A NUMERICAL MODEL OF STRATIFIED CIRCULATION IN A SHALLOW-SILLED INLET

by

DONALD STANLEY DUNBAR

B.Sc., University of British Columbia, 1975

M.Math., University of Waterloo, 1977

A THESIS SUBMITTED IN PARTIAL FULFILMENT OF

THE REQUIREMENTS FOR THE DEGREE OF

DOCTOR OF PHILOSOPHY

in

THE FACULTY OF GRADUATE STUDIES

Department of Oceanography

We accept this thesis as conforming

to the required standard

THE UNIVERSITY OF BRITISH COLUMBIA

JUNE 1985

In presenting this thesis in partial fulfilment of the requirements for an advanced degree at the University of British Columbia, I agree that the Library shall make it freely available for reference and study. I further agree that permission for extensive copying of this thesis for scholarly purposes may be granted by the head of my department or by his or her representatives. It is understood that copying or publication of this thesis for financial gain shall not be allowed without my written permission.

Department of Oceanography

The University of British Columbia
1956 Main Mall
Vancouver, Canada
V6T 1Y3

Date May 29, 1985

Abstract

A numerical model has been developed for the study of stratified tidal circulation in Indian Arm — a representative inlet on the southern coast of British Columbia. Equations for horizontal velocity, salt conservation, continuity, density (calculated as a linear function of salinity), and the hydrostatic approximation govern the dynamics. All equations have been laterally integrated under the assumption of negligible cross-inlet variability. The model is time dependent and includes nonlinear advective terms, horizontal and vertical turbulent diffusion of salt and momentum, and variations in width and depth. Provisions for surface wind stress and a flux of fresh water are also included, although neither was utilized in this study. An explicit finite difference scheme centred in both time and space was used to solve for the horizontal and vertical velocity components, salinity, and surface elevation on a staggered rectangular grid. A backward Euler scheme was used to suppress the computational mode. Tests using a semi-implicit scheme to solve the finite difference equations over realistic topography led to numerical instabilities at modest values of the time step — in spite of the unconditional stability criteria — suggesting that linear stability analysis may give misleading results for strongly nonlinear systems. Surface elevations calculated from tidal harmonic analysis and salinity timeseries derived from linearly interpolated CTD casts were prescribed at the open boundary.

Initial and boundary conditions based on observations in Burrard Inlet and Indian Arm during the winter of 1974–75 were used to study the inlet's response to tidal forcing and to simulate the deep-water renewal that occurred during this period. Coefficients for the horizontal turbulent diffusion of momentum and salt were set equal to $10^6\ cm^2\ s^{-1}$. Reducing this value by a factor of two was found to have little impact on the solution. A further reduction to $10^5\ cm^2\ s^{-1}$ led to numerical instabilities under conditions of dense water inflow. The side friction term in the momentum balance was tuned to match calculated and observed dissipation rates in Burrard Inlet; leading to good agreement between the observed and calculated barotropic tide. Contour plots of tidal amplitudes and phases for model currents and salinities revealed a standing wave pattern for the K_1 and M_2 internal

tides in Indian Arm; thus allowing for the possibility of resonance. A comparison of model results with vertical amplitude and phase profiles from harmonic analysis of Cyclesonde current meter timeseries at two locations in Indian Arm was consistent with this result. A least-squares fit was made of the vertical modal structure in the model to the complex tidal amplitudes. This led to calculations of the kinetic energy contained in each of the modes along the model inlet for the M_2 and K_1 constituents. Most of the energy was found to be contained in the barotropic and first baroclinic modes, with the latter dominating in the deep basin, and the former dominating near the sill. Second mode energy was significant for the K_1 constituent at some locations in Indian Arm. There are clear indications in the model of barotropic tidal energy being radiated into the inlet basin via the internal tide.

Simulations of the influx of dense water into Indian Arm yielded exchange rates that are consistent with observed values and suggest the possibility of fine-tuning the model coefficients to allow prediction of future overturning events.

Table of Contents

List of Tables

List of Figures

Acknowledgements

I am indebted to my wife, Judy Jansen, for her unwavering emotional and financial support during these past several years of study.

In addition, I thank Dr. N.E.J. Boston for encouraging me while at Beak Consultants Ltd. to undertake doctoral studies in Physical Oceanography, and for his support in helping me to acquire funding through the G.R.E.A.T program of the British Columbia Science Council. In addition, the part-time consulting work made available to me by Beak provided a crucial source of income during my first three years of study.

I would also like to thank my supervisor Dr. R.W. Burling for funds provided during the latter months of my research, and together with Dr. P.B. Crean for the constant guidance they provided while I carried out this research. To the other members of my committee — Dr. P.H. LeBlond, Dr. L.A. Mysak, and Dr. A.E. Lewis — I am grateful for their willingness to answer questions, and grant valuable advice.

My gratitude is extended to Dr. D.O. Hodgins of Seaconsult Marine Research Ltd. for providing me with part-time employment during the last fifteen months of my studies, and for my full-time employment afterwards.

Table of Symbols

Operators and Special Symbols

∇	The differential operator $(\partial/\partial x, \partial/\partial y, \partial/\partial z)$
$\hat{x}$	Instantaneous value
x'	Turbulent value
$\bar{x}$ or $\langle\cdot\rangle$	Ensemble average
$\tilde{x}$	Cross-inlet fluctuations
$[\cdot]_{y=Y}$	Value of bracketed expression at $y = Y$ (or $z = Z$, etc.)

Variables and Constants

$a(x,z)$	Lateral position of left wall of inlet (looking seaward)
α_0	Parameter in equation of state $(= 7.566 \times 10^{-4})$
$b(x,z)$	Lateral position of right wall of inlet (looking seaward)
$B(x,z)$	Breadth of inlet $= b - a$
$B^{(x)}$	Breadth of inlet at *u-point*
$B^{(z)}$	Breadth of inlet at *w-point*
c_0	Barotropic phase speed
c_i	Phase speed of i^{th} internal vertical mode
$\eta(x,t)$	Free surface displacement
f	Coriolis parameter
$\mathcal{F}$	Vector of frictional stresses
$\mathbf{g}$	Gravitation vector$= (0,0,g)$
$H(x)$	Maximum depth across the inlet
k_H	Bottom friction coefficient
k_s	Side friction coefficient
$K^{(x)}$	Horizontal turbulent eddy diffusivity
$K^{(z)}$	Vertical turbulent eddy diffusivity
$N^{(x)}$	Horizontal turbulent eddy viscosity
$N^{(z)}$	Vertical turbulent eddy viscosity
Ω	Earth's rotation vector$= (0,0,\Omega)$
$p(\mathbf{x},t)$	Pressure
$\phi(\mathbf{x})$	Surface corresponding to inlet side. (specified by $\phi = 0$)
R_i	Internal Rossby Radius $(i = 1,2,3\ldots)$
R_0	External Rossby Radius
$\rho(\mathbf{x},t)$	Density
$\varrho(\mathbf{x},t)$	Depth averaged density
ρ_0	Parameter in equation of state $= (0.9995)$
$S(\mathbf{x},t)$	Salinity
t	Time
$\tau_H(x)$	Bottom boundary stress
τ_W	Surface wind stress
τ_{ij}	Reynold's stress
$\tau(z)$	τ_{13} evaluated at depth z
$\mathbf{u}$	Velocity vector $= (u,v,w)$ or (u_1,u_2,u_3)
$\mathbf{x}$	Position vector $= (x,y,z)$ or (x_1,x_2,x_3)

1. Introduction

Coastlines at high latitudes (both north and south) are generally rugged and characterized by the presence of many inlets (or fjords). The inlets were created when mountain valleys — carved by advancing glaciers during the last ice age — flooded as the ice melted and the sea level rose. They are usually narrow and relatively deep — often deeper than the adjacent continental shelf. Frequently, they will have one or more *sills* consisting of former glacial moraines that restrict the exchange of water between the inlet and outside sources. They are also *estuaries*, with most having a river or stream emptying at the *head* or sides which supplies a flux of buoyant water that drives the surface layer toward the *mouth*. As this occurs, *entrainment* results in an exchange of salt and momentum between the brackish outflowing surface layer and the saltier water below. The result is a net flux of surface water out of the inlet and a compensating inflow below.

Together with this *estuarine* flow there are large periodic currents associated with the ebb and flood of the tides that can dominate inlet dynamics over short time scales and supply energy for mixing. Various mechanisms may contribute to this energy flux, including dynamic instabilities associated with small Richardson numbers, internal wave breaking, hydraulic jumps, and density currents. Mixing slowly breaks down the stratification in the deep basin that tends to inhibit the replacement of water below sill depth. This can precipitate episodic influxes of dense water which may effectively *flush*, or *overturn*, the resident bottom water over timescales of a few days, weeks, or months. Deep water replacement is observed in nearly all inlets; however the frequency and duration can vary markedly. In Indian Arm, for example, the duration between overturns has been observed to vary from one to six years (*Pickard*, 1975; *de Young*, 1985 — personal communication).

Deep water renewals may have a dramatic effect on the character of water in the inlet basin. Typically, the inflowing water will be saltier, sometimes colder, and substantially richer in oxygen than that which it replaces. This can have a significant impact on the biota of the inlet. In extreme cases — where stagnation has resulted in anoxic conditions — sulphur compounds are advected to mid-depths where they may have lethal effects.

Wind blowing over the surface of an inlet is usually aligned with the longitudinal axis due to the presence of mountains. In some inlets this can be an important source of energy for mixing in the surface layer and can lead to the breakdown in winter of the sharp pycnocline established during the spring and summer. In addition, both internal and surface seiches can be generated by the relaxation of the surface wind stress after setting up a surface slope.

Inlets are complex and highly variable systems. As part of the coastline, some are readily accessible for making measurements. The Department of Oceanography at the University of British Columbia and the Institute of Ocean Sciences at Patricia Bay have made physical, biological, chemical, and geological measurements of most of the inlets along the British Columbia coast. Data sets spanning several decades now exist for some of these, with one of the largest having been assembled for Indian Arm and Burrard Inlet. Their close proximity to Vancouver and Burrard Inlet's importance as a major harbour accounts, in part, for this interest.

1.1 Summary

The primary objective of this research has been to develop a numerical model of the laterally integrated, longitudinal (X), vertical (Z), time dependent (T), tidal- and density-driven circulation in Indian Arm and Burrard Inlet. This has been accomplished with a laterally integrated (XZT) model which calculates temporal variations in surface elevation, horizontal and vertical velocities, and salinity. It solves a system of coupled nonlinear partial differential equations that includes the effects of acceleration, advection, diffusion of momentum and salt, boundary friction, and variations in bathymetry and width. Smooth time series of salinity and surface elevations — the latter calculated from harmonic analysis of tidal records — have been applied at the open boundary at the mouth.

This investigation of tidally driven flows has focused on reproducing surface elevations, energy dissipation rates, velocity structure, and internal response observed in Indian Arm. In particular, available tide gauge, current, and density data have permitted a comprehen-

sive comparison with model results. Cyclesonde vertically profiling current meters deployed by Dr. S. Pond have, for the first time, allowed comparisons between the observed and simulated internal tide in winter. Calculations reveal which vertical modes are excited by the barotropic tide and how the partitioning of energy varies along the inlet for realistic winter stratification. An examination of the relative sizes of terms in the momentum equation during a tidal cycle reveals the principal force balances that occur as a function of time and position along the inlet.

In addition, the model has been used to simulate deep water renewal. Initial and boundary conditions have been taken from an inflow event that occurred in Indian Arm during midwinter of 1974–75 and was recorded in some detail via CTD casts and one current/salinity time series (*Davidson*, 1979). Successfully hindcasting important features of this inflow event is aimed at providing a means for predicting future renewals. This satifies both a practical need and a desire to understand the underlying physical processes involved in the functioning of a complex dynamical system.

Chapter 2 discusses the physical oceanography of Indian Arm and Burrard Inlet, including a detailed discussion of new results obtained from the harmonic analysis of existing surface elevation time series. Subsequently, the mathematical framework for the model is developed in chapter 3, after which the transformation to finite difference form is described in chapter 4. Chapter 5 presents a series of preliminary numerical experiments conducted to verify the model output before proceeding to the final simulations detailed in chapter 6. Finally, the summary and conclusions are contained in chapter 7.

1.2 Data Used in this Research

The data used to calibrate and evaluate the model performance have been assembled from several different sources. Conductivity, temperature, and depth (CTD) data collected at standard stations in Burrard Inlet and Indian Arm during the winter of 1974–75 (University of British Columbia, Department of Oceanography, *Data Report 37* (1974) and *Data report 41* (1975)) together with time series of current and salinity from a single station on the

inner sill (*Davidson*, 1979) were used to provide initial and boundary conditions for the simulation of tidal forcing and deep water renewal and for comparison with model output.

Tide gauge data obtained from the Canadian Hydrographic Service (1964–77, unpublished) were analyzed to extract amplitudes and Greenwich phase angles for tidal constituents. These were used to calculate energy dissipation rates in Burrard Inlet, and subsequently, to calibrate the friction terms in the model. In addition, the results of the harmonic analysis at the most seaward of these stations were used to reconstruct the tidal elevations at the open boundary of the model, thereby providing the barotropic forcing that drives the model.

Short time series of vertical density profiles were collected by the author at a few stations in Indian Arm and Burrard Inlet during August and September of 1982. These have been used to compare observed and calculated isopycnal displacements over a diurnal cycle.

Cyclesonde vertically profiling current meters situated at two locations in Indian Arm during the winters of 1983 and 1984 by Dr. Pond of the University of British Columbia provided crucial information on the vertical structure of along-inlet currents.

1.3 Digital Filtering of Time series

Time series of either observations or model output were sometimes filtered to remove unwanted frequencies from the signal. The method used has been described by *Graham* (1963). Briefly, the technique begins with the construction of a desired response curve for a low-pass filter. Horizontal segments above and below the desired cut-off frequency are pieced together with a quarter wavelength cosine roll-off. The roll-off occurs between two selected frequencies f_1 and f_2 ($f_1 < f_2$). An explicit inverse Fourier transform of this piecewise analytic function exists and is used to calculate a set of $N+1$ weights, W_j, which are applied to a time series $\{x_i : i = 1, 2, \ldots, n\}$ via a weighted moving average to yield the filtered estimates

$$\hat{x}_i = \sum_{j=-N}^{N} W_{|j|} x_{i+j}$$

for $i = N+1, N+2, \ldots, n-N$. The performance of the filter improves with increasing N, that is, the actual response curve approaches the theoretical curve as $N \rightarrow \infty$. Low-pass filters referred to in this thesis are specified by the notation (f_2^{-1}, f_1^{-1}, N). For example, $(6, 8.5, 40)$ refers to a digital filter with a roll-off between 6.0 and 8.5 hours employing 41 weights.

1.4 Previous Work

The study of estuarine circulation has, until the last decade, been either descriptive in nature, or concerned with theoretical models of highly simplified flows. As long ago as 1798 the explorer George Vancouver made observations from his ship of surface currents associated with estuarine circulation (*Pickard*, 1961). Since *Tully* (1949) presented his detailed study of Alberni Inlet others have discussed the distribution of physical properties in the major inlets of British Columbia (for example, *Pickard*, 1961,1963,1975 and *Gilmartin*, 1962).

Several important observations were made in these early studies, particularly regarding seasonal and interannual variability. It became clear that inlets are dynamic systems that exhibit both periodic and aperiodic changes over months or years. Specifically, it was

observed that most inlets undergo partial or complete replacement of the water occupying their deep basins at more or less infrequent intervals and with surprising rapidity. This low frequency variability is likely to be a direct result of variations in available source water present at the entrances to the inlets. Since this consists of local runoff mixed with water from the deep ocean that makes its way over the continental shelf into coastal waterways, it is possible that a link could exist between occurrences of overturning and such far removed events as equatorial El Niños.

1.4.1 Theoretical models

Early theoretical work by *Stommel and Farmer* (1952) served as one of the first steps toward understanding the mechanisms controlling circulation in estuaries. By introducing the concept of *overmixing* they demonstrated that mass exchange in two-layer flow at a constriction — such as occurs at the mouth of many fjords — is limited by hydraulic control. This follows from the constraint that $F_1^2+F_2^2 = 1$, where F_1 and F_2 are appropriate layer Froude numbers defined by $F_i^2 = u_i^2/(g'H_i)$. u_i and H_i are the horizontal speed and depth, respectively, in each layer, and $g' = g\Delta\rho/\rho_0$ is the reduced gravity resulting from the density difference $\Delta\rho$ across the interface.

Rattray and Hansen (1962) considered steady state flow in estuaries of constant width. Assuming a balance between horizontal advection of momentum, horizontal pressure gradient, and vertical diffusion together with a balance between horizontal advection and vertical diffusion of salt, they derived a similarity solution for the vertical density and velocity profiles. *Hansen and Rattray* (1965) applied these techniques to a coastal plane estuary to obtain good agreement with observations in the James River estuary. Similar methods were used by *Winter* (1973), who assumed steady-state conditions to predict isohaline depths in the near-surface zone for large runoff inlets.

Long (1975) modelled two-layer steady-state flow in inlets to predict interface depths and concluded that friction effects should dominate flow in fjords. He applied his theory to Knight Inlet with limited success — subsequent investigations by *Freeland and Farmer*

(1980) revealed significant discrepancies between the predicted and observed upper layer thickness. In addition, they found that friction effects and hydraulic control at the mouth are unimportant in Knight Inlet.

The theory of hydraulic control was extended by *Stigebrandt* (1977) to include tidal fluctuations. He found that periodic barotropic flows could enhance the transport capabilities of a constriction and thus have implications for the movement of dense water into the basin of a fjord. *Pearson and Winter* (1978) extended two-layer flow theory in high runoff inlets to include variations in depth and width. Their theory was applied to Knight Inlet, where good agreement was obtained for the pycnocline depths and layer salinities along the inlet.

Observations of three-layer flow by *Svendsen* (1977) in the upper $50\,m$ of Jøsenfjord during summer suggest that two-layer models are inadequate to describe the circulation in some inlets. He observed a net inflow-outflow-inflow structure which was established, in part, by surface wind stress. *Hansen and Rattray* (1972) derived a similarity solution for low runoff inlets which predicts a three-layer structure for steady state circulation driven by stratification at the mouth.

Stigebrandt (1981) introduced an estuarine Froude number (Fe) in order to quantify the character of flow in a fjord constriction. He describes a two-layer model which assumes hydraulic control at the mouth. Fe is defined as

$$Fe = Q_f \left[(g')^{\frac{1}{2}} B_m H_m^{\frac{3}{2}} \right]^{-1} \tag{1.1}$$

where $g' = g\Delta\rho_0/\rho_0$ is the reduced gravitational acceleration, $\Delta\rho_0$ is the density difference between salty and fresh (ρ_0) water, B_m and H_m are the inlet breadth and depth at the mouth, and Q_f is the freshwater volume flux into the head of the inlet. A small value for Fe implies a thin upper layer and weak coupling between estuarine and deep flow. *Stigebrandt* (1981) introduces the term N-fjords (normal fjords) to denote these inlets, while O-fjords (overmixed fjords) designate inlets with large values for Fe. Both Indian Arm and Burrard Inlet are examples of low runoff N-fjords. An estuarine Rayleigh number,

defined as $Ra_e = (Fe)^{-2}$, provides an indication of the degree of recirculation between the two layers.

1.4.2 Internal waves

Observations of the interaction between tidal flow and the shallow sill regions of inlets have led to the consideration of generating mechanisms for internal waves and the transfer of barotropic tidal energy to mixing processes in the deep basins. *Lee and Beardsley* (1974) considered the generation of long internal waves in dynamically stable flows. Their numerical solutions of the Korteweg-de Vries (KdV) equation and tank experiments indicate that for flow which is supercritical to all vertical modes greater than the first, a train of solitary or plain waves is generated depending on whether an initial depression or elevation, respectively, of the isopycnals is produced.

Gargett (1976) observed internal solitary waves in the Strait of Georgia which appear to be generated by the displacement of isopycnals by vertical velocities arising from tidal flow through constrictions. *Farmer and Smith* (1978) observed a variety of nonlinear internal waves in the sill region of Knight Inlet which are associated with strong shear flows. These waves transport energy and momentum to the interior of the inlet where they may break; providing a source of energy for deep mixing. *Stigebrandt* (1976) has speculated that internal waves generated at a sill may break on the sloping bottoms of inlets and thereby provide energy for mixing in a thin boundary layer. This mixed water is then capable of flowing as a density current to the interior of the fjord. Observations in Oslofjord suggest that as little as 5% of breaking wave energy contributes to mixing; with the remainder being dissipated as heat.

Farmer and Smith (1980) report acoustic measurements of the response to strong tidal flows over the sill of Knight Inlet, including lee waves and hydraulic jumps. The mixed region resulting from breaking internal waves collapses as the flow subsides, giving rise to internal bores and surges. A similar effect, although nontidal, was observed by *Hamblin* (1977) in Kamloops lake. Stratification is critical to the character of the flow

over sills, while sill shape and size, gravity flows, and perhaps wind, are also important. A densimetric Froude number, $F_i = \bar{U}/c_i$, where $\bar{U}$ is the maximum sectionally averaged tidal current and c_i is the phase speed of the i^{th} vertical mode, was found by *Farmer and Smith* (1980) to govern the response of stratified tidal flows over the sill in Knight Inlet. Pronounced seasonal variability in this response due to changes in stratification was also observed. In winter they found primarily a first mode response while in summer the second mode appeared to be important.

Internal waves generated by interactions between a sill and currents can be classified as either high frequency (discussed above), or of tidal frequency. Internal tides, as the latter are called, appear to be an important sink for energy from barotropic tidal currents interacting with a sill. *Blackford* (1978) proposes a nonlinear mechanism for the generation of internal tides which assumes no reflections at the inlet head and predicts oscillations at twice the forcing frequency. Observations in Glacier Bay cited by *Blackford* appear to support his results.

Maxworthy (1979) describes a probable mechanism for generation of internal tides through interaction of supercritical flow — in the sense of a densimetric Froude number — with an obstacle such as a sill. Supercritical flow during an ebb tide creates a stationary lee wave which may or may not break initially to generate mixing. As the flow subsides and becomes subcritical this wave will propagate inward against the flow as a series of solitary waves, and upon reversal of the flow these will be advected into the inlet. If breaking occurs during peak flows the resulting mixed region will collapse as the flow relaxes, and may generate internal waves that propagate in both directions. A critical value for F_i that determines when mixing ceases was found to be roughly 0.75 from experiments (*Maxworthy*, 1979), while another critical Froude number determines if waves will be generated. Most of the waves observed on the inlet side of a sill are generated during the preceding ebb. Stratification, tidal amplitudes, and sill shape are all crucial in determining the character of the response.

Stigebrandt (1980) presents a model of internal tide generation over a sill. Constrictions produce tidal jets on the lee side of the sill where the momentum balance is between advection and vertical diffusion. The upstream balance, on the other hand, is between acceleration and the horizontal pressure gradient. Internal tides are generated only during subcritical flow, while supercritical flow leads to hydraulic jumps and solitary waves as noted above. *Stigebrandt* proposes a mechanism for internal tide generation based on the linear superposition of a barotropic and infinitely many baroclinic waves which satisfy continuity and matching constraints at a one-dimensional sill. Linear stratification and a linear vertical depth dependence for baroclinic velocity over the sill is assumed. An expression for the amplitude of the n^{th} baroclinic component is provided by

$$a_n = \frac{4\alpha}{(n\pi r)^2}\left\{(-1)^n - \cos\left[n\pi(1-r)\right]\right\} \tag{1.2}$$

where α is the amplitude of the current and r is the ratio of sill depth to maximum basin depth.

Stacey (1984) examines the interaction of tides with the sill of Observatory Inlet using a similar approach. Again, no reflection is permitted and linear stratification is assumed. Seasonal variations in stratification were found to result in changes to the amount of energy withdrawn from the barotropic tide. A Froude number based on the amplitude of each tidal velocity constituent — rather than the maximum sectionally averaged current — is required to be subcritical. *Stacey* found that most of the energy extracted from the barotropic tide goes to the linear progressive semi-diurnal (M_2) tide.

The assumption of no reflection of the internal tide from the head of an inlet may be unrealistic for some fjords under certain conditions. Recent observations (*Lewis and Perkin*, 1982; *Keeley*, 1984) indicate that seasonal resonance of the internal tide may occur during short periods of time when the natural oscillating frequency of a mode in the inlet (the internal seiche frequency) matches a dominant forcing frequency. *Lewis and Perkin* (1982) discuss data which suggests a first mode resonance at the semidiurnal frequency when the natural period of Agfardlikavsâ Fjord was 11.0 hours. More recently, *Keeley*

(1984) has presented convincing evidence for resonance in Alice Arm.

Resonance is a standing wave phenomenon that requires high reflection coefficients and weak dissipation of energy to be pronounced. It now appears that reflection of internal tides can occur and may be a very important factor in inducing brief periods of intense mixing in the basin of an inlet as it passes through resonance. These episodes are expected to be relatively brief as the induced mixing alters the stratification and hence modifies the conditions promoting resonance.

1.4.3 Turbulent mixing

Much effort has been expended to parameterize small-scale turbulent mixing for use in both theoretical and numerical models. Owing to the wide range of mechanisms for its generation and to the lack of adequate observations this has been a difficult task, and one that has achieved limited success.

Random fluctuations in velocity components generate turbulent fluxes of momentum. These lead to Reynold's stress terms in the governing equations (chapter 3) that may be expressed as $\tau = -\rho\langle u'w'\rangle$ where primes denote turbulent fluctuations and the brackets an ensemble average. τ is used to define a friction velocity $u_* = (|\tau|/\rho)^{\frac{1}{2}}$ that provides a velocity scale for the turbulence.

Turbulence in the surface brackish layer of a fjord is used to explain the occurrence of entrainment. The turbulence may be generated by current shear relative to deeper water established by the river discharge and perhaps substantially modified by a wind stress τ_W given by

$$\tau_W = C_d \rho_a |W_{10}|^2, \tag{1.3}$$

where W_{10} is the wind speed at $10\,m$ above the surface, C_d is a drag coefficient that depends on stability conditions near the surface, and ρ_a is the density of air. Classical entrainment is a one way process wherein the turbulent surface layer is assumed to overlie a nearly quiescent bottom layer. With a constant value for τ the velocity shear in the boundary layer is assumed to be a function of τ and vertical position z only. A dimensional argument

leads to

$$\frac{du}{dz} = \frac{u_*}{\kappa z} \tag{1.4}$$

where κ is commonly called von Karman's constant. The logarithmic velocity profile follows immediately upon integration of (1.4) over the depth of the boundary layer. *Kullenberg* (1977) discusses this entrainment process in more detail and derives an expression for the entrainment velocity — the rate of thickening of the brackish surface layer due to entrainment.

Mixing below the main pycnocline is generated by many processes, including stratified shear flow, breaking internal waves, and (to a lesser degree) convective overturning. *Farmer and Freeland* (1983) give an excellent review of the mixing mechanisms in fjords. If mixing is to be included in numerical models it must either be parameterized or simulated stochastically. One of three approaches is normally used to parameterize diffusive mixing. The first, attributed to *Prandtl*, employs a length scale l_T characteristic of the mixing to express τ as

$$\tau = -\rho l_T^2 \left|\frac{\partial u}{\partial z}\right| \frac{\partial u}{\partial z}. \tag{1.5}$$

Another approach defines a coefficient of vertical eddy viscosity by

$$\tau = -\rho N^{(z)} \frac{\partial u}{\partial z}. \tag{1.6}$$

Similar expressions may be used to define a horizontal eddy viscosity coefficient $N^{(x)}$ and horizontal and vertical eddy diffusion coefficients for salt ($K^{(x)}$ and $K^{(z)}$). Equating (1.5) and (1.6) we find that $N^{(z)} = l_T^2 |\partial u/\partial z|$. It has been observed that l_T and $N^{(z)}$ ($K^{(z)}$) are not fixed values, but depend on properties of the mean flow, or on dynamic stability. The latter is quantified using the gradient Richardson number

$$R_i = \frac{N^2}{\left(\frac{\partial u}{\partial z}\right)^2}, \tag{1.7}$$

where

$$N^2 = -\frac{g}{\rho}\frac{\partial \rho}{\partial z} \tag{1.8}$$

is the Brunt-Väisälä frequency. *Odd and Roger* (1978) review several mixing length representations for diffusive terms.

A third method of specifying eddy mixing coefficients utilizes a turbulent energy equation to close the system of equations. *Smith* (1982) describes a scheme which employs an estimate of the depth mean dissipation rate to scale $N^{(z)}$ rather than using the depth mean speed as many other schemes do. *Smith and Takhar* (1981) also describe an energy closure scheme that has the advantage of allowing turbulence to persist after the mean flow has subsided.

Parameters for horizontal diffusion and viscosity are not normally considered to be dynamically important. As will be noted later, however, these provide important sinks for energy in nonlinear numerical models where finite grid lengths interrupt the cascade of energy to the scales of viscous dissipation of heat.

Okubo and Ozmidov (1970) present an empirical relationship between $N^{(x)}$ and the scale of motion being considered in the open ocean. A length scale of $1\,km$, for example, corresponds to $N^{(x)} \approx 10^4\,cm^2\,s^{-1}$, and $N^{(x)}$ was found to vary approximately as $L^{\frac{4}{3}}$. Application of these values to the more energetic flows associated with circulation in inlets may not be justified, however.

Calculations of $K^{(x)}$ and $K^{(z)}$ by *Ebbesmeyer et al.* (1975) for water parcels in Puget Sound yield values of $7.7 \cdot 10^4$ and $0.7\,cm^2\,s^{-1}$, respectively, while *Officer* (1977) observed values ranging from 0.9–41 $cm^2\,s^{-1}$ for $N^{(z)}$; from 0.1–25 $cm^2\,s^{-1}$ for $K^{(z)}$; and from 0.1–1.2 for the ratio $K^{(z)} : N^{(z)}$. In a review of vertical circulation models in estuaries *Hamilton and Rattray* (1978) cite an upper limit of $10^7\,cm^2\,s^{-1}$ for $N^{(x)}$ in a model with a $3\,km$ horizontal grid spacing, with larger values tending to smear features such as tidal jets.

In the main basin of a subarctic inlet *Muench and Heggie* (1978) note that vertical mixing with $N^{(z)} \approx 1\,cm^2\,s^{-1}$ is sufficient to explain observed reductions in salinity between deep water renewal events. *Lewis and Perkin* (1982) cite values for $N^{(z)}$ of 0.1–10 $cm^2\,s^{-1}$

for N^2 values between 10^{-3} and $10^{-5}\,s^{-2}$ based on tracer studies. *Smethie* (1981) used radon isotopes and salinity as tracers to estimate $K^{(z)}$ in five British Columbia and Washington state inlets and found that values ranged from 0.12–36 $cm^2\,s^{-1}$, with most values between 0.1 and 2. A dependence on N^2 was not obvious, although in shallow silled Narrows Inlet it appeared that $K^{(z)} \propto N^{-1}$. $K^{(z)}$ was measured as 0.23 $cm^2\,s^{-1}$ near the surface and 1.8 $cm^2\,s^{-1}$ between 5 and 35 m. *Buch* (1981) obtained a value of 0.01 $cm^2\,s^{-1}$ for $K^{(z)}$ near the pycnocline and also presents a number of empirical formulae for $K^{(z)}$.

1.4.4 Numerical models

Relatively little work has appeared regarding numerical simulation of internal tides. *De Granpré, et al.* (1981) observed an internal tide consisting primarily of a first mode response in their laterally integrated, two-dimensional model of the St. Lawrence estuary. *Niebauer* (1980) generated internal tides of at least second mode response in his model of Resurrection Bay.

Numerical models present a convenient opportunity to evaluate various formulations of the turbulent eddy coefficients. *Hamilton* (1975) modelled circulation in the Rotterdam Waterway using a model with a 2 km horizontal grid spacing. He tried constant values for $K^{(z)}$ and $N^{(z)}$; a dependence of these coefficients on the depth mean horizontal velocity $|\bar{u}|$; and a R_i dependence. He concluded that a constant $K^{(z)}$ gave better results than a $|\bar{u}|$ dependence, but was poorer than inclusion of R_i. *Bowden and Hamilton* (1975) applied a laterally integrated model with a horizontal grid spacing of 4 km to investigate several formulations of $K^{(z)}$ and $N^{(z)}$; finding that R_i dependent values led to numerical instabilities. A bulk Richardson number ($\bar{R}_i$) defined as

$$\bar{R}_i = \frac{gH\Delta\rho}{\bar{U}^2\rho_0}$$

was substituted for R_i, where H is the local depth, $\Delta\rho$ the density difference from top to bottom, $\bar{U}$ the depth mean velocity, and ρ_0 the mean density. Best results were obtained using a $|\bar{u}|H$ dependence, where H is the local inlet depth. They note, however, that for weakly stratified systems the coefficients may be depth independent. *Hamilton* (1977) tests

several formulations using horizontal grid spacings of 2 and 4 km. Variable coefficients led to asymmetry in the tidal elevations over a tidal cycle and to slightly larger amplitudes. *Festa and Hansen* (1976) found variations in the ratios $N^{(x)} : N^{(z)}$ and $K^{(x)} : K^{(z)}$ from 1–10^6 had little effect on their numerical solutions. *Niebauer* (1980) used values for $N^{(x)}$, $K^{(x)}$, and $K^{(z)}$ of $5 \cdot 10^6$, 10^5, and $5\,cm^2\,s^{-1}$, respectively, in his model of Resurrection Bay using a horizontal grid spacing of $2\,km$.

1.4.5 Density flows

The infrequent replacement of deep water in a fjord by denser water from outside a sill has been observed in many inlets and is almost certain to occur in every inlet that has a free connection with the sea. The frequency and duration of occurrence, and seasonal variations, depend critically on the supply of dense water, sill and inlet depths, tidal currents, stratification, and mixing rates throughout the inlet. *Gade and Edwards* (1978) present a thorough review of deep water renewal observations and related circulation theory.

The Strait of Georgia is the source of dense water for renewal of bottom water in the inlets of southern British Columbia. Upwelling off the west coast of Vancouver Island during late summer drives dense water through Juan de Fuca Strait to the mouths of inlets. During the period of transit from the continental shelf this water is modified in places by vigorous mixing that can be inferred from observations of internal waves (*Gargett*, 1976).

Lafond and Pickard (1975) discuss replacement of deep water in Bute Inlet where inflows are observed primarily in late fall or early winter, and may last for several months. They calculate that during one inflow episode 80% of water below $350\,m$ and 45% of water below $100\,m$ was replaced. Mean inflow currents were estimated to be from 1 to $5\,cm\,s^{-1}$.

Anderson and Devol (1973) observed inflows occuring in Saanich Inlet and concluded that little or no mixing occurs between the ambient and inflowing waters until the level of inflow density is reached. Approximately 12 days were required to replace 37% of the inlet volume.

Extensive observations of deep intrusions into Puget Sound have been made. *Cannon*

(1975) reports measurements made over two months, and notes that inflows occur over periods of 4 to 7 days and at fortnightly intervals. Intense mixing of inflowing water was found to occur over the unusually long ($30\,km$) sill connected to the deep basin (*Cannon and Ebbesmeyer*, 1978), leading to generation of strong horizontal gradients over the sill region. *Geyer and Cannon* (1982) note that maximum inflows occur during neap tides when mixing intensities are at a minimum. *Cannon et al.* (in print) and *Ebbesmeyer and Barnes* (1980) remark on the importance of recirculation over the sill resulting from intense mixing of inflowing and outflowing waters in controlling the density of available water outside the sill.

Additional observations of deep water renewal are provided by *Davidson* (1979) who discusses data related to bottom water replacement in Indian Arm during the winter of 1974–75, and *Edwards and Edelsten* (1977) who observed exchange in Loch Etive over a period of four weeks caused by low freshwater runoff.

An attempt to model the combined circulation of a coastal shelf-inlet system was made by *Klinck et al.* (1981) utilizing a two-layer numerical model which ignores the surface brackish layer, nonlinear terms, and vertical mixing. Ekman transport due to wind forcing generated coastal currents which strongly affected circulation inside the inlet. *Heggie and Burrell* (1981) have associated annual deep water renewal in Resurrection Bay with the relaxation of downwelling along the coast, while *Crean* (1983) has applied a laterally integrated numerical model to the Strait of Georgia to model fortnightly intrusions of dense water associated with coastal upwelling.

The number and variety of numerical models that have been applied to estuarine circulation are too extensive to be fully reviewed here. Models can generally be classified according to the number of spatial dimensions included and whether they are time dependent or steady state. In addition, they may utilize fixed grids or movable interfaces. The model described in this thesis is based on work by *Blumberg* (1975) and *Elliott* (1976), who applied a laterally integrated model to time dependent circulation in Chesapeake Bay.

Blumberg (1978) compared stratified and unstratified flow in a simulation of the Potomac River and found stratification to have a strong effect on residual circulation and the vertical structure of the flow.

Niebauer (1980) modelled stratified tidal flow in Resurrection Bay and the adjacent continental shelf, including topography and Coriolis terms, but ignoring alongshore advection. The inlet extends 11 km from its head — reaching a maximum depth of 250 m — to a sill at a depth of 175 m which separates the deep basin from the Gulf of Alaska. In simulations of bottom water replacement, wind forcing and river runoff were found to be unimportant for deep circulation.

Perrels and Karelse (1978) describe an **XZT** model for a tidal salinity plume which utilizes an implicit scheme with a simple geometric transformation to map the solution domain onto a rectangular grid. *Hodgins* (1979) presents results from a two-layer model of Alberni Inlet based on work by *Farmer* (1972) that emphasizes the role of wind stress on the depth of the main pycnocline.

In spite of the considerable effort made to construct both mathematical and numerical models of stratified circulation in estuaries, little work has been done to reproduce the observed internal response of a fjord to tidal forcing, or to simulate the intrusion of dense water into the deep basin of a shallow-silled inlet. This research demonstrates that such flows can be successfully simulated using numerical methods.

2. Physical Oceanography of Burrard Inlet and Indian Arm

2.1 Introduction

Indian Arm and Burrard Inlet are located in southwest British Columbia and include the major port of Vancouver (*figure* 1). Indian Arm is classified as a somewhat smaller fjord than the average of those found along the north-west coast of North America (*Pickard*, 1961). It is long, narrow, and bounded on both sides by mountain slopes extending to the bottom of the inlet. In cross-section its sides are steep and the bottom flat (*figures* 2–4). In longitudinal section the inlet bottom slopes downward from the head at the north to its maximum depth of 220 m, then upward to a shallow sill where it intersects Burrard Inlet (*figure* 3) at nearly a right angle (*figure* 1). Burrard Inlet extends eastward from this point almost 8 km and westward 22 km to the Strait of Georgia. From there it connects to the Pacific Ocean through Juan de Fuca Strait.

Burrard Inlet is not typical of British Columbia's inlets; mountains border on only one side, and it is relatively shallow, having a maximum depth of less than 100 m. It acts as an extended sill connecting Indian Arm to the Strait of Georgia, with water passing through First Narrows and Second Narrows (*figure* 1) being strongly mixed before reaching Indian Arm.

The major sources of fresh water input to Indian Arm are from the Buntzen Power Houses located midway along the inlet and the Indian River at its head. Runoff is small in comparison with other inlets in the region, however, in spite of numerous smaller creeks along the length of the inlet and a large annual precipitation (*Gilmartin*, 1962).

Figure 5(*a–l*) summarizes several physical properties of Indian Arm and Burrard Inlet. Some of the plots show cumulative integrals which allow quantities such as volume and surface area to be calculated between arbitrary points. A brief explanation of each plot in this figure is provided in *table* 1. The large peak in the graph of surface areas (*figure* 5b) corresponds to the extension of Burrard Inlet eastward of segment 11 (*figure* 1). The volume of the extension is small, however (*figure* 5d), and justifies its treatment in the

Table 1
Explanation of plots found in figure 5. The abscissa represents distance along the deepest section from the head

plot	*description*	*parameter*	*formula*
a	depth	H	
b	surface area	A_s	
c	cross-sectional area	A_x	
d	volume	V	
e	mean depth		V/A_s
f	log(surface area/X-sec area)		$\log_{10}(A_s/A_x)$
g	width from X-sec	B	A_x/H
h	horiz. width gradient		$\partial B/\partial x$
i	phase speed		$\sqrt{gH}$
j	(phase speed)$^{-1}$		$(gH)^{-\frac{1}{2}}$
k	mean depth		V/A_s
l	cumulative mean depth		$\int_0^x A_s\,dx$

model as part of section 11 rather than as a separate branch of the system.

2.2 Fresh Water Input

Fresh water enters Indian Arm via several sources, with the primary routes through the Indian River and the controlled runoff from the Buntzen Power Houses on the eastern shore of Indian Arm (*figure* 1). Secondary sources include numerous peripheral streams and direct precipitation. Runoff from the Fraser River enters Burrard Inlet through First Narrows during the late spring and early summer where it is mixed by energetic tidal currents, thus modifying the source water available to enter Indian Arm.

The freshwater budget for Indian Arm can be calculated from historical streamflow data, mean precipitation values for the region, knowledge of the drainage areas for relevant rivers and streams, and the surface area of Indian Arm (*table* 2). This budget is small in comparison with other inlets such as Knight Inlet, which has over ten times the runoff entering at its head. *Pickard* (1961) classifies Indian Arm as a low runoff inlet; hence one would expect the estuarine driven circulation to be relatively weak.

Runoff data is not available for the Indian River outside the period from November, 1912 to September, 1921. The closest river that is presently monitored, and that was also gauged during this earlier period, is the Capilano River emptying into Burrard Inlet just outside First Narrows. Runoff data was obtained for both the Indian and Capilano

Table 2
Estimated freshwater budget for Indian Arm

source	drainage area (km^2)	mean annual discharge ($m^3\ s^{-1}$)	percentage of total discharge
Buntzen Power Houses	—	23.0[a]	55
Indian River	121	11.8[b]	28
peripheral streams	44	4.3[c]	10
direct precipitation	32	3.0[d]	7
total	—	42.1	100

Notes:
(a) *Davidson*, 1979
(b) mean of 1912–21 historical streamflow data
(c) based on drainage area ratio
(d) based on 3.0 *m* annual precipitation (*Hay and Oke*, 1976)

Rivers for the period of coincident measurements, and a series of simple linear regressions performed (*table* 3). An equation relating Capilano River runoff to Indian River runoff, $R_I = a + bR_C$, was fitted by the usual least squares procedure. The values of R^2 indicate the fraction of variance in the data accounted for by the regression equation, with a value of 1.000 indicating a perfect fit (see appendix B).

Table 3
Regression of Indian river runoff (R_I) against Capilano River runoff (R_C): $R_I = a + bR_C$. R^2 is the multiple correlation coefficient

month	a	b	R^2	year	a	b	R^2
Jan	4.33	0.25	0.77	1914	3.02	0.28	0.75
Feb	-4.14	0.59	0.61	1915	1.47	0.51	0.78
Mar	1.87	0.35	0.84	1916	1.53	0.50	0.94
Apr	-0.41	0.47	0.84	1917	0.82	0.58	0.83
May	-2.74	0.62	0.87	1918	4.40	0.35	0.69
June	1.41	0.50	0.93	1919	1.47	0.44	0.89
July	2.05	0.52	0.99	1920	2.37	0.44	0.90
Aug	2.11	0.59	0.72	1921	-0.87	0.56	0.82
Sep	2.46	0.44	0.93				
Oct	2.44	0.51	0.75	**overall**	2.79	0.39	0.69
Nov	9.73	0.21	0.21				
Dec	0.98	0.53	0.89				

There is considerable variability in the regression parameter estimates, and yet there is a definite positive correlation between the two river flows. The choice of which values to use for predicting Indian River runoff is somewhat arbitrary given the large range in

calculated regression coefficients; thus, values for a and b of 1.5 and 0.5, respectively, were used. Predictions based on this relationship for the period November 25, 1974 to March 31, 1975 together with Buntzen runoff are shown in *figure* 6. Discharge levels into Indian Arm display a marked seasonal dependence, with maximum levels occuring in late fall and early winter corresponding to peak precipitaion levels. A smaller peak occurs in late summer as the snow melts in adjacent mountains.

2.3 Wind

Hay and Oke (1976) list the mean annual wind speed for the vicinity of the mouth of Indian Arm as from 1.9 to 3.7 $m\,s^{-1}$ depending on the station. *de Young* (1985, personal communication) reports measured wind speeds in Indian Arm of less than 5 $m\,s^{-1}$ during most of the winter of 1983. *Davidson* (1979) reports that monthly maximum winds rarely exceed 7 $m\,s^{-1}$, only occasionally reaching 10 $m\,s^{-1}$ in fall and winter. We therefore conclude that wind should have a minimal influence on the circulation of Indian Arm under normal conditions, and thus its effect is excluded from the model.

2.4 Cross-Inlet Variability

The assumption is often made in mathematical and numerical models of inlets, and other bodies of water with large ratios of longitudinal to lateral dimensions, that cross-inlet variations in water properties and currents are negligible. That assumption is made in this thesis in order to construct a workable mathematical framework on which a numerical model of Indian Arm and Burrard Inlet can be built. Nevertheless, the earth's rotation together with topographic variations can produce significant departures from this assumption in some regions of the system.

Few observations or studies exist of cross-inlet variability of currents in inlets. Theoretical treatment of internal tides propagating in an inlet suggest that free and trapped internal waves should be generated at tidal frequencies. The nature of internal wave propagation is governed by the dispersion relation

$$\omega^2 = f^2 + c_n^2(k_1^2 + k_2^2). \tag{2.1}$$

For free waves to propagate we require that

$$c_n^2 k_2^2 < \omega^2 - f^2 - c_n^2 k_1^2, \tag{2.2}$$

where c_n is the phase speed of the n^{th} internal mode. If (2.2) is not satisfied, then propagation occurs as trapped Kelvin waves whose amplitude decays exponentially across the inlet over a length scale equal to the corresponding internal Rossby deformation radius $R_n = c_n/f$, that is,

$$A(y) = A_0 e^{-y/R_n}.$$

Indian Arm has a typical width of about $1.6\,km$, hence for a decay in amplitude across the inlet of less than 20% (for example) we require that R_n be greater than $7.2\,km$, or equivalently, that c_n be greater than $79\,cm\,s^{-1}$. For observed winter stratification in Indian Arm c_n was calculated to be less than $50\,cm\,s^{-1}$, thus leading to values of R_n which are less than about $5\,km$, or of the same order of magnitude as the lateral dimension of the inlet.

Smith (1978) has considered a theoretical treatment of the effect of curvature, Coriolis force, and buoyancy on internal flow in narrow channels. In general, rotation results in larger densities to the left of rectilinear flow, while channel curvature causes larger densities toward the inside of the curve.

2.4.1 Cross-inlet variability in Knight Inlet

Although there are significant differences between Knight Inlet and Indian Arm it is, nevertheless, informative to examine one of the few measurements of cross-inlet variablity. A 17 day filtered time series of along inlet currents from two Cyclesonde vertically profiling current meters was obtained from Dr. Pond of the Department of Oceanography at the University of British Columbia. The two meters were located $1\,km$ apart and abreast of each other at a point in Knight Inlet where the breadth is $2.5\,km$ and the depth $195\,m$. In *figure* 18c it can be seen that there is a significant decrease in the amplitude of the M_2 constituent of along-inlet current across the inlet at all depths. This likely results from the

exponential decay of the internal tide from the shore of the inlet due to the small internal Rossby radius of deformation.

2.5 Subsurface Renewal

Figures 7–8 show the variations in temperature, salinity, and oxygen for a typical central location in the deep basin of Indian Arm at 100 m and 200 m from 1956–63 and 1968–74 respectively (from *Pickard*, 1975). *Figure* 9 shows the variations in σ_t at several depths between March 1973 and September 1975 (from *Burling*, 1982). The plots indicate both annual and interannual variability at all depths. Typically, density (salinity) increases quickly during the winter then decreases nearly linearly throughout the remainder of the year. This *saw-tooth* behaviour is also observed in other inlets, including Princess Louisa, Sechelt, and Narrows Inlet (*Pickard*, 1975). The distinguishing characteristic of these inlets, together with Indian Arm, is the shallow entrance sill. Inlets with much deeper sills tend to display a more sinusoidal variation in density at depth (*Pickard*, 1975).

The enhanced blockage offered by the shallow sill of Indian Arm limits inflows of dense water to short periods in winter when large tropic tides combine with increased density, due to cooling of source water just outside the inlet, to cause *spillage* of water over the sill and into the main inlet basin. The duration of this spillage and its influence in the basin will depend on the relative densities of source and resident waters.

Intrusions of dense water may occur at different times of the year for other inlets. In the Rupert-Holberg system, for example, overturning is more effective in summer. The time of occurrence is dependent on the period during which dense water is available outside the sill. Advection of dense water from source areas such as the upwelling zone off Vancouver Island introduces a phase lag in the time of its arrival at the vicinity of the sill. Thus, optimum conditions for renewal may occur at times other than winter if the density of the source water is the controlling factor for its occurrence.

In addition to the brief periods of inflow clearly indicated in *figures* 7–9 there are also protracted intervals during which much smaller inflows occur, and densities generally

decrease steadily over several years. This is apparent between 1957 and 1960, as well as from 1971 to 1975. In both cases the previous deep inflow had brought exceptionally dense water into the deep basin. More recent data (not shown) indicates the same behaviour between 1979 — when a very dense water mass flushed Indian Arm — and the winter of 1984–85, when once again the deep water in the basin was replaced.

During intervals when water in the deepest part of the basin is not replaced there may be significant intrusions at intermediate levels (*figure* 9). This is clearly indicated above $50\,m$ and to a lesser extent at $75\,m$. These depths compare to the sill depth of $20\,m$ in Indian Arm.

The process of water replacement in Indian Arm and some other shallow silled inlets may be summarized as follows. During periods of large winter tides coincident with the availability of relatively dense source water outside the sill, intrusions into the inlet occur to a depth of an appropriate level of buoyant equilibrium, or, if the density of the intruding water is large enough, to the bottom of the inlet. Inlets will be expected to differ from one another in their response to the same density difference across the sill, with factors influencing this difference including sill shape and length, mixing of source and resident water over the sill, relative levels of estuarine circulation, degree of refluxing of outgoing water, and magnitude of tidal currents.

2.6 Tidal Elevations

Observations of tidal elevations have been made at several locations in Indian Arm and Burrard Inlet by the Canadian Hydrographic Service, although the only permanent station is maintained at Vancouver Harbour (no. 7735). The other stations recorded at different times and for varying durations (*table* 4). The existing data have been carefully analyzed to extract information relevant to verifying the model developed in the present program.

An additional station was maintained at Buntzen Power House in Indian Arm for 29 days during 1912. The data collected there is extremely suspect, however, since harmonic analysis of this time series indicates an 11 degree phase shift for the M_2 tidal constituent

Table 4
Tidal stations in Burrard Inlet and Indian Arm. C indicates that a continuous record is maintained. Station positions are shown in figure 1.

station	*name*	*location*	*latitude*	*longitude*	*start*	*length(d)*
7765	Deep Cove	Indian Arm	49° 20′	122° 57′	04/64	29
7755	Port Moody	Burrard Inlet	49° 17′	122° 52′	10/64	369
7747	Stanovan	Burrard Inlet	49° 17′	123° 00′	04/77	45
7743	Alberta Pool	Burrard Inlet	49° 18′	123° 02′	07/56	29
7735	Vancouver	Burrard Inlet	49° 17′	123° 07′	—	*C*

over the 9 *km* separating Deep Cove and Buntzen. This is equivalent to a 22 minute lag between these stations. Since one expects the barotropic tidal response in a deep inlet to behave as a standing wave, no phase lag should be observed in the elevations. In consideration of the reasonable agreement between Deep Cove and the other stations, the analysis at Buntzen must be rejected.

Most of the periodic variability in the observed tides may be accounted for by a relatively small number of constituents. Those listed in *table* 5 account for more than 97% of the variance at all stations.

Harmonic analysis was conducted using original surface elevation data from stations 7765, 7747, and 7735, and for several sets of model and Cyclesonde time series. These analyses required the amplitude ratios and phase differences listed in *table* 6 for the method of inference used to separate constituent sets having closely spaced frequencies (see Appendix A for details). Inference requires specification of the ratios of amplitudes and differences in phases for constituent pairs in such sets. This information is best obtained from harmonic analysis of previous, longer time series at the same station. If this is not available, harmonic analysis from a nearby station must be used. In the case of velocity time series, previous current data is often lacking and constituent relationships obtained from surface elevation time series must be used under the assumption that these hold for currents as well (*Pugh and Vassie*, 1976).

The original time series for stations 7735, 7747, and 7765 were obtained in order to determine the sensitivity of harmonic analysis to inference and to calculate confidence

Table 5
Amplitudes and phases for the 6 largest constituents in Burrard Inlet and Indian Arm.

name	*Deep Cove* 7765(1)	*Pt. Moody* 7755(2)	*Stanovan* 7747(1)	*Alberta Pool* 7743(2)	*Vancouver* 7735(1,3)
Amplitude (*cm*)					
M_2	93.27	95.8	95.53	91.4	92.40
K_1	83.97	85.7	86.27	80.4	84.96
O_1	42.69	46.8	44.15	47.8	46.50
P_1	26.03	26.6	26.75	26.5	27.15
S_2	21.93	23.4	23.20	23.4	22.54
N_2	20.83	19.3	22.85	18.5	19.13
% variance	99.7	97.7	97.6	99.8	98.5
Phase (°)					
M_2	177.37	178.1	175.58	169.0	168.34
K_1	175.27	177.4	174.62	172.0	171.15
O_1	161.62	163.9	163.31	163.0	157.02
P_1	175.67	177.8	175.02	172.0	171.50
S_2	207.37	205.6	204.64	195.0	191.42
N_2	169.71	156.5	158.67	147.0	146.02

(1) from analysis of original time series
(2) from published analyses
(3) vector mean for 1964–69 (see §2.6.1)

intervals for the resulting amplitudes and phases.

The effect of inference is to resolve tidal constituent groups whose frequencies are too close to separate with the length of time series available. The K_1, P_1, S_1 group, for example, is important because the K_1 constituent is second to the M_2 in amplitude. A time series of one year is required to separate this triplet without inference. Series of this length are available only at stations 7735 and 7755. The response of the inlet between these two stations is significantly modified by the shallow constriction at Second Narrows, and the tidal response landward of this point would be expected to resemble more nearly the response at Pt. Moody than at Vancouver Harbour. For this reason, amplitude ratios and phase differences required for inference at Stanovan and Deep Cove were best calculated from the analysis at Port Moody in the absence of additional information.

The sensitivity of harmonic analysis to inference was investigated by analysing two time series of elevations using several sets of inference relationships (*table* 7). The first

Table 6
Amplitude ratios and phase differences. '' indicates values used by the Hydrographic Service for inference.*

	minimum series (d)	*Deep Cove* 7765	*Pt. Moody* 7755	*Stanovan* 7747	*Alberta Pool* 7743	*Vancouver* 7735
Amplitude ratio						
$N_2 : M_2$	27.55	.206	.201	.239	.202	.207
$S_2 : M_2$	14.77	.235	.244	.243	.256	.244
$O_1 : K_1$	13.66	.508	.546	.512	.595	.547
$P_1 : K_1$	182.62	.321*	.310	.310*	.330*	.314
$S_1 : K_1$	365.26	—	.046	—	—	.049
$L_2 : S_2$	31.81	—	.162	.207	—	.201
$K_2 : S_2$	182.62	.281*	.303	.270*	.273*	.284
$NU_2 : N_2$	205.89	—	.218	—	—	.201
Phase difference (°)						
$M_2 - N_2$	27.55	18.4	21.6	16.9	22.0	22.3
$M_2 - S_2$	14.77	330.0	332.5	330.9	334.0	336.9
$K_1 - O_1$	13.66	346.4	346.5	348.7	351.0	345.9
$K_1 - P_1$	182.62	0.0*	359.6	1.5*	0.0*	0.4
$K_1 - S_1$	365.26	—	35.8	—	—	45.6
$S_2 - L_2$	31.81	—	24.7	292.2	—	7.4
$S_2 - K_2$	182.62	0.0*	17.8	267.5*	0.0*	5.2
$N_2 - NU_2$	205.89	—	351.7	—	—	354.9

set was derived from the analysis available from the Hydrographic Service of the Institute of Ocean Sciences (values with '*' beside them in table 4). The second used relationships derived from the available analysis at Port Moody. The first two sets separate the (K_1,P_1) pair, the third set separates the (K_1, P_1, S_1) triplet, and the fourth set is the result with no inference.

It is apparent that the inclusion of the S_1 inference parameters has a significant effect on the phase of the K_1 constituent, reducing it by approximately 2°. We can estimate the expected value of the K_1 phase by looking at the phase change for the uncontaminated M_2 between 7735 and the other stations. The time lag between stations can be calculated by using the frequencies of the two constituents with

$$\Delta t_i = \frac{\Delta\theta_i}{360\,\sigma_i}, \qquad i = \begin{cases} 1 & \rightarrow K_1 \\ 2 & \rightarrow M_2 \end{cases}.$$

where $\Delta\theta_i$ is the difference in phase between stations and σ_i is the constituent frequency.

Table 7
Results of harmonic analysis with and without inference. Confidence intervals are at the 80% level

set	*pair*	*ratio*	$\Delta\theta(°)$	*constituent*	*amplitude(cm)*	*phase(°)*
Deep Cove (7765)						
1	K_1, P_1	.321	0.0	K_1	84.9± 3.1	177.7± 2.1
				P_1	27.2± 3.1	177.7± 6.5
2	K_1, P_1	.310	359.6	K_1	84.7± 3.1	177.1± 2.1
				P_1	26.2± 3.1	177.5± 6.7
3	K_1, P_1	.310	359.6	K_1	84.0± 3.1	175.3± 2.1
	K_1, S_1	.046	35.8	P_1	26.0± 3.1	175.7± 6.7
				S_1	3.9± 3.1	139.5± 45.6
4	no inference			K_1	81.0± 3.1	159.9± 2.2
Stanovan (7747)						
1	K_1, P_1	.310	1.5	K_1	86.5± 2.8	176.7± 1.9
				P_1	26.8± 2.8	175.2± 6.0
2	K_1, P_1	.310	359.6	K_1	85.8± 2.8	176.4± 1.9
				P_1	26.6± 2.8	176.8± 6.1
3	K_1, P_1	.310	359.6	K_1	86.3± 2.8	174.6± 1.9
	K_1, S_1	.046	35.8	P_1	26.7± 2.8	175.0± 6.0
				S_1	4.0± 2.8	138.8± 40.7
4	no inference			K_1	97.2± 2.8	161.2± 1.7

Thus, if we let $\Delta t_1 = \Delta t_2$ we get

$$\Delta\theta_1 = \frac{\sigma_1}{\sigma_2}\Delta\theta_2, \qquad \frac{\sigma_1}{\sigma_2} = .5190.$$

The values for $\Delta\theta_1$ listed in *table* 8 are those expected in a nondissipative, nondispersive system. The observed phase lag at Pt. Moody for K_1 is 6.25°; greater than the calculated $\Delta\theta_1$ value by 1.18°. There is quite good agreement between the calculated difference and the results of harmonic analysis.

Table 8
K_1 phase lag from Vancouver tide gauge calculated from the observed M_2 lag

station	$\Delta\theta_2$ (°)	$\Delta\theta_1$ (°)	*from table 3*
Deep Cove	9.03	4.66	4.12
Pt. Moody	9.76	5.07	6.25
Stanovan	7.24	3.76	3.47
Alberta Pool	0.66	0.34	0.85

2.6.1 Tidal analysis at Vancouver Harbour (station 7735)

Year long time series of elevations were obtained for station 7735 in Vancouver Harbour for eleven years between 1964 and 1976. Data for 1966 and 1972 were incomplete and were therefore excluded from the analysis (*table* 9).

Table 9
Harmonic analysis at Vancouver Harbour (station 7735) for 11 yearly records

	M_2		K_1	
year	*amp.(cm)*	*phase(°)*	*amp.(cm)*	*phase(°)*
64	92.48	168.31	84.17	171.48
65	92.77	168.64	85.66	171.16
66	—	—	—	—
67	91.85	168.54	84.84	171.63
68	92.31	168.33	84.92	170.97
69	92.57	167.89	85.24	170.51
70	92.89	165.77	85.97	168.81
71	93.39	163.69	86.00	168.36
72	—	—	—	—
73	94.67	165.11	86.91	168.86
74	94.22	164.55	86.54	169.82
75	94.26	165.00	87.00	169.23
76	94.19	164.54	86.11	169.88
mean(64–69)	92.40	168.34	84.96	171.15
mean(70–76)	93.93	164.78	86.42	169.16

It is interesting to note the change in mean phase for both constituents between 1969 and 1970. The variance in the data suggests that this shift is significant, and represents an advance in the arrival of high water at Vancouver Harbour of about 7 minutes. It is likely that this change is due to dredging conducted by Public Works of Vancouver in 1970. Increasing the depth of First Narrows from $12\,m$ to $15\,m$ over a $0.5\,km$ length would account for the observed phase shift. Since all but one of the time series of surface elevations used for harmonic analyses were collected before 1970 (the exception being at Stanovan), the vector mean amplitudes and phases for station 7735 between 1964 and 1969 were used for calculations, and for input to the model (*table* 9).

2.7 Energy Dissipation

The energy dissipation in Burrard Inlet and Indian Arm can be estimated from measurements of tidal elevations. Following *Farmer and Freeland* (1980), who performed similar calculations for Knight Inlet, we consider the three sections between model segments (14) and (17), (13) and (14), and between (9) and (13). Segment (9) is located near Deep Cove in Indian Arm, while segments (17), (14) and (13) are located near Vancouver Harbour, Alberta Pool, and Stanovan tide gauges respectively (*figure* 1). The harmonic constants for the M_2 and K_1 constituents are recalled for convenience in *table* 10.

Table 10
Harmonic constants for M_2 and K_1 at Indian Arm and Burrard Inlet tide stations

			M_2		K_1	
segment	*station*	*location*	*amp* (*m*)	*phase* (°)	*amp* (*m*)	*phase* (°)
9	7765	Deep cove	.9327	177.37	.8397	175.27
13	7747	Stanovan	.9553	175.58	.8628	174.62
14	7743	Alberta Pool	.9140	169.00	.8040	172.00
17	7735	Vancouver Harbour	.9240	168.34	.8496	171.15

In the following discussion the landward segment (9) is denoted by a subscript 2, while the seaward segment (one of 13, 14 or 17) is denoted by a subscript 1. The portion of Indian Arm landward of segment 9 is deep and of fairly uniform width. We thus expect that tidal currents there will be much smaller than in the relatively shallow and constricted length of Burrard Inlet, and in the region over the sill — located roughly between segments 10 and 12. Turbulent dissipation of energy is thus assumed to be negligible landward of segment 9.

The head of an inlet may act as a reflecting barrier to a long progressive wave, such as the surface tides, giving rise to a standing wave within the inlet. This results in the elevations and barotropic currents having constant phase along the inlet provided its length is less than the wavelength of the tide. For Indian Arm, with a length of 20 *km* and an average depth of over 100 *m*, the wavelength of the M_2 tidal constituent exceeds 1300 *km*. In addition, we expect the tidal currents and elevations to be in quadrature throughout Indian Arm. If ϕ denotes the phase lag in the elevations between two ends of a section,

then we can write the elevation and barotropic velocity at segment 9 as

$$\eta_2(t) = a_2 \sin(\omega t - \phi), \tag{2.3}$$

$$u_2(t) = U_2 \cos(\omega t - \phi), \tag{2.4}$$

where $\omega = 2\pi/T$ is the angular frequency of a tidal constituent.

Due to dissipation at the seaward end of each section we expect that the horizontal velocity will not be in quadrature with the surface elevation. We can represent this result as

$$\eta_1(t) = a_1 \sin(\omega t), \tag{2.5}$$

$$u_1(t) = U_1 \cos(\omega t - \epsilon). \tag{2.6}$$

Under the set of assumptions discussed in §3.2.6 the rate of energy dissipation between the seaward segment and the head of the inlet is given by an integral of (3.34), that is,

$$P = \int_{A_1} \rho g \langle u_1 \eta_1 \rangle \, dA, \tag{2.7}$$

(*Farmer and Freeland*, 1980), where the integral of the averaged product, pressure times velocity, is taken over the cross-sectional area A_1 at segment 1, and $\langle \cdot \rangle$ denotes the time average over one tidal cycle. Substituting (2.5) and (2.6) into (2.7) yields

$$P = \frac{\rho g}{2} A_1 a_1 U_1 \sin(\epsilon). \tag{2.8}$$

If the phase shift along the section is not too large we can approximate U_1 by $U_1 = S_1 a_1 \omega / A_1$ where S_1/A_1 is the ratio of the inlet surface area landward of segment 1 to the cross-sectional area at segment 1. Substituting this into (2.8) gives

$$P = \frac{\rho g}{2} S_1 a_1^2 \omega \sin(\epsilon). \tag{2.9}$$

To evaluate ϵ we consider the following two expressions for the rate of change of volume in the section.

$$\frac{\partial V}{\partial t} = A_1 U_1 \cos(\omega t - \epsilon) - A_2 U_2 \cos(\omega t - \phi), \tag{2.10}$$

$$\frac{\partial V}{\partial t} = \frac{S_1 - S_2}{B_1 + B_2} \left(B_1 \frac{\partial \eta_1}{\partial t} + B_2 \frac{\partial \eta_2}{\partial t} \right), \tag{2.11}$$

where B_i is the breadth of the inlet at the surface at segment i. The first expression requires no assumption about the shape of the inlet along the section, and should be a good approximation to the integrated continuity equation. The second expression assumes that both the elevation and width vary linearly along the section. This is not a good approximation for any of the sections; however the result is intended only as a rough measure of the rate of dissipation.

After substituting for η_i and U_i in (2.10) and (2.11) and expanding the cos and sin terms we equate the coefficients of $\cos(\omega t)$ and $\sin(\omega t)$ to get

$$\epsilon = \arctan\left[\frac{a_2 \sin(\phi)(S_2 B_1 + S_1 B_2)}{a_2 \cos(\phi)(S_2 B_1 + S_1 B_2) + (S_1 - S_2) B_1 a_1}\right]. \tag{2.12}$$

This can be simplified somewhat since ϕ and ϵ are small. To an adequate order of approximation we can write

$$\epsilon = \frac{a_2 \phi (S_2 B_1 + S_1 B_2)}{a_2 (S_2 B_1 + S_1 B_2) + (S_1 - S_2) B_1 a_1}. \tag{2.13}$$

For the special case when $a_1 \approx a_2$, $B_1 \approx B_2$, and $S_2 = 0$ (i.e., the landward end of the section is the inlet head) we have $\epsilon = \phi/2$. For the other extreme when $S_2 \approx S_1$ we have $\epsilon \approx \phi$. The additional information required to calculate the values of ϵ and P for each constituent are summarized in *table* 11.

Table 11
Values required to calculate dissipation rates in Burrard Inlet

segment	*station*	*location*	S_i (km^2)	B_i (km)	A_1 (km^2)	$U_1\,(ms^{-1})$ M_2	K_1
9	7765	Deep Cove	23.72	1.230	.0608	.05	.02
13	7747	Stanovan	39.05	1.056	.0173	.30	.18
14	7743	Alberta Pool	40.88	0.800	.0147	.36	.16
17	7735	Vancouver Harbour	52.00	3.040	.0668	.10	.05

Finally, we can calculate the dissipation rate between each pair of segments by differencing the results of the calculations listed in *table* 12.

In the section from segments 13–14, which includes the severe constriction at Second Narrows, the rate of energy dissipation per unit volume for the M_2 constituent is approx-

Table 12
Phase lags and dissipation rates for 3 sections in Burrard Inlet

	M_2			K_1		
section	$\phi(°)$	$\epsilon(°)$	$P(MW)$	$\phi(°)$	$\epsilon(°)$	$P(MW)$
9 – 17	9.03	5.56	2.96	4.12	2.51	0.59
9 – 14	8.37	7.01	2.87	3.27	2.75	0.45
9 – 13	1.79	1.46	0.63	0.65	0.53	0.10

imately 20 times greater than the value on either side, and for the K_1 constituent it is approximately 15 times greater (*table* 13).

Table 13
Dissipation rates for each subsection in Burrard Inlet

	Energy loss(MW)			*Energy loss*($mW\,m^{-3}$)	
section	M_2	K_1	$vol(km^3)$	M_2	K_1
9 – 13	0.63	0.10	.2787	2.3	0.4
13 – 14	2.24	0.35	.0279	80.3	12.5
14 – 17	0.09	0.14	.2538	0.4	0.7

The dissipation rates in *table 13* are of the same order of magnitude as those presented in *Grant, Stewart, and Moilliet* (1962). They made measurements of the dissipation rate in a section of Discovery Passage, British Columbia in current speeds ranging up to about $1.5\,m\,s^{-1}$, and found dissipation rates of from 0.15 to 100 milliwatts per cubic metre ($mW\,m^{-3}$). An estimate of the amplitude of the tidal currents in Second Narrows may be made by using the expression $U_1 = S_1 a_1 \omega / A_1$ for each constituent. This leads to speeds of approximately $1.4\,m\,s^{-1}$ and $0.6\,m\,s^{-1}$ for the M_2 and K_1 constituents, respectively.

2.8 Stratification and Vertical Modes

The vertical response of an inlet to tidal forcing is strongly dependent on the stratification as can be seen by considering a solution to the equation for the vertical velocity in a stratified fluid given by (e.g., *Keeley*, 1984)

$$\frac{\partial^2}{\partial t^2}\nabla^2 w + N^2 \nabla_h^2 w + f^2 \frac{\partial^2 w}{\partial z^2} + \gamma \frac{\partial}{\partial t}\nabla^2 w = 0, \tag{2.14}$$

where N^2 is the Brunt-Väisälä frequency, γ is a frictional drag coefficient, and the Boussinesq approximation is assumed. A separable solution to (2.14) is sought of the form

$w = T(t)G(x,y)\Phi(z)$, which upon substitution leads to

$$\frac{\partial^2 T}{\partial t^2} + \gamma\frac{\partial T}{\partial t} + \omega^2 T = 0, \tag{2.15}$$

$$\nabla_h^2 G + \alpha^2 G = 0, \tag{2.16}$$

$$\frac{\partial^2 \Phi}{\partial z^2} + \frac{N^2 - \omega^2}{c^2}\Phi = 0, \tag{2.17}$$

where $\alpha^2 = (k_1^2 + k_2^2)$ and $\omega^2 = f^2 + c^2\alpha^2$ are separation constants, and k_1 and k_2 are the longitudinal and lateral wavenumbers respectively.

The assumption that a separable solution to (2.14) exists depends on the relative steepness of the group velocity vector and the inlet bottom. If we disallow a cross-inlet wavenumber component for linear internal waves propagating in Indian Arm then the dispersion relation for low frequencies applicable to such strongly stratified bodies of water is given by

$$\left(\frac{k_3}{k_1}\right)^2 = \frac{N^2}{\omega^2 - f^2} = R^2.$$

In the special case where $f = 0$ we have

$$R^2 = \frac{N^2}{\omega^2}. \tag{2.18}$$

The slope of the rays in the direction of the group velocity — along which the energy propagates — is $1/R$, while in the direction of the wave crests it is R. The ratio of the bottom slope, s, to the group velocity vector (i.e., $|s|R$) determines whether transmission or reflection of the wave takes place. If $|s|R < 1$ then the rays are steeper than the bottom slope and the inlet will act as a waveguide with the waves propagating along the inlet. If $|s|R > 1$ then the opposite holds true and the waves will tend to be reflected back toward their origin. Since the bottom slope extends over a finite depth this situation is complicated by variations in N^2 over the slope that may result in partial reflection or transmission at different depths. It is difficult to characterize the transmissive properties of an inlet from a simple consideration of vertical profiles of N^2. Nevertheless, an attempt has been made in *table* 14 to discern whether a separable solution is valid based on $|s|R$ values calculated from near bottom values of N^2. These were taken from the density distribution in the

model on December 9, 1974, after filtering σ_t time series with a (30,50,50) digital filter. Since the internal tide will normally propagate as a Kelvin wave (see below), (2.18) has been used to calculate R.

Table 14
Transmissive properties of Indian Arm for internal tides. Slopes (s) are approximated from the model bathymetry.

				$\|s\|R$	
segment	*depth* (m)	$\|s\|$	$N^2\,(\cdot 10^{-6})$	M_2	K_1
1	45	∞	11	∞	∞
2	85	.010	17	0.29	0.56
3	105	.050	10	1.13	2.18
4	205	.005	3.5	0.07	0.13
5	215	0	0.5	0	0
6	205	.005	3.7	0.07	0.13
7	195	.010	0.5	0.05	0.10
8	155	.015	6.0	0.26	0.50
9	95	.030	16	0.85	1.64
10	75	.015	30	0.58	1.13

Solutions to (2.17) are eigenfunctions $\Phi_n(z)$, $n = 1, 2, \ldots$ with corresponding eigenvalues c_n. Free wave solutions to (2.15–17) for a real lateral wave number will exist only if $\omega^2 - f^2 > c^2 k_2^2$, otherwise trapped Kelvin wave solutions result. f has a value of $1.1 \cdot 10^{-4}\, s^{-1}$ at the latitude of Indian Arm, and the M_2 and K_1 tidal constituents have angular frequencies of $1.4 \cdot 10^{-4}$ and $0.73 \cdot 10^{-4}\, s^{-1}$ respectively. Thus, we expect the internal diurnal tide to propagate only as a Kelvin wave while the semi-diurnal internal tide will be a free wave for phase speeds $c_n < (\omega^2 - f^2)^{\frac{1}{2}}/k_2$. The width of Indian Arm is typically $1.6\, km$, thus phase speeds of greater than about $2\, cm\, s^{-1}$ will result in Kelvin waves.

CTD data collected by Dr. Pond during January and February of 1983 in Indian Arm and Burrard Inlet together with Cyclesonde vertically profiling current data from the sites shown in *figures* 1 and 2 have been analyzed to determine the modal structure during winter. *Figures* 10–15 show the CTD and modal results at station Van-34, at the sill narrows, and at Ind-1.5 for January 5 and February 1, 1983. There are significant differences in the details of the modal structure between the two dates, especially with

regard to phase speeds and zero-crossing depths. Static instabilities seen in the N^2 profiles may be due to small scale mixing effects caused by breaking internal waves, turbulence from shear instabilities, or perhaps discrepancies in the response time of the conductivity cell and thermistor in the CTD profiler.

It appears that the M_2 internal tide propagates as a Kelvin wave in Indian Arm since the smallest phase speed calculated for the third internal mode is much larger than the limit of $1\,cm\,s^{-1}$ (*table* 15).

Table 15
Phase speeds of internal modes in Indian Arm ($cm\,s^{-1}$)

	January 5, 1983			**February 2, 1983**		
mode	*Van-34*	*Narrows*	*Ind-1.5*	*Van-34*	*Narrows*	*Ind-1.5*
1	9.5	30.2	34.0	15.0	34.8	49.6
2	7.3	12.4	20.7	7.4	18.7	32.8
3	3.8	8.6	15.5	5.1	11.9	20.7

2.9 Currents

Cyclesonde vertically profiling current meter data were collected by Dr. Pond during the winters of 1982–84 at two stations in Indian Arm (*figures* 1–2, *table* 16). The location of the deep water station was close to segment 7 of the model, while the station in the shallow narrows was near segment 10 (*figure* 2). For convenience, these segment numbers will be used to distinguish the two locations. Some of these data were analyzed for comparison with model output.

Table 16
Indian Arm Cyclesonde positions for winter of 1982–83

station	*latitude*	*longitude*	*depth*(m)	*levels*	Δt (*hrs*)
7	49° 21.80′ *N*	122° 53.0′ *W*	192	17	3.0
10	48° 19.25′ *N*	122° 55.9′ *W*	75	5	1.5

Four different Cyclesondes were used over the duration of the measurements (*table* 17).

Table 17
Start and finish times for Cyclesonde measurements

station	*Cyclesonde*	*start* (h:m)	(m-d-y)	*finish* (h:m)	(m-d-y)	*delay* (h:m)
7	22	12:03	12-07-82	09:27	01-05-83	—
7	21	18:01	01-05-83	09:31	02-02-83	8:35
7	22	12:02	02-02-83	09:31	03-05-83	2:31
7	21	19:28	03-07-83	09:26	03-29-83	9:57
10	20	12:01	12-07-82	13:35	01-05-83	—
10	67	18:01	01-05-83	10:35	02-02-83	4:26
10	20	15:02	02-02-83	13:37	03-05-83	4:27
10	67	01:26	03-06-83	12:11	03-29-83	11:49

Guildline CTD casts were made at both stations in conjunction with Cyclesonde servicing (see §2.8). The interval from 10:00 January 3, 1983 to 10:00 February 3, 1983 (744 hours) was selected for detailed analysis since it corresponds to the same time of year as the primary model simulation, and because this period brackets two Cyclesonde servicings and hence two CTD casts.

Time series of east and north (u, v) current vector components were obtained at $10\,m$ depth intervals beginning at $15\,m$ below the surface at both stations. Because of the aperiodic sampling rate the time series did not have a constant time increment. Linear interpolation was used to obtain hourly values at each depth (*figure* 16a).

Instrument changes occurred during the measurement period on January 5 and February 2. At station 7 there were delays of 8.6 hours and 2.5 hours between successive time series, while at station 10 there were delays of 4.4 hours and 4.5 hours respectively. When compared to the sampling interval, series length, and dominant tidal period of 12.4 hours, neither delay introduces significant error into the analysis. The time series at each station were filtered using a $(6, 8.5, 40)$ digital filter (*figure* 16b and *figure* 17).

It was necessary to rotate the velocity coordinate system in order to calculate along-inlet velocity components. Several methods may be used to select a rotation angle θ, including

(1) Minimizing cross-inlet energy

(2) Minimizing cross-inlet transport

(3) Visual alignment with topography

The first two methods may be applied by selecting θ such that the vertically summed cross-channel variance or mean is equal to zero. When this is done for the two stations over the study period the results listed in *table* 18 are obtained.

Table 18
Calculated rotation angles for Cyclesonde current meters

station	θ (°) *for minimized* *variance*	*mean*
7	114.5	120.2
10	114.5	112.7

The angles arrived at by the two methods are comparable, and agree with simple visual alignment. Values for θ that minimized the variance were chosen such that the positive x-axis points toward the inlet mouth in agreement with the alignment used for the model (*figure* 2).

Harmonic analysis was performed on the filtered and rotated velocity profiles at each depth and location in Indian Arm for the data collected in January 1983. Argand diagrams were then plotted of calculated amplitudes and phases for the M_2 and K_1 constituents (*figure* 18a,b). If the modal analysis described in §2.8 is valid, these plots illustrate the response of the internal structure of the inlet to tidal forcing and the resulting superposition of these excited modes. Appendix B describes a procedure for fitting the calculated modes to the results of harmonic analysis and this method is applied with success in chapter 6 to the output from the model; however similar attempts using Cyclesonde data and CTD casts were not successful. This was due to a conflict between the averaging properties of the harmonic analysis — which reduces a time series spanning several days or weeks to a set of complex amplitudes — and the discerned variability in the density data between nearly instantaneous CTD casts (*figures* 10–13). The casts tend not to be synoptic because they depend on the phase of the tide to some extent, and include the transient effects of

high frequency internal waves. Analysis of output from the numerical model avoids this problem through digital filtering of nearly continuous density data to yield a mean vertical density profile.

3. The Mathematical Model

3.1 The Governing Equations

The equations governing the dynamics of fluid motion without external forcing are discussed in many texts on fluid or ocean physics (e.g. *Phillips*, 1966) and hence the following are stated without derivation.

Mass Conservation
$$\frac{d\hat{\rho}}{dt} + \hat{\rho}\nabla \cdot \hat{\mathbf{u}} = 0, \tag{3.1}$$

Momentum Balance
$$\hat{\rho}\frac{d\hat{\mathbf{u}}}{dt} + \hat{\rho}2\Omega \times \hat{\mathbf{u}} + \nabla\hat{p} + \hat{\rho}\mathbf{g} = 0, \tag{3.2}$$

Salt Balance
$$\frac{d\hat{S}}{dt} = 0, \tag{3.3}$$

where molecular viscosity has been ignored in (3.2), and d/dt is the total derivative given by

$$\frac{d}{dt} = \frac{\partial}{\partial t} + \hat{\mathbf{u}} \cdot \nabla$$

describing the rate of change of a material element positioned in a flow field. Other symbols are listed in the *table of Symbols.*

The density of a material element of seawater is constant to a high degree of precision and hence (3.1) reduces to

Continuity
$$\nabla \cdot \hat{\mathbf{u}} = 0. \tag{3.4}$$

The *kinematic boundary condition* expresses mathematically the physical requirement for no transport of fluid across either a fixed solid, or moving surface at a boundary, and is given by

Kinematic Boundary Condition
$$\frac{d\phi(\mathbf{x},t)}{dt} = 0, \tag{3.5}$$

where $\phi(\mathbf{x},t) = 0$ defines the boundary. For example, at the surface (*figure* 19) $x_3 = z = -\eta(x,t)$, which leads to $\phi(\mathbf{x},t) = \eta(x,t)+z = 0$, where the surface elevation (η) is assumed

to be independent of lateral position y. Similarly, at the fixed boundary $y = \mathcal{Y}(x,z)$ — where $\mathcal{Y}$ is one of $a(x,z)$ or $b(x,z)$ — $\phi(\mathbf{x},t) = \mathcal{Y}(x,z) - y$. In these two cases the corresponding kinematic boundary conditions become (substituting for $\mathcal{Y}$)

$$\frac{\partial \eta}{\partial t} + [u]_{z=-\eta}\frac{\partial \eta}{\partial x} + [w]_{z=-\eta} = 0, \tag{3.6}$$

$$[u]_{y=a}\frac{\partial a}{\partial x} - [v]_{y=a} + [w]_{y=a}\frac{\partial a}{\partial z} = 0, \tag{3.7}$$

$$[u]_{y=b}\frac{\partial b}{\partial x} - [v]_{y=b} + [w]_{y=b}\frac{\partial b}{\partial z} = 0. \tag{3.8}$$

We also assume the existence of an equation of state $\hat{\rho} = \hat{\rho}(S,T,p)$ which may be approximated for many inlets by a linear function of salinity

Equation of state
$$\rho = \rho_0(1 + \alpha_0 S), \tag{3.9}$$

where ρ_0 and α_0 are prescribed constants.

The second term in (3.2) accounts for the influence of the earth's rotation. For long surface gravity waves, such as tides, this term may be ignored provided the external Rossby radius, given by

$$R_0 = \frac{c_0}{f}$$

is much larger than the lateral dimensions of the inlet. The phase speed, c_0, of the barotropic tide is very nearly equal to $\sqrt{gH}$, where H is the inlet depth. H is on the order of $100\,m$, and hence c_0 will be greater than about $32\,ms^{-1}$. For $f \approx 10^{-4}\,s^{-1}$ at mid-latitudes this leads to a value of $R_0 = 320\,km$. This is approximately 100 times the typical lateral dimensions of an inlet, hence we may omit the Coriolis term from the momentum equation based on the barotropic tide. Unfortunately, for internal tides such as those observed in inlets this approximation is not strictly valid since significant cross channel variability has been observed (*Farmer and Freeland*, 1983).

The internal Rossby radii R_i, $i = 1,2,\ldots$ for Indian Arm vary seasonally due to changes in stratification. It was found in §2.8 that for the first and second modes typical values for R_i range from $0.5\,km$ to $5.0\,km$. These values are of the same order of magnitude

as the width of Indian Arm, hence the predicted internal tides should be viewed with this approximation in mind. In particular, the internal tide will propagate as a trapped Kelvin wave under normal conditions as discussed in §2.8.

3.1.1 Reynold's decomposition

$\hat{\mathbf{u}}$ can be expressed as the sum of statistically steady and unsteady terms via the

Reynold's decomposition
$$\hat{\mathbf{u}} = \bar{\mathbf{u}} + \mathbf{u}'. \tag{3.10}$$

The two terms on the right hand side of (3.10) are defined as $\bar{\mathbf{u}} \equiv \langle \hat{\mathbf{u}} \rangle$ and $\mathbf{u}' = \hat{\mathbf{u}} - \bar{\mathbf{u}}$, where $\langle \cdot \rangle$ indicates an ensemble average. A direct result of the definitions is that $\langle \mathbf{u}' \rangle = 0$. If we now substitute (3.10) into (3.4) and then ensemble average we obtain

$$\begin{aligned} \langle \nabla \cdot \hat{\mathbf{u}} \rangle &= \langle \nabla \cdot (\bar{\mathbf{u}} + \mathbf{u}') \rangle \\ &= \nabla \cdot \langle \bar{\mathbf{u}} \rangle + \nabla \cdot \langle \mathbf{u}' \rangle \\ &= \nabla \cdot \bar{\mathbf{u}} = 0. \end{aligned} \tag{3.11}$$

Similar decompositions may be made for p and ρ as well.

3.1.2 Momentum equation

Because the horizontal length scale is large compared with the depth for the slow tidal motions considered, the vertical component of (3.2) simplifies to the

Hydrostatic approximation
$$\frac{\partial \hat{p}}{\partial z} = \hat{\rho} g. \tag{3.12}$$

This approximation can be justified by the following simple scaling argument. Let U, T, L and H be scales for horizontal velocity, time, length, and depth respectively. Scaling w by HU/L and substituting into the vertical component of (3.2), that is

$$\frac{\partial \hat{w}}{\partial t} + \hat{u}_j \frac{\partial \hat{w}}{\partial x_j} + g = \hat{\rho}^{-1} \frac{\partial \hat{p}}{\partial z}, \tag{3.13}$$

leads to

$$\frac{HU}{LT} + \frac{U^2 H}{L^2} + g = \hat{\rho}^{-1} \frac{\partial \hat{p}}{\partial z},$$

where standard tensor notation is used in (3.13) implying summation over repeated indices. Representative values for the scaling parameters are $H = 10^2\,m$, $L = 10^3\,m$, $U = 1\,ms^{-1}$, and $T = 10^4\,s$. Upon substituting these values and using a value for g of $10\,ms^{-2}$ we find that

$$10^{-5} + 10^{-4} + 10 = \hat{\rho}^{-1}\frac{\partial \hat{p}}{\partial z}.$$

Thus the vertical pressure gradient is very nearly balanced by gravitation alone. This argument may not be valid in certain shallow and constricted regions where horizontal velocities and gradients are very large, however it is a very good approximation over most of Indian Arm and Burrard Inlet. We can simplify the pressure term in (3.2) by using (3.12) to get

$$\begin{aligned}\hat{p}(z) &= g\int_{-\eta}^{z}\hat{\rho}\,dz \\ &= g(z+\eta)\hat{\varrho}(z), \qquad (3.14)\end{aligned}$$

$$\text{where} \qquad \hat{\varrho}(z) = \frac{1}{(z+\eta)}\int_{-\eta}^{z}\hat{\rho}\,dz. \qquad (3.15)$$

The next step is to replace the instantaneous values in the equations with Reynold's decompositions of each term. Recalling the horizontal component of (3.2) with (3.14) substituting for $\hat{p}$, and neglecting Coriolis terms (see §3.4.1) we have

$$\frac{\partial \hat{u}}{\partial t} + \hat{u}_j\frac{\partial \hat{u}}{\partial x_j} + \frac{g}{\hat{\rho}}\frac{\partial}{\partial x}\left[(z+\eta)\hat{\varrho}\right] = 0.$$

Replacing all instantaneous values with sums, ensemble averaging, and using $\langle u' \rangle = 0$, we have

$$\frac{\partial \bar{u}}{\partial t} + \bar{u}_j\frac{\partial \bar{u}}{\partial x_j} + \frac{g}{\rho}\frac{\partial}{\partial x}\left[(z+\eta)\varrho\right] = -\frac{\partial\langle u_1' u_j'\rangle}{\partial x_j}. \qquad (3.16)$$

The term on the right of the equals sign in (3.16) is the divergence of the Reynold's stress (per unit mass), which can be written as

$$-\frac{\partial\langle u_1' u_j'\rangle}{\partial x_j} = \frac{\partial(\bar{\tau}_{1j}\rho^{-1})}{\partial x_j}. \qquad (3.17)$$

The Reynold's stresses act like friction terms and represent a flux of momentum in the fluid due to unsteady velocity fluctuations. In the interior of a fluid column we replace

these stresses with a turbulent eddy viscosity parameterization, and at the boundaries with a quadratic drag law. A turbulent eddy viscosity coefficient N_j is defined by

$$\bar{\tau}_{1j} = \bar{\rho} N_j \frac{\partial \bar{u}_1}{\partial x_j}.$$

Using (3.17) we rewrite (3.16) as

$$\frac{\partial \bar{u}}{\partial t} + \bar{u}_j \frac{\partial \bar{u}_1}{\partial x_j} + \frac{g}{\bar{\rho}} \frac{\partial}{\partial x}\left[(z+\eta)\bar{\varrho}\right] = \frac{\partial}{\partial x_j}\left(\frac{\bar{\tau}_{1j}}{\bar{\rho}}\right). \tag{3.18}$$

Equation (3.18) is the final form of the horizontal momentum equation before lateral integration.

3.2 Lateral Integration of the Equations

Proceeding further, we can decompose $\bar{\mathbf{u}}$ into laterally invariant and fluctuating terms so that

$$\bar{\mathbf{u}} = \mathbf{u}(x,z,t) + \tilde{\mathbf{u}}(\mathbf{x},t), \tag{3.19}$$

$$\text{where} \qquad \mathbf{u} = \frac{1}{B}\int_a^b \bar{\mathbf{u}}\, dy$$

and $B(x,z) = b - a$ is the breadth of the inlet. It follows directly that $\int_a^b \tilde{\mathbf{u}}\, dy = 0$. It is noted that the water element following lateral integration is a right cylinder stretching across the inlet of unit cross-sectional area (normal to the y-axis).

3.2.1 Continuity equation

Integrating (3.11) across the inlet (i.e., with respect to the y-variable) and substituting (3.19) gives

$$\begin{aligned}
\int_a^b \nabla\cdot\bar{\mathbf{u}}\, dy &= \int_a^b \nabla\cdot\mathbf{u}\, dy + \int_a^b \nabla\cdot\tilde{\mathbf{u}}\, dy \\
&= \nabla\cdot(B\mathbf{u}) + \frac{\partial}{\partial x}\int_a^b \tilde{u}\, dy + \frac{\partial}{\partial z}\int_a^b \tilde{w}\, dy \\
&\quad - [\tilde{u}]_{y=b}\frac{\partial b}{\partial x} + [\tilde{v}]_{y=b} - [\tilde{w}]_{y=b}\frac{\partial b}{\partial z} \\
&\quad + [\tilde{u}]_{y=a}\frac{\partial a}{\partial x} - [\tilde{v}]_{y=a} + [\tilde{w}]_{y=a}\frac{\partial a}{\partial z} \\
&= \frac{\partial (Bu)}{\partial x} + \frac{\partial (Bw)}{\partial z} = 0.
\end{aligned} \tag{3.20}$$

where (3.7) and (3.8) have been used.

3.2.2 Surface elevation equation

We can obtain an equation for the free surface elevation $\eta(x,t)$ by integrating (3.20) from surface to bottom. Doing this we get

$$[Bw]_{z=H} - [Bw]_{z=-\eta} = -\frac{\partial}{\partial x}\int_{-\eta}^{H} Bu\,dz + [Bu]_{z=H}\frac{\partial H}{\partial x} + [Bu]_{z=-\eta}\frac{\partial \eta}{\partial x},$$

$$\Longrightarrow \qquad \frac{\partial \eta}{\partial t} = -\frac{1}{B}\frac{\partial}{\partial x}\int_{-\eta}^{H} Bu\,dz, \tag{3.21}$$

where $z = H(x)$ is the greatest inlet depth, and (3.6) and the boundary condition $[w]_{z=H} = [u]_{z=H} = 0$ have been used.

3.2.3 Vertical velocity equation

In a similar fashion, the equation for the vertical velocity, $w(x,z,t)$, can be derived by integrating (3.20) between a depth z' and the bottom. We obtain

$$[Bw]_{z=H} - [Bw]_{z=z'} = -\frac{\partial}{\partial x}\int_{z'}^{H} Bu\,dz + [Bu]_{z=H}\frac{\partial H}{\partial x},$$

$$\Longrightarrow \qquad w = \frac{1}{B}\frac{\partial}{\partial x}\int_{z'}^{H} Bu\,dz, \tag{3.22}$$

where again the boundary condition at the bottom has been used.

3.2.4 Horizontal velocity equation

Integrating the first two terms of (3.18) with respect to y after using (3.4) to bring $\bar{u}_j$ $(= \bar{u}, \bar{v}, \bar{w}$, when $j = 1,2,3)$ inside the derivatives gives

$$\begin{aligned}
&\frac{\partial}{\partial t}\int_a^b \bar{u}\,dy + \frac{\partial}{\partial x}\int_a^b \bar{u}\bar{u}\,dy + \frac{\partial}{\partial z}\int_a^b \bar{u}\bar{w}\,dy \\
&\quad - [\bar{u}\bar{u}]_{y=b}\frac{\partial b}{\partial x} + [\bar{u}\bar{v}]_{y=b} - [\bar{u}\bar{w}]_{y=b}\frac{\partial b}{\partial z} \\
&\quad + [\bar{u}\bar{u}]_{y=a}\frac{\partial a}{\partial x} - [\bar{u}\bar{v}]_{y=a} + [\bar{u}\bar{w}]_{y=a}\frac{\partial a}{\partial z} \\
&= \frac{\partial}{\partial t}\int_a^b \bar{u}\,dy + \frac{\partial}{\partial x}\int_a^b \bar{u}\bar{u}\,dy + \frac{\partial}{\partial z}\int_a^b \bar{u}\bar{w}\,dy.
\end{aligned} \tag{3.23}$$

The last two terms on the right hand side of the equals sign in (3.23) cannot be simplified without further assumptions. Substituting (3.19) into these integrals results in

$$\frac{\partial(Bu)}{\partial t} + \frac{\partial(Buu)}{\partial x} + \frac{\partial(Buw)}{\partial z} + \frac{\partial}{\partial x}\int_a^b \tilde{u}\tilde{u}\,dy + \frac{\partial}{\partial z}\int_a^b \tilde{u}\tilde{w}\,dy. \tag{3.24}$$

The last two terms in (3.24) are included as part of the eddy viscosity terms discussed below. The remaining three terms reduce to

$$\frac{\partial(Bu)}{\partial t} + \frac{\partial(Buu)}{\partial x} + \frac{\partial(Buw)}{\partial z}. \tag{3.25}$$

Integrating the third term in (3.18) across the inlet yields

$$g\int_a^b \bar{\rho}^{-1}\frac{\partial}{\partial x}[(z+\eta)\bar{\varrho}]\,dy = \frac{gB}{\rho}\frac{\partial}{\partial x}[(z+\eta)\varrho]$$

provided that $\bar{\rho}$ and η are independent of lateral position. That is very nearly the case for η because of the large value for R_0. For $\bar{\rho}$ there will be some cross-inlet variability due to the exponential decay of the isopycnal displacements arising from the passage of internal tidal waves. Nevertheless, this variation of $\bar{\rho}$ from ρ will normally be small, and will be ignored. From this point onward we assume that $\rho = \bar{\rho}$.

The right hand side of (3.18) includes the turbulent Reynold's stress terms. Substituting $\bar{\tau}_{1j} = \tau_{1j} + \tilde{\tau}_{1j}$ and integrating across the inlet gives

$$\int_a^b \frac{\partial}{\partial x_j}\left(\frac{\bar{\tau}_{1j}}{\rho}\right)dy = \frac{\partial}{\partial x}\left(\frac{B\tau_{11}}{\rho}\right) + \frac{\partial}{\partial z}\left(\frac{B\tau_{13}}{\rho}\right)$$
$$+\rho^{-1}\left[\tilde{\tau}_{11}\frac{\partial a}{\partial x} - \tilde{\tau}_{12} + \tilde{\tau}_{13}\frac{\partial a}{\partial z}\right]_{y=a} - \rho^{-1}\left[\tilde{\tau}_{11}\frac{\partial b}{\partial x} - \tilde{\tau}_{12} + \tilde{\tau}_{13}\frac{\partial b}{\partial z}\right]_{y=b}. \tag{3.26}$$

We replace the last two terms of (3.26) with an eddy viscosity parameterization of the normal stress terms, and with a quadratic friction term, $-\rho k_s u|u|$, substituting for the stresses representing the drag against the inlet sides (k_s is an empirically derived constant). Retaining the dependence of the side friction terms on the vertical gradient of inlet width (*Blumberg*, 1975), we finally write the complete, laterally integrated, longitudinal momentum equation as

$$\frac{\partial(Bu)}{\partial t} + \frac{\partial(Buu)}{\partial x} + \frac{\partial(Buw)}{\partial z} + \frac{gB\varrho}{\rho}\frac{\partial\eta}{\partial x} + \frac{gB(z+\eta)}{\rho}\frac{\partial\varrho}{\partial x}$$
$$= \frac{\partial}{\partial x}\left(\frac{B\tau_{11}}{\rho}\right) + \frac{\partial}{\partial z}\left(\frac{B\tau_{13}}{\rho}\right) - k_s u|u|\sqrt{1+\left(\frac{\partial B}{\partial z}\right)^2}. \tag{3.27}$$

3.2.5 Salt balance equation

Equation (3.3) is decomposed into steady and fluctuating components in exactly the same way as for the momentum equation. After ensemble averaging and replacement of the Reynold's stress terms with turbulent eddy diffusion approximations we obtain

$$\frac{\partial \bar{S}}{\partial t} + \bar{u}\frac{\partial \bar{S}}{\partial x} + \bar{v}\frac{\partial \bar{S}}{\partial y} + \bar{w}\frac{\partial \bar{S}}{\partial z} = \frac{\partial}{\partial x}\left(K_x\frac{\partial \bar{S}}{\partial x}\right) + \frac{\partial}{\partial y}\left(K_y\frac{\partial \bar{S}}{\partial y}\right) + \frac{\partial}{\partial z}\left(K_z\frac{\partial \bar{S}}{\partial z}\right). \quad (3.28)$$

Applying the assumption of lateral homogeneity, noting that there is no diffusion through solid boundaries, and laterally integrating, yields

$$\frac{\partial (BS)}{\partial t} + \frac{\partial (BSu)}{\partial x} + \frac{\partial (BSw)}{\partial z} = \frac{\partial}{\partial x}\left(BK_x\frac{\partial S}{\partial x}\right) + \frac{\partial}{\partial z}\left(BK_z\frac{\partial S}{\partial z}\right). \quad (3.29)$$

3.2.6 Mechanical energy equation

The equation for the balance of mechanical energy is derived by taking the inner product of the velocity with the momentum equation. This leads to (see *Phillips*, 1966 for details)

$$\frac{\partial}{\partial t}(\tfrac{1}{2}\rho\mathbf{u}^2 - \rho g\zeta) + \nabla\cdot\left[\mathbf{u}(p + \tfrac{1}{2}\rho\mathbf{u}^2 - \rho g\zeta)\right] = \mathbf{u}\cdot\mathcal{F} \quad (3.30)$$

where $\mathbf{u}^2 = \mathbf{u}\cdot\mathbf{u}$, $\zeta(x,t)$ is the vertical displacement of a fluid element from a reference level, and $\mathcal{F}$ is the vector of Reynold's stress terms

$$\mathcal{F}_i = \frac{\partial \tau_{ij}}{\partial x_j} \quad \text{where} \quad \tau_{ij} = -\rho\langle u_i' u_j'\rangle.$$

We can derive an approximation to the laterally integrated form of (3.30) by multiplying (3.27) by ρu_1, (3.6) by $B\rho u_3$, and adding. This leads to

$$B\frac{\partial}{\partial t}(\tfrac{1}{2}\rho u_1^2) + \frac{\partial}{\partial x_j}\left\{Bu_j\left[\tfrac{1}{2}\rho u_1^2 + g(x_3+\eta)\varrho\right]\right\} - Bu_3\rho g$$

$$= \frac{\partial}{\partial x_j}(Bu_1\tau_{1j}) - \frac{B\tau_{1j}}{\rho}\frac{\partial(\rho u_1)}{\partial x_j} - \rho|u_1^3|k_s\sqrt{1+\left(\frac{\partial B}{\partial z}\right)^2}, \quad (3.31)$$

where modified tensor notation has been used with repeated indices indicating summation over indices 1 and 3 only.

The first term in (3.31) is the local rate of change of kinetic energy density. The next term is comprised of the divergence of the kinetic energy flux and rate of working by the

pressure. The third term is the total rate of change of potential energy, that is, both the local rate and divergence of potential energy flux. This can be seen by rewriting $Bu_3\rho g$ — replacing u_3 by $d\zeta/dt$ (the rate of upwards displacement) — as

$$\begin{aligned} -Bu_3\rho g = B\rho g\frac{d\zeta}{dt} &= B\frac{d(\rho g\zeta)}{dt} - Bg\zeta\frac{d\rho}{dt} \\ &= B\frac{\partial(\rho g\zeta)}{\partial t} + \frac{\partial}{\partial x_j}[Bu_j(\rho g\zeta)] \end{aligned} \tag{3.32}$$

The first term on the right hand side of (3.31) is the divergence of the horizontal diffusive flux of energy by the turbulence. The next term is the rate of dissipation of turbulent energy. In the interior of the fluid we let $\tau_{1j} = \rho N_j \partial u_1/\partial x_j$, therefore

$$-\frac{B\tau_{1j}}{\rho}\frac{\partial(\rho u_1)}{\partial x_j} = -BN_j\frac{\partial u_1}{\partial x_j}\frac{\partial(\rho u_1)}{\partial x_j} \approx -BN_j\rho\left(\frac{\partial u_1}{\partial x_j}\right)^2,$$

which is always negative. Near the bottom $\tau_{13} = -\rho k_H u_1|u_1|$, and this term becomes

$$-Bk_H u_1|u_1|\frac{\partial(\rho u_1)}{\partial x_3}.$$

Close to the bottom, in the bottom boundary layer, u_1 and $\partial(\rho u_1)/\partial x_3$ will have the opposite sign. This follows from the assumption of a constant stress layer where $\tau = \rho u_*|u_*|$, $u_* = -\kappa z\partial u/\partial x_3$, and κ is von Karman's constant. Thus, bottom friction serves as a sink for energy as well.

Several interesting results can be derived by integrating (3.31) under various assumptions. If we first assume that u_j and η are periodic with period T, and that ρ — and therefore ϱ the depth mean density (see §3.1.2 and equation 3.15) — is constant, then we find after averaging (3.31) over one period that

$$\begin{aligned} g\rho\frac{\partial}{\partial x_j}[B\langle u_j\eta\rangle] + \tfrac{1}{2}\rho\frac{\partial}{\partial x_3}[B\langle u_3u_1^2\rangle] &= \frac{\partial}{\partial x_j}[B\langle u_1\tau_{1j}\rangle] \\ -B\langle\tau_{1j}\frac{\partial u_1}{\partial x_j}\rangle - \rho k_s\sqrt{1+\left(\frac{\partial B}{\partial z}\right)^2}\langle|u_1^3|\rangle. \end{aligned} \tag{3.33}$$

A further simplification can be made by assuming that u_3 and vertical variations in u_1, k_s, and τ_{11} are all negligible. This leads to

$$g\rho\frac{\partial}{\partial x_1}[B\langle u_1\eta\rangle] = \frac{\partial}{\partial x_3}[B\langle u_1\tau_{13}\rangle], \tag{3.34}$$

which was used in §2.7 to estimate the dissipation in Burrard Inlet. The left hand side of (3.34) is the gradient of the potential energy flux into the inlet represented by the barotropic tidal current and surface elevation, while the right side is the gradient of the flux of kinetic energy lost to frictional bottom drag.

Another variation of (3.31) is better suited to numerical computation. The second and third terms may be rewritten as

$$\begin{aligned}&\frac{\partial}{\partial x_j}\left\{Bu_j\left[\tfrac{1}{2}\rho u_1^2+g(x_3+\eta)\varrho\right]\right\}-Bu_3\rho g\\&=\frac{\partial}{\partial x_j}\left[Bu_j(\tfrac{1}{2}\rho u_1^2)\right]+Bu_1\frac{\partial}{\partial x_1}\left[g(x_3+\eta)\varrho\right],\end{aligned}\tag{3.35}$$

where continuity and (3.32) have been used. The second term represents the flux of energy due to the horizontal pressure gradient or, in other words, the rate of work done on a fluid element by the pressure gradient. We can split this term into barotropic and baroclinic parts

$$Bu_1\frac{\partial}{\partial x_1}\left[g(x_3+\eta)\varrho\right]=gBu_1\varrho\frac{\partial\eta}{\partial x_1}+gBu_1(x_3+\eta)\frac{\partial\varrho}{\partial x_1}.\tag{3.36}$$

Rewriting (3.31) using (3.35) and (3.36) gives

$$\begin{aligned}&B\frac{\partial}{\partial t}(\tfrac{1}{2}\rho u_1^2)+\frac{\partial}{\partial x_j}\left[Bu_j(\tfrac{1}{2}\rho u_1^2)\right]+gBu_1\left[\varrho\frac{\partial\eta}{\partial x_1}+(x_3+\eta)\frac{\partial\varrho}{\partial x_1}\right]\\&=\frac{\partial}{\partial x_j}(Bu_1\tau_{1j})-\frac{B\tau_{1j}}{\rho}\frac{\partial\rho u_1}{\partial x_j}-\rho|u_1^3|k_s\sqrt{1+\left(\frac{\partial B}{\partial z}\right)^2}.\end{aligned}\tag{3.37}$$

The relative contribution of bottom and side friction to the dissipation of turbulent energy in the model can be estimated by vertically integrating the respective terms in (3.33) over a fluid column. If we first simplify by assuming that B and ρ are independent of x_3, then the corresponding integrals become

$$B\int_0^H\frac{\partial}{\partial x_3}\langle u_1\tau_{13}\rangle\,dx_3=-B\rho k_H\left[\langle|u_1^3|\rangle\right]_{z=H}-\rho k_s\int_0^H\langle|u_1^3|\rangle\,dx_3.$$

If the flow is nearly depth independent then the ratio of the two terms will be approximately $Bk_H : Hk_s$, and bottom friction will tend to dominate since normally $k_H \approx k_s$ and $B \gg H$. If, however, the flow is strongly depth dependent, and in particular, if maximum horizontal

speeds tend to occur away from the bottom — which we will observe in §6.4 to be the case for Burrard Inlet — then the cubic dependence on u_1 can result in side friction becoming the dominant energy sink.

3.3 Conservation of Salt in the Model

The fundamental equation governing the conservation of salt in the laterally integrated XZT numerical model is (3.29), where S(x,z,t) is the salinity (in $grams\, l^{-1}$ for example). Integrating (3.29) over a fluid volume with $\chi(x,t)$ representing the upper boundary of the cell (either fixed or free), and noting that the diffusive terms integrate to zero (except at the mouth) we get

$$\int_{\chi}^{z_0}\int_{0}^{\Delta x}\left[\frac{\partial(BS)}{\partial t}+\frac{\partial(BSu)}{\partial x}+\frac{\partial(BSw)}{\partial z}\right]dx\,dz=0,$$

or

$$\int_{0}^{\Delta x}\left\{\frac{\partial}{\partial t}\int_{\chi}^{z_0}BS\,dz+\frac{\partial}{\partial x}\int_{\chi}^{z_0}BSu\,dz+\left[BS\left(\frac{\partial\chi}{\partial t}+u\frac{\partial\chi}{\partial x}-w\right)\right]_{z=\chi}+[BSw]_{z=z_0}\right\}dx=0. \tag{3.38}$$

(3.38) will be used in the chapter 4 to derive the finite difference approximation to the salt balance equation.

4. The Numerical Method

4.1 Introduction

Finite element and finite difference techniques comprise two widely used families of methods for solving systems of partial differential equations. In this chapter, a finite difference model is described which solves the equations derived in chapter 3. Finite element methods might have worked as well, but the vast majority of related studies have used techniques similar to those employed here.

The many available finite difference methods tend to be classified according to whether they are implicit or explicit, on the order of accuracy used, and whether or not they are dissipative. Implicit methods are valuable for their savings in computer time, since linear stability analysis shows they are not restricted by a maximum time step. One must be careful, however, to limit phase errors that increase with the time step. In addition, the stability of almost all methods cannot be analysed in the case of strong nonlinearities and generalized boundary conditions. Hence, it may be found that an implicit method that should theoretically be stable under a particular set of conditions may be unstable instead.

The equations derived in chapter 3 are nonlinear, and in regions of the inlet where constrictions exist — possibly together with large gradients in the bottom slope and sides — strong nonlinearities may be expected. In numerical experiments conducted using a semi-implicit scheme developed by *Wang and Kravitz* (1980) it was found that, although their method worked well in weakly nonlinear systems, it was unstable in more realistic tidal flows and bathymetry for time steps which were not significantly larger than those allowed for an explicit scheme. For this reason an explicit scheme described by *Blumberg* (1975) and extended by *Elliott* (1976) was modified and adapted for use in this research. Its numerical properties are well known, and the separation of physically relevant results from spurious numerical artifacts is more easily accomplished.

4.2 The Model Grid

The solution domain was discretized so that finite difference approximations to the governing equations derived in chapter 3 could be numerically integrated. The total number of columns in the model representing the simulation region is denoted by J, while the number of rows in column j is n_j. Note that variables are not all calculated at the same locations in a grid (*figure* 20). In particular, u-velocities are calculated at the centre of the left edge, w-velocities at the centre of the top edge, and salinities at the centre of a grid. These three locations will subsequently be referred to as the *u-point*, the *w-point* and the *S-point* respectively. This structure more easily accomodates the calculation of the centred space differences used in the model. All model parameters are defined at one of these three locations except for $N^{(z)}$, which is at the upper left corner of each grid (*table* 19).

Table 19
Locations of model parameters

location	*parameter*
u-point	$u, B^{(x)}, K^{(x)}$
w-point	$w, B^{(z)}, K^{(z)}$
S-point	$S, \rho, \varrho, N^{(x)}$
upper left corner	$N^{(z)}$

The height (Δz) and length down-inlet (Δx) of each cell in the model is fixed. The width varies, however, and is specified at the *u-point* and *w-point* by $B^{(x)}_{i,j-1/2}$ and $B^{(z)}_{i-1/2,j}$ respectively. These are used in the model to calculate surface areas and volumes according to the following formulae.

Area of left face $$A^{(x)}_{i,j-1/2} = \Delta z B^{(x)}_{i,j-1/2} \tag{4.1}$$

Area of top face $$A^{(z)}_{i-1/2,j} = \Delta x B^{(z)}_{i-1/2,j} \tag{4.2}$$

Volume of cell $$V_{ij} = \Delta x \Delta z (B^{(z)}_{i-1/2,j} + B^{(z)}_{i+1/2,j})/2 \tag{4.3}$$

A no-flow condition was prescribed for velocity components normal to the fixed bottom boundary of the model (i.e., w at horizontal grid edges and u at vertical grid edges) by

setting them to zero. A condition for velocity components tangential to these edges was not required since only normal velocity components are located at each of the fixed boundaries corresponding to a model grid edge (*figure* 20).

4.3 Discretization of the Bathymetry

The basic dimensions of each model cell are the fixed length Δx and height Δz together with two varying widths; $B^{(x)}$ and $B^{(z)}$. Estimates of $A_{ij}^{(x)}$ and $A_{ij}^{(z)}$ were made from navigation charts of Indian Arm and Burrard Inlet and the corresponding widths calculated using (4.1–4.3). This was accomplished by first marking each model segment on the appropriate Canadian Hydrographic Service chart (nos. 3482, 3483 and 3495) (e.g., *figure* 21). Segments were spaced at 0.5 *km* intervals and appropriate areas combined to construct the coarse 2 *km* grid. This was done anticipating the possible need to construct a finer mesh model. Data is available for constructing a model with multiples of a 0.5 *km* spacing.

Within the boundaries of a model cell the area enclosed by each depth contour was calculated while making allowances for islands and raised portions of the bottom by contouring around them, and thus excluding their volume from the model cells. In addition, the cross-channel width along each segment and at each depth was measured. This area and width for cell j at depth z are denoted by $A_j(z)$ and $L_{j-1/2}(z)$ respectively (*figure* 21). The volume of cell j between depths z_i and $z_i + \Delta z$ is given by

$$V_{ij} = \int_{z_i}^{z_i+\Delta z} A_j(z)\, dz,$$

and the cross-sectional area along the column face between the same two depths by

$$A_{i,j-1/2}^{(x)} = \int_{z_i}^{z_i+\Delta z} L_{j-1/2}(z)\, dz.$$

These integrals were calculated from discretely spaced values by fitting a cubic spline under tension and integrating the fitted curve between the desired depths (see *U.B.C. Computing Centre publication UBC TSPLINE* for details of the interpolation method). Plots of these values, and others calculated from them, are shown in *figures* 5 and 42.

An estimate of the digitization error was made by repeating several of the area and length measurements. It was found that the values differed in the two cases by less than about 3%. Grids with spacings greater than 0.5 km were generated by adding contour areas from adjacent cells, and using the cross-sectional areas from the appropriate cell faces. Intertidal areas were treated by averaging two values of the surface area — one including the intertidal zone and the other excluding it — to yield a better estimate of the tidal prism volume than using either value alone.

4.4 Notation

The notation for representing finite difference equations (FDEs) is not universally agreed upon. In this thesis the following conventions will be used.

1) A parameter $P(x,z,t)$ evaluated at $x = (j-1/2)\Delta x$, $z = i\Delta z$, and at relative time level $k = 1, 2$, or 3 is denoted by P_{ijk}. Where k is omitted a value of 2 will be assumed. Values for k of 1, 2 and 3 correspond to $t = T - \Delta t$, T, and $T + \Delta t$ respectively, where $T = n\Delta t$ is the time of the n^{th} model iteration.

2) Noninteger values for i and j are permitted. For example, $P_{i+1/2,j}$ corresponds to $P[(j-1/2)\Delta x, (i+1/2)\Delta z, t]$, that is, to the centre of the lower edge of cell (i,j).

3) If parameter values are required at locations other than where defined then the following formulae are used for P defined at each of the following locations.

S-point
$$P_{i-1/2,j}=(P_{i-1,j}+P_{ij})/2$$
$$P_{i,j-1/2}=(P_{i,j-1}+P_{ij})/2$$

w-point
$$P_{i,j}=(P_{i-1/2,j}+P_{i+1/2,j})/2$$
$$P_{i,j-1/2}=(P_{i-1/2,j}+P_{i+1/2,j}+P_{i-1/2,j-1}+P_{i+1/2,j-1})/4$$

u-point
$$P_{i,j}=(P_{i,j-1/2}+P_{i,j+1/2})/2$$
$$P_{i-1/2,j}=(P_{i,j-1/2}+P_{i,j+1/2}+P_{i-1,j-1/2}+P_{i-1,j+1/2})/4$$

4) The following operators on a parameter P are defined

δ_x:
$$\delta_x P_{ij} = P_{i,j+1/2} - P_{i,j-1/2}$$

δ_x^n: $\quad \delta_x^n P_{ij} = \delta_x(\delta_x^{n-1} P_{ij}), \quad \delta_x^0 P_{ij} = P_{ij}$

e.g. $\delta_x^2 P_{ij} = P_{i,j+1} - 2P_{ij} + P_{i,j-1}$

δ_z, δ_z^n: (same as δ_x, δ_x^n but for subscript i rather than j)

δ_t: $\quad \delta_t P_{ij} = P_{ij3} - P_{ij1}$

5) If bracketed quantities are subscripted then the subscripts apply to each term within the brackets. For example

$$[B^{(x)}u]_{i,j-1/2} = B^{(x)}_{i,j-1/2} u_{i,j-1/2}$$

6) Where the product of two parameters defined at the same location must be evaluated at a location where they are undefined, the average of the products, rather than the product of the averages is used. For example

$$[B^{(x)}u]_{ij} = \frac{[B^{(x)}u]_{i,j-1/2} + [B^{(x)}u]_{i,j+1/2}}{2}$$

$$\text{rather than} \quad = \frac{(B^{(x)}_{i,j-1/2} + B^{(x)}_{i,j+1/2})(u_{i,j-1/2} + u_{i,j+1/2})}{2}$$

4.5 Finite Difference Equations

The following FDEs were used in the model to approximate the PDEs derived in chapter 3.

4.5.1 Surface Elevation

$$\eta_{j3} = \begin{cases} \eta_{j1} - (B^{(z)}_{1j})^{-1} \left(\frac{2\Delta t}{\Delta x}\right) \delta_x[U]_j & j < J, \\ \eta_{j-1,3} & j = J \text{ (closed mouth)}, \\ \text{(A.1), Appendix A} & j = J \text{ (open mouth)}, \end{cases}$$

where U_{jk} is the vertically integrated horizontal transport specified by

$$U_{j-1/2,k} = (1.5\Delta z + \eta_{jk})[B^{(x)}u]_{1,j-1/2,k} + \Delta z \sum_{i=2}^{n_j} [B^{(x)}u]_{i,j-1/2,k}. \qquad (4.4)$$

During some preliminary tests the boundary at the mouth was closed. In the case of an open boundary, elevations were specified by reconstructing the tidal elevation from a set of harmonic constants. For tidal studies — including the degenerative case with zero

tide — the elevations were calculated for real clock times using (A.1). The program was constructed so that a particular tidal station and a specified subset of constituents could be easily selected. It was found that a radiation boundary condition was not required for simulations with realistic values of the friction coefficients since the reflected wave did not have sufficient energy upon returning to the mouth to adversely affect the solution.

4.5.2 Vertical Velocity

The vertical velocities were determined from (3.22) using the approximation

$$w_{i-1/2,j,3} = \begin{cases} (B^{(z)}_{i-1/2,j})^{-1} \left(\frac{\Delta z}{\Delta x}\right) \delta_x[U]_{ij3} & \text{for all } i,\, j < J, \\ 0 & \text{for all } i,\, j = J, \end{cases}$$

where U_{ijk} is the partially integrated horizontal transport given by

$$U_{i,j-1/2,k} = \sum_{l=0}^{n_j - i} [B^{(x)} u]_{n_j - l, j-1/2, 3}. \tag{4.5}$$

4.5.3 Horizontal Velocity

The FDE for (3.27), the horizontal velocity equation, is most conveniently dealt with by considering it term by term. We therefore define the following mass balance terms

$$\begin{aligned}
\textit{Local acceleration :} \quad & M_{B1} \equiv \frac{\partial (Bu)}{\partial t} \\
\textit{Horizontal advection:} \quad & M_{B2} \equiv \frac{\partial (Buu)}{\partial x} \\
\textit{Vertical advection :} \quad & M_{B3} \equiv \frac{\partial (Buw)}{\partial z} \\
\textit{Horizontal viscosity:} \quad & M_{B4} \equiv -\frac{\partial}{\partial x}\left(\frac{B\tau_{11}}{\rho}\right) \\
\textit{Vertical viscosity :} \quad & M_{B5} \equiv -\frac{\partial}{\partial z}\left(\frac{B\tau_{13}}{\rho}\right) \\
\textit{Side friction:} \quad & M_{B6} \equiv k_s u|u| \sqrt{1 + \left(\frac{\partial B}{\partial z}\right)^2} \\
\textit{Barotropic pressure :} \quad & M_{B7} \equiv \frac{gB\varrho}{\rho} \frac{\partial \eta}{\partial x} \\
\textit{Baroclinic pressure :} \quad & M_{B8} \equiv \frac{gB(z+\eta)}{\rho} \frac{\partial \varrho}{\partial x}
\end{aligned}$$

Thus (3.27) is equivalent to

$$M_{B1} = -(M_{B2} + M_{B3} + M_{B4} + M_{B5} + M_{B6} + M_{B7} + M_{B8}).$$

At the head of the model ($j = 1$) the horizontal velocity was set to 0. At all other points the following FDEs were used.

$$M_{B2} = \frac{1}{\Delta x}\delta_x[B^{(z)}uu]_{i,j-1/2} \tag{4.6}$$

$$M_{B3} = \frac{1}{\Delta z}\delta_z[B^{(x)}uw]_{i,j-1/2} \tag{4.7}$$

$$M_{B4} = -\frac{1}{\Delta x^2}\delta_x\left[N^{(x)}B^{(z)}\delta_x(u)_{ij1}\right]_{i,j-1/2} \tag{4.8}$$

$$M_{B5} = \frac{1}{\Delta z}\delta_z[\tau_{13}]_{i,j-1/2} \tag{4.9}$$

where $(\tau_{13})_{i-1/2,j-1/2} = \begin{cases} B^{(x)}_{1j}\tau_W, & i = 1 \\ \frac{1}{\Delta z}\left[N^{(z)}B^{(x)}\delta_z(u)_{ij1}\right]_{i-1/2,j-1/2} & 1 < i \le n_j \\ H\tau_B B^{(z)}_{i-1/2,j-1/2}(u|u|)_{i-1,j-1/2,1} & i = n_j + 1 \end{cases}$

$$M_{B6} = k_s(u|u|)_{i,j-1/2,1}\sqrt{1 + \left(\frac{\delta_z B^{(z)}_{i,j-1/2}}{\Delta z}\right)^2} \tag{4.10}$$

$$M_{B7} = \frac{g}{\Delta x}\left(\frac{B^{(x)}\varrho}{\rho}\right)_{i,j-1/2}\delta_x[\eta]_{j-1/2} \tag{4.11}$$

$$M_{B8} = \left[\frac{gB^{(x)}(\eta_j + i\Delta z)}{\rho\Delta x}\right]_{i,j-1/2}\delta_x[\varrho]_{i,j-1/2} \tag{4.12}$$

In the above formulaes $u_{i,J+1,k} = u_{iJk}$ was used to define the horizontal velocity beyond the last column of the model. This implies that both horizontal advective and diffusive terms are zero at the open boundary. Individual terms were then combined using

$$u_{i,j-1/2,3} = u_{i,j-1/2,1} - \frac{2\Delta t}{B^{(x)}_{i,j-1/2}}(M_{B2} + M_{B3} + M_{B4} + M_{B5} + M_{B6} + M_{B7} + M_{B8}).$$

4.5.4 Salinity

As with the horizontal velocity equation it is convenient to consider the distinct terms in the salt balance equation (3.29). Define

$$\begin{aligned}
\textit{Local rate of change:} \quad & S_{B1} \equiv \frac{\partial(BS)}{\partial t} \\
\textit{Horizontal advection:} \quad & S_{B2} \equiv \frac{\partial(Buu)}{\partial x} \\
\textit{Vertical advection :} \quad & S_{B3} \equiv \frac{\partial(BSw)}{\partial z} \\
\textit{Horizontal diffusion:} \quad & S_{B4} \equiv -\frac{\partial}{\partial x}\left(BK^{(x)}\frac{\partial S}{\partial x}\right) \\
\textit{Vertical diffusion :} \quad & S_{B5} \equiv -\frac{\partial}{\partial z}\left(BK^{(z)}\frac{\partial S}{\partial z}\right)
\end{aligned}$$

Thus (3.29) is equivalent to

$$S_{B1} = -(S_{B2} + S_{B3} + S_{B4} + S_{B5}).$$

Equation (3.38) governs the conservation of salt in the finite volume cells of the model. In the interior of the model (below row 1) both the lower and upper boundaries are stationary. In the surface layer (row 1), on the other hand, the upper boundary is free to move.

Before listing the expressions for each term in the salt balance equation for these two cases we define the following functions:

$$\begin{aligned}
[f_1(Su)]_{i,j-1/2} &= [Su]_{i,j-1/2}, \\
[f_2(Su)]_{i,j-1/2} &= H_+(u_{i,j-1/2})S_{i,j-1} + H_-(u_{i,j-1/2})S_{ij}, \\
H_+(x) &= (x + |x|)/2, \\
H_-(x) &= (x - |x|)/2,
\end{aligned}$$

f_1 and f_2 are, respectively, centred and *upwind* expressions for the salt flux at a grid edge. The former leads to second order FDEs which are non*transportive*, while the latter leads to first order FDEs that are *transportive*. Transportive finite difference schemes for the pure advection of a tracer (such as salt) have the physically sensible property that perturbations in the tracer concentration do not propagate against the direction of the flow

field. Nontransportive schemes, on the other hand, have a tendency to move a perturbation against the direction of the fluid velocity field — a physically unrealistic result. This can lead to the calculation of salinities that are higher than any salinity that is initially present.

Upwind differences avoid this undesirable effect, but tend to exhibit *numerical diffusion* due to the second order derivative in the truncation error. This term acts like physical diffusion and will cause the solution to be smeared.

In selecting one of these schemes over the other, the relative merits and disadvantages of each were compared. The nontransportive property of the centred difference scheme was found to be of minimal detriment in extensive tests using both schemes. On the other hand, numerical diffusion in the upwind scheme was found to be severe. Considerable effort was spent in an attempt to mimimize this effect, and in particular, a scheme described by *Smolarkiewicz* (1983) was utilized, but with little success. His method requires an additional step in the solution procedure which introduces an *antidiffusion velocity* $\tilde{u}$ in a synthetic advection equation to reverse the effect of the artificial diffusion. Tests were performed with spreading of an initially static *lump* of dense water in a closed rectangular basin of constant width and depth. The results with the *Smolarkiewicz* scheme were inconclusive; showing no apparent improvement in performance over the original upwind scheme. Further tests with this scheme in tidally forced flows were not undertaken due to the very satisfactory performance and inherently simpler construction of the centred difference scheme. The centred scheme tended to work very well in the interior of the model while at the column just inside the open boundary (at the mouth) upwind differencing was used. This was found to be necessary for generating satisfactory salinities in the model interior. In particular, during the period of outflow which occurs during ebb tides the salinity external to the model (i.e., the salinity prescribed as an open boundary condition) should not influence the interior solution — as observed in nature. This is most readily accomplished by means of the upwind differencing scheme. Other methods — most notably *flux corrected transports* — have been developed as a means for eliminating the effect of artificial diffusion while retaining the desirable transportive property of upwind

differencing. These were not investigated in the present research due to the apparent success of the methods employed.

4.5.4.1 Case 1: The subsurface region ($i > 1$)

Let $\chi(x,t) = z_1 \equiv$ constant, $z_0 - z_1 = \Delta z$. Therefore (3.38) becomes

$$\int_0^{\Delta x} \left\{ \frac{\partial}{\partial t} \int_{z_1}^{z_0} BS\, dz + \frac{\partial}{\partial x} \int_{z_1}^{z_0} BSu\, dz - [BSw]_{z=z_1} + [BSw]_{z=z_0} \right\} dx = 0. \qquad (4.13)$$

Assume that the volume is small enough such that

$$\int_{z_1}^{z_0} BS\, dz \approx BS\Delta z,$$
$$\int_{z_1}^{z_0} BSu\, dz \approx BSu\Delta z.$$

Making a similar assumption about the horizontal integrals we get

$$\Delta x \Delta z B \frac{\partial S}{\partial t} + \Delta z \left\{ [BSu]_{x=\Delta x} - [BSu]_{x=0} \right\} + \Delta x \left\{ [BSw]_{z=z_1} - [BSw]_{z=z_0} \right\} = 0$$

which we can rearrange to derive

$$\frac{\partial S}{\partial t} = -\frac{1}{B} \left(\frac{[BSu]_{x=\Delta x} - [BSu]_{x=0}}{\Delta x} + \frac{[BSw]_{z=z_1} - [BSw]_{z=z_0}}{\Delta z} \right). \qquad (4.14)$$

$$S_{B2} = \frac{1}{\Delta x} \delta_x \left[B^{(x)} f_k(Su) \right]_{ij}, \qquad k = \begin{cases} 1 & j < J \\ 2 & j = J \end{cases} \qquad (4.15)$$

$$S_{B3} = \frac{1}{\Delta z} \delta_z \left[B^{(z)} f_k(Sw) \right]_{ij}, \qquad k = \begin{cases} 1 & j < J \\ 2 & j = J \end{cases} \qquad (4.16)$$

$$S_{B4} = -\frac{1}{(\Delta x)^2} \delta_x \left[B^{(x)} K^{(x)} \delta_x (S)_{ij} \right]_{ij}, \qquad (4.17)$$

$$S_{B5} = -\frac{1}{(\Delta z)^2} \delta_z \left[B^{(z)} K^{(z)} \delta_z (S)_{ij} \right]_{ij}. \qquad (4.18)$$

These are combined to give

$$S_{ij3} = S_{ij1} - \frac{2\Delta t}{B_{ij}^{(z)}} (S_{B2} + S_{B3} + S_{B4} + S_{B5}). \qquad (4.19)$$

4.5.4.2 Case 2: The surface layer ($i = 1$)

Let $\chi(x,t) = -\eta(x,t)$. Using the free surface condition (3.6), (3.38) becomes

$$\int_0^{\Delta x} \left\{ \frac{\partial}{\partial t} \int_{-\eta}^{z_0} BS\, dz + \frac{\partial}{\partial x} \int_{-\eta}^{z_0} BSu\, dz + [BSw]_{z=z_0} \right\} dx = 0.$$

Making similar assumptions to those in Case 1 we can reduce this to

$$B\Delta x \frac{\partial}{\partial t}[(z_0+\eta)S] + [(z_0+\eta)BSu]_{x=\Delta x} - [(z_0+\eta)BSu]_{x=0} + \Delta x\,[BSw]_{z=z_0} = 0$$

which can be rearranged to read

$$\frac{\partial}{\partial t}[(z_0+\eta)S] = -\frac{1}{B}\left\{ \frac{[(z_0+\eta)BSu]_{x=\Delta x} - [(z_0+\eta)BSu]_{x=0}}{\Delta x} + [BSw]_{z=z_0} \right\}. \quad (4.20)$$

The terms in the salt balance become

$$S_{B2} = \frac{1}{\Delta x}\delta_x \left[B^{(x)}(1.5\Delta z + \eta) f_k(Su) \right]_{1j}, \qquad k = \begin{cases} 1 & j < J \\ 2 & j = J \end{cases} \quad (4.21)$$

$$S_{B3} = B^{(z)}_{3/2,j} [f_k(Sw)]_{1j}, \qquad k = \begin{cases} 1 & j < J \\ 2 & j = J \end{cases} \quad (4.22)$$

$$S_{B4} = -\frac{1}{(\Delta x)^2}\delta_x \left[B^{(x)}(1.5\Delta z + \eta) K^{(x)} \delta_x (S)_{1j} \right]_{1j}, \quad (4.23)$$

$$S_{B5} = -\frac{1}{(\Delta z)^2} \left[B^{(z)} K^{(z)} \delta_z (S)_{1j} \right]_{1j}. \quad (4.24)$$

These are combined in the expression for the updated salinity in the surface layer

$$S_{1j3} = \frac{(1.5\Delta z + \eta_{j1})}{(1.5\Delta z + \eta_{j3})} S_{1j1} - \frac{2\Delta t}{(1.5\Delta z + \eta_{j3}) B^{(z)}_{1j}} (S_{B2} + S_{B3} + S_{B4} + S_{B5}). \quad (4.25)$$

4.5.4.3 Conservation with constant S

Consider both (3.17) and (3.19) for a constant value of S.

$$(3.17) \quad \Rightarrow \quad S_{ij3} = S - \frac{2\Delta t S}{B^{(z)}_{ij}} \left(\frac{1}{\Delta x}\delta_x [B^{(x)}u]_{ij} + \frac{1}{\Delta z}\delta_z [B^{(z)}w]_{ij} \right) = S$$

by the continuity equation which is satisfied exactly by the method for calculating w. For (3.19) we have

$$S_{1j3} = \frac{z_0 + \eta_{j1}}{z_0 + \eta_{j3}} S - \frac{2\Delta t S}{B^{(z)}_{1j}(z_0 + \eta_{j3})} \left(\frac{1}{\Delta x}\delta_x \left[(z_0+\eta) B^{(x)} u \right]_{1j} + [B^{(z)}w]_{3/2,j} \right).$$

Carrying out substitutions using the FDEs for w and η reduces the right hand side of this expression to S. This shows that the finite difference schemes used in the model preserve salt in the simplest situation of homogeneous salt distribution.

Although salt is conserved in principle, some difficulty was encountered in realizing this result in practice. Numerical truncation errors caused a slow leak of salt out of the model in early test runs. This problem was overcome by performing calculations in double precision arithmetic.

4.6 Static Instabilities

During preliminary tests of the model it became apparent that static instabilities (regions of denser water overlying regions of less dense water) could develop and intensify with time. It was found that layers of relatively dense water accumulated between layers of less dense water. Such occurrences are not observed in nature to the same degree since convective overturning will eventually mix denser water downward. To rectify this situation instabilities of greater than 0.01‰ in salinity were eliminated by homogenizing the two layers where the inversion occurred. By an iterative process lower layers were checked and included, if necessary, until the inversion was removed.

4.7 Boundary Conditions

No fluxes of momentum or salt were permitted through either the free surface or solid boundary comprising the inlet bottom. This was accomplished by setting normal derivatives at these locations to zero. Other boundary conditions are described below.

4.7.1 Salinity at the Mouth

The open boundary condition at the mouth of the model requires that the salinity be specified at each time step. One way to do this is to prescribe a constant or slowly varying mean salinity at each depth. This is unsatisfactory because the barotropic tide will not only displace the surface, but also the isopycnals as well. The magnitude of the displacement at each depth will also depend on the baroclinic response and hence the modal structure. As

a first approximation, however, we can use continuity to calculate the displacement at a specified depth due to the barotropic response. As mentioned in §4.5.4, upwind differencing — a transportive finite difference scheme — is required for the last column of the model for which the salinity is calculated (i.e., the column immediately inside the one where salinities are prescribed). This is necessary to eliminate the influence of the prescribed salinities during periods of outflow.

Letting $\varsigma(z,t)$ be the displacement of an isopycnal from a reference depth z at time t we have upon integrating (3.20)

$$\frac{\partial \varsigma}{\partial t} = \frac{1}{B}\frac{\partial}{\partial x}\int_{\varsigma}^{H} Bu\,dz. \tag{4.26}$$

If B varies slowly along the inlet and u is constant with depth then (4.26) can be written as

$$\frac{\partial \varsigma}{\partial t} = \frac{\partial}{\partial x}[(H-\varsigma)u] \tag{4.27}$$

If we write $\varsigma = \varsigma' + z$ for constant depth z then (4.27) becomes

$$\frac{\partial \varsigma'}{\partial t} = (H-z)\frac{\partial u}{\partial x} - \frac{\partial(\varsigma' u)}{\partial x} \approx (H-z)\frac{\partial u}{\partial x}, \quad \text{if } \varsigma' \ll (H-z).$$

For $z = 0$ we have $\varsigma' = -\eta$,

$$\frac{\partial \eta}{\partial t} = -H\frac{\partial u}{\partial x}, \quad \text{and thus} \quad \frac{\partial \varsigma'}{\partial t} = -\frac{(H-z)}{H}\frac{\partial \eta}{\partial t}.$$

If we further assume that at $t = 0$, $\eta = \varsigma' = 0$ then we can write

$$\varsigma' = -\frac{(H-z)}{H}\eta.$$

In other words, the isopycnal displacements are proportional to the surface displacement and vary linearly with depth. Although this result assumes a purely barotropic response, it leads to better estimates of boundary salinities than simply prescribing values that vary independently of the flow conditions. Since the baroclinic response of the inlet at the mouth will not, in general, be known *a priori* this would seem to be the best that can be done for specifying more realistic boundary salinities. Data from CTD casts taken in

Burrard Inlet and Indian Arm between November 25, 1974 and March 7, 1975 were used to provide boundary conditions at the model mouth. Values of σ_t calculated from salinity and temperature at each standard depth were converted to model salinities using the linear equation of state (3.9).

Depths from CTD measurements are referenced from the surface, whereas model depths are referenced from a fixed datum. It was therefore necessary to transform the σ_t values to the model coordinate system.

Consider a CTD cast made when the tidal elevation is η. An isopycnal at depth d' as measured from the surface will be at depth $d = d' - \eta$ measured from the model datum. In addition, the isopycnal will be displaced a vertical distance $\varsigma(z_0)$ from a depth z_0 due to the barotropic tide. We can write

$$d = d' - \eta = z_0 - \varsigma(z_0),$$

$$\text{or} \quad z_0 = d' + \varsigma(z_0) - \eta. \tag{4.28}$$

Let us assume that $\varsigma(z)$ varies linearly with depth and satisfies $\varsigma(0) = \eta$ and $\varsigma(H) = 0$, where H is the local depth. Thus, we have $\varsigma(z) = \eta(H - z)/H$. Substituting for $\varsigma(z_0)$ in (4.28) yields

$$z_0 = d' - \eta\frac{z_0}{H},$$

$$\text{or} \quad z_0 = d'\left(\frac{H}{H+\eta}\right).$$

If H' is the measured depth at the time of the CTD cast then $H' = H + \eta$ and

$$z_0 = d'\left(\frac{H'-\eta}{H'}\right).$$

This gives the depth, measured from the datum, at which an isopycnal would be located if the tidal elevation was zero — assuming a purely barotropic response.

The first step in applying this result involved calculating z_0 for each depth d' and for each time at the station Van-24, which is the closest to the mouth of the model. Given these depths the corresponding σ_t values were linearly interpolated onto model depths

$z_i = i\Delta z$, where $\Delta z = 10\,m$. σ_t values were converted to salinity values using the equation of state.

Salinity values corresponding to six times and four depths were interpolated in time using a cubic spline under tension. Spline coefficients were stored and inputed by the model to reconstruct boundary salinities at any time within the sampling interval. The values $S_i'(t)$ corresponding to the salinity at time t were assumed to be at a depth $d_i = z_i - \zeta_i(t)$, where $\zeta_i(t) = (H - z_i)\eta(t)/H$. The salinity at z_i was then calculated by linear interpolation using

$$\begin{aligned} S_i(t) &= S_i'(t) + \frac{z_i - d_i}{d_{i+1} - d_i}[S_{i+1}'(t) - S_i'(t)] \\ &= S_i'(t) + \frac{(H - Z_i)\eta}{\Delta z(H + \eta)}[S_{i+1}'(t) - S_i'(t)]. \end{aligned}$$

4.7.2 River discharge

Provision was made for the addition of fresh water discharge at the surface of any of the model columns. As with the salinity at the mouth, tensioned splines were fitted to prescribed time series of river volume discharge (in $m^3\,s^{-1}$) for each location where it was to be added. In the model an elevation increment $\Delta\eta_j = Q_j(t)\Delta t/A_j$ was added to column j at each time step for volume discharge $Q_j(t)$, and surface area A_j.

4.8 Numerical Stability

The stability properties of the FDEs used in the model cannot be easily investigated analytically due to the presence of nonlinear terms. The usual approach in this situation is to consider a linearized set of equations. In general we seek to express the system of FDEs in the form

$$\mathbf{X}_1^{n+1} = \mathbf{\Gamma}_1\mathbf{X}_1^n + \mathbf{\Gamma}_2\mathbf{X}_1^{n-1}, \tag{4.29}$$

where $\mathbf{X}_1^n$ is the vector of all variables at time step n and the $\mathbf{\Gamma}_i$ are coefficient matrices. Defining $\mathbf{X}_2^n \equiv \mathbf{X}_1^{n-1}$ we can write

$$\mathbf{X}^{n+1} \equiv \begin{pmatrix} \mathbf{X}_1 \\ \mathbf{X}_2 \end{pmatrix}^{n+1} = \begin{pmatrix} \mathbf{\Gamma}_1 & \mathbf{\Gamma}_2 \\ \mathbf{I} & \mathbf{0} \end{pmatrix} \begin{pmatrix} \mathbf{X}_1 \\ \mathbf{X}_2 \end{pmatrix}^n \equiv \mathbf{\Gamma}\mathbf{X}^n, \tag{4.30}$$

where $\mathbf{\Gamma}$ is the *coefficient* matrix for the system.

An *amplification* matrix, $\mathbf{G}$, for the system of finite difference equations presented by (4.30) can be defined by substituting a Fourier component, $\mathbf{X}_j^n \equiv \alpha^n e^{ij\theta}$, of $\mathbf{X}^n$ into (4.30), where α is a complex constant. This yields the linear system

$$\mathbf{X}_j^{n+1} = \mathbf{G}\mathbf{X}_j^n.$$

For stability we require that the spectral radius, λ, of $\mathbf{G}$ satisfies $\lambda \leq 1$, where the spectral radius is defined as $\max_i\{|\lambda_i| : \lambda_i \text{ is an eigenvalue of } \mathbf{G}\}$. $\mathbf{G}$ is a sparse, square matrix of dimension equal to the number of independent governing equations.

Although this provides a concise mathematical formulation of the stability criterion, the problem of determining λ makes this general approach difficult to apply in practice. Considerable success has been achieved by combining stability calculations for much simpler decoupled systems with numerical tests. In practice, the former provides an approximate guideline for specifying the time increment which may be refined by trial and error.

As an example, consider the one-dimensional, linearized advection-diffusion equation for a variable $\Phi(x,t)$: $\quad \Phi_t + c\Phi_x + K\Phi_{xx} = 0$ where c and K are constants. In centred finite difference form this becomes

$$\Phi_{j,n+1} = \Phi_{j,n-1} - \frac{2\Delta t}{\Delta x} c\,(\Phi_{j+1,n} - \Phi_{j-1,n}) - \frac{2\Delta t}{\Delta x^2} K\,(\Phi_{j+2,n-p} - 2\Phi_{j,n-p} + \Phi_{j-2,n-p}) \tag{4.31}$$

for grid i and time step n, and where we allow $p = 0$ (unlagged) or 1 (lagged). Using von Neuman analysis we substitute a single Fourier component of Φ into (4.31) given by

$$\alpha^n e^{ij\theta} \equiv A_{jn} e^{2\pi i(jk\Delta x - n\omega\Delta t)},$$

where α is complex. Upon substitution we obtain

$$\alpha^2 + \alpha 2ia \sin\theta + \alpha^{1-p} b(\cos 2\theta - 1) - 1 = 0, \tag{4.32}$$

where $a = 2c\Delta t/\Delta x$ and $b = 4K\Delta t/\Delta x^2$. Of interest are the two solutions to (4.32). For stability we require that $|\alpha| \leq 1 \quad \forall\theta$. The existence of two solutions is characteristic of

centred time schemes, and may lead to severe problems through the appearance of two distinct solutions at alternate time steps — eventually leading to instabilities. The unwanted solution is referred to as the *computational mode* and must be filtered out periodically using some form of smoothing. Further discussion of this aspect of the computation is postponed to the next section. Consider first the purely advective case (K=0). (4.32) reduces to

$$\alpha^2 + \alpha 2ia \sin\theta - 1 = 0,$$

which has the roots

$$\alpha = -ia \sin\theta \pm \sqrt{1 - a^2 \sin^2\theta}.$$

If $a^2 > 1$ then letting $\theta = \pi/2$ yields a root $|\alpha| = a + \sqrt{a^2 - 1} > 1$, and the scheme is unstable. If $a^2 \leq 1$, on the other hand, then $|\alpha|^2 = a^2 \sin^2\theta + (1 - a^2)\sin^2\theta = 1 \quad \forall\theta$, and the method is stable. Thus, we require that $\Delta t \leq \Delta x/(2c)$ — the C.F.L. criterion. The largest value of c to be found in the model will be associated with the phase speed of a shallow water wave given by $c = \sqrt{gH}$, where H is the maximum depth in the model.

The second case arises when $c = 0$ and $K > 0$. (4.32) then reduces to

$$\alpha^2 + \alpha^{1-p} b(\cos 2\theta - 1) - 1 = 0. \tag{4.33}$$

Letting $p = 0$ we obtain the root

$$\alpha = \frac{-b(\cos 2\theta - 1) + \sqrt{b^2(\cos 2\theta - 1)^2 + 4}}{2},$$

which is greater than 1 for all values of b when $\cos 2\theta \neq 1$. Thus, for unlagged diffusion the scheme is always unstable. Letting $p = 1$ (lagged case) leads to

$$\begin{aligned} |\alpha|^2 &= |1 + b(1 - \cos 2\theta)| \\ &= |1 - 2b \sin^2\theta| \\ &\leq |1 - 2b| \leq 1 \end{aligned}$$

provided $2b \leq 1$ or $\Delta t \leq \Delta x^2/(8K)$.

A more general discussion of numerical properties for the finite difference schemes used in the surface (barotropic) mode calculations — including accuracy and phase errors — is presented in Appendix C.

4.9 Time-splitting instability

The problem arising from the generation of the computational mode mentioned above was removed by periodically smoothing the solution. Every 25 iterations each dependent variable (denoted by Φ) was adjusted using the following steps (*Kurihara*, 1965).

1. $\Phi_{ij2} \longleftarrow 0.5\Phi_{ij2} + 0.25(\Phi_{ij1} + \Phi_{ij3})$

2. $\Phi^*_{ij} \longleftarrow \Phi_{ij1} + \Delta tE(\Phi_{ij2})$

3. $\Phi_{ij3} \longleftarrow \Phi^*_{ij} + \Delta tE(\Phi^*_{ij})$

Here, $\Delta tE(\Phi)$ denotes the increment from the relevant *forward* (first order accurate) time stepping finite difference scheme evaluated using the prescribed value of Φ. This process — called the *Euler backward method* — has been used by *Blumberg* (1975). Prior to implementing this approach the time-splitting could only be controlled using extremely large values for the diffusion coefficients.

5. Preliminary Numerical Experiments

Four classes of simulations were performed using the laterally integrated (XZT) numerical model with increasingly complex geometries, initial, and boundary conditions. This was done to validate the model before advancing to analytically intractable problems and to simulate dynamics under relatively simple conditions where the lack of complexity allows for a better understanding of model performance. The first simulation class was unique in that an exact analytical solution was compared with the output from the model. *Table* 20 summarizes the various parameter values used in each simulation class.

Table 20
Summary of parameter values for each XZT model simulation class

			Simulation class			
param.	*definition*	*units*	1	2	3	4
Δt	Time increment	*seconds*	1200	30	20	20
Δx	Horiz. grid spacing	*km*	40	2	2	2
Δz	Vert. grid spacing	*m*	2	10	10	10
N	No. of columns	—	36	18	19	17
M	Max. no. of rows	—	4	10	19	21
ρ	density	$g\,cm^{-3}$	1.0	varies	varies	varies
$N^{(x)}$	Horiz. eddy viscosity	$cm^2\,s^{-1}$	0	0	10^5–10^6	10^5–10^6
$K^{(x)}$	Horiz. eddy diffusion	$cm^2\,s^{-1}$	0	0	10^5–10^6	10^5–10^6
$N^{(z)}$	Vert. eddy viscosity	$cm^2\,s^{-1}$	0	0	1	0–1
$K^{(z)}$	Vert. eddy diffusion	$cm^2\,s^{-1}$	0	0	1	0–1
k_H	Bottom friction	—	linear	no	no	varies
k_S	Side friction	—	no	no	no	varies
	Nonlinear	—	no	yes	yes	yes
	Periodic forcing	—	12 *hr*	none	M_2	K_1,O_1,P_1 M_2,N_2,S_2

5.1 Class 1: Linear bottom friction. Constant width

This experiment simulated unstratified tidal flow in a rectangular box of constant depth (H) with linearized bottom friction and a single forcing frequency of small amplitude used to drive the surface elevation at the mouth. Lateral homogeneity was assumed together with a balance in the horizontal momentum equation between local acceleration, the horizontal pressure gradient, and the vertical gradient of a linearized stress term. Formally, we have

$$\frac{\partial u}{\partial t} = -g\frac{\partial \eta}{\partial x} - \frac{\partial \tau}{\partial z}, \tag{5.1}$$

$$\frac{\partial w}{\partial z} = -\frac{\partial u}{\partial x}. \tag{5.2}$$

Integrating (5.1) vertically from the surface to the bottom yields

$$\int_{-\eta}^{H} \frac{\partial u}{\partial t}\, dz = -g(H+\eta)\frac{\partial \eta}{\partial x} - [\tau(H) - \tau(-\eta)].$$

Assuming that $\tau(-\eta) = 0$, denoting $\tau(H)$ by τ_H, and defining

$$U = H^{-1}\int_0^H u\, dz$$

we have

$$\frac{\partial U}{\partial t} + H^{-1}\left(\frac{\partial}{\partial t}\int_{-\eta}^{0} u\, dz - u(-\eta)\frac{\partial \eta}{\partial t}\right) = -g\frac{(H+\eta)}{H}\frac{\partial \eta}{\partial x} - \frac{\tau_H}{H}.$$

For $\eta \ll H$ and slowly varying with time, we can ignore the bracketed term to the left of the equals sign, and replace $(H+\eta)/H$ by 1. Vertically integrating (5.2) yields

$$w(H) - w(-\eta) = -\int_{-\eta}^{H} \frac{\partial u}{\partial x}\, dz$$

which we can rewrite using $w(H) = 0$ and $w(-\eta) = -d\eta/\,dt$ as

$$\frac{\partial \eta}{\partial t} = -H\frac{\partial U}{\partial x} - \frac{\partial}{\partial x}\int_{-\eta}^{0} u\, dz.$$

The vertically averaged equations corresponding to (5.1) and (5.2) under the same assumptions as above are

$$\frac{\partial U}{\partial t} = -g\frac{\partial \eta}{\partial x} - \frac{\tau_H}{H}, \tag{5.3}$$

$$\frac{\partial \eta}{\partial t} = -H\frac{\partial U}{\partial x}. \tag{5.4}$$

Assuming τ_H, the bottom stress per unit mass, to have the linear form

$$\tau_H = Hk_H U, \tag{5.5}$$

a solution to (5.3) and (5.4) using (5.5) — with periodic forcing at the mouth of amplitude δH and angular frequency ω — is given by *Ippen* (1966) as

$$\eta(x,t) = \delta H e^{-\mu x}\cos(\omega t - kx), \tag{5.6}$$

$$U(x,t) = \delta c_0 e^{-\mu x}\frac{k_0}{\sqrt{\mu^2 + k^2}}\cos(\omega t - kx + \alpha), \tag{5.7}$$

Table 21
Additional parameters required for Class 1 runs

parameter	*definition*	*value*
ω	$2\pi/T$	$1.45 \cdot 10^{-4}\, s^{-1}$
T	wave period	$12\, hours$
c_0	$\sqrt{gH}$	$9.40\, ms^{-1}$
k_0	ω/c_0	$1.47 \cdot 10^{-7}\, cm^{-1}$
k	$k_0(1-\beta^2)^{-\frac{1}{2}}$	$1.57 \cdot 10^{-7}\, cm^{-1}$
μ	$k\beta$	$2.62 \cdot 10^{-8}\, cm^{-1}$
β	$(-\omega + \sqrt{\omega^2 + k_H^2})/k_H$	0.168
α	$\tan^{-1}(\mu/k)$	9.49°
δ		10^{-4}
A_{mouth}		$9 \cdot 10^7\, cm^2$
$\langle U\eta \rangle$		$-3.303 \cdot 10^{-6}\, cm^2 s^{-1}$
$\langle U\tau \rangle$		$7.403 \cdot 10^{-7}\, cm^4 s^{-3}$

where definitions, and values of parameters used in (5.6) and (5.7) are listed separately in *table* 21.

Solution (5.6) and (5.7) is a damped, purely progressive wave. To simulate this solution with a model having a reflecting boundary condition it is necessary to have sufficient damping so that the wave amplitude at the closed boundary is negligible. The parameter values in *table 21* provide for an e-folding length of 382 *km*, and a total damping factor over the length of 0.023.

The simulation was run for 216 iterations (12 periods). *Figure* 22 shows graphs of the analytical and model solutions at hour 96 as a function of distance from the mouth. The error in the model ranges from 1–5% of the value at the mouth.

There is a steady state balance between the flux of energy into the inlet across the mouth and the dissipation within the inlet. Recalling equation (3.34) and integrating over the inlet volume leads to

$$\int_{mouth} \rho g \langle U\eta \rangle \, dA = -\int_{bottom} \rho \langle U\tau \rangle \, ds \tag{5.8}$$

where the time average is taken over a tidal cycle, and the integrals are over the cross-sectional area at the mouth, and the length of the inlet between the mouth and head,

respectively. The results for the simulation are given by (*table 21*)

$$\int_{mouth} \rho g \langle U\eta \rangle \, dA = -2.92 \cdot 10^5 \, g\, cm^2\, s^{-3} \quad (erg\, s^{-1}),$$
$$-\int_{bottom} \rho \langle U\tau \rangle \, ds = -2.96 \cdot 10^5 \, g\, cm^2\, s^{-3} \quad (erg\, s^{-1}).$$

We conclude that the flux of energy into the system is very nearly balanced by the dissipation due to bottom friction.

5.2 Class 2: Nontidal density flow down a slope (nondissipative)

The first calculations using the baroclinic option in the model investigated the intrusion of dense water into a flat bottomed basin of constant width with a linear slope leading down from the open boundary (*figure* 23). Dissipation, initial velocities, and velocities at the mouth were set to zero.

The development of the flow shown in *figure* 24 illustrates the model's ability to simulate realistic density currents, and reveals several interesting features. A clockwise circulation is quickly established in the vicinity of the dense water mass as the flow begins. Maximum currents at hour 5 are close to $20\, cm\, s^{-1}$ and as the water mass flows down the gentle slope (0.29°), a pronounced elevated head is established along the leading edge. By hour 10 there is evidence of internal waves in the highly stratified surface layer, and currents are less than $25\, cm\, s^{-1}$. At hour 20 there is an indication that the the density flow is separating into a train of distinct waves. This becomes quite clear by hour 30 when interfacial waves are visible with wavelengths of approximately $6\, km$. The waves near the bottom have the same length, but are 180° out of phase with the interfacial waves. A third wave begins to appear before hour 40, and by hour 60 the leading wave has reached the far wall, and begun to rise up due to its momentum. Maximum velocities during this interval are typically $25\, cm\, s^{-1}$, and are found near the bottom of the main density flow. By the end of the simulation the wave crest has moved to within $30\, m$ of the surface.

The mean flow speed estimated from successive positions of the leading edge of the dense water mass is approximately $15\, cm\, s^{-1}$. The density difference between the water

mass and the surrounding fluid is about $0.1\,kg\,m^{-3}$. According to *Benjamin* (1968) the theoretical propagation speed (c) for this type of flow should be given by

$$c^2 = 2gH\frac{\Delta\rho}{\rho_0},$$

where H is the height of the flow behind the head. The wave-like behaviour of the flow in this region makes it difficult to accurately determine a value for H. A nominal value of $15\,m$ was selected based on a visual inspection of *figure* 24. Using this value and setting $\rho_0 \approx 1020\,kg\,m^{-3}$ leads to a value for c of $17\,cm\,s^{-1}$. Thus, there is good agreement between the observed and theoretical flow speeds.

5.3 Class 3: Circulation in a constant width inlet.

These simulations were performed to investigate the behaviour of the model using more realistic geometry, but without the complication of variations in breadth. The basin geometry was selected to approximate Indian Arm and Burrard Inlet (*Figure* 25).

Initial velocities and surface elevations were set to zero, and the initial salinity distribution was selected to yield a constant squared Brunt-Väisälä frequency (N^2) equal to $5.19 \cdot 10^{-5}\,(\mathrm{rad/sec})^2$ throughout the basin. For an M_2 internal tide this leads to a first mode wavelength (λ_1) equal to $2\pi\omega/c_1 = 20\,km$, where $\omega = 1.405 \cdot 10^{-4}\,s^{-1}$, and $c_1 = 44.7\,cm\,s^{-1}$. This value for c_1 is derived from the solution of (B.12) with $w(0) = w(H) = 0$, which for constant N^2 admits the solution

$$w_n(z) = \sin\left(\frac{\sqrt{N^2-\omega^2}}{c_n}\,z\right), \qquad c_n = \frac{H\sqrt{N^2-\omega^2}}{n\pi}.$$

This stratification should give rise to long internal waves for simulations with tidal forcing.

5.3.1 Class 3.1: Nontidal density flows

The first test modelled the effect of a density flow resulting from the presence of a more saline parcel of water at the top of a gentle slope in the absence of tidal forcing. *Figure* 26 shows the evolution of the density field at 25 hour intervals, while *Figures* 27–30 show time series at four model segments. The surface elevation at the mouth was held fixed at zero while the salinity there was increased linearly over 50 hours, then held constant (*figure* 27e). The density increase at the mouth was approximately one σ_t unit — a larger increase than would normally occur in nature, but one which results in a rapid exchange.

The upward displacement of the isopycnals by the flow is clearly evident in the snapshots. The time series, however, reveal that the density does not increase monotonically at each position in the inlet; rather it displays a complex wave-like behaviour superimposed upon a generally increasing trend. The plots of σ_t landward of the sill (columns 2, 7 and 10; *figures* 28–30c) all show an initial lag of from 1.5 to 2.5 days before the density begins to increase — reflecting the blocking action of the sill. There is an additional phase lag with increasing depth after the inflow begins. The isopycnals for different depths occasionally meet and combine due to the requirement that static instabilities are not permitted. In several instances the isopycnals separate a short time later.

Velocities reach their greatest magnitude a few days after the start of the inflow, then exhibit a complex decay. The largest speeds are in excess of $60\,cm\,s^{-1}$ and generally decrease away from the mouth. Speeds near the middle of the basin do not exceed $30\,cm\,s^{-1}$ and at the head are less than $6\,cm\,s^{-1}$. At column 19 there is an initial period of inflow below $30\,m$, and outflow above, that lasts for two days. The outflow continues after this between $20\,m$ and $30\,m$, and the inflow at $50\,m$. At $10\,m$ and $40\,m$, however, there is a periodic reversal in flow every 20 hours that lasts for a few cycles. The velocities inside the sill exhibit an extremely complex vertical structure (*figures* 28–29) with frequent reversals due, perhaps, to a modal response that varies continuously with the stratification. The flow near the head (*figure* 30) reverses after 6.5 days accompanied by the velocities at all depths approaching zero. This is required by continuity under conditions of very small

surface elevation changes.

The vertical fields of velocity vectors and isopycnals reveal an initial compression and tilting of the isopycnals seaward of the sill as the density flow develops. The strong stratification at the mouth evident beginning at hour 25 is an artifact of the boundary condition, and is strongly modified away from this region. A sharp pycnocline has developed by hour 50 just seaward of the sill within the first $20\,m$. A depression in the isopycnals is also evident in the lee of the sill — a feature that persists until hour 125. The isopycnals inside the inlet exhibit significant tilts between hours 50 and 175, after which they are nearly level again. The inflow penetrates to a depth of $150\,m$ by the end of the simulation, at which time water denser than at the bottom of the inlet exists only outside the sill, and below sill depth. In the absence of a further increase in density at the mouth, or tidal forcing, no further intrusion of dense water would be expected.

The velocity vectors indicate the development of a strong flow at middepths by hour 75, where currents in excess of $10\,cm\,s^{-1}$ persist through hour 125 below $50\,m$. The depth of this flow increases during this period from $110\,m$ to $150\,m$, and then diminishes rapidly in strength as the horizontal density gradient across the sill vanishes. An internal Froude number F_i can be defined as

$$F_i = \frac{U_{\max}}{c_i}, \tag{5.9}$$

where $U_{\max}$ is the maximum speed of the inflow in a vertical column, and c_i is the phase speed of the i^{th} vertical mode calculated using (B.12) and profiles of σ_t extracted at desired times. A plot of F_i (*figure* 31) for the first and second modes over the sill (column 12) against time indicates that a transition from supercritical to subcritical flow occurs between hours 50 and 100 for the first mode, while the flow is supercritical relative to the second mode until hour 125, and supercritical for all higher modes throughout the simulation. The first mode transition is evident in the fields of velocity vectors and isopycnals between hours 50 and 100 as a severe compression of the isopycnals over the sill, together with the formation of a depression in the isopycnals just landward of this location. The flow remains subcritical with respect to the first mode beyond hour 100, while it alternates

between subcritical and supercritical for the second mode. This behaviour is caused by the short period fluctuations in density and velocity noted above in the discussion of the time series.

5.3.2 Class 3.2: Unstratified tidal flow.

The next simulation applied semi-diurnal tidal forcing of the surface elevation at the mouth to drive the inlet circulation without stratification, and using the same constant width geometry described in the last section. The final velocity field and surface elevations were used to initialize subsequent stratified runs.

The residual circulation for this simulation was calculated by digitally filtering time series of velocity components and elevations at each grid point of the model in order to remove motions of diurnal period or shorter (*figure* 32). A circulation pattern consisting of counter rotating vertical eddies results in a surface divergence and subsurface convergence at the sill. This is in close qualitative agreement with analytical results obtained by *Ianniello* (1979) for a constant width inlet having depth variations. An additional region of inward flow exists in the basin below 120 m. The residual surface elevation is very nearly flat, with a range over the inlet of only 0.04 cm.

5.3.3 Class 3.3: Stratified tidal flow (Varying $N^{(x)}$ and $K^{(x)}$)

Two runs were performed using initial and boundary conditions that were identical except for values of the horizontal eddy coefficients, which were set to 10^5 and $10^6\ cm^2\ s^{-1}$ respectively. The density at the mouth was increased linearly over a period of 50 hours (*figure* 33). *Figures* 34–35 illustrate the effect on horizontal velocity and density of varying these coefficients. For the first 75 hours or so of the simulation there is little difference between the time series pairs. Amplitudes for the smaller value of $N^{(x)}$ and $K^{(x)}$ are perceptibly larger due to decreased dissipation of energy. As the intrusion begins, the amplitudes increase in both cases. For the weaker diffusion, however, this increase becomes unbounded — indicating for this simulation that a value in excess of $10^5\ cm^2\ s^{-1}$ is required to maintain numerical stability during the intrusion of dense water.

5.3.4 Class 3.4: Stratified tidal flow (long term simulation)

The final simulation with this geometry was designed to investigate the long term evolution of the density field subject to nearly stepwise increases in density at the mouth. Time series of horizontal velocity and σ_t have been plotted at four segments of the model, and fields of filtered velocities and isopycnals have been plotted at six times (*figures* 36–39 and *figure* 40).

The salinity at the mouth was increased linearly over 50 hours at two times in the simulation (*figure* 36). The density increase along the inlet in response to the resulting intrusion exhibits a significant phase lag, with the maximum densities at columns 10, 7, and 2 occuring approximately 3.5, 4.5, and 5.5 days, respectively, after the end of the density increase at the mouth. The strong inflow generates large amplitude waves at column 10 as indicated by the $10\,m$ time series in *figure* 37, but smaller amplitude waves at the other two locations inside the sill, where internal wave generation appears to be suppressed. Internal wave amplitudes above sill depth inside the inlet are larger after the inflow in response to the altered stratification, which has intensified above the sill and weakened below. Stratification near the sill is characterized by strong horizontal gradients (*figure* 40, hours 360, 420 and 840), which resemble those present in the purely density driven flow (*figure* 26, hour 50).

As with purely density driven flow, we find that the vertical velocity structure is complex. Inflow during the first intrusion of dense water occurs below $30\,m$ at the mouth (*figure* 36) and below $50\,m$ inside the sill (*figure* 37). Three tidal cycles after the time of peak outflow at $10\,m$ the flow at this depth reverses until the next intrusion event, and a three-layer flow structure develops at the mouth with outflow occuring at 20 and 30 metres. The flow inside the sill is multi-layered throughout the intrusion, with inflow below $60\,m$ at columns 7 and 10 (*figure* 40, hour 420). The residual isopycnals and velocity structure closely resemble the purely density driven flow described above (*figure* 26, hours 75–125).

The effect of the first intrusion was to strengthen the stratification above sill depth,

while weakening it below this level (*figure* 40, hour 720). The isopycnals have become level by this time and the residual velocities are markedly smaller.

The response to the second intrusion closely resembles the response to the first, particularly at columns 10, 7 and 2 (*figures* 37–39). In general, a similar vertical velocity structure results and σ_t time series exhibit a very similar response. A notable exception occurs at column 7, where the flow at 50 m is much different during the second intrusion. A comparison of *figure* 40 (hour 420) and *figure* 40 (hour 840) reveals comparable circulation patterns, although the later of the two extends deeper due to the weakened stratification.

5.4 Other tests of the model

Blumberg (1975) describes examples of other test simulations conducted with the XZT model. In a variation of the Class 1 test for linearized bottom friction in a box of rectangular cross-section a channel with linearly varying width was used. The solution for the surface elevation in this case becomes $\eta(x) = \eta_0\sqrt{B_0/B(x)}$. *Blumberg* finds good agreement between the model and analytical solution.

In another test, a comparison is made with observations of circulation in a flume connected at one end to a large resevoir where sinusoidal tides were generated, and at the other end to a vertical wall. Vertical eddy viscosity and bottom friction coefficients were set to values calculated from the observations. The horizontal and vertical grid spacings in the model were 6.45 m and 3.05 cm respectively, with the total flume length being 100 m. Good agreement was obtained for observed and modelled surface elevations.

The final test result discussed by *Blumberg* consisted of tidally-forced density flow in a channel of constant width and depth. Vertical eddy coefficients $K^{(z)}$ and $N^{(z)}$ were set to 1 and 2 $cm^2\,s^{-1}$ respectively, and the horizontal and vertical grid spacings were 4 km and 1.5 m respectively. The total length was 185 km, the depth 10 m, and the width 4 km. Comparison of the vertical profile of horizontal velocity with an analytical solution of the linearized governing equations was surprisingly good.

5.5 Conclusions

The model has been applied to several different geometries using a variety of initial and boundary conditions. Results have compared well with analytical solutions where these exist. The simulations of density and tidal flows for a constant width inlet have indicated the ability of the model to carry out long-term integrations with little apparent artificial diffusion, and to produce complex flows that exhibit properties consistent with those observed in nature. In addition, the final simulation revealed that properties of the residual flow structure are preserved under significantly different stratification conditions. Dense water intrusions penetrating to near bottom depths over periods of several days have been simulated. It was noted that the presence of a sill at the entrance to an inlet can effectively block or delay the intrusion of dense water into the basin, and clearly modifies the flow characteristics by introducing a constriction. Evidence of supercritical flow as measured by an appropriate internal Froude number was discussed, and the resulting effect on stratification over the sill noted. The definition of F_i in terms of the maximum horizontal current speed in a vertical column for nontidal density flows provides a convenient and effective description of the hydraulic nature of the flow. It was seen that for $F_i > 1$ the vertical density gradient increases dramatically (i.e., the isopycnals become *squeezed* together), while for periods and locations where $F_i < 1$ these gradients are reduced. Stratification below sill depth was significantly weakened by the simulated density flows, while above this level it was intensified.

Order of magnitude variations in the coefficients of horizontal diffusion of salt and momentum were found to weakly affect the amplitudes of the horizontal velocity and σ_t time series under pre-inflow conditions. Minimum values determined through experimentation were subsequently required to maintain numerical stability. A discussion of the effect on the solution of varying the vertical eddy coefficients is postponed to §6.2.4.

Finally, additional test results presented by *Blumberg* verify the performance characteristics of the XZT model under a variety of initial and boundary conditions, and within a wide range of basin geometries.

6. The Indian Arm, Burrard Inlet model

The final class of simulations modelled realistic flow dynamics in Indian Arm and Burrard Inlet by incorporating variations in topography (*figures* 41–42); elevations at the mouth (column 17) calculated from the seven largest tidal constituents (Z_0, M_2, K_1, P_1, O_1, S_2, and N_2); and initial stratification and time dependent density at the mouth based on CTD casts. Simulations were performed for both unstratified and stratified conditions; thereby providing a basis for comparing the barotropic and baroclinic response of Indian Arm. An extension of the simulation of stratified flow was designed to model the intrusion of dense water which occurred in mid-winter of 1974–75.

6.1 Initial and boundary values

Initial densities were prescribed at all internal grid points of the model using CTD cast data for November 25, 1974. Data were available for the standard stations and depths listed in *table* 22.

Table 22
σ_t data available for November 25, 1974 initial conditions used in Class 4 simulations (University of British Columbia, Dept. of Oceanography data report 37, 1974). See figures 1 and 3 for locations

station	*Depths (m)*
Van-24	0,2,5,10,15,20,30,40,50
Van-27	0,2,5,10,15,20,25
Van-34	0,2,5,10,15,20,30,40,50
Ind-0	0,2,5,10,15,20
Ind-1	0,5,10,15,20,30,40,50,60
Ind-1.5	0,5,10,20,30,50,75,100,125,150,175
Ind-2	0,5,10,20,30,50,75,100,125,150,175,200

Densities at these stations were converted to salinities using (3.9) with $\alpha_0 = 7.566 \cdot 10^{-4}$ and $\rho_0 = 0.9995$ (*Blumberg*, 1975). Linear spatial interpolation was used when possible where data were not available, otherwise values at a given depth at the nearest station were used (for example, landward of Ind-2).

The initial component velocity fields in the model were set to zero and a horizontal sea surface was prescribed for each of the first two model time steps (designated as relative

time levels 1 and 2 (or *past* and *present*), respectively). These were required to calculate the values of the solution variables for the first model iteration (relative time level 3 — or *future*). The initial surface elevations at each column of the model for the first two time levels were set to the corresponding tidal elevations calculated at station 7735 (Vancouver Harbour) using the six largest harmonic constants from the results of harmonic analysis (see §3.2.2). After several iterations of the model (less than a diurnal cycle) these initial conditions adjusted to a solution of the governing equations.

Prescribed boundary values consisted of surface elevation and salinities at column 17 — near tide gauge 7735, and CTD station Van-24. σ_t data from six CTD casts at Van-24 were linearly interpolated both vertically and in time to prescribe continuous open boundary salinities (*table* 23). Spatial interpolation was required because depths in the model, and for the CTD data, are referenced from different origins. The former references depths from a fixed datum in the model grid, while the field data is referenced from a sea surface elevation that fluctuates with the tide. The method of correction is detailed in §4.7.1. Base salinities were calculated by linearly interpolating the data listed for Van-24 in University of British Columbia Department of Oceanography cruise reports nos. 37 and 41. As in the previous simulations, upwind differencing of the finite difference expressions for the advective terms in the salt balance equation was done for the model column just inside the mouth in order to remove the influence of prescribed salinities during ebb tides.

Table 23
Base salinities prescribed at the open boundary of the model for Class 4 simulations. Actual salinities were modified according to details provided in §4.7.1

Time	Date	Depth (m)				
		10	20	30	40	50
13:50	Nov. 25, 1974	25.602	30.295	30.932	31.103	31.168
17:00	Dec. 05, 1974	27.481	28.080	29.754	30.163	30.163
11:40	Jan. 03, 1975	29.125	29.558	30.060	30.292	30.401
11:52	Jan. 23, 1975	29.178	30.821	31.050	31.166	31.221
14:06	Feb. 19, 1975	29.690	31.068	31.120	31.156	31.208
17:07	Mar. 07, 1975	28.910	30.982	31.125	31.206	31.261

6.2 Selection of coefficient values

The freely adjustable parameters in the XZT model consist of the vertical and horizontal grid spacings, time step, coefficients of horizontal and vertical eddy diffusion and viscosity, and bottom and side friction.

6.2.1 Grid spacings

The grid spacings were selected to be the same as for the Class 3 simulations described in the previous chapter. This choice was based on measurements taken in Indian Arm which indicate that water properties such as salinity and temperature vary sufficiently slowly over a horizontal spatial scale of 2 *km* (for example, *Gilmartin*, 1962 and *Davidson*, 1979). In addition, calculations of the wavelengths of the internal tidal constituents for winter stratification yield values of a few tens of kilometres, or several mesh lengths. A vertical spacing of 10 *m* provides a sufficient number of layers in the model to resolve the modal response of the inlet, although it is too large to resolve the thin, brackish, surface layer associated with freshwater discharge, and hence, cannot be used to model estuarine circulation in Indian Arm, where this layer is only a few metres deep.

6.2.2 Time step

The selected time step of 20 seconds satisfies the CFL criteria for explicit finite difference schemes discussed in chapter 4, which were found to be numerically stable. Fields of current vectors, isopycnals, and elevations from the model for each of the three relative time levels mentioned above were stored on 9-track magnetic tape at every hour of simulation time (180 iterations) for subsequent analysis. Saving values at all three time levels permitted the calculation of time gradients for each of the model variables.

6.2.3 Eddy diffusion and viscosity

Numerous studies of eddy diffusion and viscosity coefficients have been done, some of which are cited in the introduction to this thesis. No consensus exists as to a generalized dependence of these parameters on the stratification, mean flow, and model mesh size. While it has become clear that these coefficients almost certainly do not remain constant

in strongly stratified tidal flows, it has also become apparent that their specification in tidal models often becomes an exercise in fine-tuning model output to observations. It was decided that the use of constant coefficients in this study would simplify the analysis of model output, since the effect of variable coefficients on the solution might otherwise be difficult to isolate from other effects. It was also decided that it was not an objective of this research to perform an exhaustive evaluation of different methods for calculating eddy coefficient values, and more importantly, the observations needed to pursue such an objective must await future work planned on the results of studies like the present one.

6.2.3.1 Horizontal coefficients

A comparison of model results using four values of $N^{(x)}$ and $K^{(x)}$ indicates that a threshold exists below which excessive spatial oscillations eventually lead to numerical instabilities (*figures* 43–45). For the Indian Arm model this value is somewhat greater than $10^5\, cm^2\, s^{-1}$. Below this there is local intensification of salt on the upward slope, severe distortion of isopycnals, and irregular distribution of velocity directions and magnitudes (*figures* 43–45, a and b). These features are not present using values of $5 \cdot 10^5$ and $10^6\, cm^2\, s^{-1}$ (*figures* 43–45, c and d). Furthermore, the results using the latter two values are very similar, indicating a weak dependence of the solution on the value of the horizontal eddy coefficients. Based on these tests, as well as those discussed in the preceding chapter, a nominal value of $10^6\, cm^2\, s^{-1}$ was selected for $N^{(x)}$ and $K^{(x)}$. It was felt that this choice would provide sufficient protection against numerical instabilities that appear for values near $10^5\, cm^2\, s^{-1}$, without adversely affecting the solution.

6.2.4 Vertical coefficients

Guided by the experimental and observed values of $N^{(z)}$ and $K^{(z)}$ discussed in the introduction, these coefficients were set at 0.0, 0.2 and $1.0\, cm^2\, s^{-1}$ to determine the effect of different values on the solution. In general the solution was insensitive to values in this range as shown by *figure* 75. In contrast, the residual plots showed significant differences in the details of the velocity field, although the distribution of density was not strongly

affected (*figure* 76).

As the analysis will show, these constant values for the horizontal and vertical eddy coefficients lead to good agreement with observations. In anticipation of future work, however, the equations were implemented in a way that permits variable coefficients to be easily included.

6.2.5 Friction coefficients

Selection of the bottom and side friction coefficients is included in the following discussion of the surface elevations in the model.

6.3 Surface Elevations

In §2.7 the dissipation of barotropic tidal energy in Burrard Inlet was estimated using the phase shift of the M_2 and K_1 tidal constituents between several tide gauge sites. Most of the dissipation was found to occur in the vicinity of Second Narrows as a result of the high velocities and resulting frictional drag that arises there.

It is shown below that there is no appreciable phase shift in either of these constituents across Second Narrows in the absence of side friction in the model. Horizontal and vertical diffusive terms do not provide a large enough sink for energy to account for the observed phase change. As well, the bottom friction term does not contribute significantly to dissipation in the model due to the relatively small velocities that occur there. In contrast, velocities at mid-depths were observed to be much larger; hence side drag at these depths leads to large dissipation rates (§3.2.6).

Side friction was found to be the controlling term in adjusting the dissipation rate to observed values, and agreement is good between observed and calculated surface elevation amplitudes and phases for the M_2 and K_1 tidal constituents after fine-tuning the side friction coefficient along the inlet (*figures* 46–47). Exact agreement between the model and station 7735 occurs since harmonic analysis at this station was used to calculate surface elevations at the mouth of the model. Error bars are not provided at station 7747 because the original time series was unavailable, and observed amplitudes for both constituents at

this station are somewhat smaller than adjacent values.

6.4 Tidal flow during a diurnal cycle

Figure 48 shows a diurnal cycle of model surface elevations and first three internal Froude numbers (F_i) over the inner sill, where $F_i = |\bar{U}|/c_i$, $\bar{U}$ is the vertically averaged horizontal velocity, and c_i is the phase speed of the i^{th} internal vertical mode. Times for a series of plots of surface elevation, velocity vectors, isopycnals, and momentum equation terms are indicated on this figure by the solid circles (*figures* 49–50). The upper (a) and lower (b) plots in *figures* 49–50 correspond to unstratified and stratified model simulations respectively. The fields of velocity vectors, isopycnals, and elevations (*figure* 49) have an inset showing the stage of the tide at the mouth (column 17); while the inset in *figure* 50 describes the position of each momentum equation term in the bar graphs. Each bar represents the sign (positive upward) and local *relative* magnitude of the corresponding term; that is, each bar graph has been normalized (scaled) to show the local balances.

Fields of velocity vectors, isopycnals and elevations are presented at eight stages of the tide: lower low water (LLW), maximum flood (LLW+4), higher high water (HHW), secondary ebb (HHW+3), higher low water (HLW), secondary flood (HLW+2), lower high water (LHW), and maximum ebb (LHW+4). These labels have been printed on the inset of each plot in *figure* 49.

For convenience, the following descriptive phrases are used in the subsequent discussions of model simulations: The *head* is at column 1; the *downward slope* refers to the bottom between columns 1 and 3 inclusive; the *upward slope* refers to the bottom between columns 6 and 10 inclusive; the *inner sill* refers to column 11; the *outer sill* refers to columns 14 and 15; and the *mouth* is at column 17.

6.4.1 LLW (hour 272)

The ebb has nearly finished, and the surface slopes gradually down from the mouth as the flow is about to turn to the flood. Currents are small and generally outward at all depths, with notable exceptions to this occurring in (b) near the bottom between the two sills, and at the mouth. In general, however, the velocity fields for the two cases are similar. The stratified flow is subcritical for all modes, and is characterized over the sill by a lifting of the isopycnals. Vertical displacement of isopycnals inside Indian Arm indicates the presence of internal waves.

The momentum balance (*figure* 50) in the deep basin in (a) is between the acceleration and barotropic pressure gradient everywhere except near the middle of the upward slope, where horizontal advection and viscosity are important. The balance between the sills is supplemented by friction and advective terms. Side friction dominates in the narrows just outside the inner sill.

The baroclinic pressure gradient in (b) dominates (except close to the surface) in the main basin (between segements 3 and 7), but elsewhere balances remain primarily between the barotropic pressure gradient and local time acceleration.

6.4.2 LLW+4 (hour 276)

Velocities (*figure* 49) at maximum flood over the outer sill have reached nearly $80\,cm\,s^{-1}$, and the flow is critical or supercritical (*figure* 48) for all internal modes. Currents are directed inward everywhere except below $40\,m$ between the sills, where weak flow reversals occur in both (a) and (b). Strong horizontal and vertical density gradients are apparent in (b) seaward of the inner sill and large isopycnal displacements are evident below middepths in the deep basin, and near the inner sill. A level of small velocities exists in the basin at $40\,m$. The velocity fields are again similar for the two cases except in the region between the sills.

The momentum balance in (a) has been complicated by major contributions from viscous and advective terms at almost all locations. Horizontal viscosity is important near

the head, while vertical advection is important at several shallower locations in the deep basin, and at the bottom inside the sill. Side friction is significant over most of the region near, and seaward of the inner sill.

The baroclinic pressure term in (b) is large in the deep basin, but of decreasing importance toward the surface. A complex balance exists on the upward slope near the inner sill. At the bottom between the sills the balance is almost purely between the two pressure gradients — contrasting with the unstratified case where side friction and vertical advection are important.

6.4.3 HHW (hour 279)

The surface is very nearly flat (within about $0.6\,cm$), and currents are small — the flow having once again become subcritical for all modes. Weak vertical eddies are in evidence on either side of the inner sill, while currents in the basin show no preferred direction in (a). Currents in (b) closely resemble those in (a) at most locations, except near the bottom of the upward slope where significantly larger velocities are apparent in (b) at $50\,m$. In addition, there is a weak jet extending halfway along the basin in (b), that is much less in evidence in (a). Depression of the isopycnals occurs just inside the inner sill, and strong horizontal density gradients are evident over the sill region.

The dominant balance between acceleration and surface slope has returned throughout most of the inlet in (a). In the shallows, and on the upward slope near the sill, contributions from other terms are important, however. In general, the balances resemble those found at LLW. As before, we find that the baroclinic term in (b) is of greater importance at shallower depths throughout most of the basin, although the opposite is true at the head. Acceleration is balanced by both pressure terms immediately landward of the inner sill.

6.4.4 HHW+3 (hour 282)

The surface elevation drops 12 cm between the inner sill and the mouth, and velocities are outward everywhere — reaching 30 $cm\,s^{-1}$ near the outer sill. The flow over the sill is subcritical for the first two modes, and is once again larger for (b) inside the basin below middepths than in (a). Currents in the shallows are similar in both cases. Isopycnal displacements are greater than 10 m below 80 m in the basin, and evidence of wavelike features with an approximate length of 20 km appears at this depth. The slope of the isopycnals in this region is opposite to that found three hours earlier near slack water.

The momentum balance is complex, with most locations having three or more significant terms. Near the inner sill the surface slope is balanced by side friction in both simulations. Side friction is important between the sills in (a), while it is replaced by the baroclinic pressure gradient in (b). A simple balance between acceleration and the surface slope exists in (b) near the surface of the deep basin. The flow is also accelerating near the head and bottom of Indian Arm.

6.4.5 HLW (hour 285)

The surface slope and currents are small — although the latter are somewhat larger seaward of the inner sill — and flow is subcritical everywhere. Isopycnal displacements are large, however, with a range in excess of 20 m below middepth. Again there is evidence of waves with lengths close to 20 km, or approximately twice the length of the deep basin. A somewhat stronger flow is evident in (b) at the bottom between the sills, and near the bottom of the upward slope.

The momentum balances have simplified to that of other slack times, and share many similar features. The only region of (a) that is somewhat complex is immediately landward of the inner sill, where horizontal advection and viscosity are important. The balance for stratified flow includes a contribution from the baroclinic pressure gradient that once again dominates near the bottom of the basin, while becoming less important near the surface.

6.4.6 HLW+2 (hour 287)

The surface slope has changed little, currents remain small, and flow is subcritical for the first two modes. Currents in (b) are noticeably larger than in (a) at the bottom between the sills, and at the bottom of the upward slope — a pattern observed at other peak flow times. Isopycnal displacement ranges have decreased in two hours from $20\,m$ to $10\,m$.

The momentum balances in (a) are significantly less complex than at other peak flow periods due to the small change in surface elevation. A balance between acceleration and surface slope dominates throughout most of the basin, with areas on the upward slope and near the inner sill being notable exceptions. Side friction is again important in the shallows as are advective and diffusive terms. Local acceleration is of importance in this region only between the sills and below sill level. The region in (b) at the bottom of the basin exhibits a complex balance.

6.4.7 LHW (hour 290)

The surface slope has reversed as the flow is changing to an ebb, and flow is subcritical everywhere. The strongest currents are found at the bottom between the sills, and in (b) there is once again evidence of stronger flows at the bottom of the upward slope. In addition, there is a weak jet at $50\,m$ in (b) that is likely a result of a small density flow. Isopycnals have reversed their slope, displacement ranges are $15\,m$, and wavelengths of close to $20\,km$ are still in evidence.

The simple momentum balance in (a) resembles that of HLW. Acceleration and surface slope dominate except between the sills and on the upward slope near the sill. The balance in (b) is much more complicated, with the baroclinic pressure gradient becoming important near the head and at the bottom of the basin. Advective and diffusive terms are important for a small region near the head.

6.4.8 LHW+4 (hour 294)

This last phase represents the second period of strong flow. Currents are outward at all depths, with no flow reversals occurring, and the flow is subcritical for only the first mode. This is in contrast to LLW+4 where a reversal was found at depth between the sills. Isopycnal displacements are small inside the basin — attaining a maximum range of $5\,m$. Isopycnals strongly resemble those at hour 272, with a large upward displacement over the sill.

The momentum balance inside the basin is somewhat more complex in (a) than in (b). There are significant contributions from advective and diffusive terms throughout this region in (a), while in (b) the balance is primarily between the two pressure gradients. Closer to the inner sill region and narrows the balance is increasingly influenced by nonlinear and diffusive terms.

6.4.9 General Conclusions

This series of velocity vectors, surface elevations, and isopycnals from unstratified and stratified flow illustrate the complexity of inlet flow dynamics in the model. Rarely is the momentum balance dominated by a simple combination of terms as is often assumed for the analytical treatment of real flows. This is true not only in the shallow constrictions where nonlinearities would be expected to occur, but also in the deeper parts of the main basin during strong flows.

The specification of mixed tidal forcing, together with a fortnightly cycle, is important to the inlet response as indicated by the different balances that evolve for small and large changes in surface elevation. The higher velocities associated with the larger changes generate significant nonlinear and diffusive terms.

It is clear from these results that stratification is of fundamental importance to the flow field calculated by the model, and presumably in nature as well. Significant near-bottom currents were observed in the deep basin only in the stratified run. These currents — although less than 10 $cm\,s^{-1}$ — are significantly larger than those found in the unstratified

case. In addition, they exhibit a large phase shift with depth — a point that will be discussed again in §6.8 in the context of a modal response for Indian Arm. The isopycnal displacements exhibit persistent wavelike displacements with a typical amplitude of $10\,m$ and length close to $20\,km$.

The strong horizontal density gradients between the sills dominate the momentum balance in this region. Side friction is significant in the balance near the inner sill, while other terms contribute to varying degrees elsewhere.

Principal areas of complexity — as characterized by the momentum balance — occur on the slope leading up to the inner sill; in all regions between the sills; and, at times, in the deepest part of the inlet. The slight differences evident between hours 272 and 297 arise because the length of a diurnal cycle is not an integral number of solar days, and also because of longer period — for example fortnightly — variability in the signal.

6.5 Residual Flows

Quasi-residual flow fields and density distribution were calculated by digitally filtering time series from the unstratified and stratified runs described in the previous sections. A (30,50,40) digital filter (§1.3) was used to remove diurnal and higher frequencies at each grid point of the model. Thus, timeseries of 80 hours length at each grid point were passed through a filter with a roll-off between 30 and 50 hours. All plots of residual fields discussed in this thesis were derived in this way. Longer periods — primarily fortnightly — will still be present; affecting the magnitude of the residuals, although not the general conclusions. For example, the ratio between surface elevation amplitudes for the largest fortnightly constituent — the MF arising from the interaction of the K_1 and O_1 diurnal constituents — and the K_1 constituent at station Van-24 is about 0.02.

Figure 51 shows the filtered velocities and isopycnals for a time series of 100 hours centred at 14:00 December 2, 1974. The inset shows the response characteristics of the digital filter used. The residuals in (a) indicate a net landward inflow at the surface in the basin countered by a seaward flow below sill level. Very complex flow occurs at sill depth,

although with insufficient resolution to clearly isolate small, vertical, residual eddies such as appear to exist between the sills. Seaward of the outer sill the surface and deepest flows are outward with a compensating inflow at middepth. The residual flow below sill depth in the basin is relatively strong at about $1\,cm\,s^{-1}$, and a point of no motion seems to exist midway along the basin at a depth of $60\,m$. The largest residual velocities of $10\,cm\,s^{-1}$ occur between the two sills, and are directed toward the mouth.

The residual flow calculated from the stratified run is significantly different from the unstratified case, with numerous flow reversals in evidence inside the basin, and with horizontal flows tending to be more highly stratified, and in thinner layers than in the case of homogeneous density. A strong jet exists at a depth of $50\,m$ inside the sill, and persists throughout the length of the basin. Flows from $70\,m$ to $160\,m$ are very weak in (b), but increase markedly between $160\,m$ and $180\,m$, where a thin, cellular circulation system is present.

Contours of residual horizontal velocity for the same period appear in *figure* 52. These enhance the different flow regimes, and isolate areas of net inflow (dashed) and outflow (solid). The most noticeable difference occurs in the surface layer, where flow is in opposite directions. The residual surface displacement is very nearly the same in both cases — indicating that the dominant difference between the two is caused by the baroclinic pressure gradient. A comparison between *figure* 52a and *figure* 32b reveals the influence of variations in width on the residual circulation. While there is some qualitative similarity between the two figures — particularly in the near surface zone — there are many substantial differences. In particular, the latest model exhibits much more complicated vertical structure — leading one to question the validity of models based on simple geometry, and simple tidal forcing.

6.6 Time series plots

To complement the previous discussion of spatial variability in the model, time series of surface elevations and isopycnals were plotted for each column in the model (*figure* 53). The duration of each time series is 100 hours — approximately 4 diurnal cycles — and spans the period from 12:00 November 30, 1974 to 16:00 December 4, 1974. The midpoint — 14:00 December 2, 1974 — corresponds to the time of the residual plots in the previous section, which were obtained by digitally filtering the time series. In addition, time series of σ_t from three stations in Indian Arm and Burrard Inlet collected in the fall of 1983 over approximately a diurnal cycle have been plotted for comparison with output from the closest model locations (*figure* 54).

Time series of model output for columns 1–8 display regular diurnal and semi-diurnal fluctuations. Amplitudes are smallest at column 5 because — as will be shown later — this location is very near a horizontal node in a two-dimensional standing wave pattern established by the internal tide. Maximum amplitudes are on the order of $10\,m$ at columns 7 and 8, and generally increase with depth throughout the interior region. Column 5 appears to be an exception in that amplitudes are slightly larger in the surface layer. In a purely barotropic response it is expected that this would be observed since the vertical velocity decreases linearly with depth to a value of zero at the bottom. The distribution at column 5 is consistent with a mainly barotropic response.

Phase shifts with depth and the changing phase relationship between the isopycnals and the surface elevations are visible, but difficult to quantify from these plots. These properties are clearly visible in the cophase plots discussed in the next section.

From column 9 to the mouth, displacements become highly nonlinear in appearance. Fine details of the contour plots should be interpreted carefully in this region since many of the loops and closed regions result from the contouring program having to cope with regions of strong gradients and curvature. The general trends, however — especially the prominent semi-diurnal signal — are clearly real. The contours at column 17 reflect the

open boundary conditions provided to the model, showing how densities were increased linearly near the bottom with time, although this effect does not persist away from the mouth. The linear increase in the isopycnal displacements at the mouth as one approaches the surface can be readily seen, as can the in-phase relationship between surface elevations and isopycnals.

The plots comparing observations with model output indicate comparable isopycnal displacements and periods. There is likely to be significant aliasing of higher frequency internal wave motions in the observations since the sampling period in all cases was on the order of one hour or more. This would account for much of the irregularity apparent in the contours (esp. *figure* 54b, column 9). Nevertheless, there is a clear and strong semi-diurnal signal in the records. Measured isopycnal displacements have been corrected for the surface tide by subtracting the local tidal elevation — as calculated from harmonic analysis — from the measured depths to allow direct comparison with model output. Amplitudes at all three stations show good quantitative agreement, although phases are not in agreement; presumably because of differences in stratification between the model and Indian Arm at the time the data was collected.

6.7 Harmonic analysis

Harmonic analysis of the 14 day density and horizontal velocity time series discussed in the previous sections was performed at each grid in the model.

6.7.1 Horizontal Currents

Figure 55 shows the amplitudes and phases of the M_2 and K_1 constituents for both Cyclesonde and model current time series at two stations in Indian Arm. The Cyclesonde time series are from January, 1983, while the model series are from a simulation for December, 1974. This set of Cyclesonde data was extracted from the only one in existence — at the time of this analysis — for the mid-winter period in Indian Arm. The model simulation is part of a longer simulation of the renewal which occured in Indian Arm during the winter of 1974–75. A comparison of vertical density profiles and resulting modal structure at these

two times indicates similar stratification at column 7, while there is poorer agreement for column 10 (*figures* 10 and 12, and *figures* 56–57).

The overall trend of phase angle with depth for model and data is very similar. Small discrepancies can be attributed primarily to differences in stratification and statistical uncertainties. The Cyclesonde data, in particular, contains noise — in the form of nontidal signals — which increase the confidence intervals around the estimates.

In general, the plots of amplitude show poorer agreement than the phases. Several factors may contribute to this discrepancy. Differences in stratification may have a significant effect on the inlet response, particularly if a near resonance condition exists for one of the frequencies. Discrepancies in inlet cross-sectional area in the model and at the two locations would scale the amplitudes proportionately. Also, *Waldichuk* (1965) found significant cross-inlet variability for tidal currents in the narrows leading into Port Moody where currents are fairly large, with mid-channel speeds found to be approximately 1.3 times the cross-channel mean. Thus, the Cyclesonde at station 10 may have measured current speeds that exceed the lateral mean value. Finally, amplitudes are affected by the dissipation rate, which in turn is controlled by the coefficients of turbulent viscosity. It is felt that the agreement is as good as can be expected given the number and variety of the sources of error.

The agreement at station 7 for both constituents is quite good. In particular, the variability with depth of the K_1 constituent for both data and model match up well, although the model amplitude is consistently smaller. Agreement for the M_2 constituent is generally good as well, with the trend and magnitude for both amplitude and phase being comparable. At station 10 the data amplitudes are larger than for the model at all depths. Some of this can be accounted for by the differences in bottom profile and cross-sectional area between the Cyclesonde location and column 10 of the model. Amplitudes for the Cyclesonde should be approximately 10% greater because of this effect.

Plots drawn on the complex plane of amplitude and phase at various depths — some-

times called *Phase*, or *Argand* diagrams — for harmonic constants arising from the harmonic analysis of horizontal velocities were made for each column of the model. Argand diagrams from the unstratified simulation show small phase changes with depth (*figure* 58). Exceptions to this occur near the bottom — due to the presence of bottom friction — and at column 8. Greenwich phase angles for all columns are approximately 265° (see Appendix A for an explanation of Greenwich phases). The results for the stratified case are markedly different (*figure* 59), as large phase changes occur with depth at all stations within the deep basin. Seaward of column 10, however, the response differs little from the unstratified case.

Certain trends are apparent inside Indian Arm. Phase generally decreases with depth (anticlockwise being positive) for both constituents. Exceptions to this occur for the M_2 constituent at columns 2 and 3, and for some isolated points in the model. The trend at columns 2 and 3 is very pronounced, however.

An overall view of the variability of amplitude and phase along the inlet is obtained by plotting contours of these parameters (*figures* 60–63). Amplitudes and phases for the unstratified case show little variability within the main basin, are uniformly small, and approximately depth independent (*figures* 60–61). Large phase changes occur for the stratified case, however, in both the vertical and horizontal (*figures* 62–63). In addition, there is intensification of the amplitude in the vicinity of the upward slope — near the bottom of column 7. In particular, the amplitude of the M_2 constituent has increased by a factor of up to about four relative to the same point for the unstratified case (*figure* 62a). A somewhat weaker, but significant, intensification is also apparent for the K_1 constituent (*figure* 63a). This supports the observed current intensification remarked upon in the discussion of a representative diurnal cycle.

6.7.2 Salinity

Time series of salinity at each point in the model were harmonically analyzed in the same way as the horizontal currents; however no equivalent data sets were available for comparison. Several interesting features are visible in the resulting co-range and co-phase plots for the M_2 and K_1 constituents. (*figures* 64–65). The most striking features are pronounced 180° phase shifts in the vicinity of columns 4 and 5 below $40\,m$; between columns 5 to 10 above $40\,m$; and — for the M_2 constituent only — near the head, and on the inside of the inner sill. In addition, at column 5 there is a vertical jump of 180° in the phase at $130\,m$ for the M_2, and at $70\,m$ for the K_1. Sudden shifts of 180° are indicative of a standing wave pattern, and in the vicinity of these shifts the amplitudes should be at a minimum. This is clearly evident in *figures* 64a and 65a. A pure standing wave should not exhibit any phase change between nodes. This is approximately the case for both constituents, although there is some indication of small along-inlet phase changes between nodes characteristic of progressive waves. Clearly, the internal tide generated by the model inside Indian Arm is very complicated, and cannot be simply characterized.

In general, evidence of a progressive internal tide in an inlet indicates that energy is being dissipated, either due to absorption at solid boundaries, or by a transfer of energy to different frequencies through nonlinear processes. *Stigebrandt* (1976) has proposed breaking of internal waves at solid boundaries of an inlet as a mechanism for mixing. The co-phase diagrams for the model simulation indicate that the internal tide is not releasing a substantial amount of energy by breaking against the bottom. This leaves open the interesting possibility of resonance inside the inlet given suitable matching between the natural periods of internal oscillation for the Indian Arm model and the tidal forcing periods. Observations of internal resonance cited in the introduction for other inlets support the *possibility* — without indicating the *likelihood* — of this occurring in Indian Arm. Of particular concern to conclusions formed from model results are the influence of islands — which are omitted from the model — bends, other topographical features, and discretization of the bathymetry, on the reflection criteria for internal tides in Indian Arm. Only

further observations of the inlet response will allow speculations concerning standing wave and resonant phenomena in Indian Arm to become definite conclusions.

6.8 Modal structure in the Indian Arm model

A vertical mode decomposition of the along-inlet current from the model was performed to investigate the modal response of the Indian Arm model to tidal forcing. Time series of σ_t at each point in the model — centred at the same time as the series used in the harmonic analysis described above — were smoothed using a (30,50,40) digital filter to yield residual, vertical profiles of density. Subsequently, the method described in Appendix B was applied to these profiles to yield estimates of the barotropic and first 5 baroclinic modes. The modes were then fitted to the results of the harmonic analysis (*figures* 66–67), and the distribution of kinetic energy between modes for each column in the model was calculated as described in Appendix B (*figures* 68–71). In most cases the modes fit the harmonic analysis results very well. The principal exceptions occur at column 9, where the fitted functions for both M_2 and K_1 constituents display excessive curvature due to the inclusion of higher modes. This was required by the least-squares fitting routine to cope with the large amount of scatter in the calculated harmonic constants. The plots of energy distribution suggest several conclusions.

The main energy balance for the M_2 constituent from column 3 to 7 (i.e., inside the deep basin) is between the barotropic and first baroclinic modes (*figure* 70). The first baroclinic mode dominates at the head, while the barotropic mode dominates seaward of column 7. The contribution of higher modes is less than 10% at all positions along the inlet.

The K_1 constituent displays a somewhat different behaviour along the inlet. The contribution near the head from the barotropic mode is greater than 60% — in contrast to less than 20% for the M_2. The contribution from the first baroclinic mode increases monotonically as one progresses toward the inner sill to a maximum of more than 80% near column 7; then decreases dramatically as the contribution from the barotropic mode

increases. In addition, the contribution from the second mode is greater throughout the inlet than for the M_2 — reaching a maximum contribution of 25% in the deepest part of the inlet.

The excitation of the baroclinic modes is most apparent in the deepest sections of the basin where the bottom is relatively flat; whereas seaward of the inner sill the flow is dominated by the barotropic component, and total energy levels are one to two orders of magnitude higher than in the basin (*figures* 68 and 69). *Stigebrandt* (1981) has derived an expression for the contribution of each baroclinic mode to the total energy based on a linear model for a flat bottomed inlet with a one-dimensional sill (equation 1.2). A comparison between his results and those from the model yields poor agreement for the M_2 constituent, but reasonable agreement at several points in the deep basin for the K_1 constituent (*figure* 71). That any agreement is obtained at all is surprising given the assumptions of simplified stratification, geometry, and tidal forcing that led to the theoretical result. Agreement becomes progressively poorer away from the vicinity of the deepest part of the basin, however.

6.9 Deep Water Renewal

The second major objective of this modelling study was to investigate the ability of the model to simulate the intrusion of dense water into Indian Arm through Burrard Inlet. The observations supporting the occurrence of this have been described in §2.9. The results described so far in this chapter for high frequency variability in the model have been taken from the early part of a longer simulation.

The same values for the model free parameters discussed at the beginning of this chapter, and summarized in *table 20*, were used for this simulation. Data available for comparison with model results consists of CTD casts at several locations and times in Indian Arm and Burrard Inlet; and time series of near bottom current, salinity and temperature near station Ind-0 (*figures* 1 and 3) — discussed in detail by *Davidson* (1979). After a short run-in time during which initial transients were allowed to decay, a simula-

tion was performed extending from December 1, 1974 to February 1, 1975. Time series of σ_t have been plotted for four CTD stations together with the corresponding model locations (*figure* 72). The prescribed boundary conditions are illustrated in *figure* 72a, with the oscillatory behaviour reflecting the boundary condition discussed in §4.7.1. This also accounts for the slight discrepancies between the values used by the model and the CTD data. The model segment corresponding to Van-34 is approximately $7\,km$ landward of the mouth in Burrard Inlet. It is perhaps not surprising then, that good agreement is obtained between the rate of increase of density in the model and the data (*figure* 72b). The unfiltered trace shows large oscillations throughout the duration of the simulation, and the final stratification in the model is somewhat weaker than observed — no doubt due to the influence of local freshwater inflow at that time; a feature not included in the model.

The time series of CTD and current data collected during the inflow period were collected near station Ind-0. The trace of σ_t for this position — filtered to remove the diurnal and higher frequency tidal signals — shows a great deal of variance, with several periods of sharp fluctuations of up to 0.6 σ_t units (*figure* 72c). There is quite good agreement, nevertheless, in the long-term trend of this series, the linearly connected CTD cast data, and the model results. The large, observed variability suggests that the model boundary conditions — based on interpolated CTD cast data — do not contain all the natural features forcing variations in the system, and therefore introduce considerable uncertainty into the prescribed values of salinity at the mouth. In particular, there would appear to be a severe aliasing problem arising from the infrequent rate of sampling represented by the CTD casts. It is apparent that because of this aliasing, the interpolated CTD cast data represents only one of many possible time evolutions of the density structure at the entrance to Indian Arm, depending on the random times of the individual CTD casts. Major discrepancies between the observations and the output from the model could be due to missing observations during entire periods of strong inflow.

The traces for Ind-2.0 (*figure* 72d) reveal some departure of the model densities from

observations. There is quite good agreement for all depths until the middle of January, when the model density at 200 m does not increase as observed. Until this time the rate of increase in density is approximately as observed, although the model stratification is generally weaker. After the third week in January the density at 200 m increases at the observed rate once again, but now the stratification in the water column of the model has almost vanished, that is, the column has become nearly homogeneous. The observations support extensive weakening of the stratification over the inflow period, but indicate that the water column does not become as nearly homogeneous.

Figure 73 reveals good qualitative and fair quantitative agreement between the observed and calculated along-inlet currents at Ind-0 during the simulation period. Both time series have been digitally filtered to reduce the amplitudes of components with frequencies greater than diurnal. In addition, the observed currents — sampled at 15 minute intervals — have been vector averaged over 6 hour periods to reduce the plot density. Again, the observations reveal more variability than contained in the model. In general, while the two data sets agree generally on the direction of the flow, short periods of weak outflow in the observed record are not evident in the simulated series. Also, the average over ten days is too small by a factor of 2 or 3 except near the end of the period.

Fields of filtered residual velocity vectors, isopycnals, and surface elevations plotted at 10 day intervals reveal details of the evolution of these variables (*figure* 74). During the initial period — up to the end of December — there is a steady increase in the flow in Indian Arm below sill level, while below 100 m the flow is little changed. The stratification above middepth is weakened throughout this period and reflects a steady increase in density at depths down to 80 m (*figures* 72b,c,d show that the model increased densities at 20 m and 50 m more rapidly than observed). Below 100 m, on the other hand, the stratification remains virtually constant. Beginning about a week or more after the start of January there is a rapid intensification and deepening of the flow from middepths to 180 m. By January 20 (hour 1447) a strong vertical circulation pattern has developed. The surface outflow has also intensified up to this date. In the depression between the inner and outer

sills the flow suggests a vertical residual eddy.

By the end of the simulation (hour 1687) the inlet has become nearly homogeneous below sill depth. There are strong horizontal density gradients extending from the outer sill to column 8. The earlier strong and coherent flow structure in the deep basin has evolved into a chaotic distribution of velocity vectors — possibly a consequence of the unrealistic density stratification in the deep water — with a single, deep jet remaining at $140\,m$.

Figure 75 illustrates the effect on the model solution of changing the values of $N^{(z)}$ and $K^{(z)}$ both from (a) 0 to (b) $1\,cm^2\,s^{-1}$. Both pairs of plots were made after running the model from the same initial conditions with the two different values for the coefficients. They show that the solution depends weakly on the change to a value of 1.0, with the exception of some weakening of the stratification in the surface layer for this value. In addition, the inflow has progressed somewhat faster in the case of a zero value as indicated by comparison with the relative positions of the 21.2 and 21.3 isopycnals in *figure* 75.

An additional comparison for residual circulation using values of 0 and $0.2\,cm^2\,s^{-1}$ reveals significant differences in the details of the mean flow structure, although the mean stratification is only weakly affected (*figure* 76). The flow field for the nonzero value (b) exhibits a layered structure within the inlet beginning at hour 1207 that is completely absent in (a).

7. Summary and Conclusions

The basic objective of this research was to numerically model the time-dependent, tidally forced, stratified circulation in Indian Arm, with the specific aims of reproducing observed barotropic elevations and currents; observed vertical structure of the baroclinic response as revealed by Cyclesonde current meter time series; and the replacement of bottom water observed during the winter of 1974–75. A detailed analysis of surface elevation time series was undertaken to determine the barotropic response in Indian Arm and Burrard Inlet, and to calculate rates of energy dissipation. It was found that there is a large sink of energy in the vicinity of Second Narrows in Burrard Inlet, where the total dissipation rate is on the order of 10^2 m$W\ m^{-3}$. The analysis also revealed a significant decrease in the phase of the diurnal and semi-diurnal constituents at the Vancouver Harbour station between 1969 and 1970 in response to dredging of First Narrows during this period.

The method of modelling the inlet dynamics utilized a laterally integrated, time-dependent numerical model which includes horizontal and vertical advection of momentum and salt; turbulent diffusion of momentum and salt (both horizontally and vertically); and frictional drag. Formulation of the mathematical framework assumed that across-inlet variations in velocity and density due to the earth's rotation are negligible. This was justified for barotropic motions by a comparison between the lateral length scale and the external Rossby radius. For baroclinic motions, exponential decay of Kelvin waves associated with the internal tide was expected to result in discrepancies between model results and observations — an effect of the comparable lateral length scale and internal Rossby radii. In addition, lateral variability arising from curvature and other topographical effects has been ignored. This is a poor approximation in Burrard Inlet near the entrance to Indian Arm, and where bays and islands are present. Pressures were calculated using the hydrostatic approximation, with departures from this expected to be minimal for the types of flows being modelled — except, perhaps, in the vicinity of the sill, where strong vertical currents may occur.

The numerical model was formulated using proven explicit finite difference techniques.

Centred difference formulae for the advective terms in the salt balance were compared with upwind differencing, and the former — although nontransportive — were found to give superior results. This was in spite of attempts to limit numerical diffusion present in the upwind scheme (*Smolarkiewicz*, 1983). Efforts were also made to utilize a semi-implicit formulation of the surface elevation equation described by *Wang and Kravitz* (1980) to permit an increased time step. Although the scheme improved model efficiency in test cases — typified by simple topography, and weak nonlinearity — it was found that the method did not permit advantageous increases in the time step for the highly nonlinear flows found in Burrard Inlet and in other regions of complex topography.

Initial use of centred time differencing led to problems with time-splitting of the solution due to the generation of a computational mode. This could be suppressed at first only by increasing both horizontal and vertical diffusion coefficients to unrealistically large values. Excellent results were eventually obtained by implementing a smoothing procedure sometimes called the *Euler backward* method. This permitted the use of reasonable horizontal diffusion coefficients and arbitrarily small vertical coefficients.

Several test runs were made to verify the model performance using simple geometries and initial conditions. The first compared an exact solution of the vertically integrated momentum equation — with linear bottom friction — to the corresponding model simulation for unstratified flow forced by a small, semi-diurnal oscillation of the surface elevation at the open boundary at the mouth. Agreement was found to be very good for both elevations and horizontal velocities.

The second simulation modelled a density flow down a very gradual slope in an enclosed box of constant width and depth, in the absence of tidal forcing. This confirmed the model's ability to preserve salt through several thousand iterations, and to produce realistic, inviscid density flows. Calculation of the flow speed agreed well with the theoretical result of *Benjamin* (1968). Observed diffusion of salt due to numerical effects during the simulation proved to be minimal.

The last test series modelled unstratified and stratified flow in a constant width inlet having gross dimensions similar to Indian Arm and Burrard Inlet, and with a shallow sill at the inlet mouth. A simulation of nontidal density flow produced lifting of plotted isopycnals as dense water flowed under and replaced less dense water. A second simulation of tidally forced, unstratified flow using the same geometry generated a vertical residual circulation pattern that compared very well with theoretical results of *Ianniello* (1979) for constant width inlets of varying depth.

Investigation of the effect of varying the coefficients of horizontal eddy viscosity and diffusion ($N^{(x)}$ and $K^{(x)}$), with vertical coefficients $N^{(z)}$ and $K^{(z)}$ held constant, revealed a threshold value of $10^4\ cm^2\ s^{-1}$ for this geometry, below which the model was numerically unstable, or gave rise to excessively high spatial frequency fluctuations of velocity and isopycnal displacements.

A 40 day simulation was then performed, again using the constant width inlet, to investigate episodic intrusions (short *bursts*) of dense water lasting 50 hours, and with increases in density of up to one σ_t unit at the mouth. It was noted that a rapid increase in density occurred throughout the main basin of the inlet accompanied by a large increase in horizontal velocities and kinetic energy. The stratification above sill level intensified during these inflows as dense water from below sill depth was flushed up and out. Below sill depth the stratification was observed to weaken due to mixing. Upon cessation of the density flow horizontal currents were observed to decay gradually over several days.

The final study involved a model of Indian Arm and Burrard Inlet incorporating realistic width and depth variations. Each of the pairs $N^{(x)}$, $K^{(x)}$; and $N^{(z)}$, $K^{(z)}$ was separately set to equal, constant values. This approach was justified by the general lack of knowledge concerning their dependence on flow parameters and stratification, and by the benefits gained at the present stage of simulation by the resulting simplified analysis. Trials with several values of the horizontal coefficients led to the conclusion that values in excess of $10^5\ cm^2\ s^{-1}$ were required to remove the high spatial frequency fluctuations in the

solution, and to suppress local intensification of the density field. A value of $10^6\ cm^2\ s^{-1}$ was selected for all subsequent runs based on this reasoning.

The dissipation in the model was made to agree with observed values by *tuning* the side friction coefficient for each column of the final tidal model. A basis for comparison was established by performing harmonic analysis on surface elevation time series obtained for several stations along Burrard Inlet and Indian Arm. Good agreement was obtained for the amplitudes and phases of the M_2 and K_1 constituents. Detailed calculation of the dissipation rates in Burrard Inlet indicate that 76% of the M_2 tidal energy lost to friction in Burrard Inlet occurs in the constriction at Second Narrows. The corresponding figure for the K_1 constituent is 59%. Energy loss densities agreed well with measurements made in Seymour Narrows by *Grant, et. al.* (1961).

A detailed examination was undertaken of the model response over a diurnal tidal cycle. Initial stratification and boundary values were obtained from measurements made in Indian Arm and Burrard Inlet during the winter of 1974–75. The vertical modes for this stratification were calculated at each model grid along Indian Arm, together with the resulting internal phase speeds — leading to the determination of an internal Froude number which characterized the internal response during the period examined. A sequence of plotted parameter fields at various stages of the tide was discussed, paying particular attention to the response near the sill and the generation of the internal tide. Internal waves of tidal frequency with amplitudes up to $10\,m$ were noted. Distortion of isopycnals in the vicinity of the sill was observed during periods of strong inflow. The spatial resolution of the model was insufficient to examine this region in detail; however distortion of the flow reminds one of features observed in other inlets (for example in Knight Inlet by *Farmer and Smith*, 1978), although one must be very cautious about forming conclusions about the similarity between observations and such poorly resolved features of the model. It appears, however, that the model has successfully simulated the intrusion of a dense plume of water from the sill into the deep basin of the inlet.

A qualitative comparison between the results for the same period from a simulation of unstratified flow revealed that the density structure has a strong influence on the velocity field, while having a negligible effect on the surface elevations, which arise almost entirely from the barotropic response. Of particular note was an intensification of the current in the deep part of the basin associated with the internal tide.

An examination of the time-dependence of the various terms in the momentum equation revealed few periods or locations where a simple balance of terms occurs. During slack periods the balance is well approximated in the deep basin by local time acceleration and pressure gradient terms. During other periods complex balances result that raise questions concerning the applicability of simplified analytical models to realistic barotropic and stratified tidal flows in some inlets.

The residual circulation from the simulation of unstratified flow revealed the complications induced by the addition of realistic geometry and mixed tidal forcing. Little similarity was apparent between the vertical residual circulation for this case and the model of a constant width inlet. The addition of stratification caused a reversal in the residual flow near the surface, and intensification of an inward flowing residual jet below sill depth. Intensity of the flow was significantly reduced below the level of the jet in this latter case — suggesting that stratification suppresses the downward flux of momentum. The residual flow seaward of the sill was observed to be very nearly the same in both these cases.

Time series of isopycnal displacements from the model confirmed the amplitude and frequency of the internal tide seen in the series of plotted fields. The displacements were observed to vary significantly along Indian Arm, with a minimum appearing near column 5 of the model. This was later explained in terms of a standing wave pattern established by the internal tide in the inlet basin. Column 5 is located near a horizontal node, thus accounting for the observed amplitude minimum. The standing wave pattern was clearly evident in contour plots of amplitude and phase from harmonic analysis of horizontal velocities and σ_t time series.

No conclusive evidence is available to confirm this model result; however, observed depth variations in the harmonic analysis of Cyclesonde current meter time series at a station near one of the model columns is consistent with the model variations. Additional support is provided by observations made by the author of short time series of CTD data at three stations in Indian Arm over a diurnal cycle that reveal internal tide amplitudes consistent with the model results. Vertical variations in the phase of the M_2 and K_1 tidal constituents from harmonic analysis of horizontal velocities indicate very good agreement between observations and modelled results.

The model predicts that the internal tide in Indian Arm can form a standing wave pattern under winter stratification. It remains to be seen whether this result will be verified by future observations. As noted in §6.8 — and recalled here for emphasis — the exclusion of islands and other variations in topography from the model combined with errors introduced by discretization of the bottom have an unknown impact on the reflection criteria for the internal tide and, it has been argued, may preclude its occurrence in Indian Arm. There are encouraging indications from this study, however, that reflection does occur. If this is the case, then resonance of the internal tide in Indian Arm may be possible. This has been observed in at least one other inlet (*Keeley*, 1984) and probably in one other as well (*Lewis and Perkin*, 1982).

The vertical modal structure at each column of the model was calculated from synoptic density profiles; yielding the barotropic and first five baroclinic modes. Using the assumption of a barotropic standing wave in Indian Arm — well supported by observations — the phase of the barotropic component was specified, and the remaining amplitudes and phases solved for by performing a least squares fit to the harmonic analysis. The results for the M_2 and K_1 constituents from the harmonic analysis of model velocities were found to be in very good agreement at most points in the inlet, with the exceptions being at column 9, and possibly at column 8. It is likely that nonlinearity at these locations — particularly at column 9 — cause the harmonic and modal analysis to fail (see §6.8 for a discussion). Where this approach succeeded, however, estimates were made of the parti-

tioning of kinetic energy between the various modes. We saw that in the deepest part of the basin most of the energy is in the first baroclinic mode, while the barotropic and second baroclinic modes contribute to a lesser degree. Closer to the sill, the energy is primarily in the barotropic mode. This was apparent in the comparison between the simulations of unstratified and stratified flow, which showed little difference in response seaward of the inner sill. These results suggest that energy in the primarily barotropic flow near the sill is radiated into the inlet as the internal tide. Analytical models by others (e.g., *Stigebrandt*, 1981, and *Stacey*, 1984) have come to the same conclusion for simplified geometries and flows.

The fate of this energy in the model is reflection from the head; thus giving rise to the observed standing wave. Dissipation of energy in the deep model basin occurs primarily through turbulent diffusion of momentum — a gross approximation to the cascade of turbulent energy to dissipative scales.

The simulation of dense water intrusion into Indian Arm qualitatively reproduced the observed rates of increase in density during the first two months of the simulation. The stratification in the model became unrealistically weakened — nearing homogeneity — toward the end in the main basin. This is due to the artificial requirement in the model for static instabilities to be removed by instantaneous vertical mixing. This requirement yielded unrealistic results only after the stratification had become very weak. Trials made without this constraint yielded unrealistic density inversions that tended to intensify, rather than disperse. It is probable that this is caused by the limitations of the centred differencing scheme which allows for nondiffusive transport of salt against the direction of flow. Although unrealistic, this defect was found to result in fewer problems than the artificial viscosity associated with upwind differencing. The good agreement obtained throughout most of the simulation suggests that the methods adopted are adequate during much of the inflow event. Future extensions to this work should investigate the effect of refining both vertical and horizontal spatial scales on the simulation of density flows. Improved performance can be expected with a better approximation to the slope leading down from

the sill to the bottom of the inlet basin. In addition, tolerance of static instabilities, combined with judicious implementation of vertical mixing — perhaps combined with upwind finite difference schemes in these special cases — may help to improve the simulation of density flows by the model.

Comparisons between time series of σ_t and current from the model with observations during the inflow revealed far more temporal variability in the latter — even when filtered to remove tidal oscillations. This suggests that CTD casts widely spaced in time — used to prescribe the boundary salinities to the model — provide temporal resolution of the density field that is inadequate for prescribing accurate boundary conditions. The model can do no better than the prescribed boundary conditions, and more realistic results would be expected if higher frequency time series of salinity (for example hourly) could be obtained for future simulations. Although the observed variance was not reproduced by the model, general trends in both density and along-inlet current were.

7.1 Closing Remarks

It has been shown — using a coarsely gridded numerical model of multi-level, stratified flow in a representative inlet on the coast of British Columbia — that important properties of the observed vertical density and current structure, residual flow fields, modal response, and intrusion of dense water, can be reproduced. The results from this study have shown the usefulness of this class of numerical model in the study of inlet dynamics, and suggests its applicabilty to inlets similar to Indian Arm and Burrard Inlet. In particular, the model is suitable for small runoff inlets where the brackish surface layer — and associated estuarine circulation — may be ignored. This will most often be satisfied during the winter when relatively well-mixed conditions tend to prevail. The model has also demonstrated its usefulness as a tool for suggesting field measurements that could be used to verify model predictions.

In spite of the successful application of this model to the study of Indian Arm, it has been made clear that several deficiencies remain that limit its applicability. These may

profit from further research into the parameterization of turbulent mixing and diffusion of momentum and salt, and an examination of the effect of reducing the spatial scales of the model in order to resolve finer features of the flow — such as lee waves near the sill. It is apparent from this study that the problems associated with using a small model time increment cannot be easily removed by a simple conversion from an explicit to implicit finite difference scheme. Strong nonlinearities in the governing equations associated with rapid variations in depth and width invalidate the linear stability analysis upon which the unconditional stability of implicit and semi-implicit schemes is based. Only the use of larger, more economical computers will permit the detailed studies of stratified flow in inlets that will be required to enhance our understanding of these very interesting dynamical systems.

Cited References

Anderson, J.J., and A.H. Devol. 1973. Deep water renewal in Saanich Inlet, an intermittently anoxic basin. *Est. Coast. Mar. Sc.* 1:1–10

Benjamin, T.B. 1968. Gravity currents and related phenomena. *J. Fluid Mech.* 31:209–248

Blackford, B.L. 1978. On the generation of internal waves by tidal flow over a sill — a possible nonlinear mechanism. *J. Mar. Res.* 36:529–549

Blumberg, A.F. 1975. A numerical investigation into the dynamics of estuarine circulation. *Chesapeake Bay Institute, The John's Hopkins University, tech. rept.* 91

———. 1978. The influence of density variations on estuarine tides and circulations. *Est. Coast. Mar. Sc.* 6:209–215

Bowden, K.F., and P. Hamilton. 1975. Some experiments with a numerical model of circulation and mixing in a tidal estuary. *Est. Coast. Mar. Sc.* 3:281-301

Buch, E. 1981. On entrainment and vertical mixing in stably stratified fjords. *Est. Coast. Shelf Sc.* 12:461-469

Burling, R.W. 1982. Deep circulations in inlets: Indian Arm as a case study. *In: Marine Tailings Disposal* (ed., D.V. Ellis). Ann Arbor Science, Ann Arbor Michigan. 85–132

Cannon, G.A. 1975. Observations of bottom-water flushing in a fjord-like estuary. *Est. Coast. Mar. Sc.* 3:95–102

Cannon, G.A., and C.C. Ebbesmeyer. 1978. Winter replacement of bottom water in Puget Sound. *In: Estuarine Transport Processes* (ed., Kjerfve). University of South Carolina Press, Columbia, South Carolina: 229–238

Cannon, G.A., D.E. Bretschneider, and J.R. Holbrook. 1985. Transport variability in a fjord. (in print)

Crean, P.B. 1983. A numerical approach to simulating the estuarine circulation in a strongly tidal deep coastal sea between Vancouver Island and the mainland. *In: Hydrothermodynamic Modelling of Natural Waters. Proc. 3rd Intl. Conf. Appl. Math. Modelling. Hamburg: Feb. 1983*: 88–116

Davidson, L.W. 1979. On the Physical Oceanography of Burrard Inlet and Indian Arm. *Master of Science, Dept. of Physics and Institute of Oceanography, University of British Columbia*

Draper, N.R., and H. Smith. 1966. Applied Regression Analysis. J. Wiley and Sons. 407 pages

Ebbesmeyer, C.C., C.A. Barnes, and C.W. Langley. 1975. Application of an advective-diffusive equation to a water parcel observed in a fjord. *Est. Coast. Mar. Sc.* 3:249–268

———, and C.A. Barnes. 1980. Control of a fjord basin's dynamics by tidal mixing in embracing sill zones. *Est. Coast. Mar. Sc.* 11:311–330

Edwards, A., and D.J. Edelsten. 1977. Deep water renewal of Loch Etive: a three basin Scottish fjord. *Est. Coast. Mar. Sc.* 5:575–595

Elliott, A.J. 1976. A numerical model of internal circulation in a branching tidal estuary. *Chesapeake Bay Institute, The John's Hopkins University, tech. rept.* 54

Farmer, D.M. 1972. The influence of wind on the surface waters of Alberni Inlet. *Ph.D. Thesis, University of British Columbia*, 92 pages

Farmer, D.M., and H.J. Freeland. 1983. The physical oceanography of fjords. *Progress Oceanog.* 12:147–220

Farmer, D.M., and J.D. Smith. 1978. Nonlinear internal waves in a fjord. *In: Hydrodyn. Est. Fjords* (ed., Nihoul): 465–494

———. 1980. Tidal interaction of stratified flow with a sill in Knight Inlet. *Deep Sea Research* 27A:239–254

Festa, J.F., and D.V. Hansen. 1976. A two-dimensional numerical model of estuarine circulation: the effects of altering depth and river discharge. *Est. Coast. Mar. Sc.* 4:309–323

Foreman, M.G.G. 1979. Manual for tidal currents analysis and prediction. *Pacific Marine Science Rept.* 78–6, Institute of Ocean Sciences, Sidney, British Columbia

Freeland, H.J., and D.M. Farmer. 1980. Circulation and energetics of a deep, strongly stratified inlet. *Can. J. Fish. Aquat. Sc.* 37:1398–1410

Gade, H.G. 1973. Deep water exchanges in a sill fjord: a stochastic process. *J. Phys. Oceanogr.* 3:213–219

———, and A. Edwards. 1980. Deep water renewal in fjords. *In: Fjord Oceanography* (ed., Freeland, Farmer, and Levings). Plenum Press, New York and London. 453–490

Gargett, A.E. 1976. Generation of internal waves in the Strait of Georgia, British Columbia. *Deep Sea Research* 23:17–32

Geyer, W.R., and G.A. Cannon. 1982. Sill processes related to deep water renewal in a fjord. *J. Geophys. Res* 87:7985–7996

Gilmartin, M. 1962. Annual cyclic changes in the physical oceanography of a British Columbia fjord. *J. Fish. Res. Bd. Canada* 19:921–974

Graham, R.J. 1963. Determination and analysis of numerical smoothing weights. *NASA tech. rept. R-179, Marshall Space Flight Center, 28 pages*

de Grandpré, C.DeB., and M.I. El-Sabh. 1981. A two-dimensional numerical model of the vertical circulation of tides in the St. Lawrence Estuary. *Est. Coast. Shelf Sc.* 12:375–387

Grant, H.L., R.W. Stewart, and A. Molliet. 1961. Turbulence spectra from a tidal channel. *J. Fluid Mech.* 12:241–263

Hamblin, P.F. 1977. Short-period internal waves in the vicinity of a river-induced shear zone in a fjord lake. *J. Geophys. Res* 82:3167–3174

Hamilton, P. 1975. A numerical model of the vertical circulation of tidal estuaries and its application to the Amsterdam Waterway. *Geophys. J. Roy. Astron. Soc.* 40:1–21

———. 1977. On the numerical formulation of a time-dependent multi-level model of an estuary, with particular reference to boundary conditions. *In: Estuarine Processes II* (ed., Wiley): 347–364

———, and M. Rattray. 1978. A numerical model of the depth-dependent wind-driven upwelling circulation on a continental shelf. *J. Phys. Oceanogr.* 8:437–457

———. 1978. Theoretical aspects of estuarine circulation. *In: Estuarine Transport Processes* (ed., Kjerfve). University of South Carolina Press, Columbia, South Carolina: 37–73

Hansen, D.V., and M. Rattray. 1965. Gravitational circulation in straits and estuaries. *J. Mar. Res.* 23:104–122

———. 1972. Estuarine circulation induced by diffusion. *J. Mar. Res.* 30:281–294

Hay, J.E., and T.R. Oke. 1976. The climate of Vancouver. British Columbia geographical series; No. 23. Tantalus Research Ltd. 49 pages

Heggie, D.T., and D.C. Burrell. 1981. Deep water Renewals and oxygen consumption in an Alaskan fjord. *Est. Coast. Shelf Sc.* 13:83–99

Hodgins, D.O. 1979. A time-dependent two-layer model of fjord circulation and its application to Alberni Inlet, British Columbia. *Est. Coast. Mar. Sc.* 8:361–378

Ianniello, J.P. 1979. Tidally induced residual circulation in estuaries of variable breadth and depth. *J. Phys. Oceanogr.* 9:962–974

Ippen, A.T., and D.R.F. Harleman. 1966. Tidal dynamics in estuaries. *In: Estuary and Coastline Hydrodynamics* (ed., Ippen). McGraw-Hill: 493–545

Keeley, J.R. 1984. Observations of an internal resonance in a fjord. *J. Mar. Res.* 42:873–891

Klinck, J.M., J.J. O'Brien, and H. Svendsen. 1981. A simple model of fjord and coastal circulation interaction. *J. Phys. Oceanogr.* 11:1612–1626

Kullenberg, G. 1977. Entrainment velocity in natural stratified vertical shear flow. *Est. Coast. Mar. Sc.* 5:329–338

Kurihara, Y. 1965. On the use of implicit and iterative methods for the time integration of the wave equation. *Monthly Weather Rev.* 93:33–46

Lafond, C.A., and G.L. Pickard. 1975. Deepwater exchanges in Bute Inlet, British Columbia. *J. Fish. Res. Bd. Canada* 32:2075–2089

LeBlond, P.H., and L.A. Mysak. 1978. Waves in the Ocean. Elsevier Scientific Publishing Co., Amsterdam. 602 pages

Lee, C.Y., and R. Beardsley. 1974. The generation of long nonlinear internal waves in a weakly stratified shearflow. *J. Geophys. Res* 79:453–462

Lewis, E.L., and R.G. Perkin. 1982. Seasonal mixing processes in an arctic fjord system. *J. Phys. Oceanogr.* 12:74–83

Long, R.R. 1975. Circulations and density distribution in a deep strongly stratified, two-layer estuary. *J. Fluid Mech.* 71:529–540

Maxworthy, T. 1979. A note on the internal solitary waves produced by tidal flow over a three-dimensional ridge. *J. Geophys. Res* 84:338–346

Muench, R.D., and D.T. Heggie. 1978. Deep water exchange in Alaskan subarctic fjords. *In: Estuarine Transport Processes* (ed., Kjerfve). University of South Carolina Press, Columbia, South Carolina: 239–268

Munk, W., and D. Cartwright. 1966. Tidal spectroscopy and prediction. *Phil. Trans. Roy. Soc.* (London), Ser. A 259: 533–581

Niebauer, H.J. 1980. A numerical model of circulation in a continental shelf-silled fjord coupled system. *Est. Coast. Mar. Sc.* 10:507–521

Odd, N.V.M., and J.G. Rodger. 1978. Vertical mixing in stratified tidal flows. *J. Hydr. Div., Proc. ASCE* 104:337–351

Officer, C.B. 1977. Longitudinal circulation and mixing relations in estuaries. *In: Estuaries, Geophys. and the Environ.*: 13–21

Okubo, A., and R.V. Ozmidov. 1970. Emprical dependence of the coefficient of horizontal turbulent diffusion in the ocean on the scale of the phenomenon in question. *Atmosphere and Oceanic Phys.* 6:534–536

Pearson, C.E., and D.F. Winter. 1978. Two layer analysis of steady circulation in stratified fjords. *In: Hydrodyn. Est. Fjords* (ed., Nihoul): 495–514

———. 1984. On tidal motion in a stratified inlet, with particular reference to boundary conditions. *J. Phys. Oceanogr.* 14:1307–1314

Perrels, P.A.J., and M. Karelse. 1978. A two-dimensional numerical model for salt intrusion in estuaries. *In: Hydrodyn. Est. Fjords* (ed., Nihoul): 107–126

Phillips, O.M. 1977. The dynamics of the upper ocean (2^{nd} edition). Cambridge University Press. 336 pages

Pickard, G.L. 1961. Oceanographic features of inlets in the British Columbia mainland coast. *J. Fish. Res. Bd. Canada* 18:907–999

———. 1963. Oceanographic characteristics of inlets of Vancouver Island, British Columbia. *J. Fish. Res. Bd. Canada* 20:1109–1144

———. 1975. Annual and longer term variations of deepwater properties in the coastal waters of southern British Columbia. *J. Fish. Res. Bd. Canada* 32:1561–1587

Pugh, D.T., and J.M. Vassie. 1976. Tide and surge propagation off-shore in the Dowsing region of the North Sea. Sonderdruck der Deutshen Hydrographischer Zeitschrift. 29:163-213

Rattray, M., and D.V. Hansen. 1962. A similarity solution for circulation in an estuary. *J. Mar. Res.* 20:121–133

Smethie. W.M. 1981. Vertical mixing rates in fjords determined using radon and salinity as tracers. *Est. Coast. Shelf Sc.* 12:131-153

Smith, R. 1978. Coriolis, curvature and boundary effects upon dispersion in a narrow channel. *In: Hydrodyn. Est. Fjords* (ed., Nihoul): 217–232

Smith, T.J. 1982. On the representation of Reynold's stress in estuaries and shallow coastal seas. *J. Phys. Oceanogr.* 12:914–921

———, and H.S. Takhar. 1981. A mathematical model for partially mixed estuaries using the turbulence energy equation. *Est. Coast. Shelf Sc.* 13:27–45

Smolarkiewicz, P.K. 1983. A simple positive definite advective scheme with small implicit diffusion. *Monthly Weather Rev.* 111:479–486

Stacey, M.W. 1984. The interaction of tides with the sill of a tidally energetic inlet. *J. Phys. Oceanogr.* 14:1105–1117

Stigebrandt, A. 1976. Vertical diffusion driven by internal waves in a sill fjord. *J. Phys. Oceanogr.* 6:486–495

———. 1977. On the effect of barotropic current fluctuations on the two-layer transport of a constriction. *J. Phys. Oceanogr.* 7:118–122

———. 1979. Observational evidence for vertical diffusion driven by internal waves of tidal origin in the Oslo Fjord. *J. Phys. Oceanogr.* 9:435–441

———. 1980. Some aspects of tidal interaction with fjord constrictions. *Est. Coast. Mar. Sc.* 11:151–166

———. 1981. A mechanism governing the estuarine circulation in deep, strongly stratified fjords. *Est. Coast. Mar. Sc.* 13:197–211

Stommel, H., and H.G. Farmer. 1952. Abrupt change in width in a two layer open channel flow. *J. Mar. Res.* 11:205–214

Svendsen, H. 1977. A study of the circulation in a sill fjord on the west coast of Norway. *Mar. Sc. Comm.* 3:151–209

University of British Columbia, Department of Oceanography. 1974. Data report 37.

University of British Columbia, Department of Oceanography. 1975. Data report 41.

Tully, J.P. 1949. Oceanography and prediction of pulp mill pollution in Alberni Inlet. *Bull. Fish. Res. Bd., Canada*, 83, 169 pages

Waldichuk, M. 1965. Water exchange in Port Moody, British Columbia and its effect on waste disposal. *J. Fish. Res. Bd. Canada* 22:801–822

Wang, D-P., and D.W. Kravitz. 1980. A semi-implicit two-dimensional model of estuarine circulation. *J. Phys. Oceanogr.* 10:441–454

Winter, D.F. 1973. A similarity solution for steady state gravitational circulation in estuaries. *Est. Coast. Mar. Sc.* 1:387–400

Appendix A: Harmonic analysis of tidal records

A.1 Method

Tidal records consisting of time series of currents or surface elevations are often analyzed by a technique known as harmonic analysis. The objective of this technique is to decompose the measured signal into a finite sum of tidal constituents of specified frequency such that the fit is optimized in the sense of a minimized residual sum of squares. This approach differs from standard Fourier analysis in that frequencies are not equally spaced and are selected *a priori* based on astronomical observations.

The most complete description of the tidal potential in terms of astronomical arguments, and the one which is used most frequently in tidal analysis was developed by *Doodson* (1921), although other approaches — for example *Munk and Cartwright* (1966) — are also used. Doodson specifies tidal frequencies in terms of astronomical variables (*table* 24).

Table 24
Doodson's astronomical variables

argument	*description*
$S(t)$	the mean longitude of the moon
$H(t)$	the mean longitude of the sun
$P(t)$	the longitude of the lunar perigee
$N'(t)$	the negative of the longitude of the ascending node
$P'(t)$	the mean longitude of the perihelion

All longitudes are measured relative to the vernal equinoctial point on the ecliptic. These variables, together with their rates of change, permit the calculation of constituent frequencies, astronomical phase angles, and nodal modulation phase and amplitude corrections. The astronomical phase angle (θ), and frequency (σ), are defined for constituent j as

$$\theta_j = i_0\tau + j_0 S + k_0 H + l_0 P + m_0 N' + n_0 P',$$

$$\sigma_j = \frac{\partial V_j}{\partial t},$$

where τ is the angular distance between the moon's position and a point on the earth's surface at a particular time, and the subscripted letters represent integers called Doodson numbers. i_0 may take values from 0 to 3, while the remainder range from -6 to 6. Additional values, called geodetic coefficients G_{i_0} and G'_{i_0}, are required to specify the complete tidal potential.

Each tidal constituent is uniquely and completely specified by the set of six Doodson numbers. Constituents may be grouped into species, groups, and subgroups depending on whether they have common values of i_0, $i_0 j_0$, or $i_0 j_0 k_0$ respectively.

The values taken by i_0 specify four species of constituents; low frequency ($i_0 = 0$), diurnal ($i_0 = 1$), semidiurnal ($i_0 = 2$), and terdiurnal ($i_0 = 3$). Traditionally, important constituents have been assigned names. Several of the major constituents are listed in *table* 25 together with their frequencies and Doodson numbers.

Table 25
frequencies and Doodson numbers for several tidal constituents

constituent	*freq*(hr^{-1})	species	i_0	j_0	k_0	l_0	m_0	n_0
Mm	.0015121518	low-freq	0	1	0	-1	0	0
O_1	.0387306544	diurnal	1	-1	0	0	0	0
P_1	.0415525871	diurnal	1	1	-2	0	0	0
S_1	.0416666721	diurnal	1	1	-1	0	0	1
K_1	.0417807462	diurnal	1	1	0	0	0	0
M_2	.0805114007	semidiurnal	2	0	0	0	0	0
L_2	.0820235525	semidiurnal	2	1	0	-1	0	0
S_2	.0833333333	semidiurnal	2	2	-2	0	0	0
M_3	.1207671010	terdiurnal	3	0	0	0	0	0

The principal effects of the sun and moon on the earth's tides are due to orbital periods, declination of the orbit to the celestial equator, and eccentricities in the orbits. Secondary effects such as precession of the orbital perigee and wobbling of the earth's axis cause smaller, very low frequency changes in the tides.

An adequate representation of the surface tide can be obtained with the set of 45 main constituents. Where nonlinear effects are significant, new harmonics will be generated at frequencies which are sums and differences of main constituent frequencies. As an example,

consider the M_2 and S_2 constituents. Nonlinear interactions give rise to the constituents listed in *table* 26.

Table 26
Some constituents generated by M_2 and S_2 interactions

constituent	*freq* (hr^{-1})	*source*
M_2	.0805114007	—
S_2	.0833333333	—
M_6	.2415342020	$3 \cdot M_2$
S_6	.2500000000	$3 \cdot S_2$
$2MS_6$	.2443561347	$S_2 + 2 \cdot M_2$
$2SM_6$	.2471780673	$2 \cdot S_2 + M_2$
$2SM_2$	.0861552660	$2 \cdot S_2 - M_2$

A nearly continuous spectrum of harmonics may be generated in this way, although a few tens of shallow water constituents are normally adequate to include in the analysis.

Harmonic analysis is routinely performed by computer programmes which select constituents to be included in the analysis and fit the corresponding complex amplitudes via a least squares procedure. The fitted series may be constructed by summing the individual terms for each constituent. These have the form

$$A_j \cos 2\pi(\sigma_j t - \phi_j)$$

where A_j and ϕ_j are determined from the least squares fit. A further complication necessitates an additional step before the actual constituent amplitude and phase may be determined. Because of the large number of constituents in the Doodson development of the tidal potential a very long time series is required to separate them all. In particular, subgroups of constituents — those with the same values of i_0, j_0 and k_0 — are lumped together under the dominant constituent of the subgroup and the effect of all members is reflected in the values for A_j and ϕ_j. To resolve the principal constituent the amplitude and phase relation from tidal potential theory are used to calculate a complex nodal amplitude correction. The calculated and true amplitudes and phases are related through

$$a_j = \frac{A_j}{f_j},$$

$$g_j = \theta_j + \delta_j - \phi_j,$$

where f_j is the nodal amplitude correction, δ_j the nodal phase correction, and θ_j the astronomical phase angle. The values a_j and g_j are the corrected amplitude and phase angle for the analysed constituent. g_j is commonly referred to as the *Greenwich phase lag* and is the phase angle tabulated in lists of harmonic contants, or calculated by the harmonic analysis program used in this research.

A.2 Tidal Predictions

The results of harmonic analysis may be used to predict tidal elevations or currents for arbitrary times using

$$\chi(t) = \sum_{j=1}^{n} f_j(t_0) A_j \cos\left\{2\pi\left[\theta_j(t_0) + \delta_j(t_0) + \sigma_j(t - t_0) - g_j\right]\right\} \qquad (A.1)$$

where $\chi(t)$ is either a predicted elevation or current value, t_0 is a reference time selected to be near the desired range of prediction times, and the sum is over a selected set of n tidal constituents.

A.3 Inference

The length of the tidal record determines the minimum frequency separation that may be resolved between two constituents. If the length of the record is T hours then two constituents with frequencies σ_1 and σ_2 may be separated only if they satisfy $|\sigma_1 - \sigma_2|T \leq 1$. If this condition is not met and one of the pair is included in the analysis, then the result will include the effect of both constituents, and the included constituent will be *contaminated* by the one excluded.

As an example, consider the K_1, P_1, S_1 constituents. The minimum time required to separate these three constituents is one year. Shorter records will not yield correct results unless the phase and amplitude relationships between the main constituent (in this case K_1) and its satellite constituents (S_1 and P_1) are known, and the analysis performed by *inference*. Specifically, if a main constituent (subscript 0) is contaminated by n satellite constituents, and the amplitude ratios $r_{i0} = a_i/a_0$ and phase differences $\zeta_{i0} = g_0 - g_i$ are

known then we can write

$$A_0' \cos 2\pi(\sigma_0 t - \phi_0') = \sum_{i=0}^{n} A_i \cos 2\pi(\sigma_i t - \phi_i),$$

where the primes denote quantities which result from the analysis of the contaminated constituent, and unprimed quantities denote the values to be inferred. Using $A_i = (f_i/f_0) r_{i0} A_0$ and $-\phi_i = \zeta - \theta_0 - \phi_0 + \theta_i$ we get

$$\begin{aligned} & A_0' \cos 2\pi(\sigma_0 t - \theta_0') \\ &= \frac{A_0}{f_0} \sum_{i=0}^{n} f_i r_{i0} \cos 2\pi\left[(\sigma_i - \sigma_0)t + \theta_i - \theta_0 + \zeta_i + (\sigma_0 t - \phi_0)\right] \\ &= \frac{A_0}{f_0}\Big\{ \cos 2\pi(\sigma_0 t - \phi_0) \sum_{i=0}^{n} f_i r_{i0} \cos 2\pi\left[(\sigma_i - \sigma_0)t + \theta_i - \theta_0 + \zeta_i\right] \\ &\quad - \sin 2\pi(\sigma_0 t - \phi_0) \sum_{i=0}^{n} f_i r_{i0} \sin 2\pi\left[(\sigma_i - \sigma_0)t + \theta_i - \theta_0 + \zeta_i\right]\Big\}. \end{aligned}$$

Since $|\sigma_1 - \sigma_2| < 1\, hr^{-1}$ we have the approximations

$$\begin{aligned} \cos 2\pi\left[(\sigma_i - \sigma_0)t + \theta_i - \theta_0 + \zeta_i\right] &\approx \frac{\sin \pi T(\sigma_2 - \sigma_1)}{\pi T(\sigma_2 - \sigma_1)} \cos 2\pi(\theta_i - \theta_0 + \zeta_i), \\ \sin 2\pi\left[(\sigma_i - \sigma_0)t + \theta_i - \theta_0 + \zeta_i\right] &\approx \frac{\sin \pi T(\sigma_2 - \sigma_1)}{\pi T(\sigma_2 - \sigma_1)} \sin 2\pi(\theta_i - \theta_0 + \zeta_i). \end{aligned}$$

Let

$$\begin{aligned} C_i &= \frac{f_i}{f_0} r_{i0} \frac{\sin \pi T(\sigma_2 - \sigma_1)}{\pi T(\sigma_2 - \sigma_1)} \cos 2\pi(\theta_i - \theta_0 + \zeta_i), \\ S_i &= \frac{f_i}{f_0} r_{i0} \frac{\sin \pi T(\sigma_2 - \sigma_1)}{\pi T(\sigma_2 - \sigma_1)} \sin 2\pi(\theta_i - \theta_0 + \zeta_i). \end{aligned}$$

Therefore

$$\frac{A_0'}{A_0} \cos 2\pi(\sigma_0 t - \phi') = \cos 2\pi(\sigma_0 - \phi_0) \sum_{i=0}^{n} C_i - \sin 2\pi(\sigma_0 t - \phi_0) \sum_{i=0}^{n} S_i,$$

or rearranging we get

$$\begin{aligned} & \cos 2\pi\sigma_0 t \left[\frac{A_0'}{A_0} \cos 2\pi\phi_0' - \left(\sum_{i=0}^{n} C_i\right) \cos 2\pi\phi_0 - \left(\sum_{i=0}^{n} S_i\right) \sin 2\pi\phi_0\right] \\ &= \sin 2\pi\sigma_0 t \left[\frac{-A_0'}{A_0} \sin 2\pi\phi_0' - \left(\sum_{i=0}^{n} C_i\right) \sin 2\pi\phi_0 - \left(\sum_{i=0}^{n} S_i\right) \cos 2\pi\phi_0\right]. \end{aligned}$$

Since this relationship must hold true for all times t, the terms in square brackets must be equal to zero. Thus we have

$$\frac{A'_0}{A_0}\cos 2\pi\phi'_0 = \left(\sum_{i=0}^{n} C_i\right)\cos 2\pi\phi_0 + \left(\sum_{i=0}^{n} S_i\right)\sin 2\pi\phi_0,$$

$$\frac{A'_0}{A_0}\sin 2\pi\phi'_0 = \left(\sum_{i=0}^{n} C_i\right)\sin 2\pi\phi_0 + \left(\sum_{i=0}^{n} S_i\right)\cos 2\pi\phi_0,$$

and therefore

$$A_0 = \frac{A'_0}{\sqrt{\left(\sum_{i=0}^{n} C_i\right)^2 + \left(\sum_{i=0}^{n} S_i\right)^2}},$$

$$\phi_0 = \phi'_0 + \arctan\left(\frac{\sum_{i=0}^{n} S_i}{\sum_{i=0}^{n} C_i}\right),$$

$$A_i = r_{i0}\left(\frac{f_i}{f_0}\right)A_0,$$

$$\phi_i = \theta_0 - \theta_i + \phi_0 - \zeta.$$

Inference can substantially improve the fit of the harmonic series to the data. However, reliable values for phase differences and amplitude ratios must be obtained from prior analysis or nearby stations where a longer series length has resulted in separation of the contaminating constituent(s) from the main constituent.

The computer programme used to perform the harmonic analysis on both tidal elevations and current data was adapted by the author while employed by Beak Consultants Ltd. (now IEC Beak Consultants Ltd.) from a programme written by M. Foreman of the Institute of Ocean Sciences at Sidney, British Columbia. Details of the least squares fit and other features of the analysis technique are described by *Foreman* (1979).

A.4 Confidence Intervals

It is important when calculating the harmonic constants to have an estimate of their reliability. This requires determining how well the set of harmonics fits the observations and what the confidence intervals are for each calculated amplitude and phase. The method used to calculate the constants is a standard least-squares technique, thus the associated statistical theory may be applied to the results.

The problem is one of fitting the set of parameters $\{A_j, \phi_j : j = 1, 2, \ldots, n\}$ described above such that the sum

$$z_i' = \sum_{j=1}^{n} A_j \cos 2\pi(\sigma_j t_i - \phi_j)$$

minimizes the squared residual error, that is

$$\epsilon^2 = \sum_{i=1}^{N} (z_i - z_i')^2$$

is minimized where $\{z_i : i = 1, 2, \ldots, N\}$ are the observed time series. The problem is reformatted in Cartesian coordinates so that

$$z_i' = \sum_{j=1}^{n} \left[C_j \cos(2\pi\sigma_j t_i) + S_j \sin(2\pi\sigma_j t_i) \right],$$

with the relationships $A_j = \left(C_j^2 + S_j^2\right)^{\frac{1}{2}}$, $\phi_j = \arctan(-S_j/C_j)$. Let

$$\mathbf{x} = (C_1, \ldots, C_n, S_1, \ldots, S_n)$$

be the vector of calculated least squares coefficients. Let $V_{ij}^x = \mathrm{cov}(x_i, x_j)$ be the variance-covariance matrix for $\mathbf{x}$. V^x is a block diagonal matrix of the form

$$V^x = \begin{pmatrix} V_c^x & 0 \\ 0 & V_s^x \end{pmatrix}$$

where V_c and V_s are $n \times n$ matrices. Let $\mathbf{y} = (A_1, \ldots, A_n, \phi_1, \ldots, \phi_n)$ be the vector of amplitude and phases derived from $\mathbf{x}$, that is

$$y_i = \mathcal{G}_i(\mathbf{x}) \quad \text{where} \quad \mathcal{G}_i(\mathbf{x}) = \begin{cases} A_j & i = 1, \ldots, n \\ \phi_j & i = n+1, \ldots, 2n. \end{cases}$$

Let $J = [\partial \mathcal{G}_i / \partial x_j]$ be the Jacobian of $\mathcal{G}$. Therefore

$$J = \begin{pmatrix} D^1 & D^2 \\ D^3 & D^4 \end{pmatrix} \quad i = 1, 2, \ldots, n$$

where each of the D^j is a diagonal $n \times n$ matrix. We have the following relationships:

$$D_{ii}^1 = \frac{\partial A_i}{\partial C_i} = \frac{C_i}{\sqrt{C_i^2 + S_i^2}} = \cos(\phi_i),$$

$$D_{ii}^2 = \frac{\partial A_i}{\partial S_i} = \frac{S_i}{\sqrt{C_i^2 + S_i^2}} = \sin(\phi_i),$$

$$D_{ii}^3 = \frac{\partial \phi_i}{\partial C_i} = \frac{S_i}{C_i^2 + S_i^2} = \frac{\sin(\phi_i)}{A_i},$$

$$D_{ii}^4 = \frac{\partial \phi_i}{\partial S_i} = \frac{-C_i}{C_i^2 + S_i^2} = \frac{-\cos(\phi_i)}{A_i}.$$

The variance-covariance matrix V^y for $\mathbf{y}$ is given by

$$V^y = J\,V^x\,J^\top, \quad V^y_{ii} = \sum_{k=1}^{2n} J_{ik}\left(\sum_{l=1}^{2n} V^x_{kl}J_{il}\right).$$

Consider the following two cases.

$$\begin{aligned}
a)\, i \le n \qquad V^y_{ii} &= J_{ii}\sum_{l=1}^{2n} V^x_{il}J_{il} + J_{i,i+n}\sum_{l=1}^{2n} V^x_{i+n,l}J_{il} \\
&= J^2_{ii}V^x_{ii} + J^2_{i,i+n}V^x_{i+n,i+n} \\
&= \cos^2(\phi_i)V^x_{ii} + \sin^2(\phi_i)V^x_{i+n,i+n} \\
b)\, i > n \qquad V^y_{ii} &= J_{i,i-n}\sum_{l=1}^{2n} V^x_{i-n,l}J_{il} + J_{ii}\sum_{l=1}^{2n} V^x_{il}J_{il} \\
&= J^2_{i,i-n}V^x_{i-n,i-n} + J^2_{ii}V^x_{ii} \\
&= \frac{\sin^2(\phi_i)V^x_{i-n,i-n} + \cos^2(\phi_i)V^x_{ii}}{A^2_i}.
\end{aligned}$$

The $100(1-\alpha)\%$ confidence level $(0 < \alpha < 1)$ for y_i is given by $y_i + t_\nu(1-\alpha/2)\sqrt{V^y_{ii}}$ where ν is the residual degrees of freedom equal to $N-n$; N being the length of the time series, and $t_\nu(x)$ is student's t-distribution (*Draper and Smith*, 1966).

Appendix B: Modal Analysis

This appendix provides the details of the procedure used to perform an optimal fit of the vertical modes — as calculated from a density profile — to the vertical distribution of amplitude and phase obtained from harmonic analysis of horizontal velocity time series.

B.1 The governing equations

The equations governing the vertical structure in a laterally homogeneous inlet of varying breadth $B(z)$ may be derived with the linearized, laterally integrated equations of motion and proceeding by a separation of variables technique. Strictly speaking, B depends on position (x) along the inlet as well as depth. We assume, however, that this variability is gentle enough to be ignored. Thus, we have

$$\rho_0 u_t + p_x = 0, \tag{B.1}$$

$$\rho_0 w_t + p_z = -\rho g, \tag{B.2}$$

$$\rho_t + w\rho_{0z} = 0, \tag{B.3}$$

$$(Bu)_x + (Bw)_z = 0, \tag{B.4}$$

where all variables are lateral averages. The following derivation parallels *LeBlond and Mysak* (1978) with the addition of width variations. Taking the time derivative of (B.2), assuming a harmonic time dependence $e^{-i\sigma t}$, and combining the result with (B.3) to eliminate ρ leads to

$$-\sigma^2 \rho_0 w - i\sigma p_z = wg\rho_{0z},$$

or

$$\rho_0 w(\sigma^2 - N^2) = -i\sigma p_z, \tag{B.5}$$

where

$$N^2 = -\frac{g}{\rho}\frac{\partial \rho}{\partial z}$$

is the Brunt-Väisälä frequency. We also have from (B.1) that

$$-i\sigma\rho_0 u + p_x = 0. \tag{B.6}$$

Define $D(z)$, $U(x)$, $Z(z)$, $P(x)$ via

$\rho_0 u = DU$ $\quad$ D has units of density,

$p = DP$ $\quad$ P has units of pressure/density,

$w = \frac{i\sigma}{g} ZP$ $\quad$ Z is dimensionless.

Substitution into (B.4–6) gives

$$\frac{DBU_x}{\rho_0} + \frac{i\sigma}{g}(BZ)'P = 0, \tag{B.7}$$

$$\rho_0(\sigma^2 - N^2)Z = -gD', \tag{B.8}$$

$$-i\sigma U = -P_x, \tag{B.9}$$

where primes denote differentiation with respect to z. We can rearrange (B.7) as

$$\frac{gU_x}{i\sigma P} = \frac{-\rho_0(BZ)'}{BD} = \frac{1}{h_n}, \tag{B.10}$$

where h_n is a separation constant with units of length. This leads to

$$D = -h_n\rho_0\left(\frac{B'}{B}Z + Z'\right),$$

$$D' = -h_n\rho_0\left[Z'' + Z'\left(-\frac{N^2}{g} + \frac{B'}{B}\right) + Z\left(-\frac{N^2}{g}\frac{B'}{B} + \frac{B''}{B} - \frac{(B')^2}{B^2}\right)\right]. \tag{B.11}$$

Substitution of (B.11) into (B.8) and rearranging, we get

$$Z'' - Z'\left(\frac{N^2}{g} - \frac{B'}{B}\right) + Z\left(\frac{N^2 - \sigma^2}{gh_n} - \frac{N^2}{g}\frac{B'}{B} + \frac{B''}{B} - \frac{(B')^2}{B^2}\right) = 0. \tag{B.12}$$

A dispersion relation may be derived by seeking solutions to (B.9–10) of the form

$$\begin{pmatrix} U \\ P \end{pmatrix} = \sum_{k_1} \begin{pmatrix} a \\ b \end{pmatrix} e^{ik_1 x}.$$

This leads to

$$-i\sigma U + ik_1 P = 0,$$

$$ik_1 gh_n U - i\sigma P = 0.$$

This is a system of two equations in two unknowns, and the dispersion relation is obtained by setting the determinant of the coefficients to 0, that is

$$\det\begin{pmatrix} -i\sigma & ik_1 \\ ik_1 gh_n & -i\sigma \end{pmatrix} = -\sigma^2 + k_1^2 gh_n = 0,$$

$$\frac{\sigma^2}{k_1^2} = gh_n \Rightarrow c_n = \sqrt{gh_n}. \tag{B.13}$$

The phase speed of the internal wave associated with the n^{th} mode is given by (B.13).

B.2 Modal decomposition of density profiles

Computer software was written to solve the modified boundary value problem for the vertical dependence given by (B.12), together with the boundary conditions

$$Z(H) = 0, \tag{B.14a}$$

$$Z' - Z\left(\frac{1}{h_n} - \frac{B'}{B}\right) = 0 \quad \text{for } z{=}0. \tag{B.14b}$$

The method uses a combination of an adaptive Runge-Kutta technique to solve the initial value problem posed by fixing the bottom boundary condition, and a *shooting* method to calculate the unique solution which satisfies the free surface condition.

The CTD data provide a vertical profile of N^2 — the Brunt-Väisälä frequency. These are smoothed using a least squares fit of piecewise cubic polynomials. The purpose of this step is to replace an instantaneous profile with a more representative, quasi-mean profile. The least squares fit also provides a continuous functional representation of N^2 which is then used in solving the ordinary differential equation. Similarly, breadths were interpolated with piecewise cubic splines to provide a continuous function with depth, and thus permit the calculation of higher order derivatives as required.

The angular frequency, σ, is normally much smaller than N for the tidal frequencies being considered here, hence the modal structure is nearly independent of the particular tidal constituent being examined.

Corresponding vertical modes for the horizontal velocity can be derived from the solution to (B.10) by using the continuity equation, that is

$$u = -\int_{x_1}^{x_2} \frac{\partial w}{\partial z}\, dx \propto \frac{\partial w}{\partial z}, \tag{B.15}$$

provided there is negligible lateral velocity, and w is only weakly dependent on longitudinal position.

The modes calculated from (B.12) and (B.14) were evaluated and normalized so that

$$\int_0^H \Phi_i(z)\Phi_j(z)\,dz = \begin{cases} 1, & \text{if } i = j; \\ 0, & \text{if } i \neq j. \end{cases} \qquad j = 0, 1, \ldots, m$$

Values of each modal function were then saved at $1m$ intervals.

It was found that the modal solutions for Indian Arm are only weakly affected by the variations in width. In comparisons made with solutions from the width-independent solutions it was found that phase speeds changed by only a few percent, and the shapes of the modes were essentially unaltered. It is possible, however, that for other inlets or bodies of water with sudden width changes over small depth intervals the inclusion of these effects in the modal equations may be significant.

Modal decomposition provides information only on the shapes of possible modes, and not on which modes are actually excited. This may be estimated, however, by fitting the calculated modes to the results of harmonic analysis.

B.3 The Least Squares Fit to Harmonic Analysis

Vertical profiles of horizontal current provided by Cyclesonde vertically profiling current meters, or XZT model output, can be used to calculate possible modal excitations if accompanying density data is available.

Harmonic analysis of time series at each of n discrete depths in a vertical profile of horizontal velocities is first performed to calculate amplitude and phase estimates $\{A_i, \theta_i : i = 1, 2, \ldots, n\}$. These are transformed to rectangular coordinates to provide vectors $\mathbf{U}^{(x)}$ and $\mathbf{U}^{(y)}$ according to

$$U_i^{(x)} = A_i \cos(\theta_i) \qquad (B.16)$$

$$U_i^{(y)} = A_i \sin(\theta_i) \qquad (B.17)$$

The set of $m + 1$ modal functions, $\Phi_j(z), j = 0, 2, \ldots, m$, calculated from the stratification is selected as a basis for a least squares fit to the results of the harmonic analysis.

The objective is to determine complex coefficients $\{C_j : j = 0, 1, \ldots, m\}$ such that

$$\sum_{j=0}^{m} C_j \Phi_j(z)$$

provides a best fit to the observed vertical profile $\mathbf{U}$ in a least squares sense. The values of $\Phi_j(z)$ at each depth in the velocity profile are extracted to form a matrix $\mathbf{M}$, where $\mathbf{M}_{ij}$ is the value at depth i of the j^{th} mode. Writing the real part of $\mathbf{C}$ as $\mathbf{C}^{(x)}$, and the imaginary part as $\mathbf{C}^{(y)}$, we can formulate the two linear model equations

$$\mathbf{U}^{(x)} = \mathbf{M}\mathbf{C}^{(x)} + \epsilon^{(x)}, \tag{B.18}$$

$$\mathbf{U}^{(y)} = \mathbf{M}\mathbf{C}^{(y)} + \epsilon^{(y)}, \tag{B.19}$$

where $\epsilon^{(x)}$ and $\epsilon^{(y)}$ are vectors of residuals. These two sets of equations can be combined as

$$\begin{pmatrix} \mathbf{U}^{(x)} \\ \mathbf{U}^{(y)} \end{pmatrix} = \begin{pmatrix} \mathbf{M} & 0 \\ 0 & \mathbf{M} \end{pmatrix} \begin{pmatrix} \mathbf{C}^{(x)} \\ \mathbf{C}^{(y)} \end{pmatrix} + \begin{pmatrix} \epsilon^{(x)} \\ \epsilon^{(y)} \end{pmatrix}$$

which we write in the compact form

$$\mathbf{U} = \mathcal{M}\mathbf{C} + \epsilon.$$

The least squares estimates $\hat{\mathbf{U}}$ are then given by $\hat{\mathbf{U}} = \mathcal{M}\mathbf{C}$, and the corresponding amplitude and phase estimates for each depth are given by $\hat{A}_i = \sqrt{(U_i^{(x)})^2 + (U_i^{(y)})^2}$, $\theta_i = \arctan(U_i^{(x)}/U_i^{(y)})$. The phase of the barotropic mode, θ_0, is known quite well from observations, since the barotropic velocity is very nearly in quadrature with the surface elevation due to the very low rates of energy dissipation found in the deep basin of the inlet. This information was incorporated in the least squares problem. The 0^{th} column of $\mathbf{M}$, corresponding to the barotropic mode, was removed. The least squares problem was then formulated as

$$\begin{pmatrix} \mathbf{U}^{(x)} \\ \mathbf{U}^{(y)} \end{pmatrix} = \begin{pmatrix} \mathbf{b}^{(x)} & \mathbf{M} & 0 \\ \mathbf{b}^{(y)} & 0 & \mathbf{M} \end{pmatrix} \begin{pmatrix} C_0 \\ \mathbf{C}^{(x)} \\ \mathbf{C}^{(y)} \end{pmatrix} + \begin{pmatrix} \epsilon^{(x)} \\ \epsilon^{(y)} \end{pmatrix} \tag{B.20}$$

where

$$b_i^{(x)} = \cos(\theta_0)\Phi_{i0},$$

$$b_i^{(y)} = \sin(\theta_0)\Phi_{i0},$$

and θ_0 is specified. C_0 is the unknown amplitude of the barotropic coefficient.

Following the usual least squares analysis (e.g., *Draper and Smith*, 1966) we minimize the squared residual error by calculating the solution as

$$\mathbf{C} = (\mathcal{M}'\mathcal{M})^{-1}\mathcal{M}'\mathbf{U}, \tag{B.21}$$

where a prime denotes the transposed matrix or vector, and $\mathcal{M}$ is now the modified coefficient matrix given in (B.20). The adequacy of the least squares fit may be evaluated by construction of an analysis of variance (ANOVA) table ilustrated in *table* 27.

Table 27
ANOVA table structure (adapted from Draper and Smith, 1966)

Source	*Symbol*	*Formula*	*Deg. Freedom*	*Mean Square*
C_0	$SS(C_0)$	$(\sum C_i)^2/n$	1	
Regression$\|C_0$	$SS(Reg\|C_0)$	$\mathbf{C}\mathcal{M}'\mathbf{U} - SS(C_0)$	$m-1$	$MS(Reg\|C_0)$
Residual	SS_E	$\mathbf{U}'\mathbf{U} - \mathbf{C}\mathcal{M}'\mathbf{U}$	$n-m$	MS_E
Total	SS_T	$\mathbf{U}'\mathbf{U}$	n	

The adequacy of the solution $\mathbf{C}$, together with the set of basis functions $\{\Phi_j\}$, in modelling the observed vertical distribution of velocities may be checked by testing the hypothesis $H_0 : C_1 = C_2 = \cdots = C_m = 0$ against H_1 : not all $C_i = 0$. The ratio

$$\frac{[SS(Reg|C_0)/(m-1)]}{MS_E}$$

is destributed as $F(m-1, n-m)$. A 95% significance level was selected for the F-distribution in order to filter out models which did not satisfy the hypothesis. In addition, the value of

$$R^2 = \frac{SS(Reg|C_0)}{\mathbf{U}'\mathbf{U} - SS(C_0)} \tag{B.22}$$

indicates the success of the model in accounting for the variation in the data. A value of 1.0 indicates a perfect fit while a value of 0.0 indicates that the model accounts for none of the variation. It should be remembered when interpreting R^2 that a value close to 1.0 is always achieved if m is close to n. Normally, the number of depths was much greater than

the number of modes being fitted, and the R^2 values were considered to be meaningful in determining the goodness of fit.

Analysis was limited to the barotropic and first 5 baroclinic modes since these were expected to contain most of the energy. Fits were calculated and plotted for comparison with the data.

B.4 Energy distribution

The above procedure allows an estimate of the kinetic energy in each mode to be calculated. This follows from the expression for the kinetic energy density per unit length along the inlet given by

$$E = \frac{\rho}{2}\int_0^H B(z)|u(z)|^2\,dz = \frac{\rho}{2}\int_0^H B(z)A^2\,dz, \qquad (B.23)$$

where ρ is assumed independent of depth, and $u(z) = [A(z), \theta(z)]$ is the polar representation of the complex amplitude for a tidal constituent. Letting $\hat{u} = \sqrt{B}u$ ($|\hat{u}|^2 = B|u|^2$), we have from the least squares modal fit that

$$\hat{u} = \sum_{j=0}^{m} C_j \Phi_j(z),$$

which leads to

$$\int_0^H |\hat{u}|^2\,dz = \int_0^H |\sum_{j=0}^{m} C_j\Phi_j(z)|^2 = \sum_{j=0}^{m}|C_j|^2,$$

where the orthogonality of the Φ_j has been used. The percentage of energy in each mode then becomes

$$P_j = 100 \cdot \frac{|C_j|^2}{\sum_{k=0}^{m}|C_k|^2}. \qquad (B.24)$$

Appendix C: Properties of the finite difference equations

Recalling the laterally integrated equations for continuity and horizontal momentum given by (3.25) and (3.27) respectively, and vertically integrating both from the surface $(-\eta)$ to the bottom (H) yields

$$\frac{\partial U}{\partial x} + B_0 \frac{\partial \eta}{\partial t} = 0, \tag{C.1}$$

$$\frac{\partial U}{\partial t} + gA \frac{\partial \eta}{\partial x} = R, \tag{C.2}$$

where

$$U(x,t) = \int_{-\eta}^{H} Bu \, dz, \tag{C.3}$$

$$A(x,t) = \int_{-\eta}^{H} B \frac{\varrho}{\rho} \, dz, \tag{C.4}$$

$$R(x,t) = \int_{-\eta}^{H} (other\ terms) \, dz. \tag{C.5}$$

(C.1) and (C.2) may be combined to yield an equation for η alone

$$\frac{\partial^2 \eta}{\partial t^2} = \frac{g}{B_0} \frac{\partial}{\partial x} \left(A \frac{\partial \eta}{\partial x} \right) - \frac{1}{B_0} \frac{\partial R}{\partial x}. \tag{C.6}$$

A generalized finite difference expression for (C.6) can be written as

$$\delta_t^2 [\eta]_j^n = \frac{g}{B_{0j} \lambda^2} \delta_x \left[A \left\{ \theta \left(\beta \delta_x [\eta]_j^{n+1} + (1-\beta) \delta_x [\eta]_j^{n-1} \right) + (1-\theta) \delta_x [\eta]_j^n \right\} \right]_j^n \tag{C.7}$$

where $\lambda = \Delta x / \Delta t$, B_{0j} is the width at the surface for column j, and $0 \leq \theta, \beta \leq 1$ are prescribed weights ($[\theta, \beta] = [0,0]$ in the model described in this thesis). The notation of chapter 4 has been modified slightly so that a variable superscript — such as $n+1$ in A^{n+1} — refers to the relative time level. It can be noted that (C.7) is explicit (the right hand side independent of time level $n+1$) if either $\theta = 0$, or $\beta = 0$. If both of these parameters are nonzero then (C.7) is implicit and must be solved by effectively solving a tri-diagonal system of linear equations — a procedure that can be done very efficiently. Rearranging (C.7) yields

$$\begin{aligned} \frac{\lambda^2 B_{0j}}{g} \delta_t^2 [\eta]_j^n = {} & \theta\beta \delta_x \left[A^n \delta_x [\eta]_j^{n+1} \right]_j + (1-\theta) \delta_x \left[A^n \delta_x [\eta]_j^n \right]_j \\ & + \theta(1-\beta) \delta_x \left[A^n \delta_x [\eta]_j^{n-1} \right]_j - \frac{\Delta x}{g} \delta_x [R]_j^n, \end{aligned} \tag{C.8}$$

and finally,

$$\theta\beta A^n_{j-\frac{1}{2}}\eta^{n+1}_{j-1} - \left(\frac{\lambda^2 B_{0j}}{g} + 2\theta\beta A^n_j\right)\eta^{n+1}_j + \theta\beta A^n_{j+\frac{1}{2}}\eta^{n+1}_{j+1}$$
$$= \delta_x\left[\frac{\Delta x}{g}R - A\left[\theta(1-\beta)\delta_x[\eta]^{n-1}_j + (1-\theta)\delta_x[\eta]^n_j\right]\right]^n_j + \frac{\lambda^2 B_{0j}}{g}(\eta^{n-1}_j - 2\eta^n_j). \quad (C.9)$$

For the purposes of analysis (C.9) can be simplified by assuming that $\eta \ll H$, $B_{ij} \equiv B$ (a constant), $\varrho = \rho = 1$, and $R \equiv 0$. Thus, $A^n_j = BH$, $R^n_j = 0$, and (C.9) becomes

$$\delta_t^2[\eta]^n_j = r^2\left\{\theta\beta\delta_x^2[\eta]^{n+1}_j + (1-\theta)\delta_x^2[\eta]^n_j + \theta(1-\beta)\delta_x^2[\eta]^{n-1}_j\right\}, \quad (C.10)$$

where $r^2 = gH/\lambda^2 = c^2/\lambda^2$. Finally we can write

$$r^2\theta\beta(\eta^{n+1}_{j+1} + \eta^{n+1}_{j-1} - (1+2\theta\beta r^2)\eta^{n+1}_j = 2\left[(1-\theta)r^2 - 1\right]\eta^n_j - r^2(1-\theta)(\eta^n_{j+1} + \eta^n_{j-1})$$
$$-\theta(1-\beta)r^2(\eta^{n-1}_{j+1} + \eta^{n-1}_{j-1}) + \left[1 + 2\theta(1-\beta)r^2\right]\eta^{n-1}_j. \quad (C.11)$$

C.1 Accuracy

Expansion of $\eta^{n\pm1}_{j\pm1}$ in a finite Taylor's series expansion to 3^{rd} order yields

$$\eta^{n\pm1}_{j\pm1} = \eta^n_j \pm \Delta x\frac{\partial\eta}{\partial x} \pm \Delta t\frac{\partial\eta}{\partial t} + \frac{\Delta x^2}{2}\frac{\partial^2\eta}{\partial x^2} + \frac{\Delta t^2}{2}\frac{\partial^2\eta}{\partial t^2} \pm \Delta x\Delta t\frac{\partial^2\eta}{\partial x\partial t}$$
$$\pm\frac{\Delta x^3}{6}\frac{\partial^3\eta}{\partial x^3} \pm \frac{\Delta x^2\Delta t}{2}\frac{\partial^3\eta}{\partial x^2\partial t} \pm \frac{\Delta x\Delta t^2}{2}\frac{\partial^3\eta}{\partial x\partial t^3} \pm \frac{\Delta t^3}{6}\frac{\partial^3\eta}{\partial t^3} + \text{higher order terms.} \quad (C.12)$$

Substituting (C.12) into (C.10) and rearranging yields

$$\frac{\partial^2\eta}{\partial t^2} = gH\left\{\frac{\partial^2\eta}{\partial x^2} + \theta(2\beta-1)\Delta t\frac{\partial^3\eta}{\partial x^2\partial t}\right\} + O(\Delta x^2) + O(\Delta t^2). \quad (C.13)$$

Thus for $\theta = 0$ (and all β), or for $\beta = \frac{1}{2}$ (and all θ) the finite difference scheme is 2^{nd} order in both Δx and Δt. In particular, the difference scheme used for the model is 2^{nd} order accurate.

C.2 Stability

Let η_j^n be a solution to (C.11) where $\eta_j^n \equiv \eta\left[(j-\frac{1}{2})\Delta x, n\Delta t\right]$, $(1 \le j \le N)$. Expand η_j^n in a Fourier series:

$$\eta_j^n = \sum_{l=-\infty}^{\infty} a_l \exp\left\{i(k_l x_j - \omega_l t_n)\right\}, \qquad (C.14)$$

where $k_l = 2\pi/L_l$, $L_l = 2N\Delta x/l$, $x_j = j\Delta x$, $t_n = n\Delta t$, $\omega_l = 2\pi/T_l$, and the a_l are real. Let $V_l \equiv a_l^{\frac{1}{n}} e^{-i\omega_l \Delta t}$, and $\phi_l \equiv k_l \Delta x = l\pi/N$. Taking one harmonic term from (C.14) and substituting into (C.11) we have (ignoring subscripts for clarity)

$$V^{n+1}\left[2r^2\theta\beta\cos\phi - (1+2\theta\beta r^2)\right] = 2V^n\left[(1-\theta)r^2(1-\cos\phi) - 1\right]$$
$$+V^{n-1}\left[2r^2\theta(1-\beta)(1-\cos\phi) + 1\right]. \qquad (C.15)$$

Defining $\mathbf{W}$ by

$$\mathbf{W}^{n+1} = \begin{pmatrix} V^{n+1} \\ V^n \end{pmatrix}$$

we can rewrite (C.15) as

$$\begin{pmatrix} V^{n+1} \\ V^n \end{pmatrix} = \begin{pmatrix} c_1 & -c_2 \\ 1 & 0 \end{pmatrix} \begin{pmatrix} V^n \\ V^{n-1} \end{pmatrix} \quad \Rightarrow \quad \mathbf{W}^{n+1} = \mathbf{G}\mathbf{W}^n$$
$$\mathbf{W} = \begin{pmatrix} V \\ 1 \end{pmatrix}, \qquad c_1 = \frac{2\left[1-(1-\theta)\psi\right]}{1+2\theta\beta\psi}, \qquad c_2 = \frac{1+2\theta(1-\beta)\psi}{1+2\theta\beta\psi},$$

where $\psi \equiv r^2(1-\cos\phi) : 0 \le \psi \le 2r^2$. Stability of the finite difference scheme requires that the spectral radius of $\mathbf{G}$ — $SP(\mathbf{G})$ — satisfies $SP(\mathbf{G}) \le 1$, that is, $|\alpha| \le 1 \quad \forall \alpha : \alpha$ an eigenvalue of $\mathbf{G}$. Since

$$\begin{pmatrix} V^2 \\ V \end{pmatrix} = \mathbf{G}\begin{pmatrix} V \\ 1 \end{pmatrix} \quad \Rightarrow \quad V\begin{pmatrix} V \\ 1 \end{pmatrix} = \mathbf{G}\begin{pmatrix} V \\ 1 \end{pmatrix}$$

it is clear that V is an eigenvalue of $\mathbf{G}$, and $[V,1]^T$ is an eigenvector for V which must satisfy

$$|\mathbf{G} - V\mathbf{I}| = 0 \quad \Rightarrow \quad (c_1 - V)(-V) + c_2 = 0 \quad \Rightarrow \quad V^2 - c_1 V + c_2 = 0.$$

This leads to the solution

$$V_{\pm} = \frac{c_1 \pm \sqrt{c_1^2 - 4c_2}}{2}.$$

Assuming that $c_1^2 > 4c_2$, and substituting for c_1 and c_2 leads to

$$\left[1-(1-\theta)\psi\right]^2 - \left[1+2\theta(1-\beta)\psi\right]\left[1+2\theta\beta\psi\right] > 0,$$

or

$$\theta^2\left[1-4\beta(1-\beta)\right] - 2\theta + 1 > \frac{2}{\psi} \qquad \forall\psi. \tag{C.16}$$

However, $\psi = c^2(1-\cos\phi)/\lambda^2 \geq 0$, and in particular; $\forall\theta,\beta : 0 \leq \theta,\beta \leq 1 \quad \exists\psi > 0$ such that $\theta^2\left[1-4\beta(1-\beta)\right] - 2\theta + 1 \leq \frac{2}{\psi}$. This contradicts (C.16), and hence it must be that $c_1^2 - 4c_2 \leq 0$. $V_\pm$ can therefore be written as

$$V_\pm = \frac{c_1 \pm i\sqrt{4c_2 - c_1^2}}{2}, \quad \text{and hence} \quad |V_\pm| = \sqrt{c_2},$$

where the root is real.

For stability we require that $|V_\pm| \leq 1$. This leads to $c_2 \leq 1$, and $1 + 2\theta(1-\beta)\psi \leq 1 + 2\theta\beta\psi$. This is satisfied if $\theta = 0$ (β arbitrary), or if $\beta \geq \frac{1}{2}$ (θ arbitrary). As shown above, $c_1^2 - 4c_2 \leq 0$ leads to

$$\theta^2\left[1-4\beta(1-\beta)\right] - 2\theta + 1 \leq \frac{2}{\psi}. \tag{C.17}$$

(C.17) is true for all ψ provided that

$$\theta \geq \frac{1-\sqrt{1-\left[1-\lambda^2/c^2\right]\left[1-4\beta(1-\beta)\right]}}{1-4\beta(1-\beta)}. \tag{C.18}$$

For $0 \leq \beta \leq 1$ we have $1-4\beta(1-\beta) \geq 0$. Assume $\lambda^2/c^2 \geq 1$ so that $\Delta t \leq \Delta x/\sqrt{gH}$. Therefore, $\theta \geq 0$ and $\beta \geq \frac{1}{2}$ is sufficient for the numerical scheme to be stable. Setting $\lambda^2/c^2 = 0$ leads to $\theta \geq \left[1+2\sqrt{\beta(1-\beta)}\right]^{-1}$. Thus, since $\lambda^2/c^2 > 0$, this is a criterion for unconditional stability. In the case of the scheme used in the model we have conditional stability since $\theta = 0$, and thus Δt must satisfy the C.F.L. criterion given by $\Delta t \leq \Delta x/\sqrt{gH}$.

C.3 Phase errors

Using the definition of V leads to

$$a_n^{\perp} e^{-i\omega\Delta t} = \frac{c_1 \pm i\sqrt{4c_2 - c_1^2}}{2},$$

and solving for ω yields the following (numerical) dispersion relation:

$$\omega_N = \frac{1}{\Delta t} |\arctan\left(\frac{\sqrt{4c_2 - c_1^2}}{c_1}\right)|. \qquad (C.19)$$

The relative error in the numerical phase speed $c_n = \omega_N/k$ is given by

$$\frac{c_N - c_s}{c_s} = \frac{\omega_N - \omega_s}{\omega_s} = \frac{\omega_N}{\omega_s} - 1$$

for fixed values of k.

For the case of $\theta = \beta = 0$, $c_1 = [1 - r^2(1 - \cos\phi)]$, and $c_2 = 1$. Using the values $\Delta x = 2\,km$, $\Delta t = 20\,s$, $g = 9.8\,m\,s^{-2}$, and $H = 200\,m$ leads to the relative phase errors for the Indian Arm model listed in *table* 28 for a sample of different wave lengths.

Table 28
Relative error in phase speeds for Indian Arm numerical model

wave length (*km*)	*% relative error*
2	-100
5	-23
10	-5.9
15	-2.6
20	-1.5

For the wave lengths found in the model we expect from these results that phase errors will be minimal.

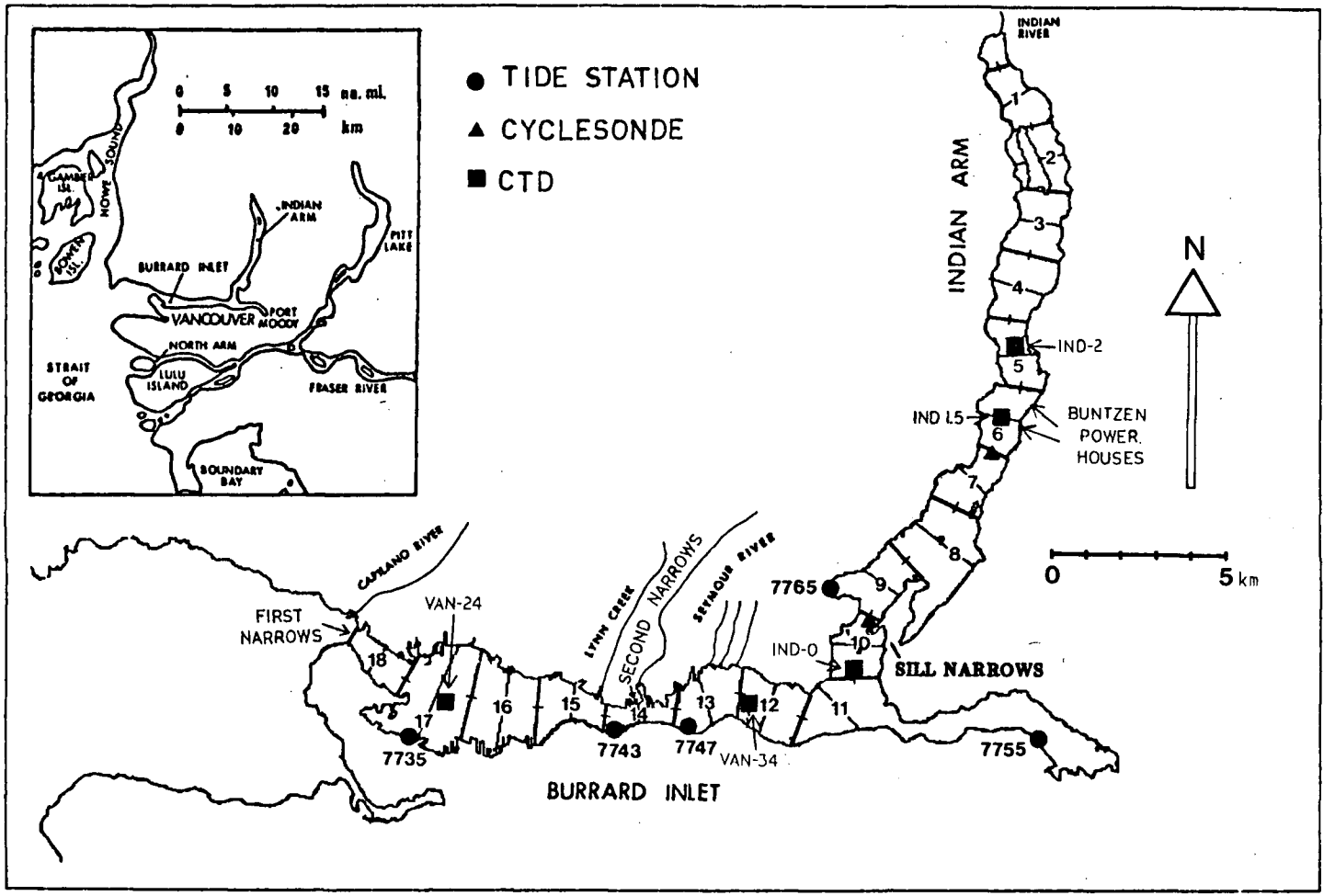

Figure 1. Plan view of Indian Arm and Burrard Inlet. Numbered sections correspond to the numerical model described in chapter 4 of the text.

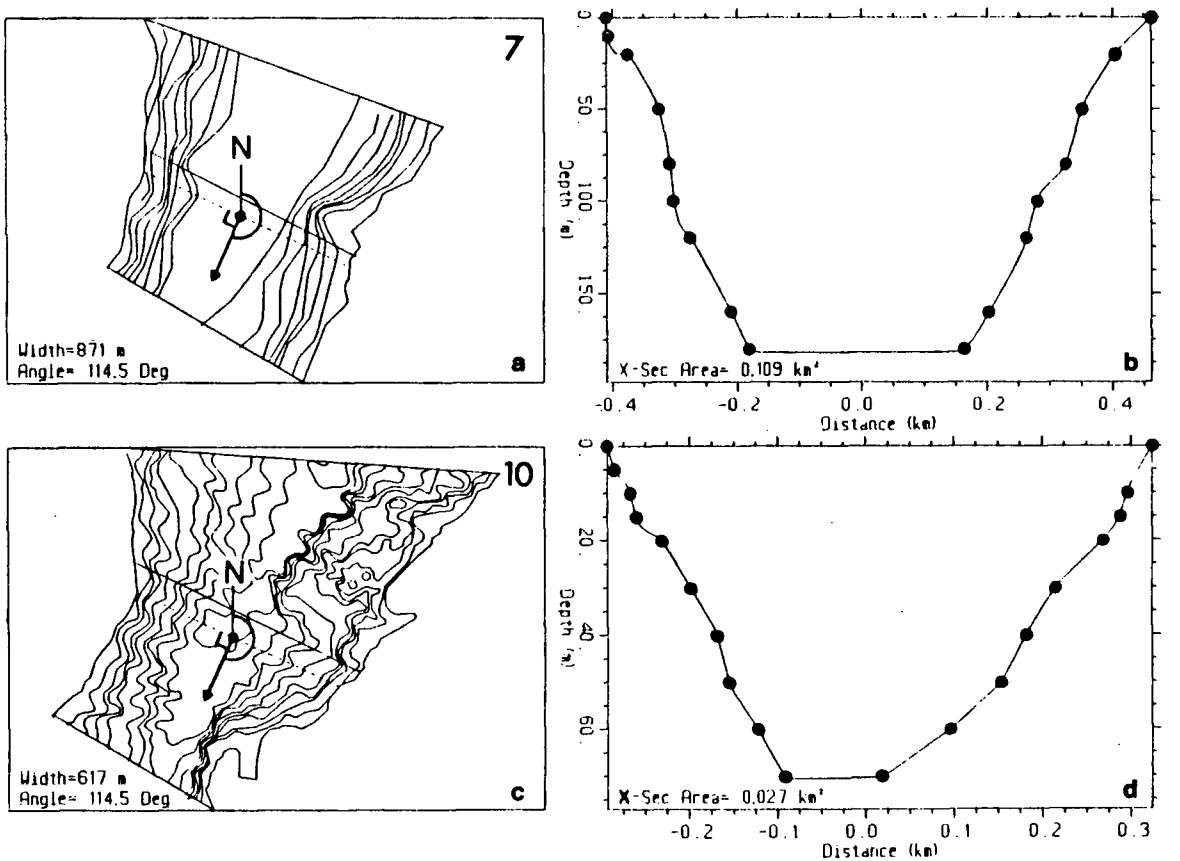

Figure 2. Plot (a): plan view of Indian Arm near Cyclesonde current meter location adjacent to model *S–point*for section 7. Contours are for depths indicated in plot (b) by solid circles. The arrow indicates the positive x-axis (out of inlet) direction in the model. Plot (b): Cross-inlet bottom profile along section 7 shown in (a). Vertical exaggeration is approximately 6 : 1. Circles indicate the depths of contours in (a). Plots (c) and (d): Same as plots (a) and (b), but for Cyclesonde location near model section 10.

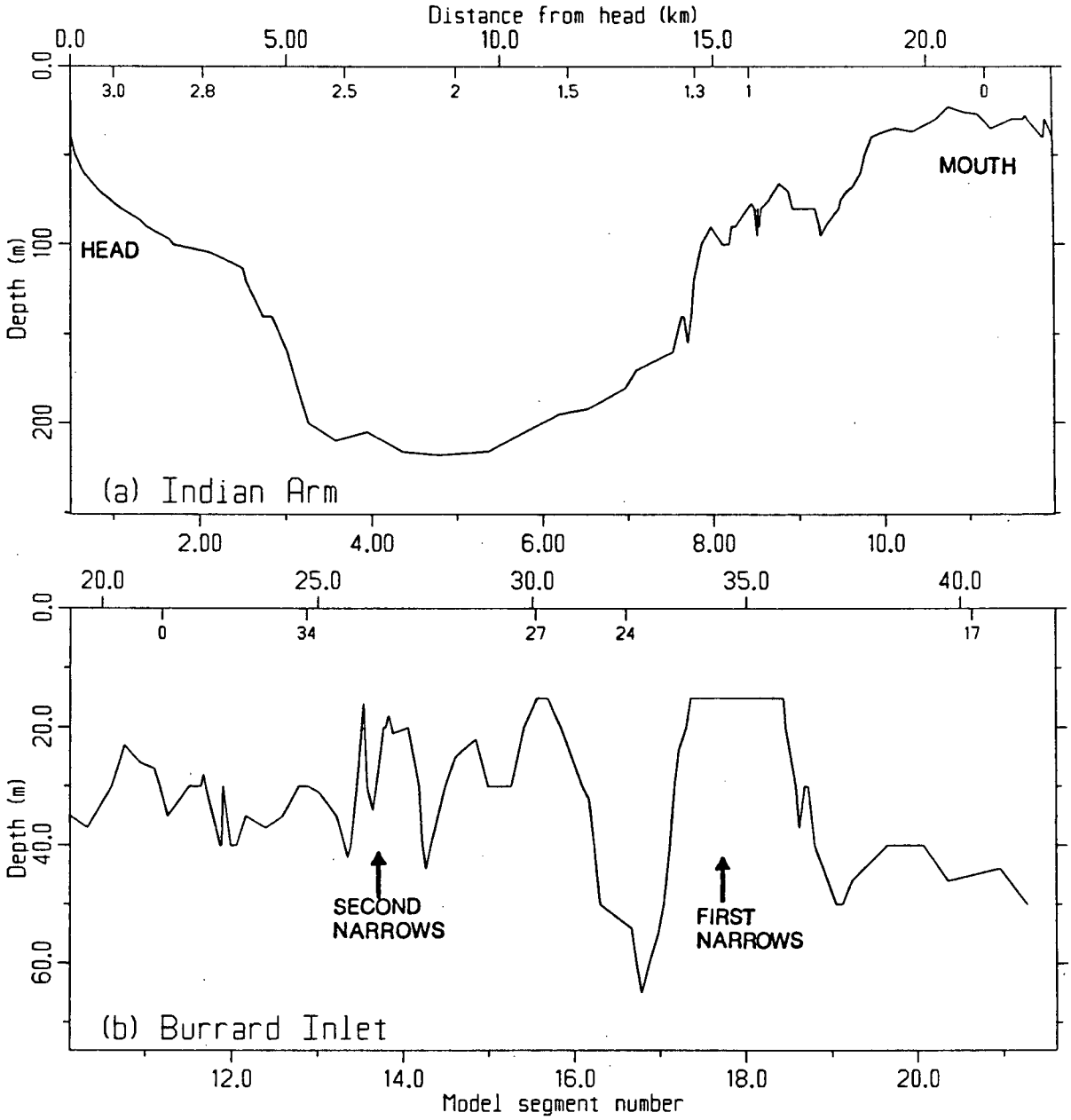

Figure 3. Longitudinal section of (a) Indian Arm and (b) Burrard Inlet. Note change in vertical scales between plots. Locations of standard CTD stations are indicated below the upper scale for *Distance from head*

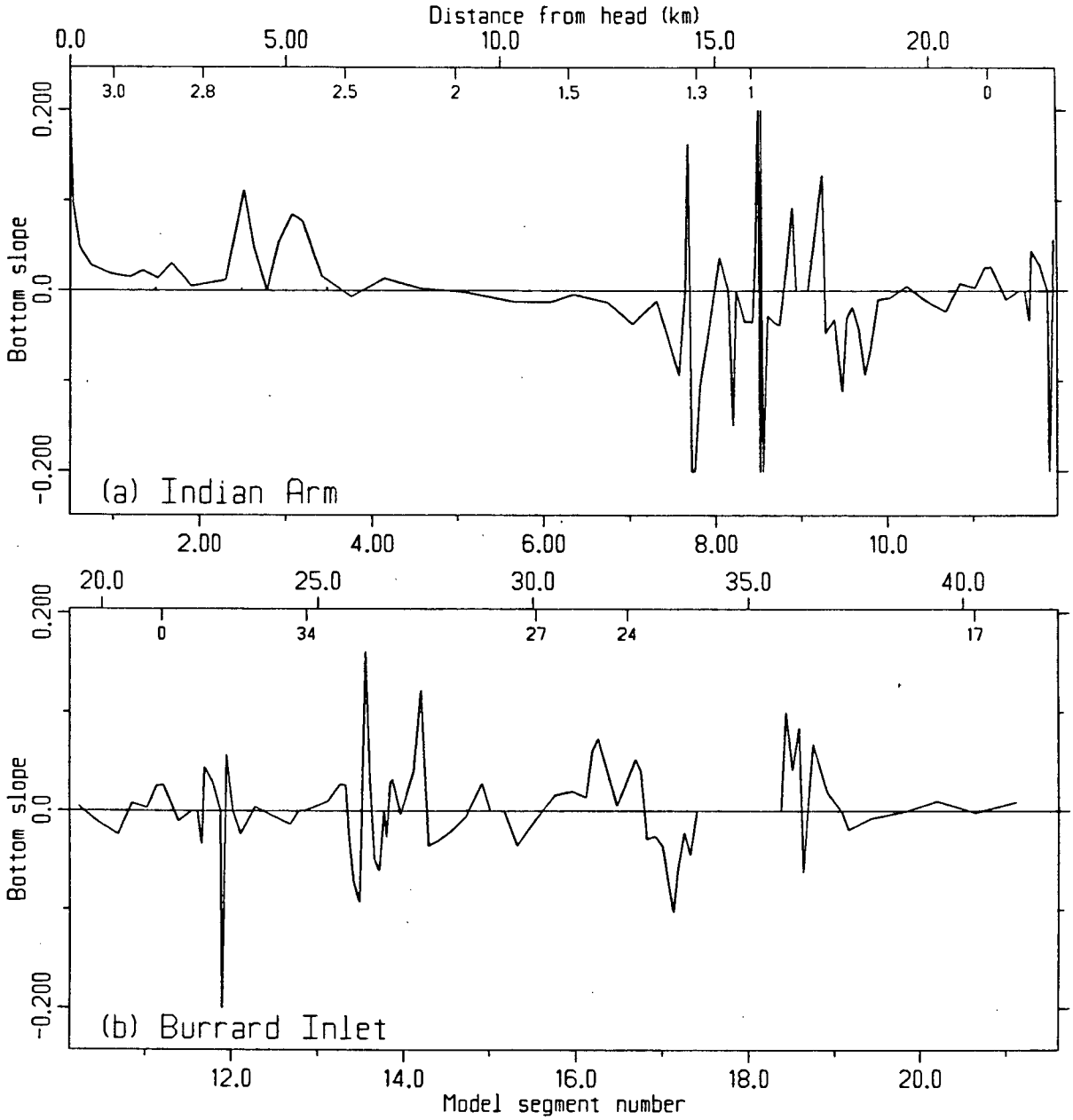

Figure 4. Bottom slope for (a) Indian Arm and (b) Burrard Inlet. Locations of standard CTD stations are indicated below the upper scale for *Distance from head*

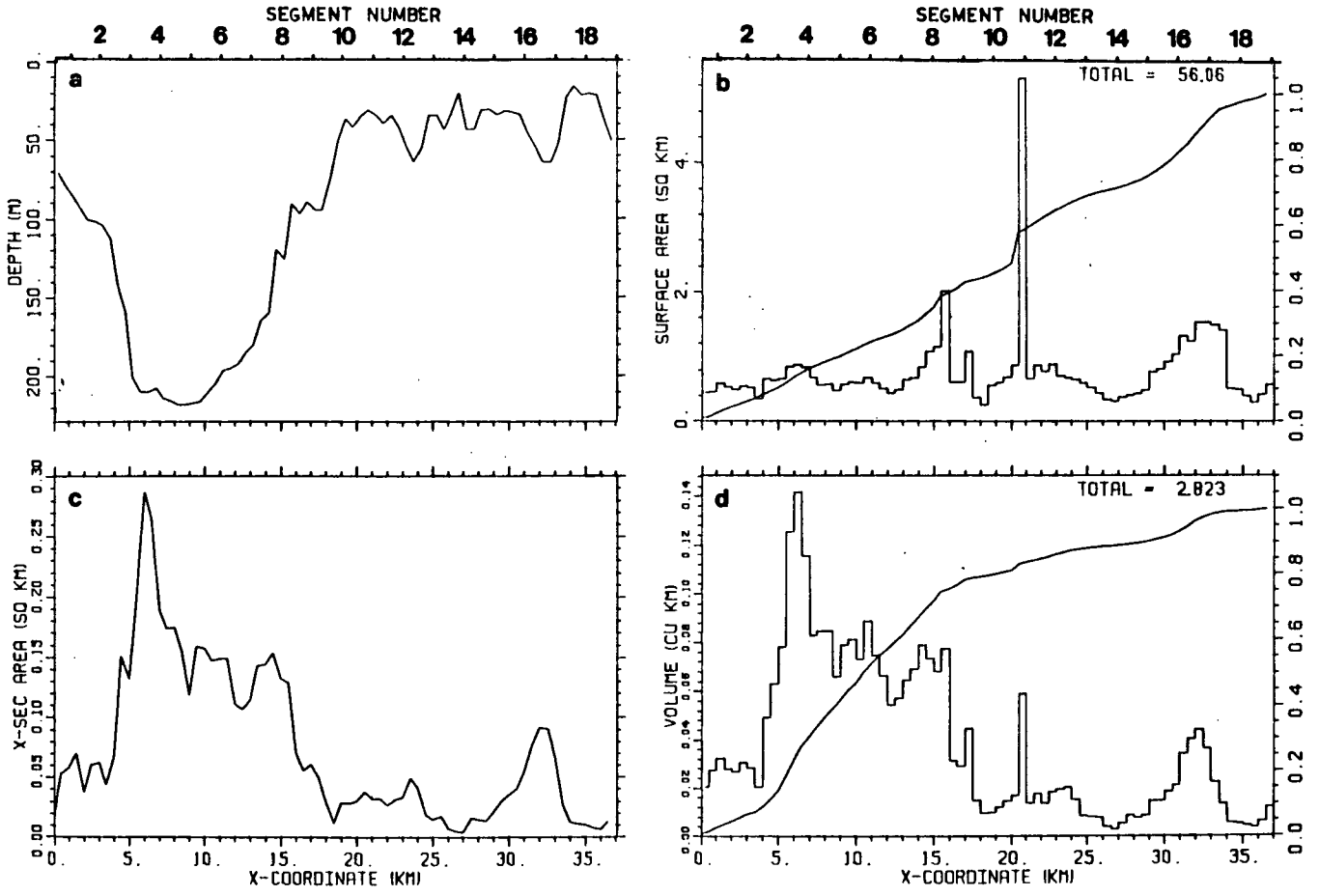

Figure 5. Summary of physical features for Indian Arm and Burrard Inlet (see text and Table 1 for details). The locations of model *segment numbers* are show in *figure* 1. TOTAL values are integrals from the head to the mouth. This value, together with the corresponding cumulative integral curve and scale to the right of the plot may be used to calculate partial integrals along the inlets.

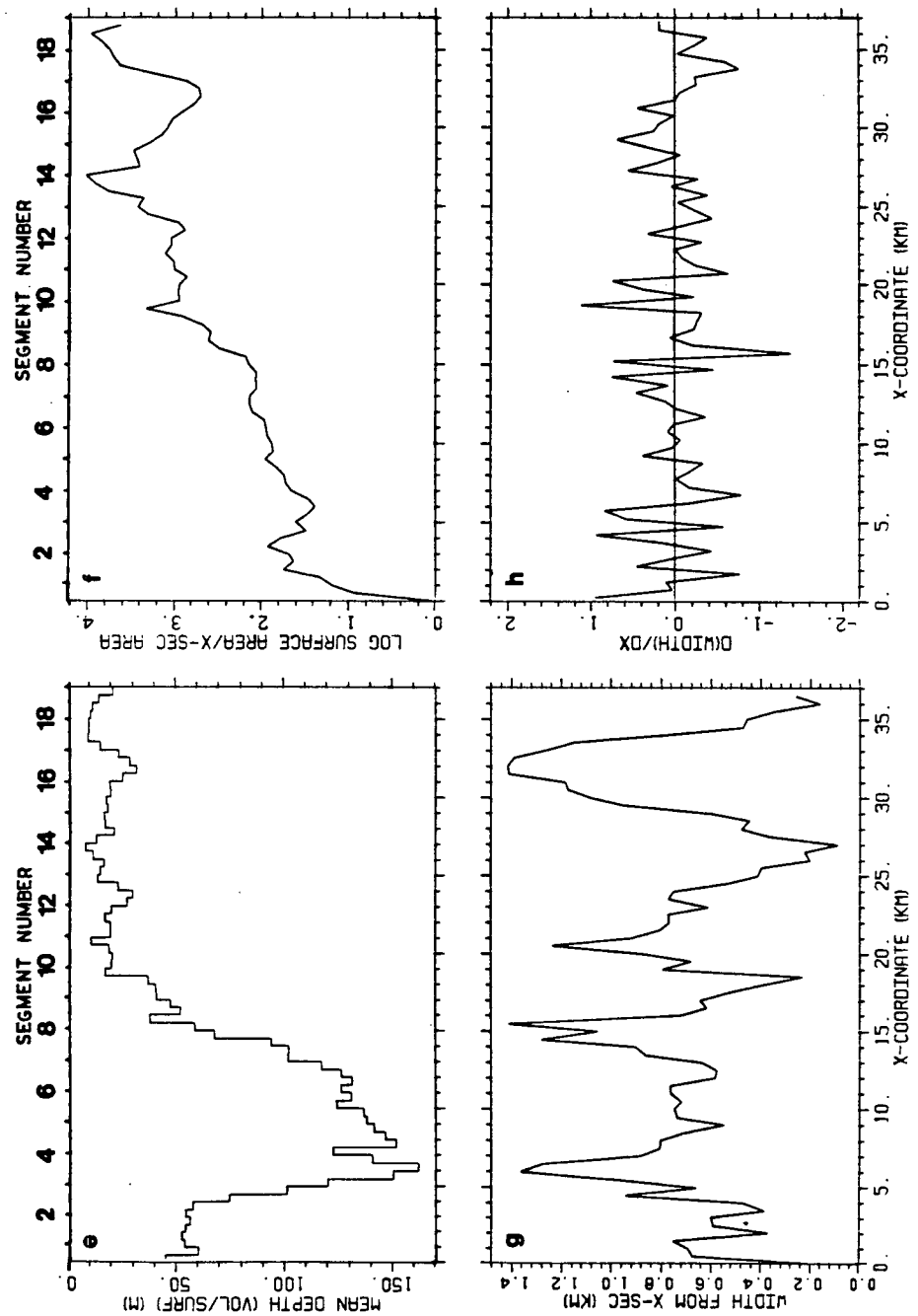

Figure 5(continued)

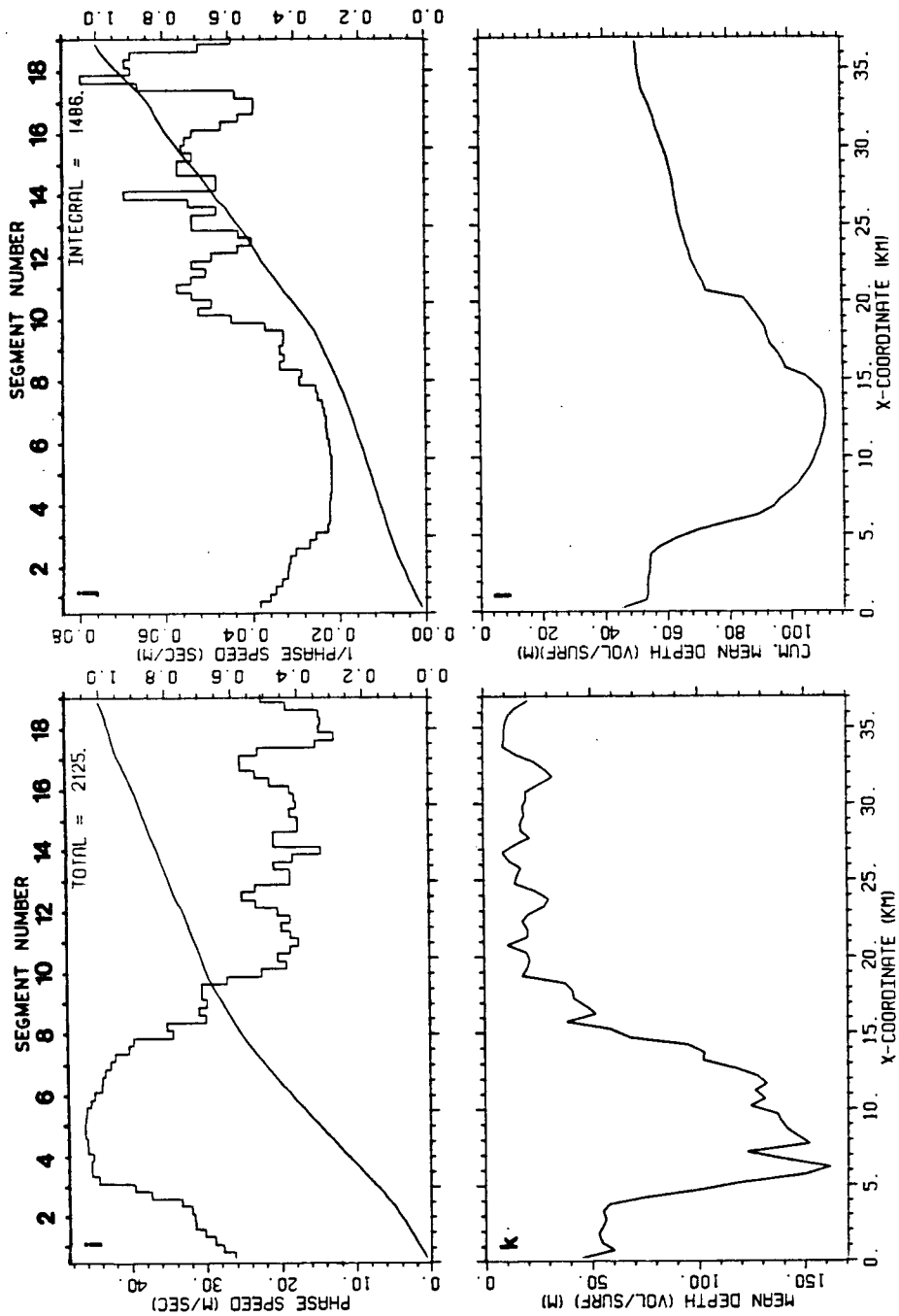

Figure 5(continued)

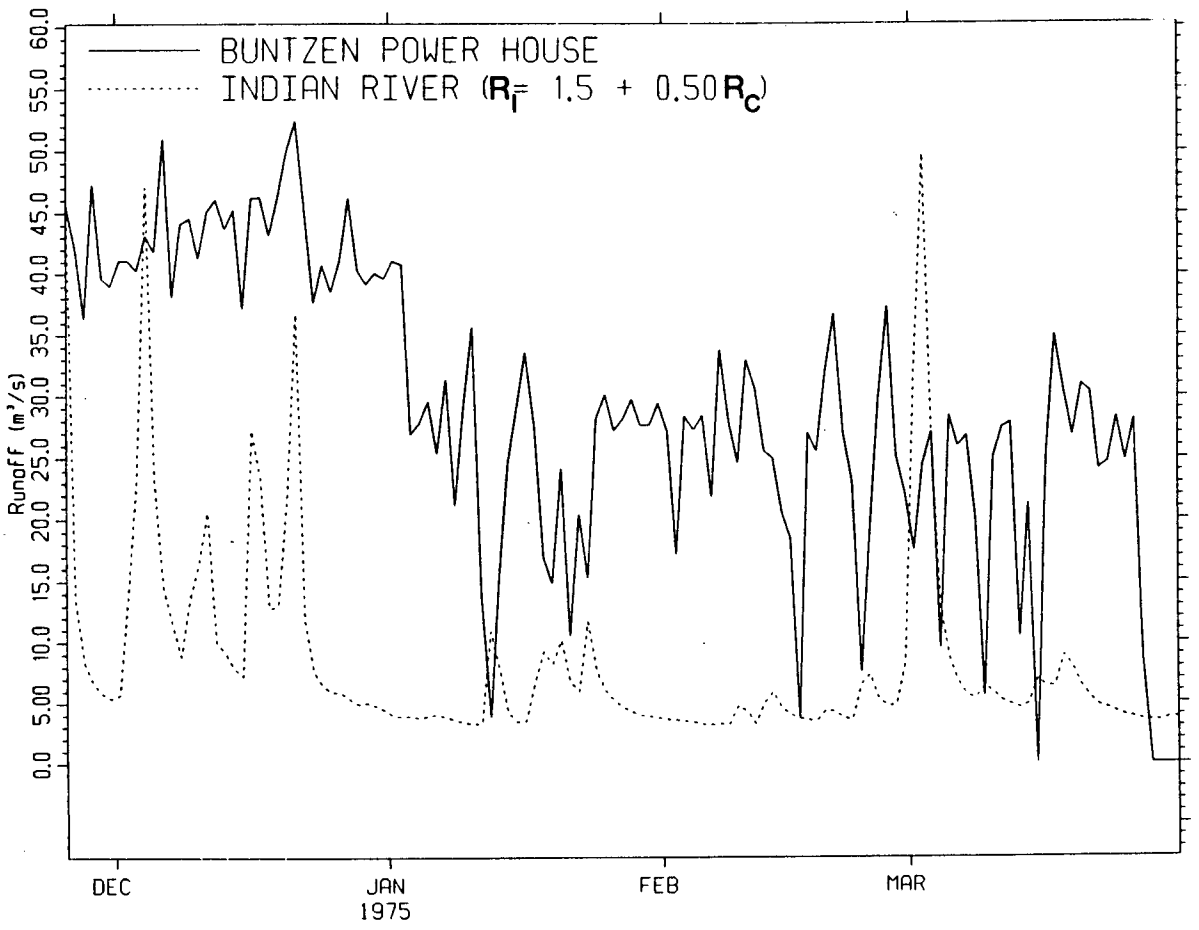

Figure 6. Freshwater discharge data for the Buntzen Power House and Indian River (R_I). The latter is estimated from Capilano River data (R_C) using the regression equation shown (see sec 2.2)

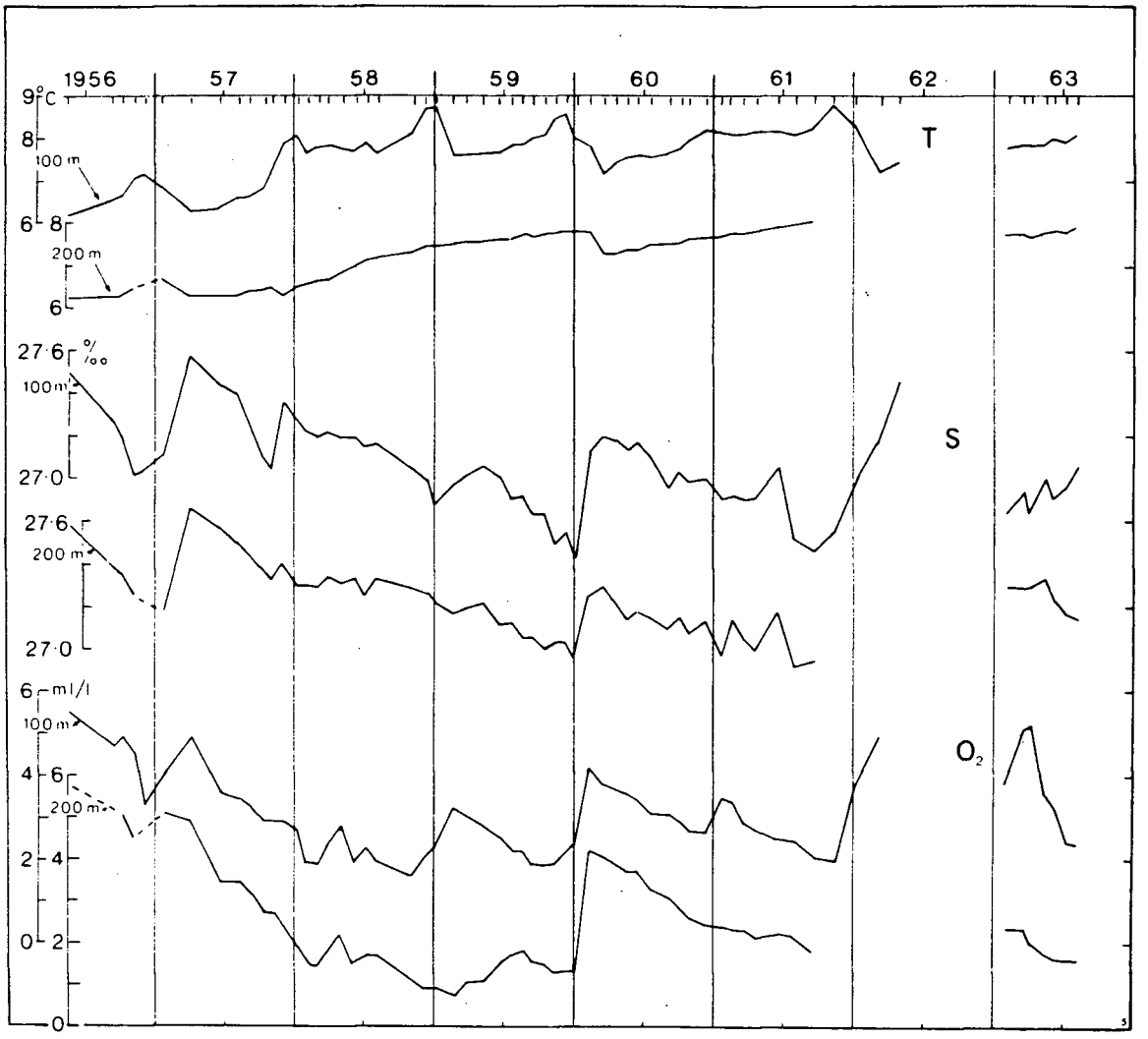

Figure 7. **Annual variations in temperature (T), Salinity (S) and oxygen (O_2) at depths 100 *m* and 200 *m* for a central representative location in the deep basin of Indian Arm for the period 1956–63.**

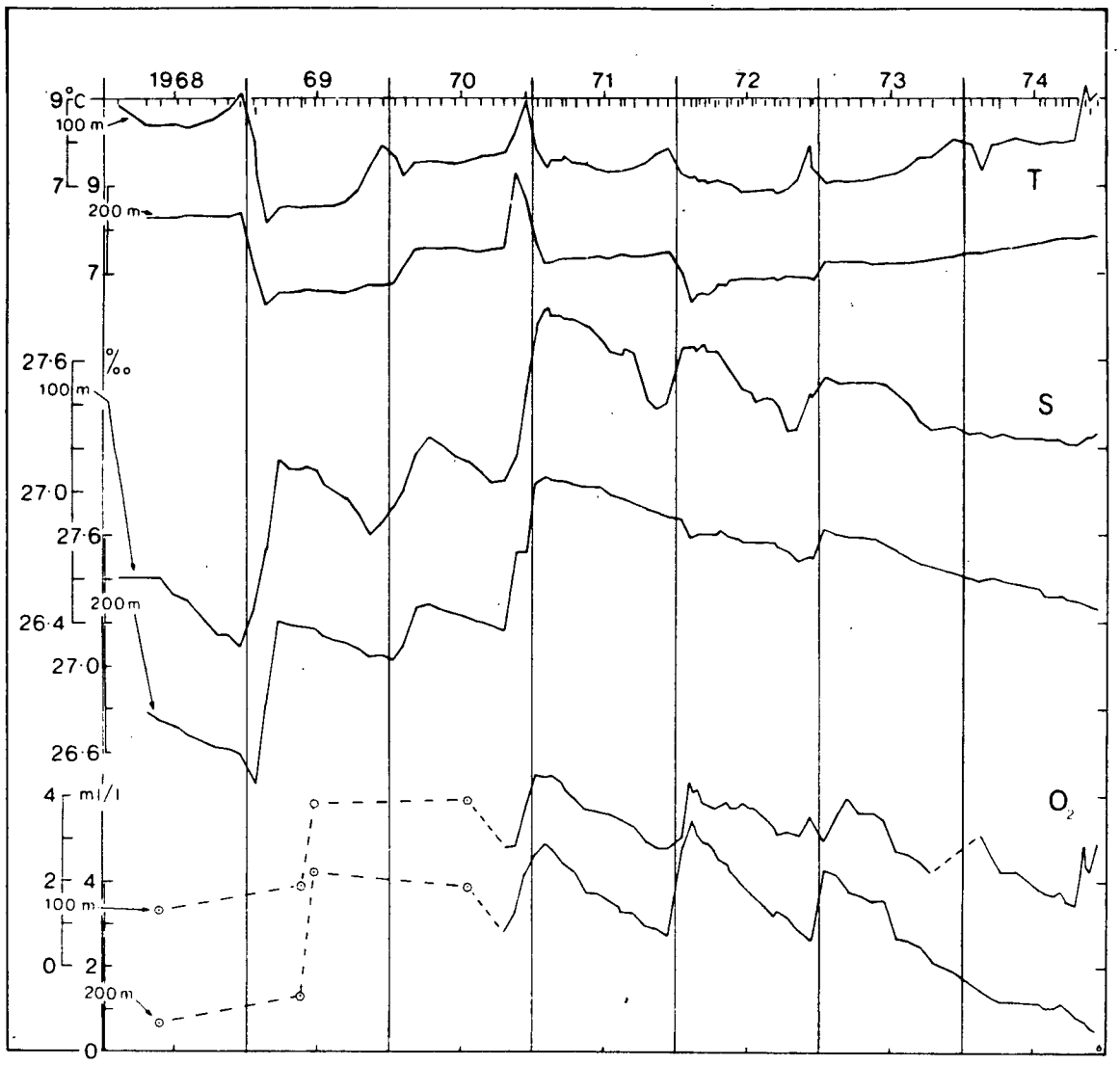

Figure 8. Annual variations in temperature (T), Salinity (S) and oxygen (O_2) at depths 100 *m* and 200 *m* for a central representative location in the deep basin of Indian Arm for the period 1968–74.

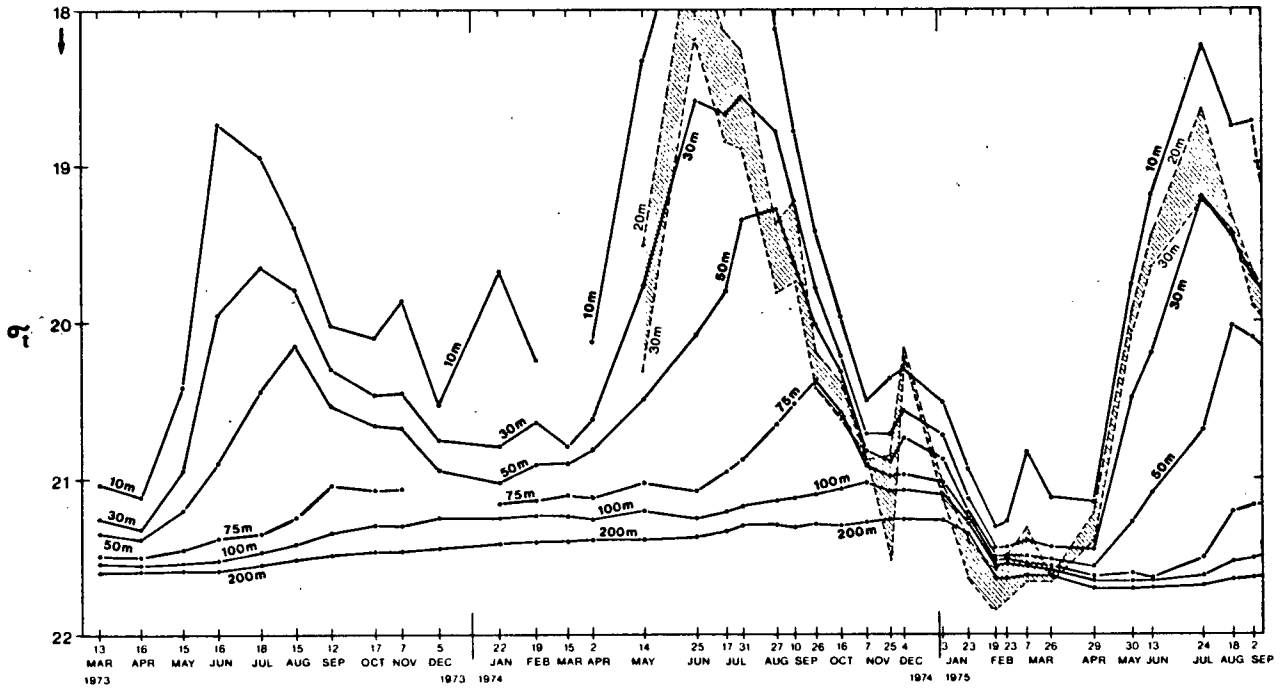

Figure 9. Annual variations in σ_t at depths 100 m and 200 m for a central representative location in the deep basin of Indian Arm between March 1973 and September 1975. Shaded area corresponds to outside source water above sill depth

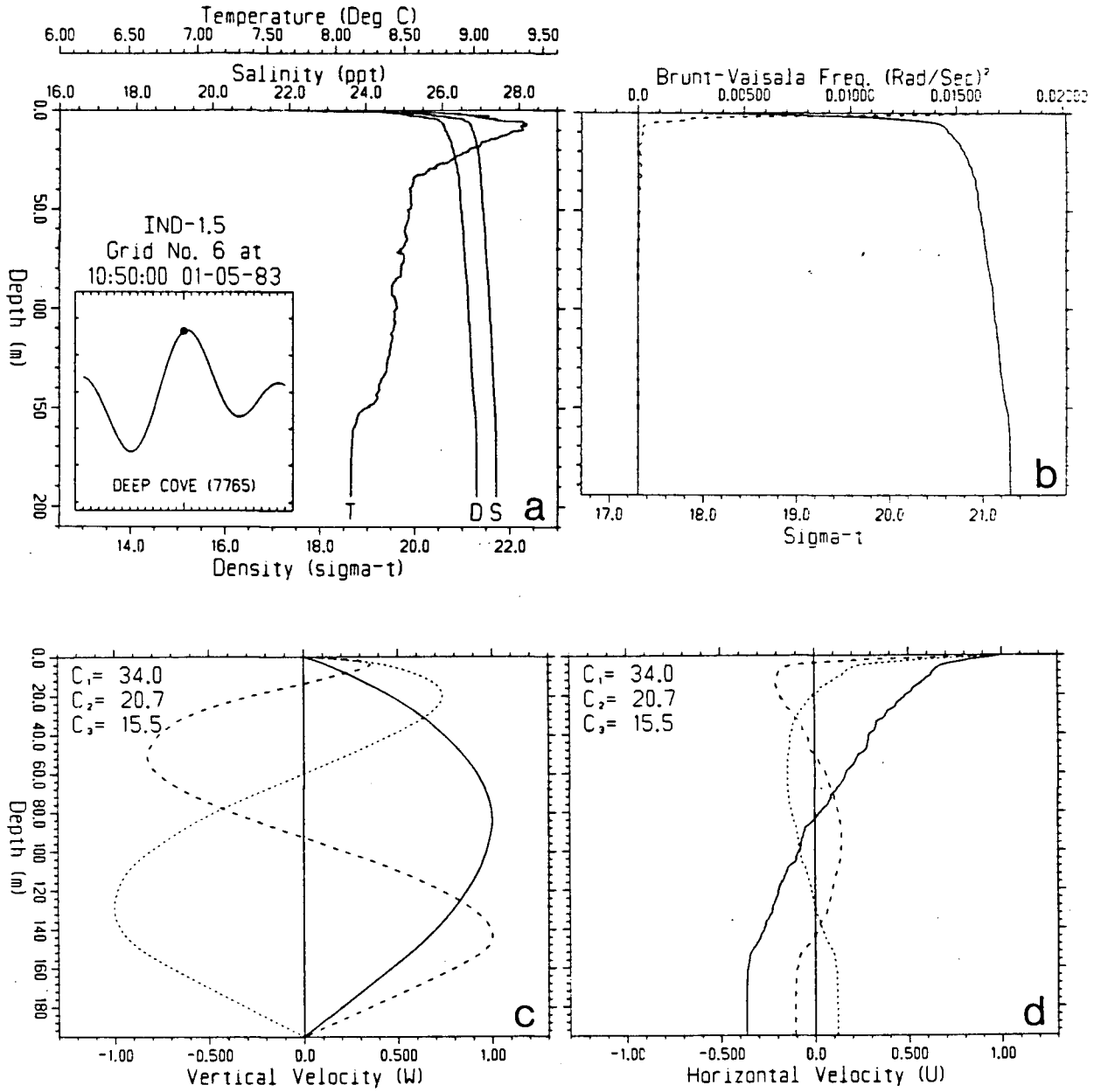

Figure 10. Observed profiles at station Ind-1.5 on January 5, 1983. Plot (a): Temperature (T), σ_t (D) and salinity (S). Plot (b): N^2 (dashed line) and σ_t (solid line). Plot (c): Vertical modes for w (arbitrary scale). Plot (d): Vertical modes for u (arbitrary scale). Phase speeds c_1, c_2, c_3 for (c) and (d) are in $cm\,s^{-1}$. Modes 1, 2 and 3 are plotted respectively as solid, dotted and dashed lines. The phase of the tide at the time of the CTD cast is shown in the inset for (a).

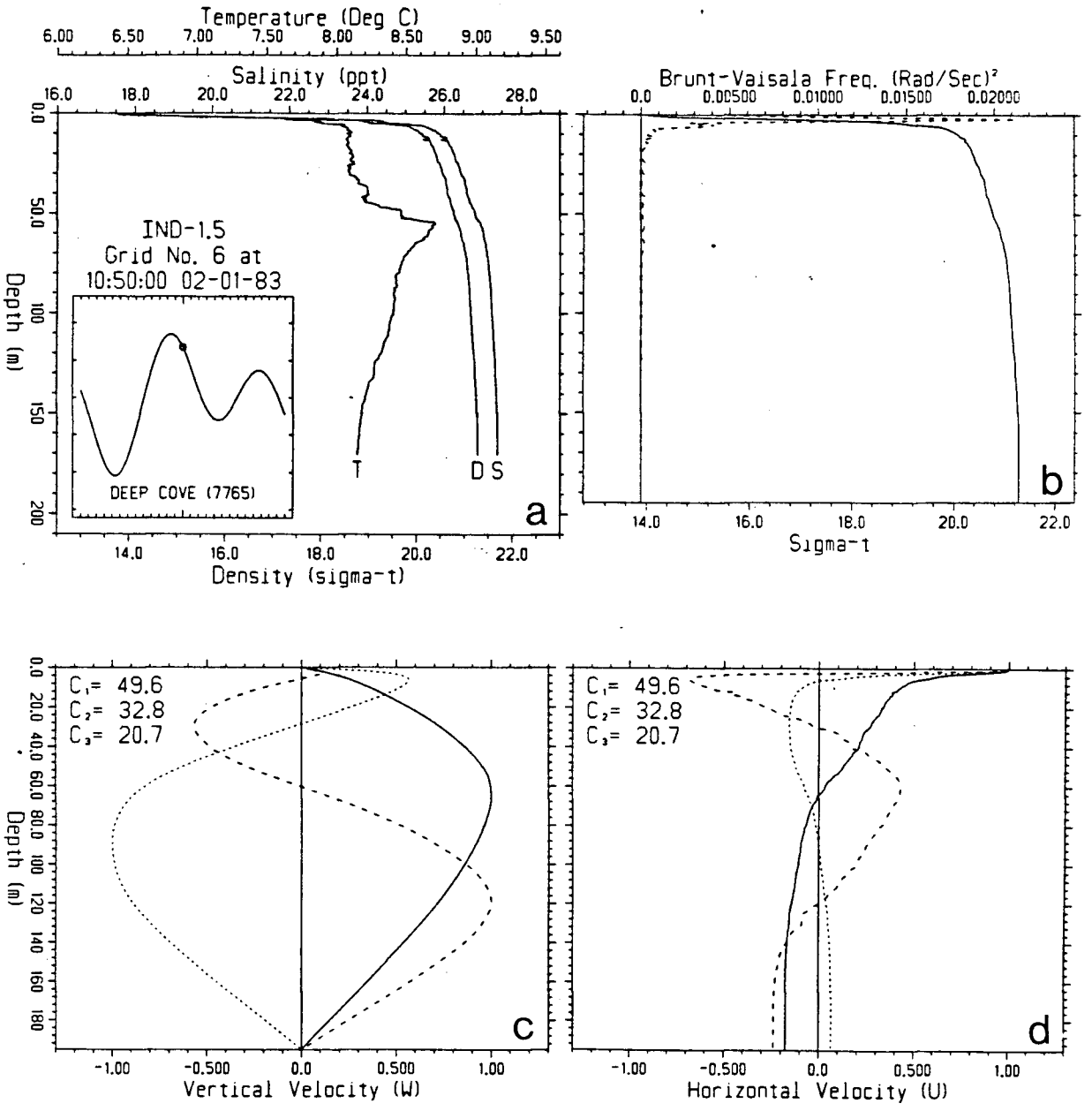

Figure **11. Profiles at station Ind-1.5 on February 1, 1983 (for legend see figure 10).**

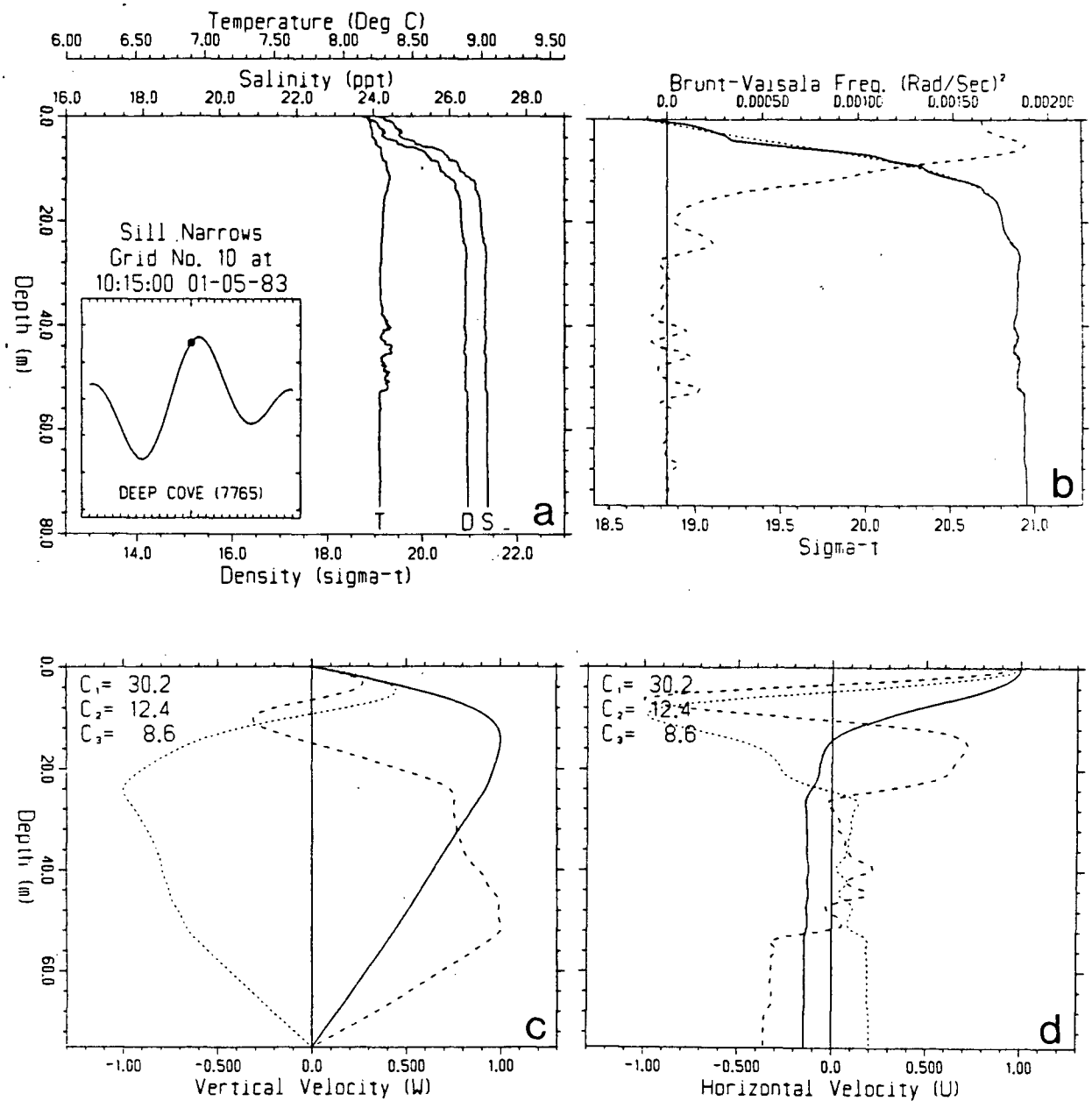

***Figure* 12. Profiles at the Sill Narrows on January 5, 1983 (for legend see figure 10).**

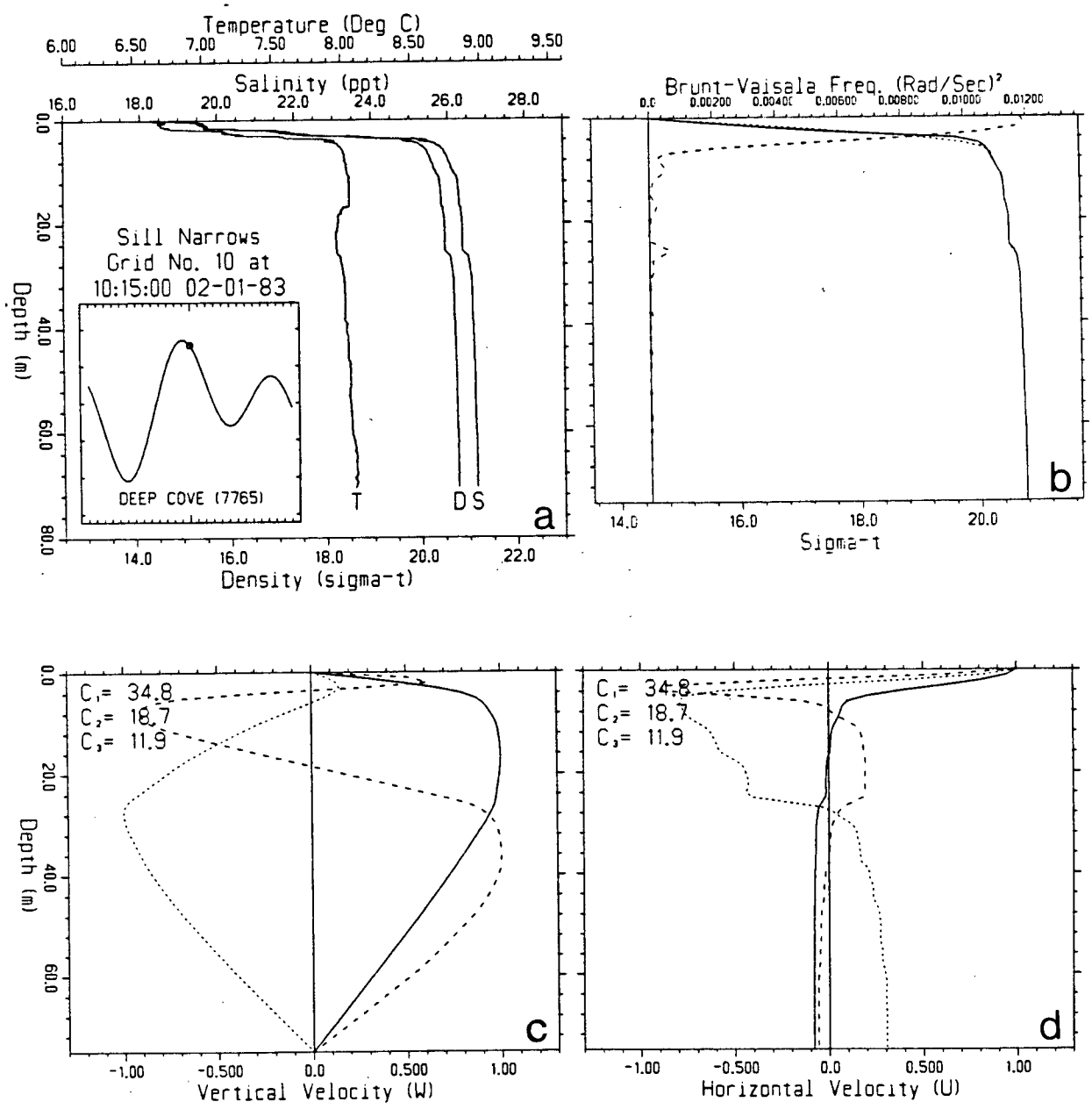

***Figure* 13. Profiles at the Sill Narrows on February 1, 1983 (for legend see figure 10).**

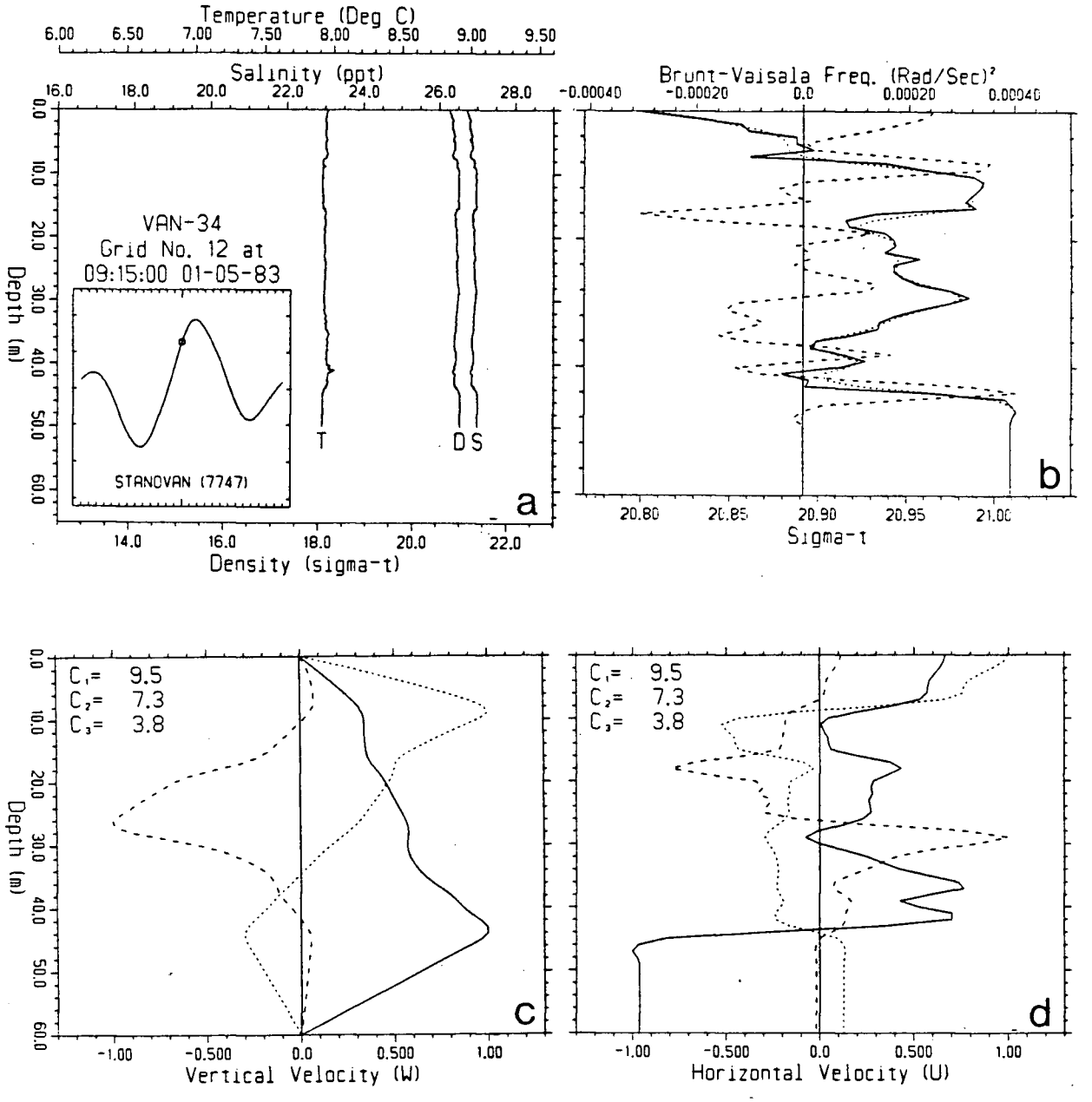

Figure **14. Profiles at station Van-34 on January 5, 1983 (for legend see figure 10).**

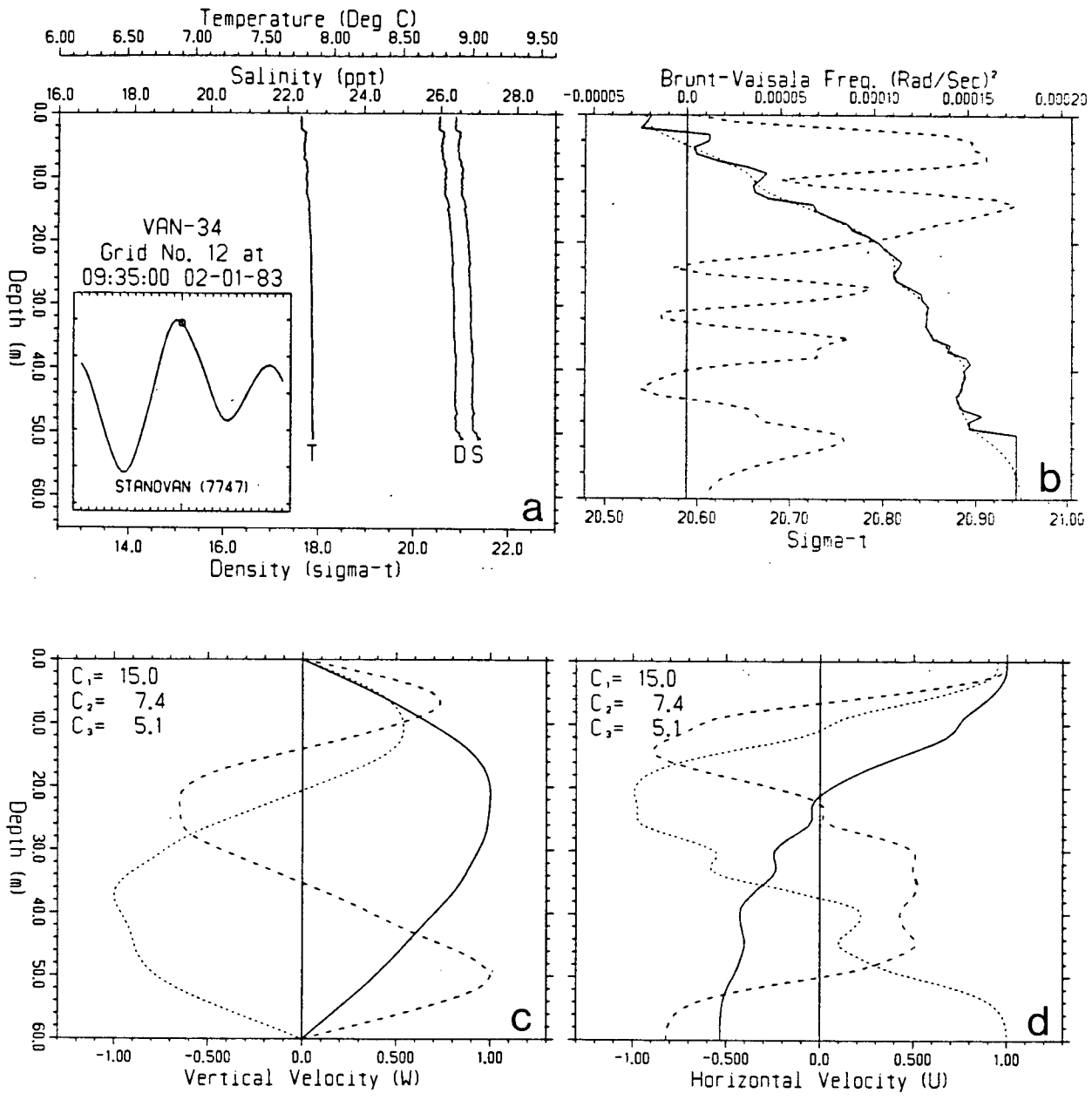

Figure 15. **Profiles at station Van-34 on February 1, 1983 (for legend see figure 10).**

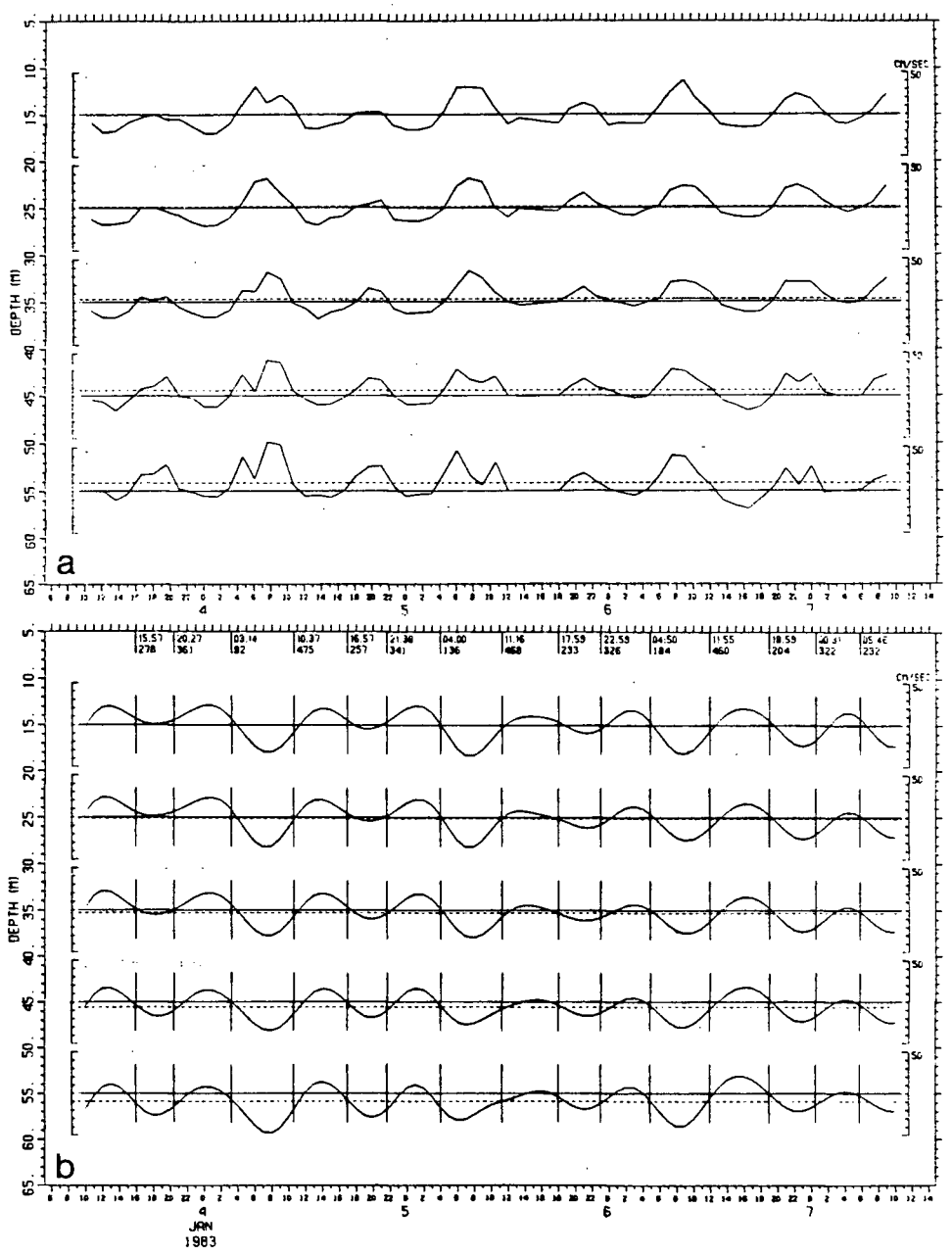

Figure 16. Sample of Cyclesonde current meter time series. Velocity scale ($cm\ s^{-1}$) is at right hand edge of each trace. Plot (a): unfiltered v-component (positive northward). Plot (b): filtered and rotated along-inlet component (positive is out of Indian Arm). Vertical lines indicate surface elevation extrema calculated from harmonic analysis at station 7765. Local time and elevation (cm) are shown at top; dashed horizontal lines indicate mean velocities.

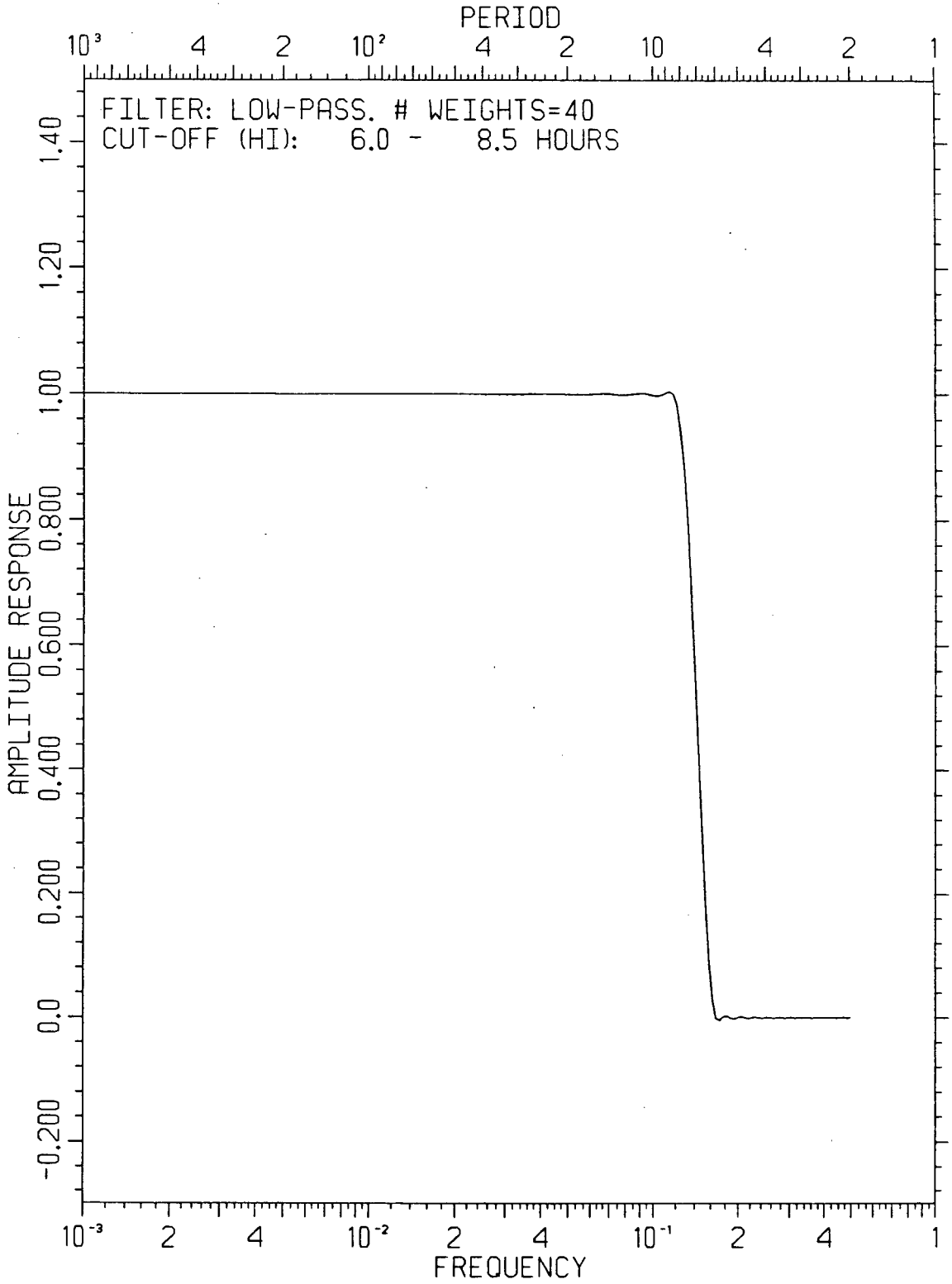

Figure 17. Sample response curve for the digital low-pass filter used in the study. Filter type is (6,8.5,40) (see §1.3 for description and explanation of notation).

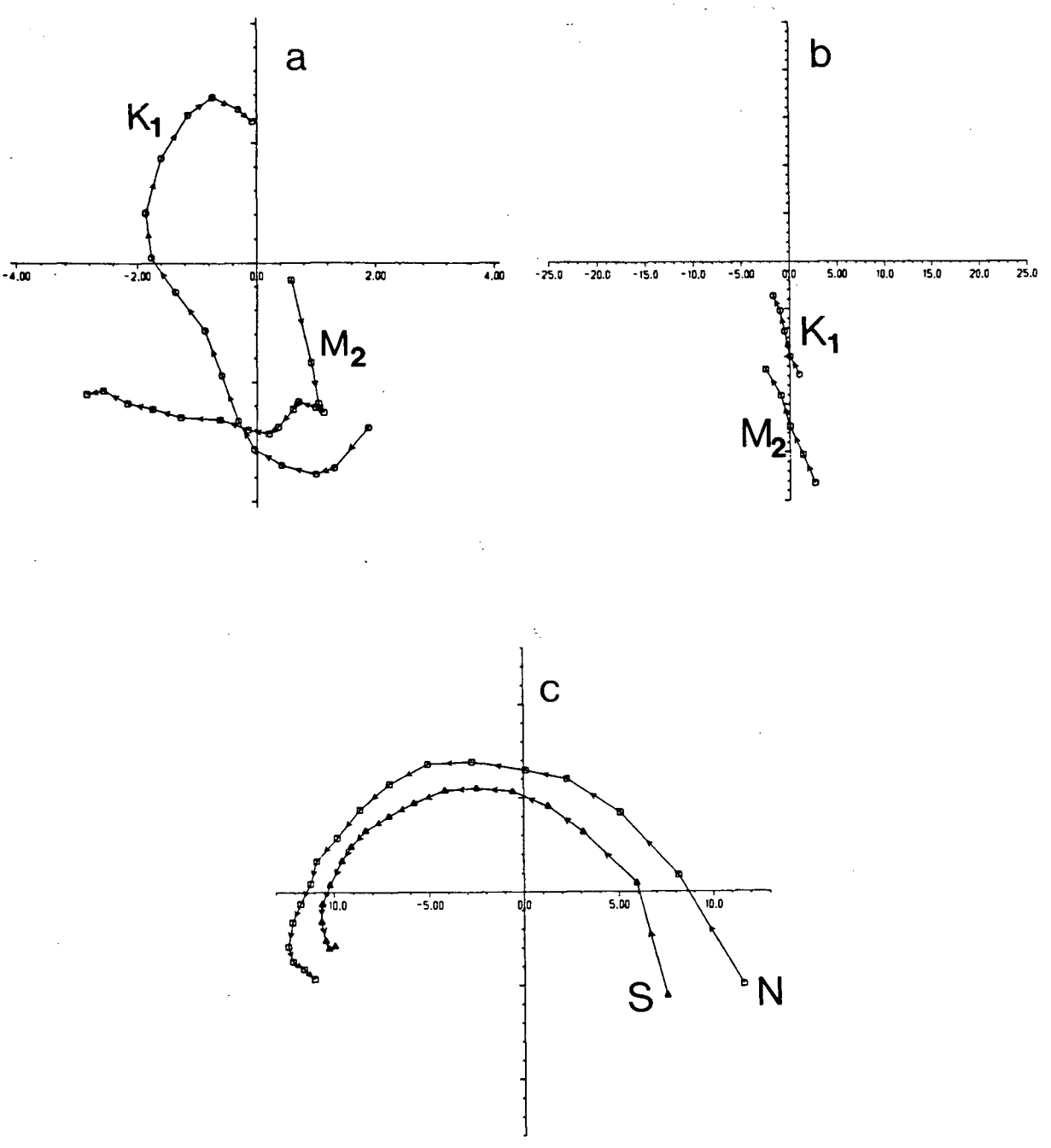

Figure 18. Argand diagrams showing depth dependence of amplitude (axes ticks indicate the scale in $cm\,s^{-1}$) and phase from harmonic analysis of Cyclesonde current meter time series. Arrows along curves indicate direction of increasing depth, starting at $15\,m$, and with a $10\,m$ spacing between symbols. Plot (a): Indian Arm near segment 7 at 12:00 January 19, 1983 (series length is 579 hours). Plot (b): Indian Arm near segment 10 at 22:00 January 18, 1983 (series length is 745 hours). Plot (c): M_2 constituent for Knight Inlet near Tomakstum Island at 06:00 September 14, 1983 (series length is 539 hours). N–north station, S–south station.

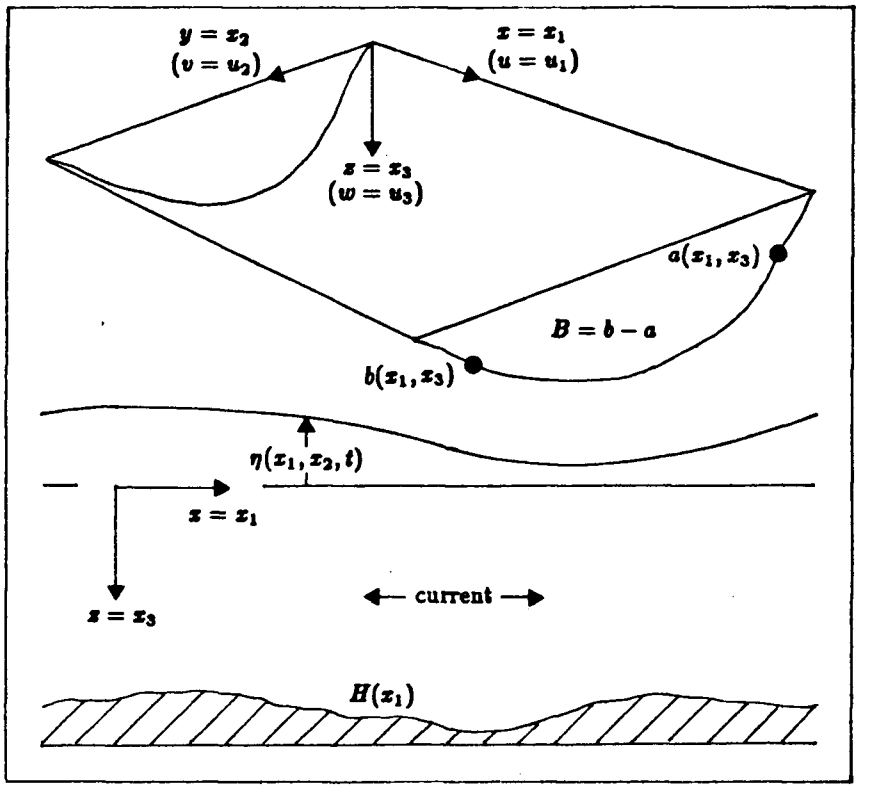

Figure 19. Frame of reference for the XZT numerical model

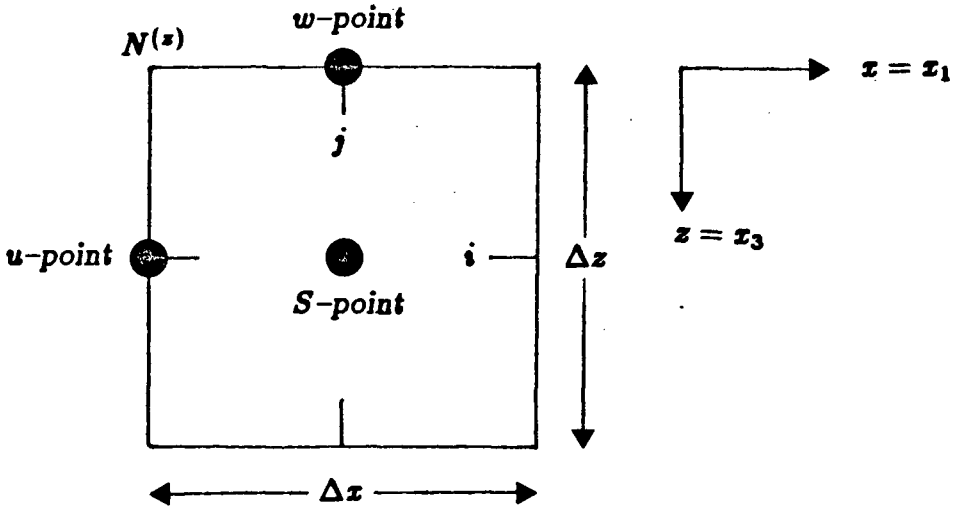

Figure 20. Staggered grid used in finite difference solution to governing equations.

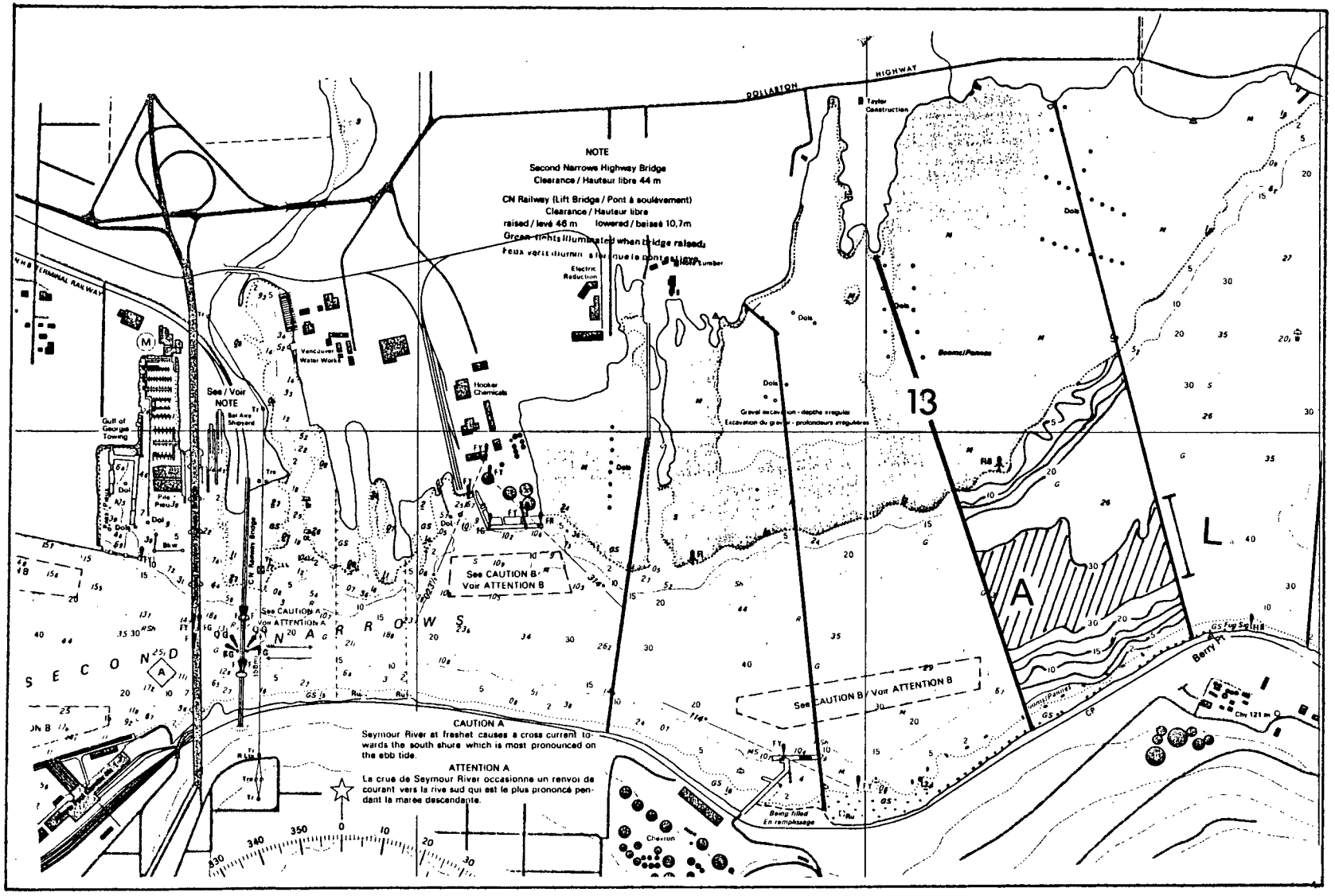

Figure 21. Detail of Canadian Hydrographic chart No. 3483 showing 0.5 *km* spaced model sections. Depth contours were digitized to give areas (A) and model segment lengths (L) at a fixed depth (example shown is for 30 *m* contour).

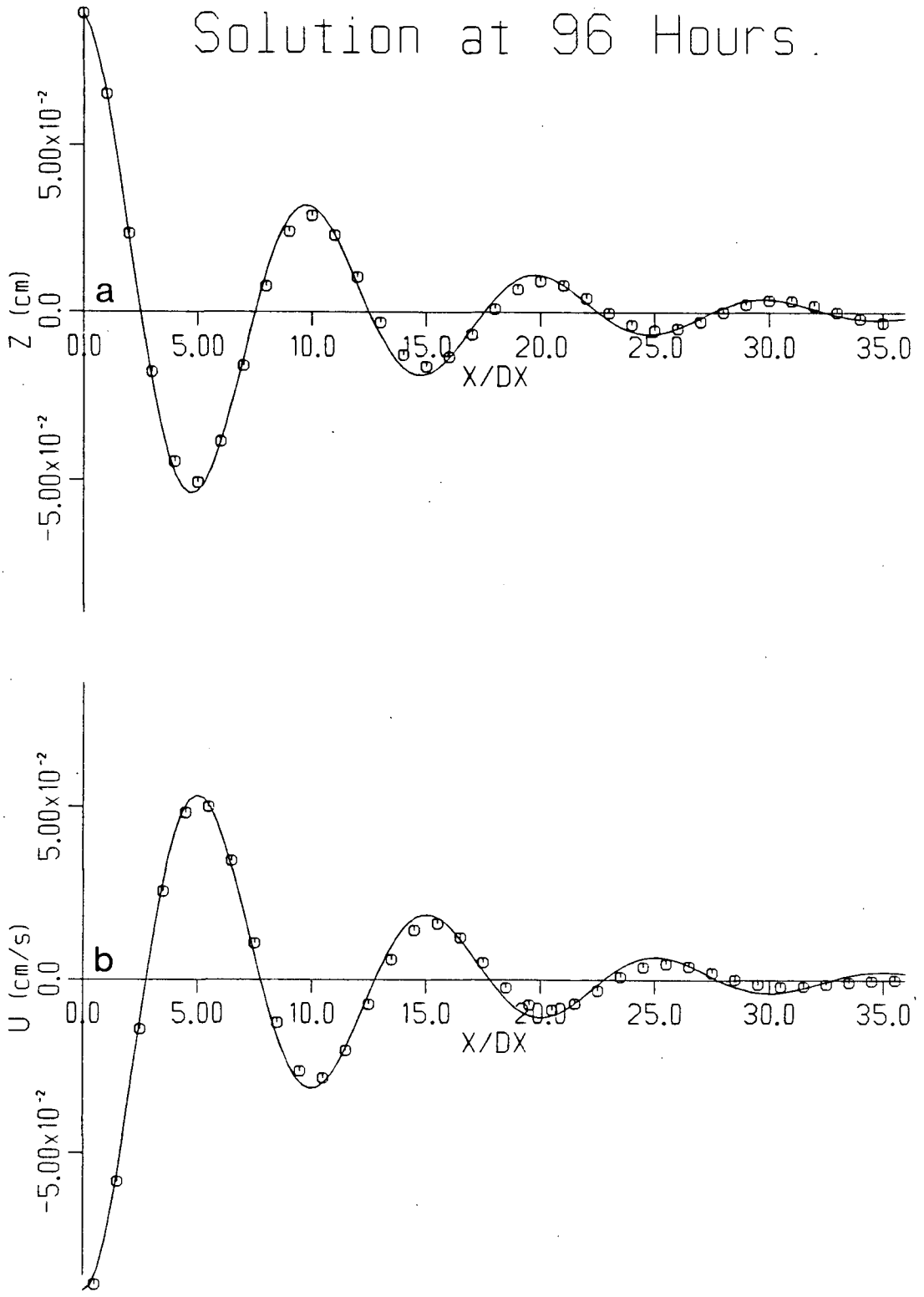

Figure 22. Comparison of calculated (circles) and analytical (solid line) solutions for Class 1 simulation of linear, unstratified tidal circulation with linear bottom friction in a basin of constant rectangular cross-section. Plot (a): Surface elevation. Plot (b): Horizontal velocity.

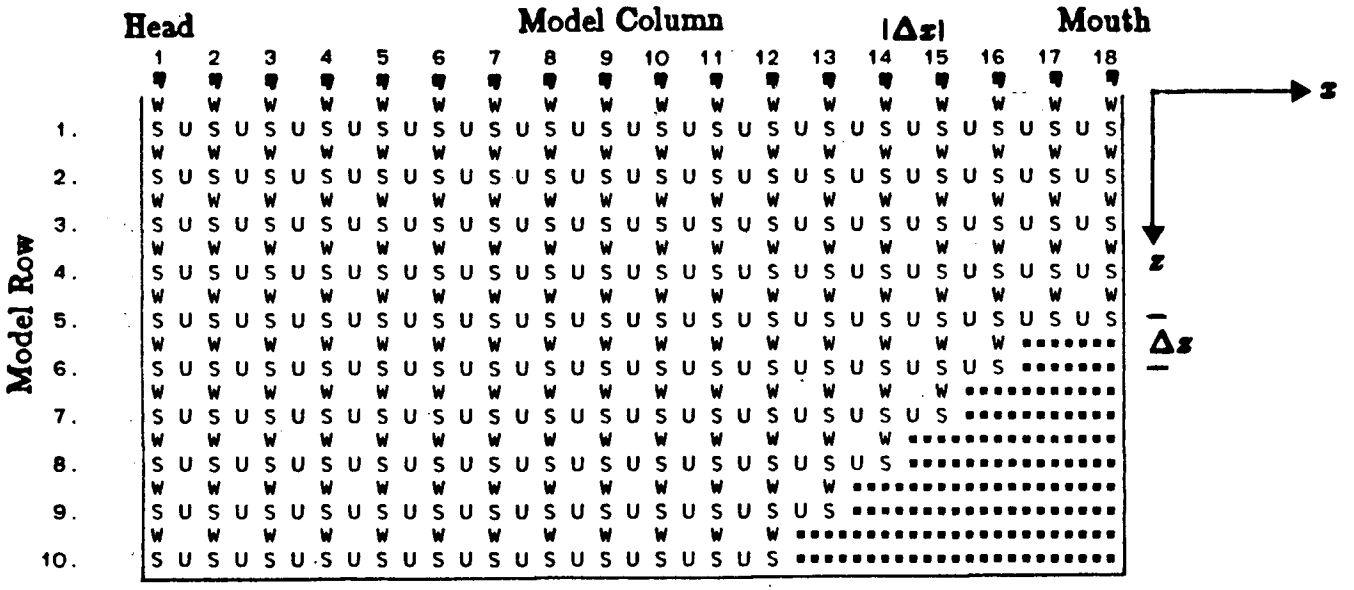

Figure 23. Geometry for Class 2 simulation of nontidal, stratified flow down a gentle slope in a closed basin of uniform width showing locations of variables for horizontal velocity (U), vertical velocity (W) and salinity (S). $\Delta x = 2\,km$, $\Delta z = 10\,m$

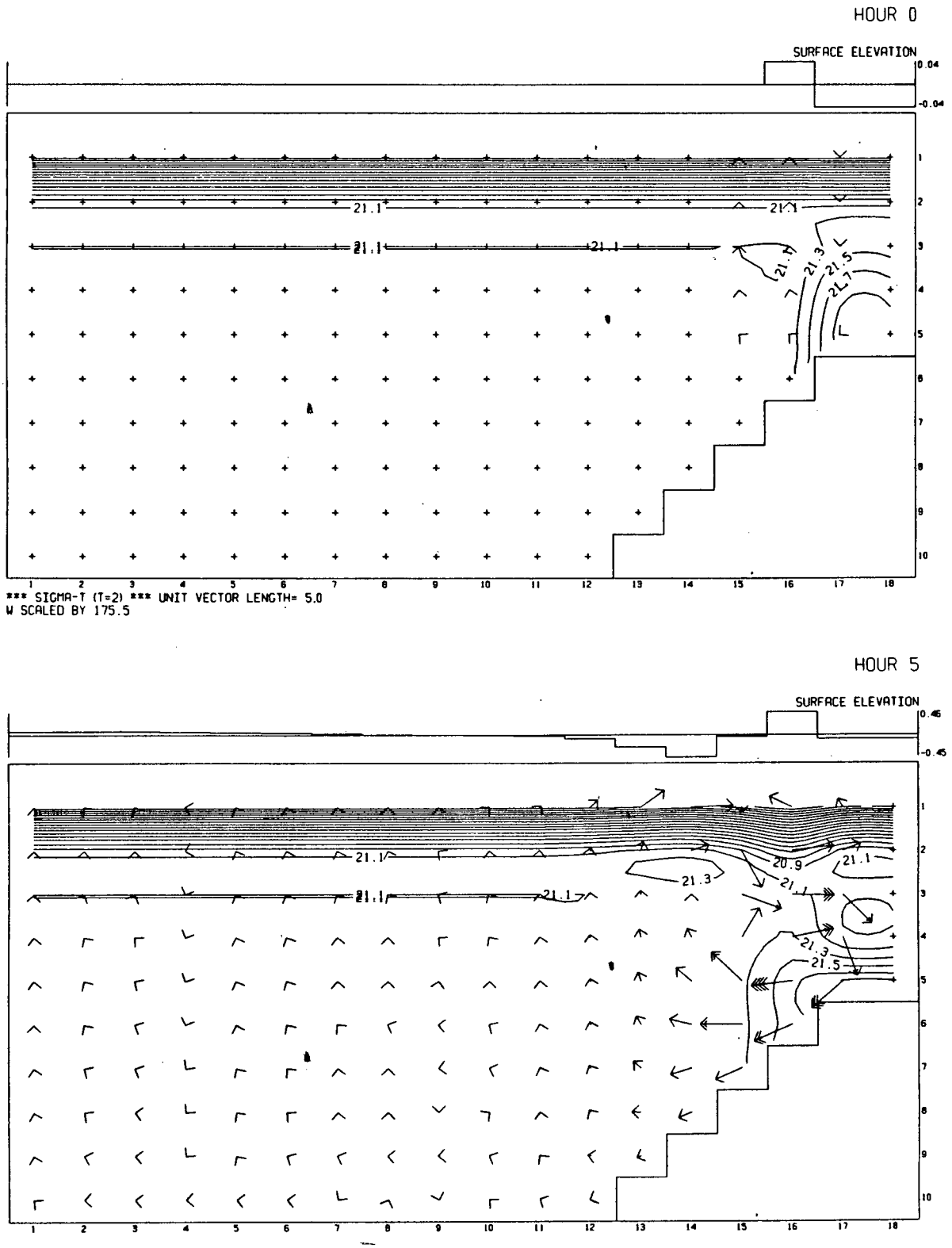

Figure 24. Fields of surface elevations, current vectors and isopycnals at 5 hour intervals for Class 2 model simulation of nontidal, stratified flow down a gentle slope in a closed basin of uniform width. Vertical exaggeration is 175.5. Elevations are in *cm* (note the change in scale between plots). The unit vector length is 5 $cm\,s^{-1}$, with extra arrowheads indicating speeds which are multiples of this value (e.g. 3.5 arrowheads indicates a speed of 17.25 $cm\,s^{-1}$). The contour interval is 0.2 σ_t units.

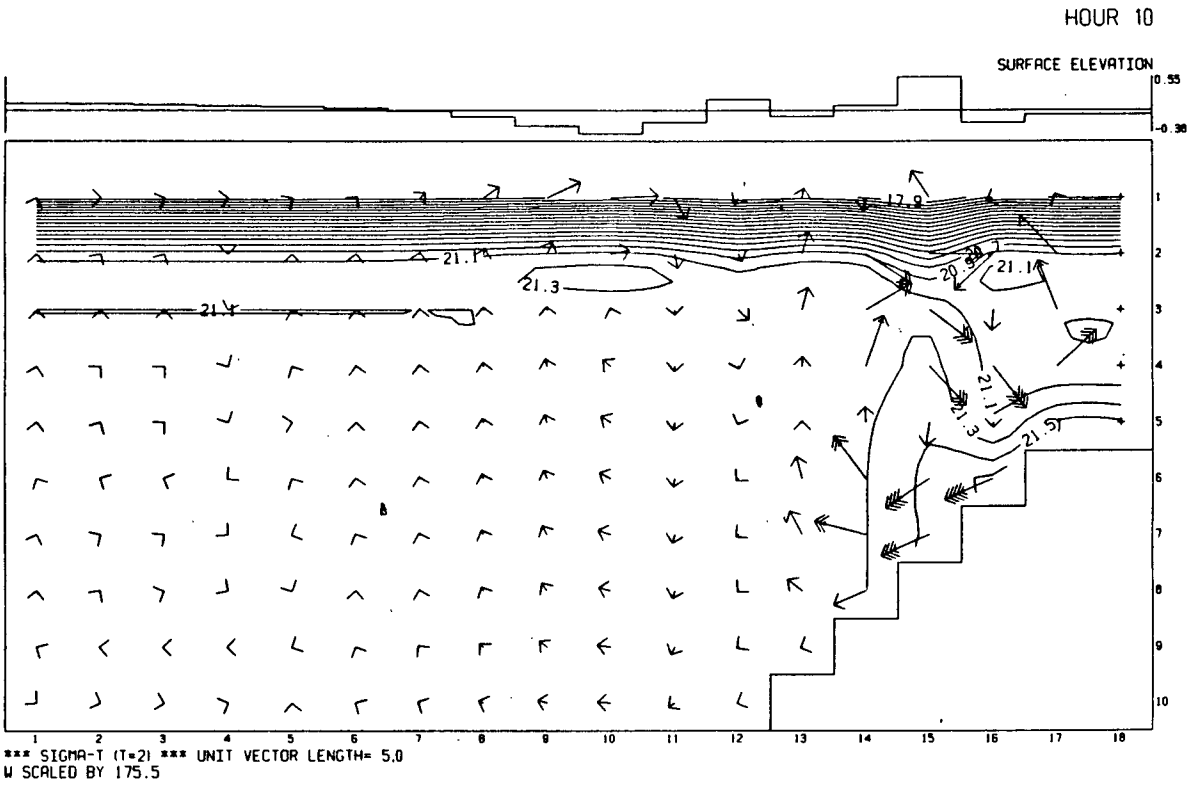

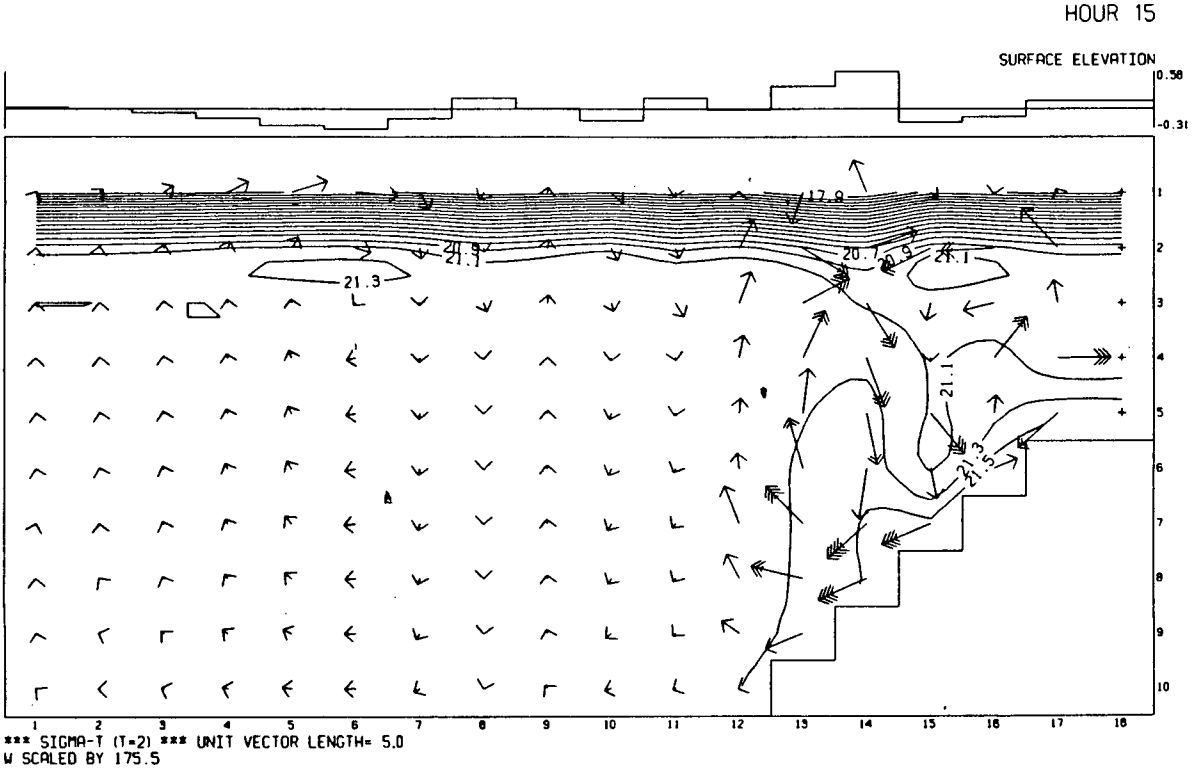

Figure 24(continued)

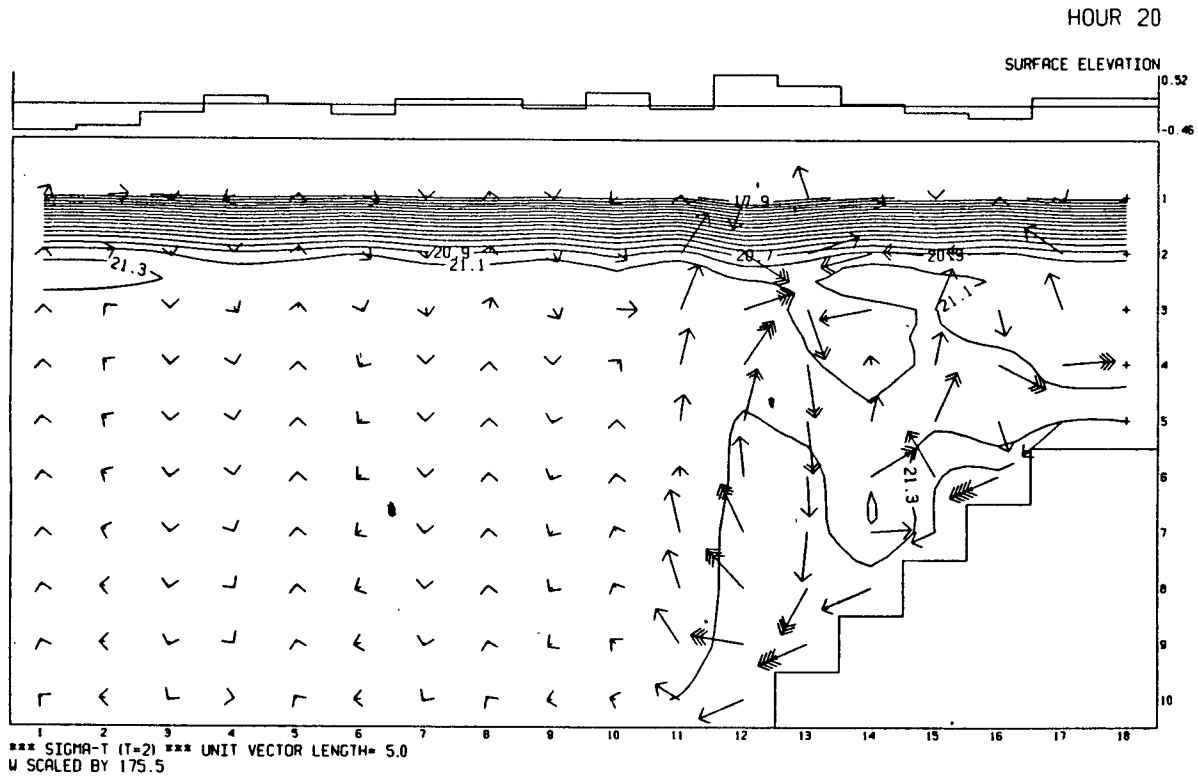

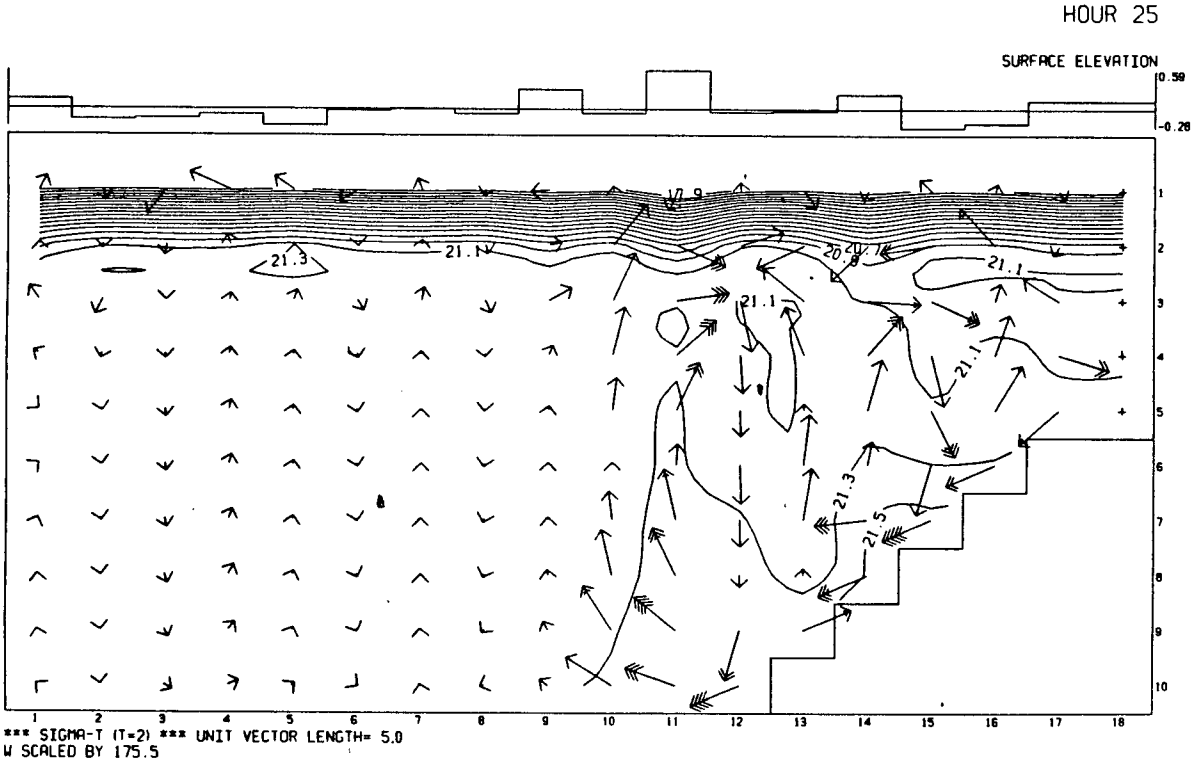

Figure 24(continued)

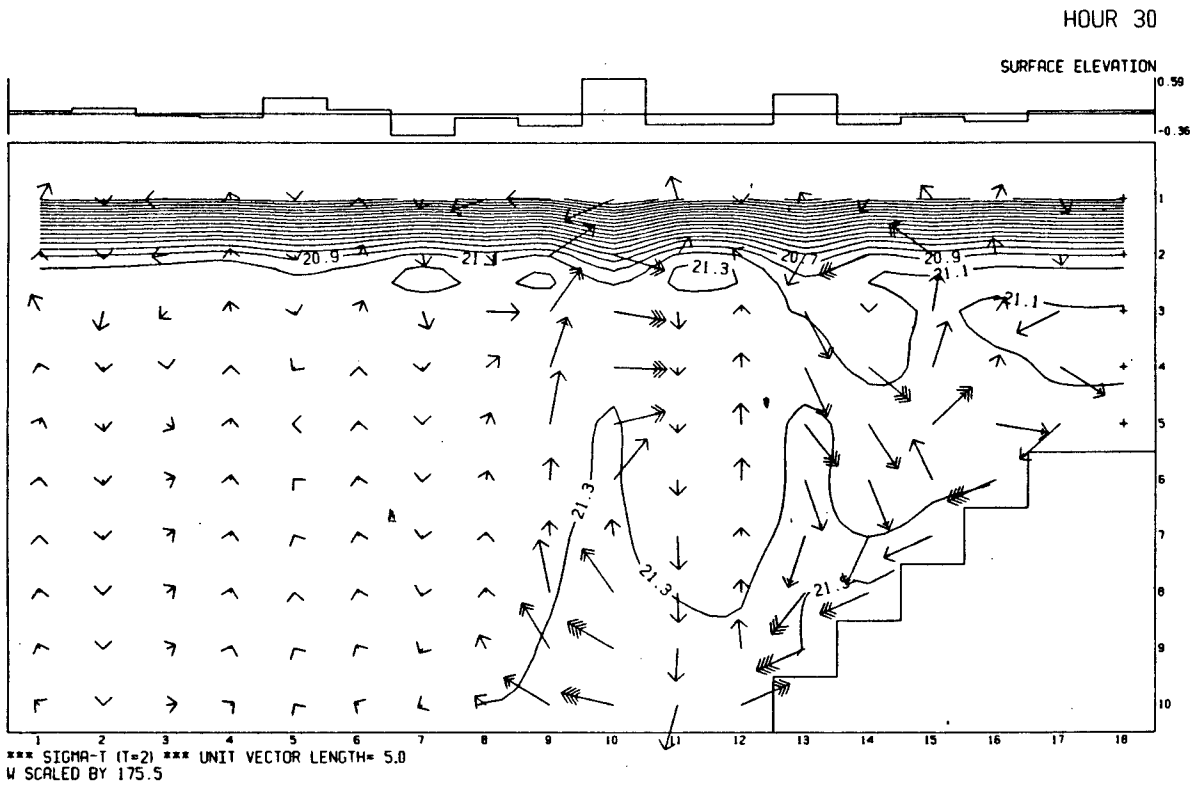

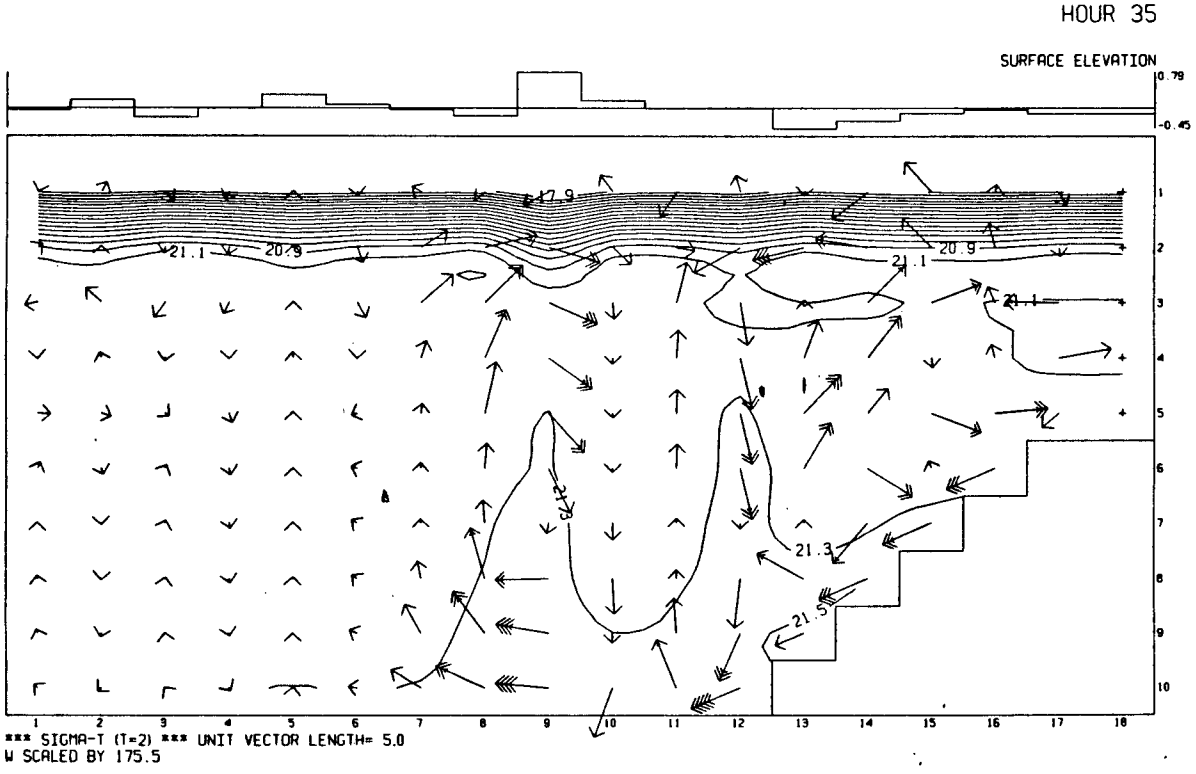

Figure 24(continued)

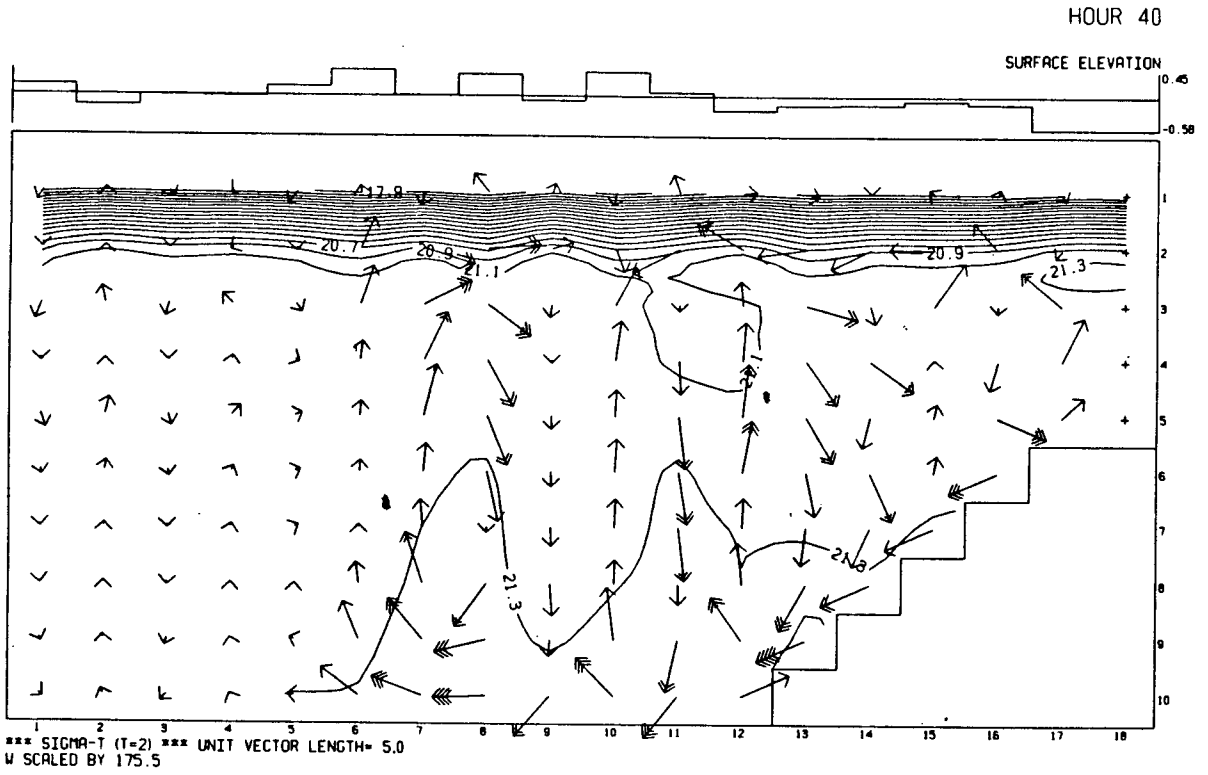

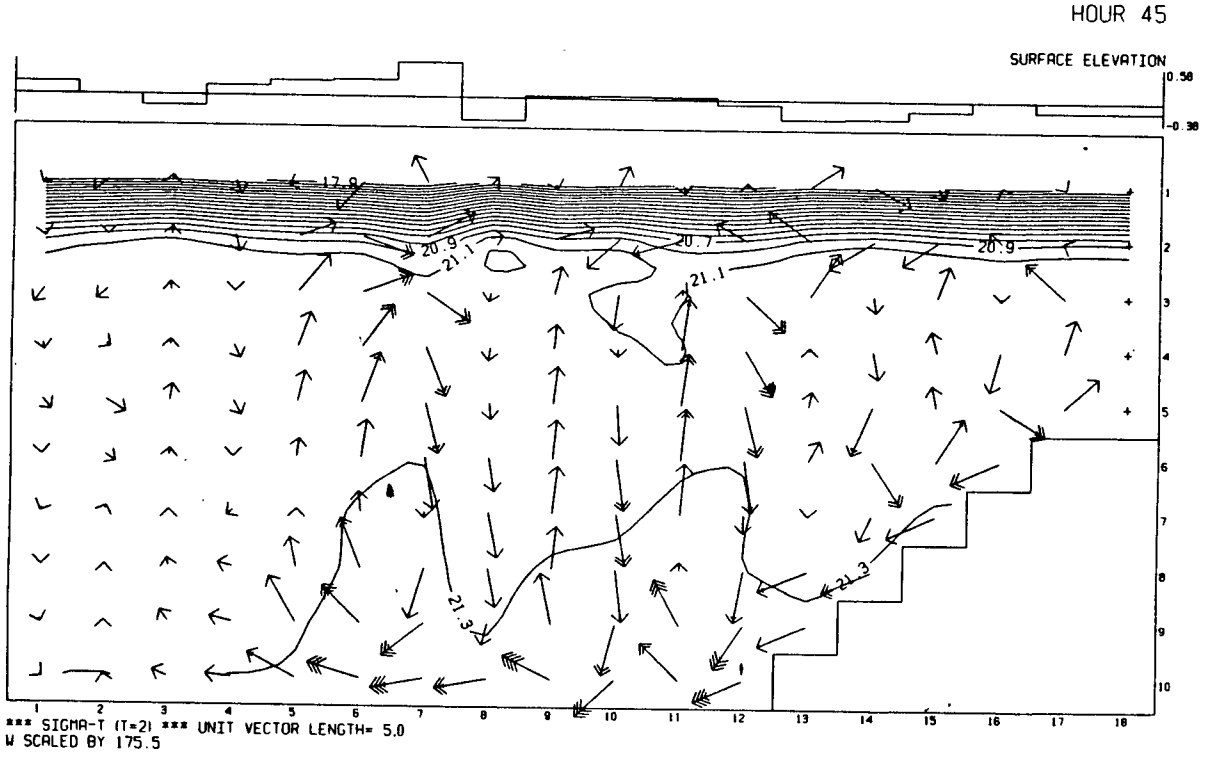

Figure 24(continued)

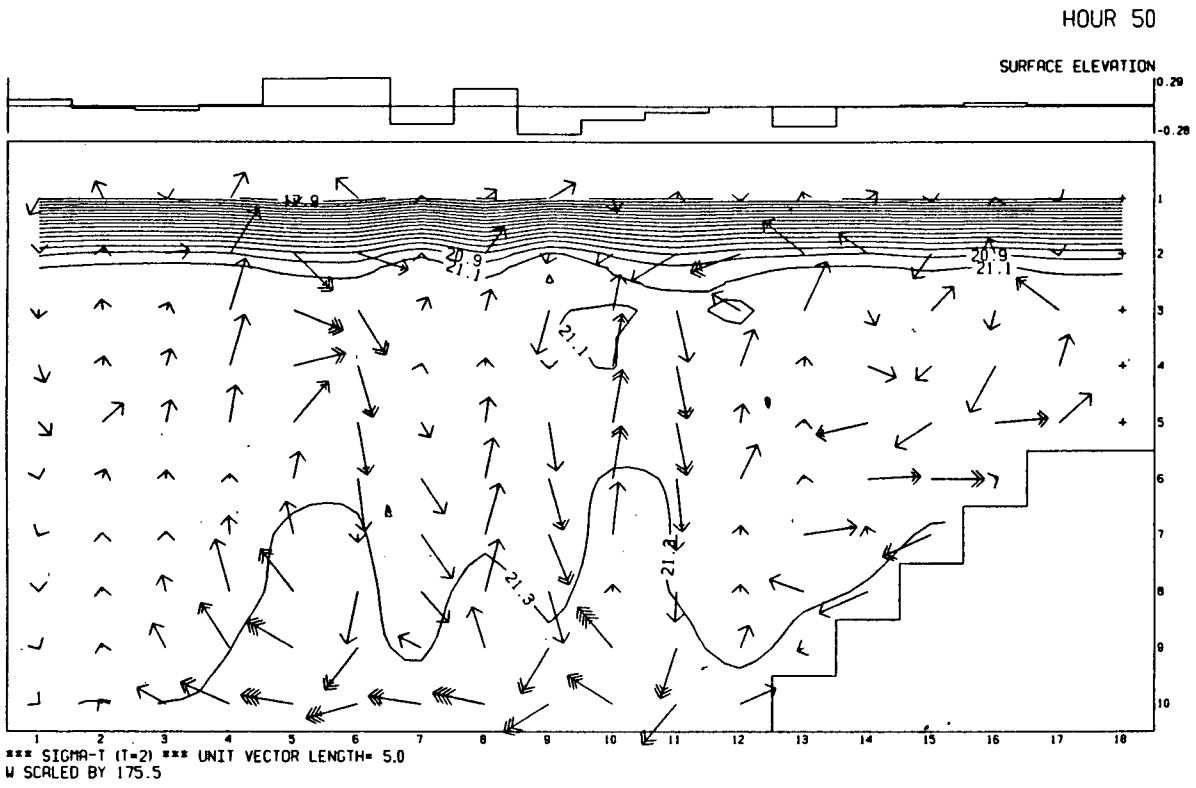

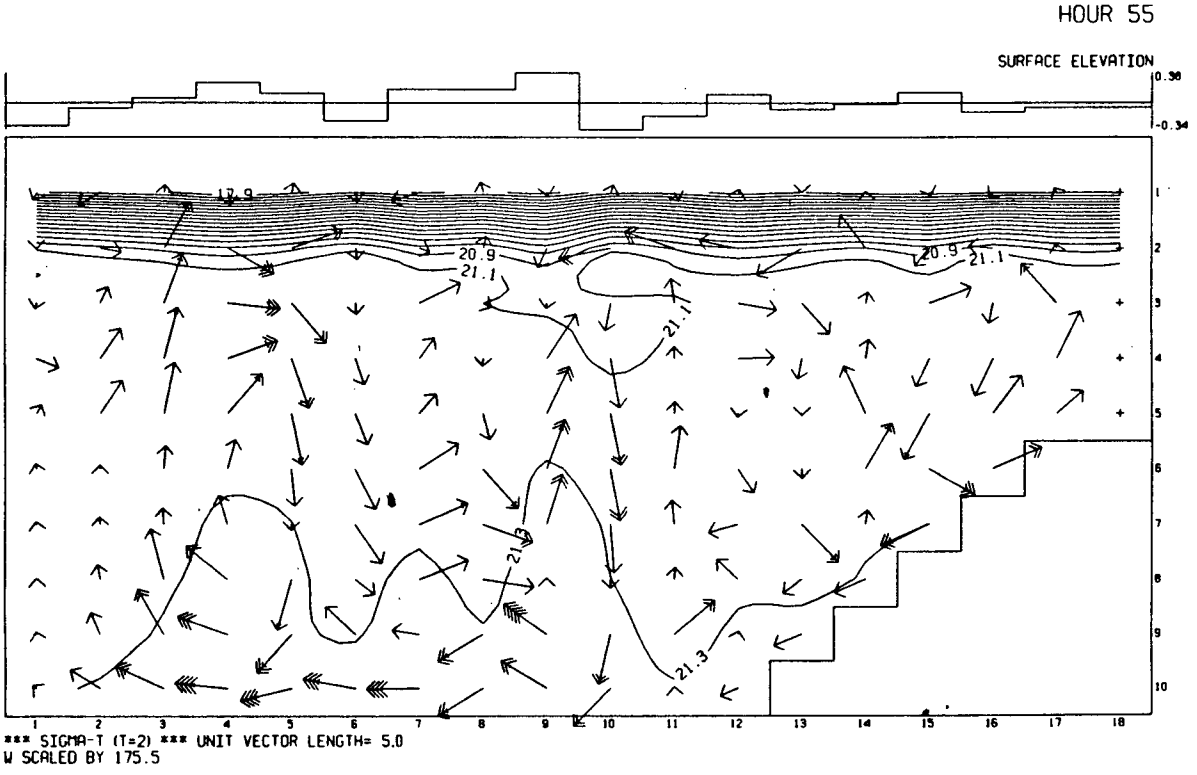

Figure 24(continued)

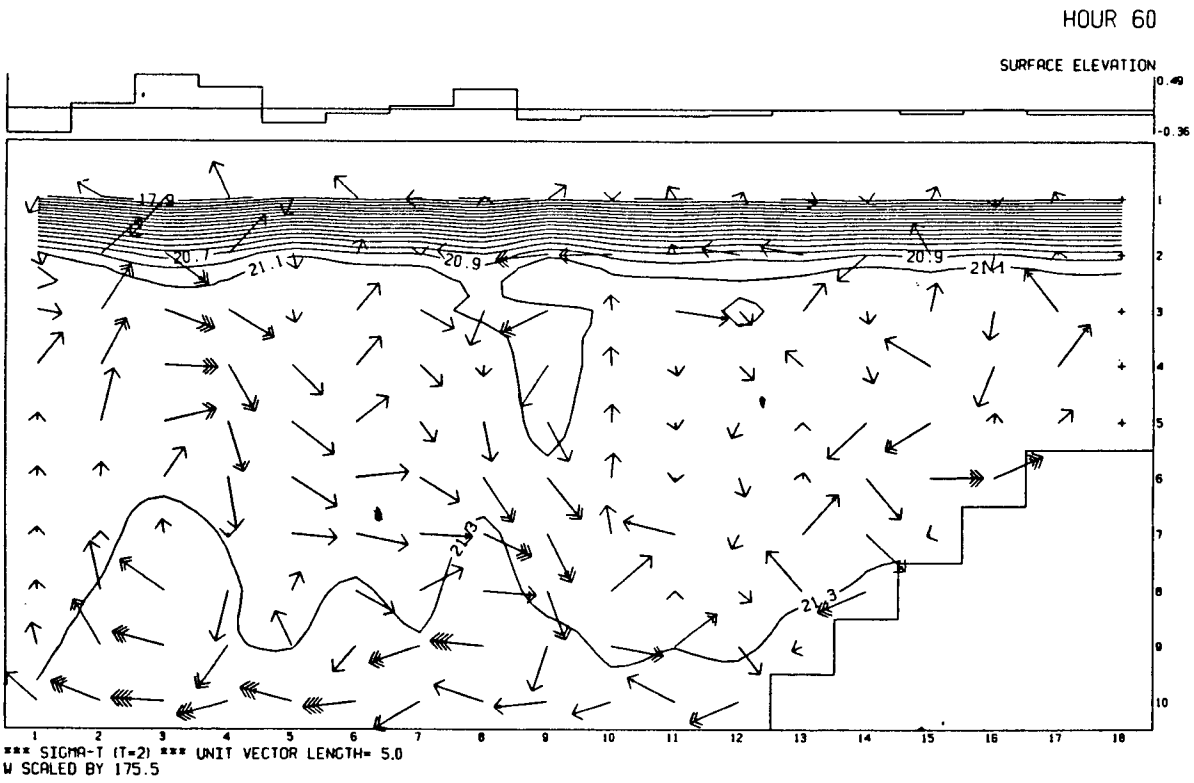

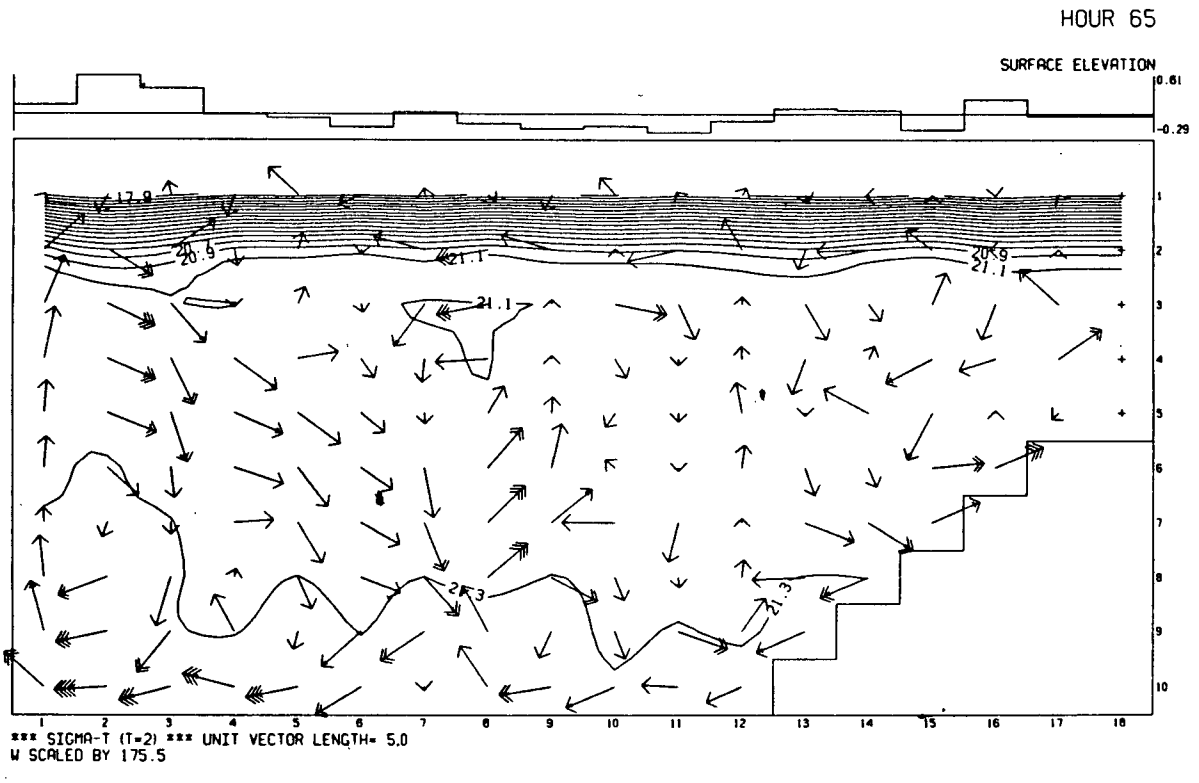

Figure 24(continued)

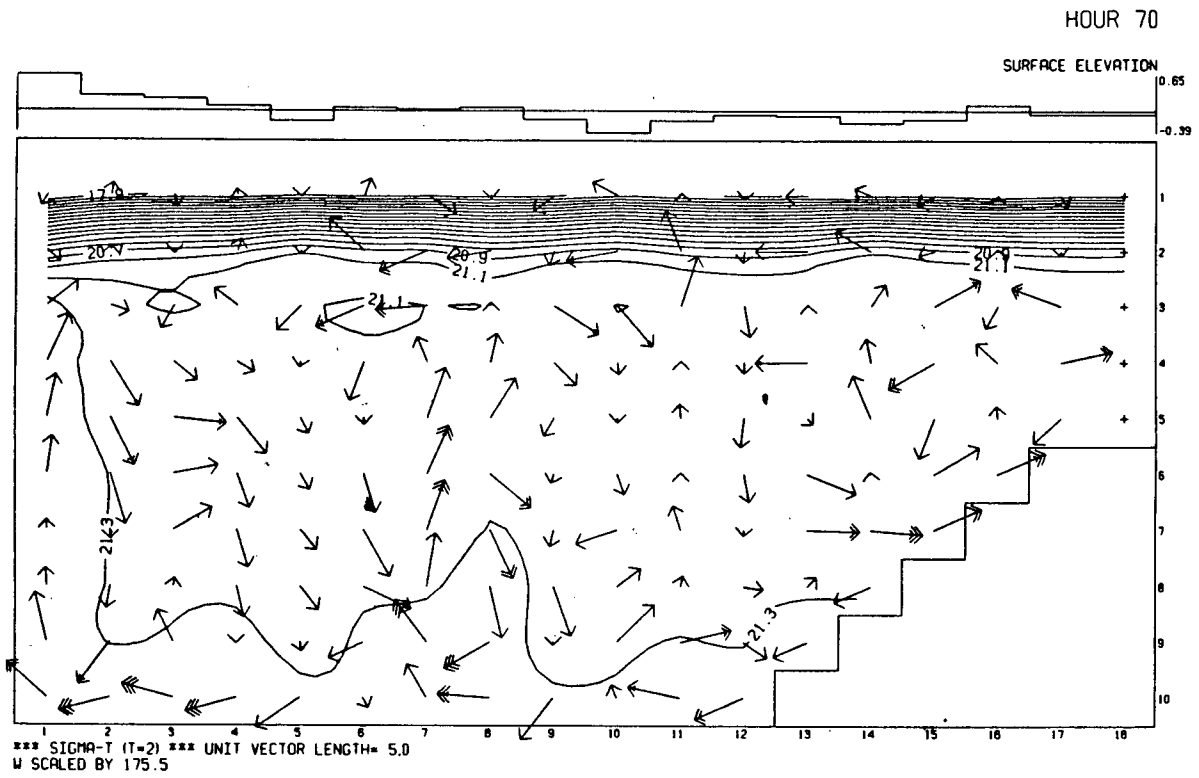

Figure 24(continued)

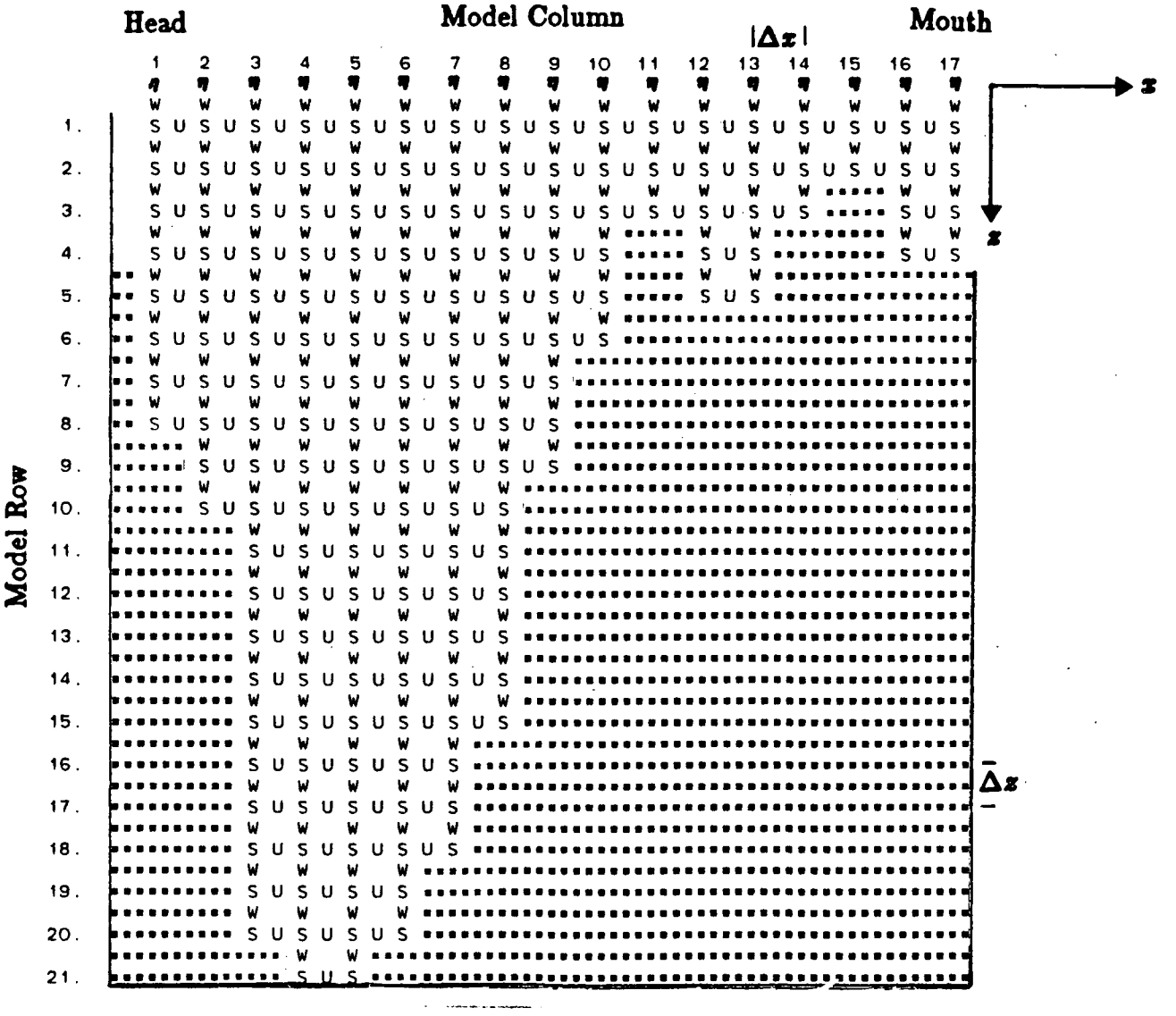

Figure 25. Geometry for Class 3 simulations of circulation in a representative inlet of uniform width showing locations of variables for horizontal velocity (U), vertical velocity (W), salinity (S), and surface elevation (η). $\Delta x = 2\,km$, $\Delta z = 10\,m$

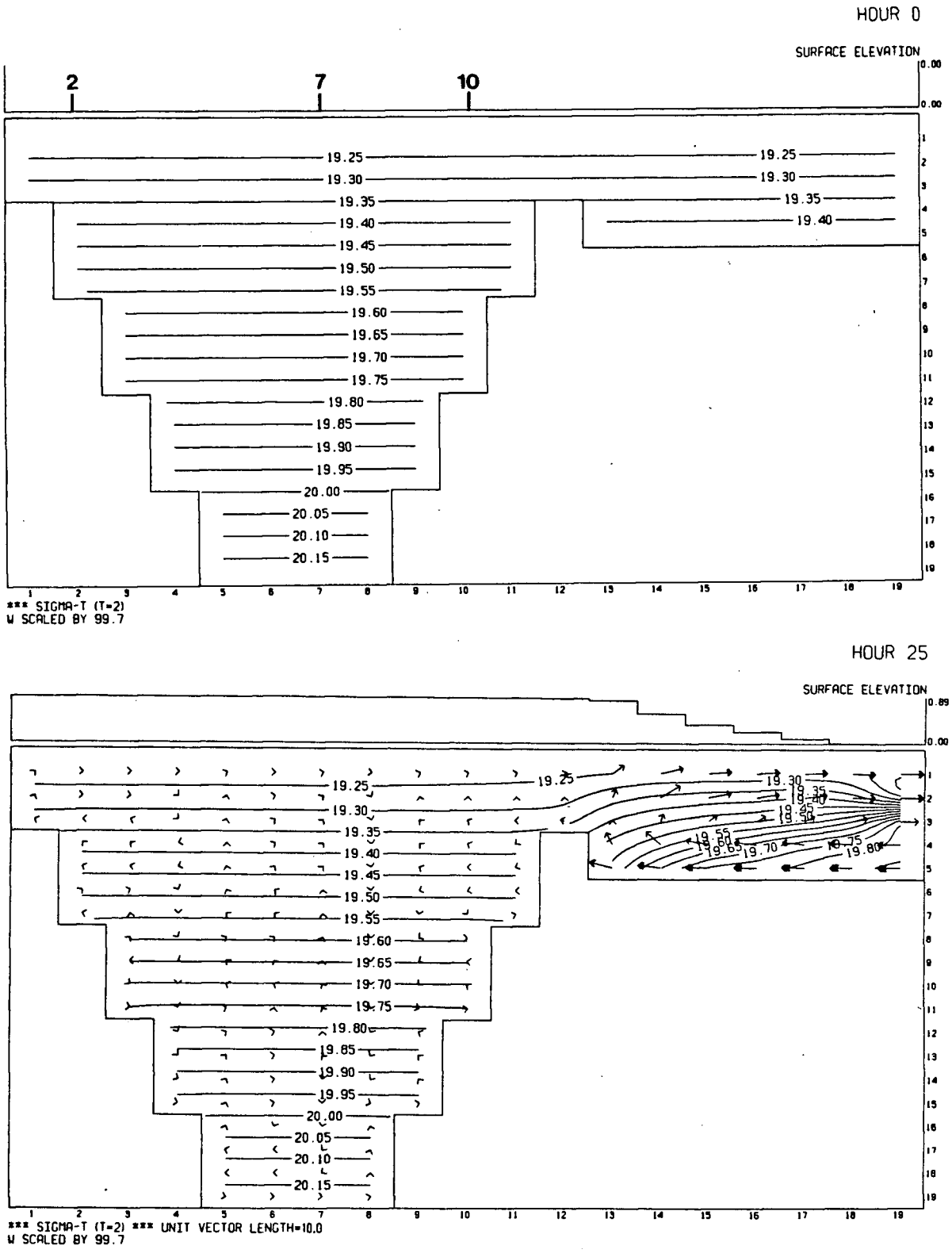

Figure 26. Fields of surface elevations (cm), current vectors and isopycnals at 25 hour intervals for Class 3.1 model simulation of nontidal, stratified circulation in a representative inlet of uniform width. Vertical exaggeration is 99.7. Unit vector length is 10 $cm\,s^{-1}$. Contours are in σ_t units (0.05 increment).

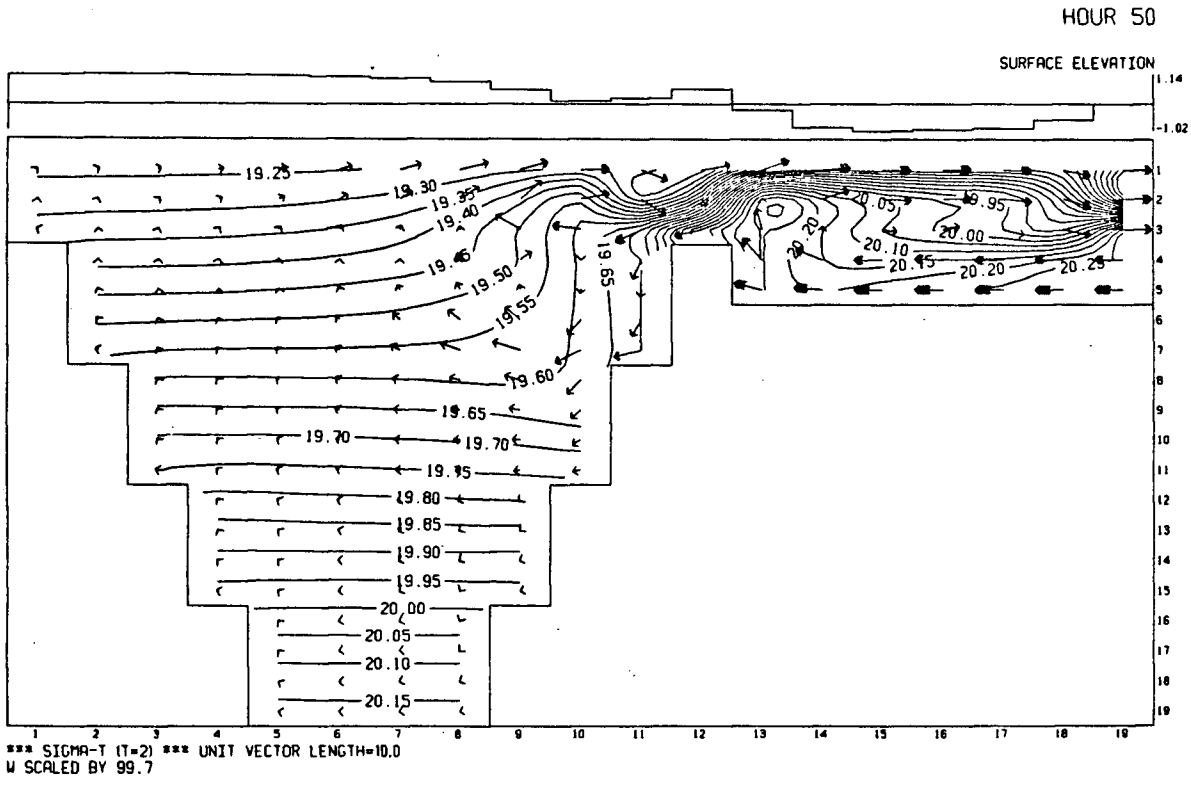

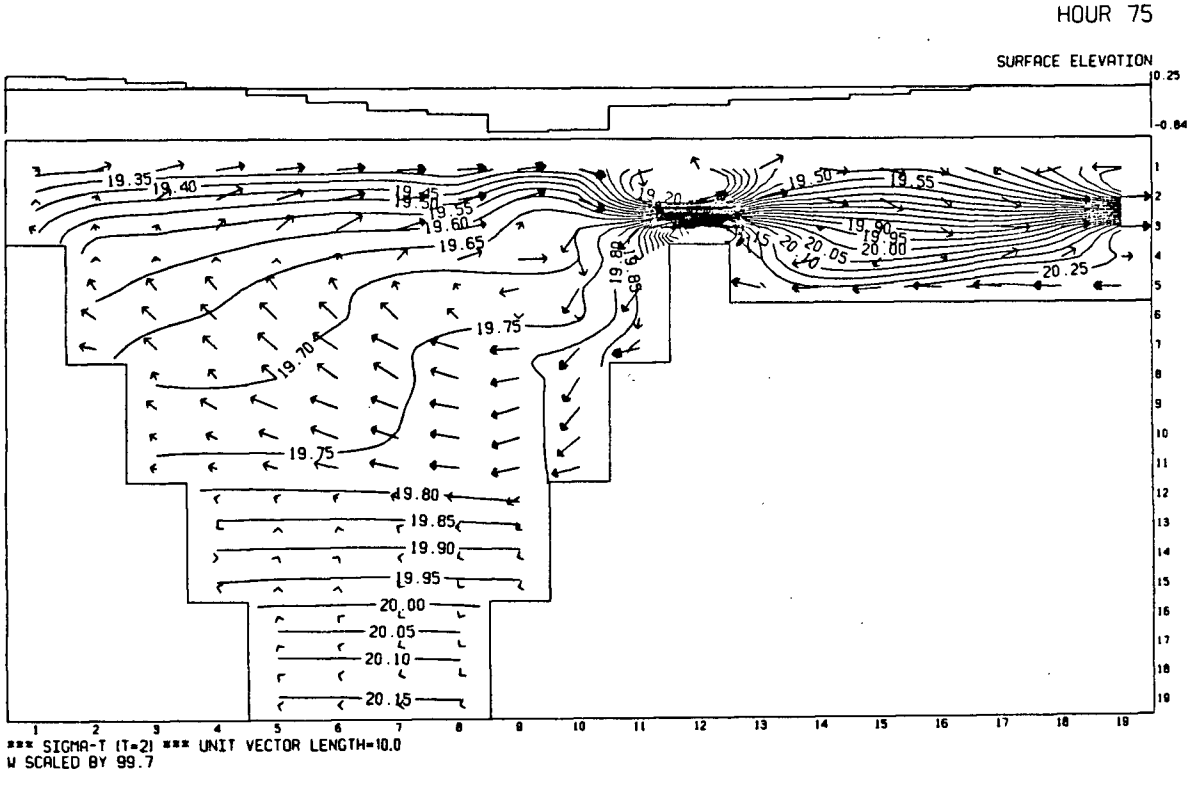

Figure 26(continued)

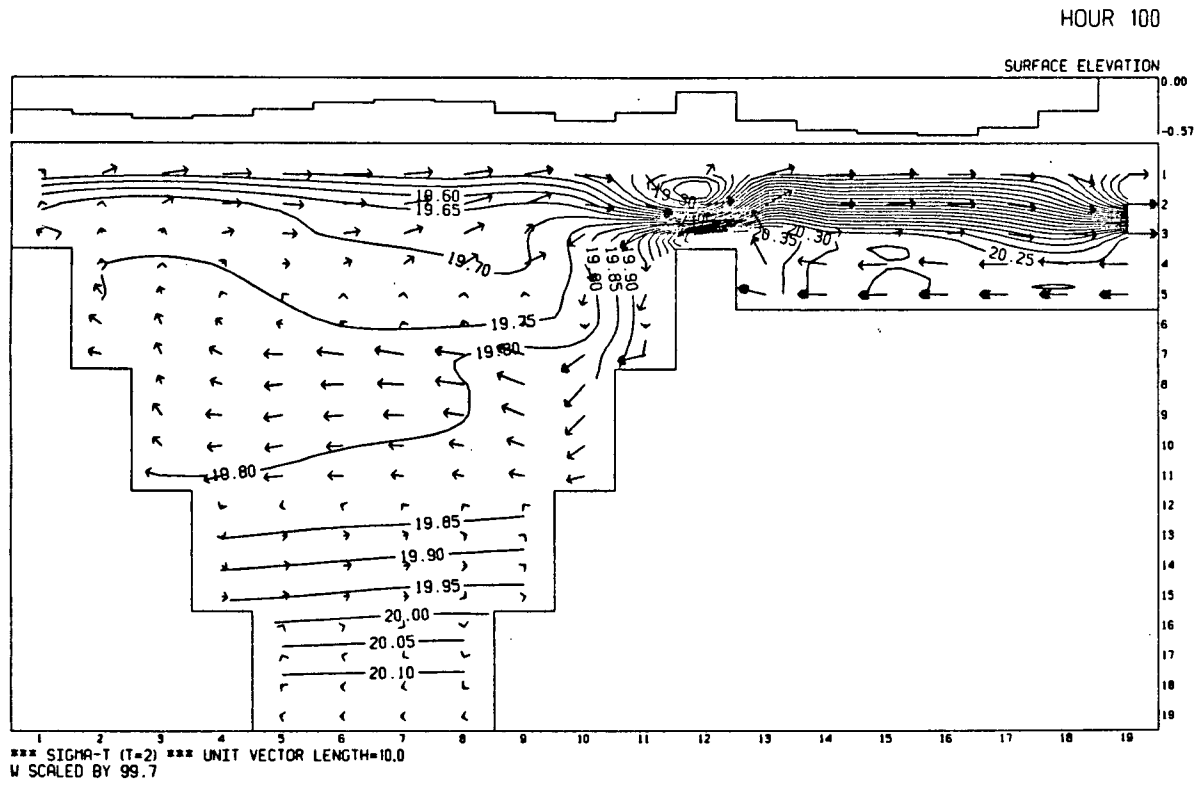

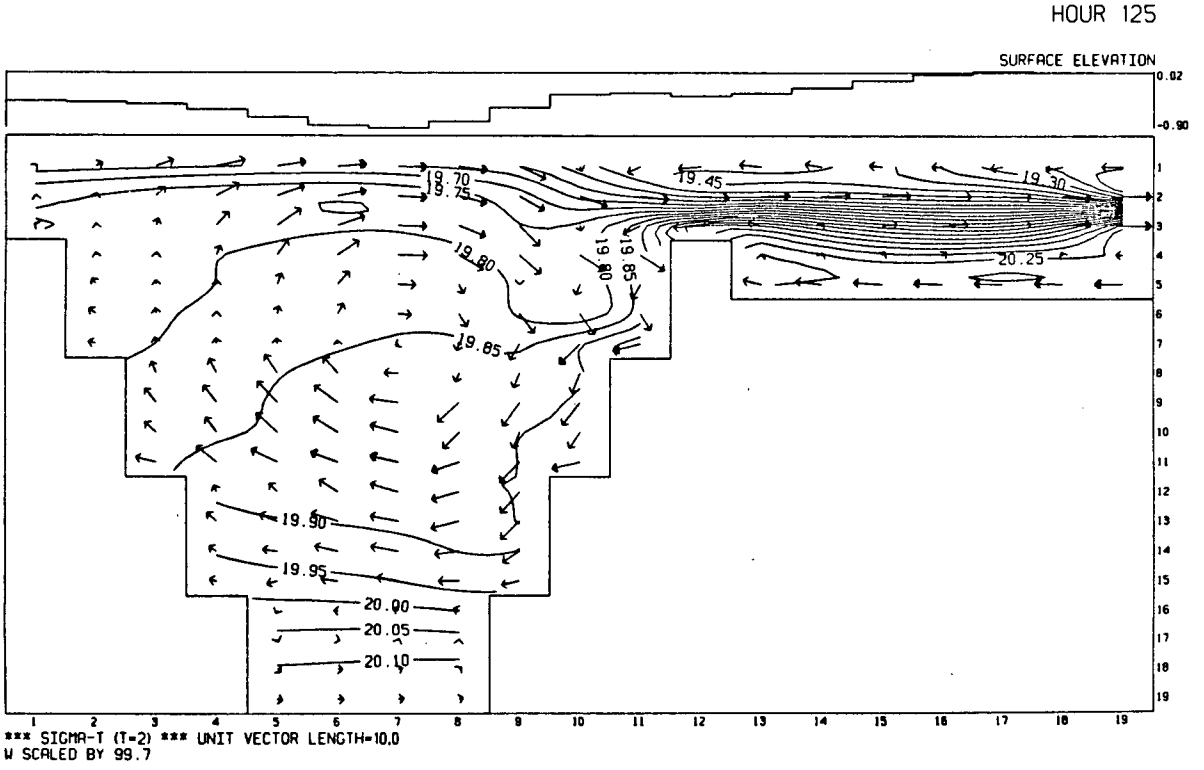

Figure 26(continued)

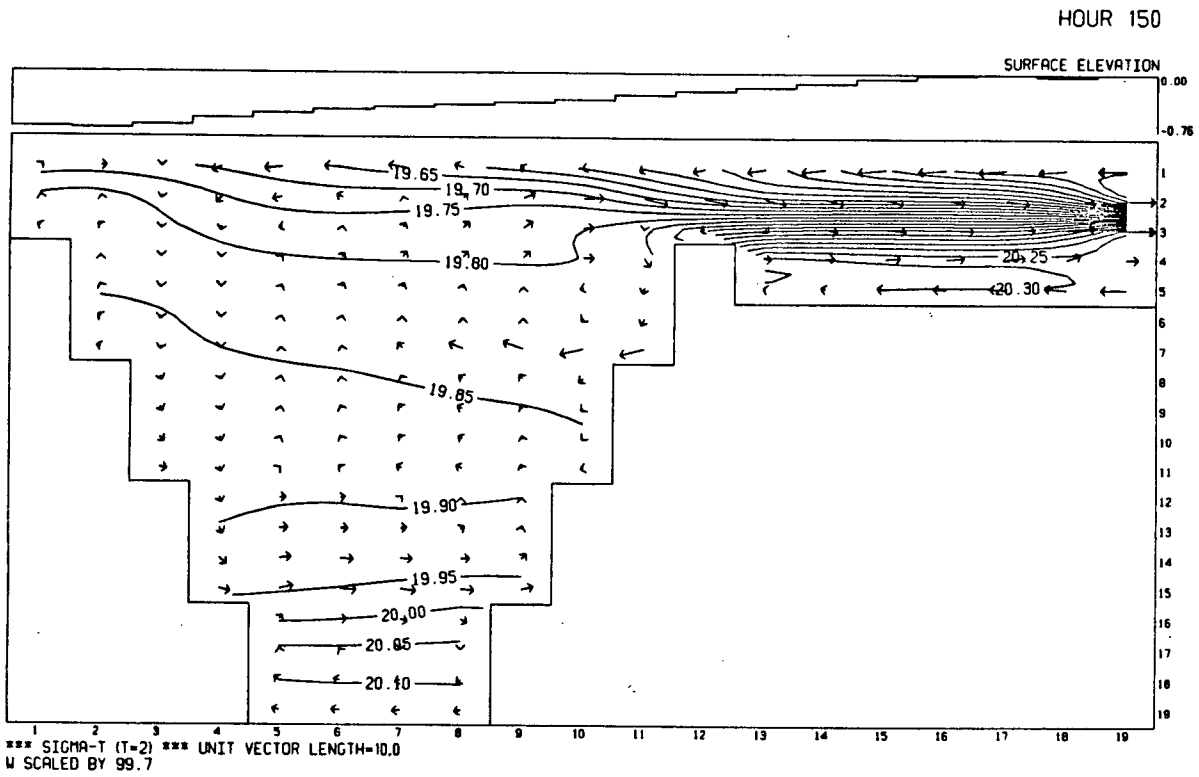

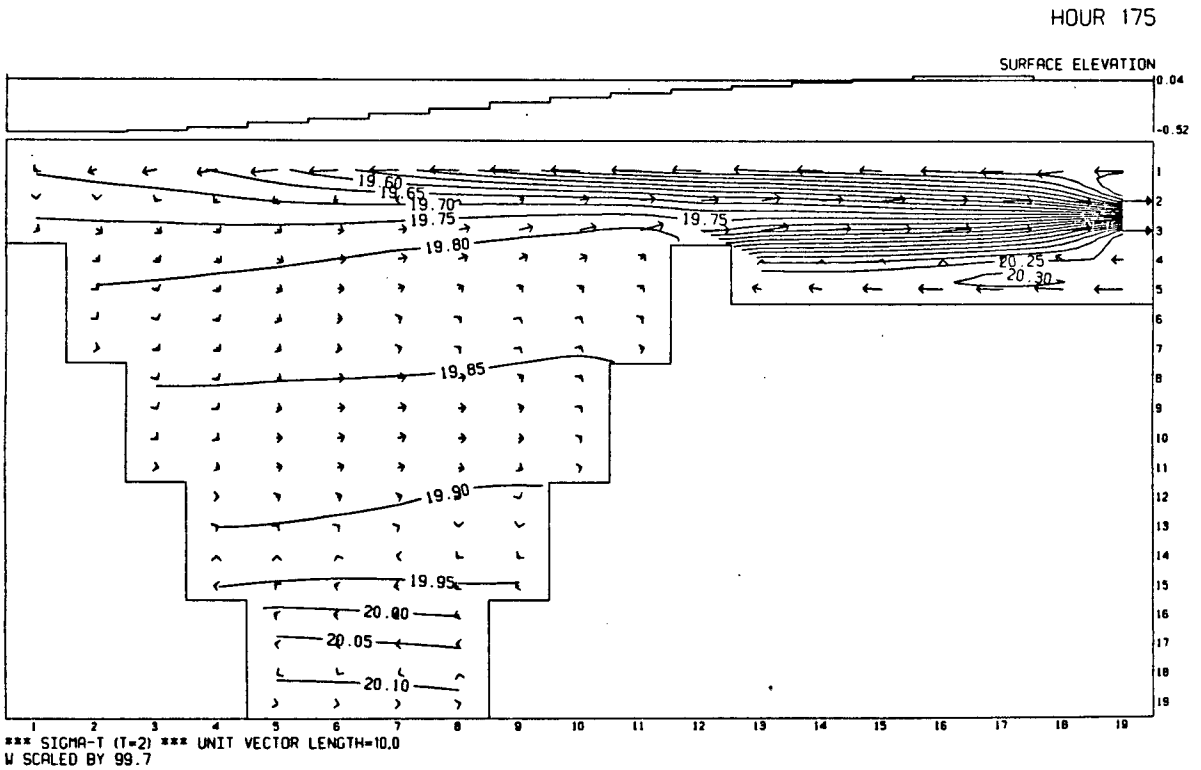

Figure 26(continued)

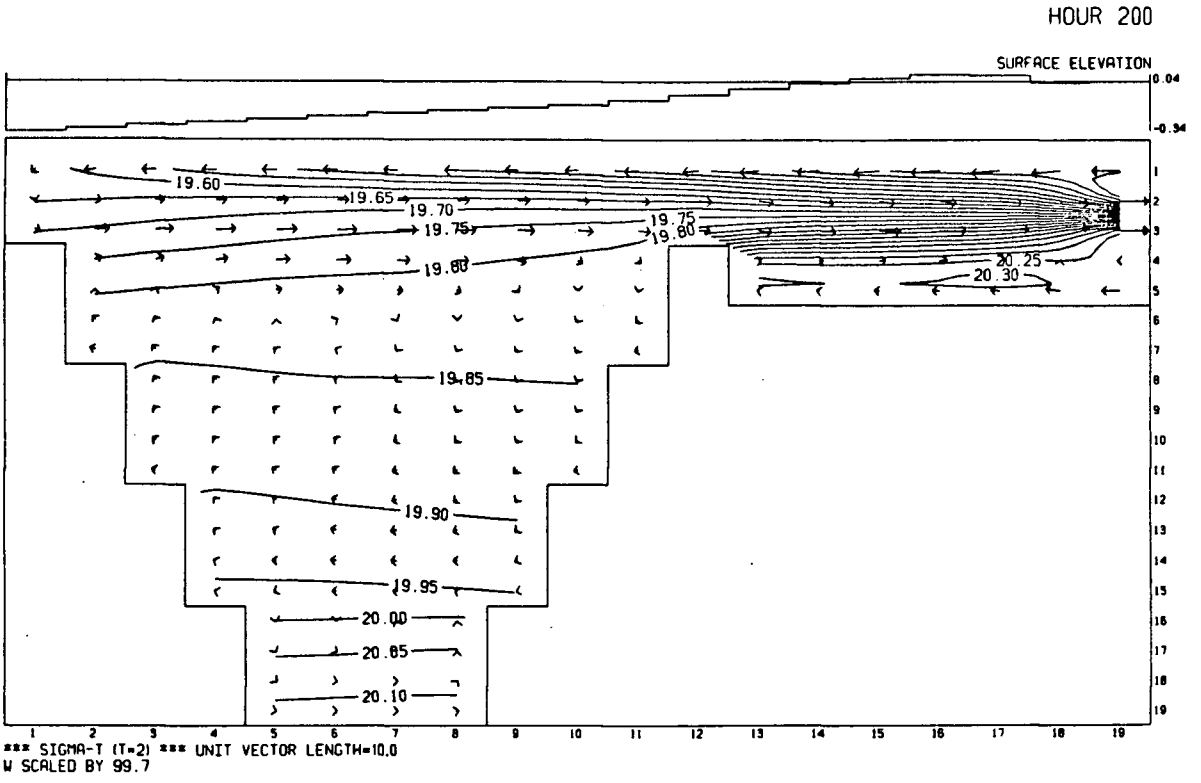

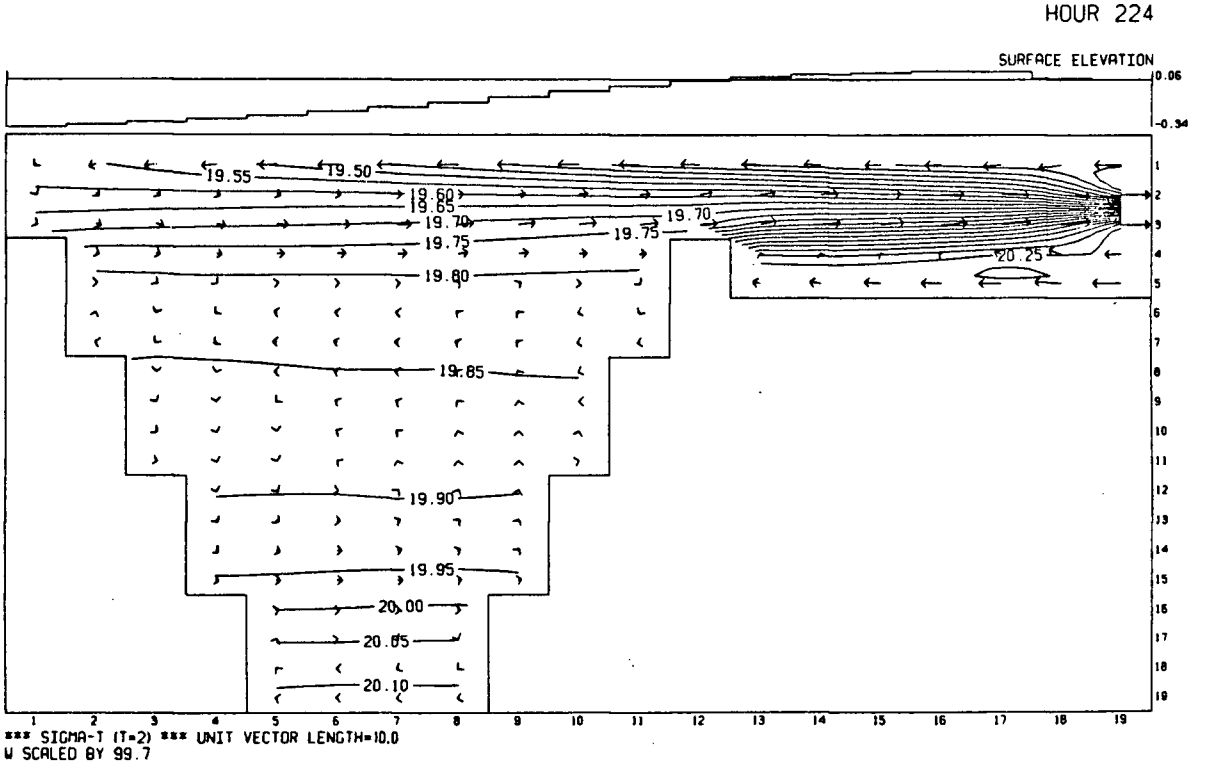

Figure 26(continued)

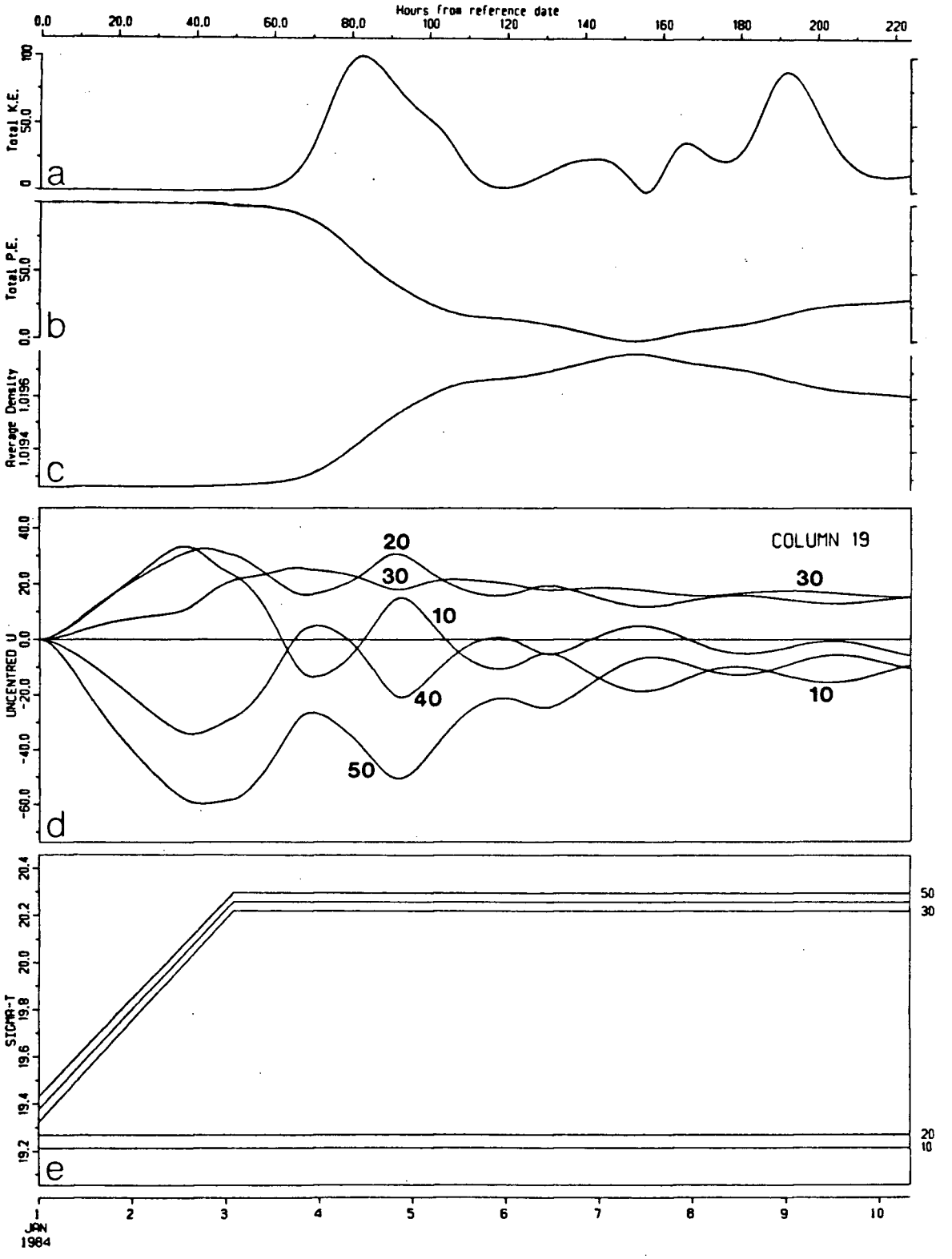

Figure 27. Time series at column 19 (the mouth) for Class 3.1 simulation of nontidal, stratified circulation in a representative inlet of uniform width. Model hours are shown on top axis. Plot (a): kinetic energy integrated over the inlet volume (arbitrary units). Plot (b): potential energy integrated over the inlet volume (arbitrary units). Plot (c): mean density in the inlet. Plot (d): horizontal velocity (depths (m) are shown next to curves). Plot (e): σ_t (depths (m) are shown at right).

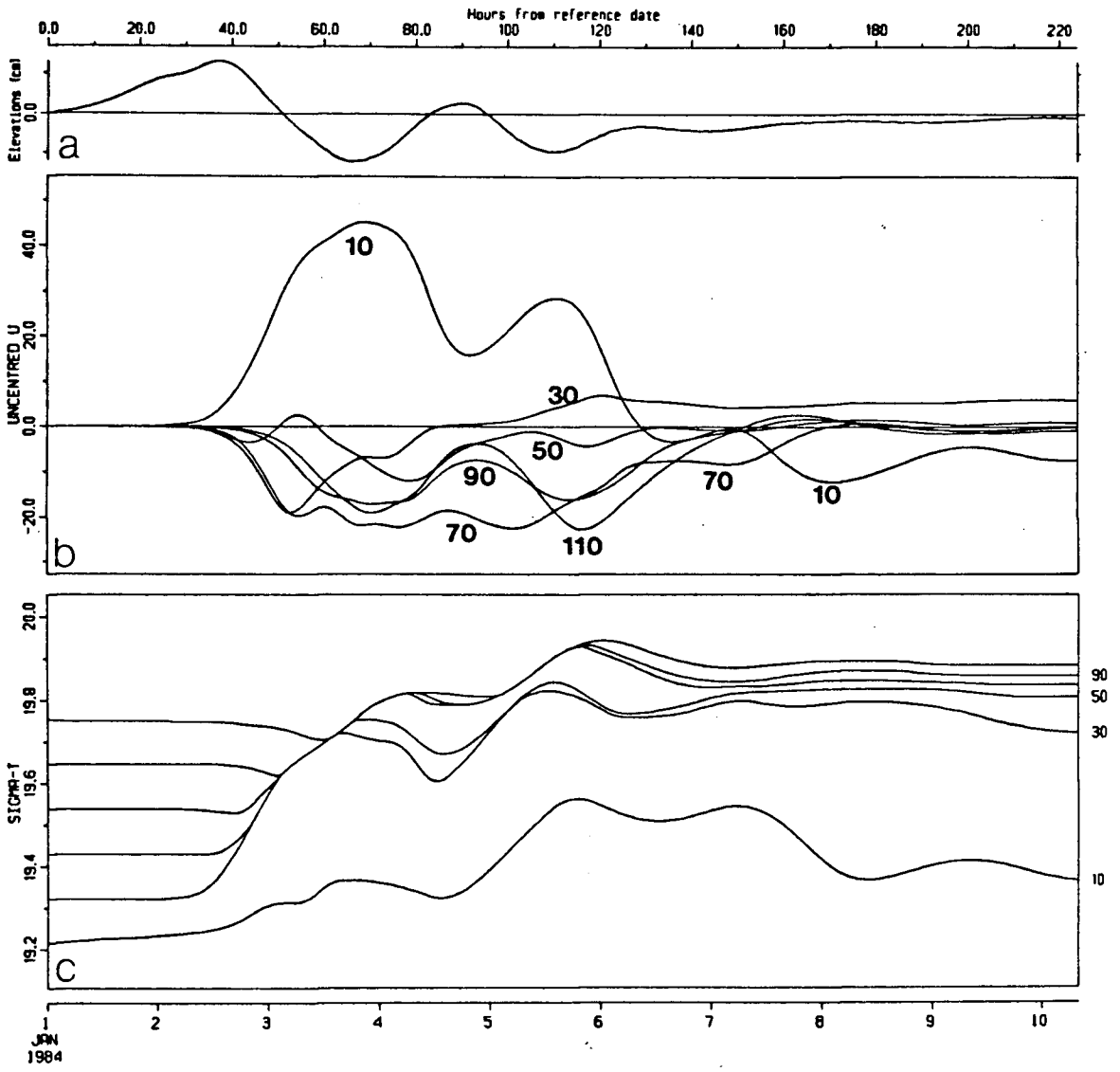

Figure 28. Time series at column 10 for Class 3.1 simulation of nontidal, stratified circulation in a representative inlet of uniform width. Model hours are shown on top axis. Plot (a): surface elevation (*cm*). Plot (b): horizontal velocity (depths (*m*) are shown next to curves). Plot (c): σ_t (depths (*m*) are shown at right).

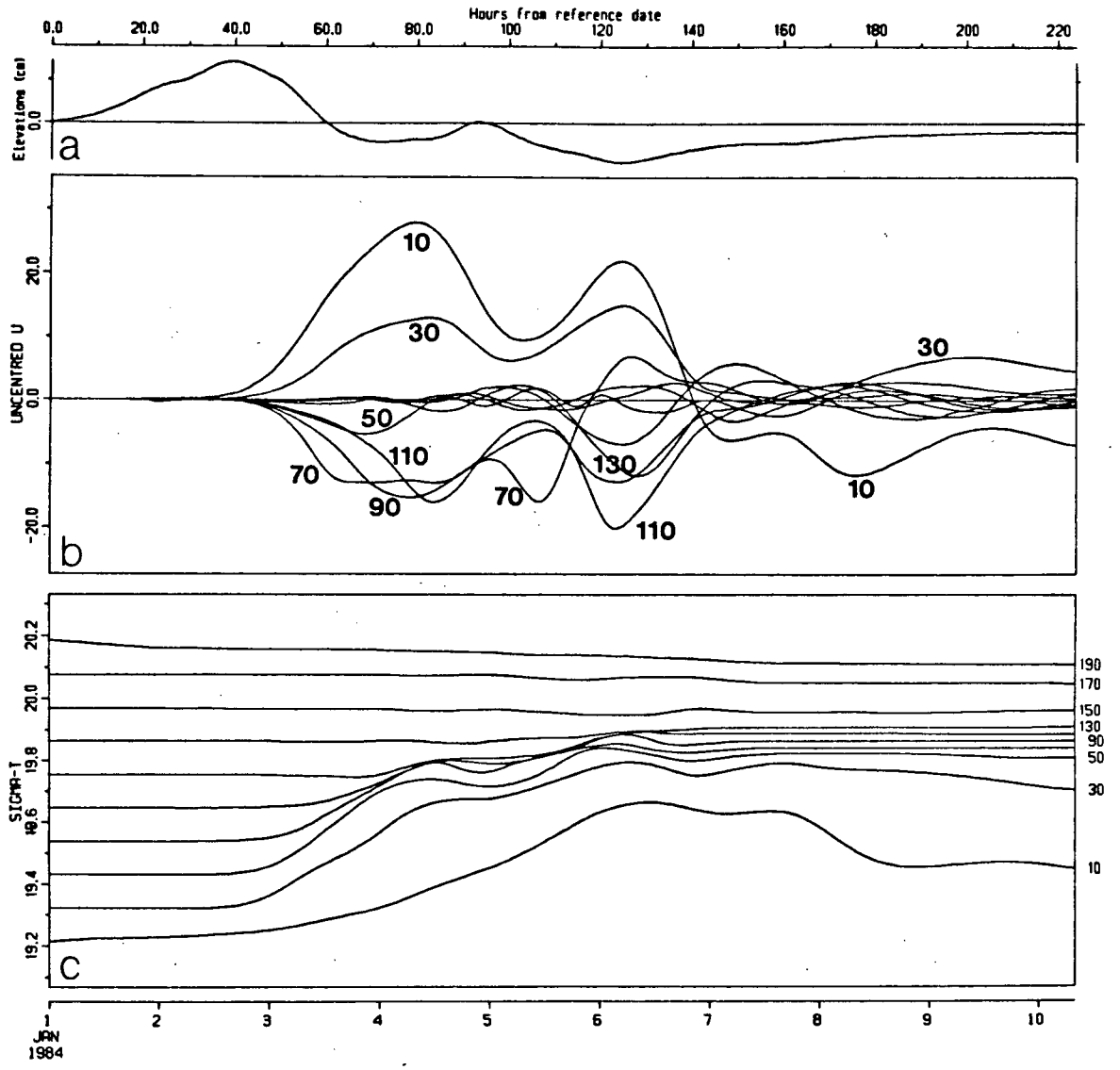

Figure 29. Time series at column 7 for Class 3.1 simulation of nontidal, stratified circulation in a representative inlet of uniform width. Model hours are shown on top axis. Plot (a): surface elevation (cm). Plot (b): horizontal velocity (depths (m) are shown next to curves). Plot (c): σ_t (depths (m) are shown at right).

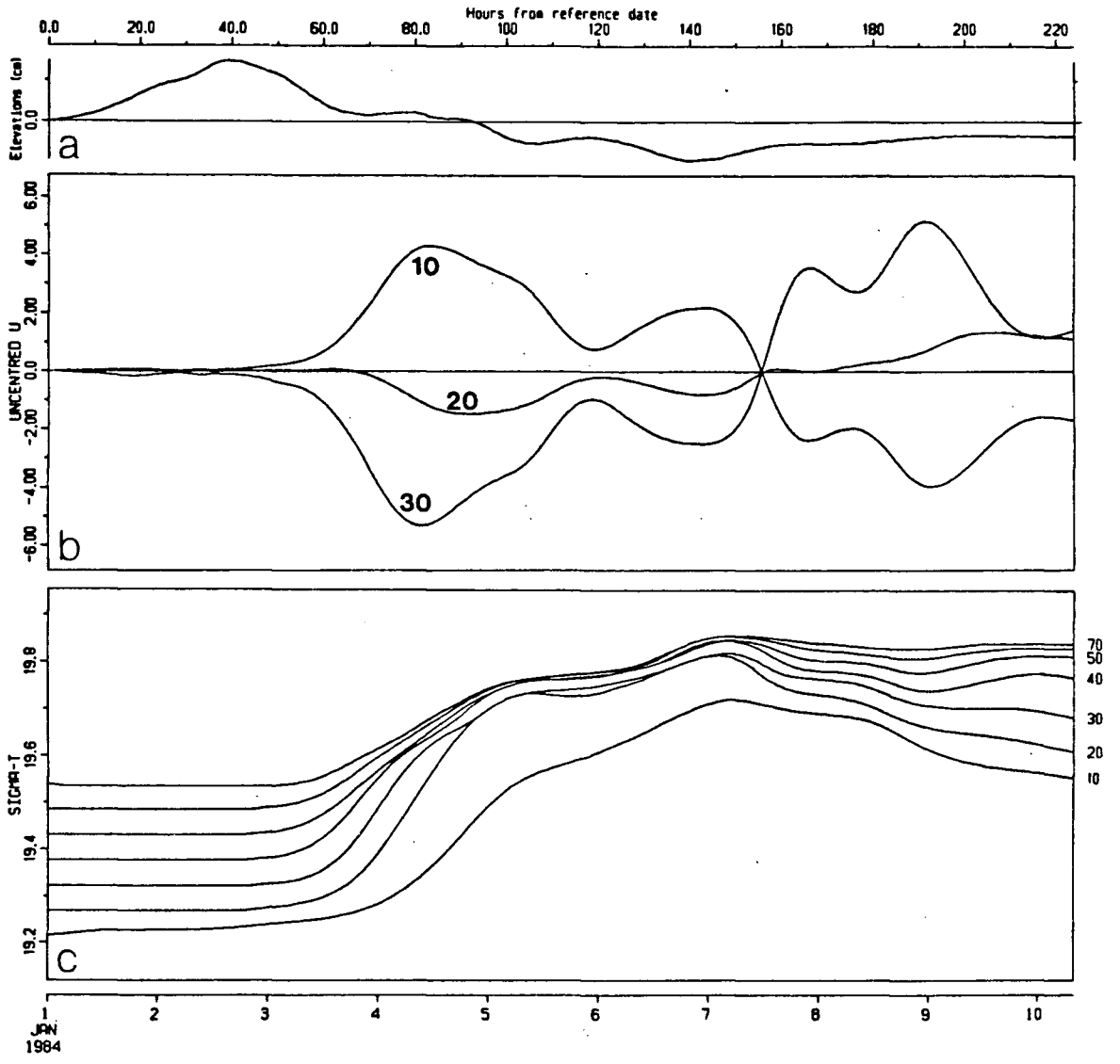

Figure 30. Time series for Class 3.1 simulation of nontidal, stratified circulation in a representative inlet of uniform width at column 2. Model hours are shown on top axis. Plot (a): surface elevation (*cm*). Plot (b): horizontal velocity (depths (*m*) are shown next to curves). Plot (c): σ_t (depths (*m*) are shown at right).

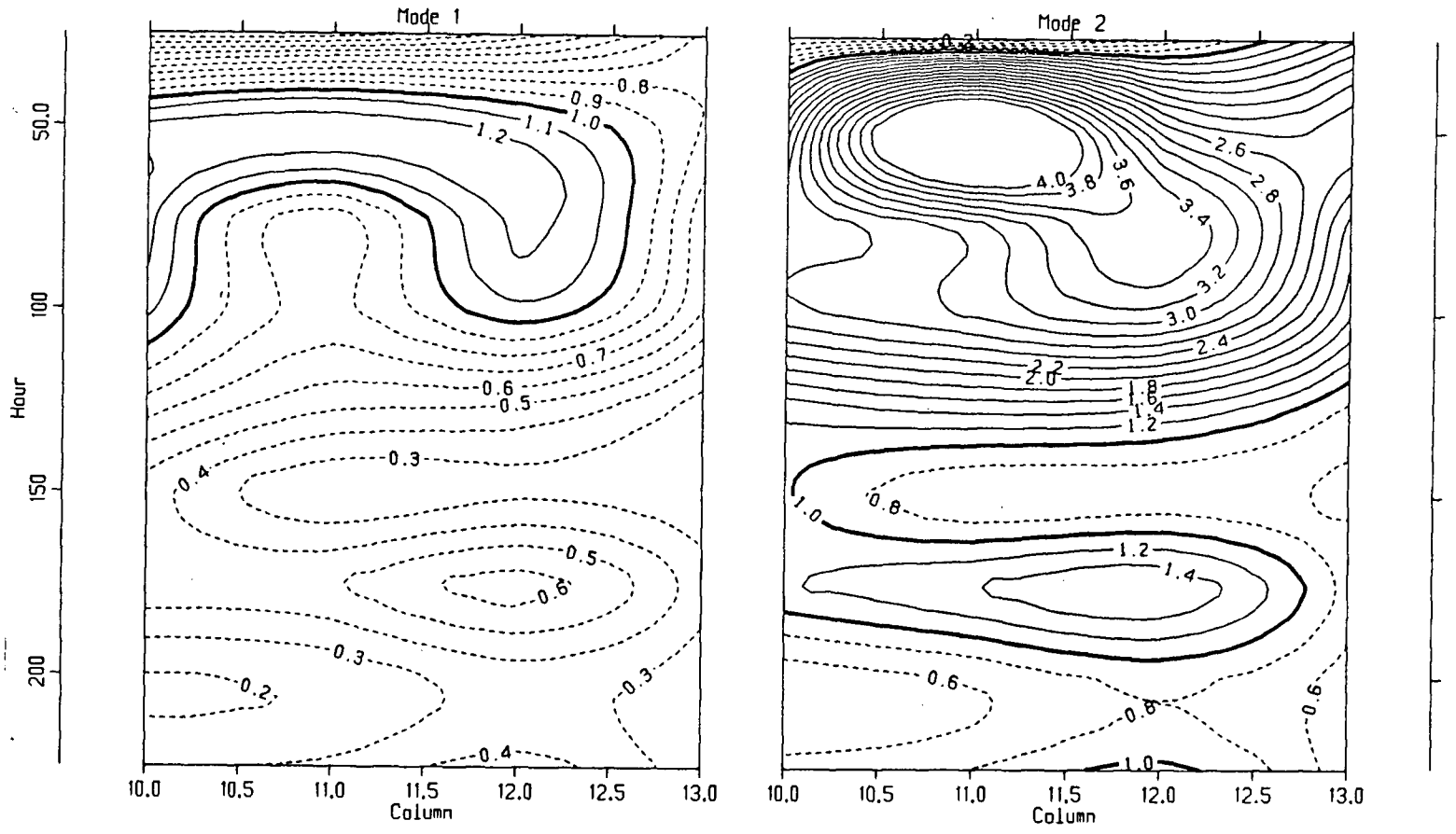

Figure 31. Contours of internal Froude number F_i for Class 3.1 simulation of nontidal, stratified circulation in a representative inlet of uniform width for the first two baroclinic modes in the vicinity of the sill as a function of time. Solid line: supercritical flow. Heavy line: critical flow. Dashed line: subcritical flow.

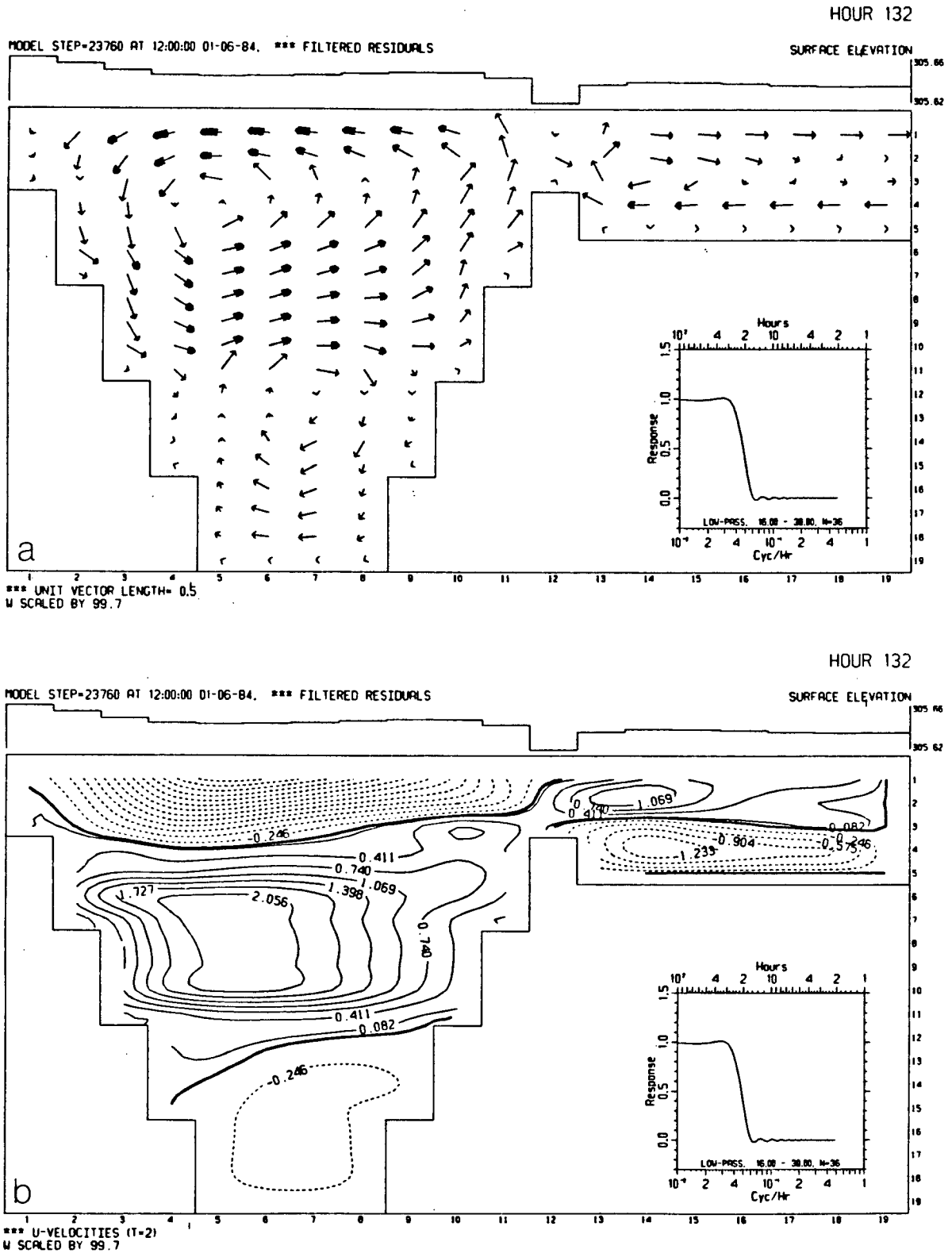

Figure 32. Residual circulation (§6.5) for Class 3.2 simulation of unstratified tidal flow. Plot (a): Current vectors (unit length = $0.5\,cm\,s^{-1}$). Plot (b): Contours of horizontal velocity; inflow (dashed line); outflow (solid line); zero value (heavy line). Inset shows response curve of digital filter used to calculate residuals.

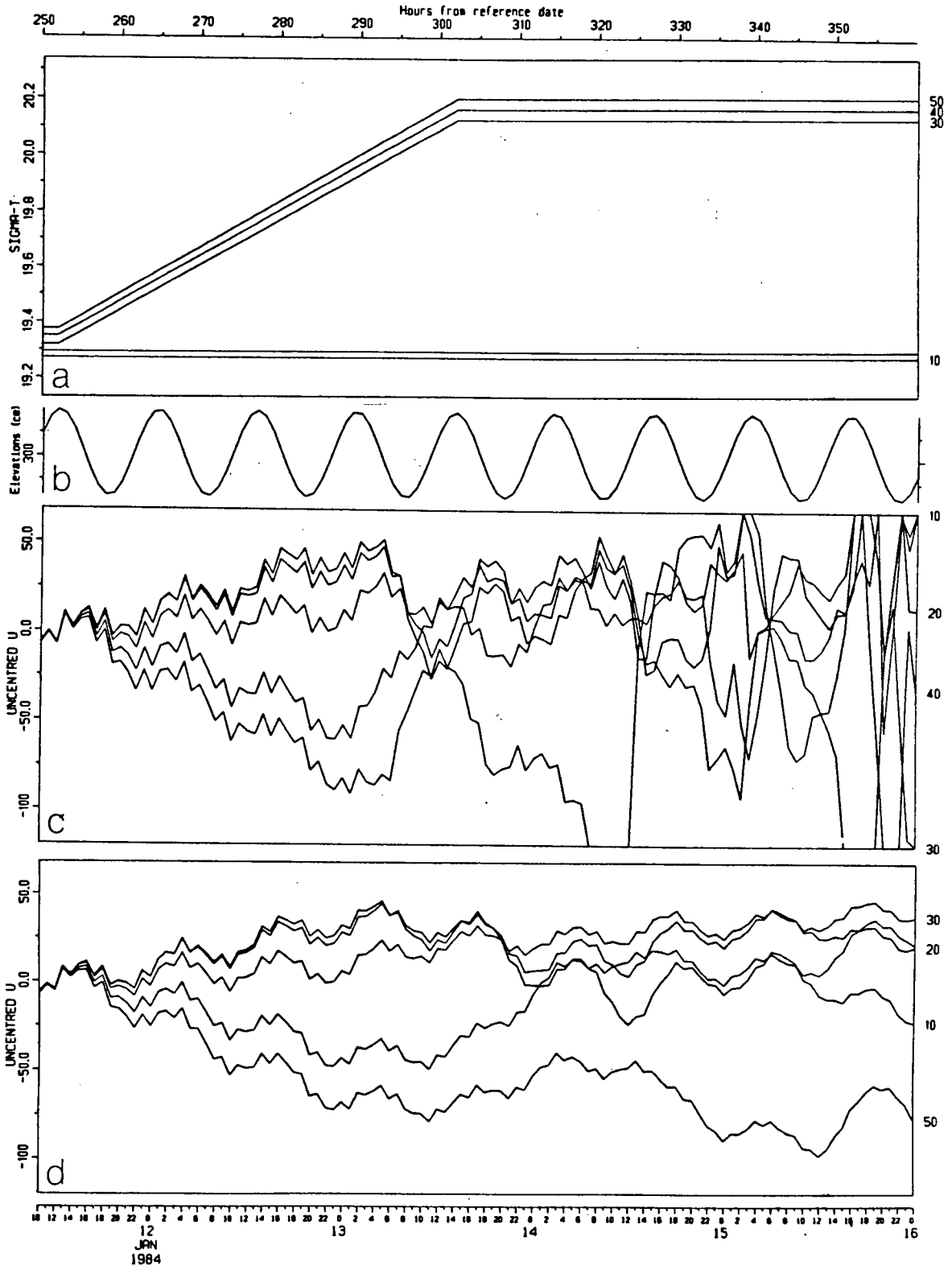

Figure 33. Time series for Class 3.3 simulation of stratified tidal flow at column 19 (the mouth). Model hours are shown on top axis, depths (m) are shown at right. Plot (a): σ_t. Plot (b): surface elevation (cm). Plot (c): horizontal velocity ($cm\,s^{-1}$) ($N^{(x)} = K^{(x)} = 10^5\,cm^2\,s^{-1}$). Plot (d): horizontal velocity ($cm\,s^{-1}$) ($N^{(x)} = K^{(x)} = 10^6\,cm^2\,s^{-1}$).

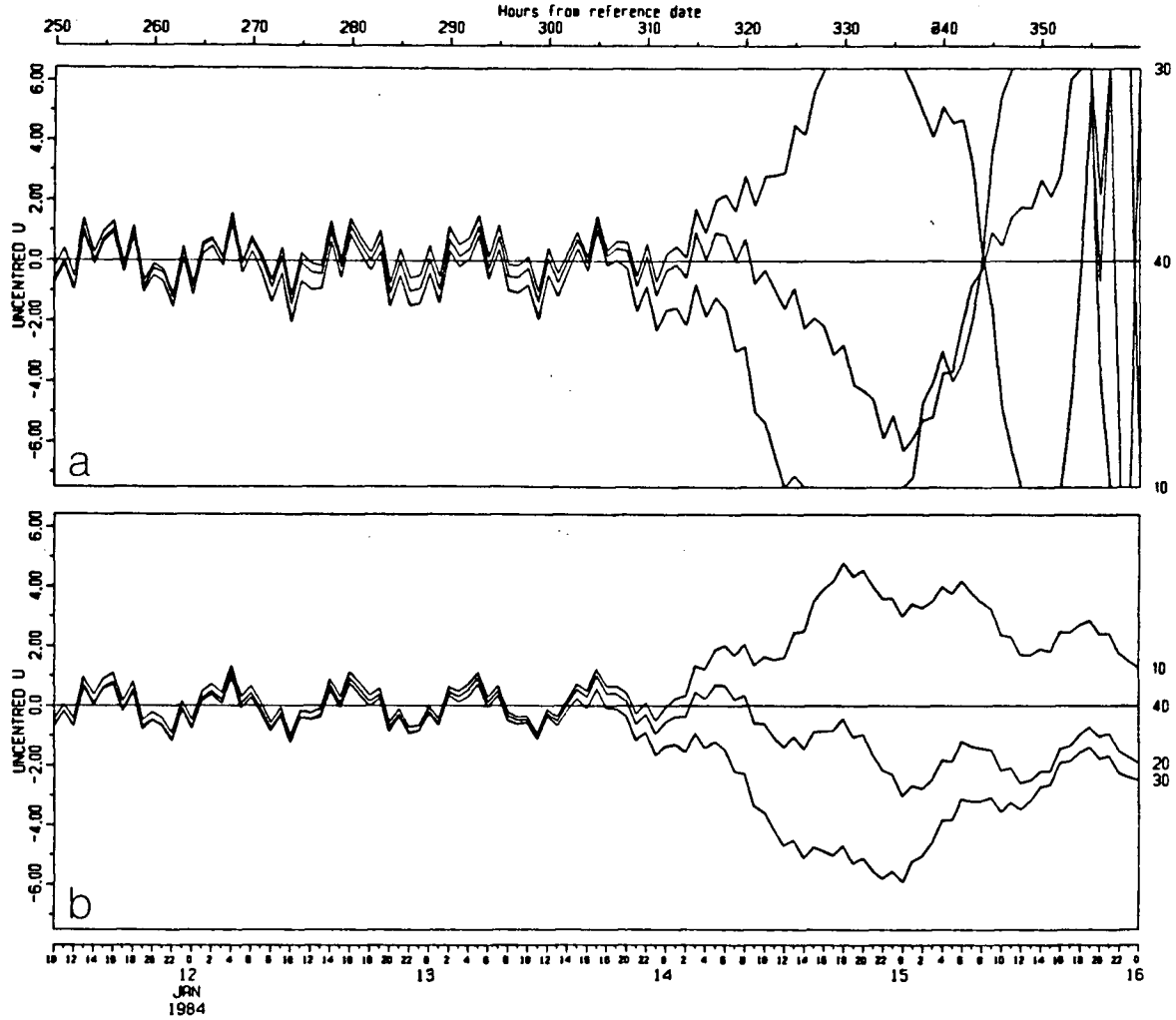

Figure 34. Time series for Class 3.3 simulation of stratified tidal flow at column 2. Model hours are shown on top axis, depths (m) are shown at right. Plot (a): horizontal velocity ($cm\,s^{-1}$) ($N^{(x)} = K^{(x)} = 10^5\,cm^2\,s^{-1}$). Plot (b): horizontal velocity ($cm\,s^{-1}$) ($N^{(x)} = K^{(x)} = 10^6\,cm^2\,s^{-1}$).

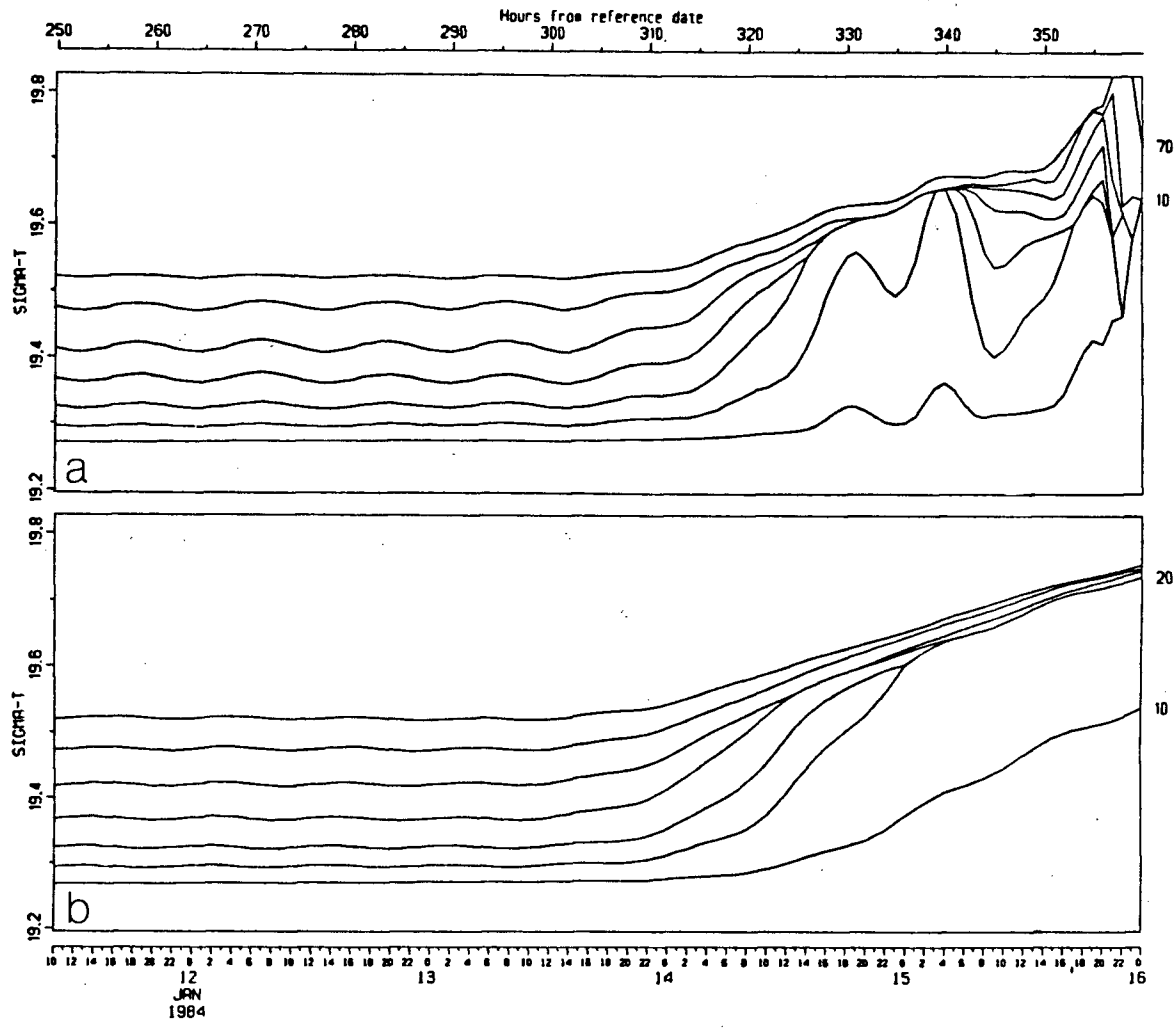

Figure 35. Time series for Class 3.3 simulation of stratified tidal flow at column 2. Model hours are shown on top axis, depths (m) are shown at right. Plot (a): σ_t ($N^{(x)} = K^{(x)} = 10^5\, cm^2\, s^{-1}$). Plot (b): σ_t ($N^{(x)} = K^{(x)} = 10^6\, cm^2\, s^{-1}$).

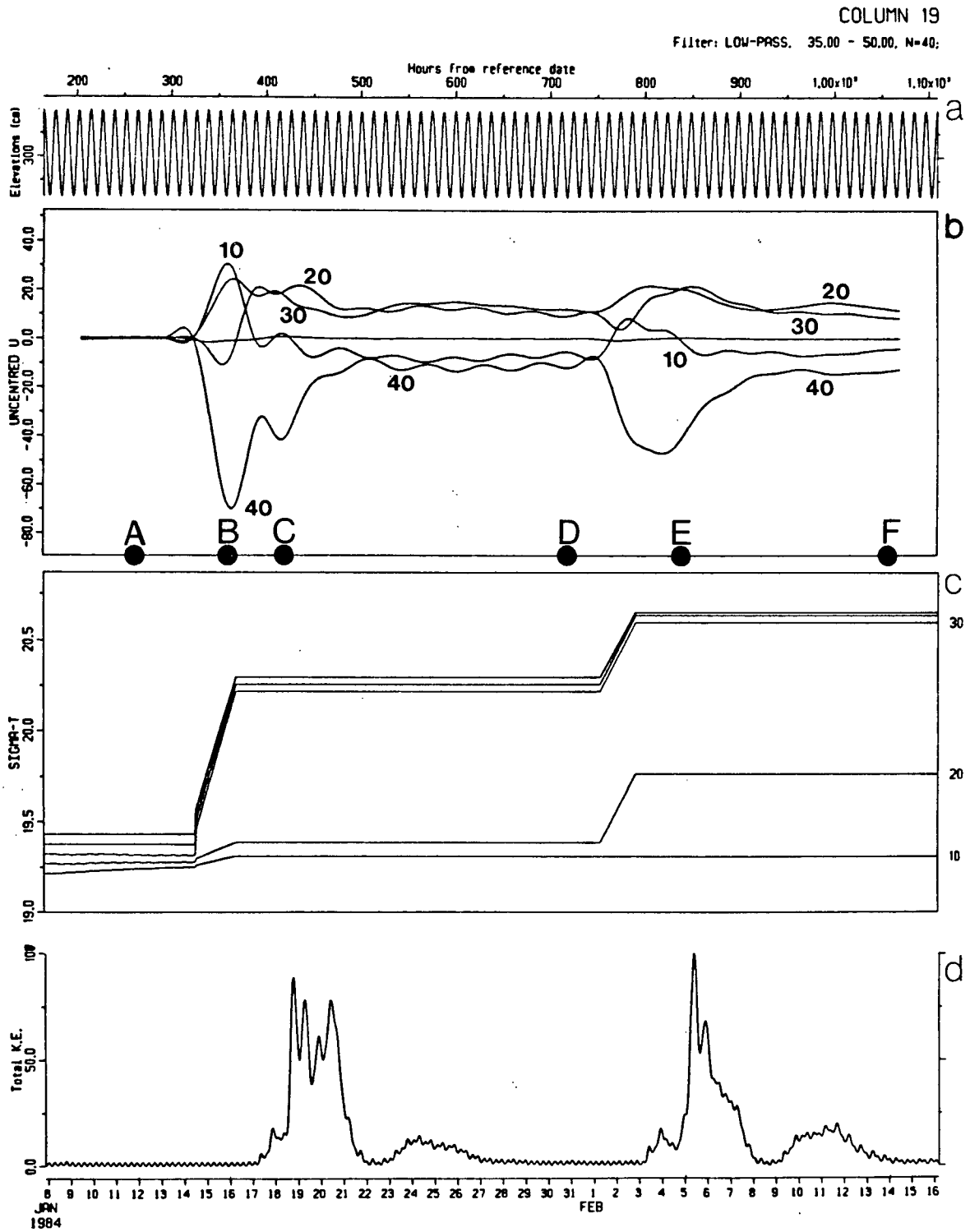

Figure 36. Time series for Class 3.4 simulation of tidally driven dense water intrusion at column 19 (the mouth). Model hours are shown on top axis. Plot (a): surface elevation (cm). Plot (b): (35,50,40) filtered horizontal velocity ($cm\,s^{-1}$) (depths (m) are marked next to curves. Circles indicate plot times). Plot (c): σ_t. Plot (d): kinetic energy integrated over the inlet volume (arbitrary units).

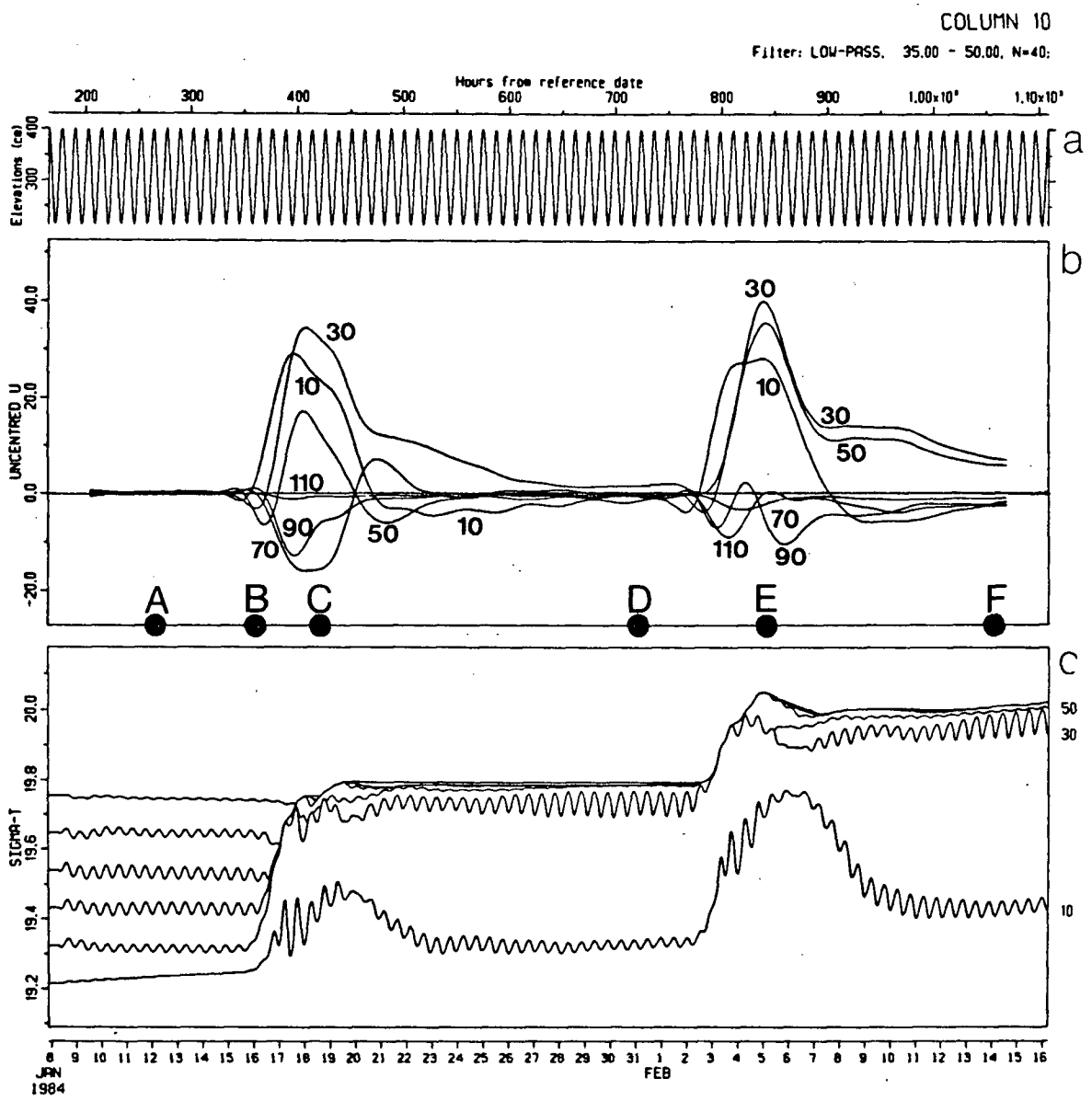

Figure 37. Time series for Class 3.4 simulation of tidally driven dense water intrusion at column 10. Model hours are shown on top axis. Plot (a): surface elevation (cm). Plot (b): (35,50,40) filtered horizontal velocity ($cm\,s^{-1}$) (depths (m) are marked next to curves. Circles mark plot times). Plot (c): σ_t.

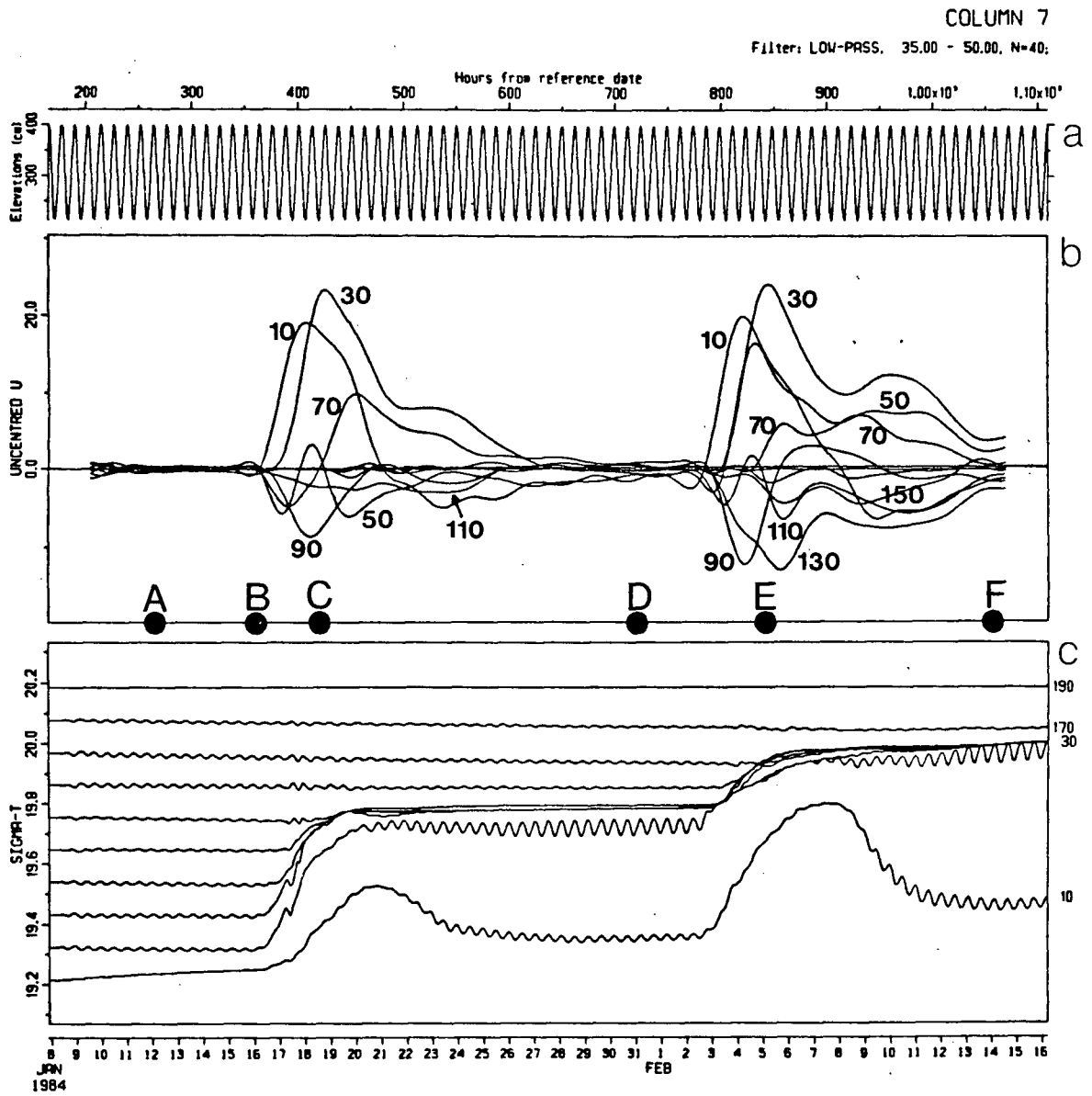

Figure 38. Time series for Class 3.4 simulation of dense water intrusion at column 7. Model hours are shown on top axis. Plot (a): surface elevation (cm). Plot (b): (35,50,40) filtered horizontal velocity ($cm\,s^{-1}$) (depths (m) are marked next to curves. Circles mark plot times). Plot (c): σ_t.

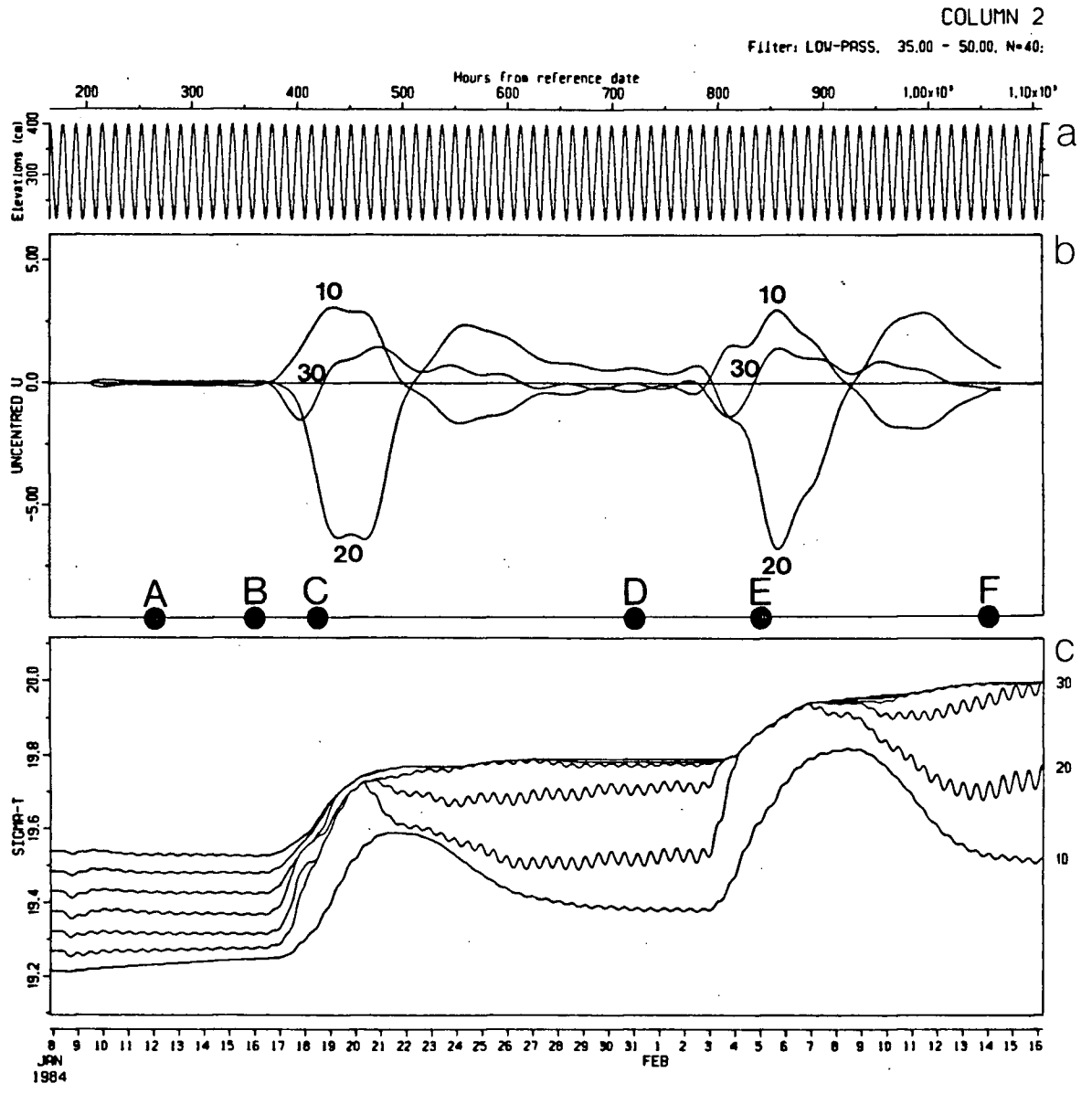

Figure 39. Time series for Class 3.4 simulation of dense water intrusion at column 2. Model hours are shown on top axis. Plot (a): surface elevation (cm). Plot (b): (35,50,40) filtered horizontal velocity ($cm\,s^{-1}$) (circles mark plot times). Plot (c): σ_t.

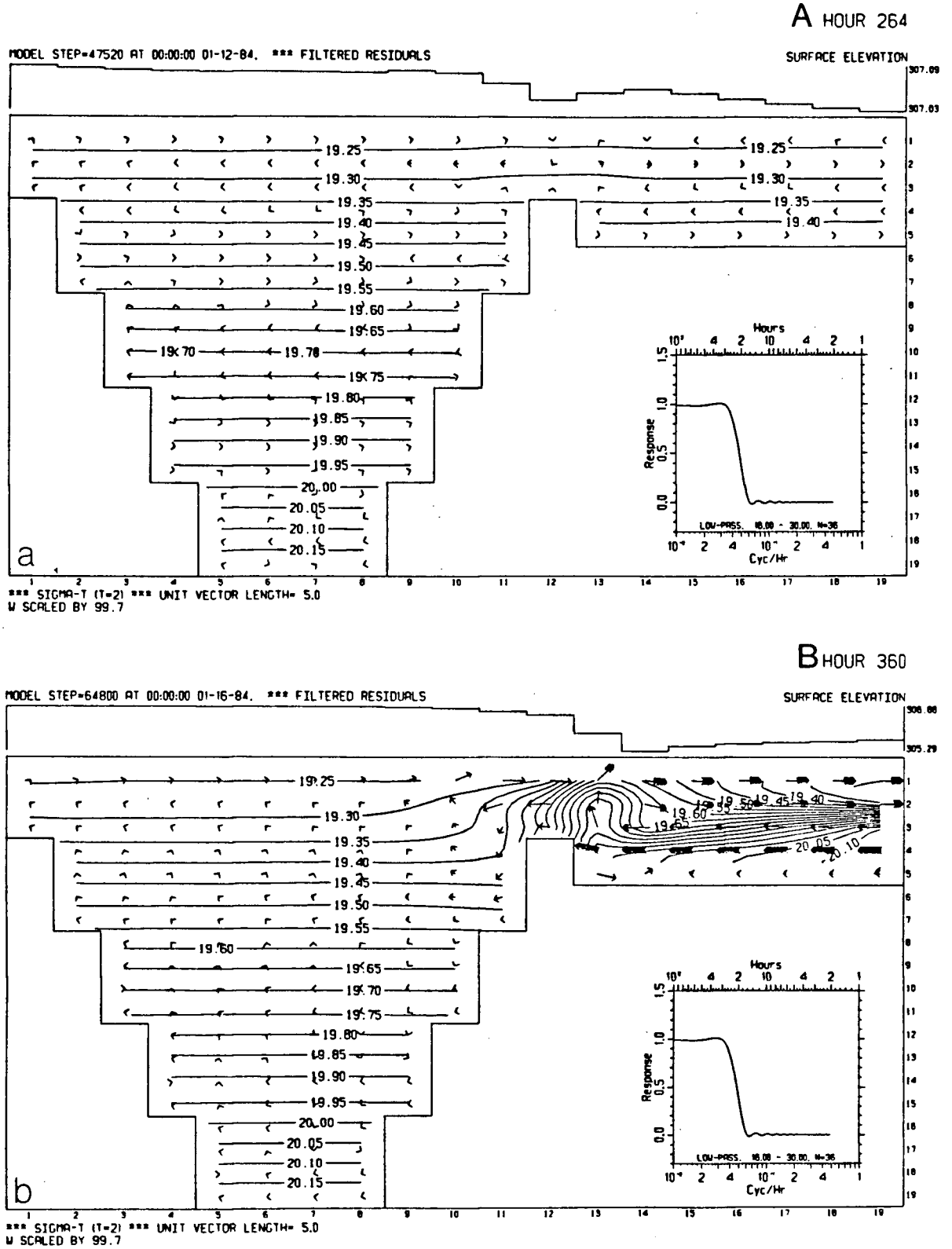

Figure 40. Fields of residual surface elevations (*cm*), velocity vectors, and isopycnals for the Class 3.4 simulation of tidally driven dense water intrusion at times indicated by circles shown on figures 38 and 39. Unit vector length is 5.0 $cm\,s^{-1}$, contours are in σ_t units. Inset shows the transfer function of the applied digital filter.

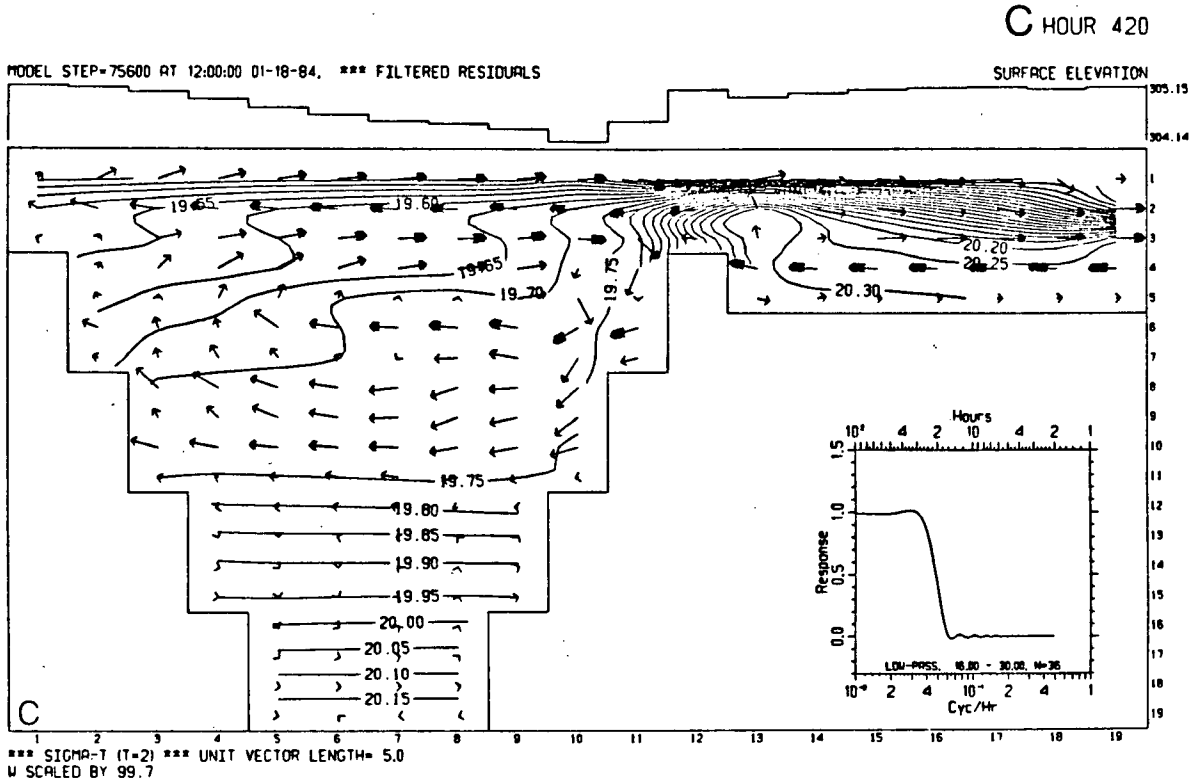

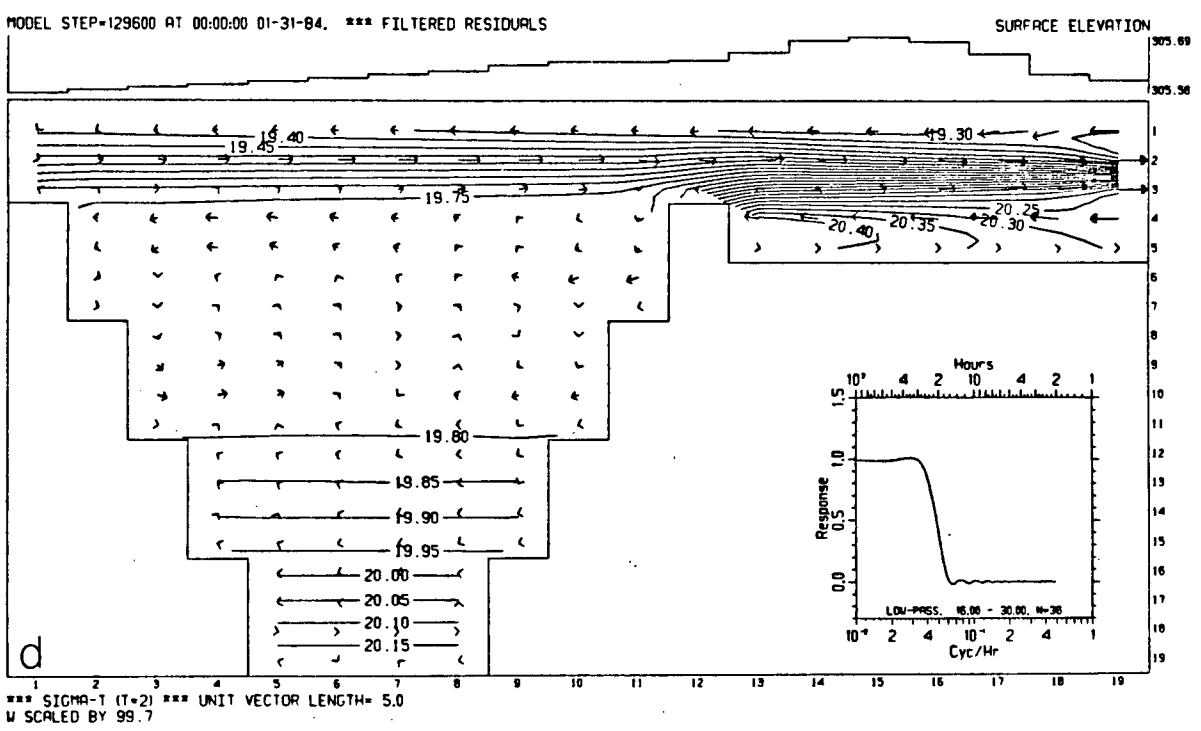

Figure 40(continued)

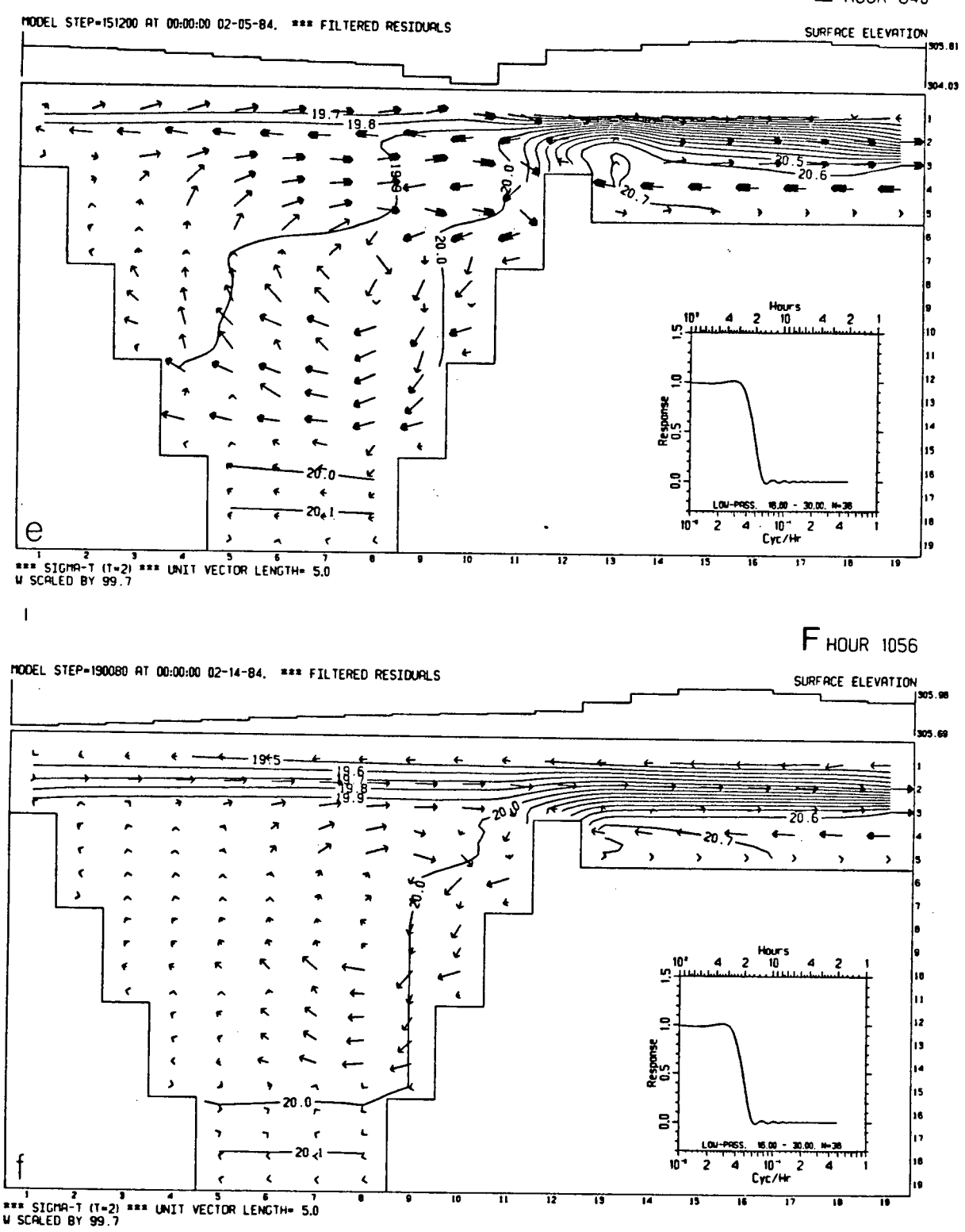

Figure 40(continued)

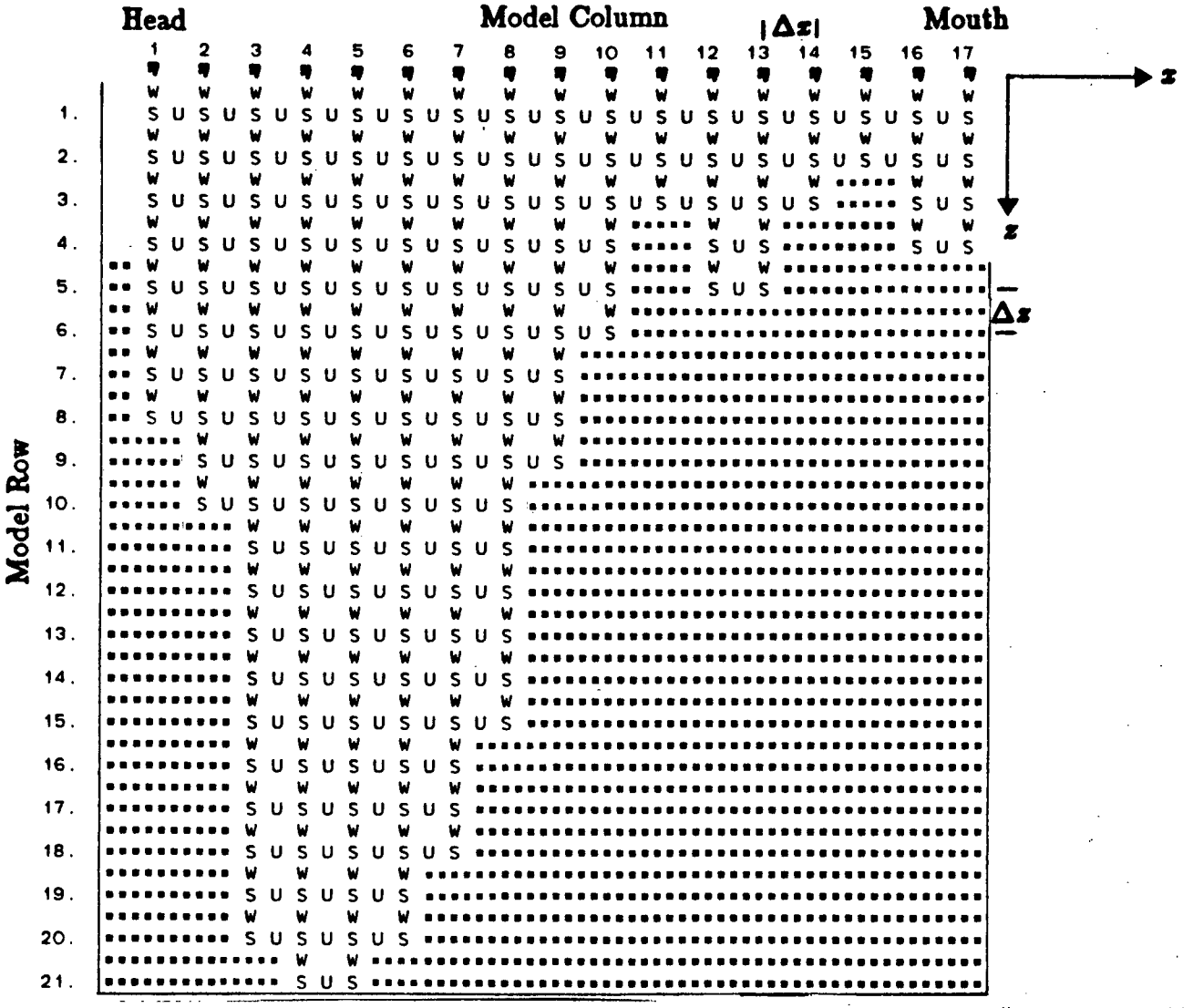

Figure 41. Geometry for Class 4 simulations showing locations of variables for horizontal velocity (U), vertical velocity (W) salinity (S), and surface elevation (η). $\Delta x = 2\,km$, $\Delta z = 10\,m$

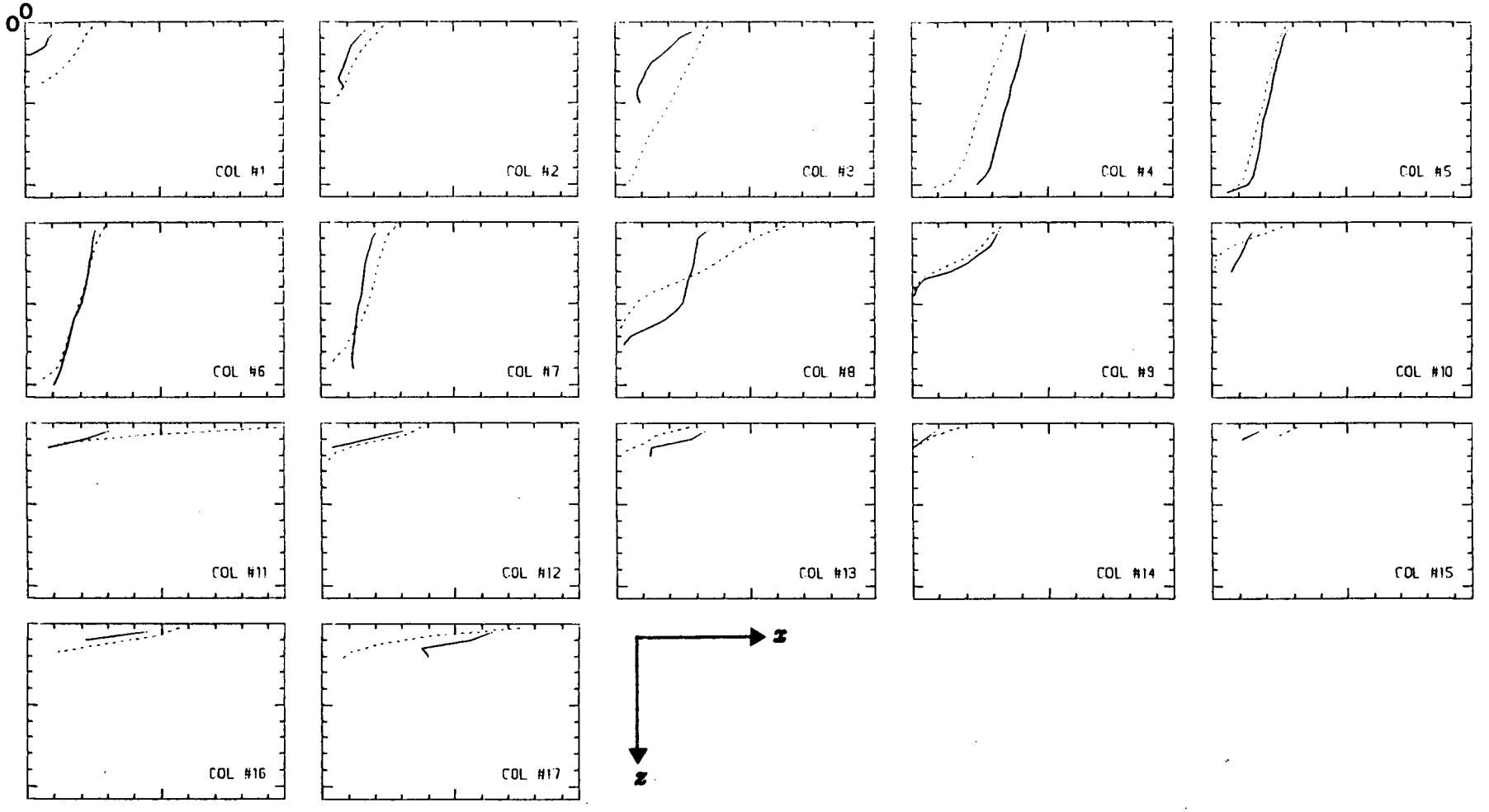

Figure 42. Depth vs. width at each column for the Class 4 simulation of Indian Arm and Burrard Inlet. Solid lines are widths at $u\text{-}point(B^{(x)})$; dashed lines are widths at $w\text{-}point(B^{(z)})$. Horizontal ticks are spaced every $100\,m$; vertical ticks are spaced every $20\,m$.

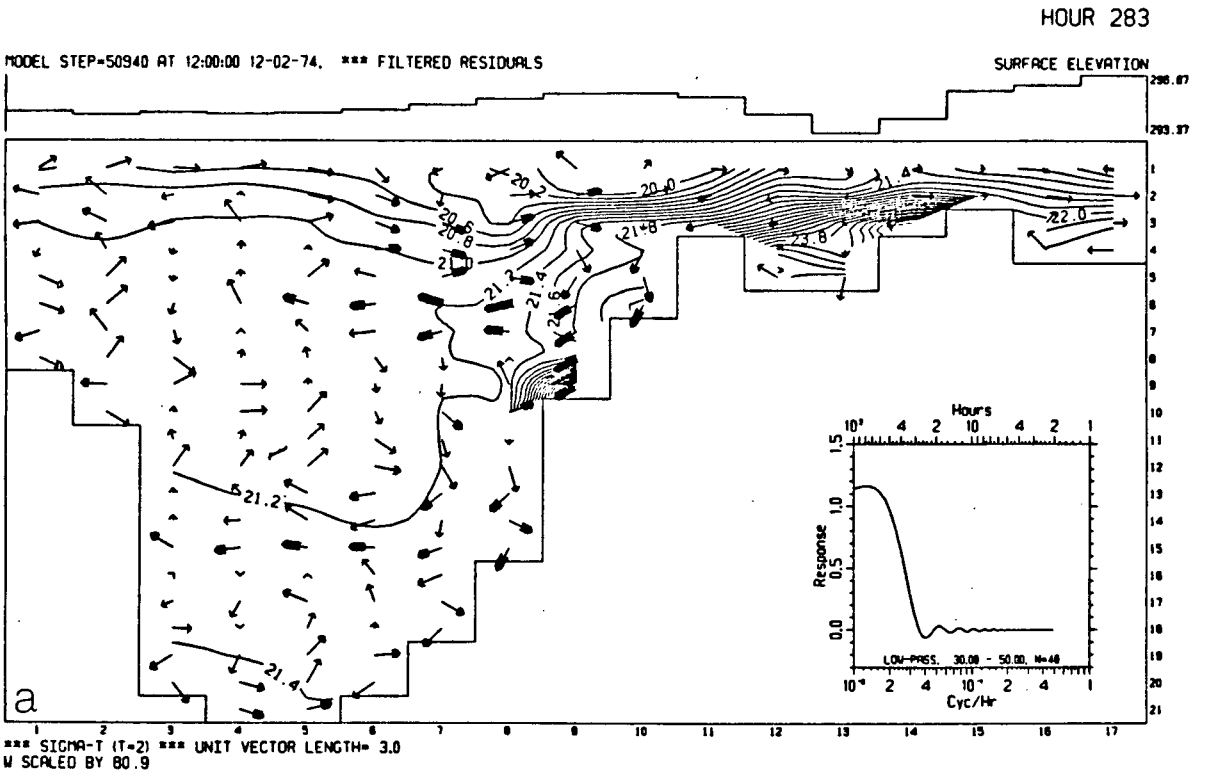

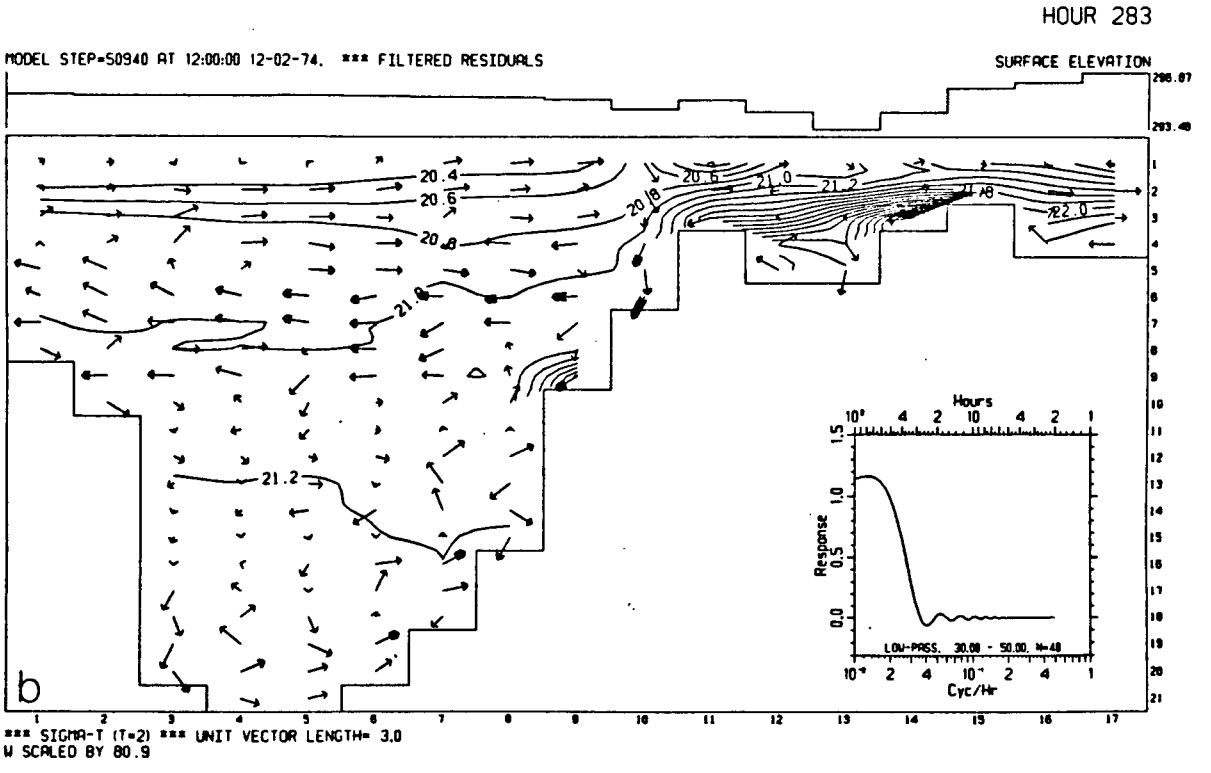

Figure 43. Residual surface elevation, current vectors and isopycnals for Class 4 simulation of Indian Arm and Burrard Inlet using different values of $N^{(x)} = K^{(x)}$. Plot (a): 10^4. Plot (b): 10^5. Plot (c): $5 \cdot 10^5$. Plot (d): 10^6. (in $cm^2\, s^{-1}$)

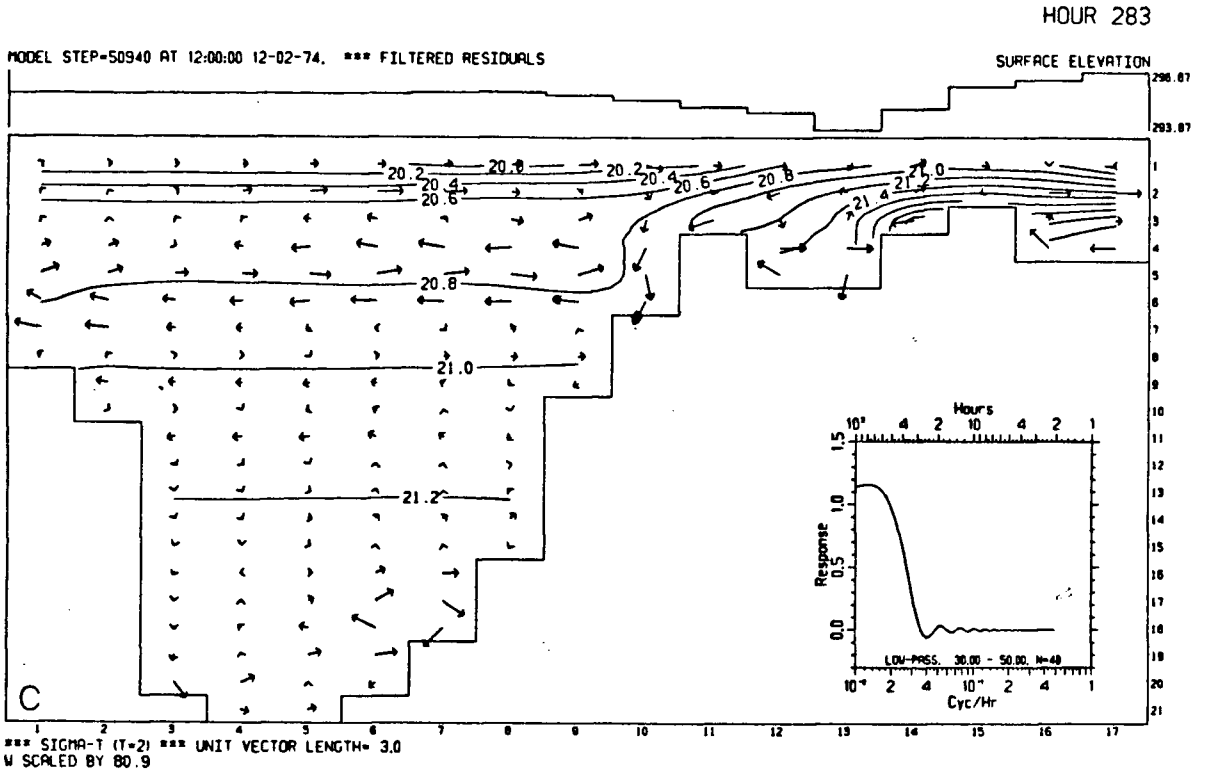

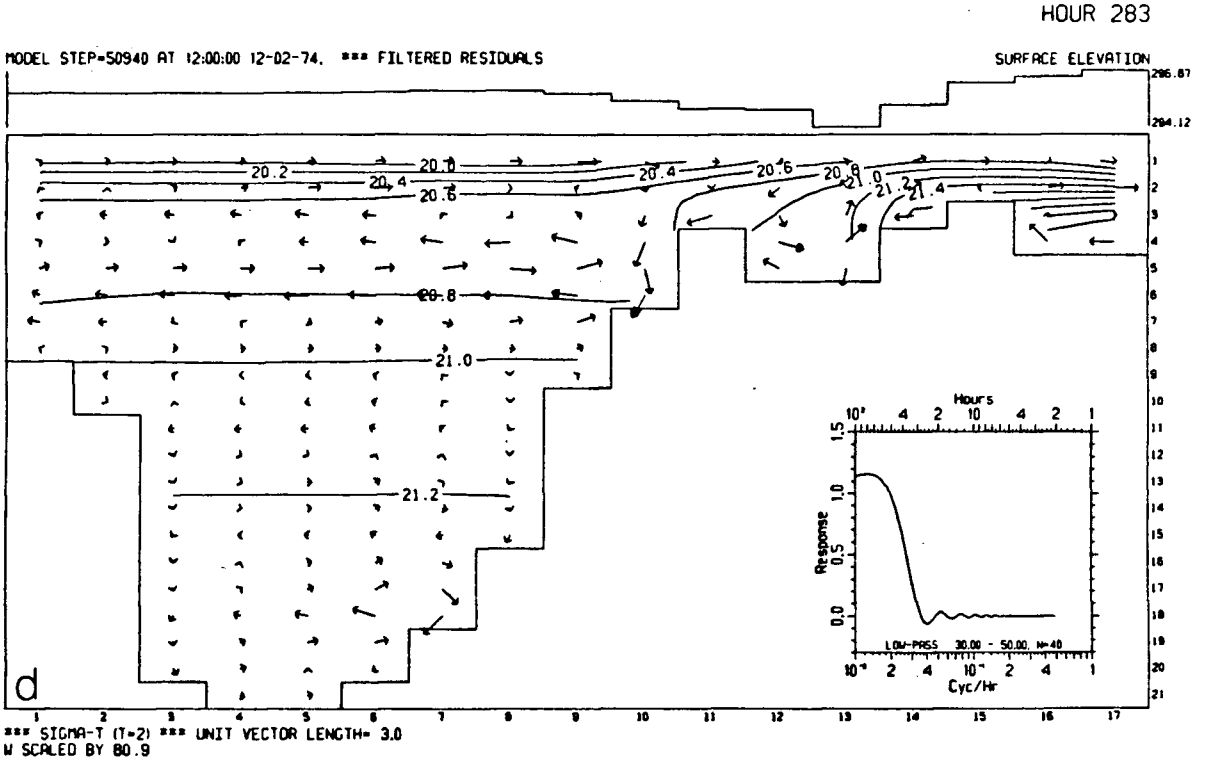

Figure 43(continued)

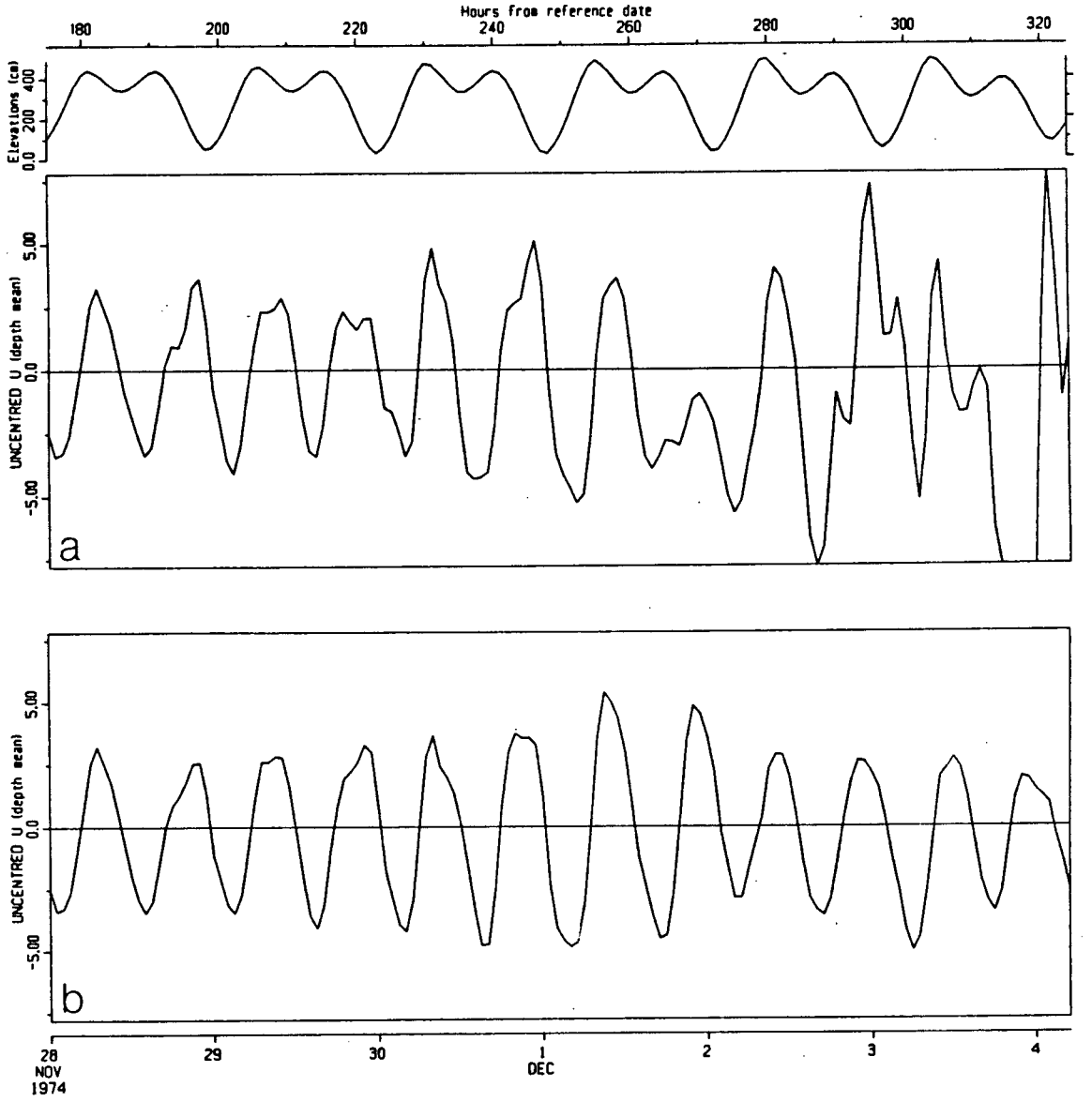

Figure 44. Vertical mean horizontal velocity at column 7 for Class 4 simulation of Indian Arm and Burrard Inlet using different values of $N^{(x)} = K^{(x)}$ (see figure 43 for legend).

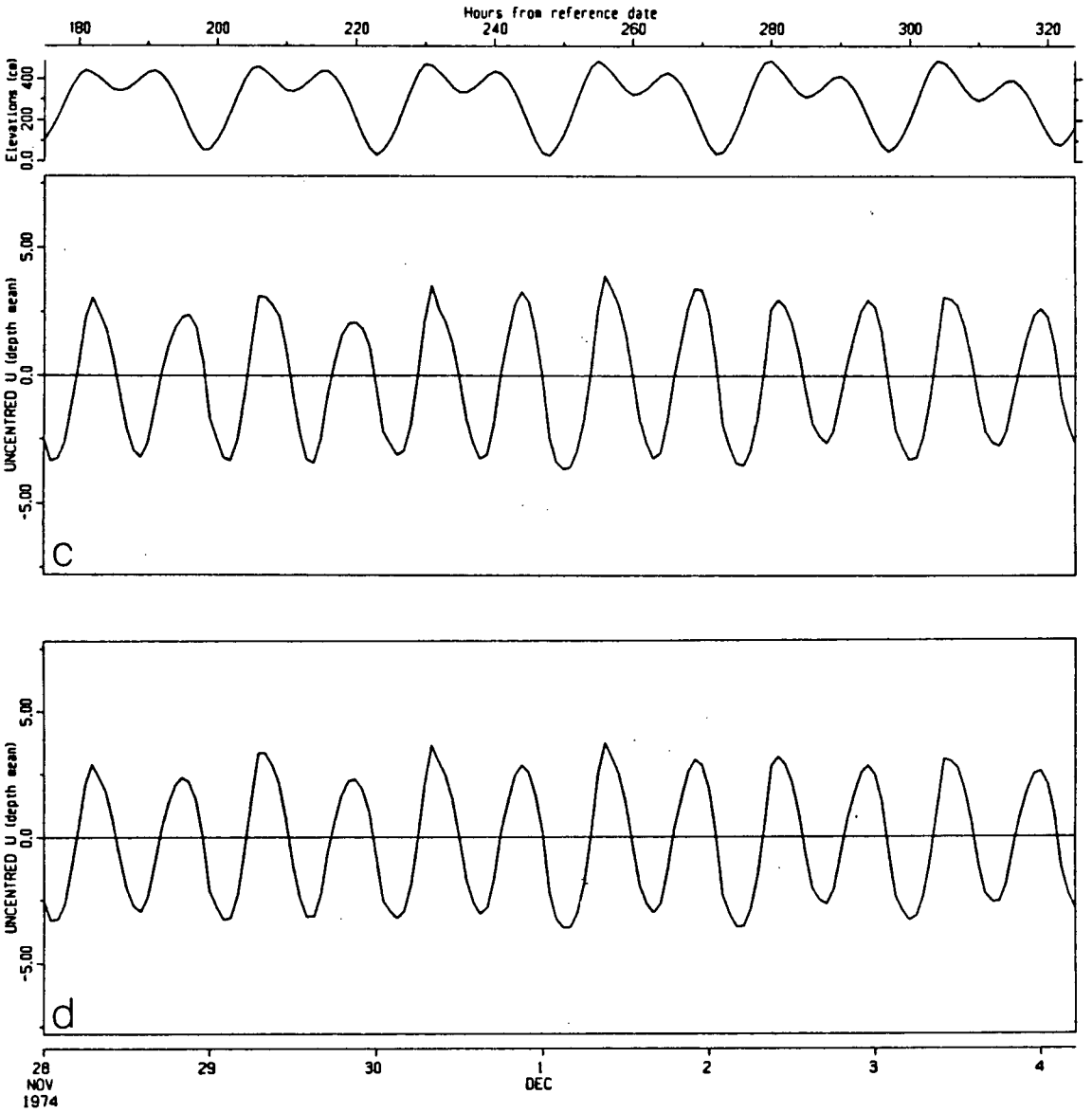

Figure 44(continued)

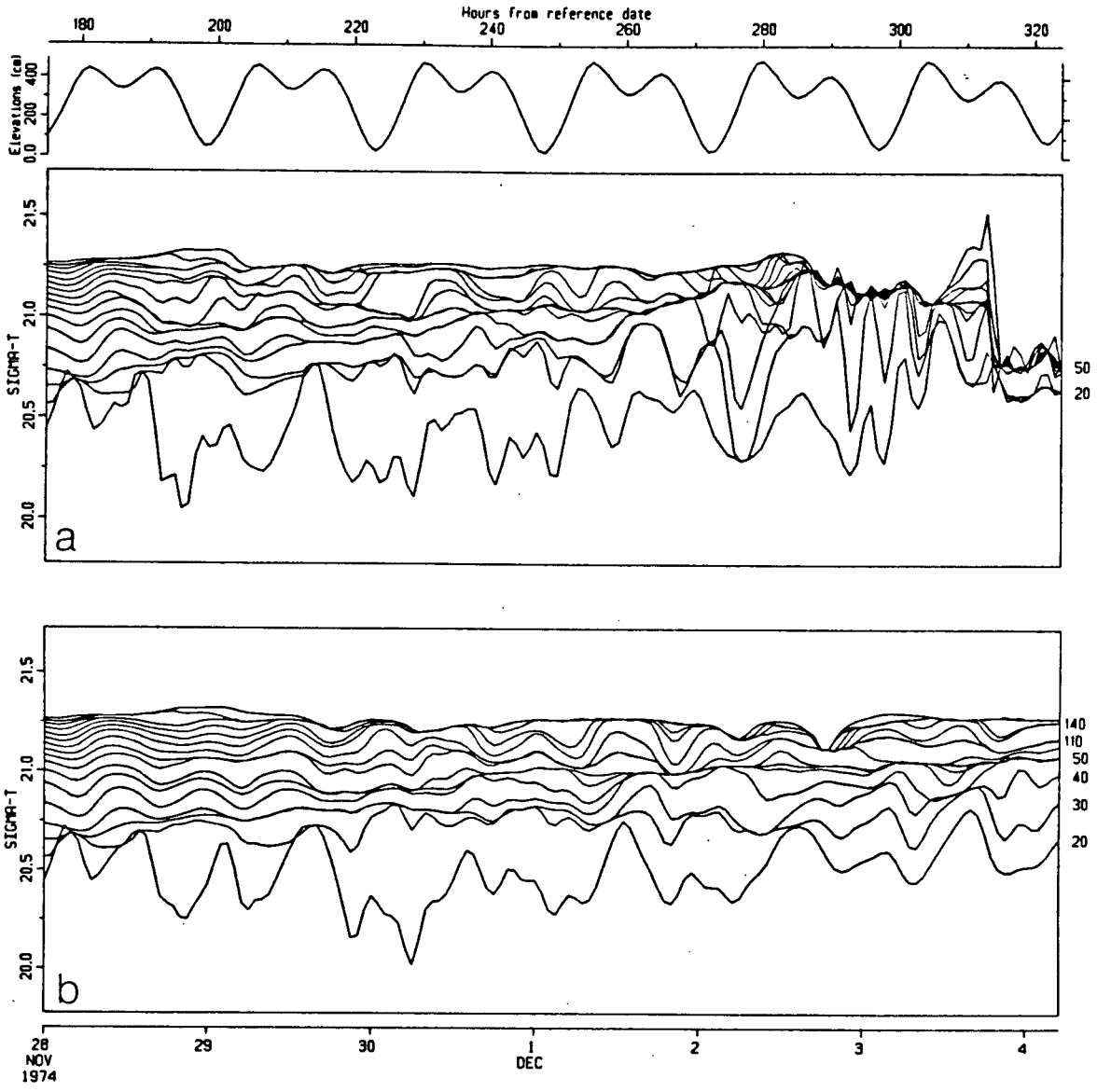

Figure 45. σ_t at column 7 for Class 4 simulation of Indian Arm and Burrard Inlet using different values of $N^{(x)} = K^{(x)}$ (see figure 43 for legend).

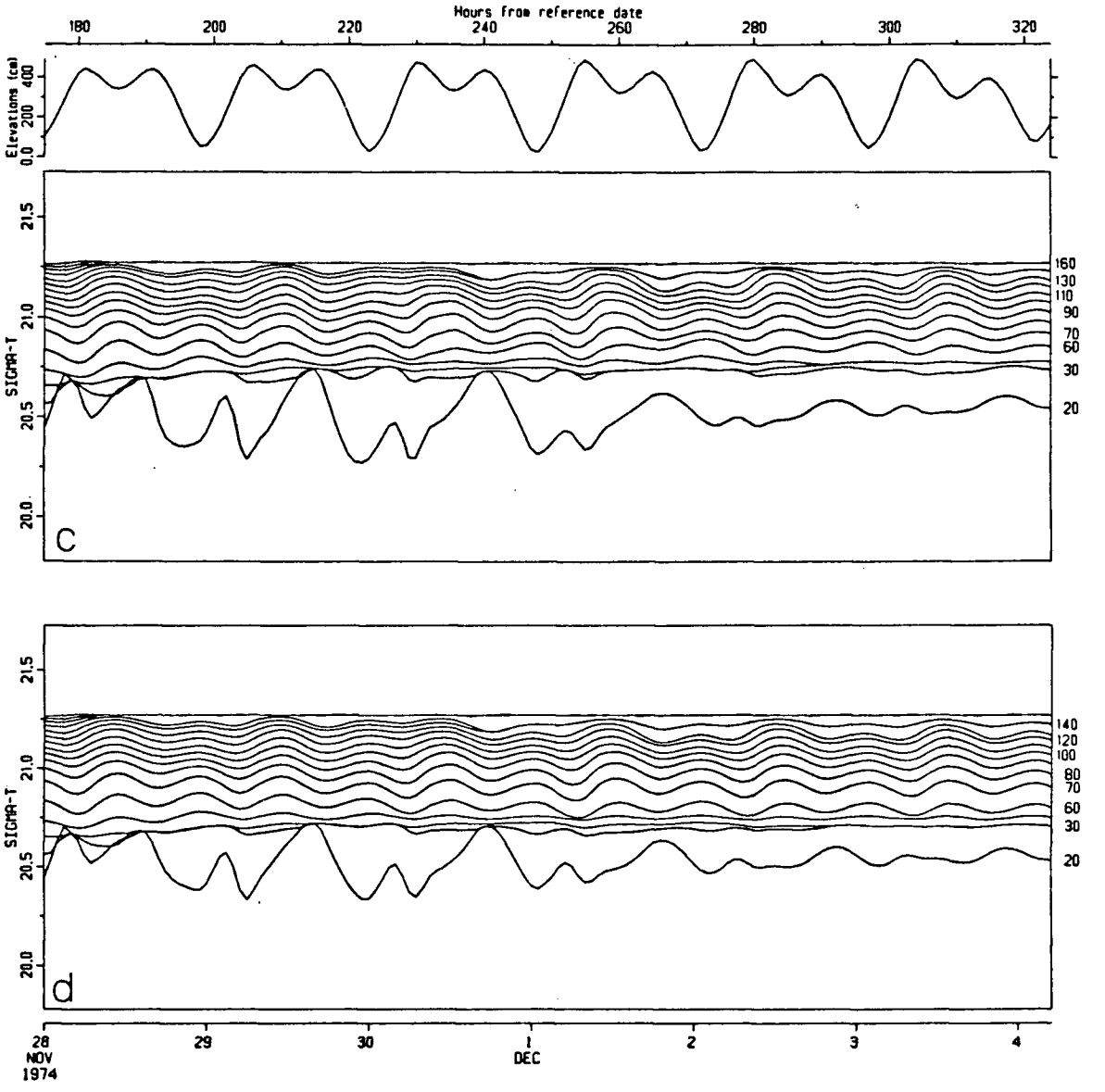

Figure 45(continued)

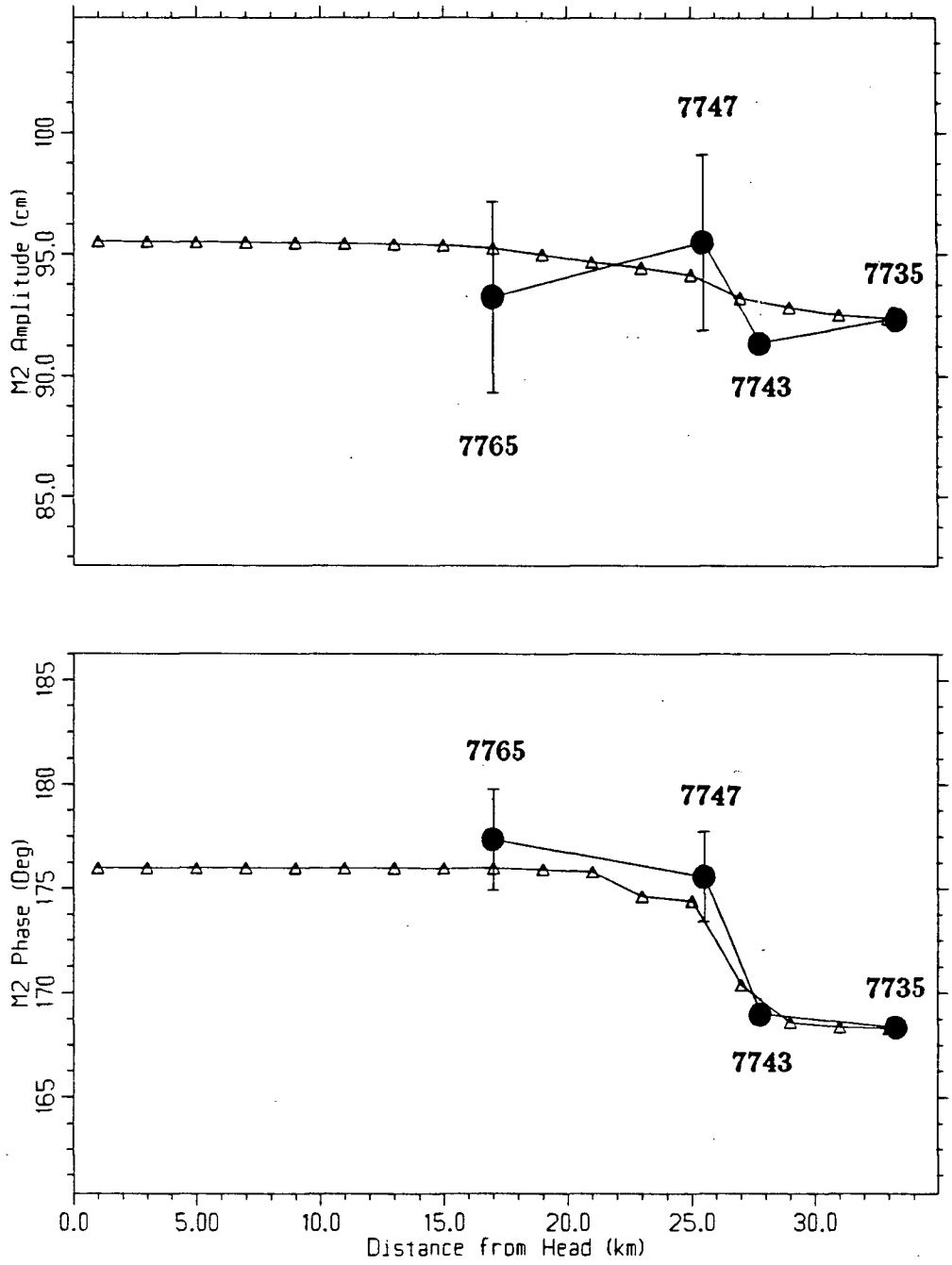

Figure 46. M_2 surface elevation amplitudes and phases for tide gauge data (circles) and model (triangles). Error bars are 90% confidence intervals. The error bar for station 7743 is missing due to lack of data, and for 7735 because this is the open boundary of the model (exact fit required).

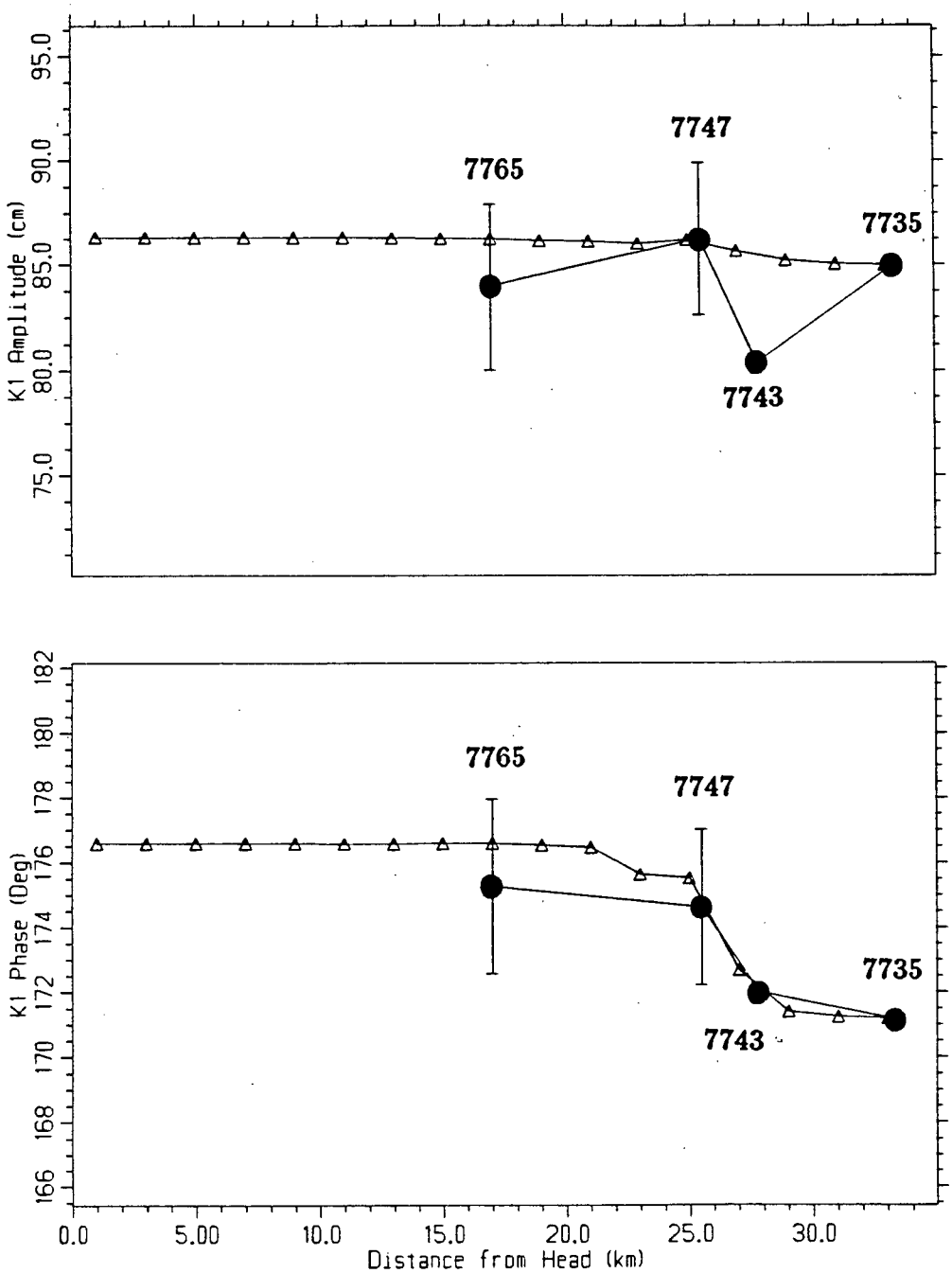

Figure 47. K_1 surface elevation amplitudes and phases for tide gauge data (circles) and model (triangles). Error bars are 90% confidence intervals. The error bar for station 7743 is missing due to lack of data, and for 7735 because this is the open boundary of the model (exact fit required).

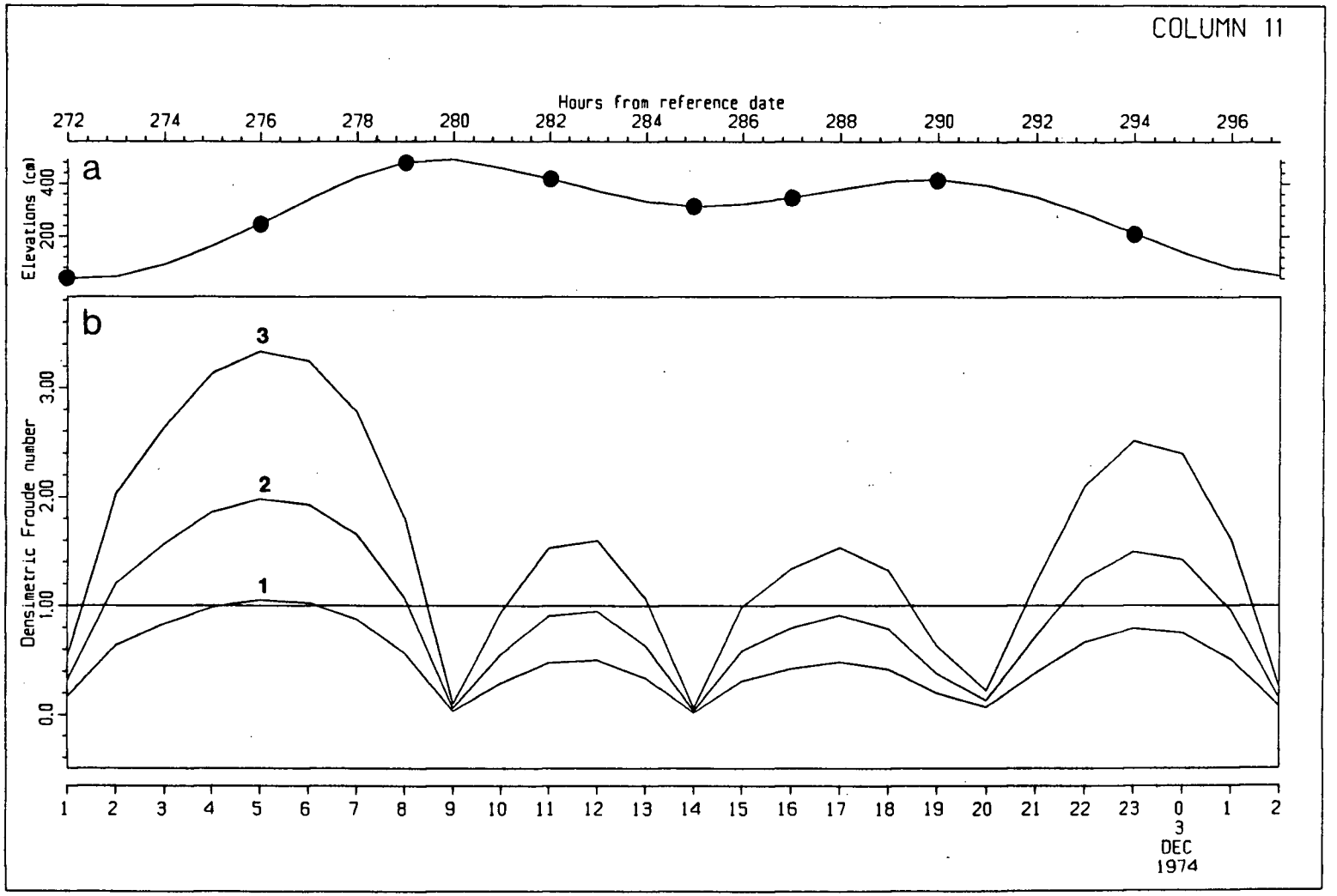

Figure 48. Time series for Class 4 simulation over a diurnal cycle at the inner sill. Plot (a): surface elevation. Times of plots (*figures* 49–50) are marked with solid circles. Plot (b): densimetric Froude number ($F_i = |\bar{U}|/c_i$) for the first three baroclinic modes, where $|\bar{U}|$ is the depth mean horizontal current velocity, and c_i is the phase speed for the i^{th} baroclinic mode.

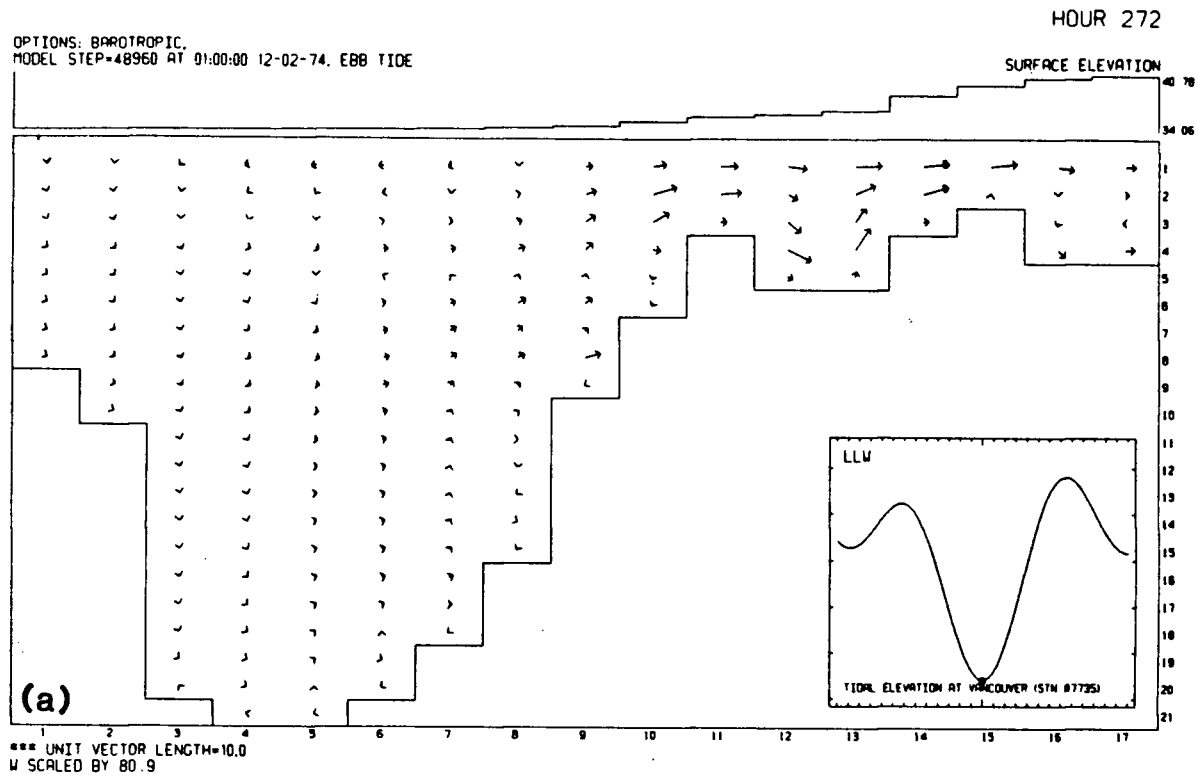

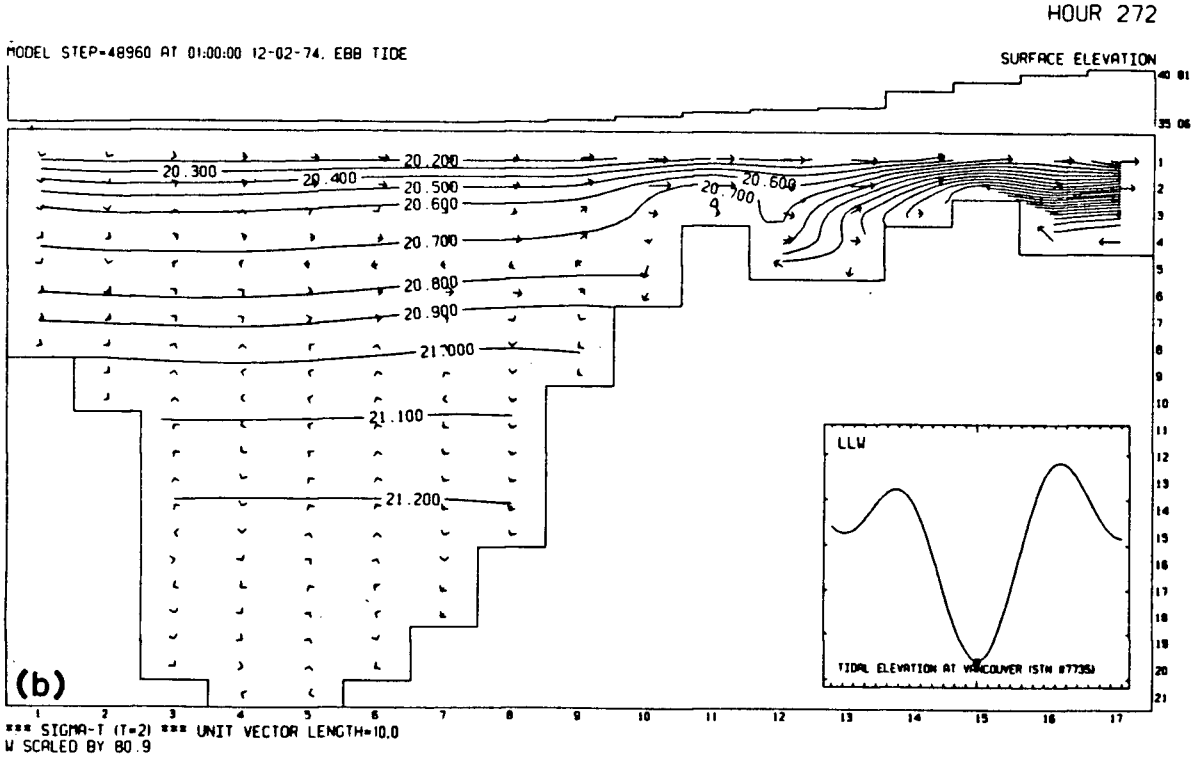

Figure 49. Fields of surface elevations, current vectors and isopycnals for Class 4 simulation of Indian Arm and Burrard Inlet over a diurnal cycle. Vertical exaggeration is 80.9. Elevations are in *cm*. Unit vector length is 10 $cm\,s^{-1}$. Contours are in σ_t units. Inset shows position in tidal cycle. Plot (a): unstratified run. Plot (b): stratified run.

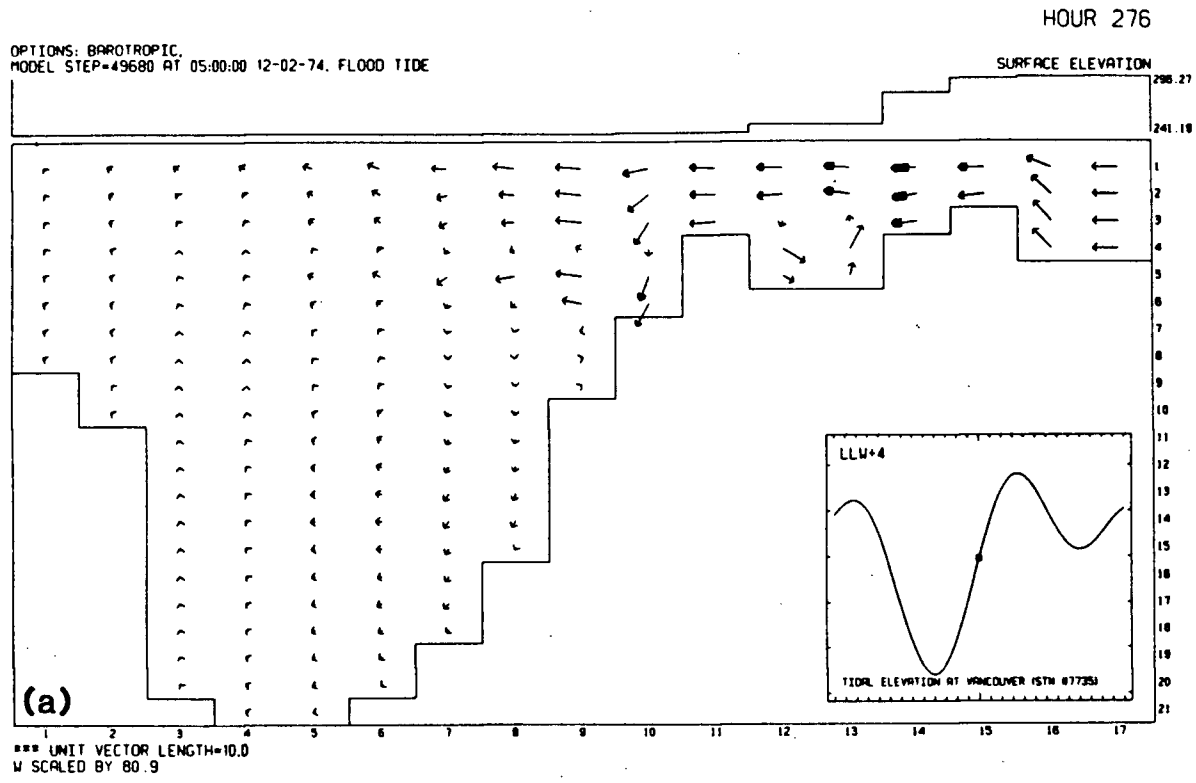

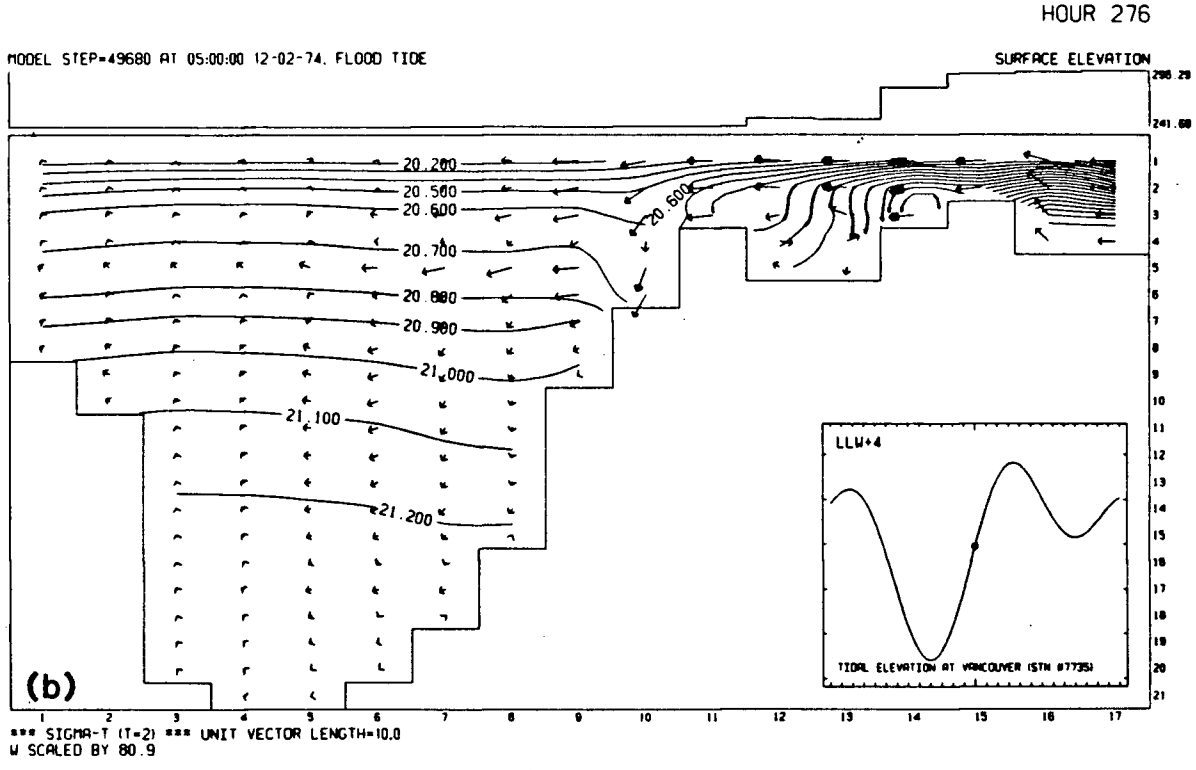

Figure 49(continued)

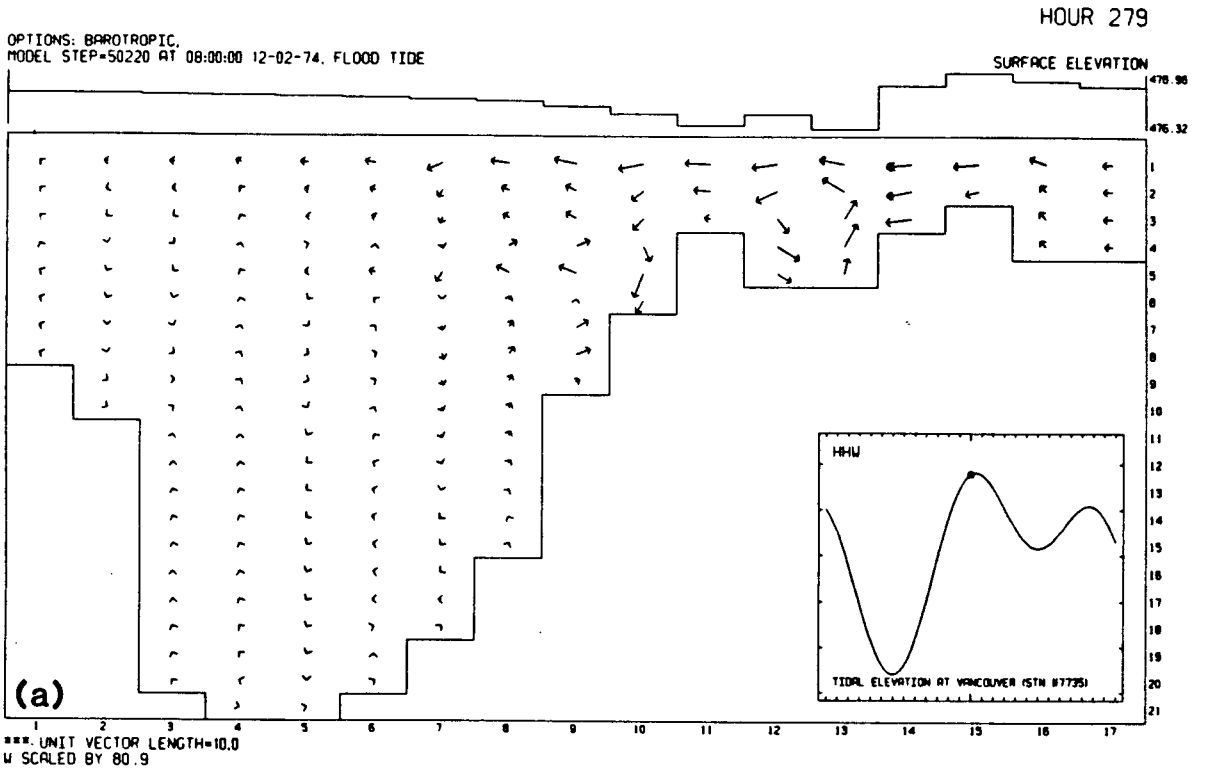

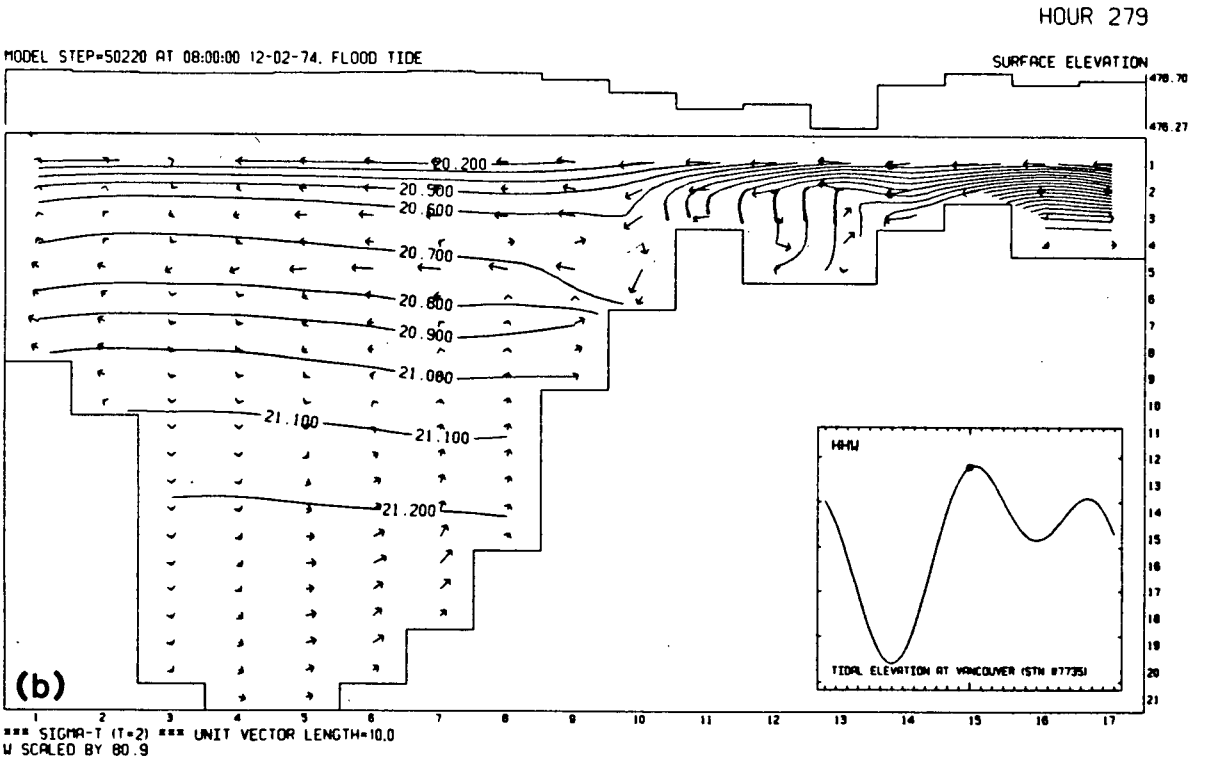

Figure 49(continued)

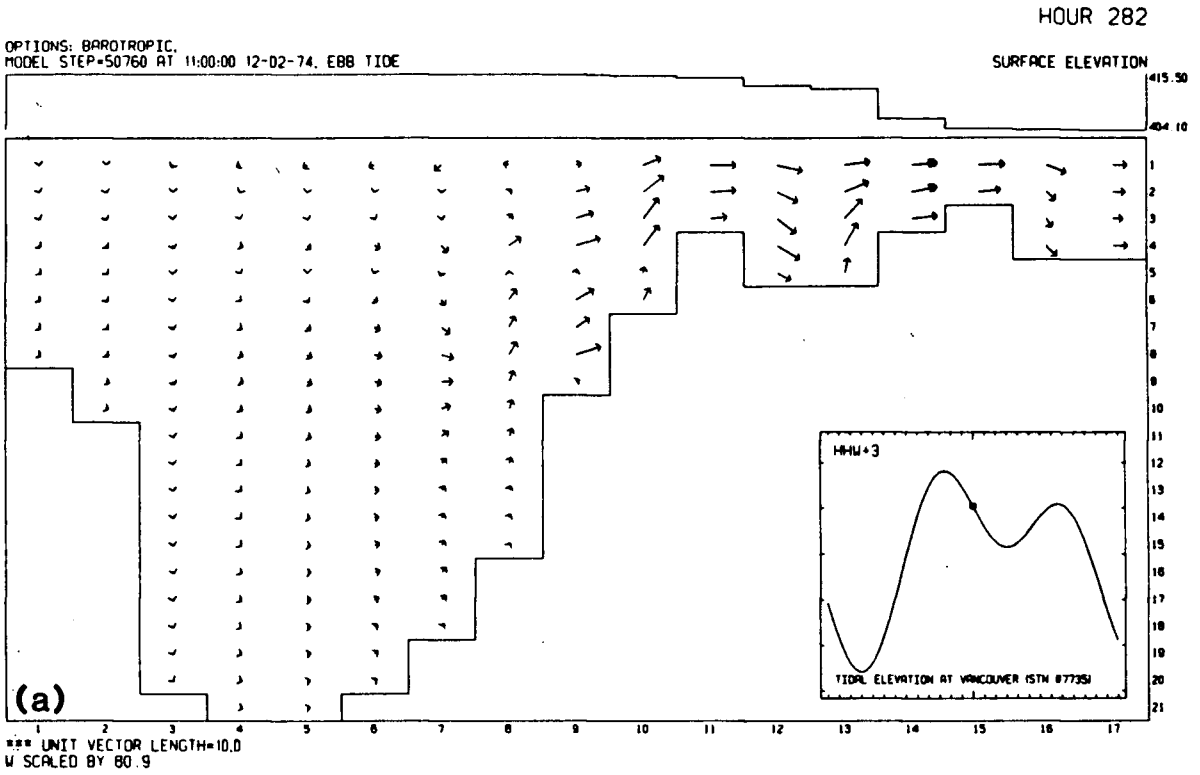

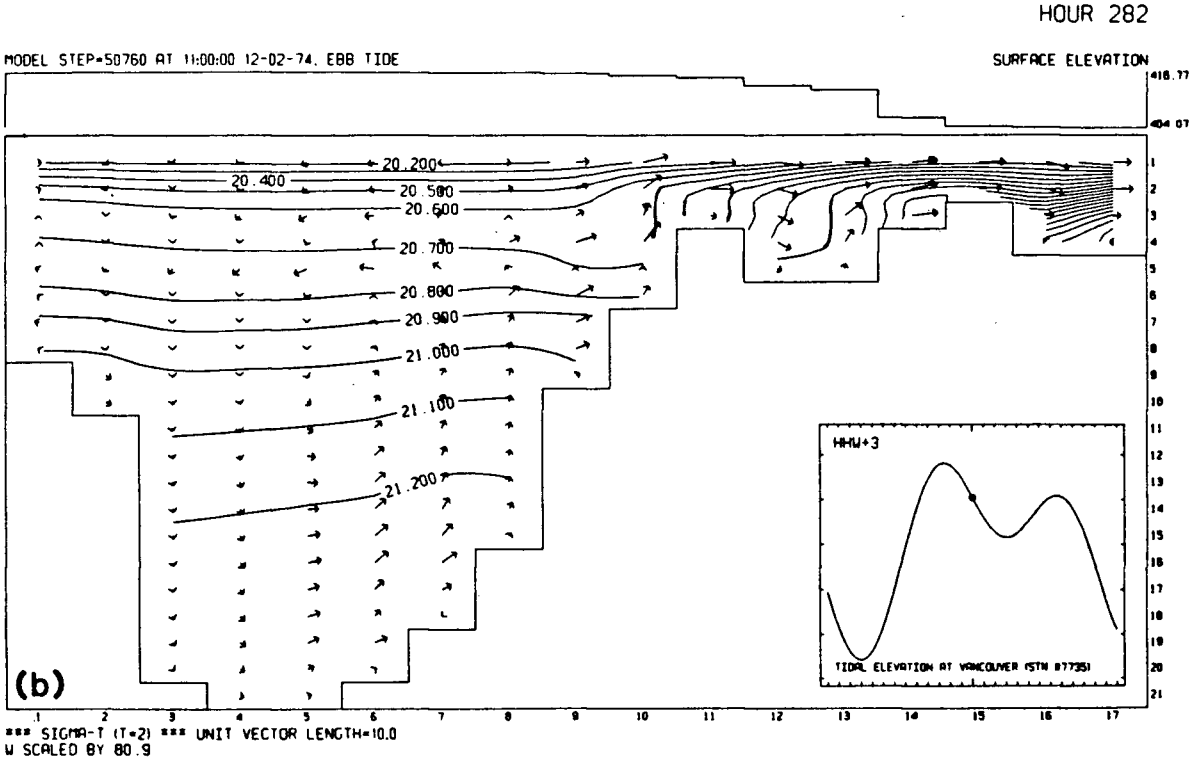

Figure 49(continued)

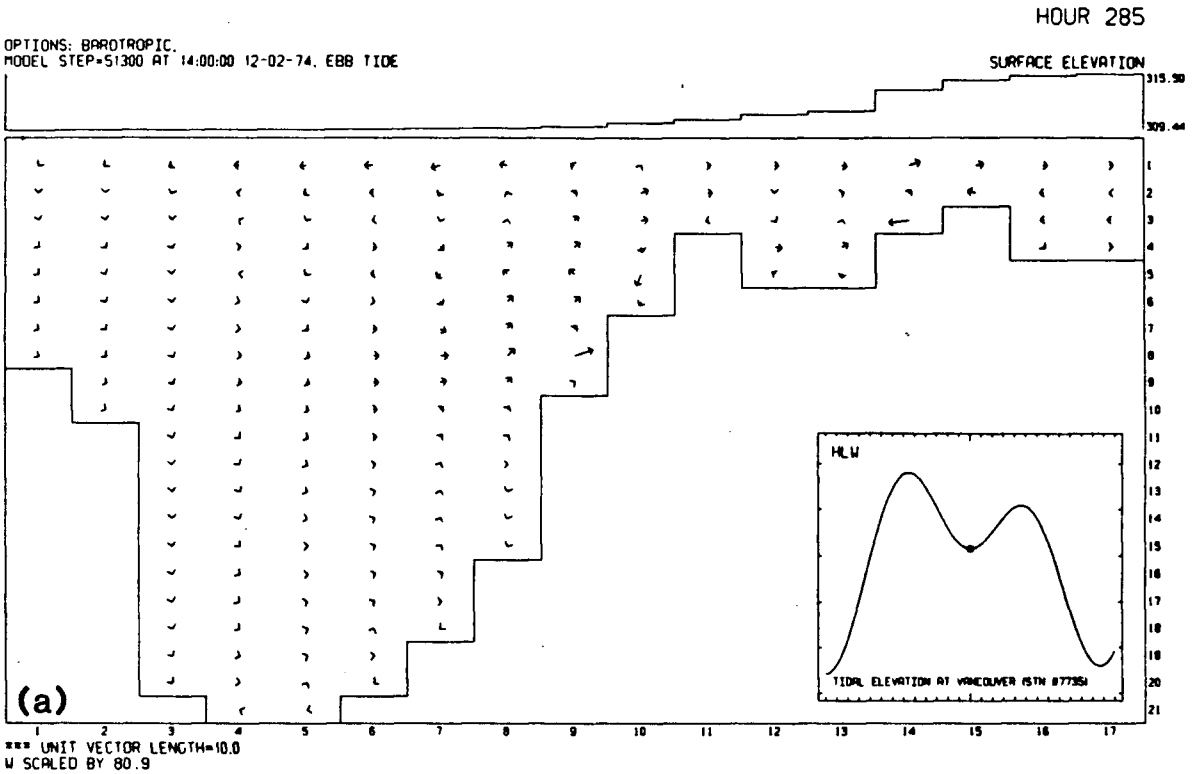

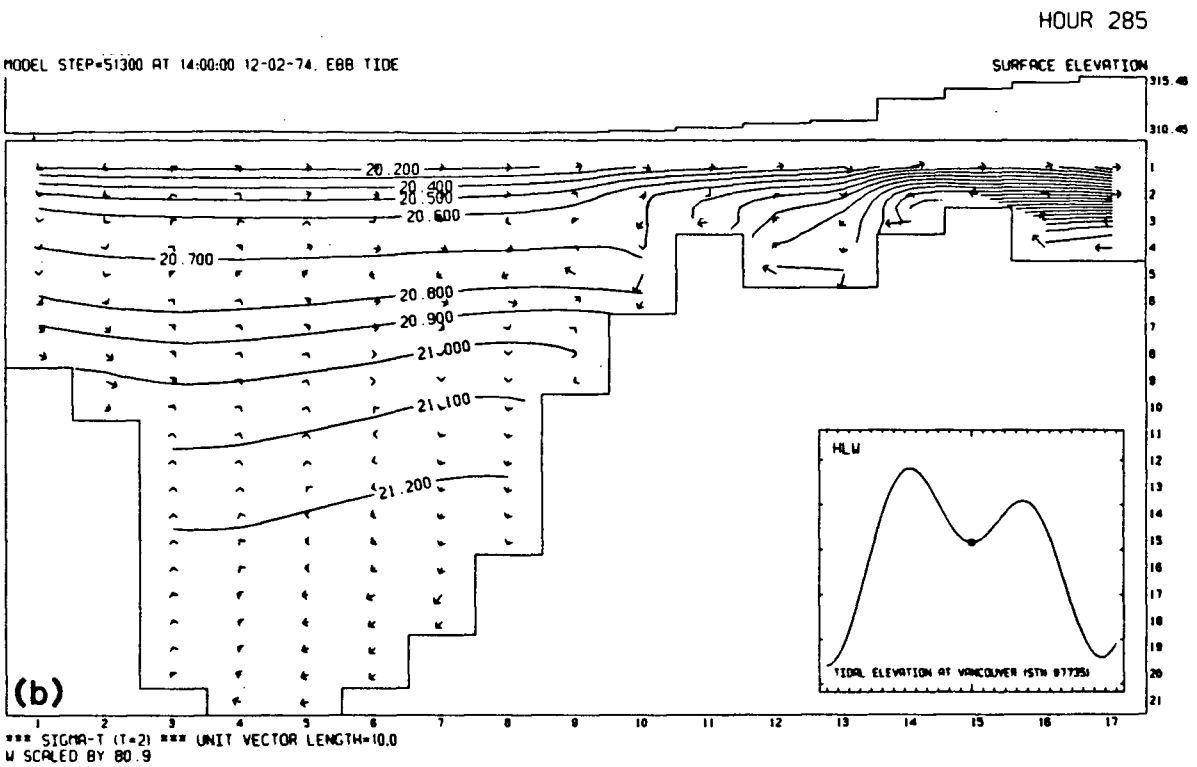

Figure 49(continued)

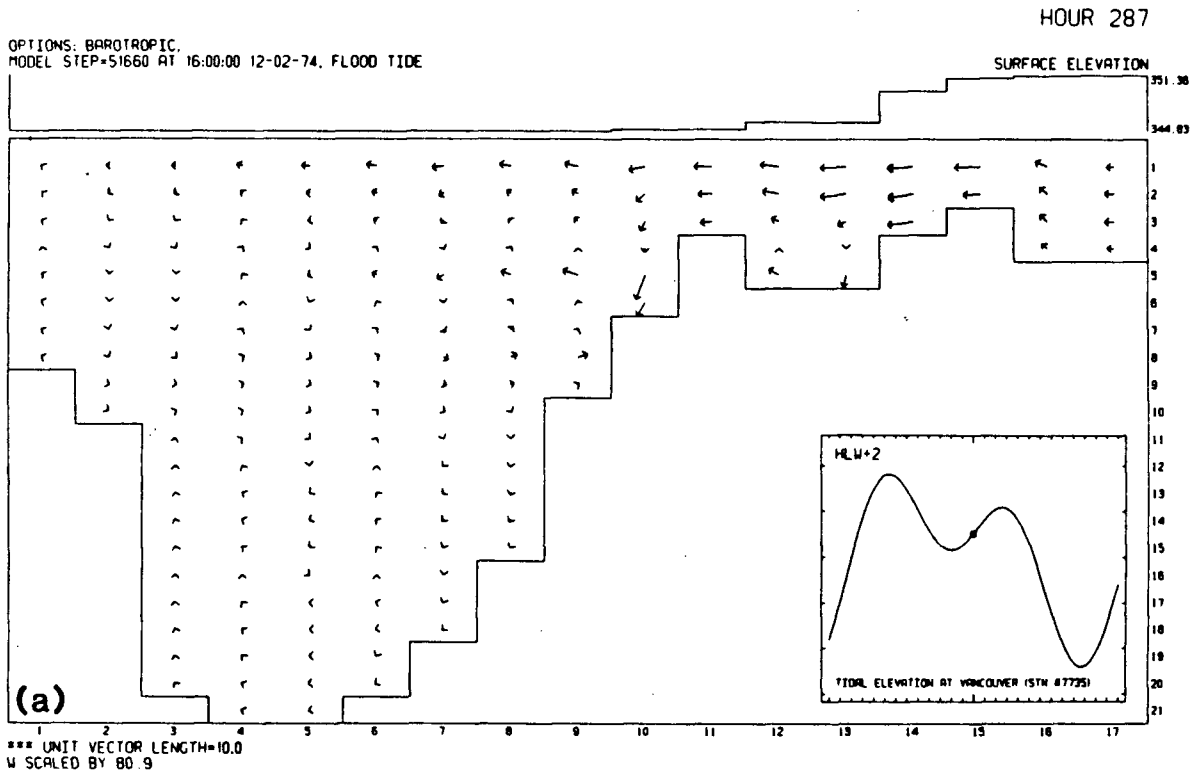

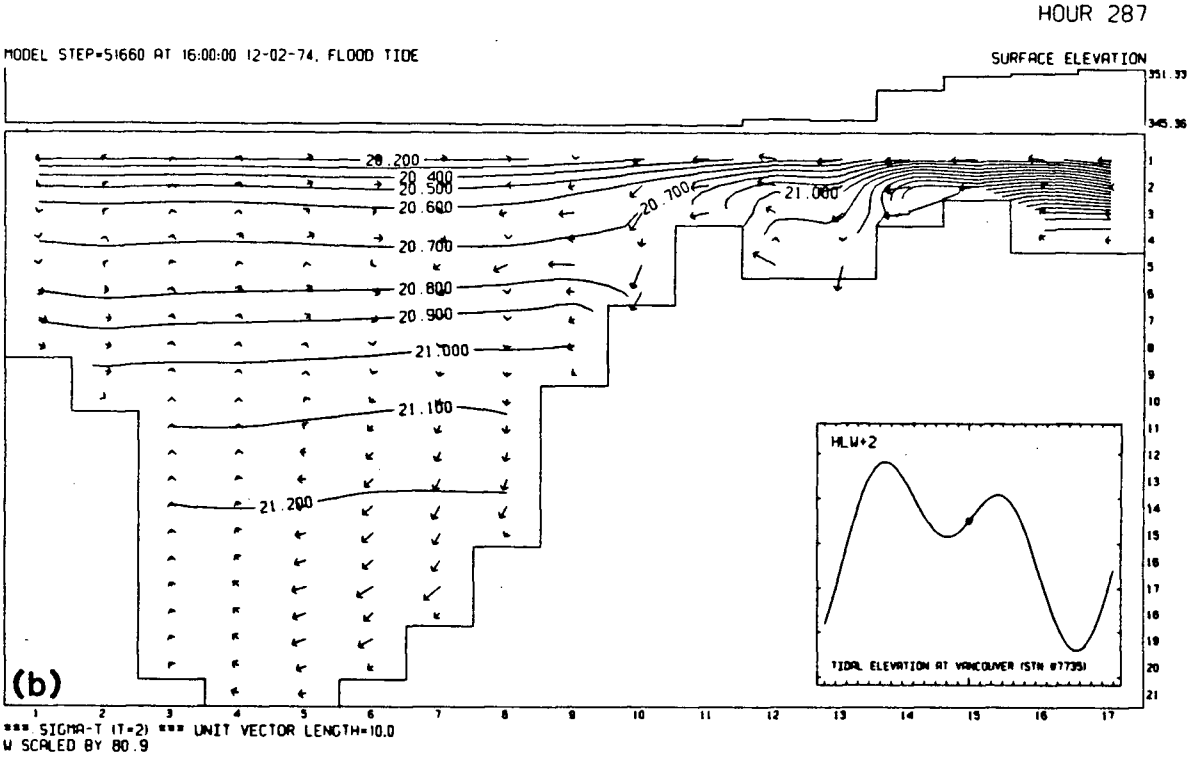

Figure 49(continued)

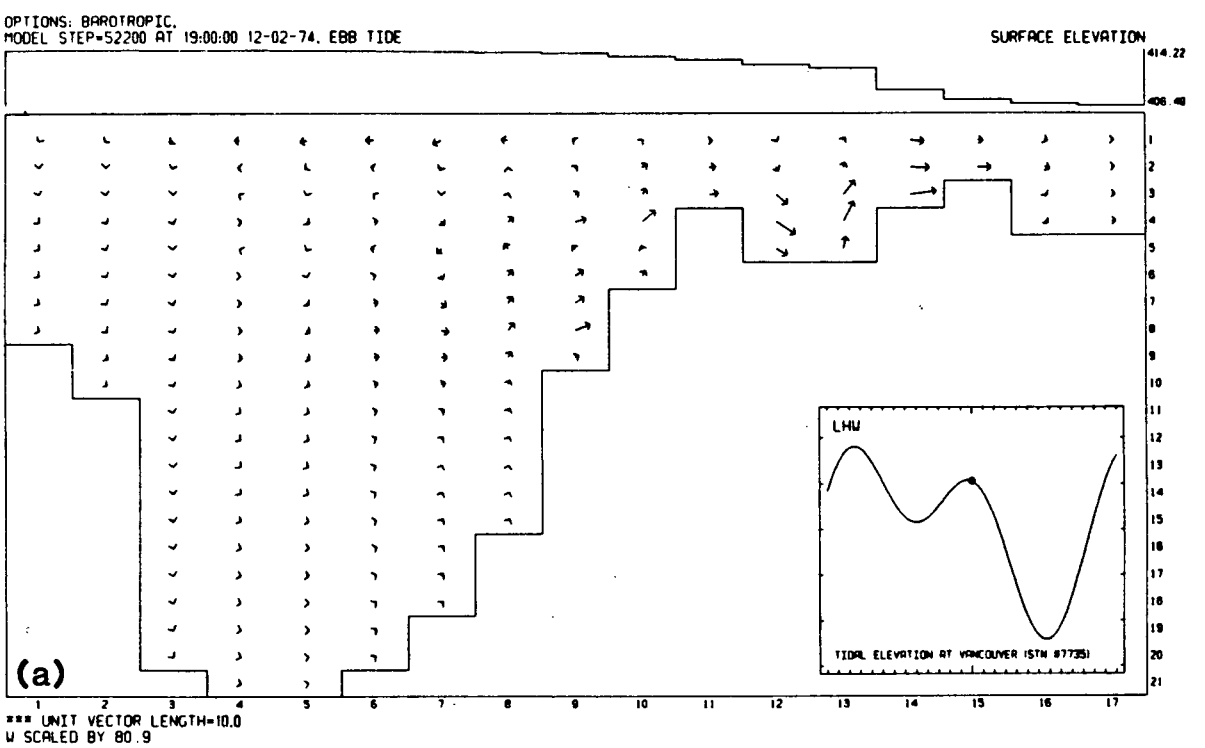

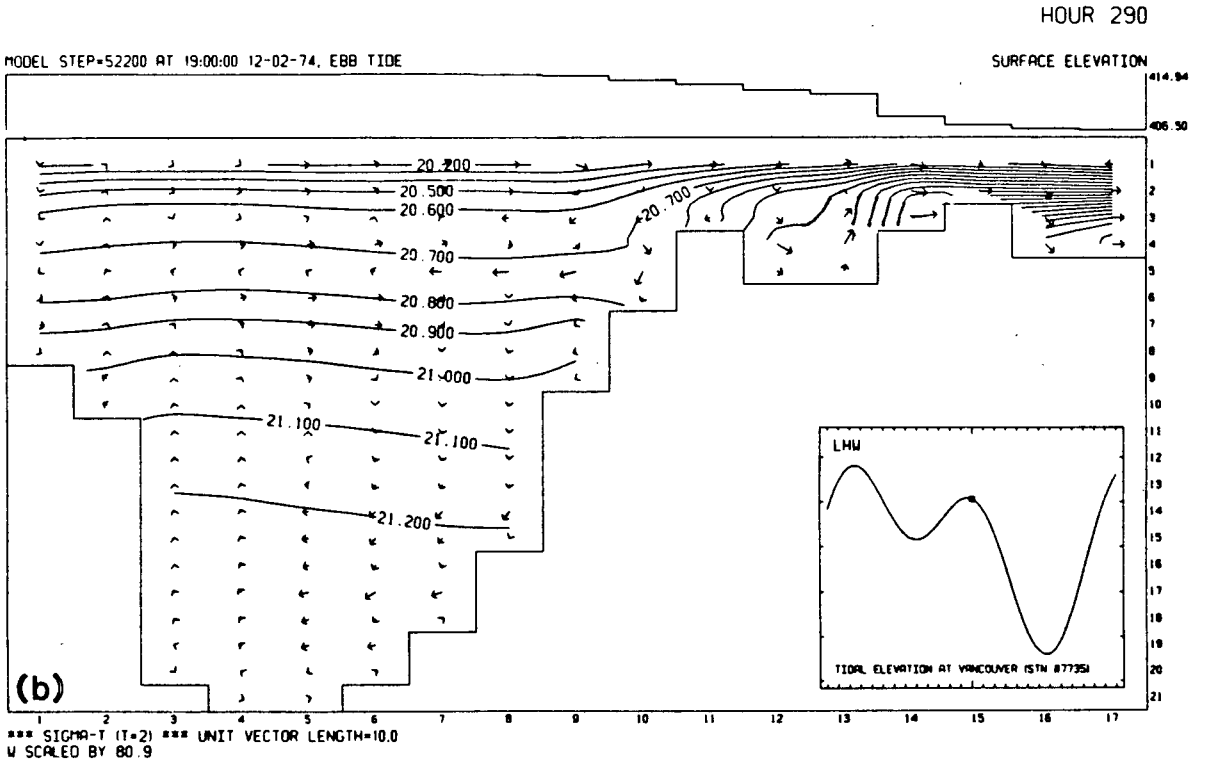

Figure 49(continued)

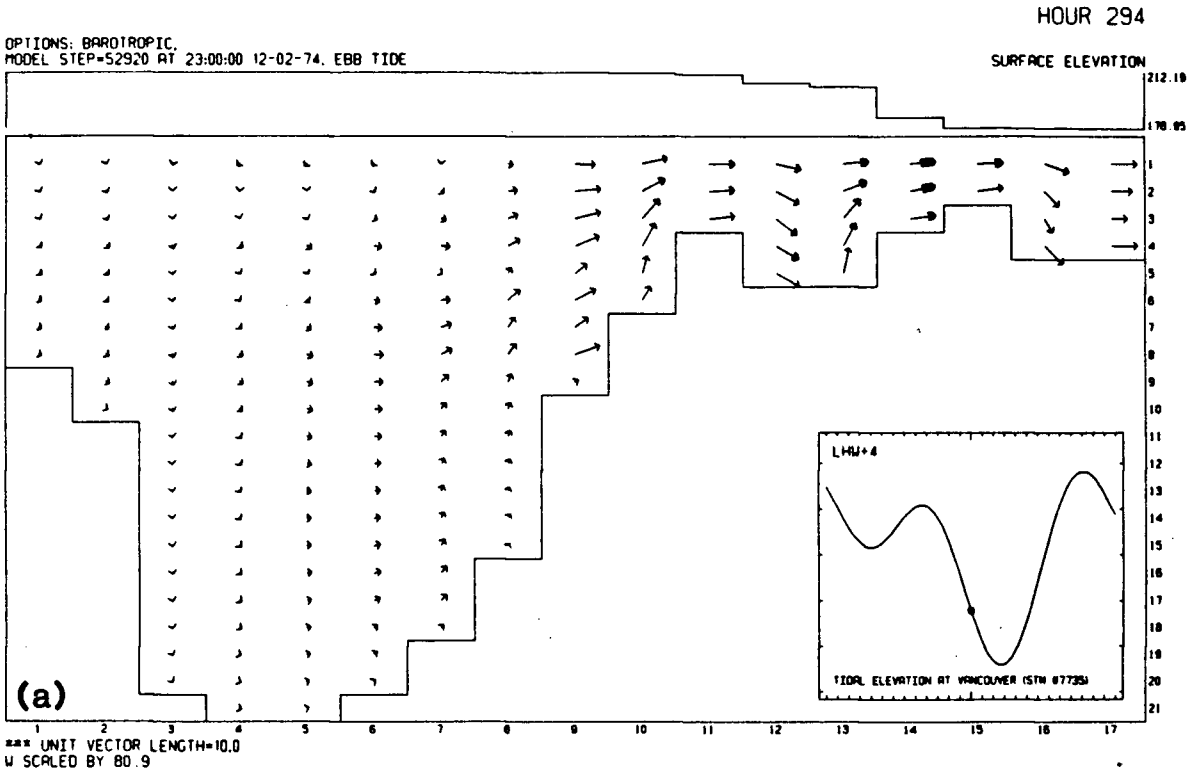

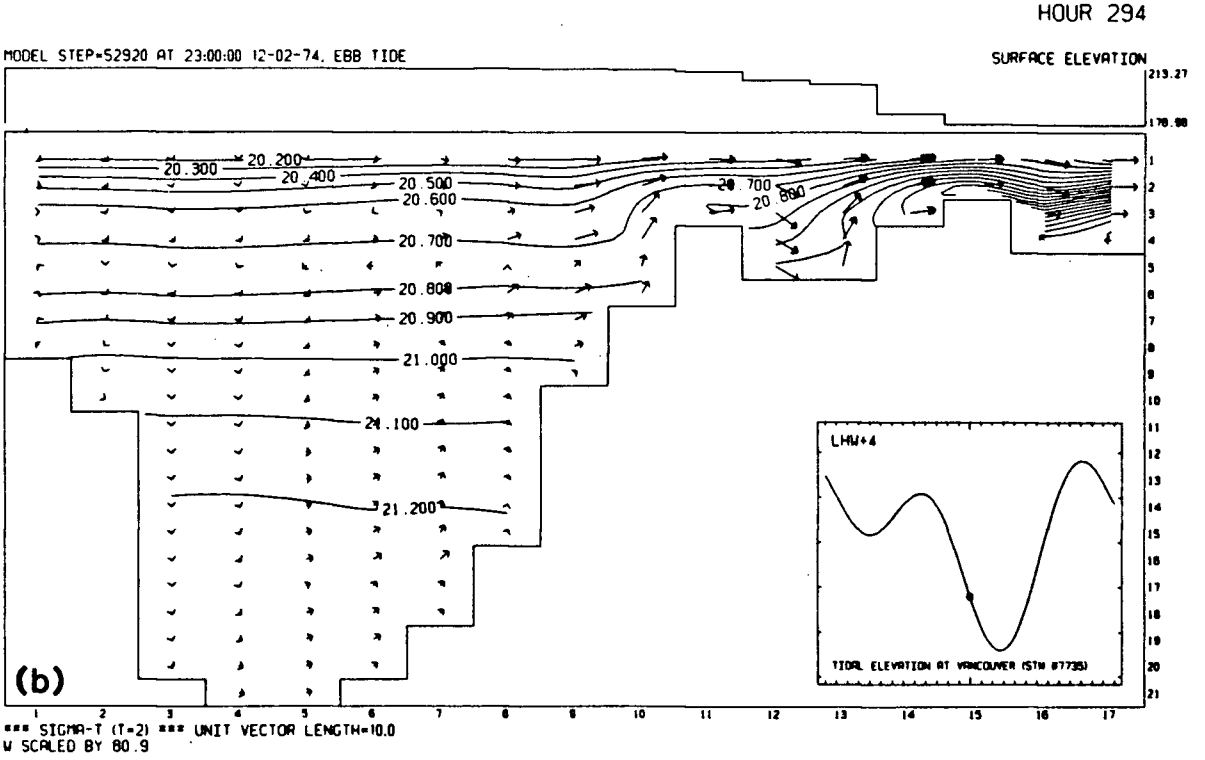

Figure 49(continued)

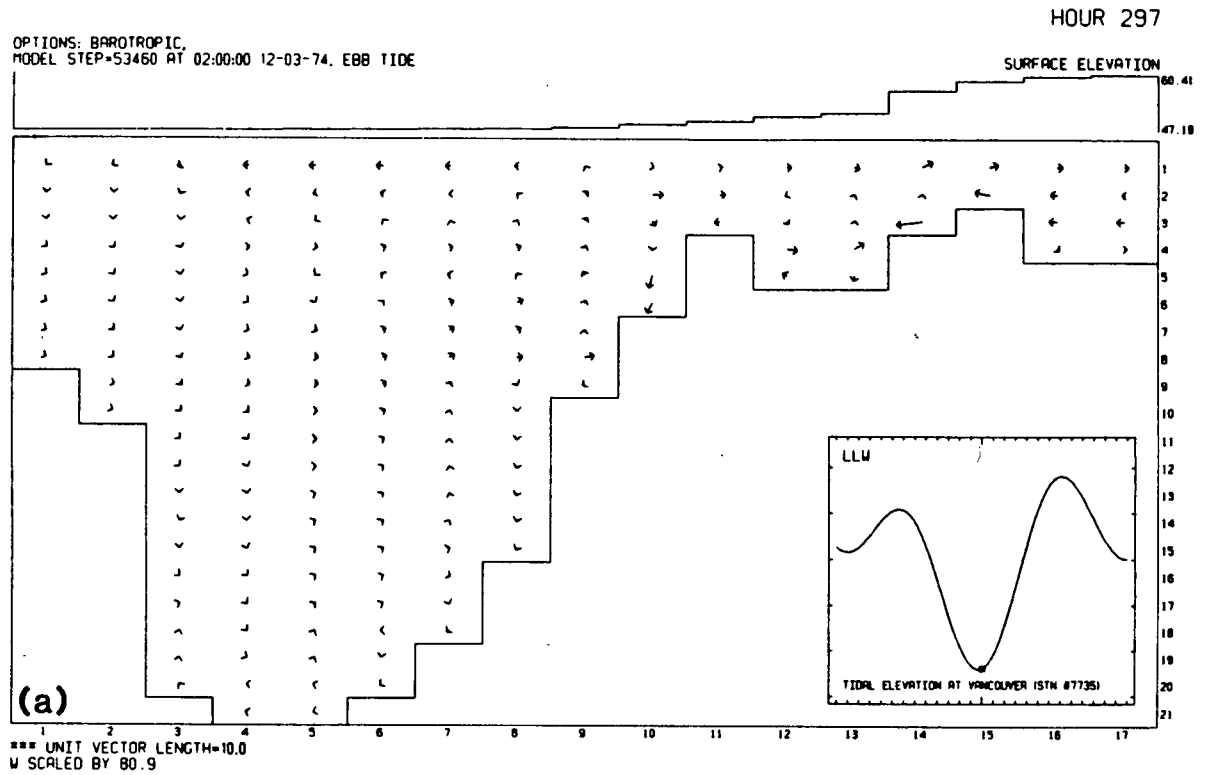

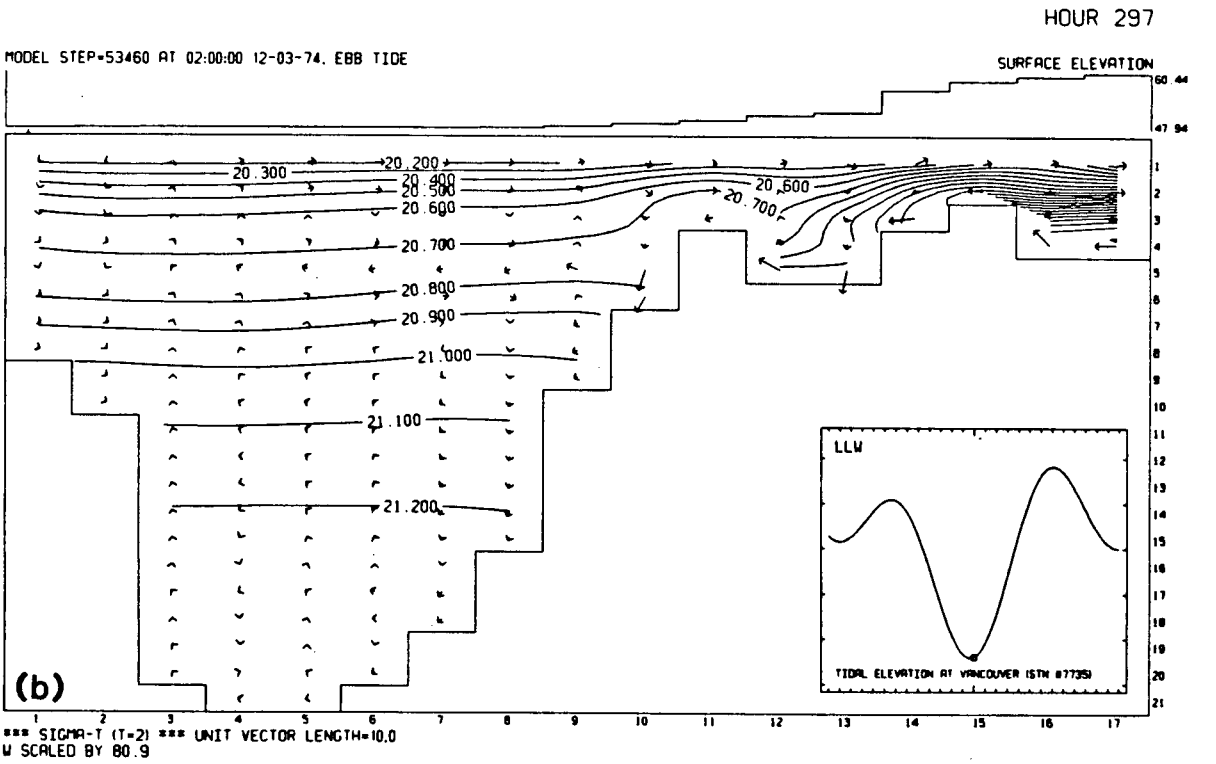

Figure 49(continued)

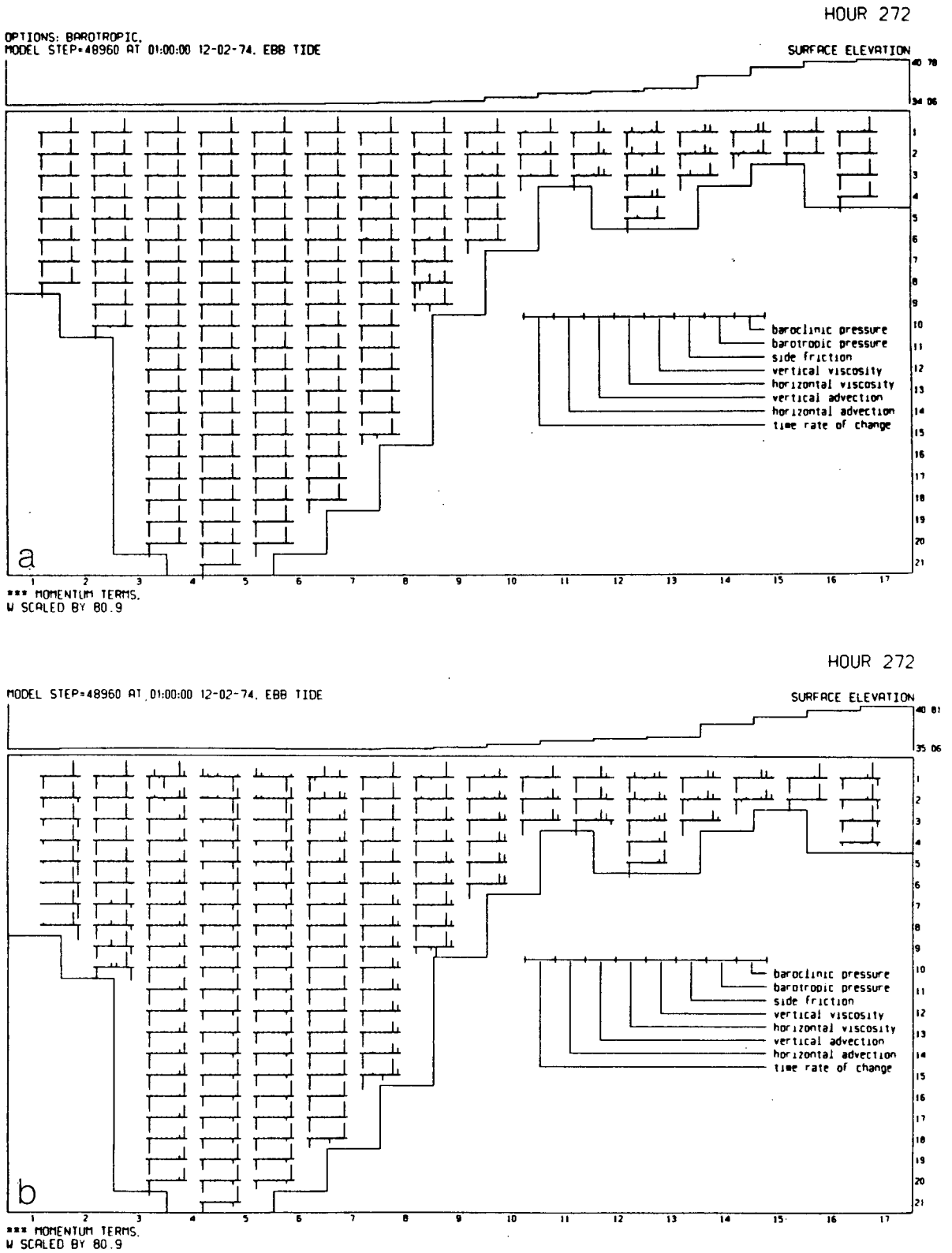

Figure 50. Fields of surface elevations and momentum balance terms for Class 4 simulation of Indian Arm and Burrard Inlet over a diurnal cycle. Vertical exaggeration is 80.9. Elevations are in *cm*. Bar graphs are separately scaled for each location in the grid. Inset identifies the position of each momentum balance term. Plot (a): unstratified run. Plot (b): stratified run. (see *figure* 49 for tidal phase).

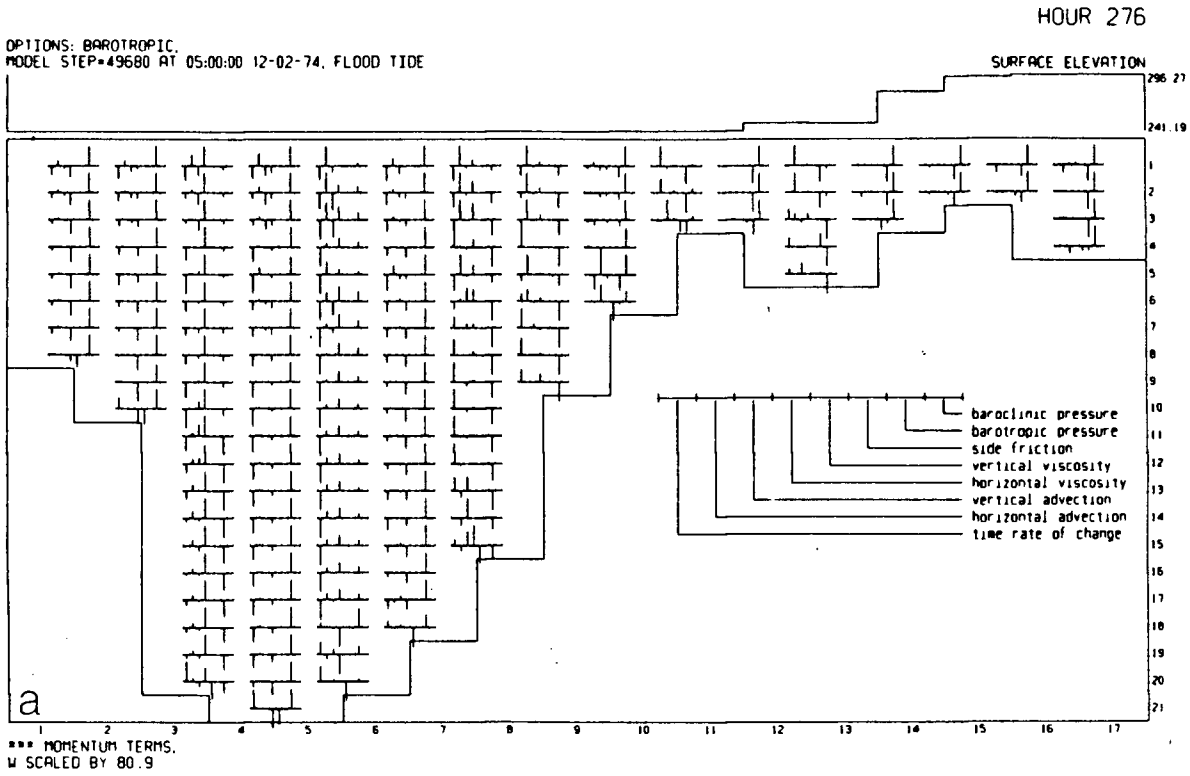

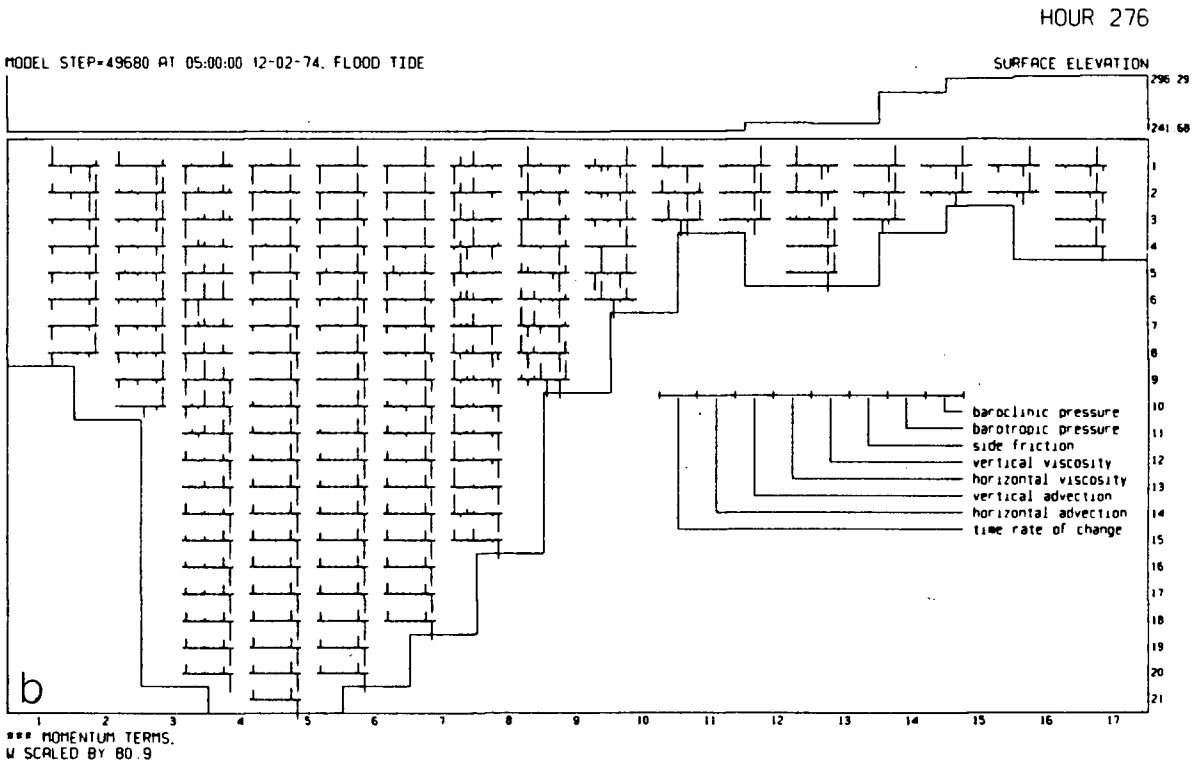

Figure 50(continued)

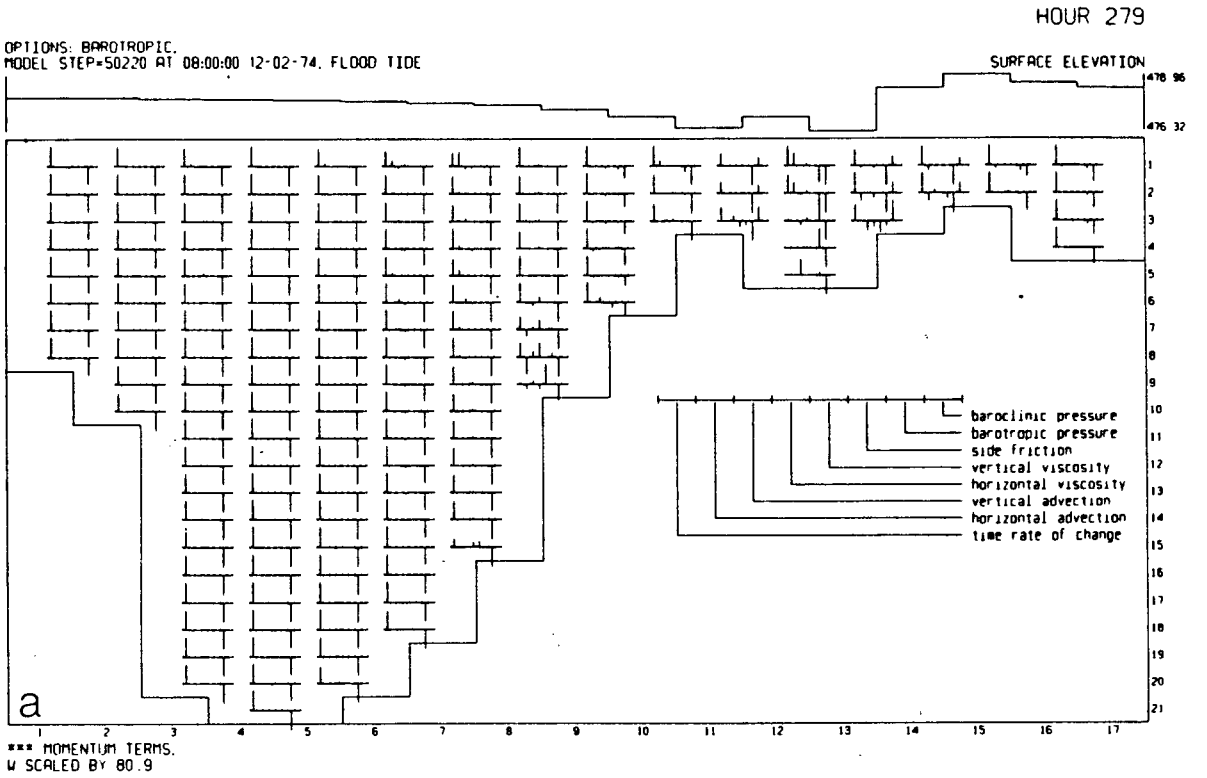

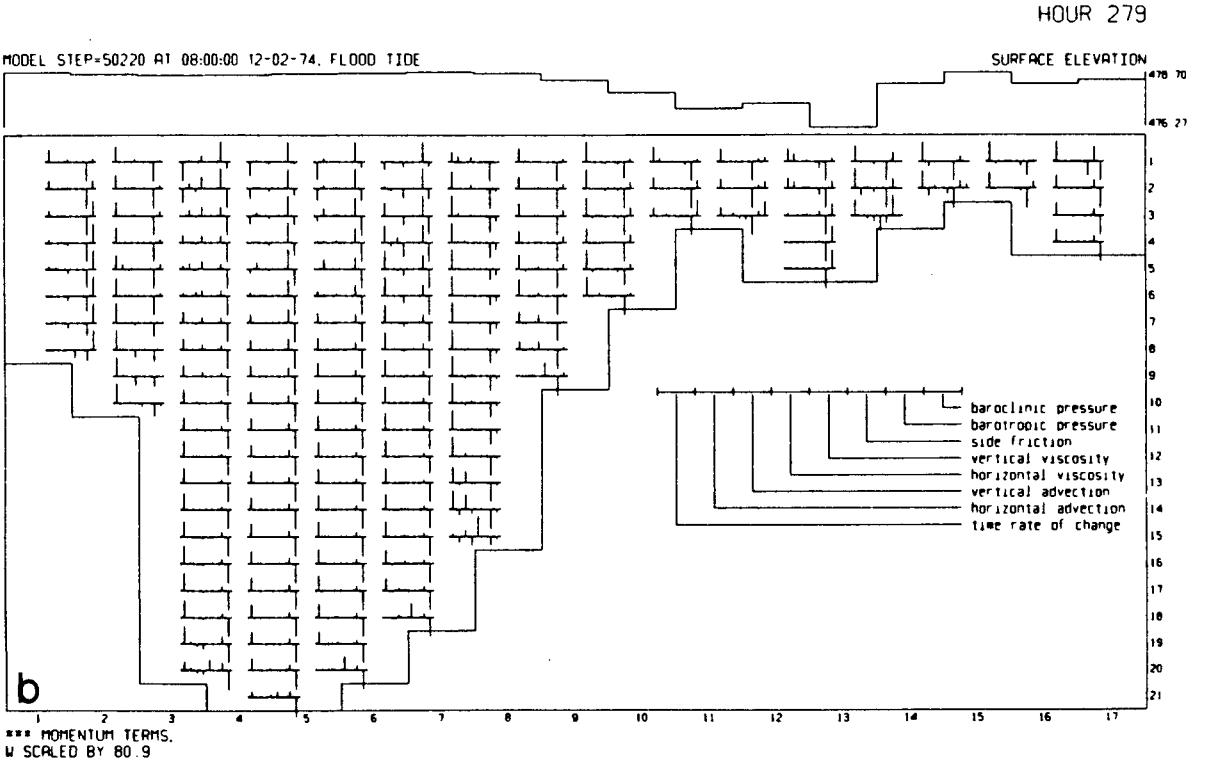

Figure 50(continued)

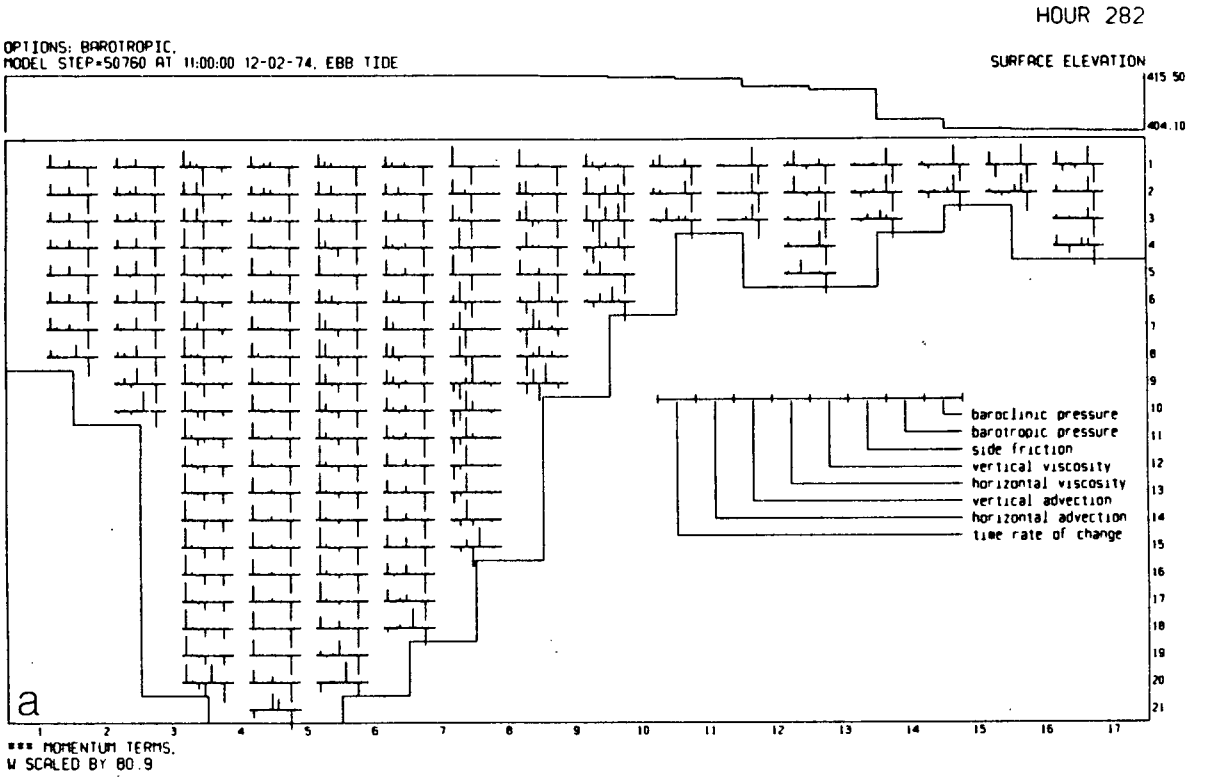

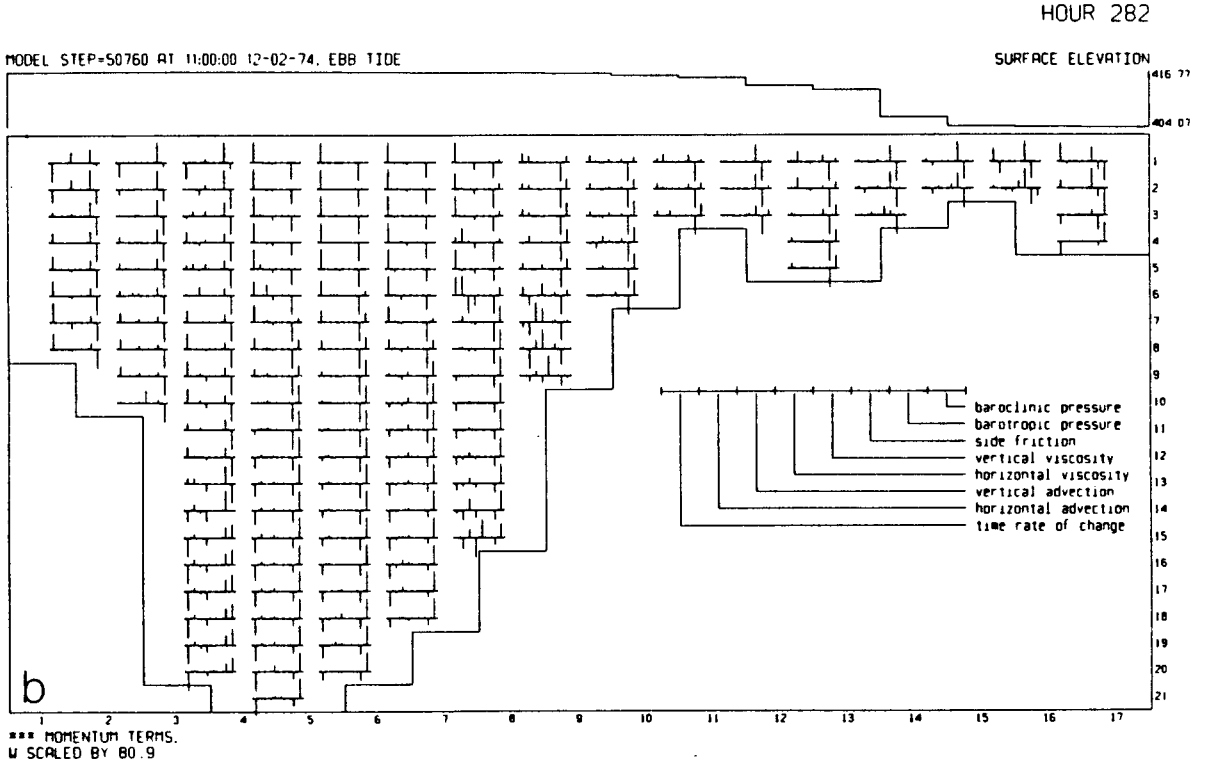

Figure 50(continued)

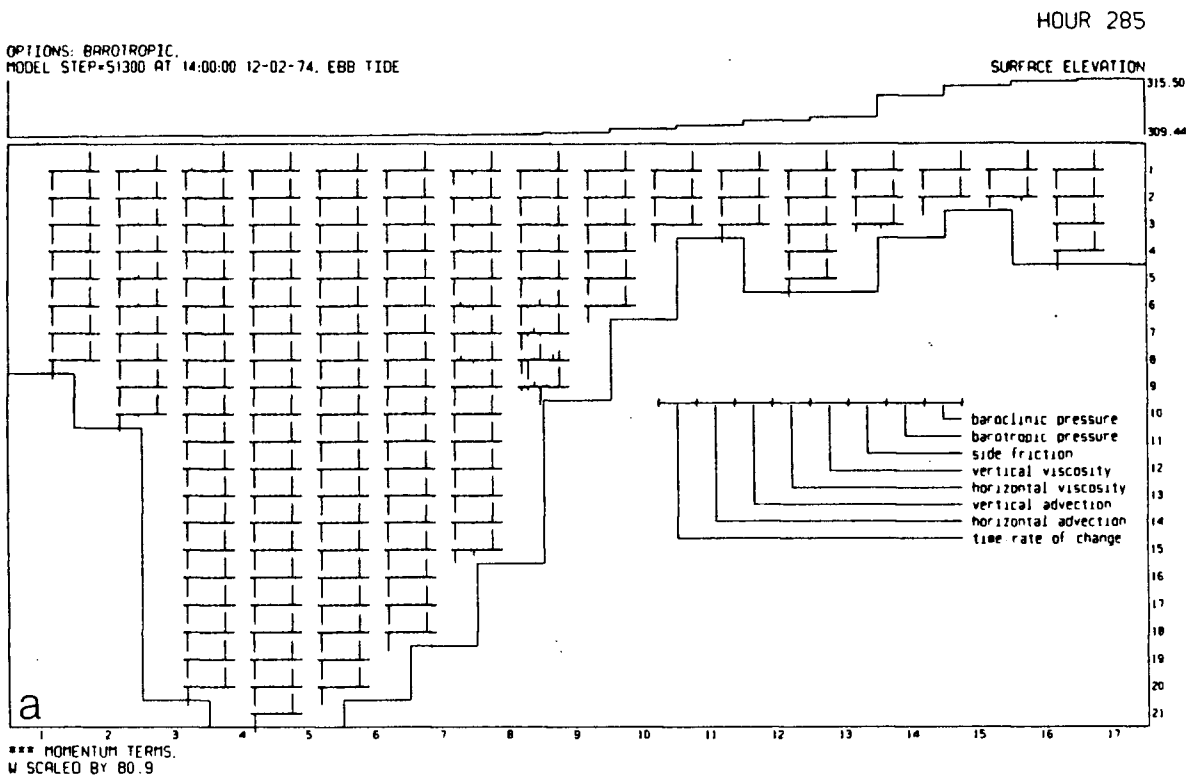

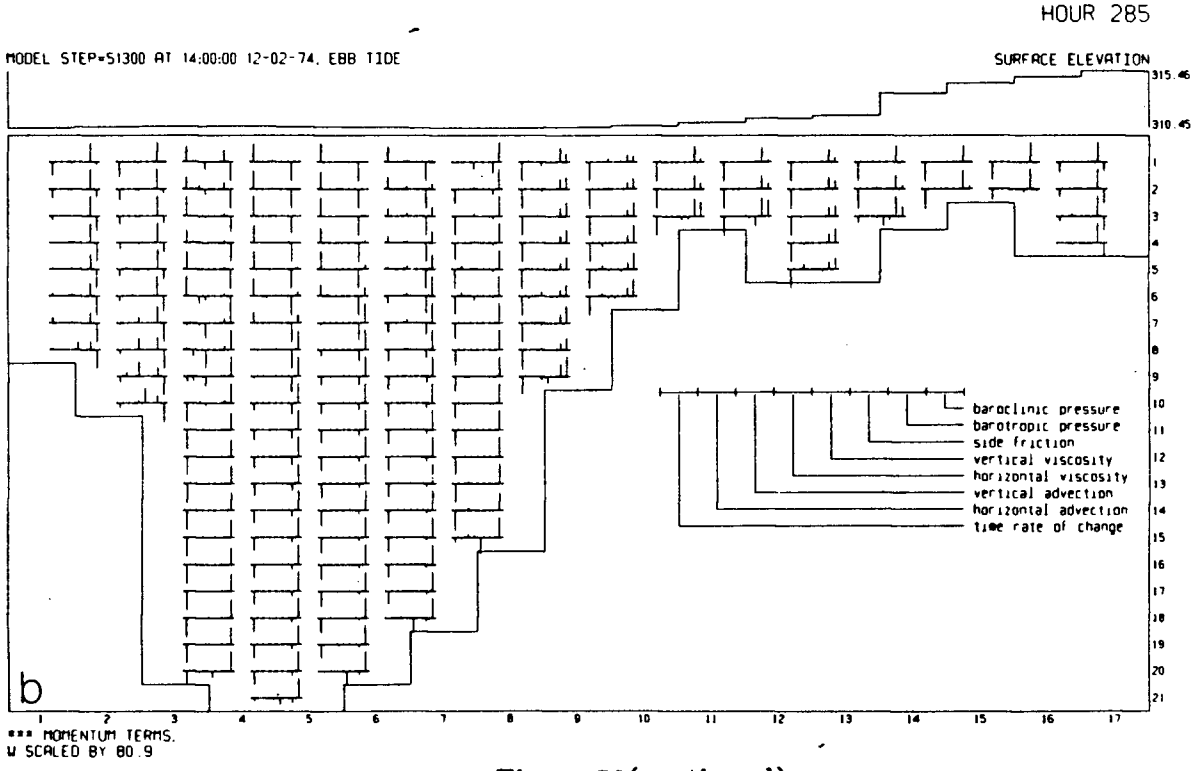

Figure 50(continued)

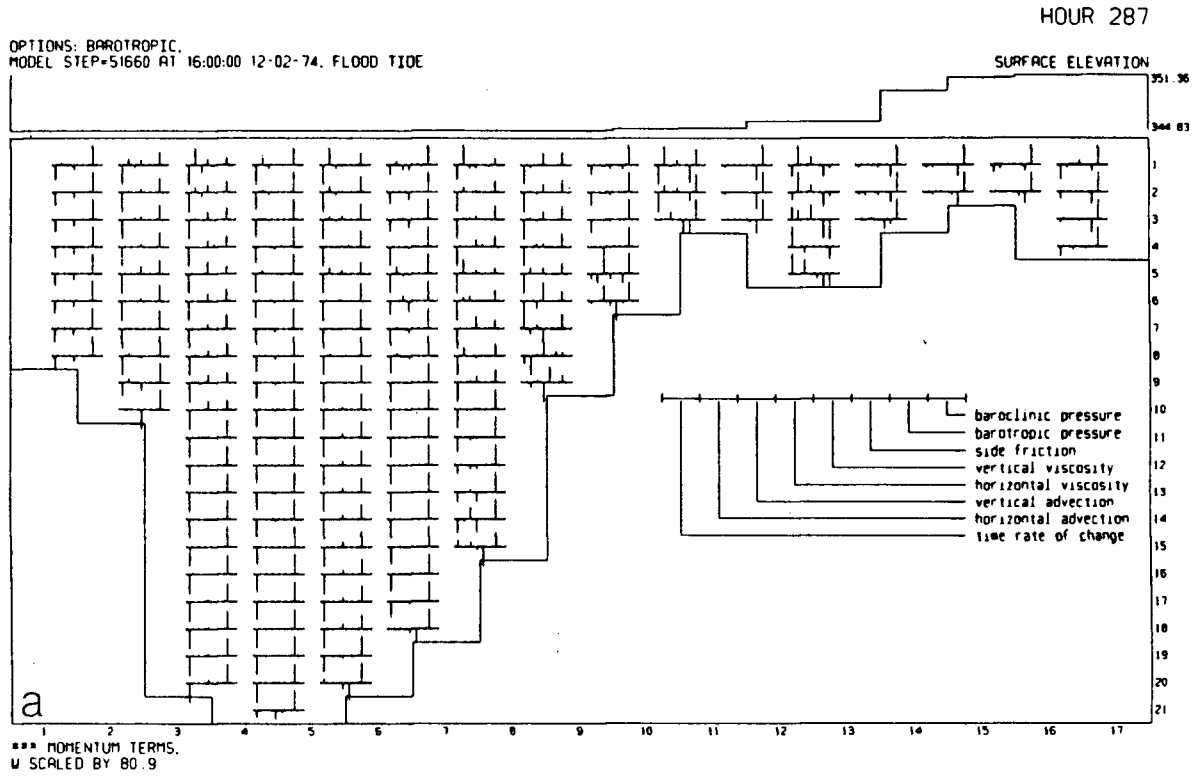

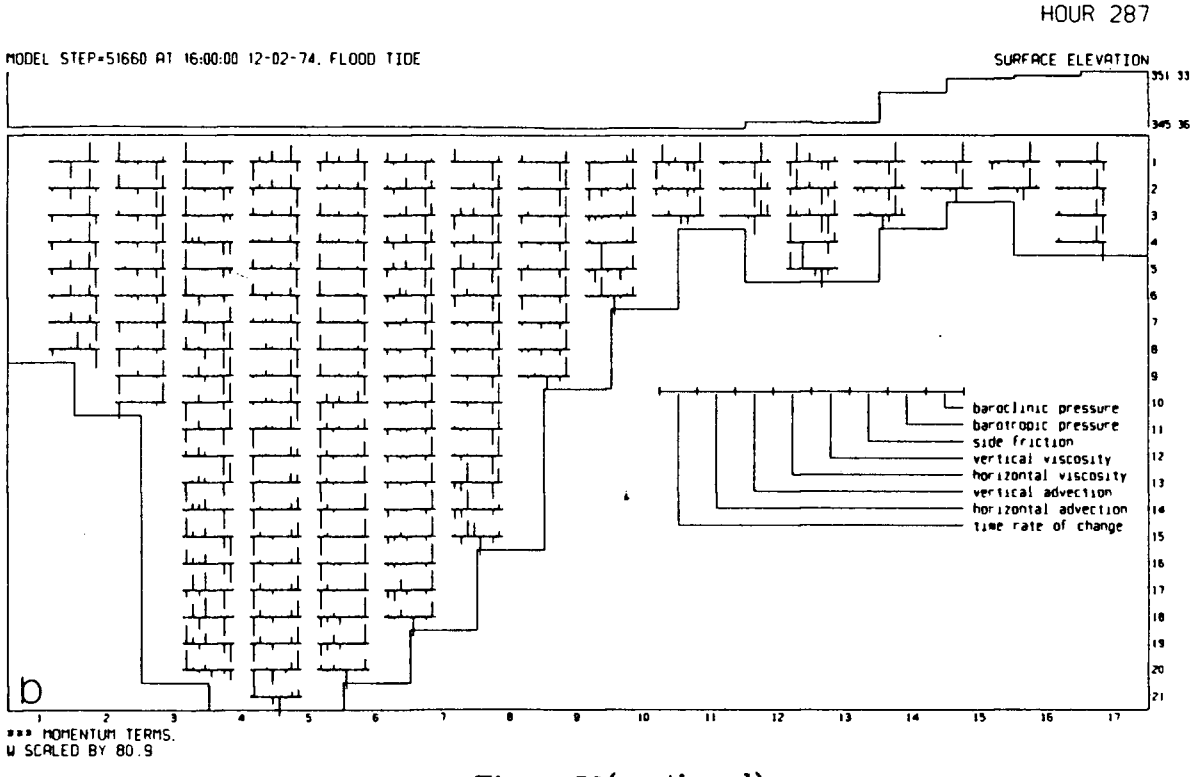

Figure 50(continued)

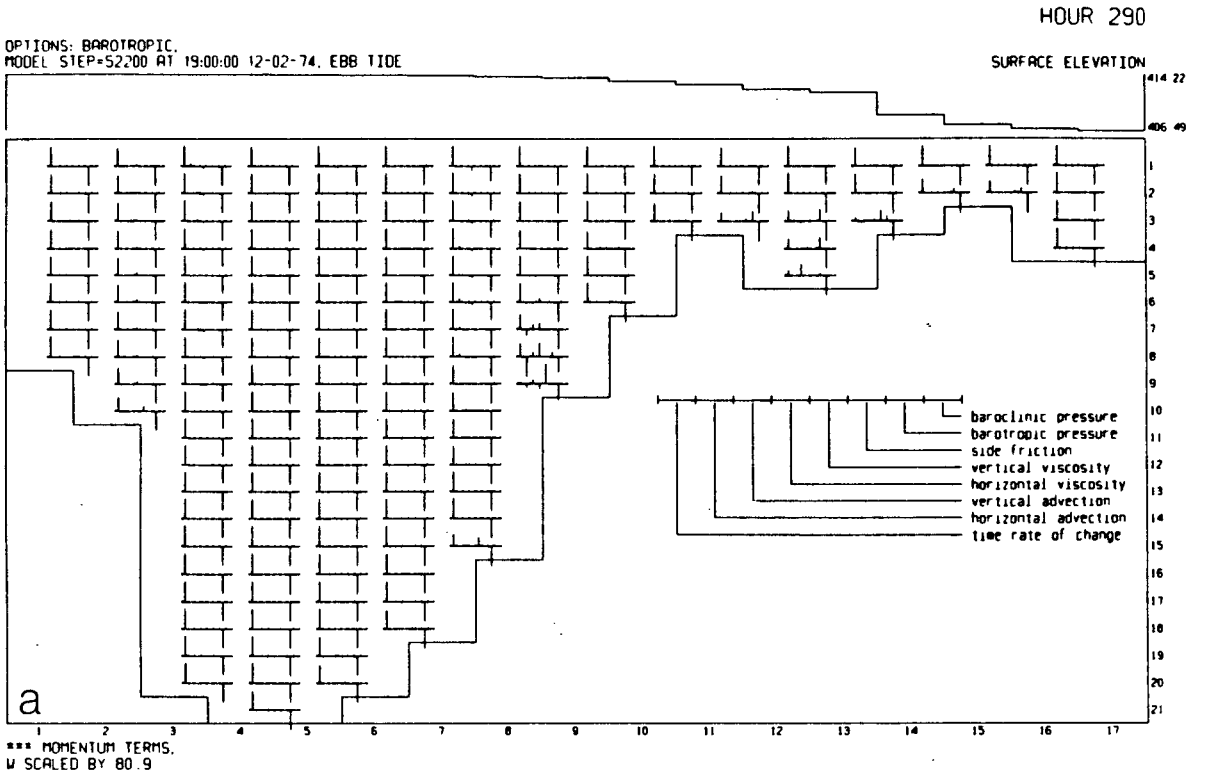

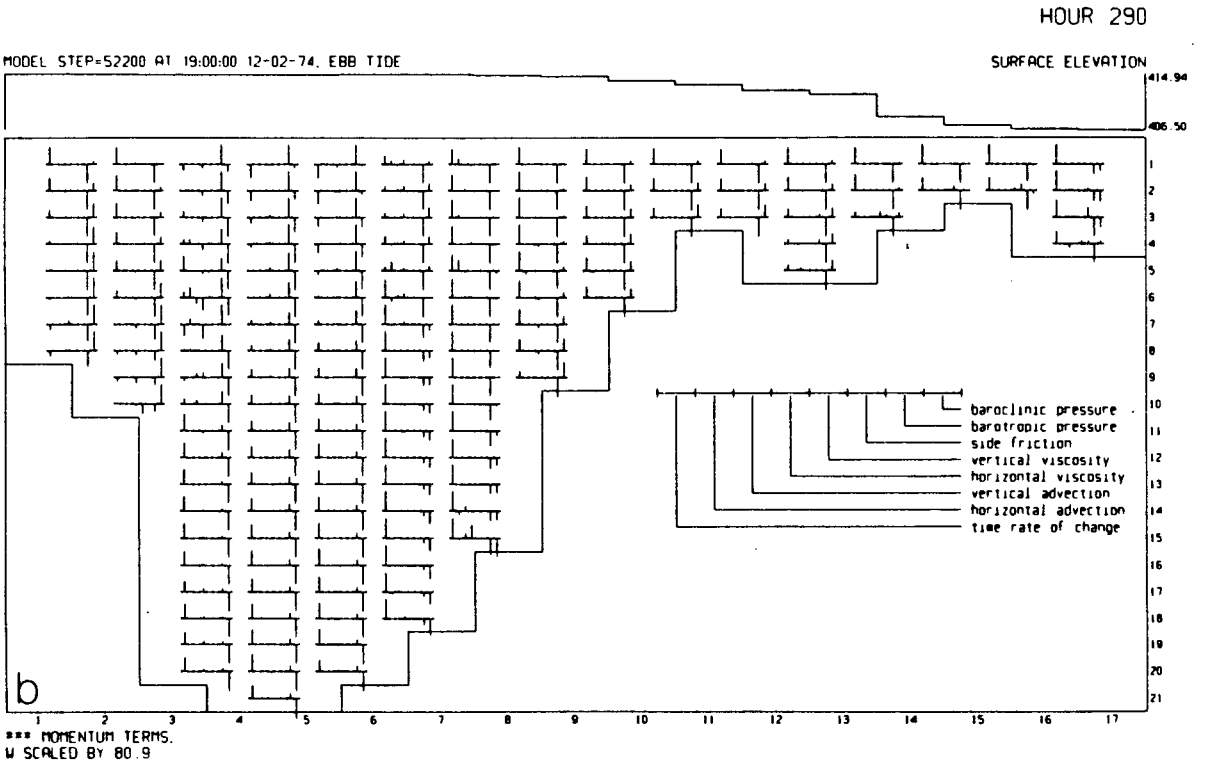

Figure 50(continued)

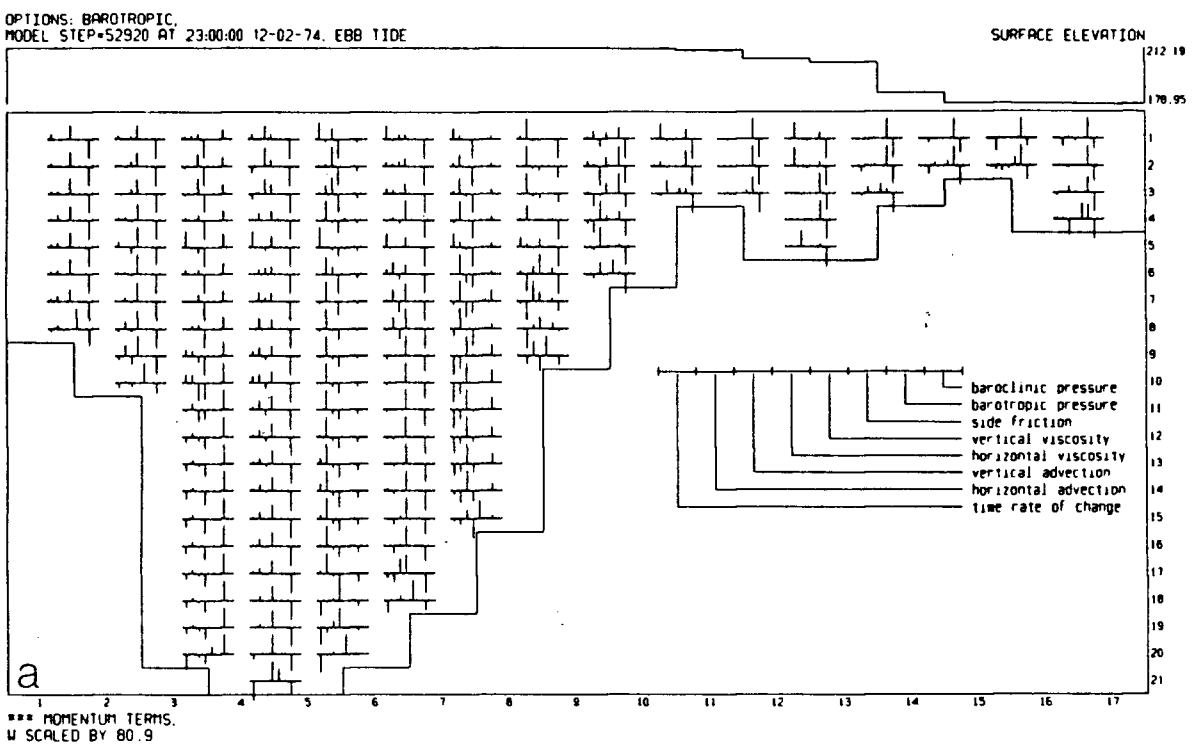

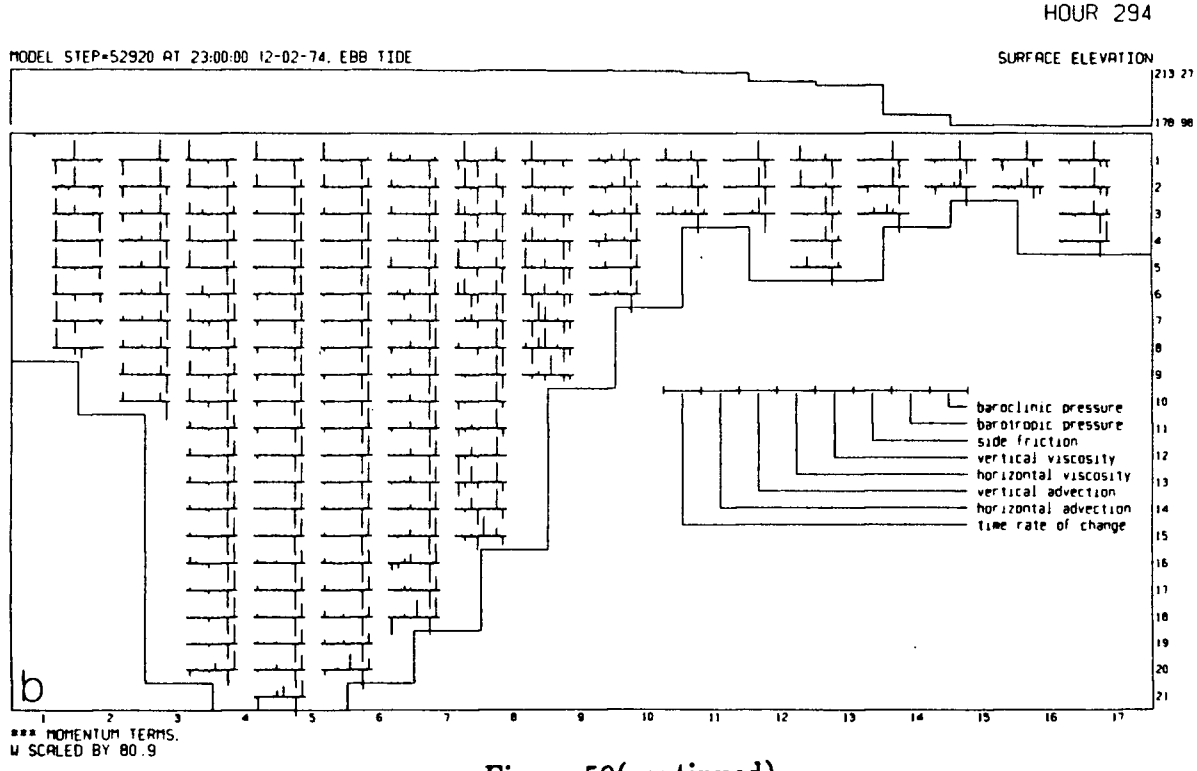

Figure 50(continued)

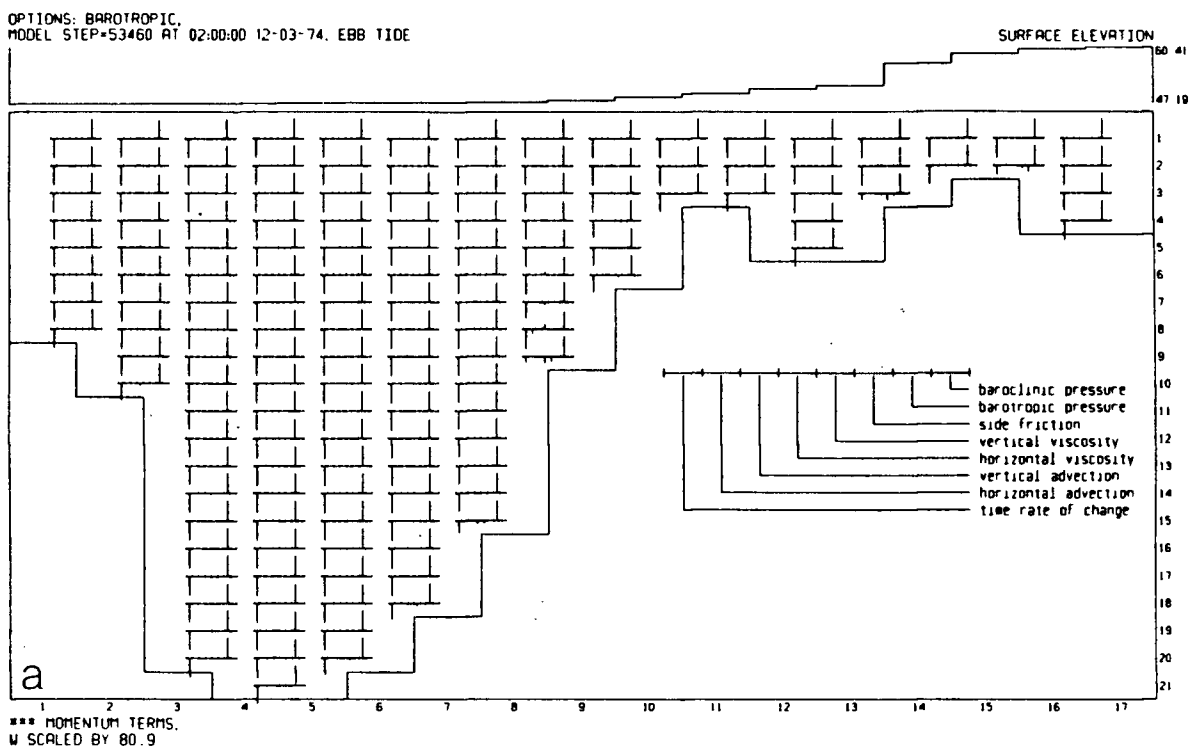

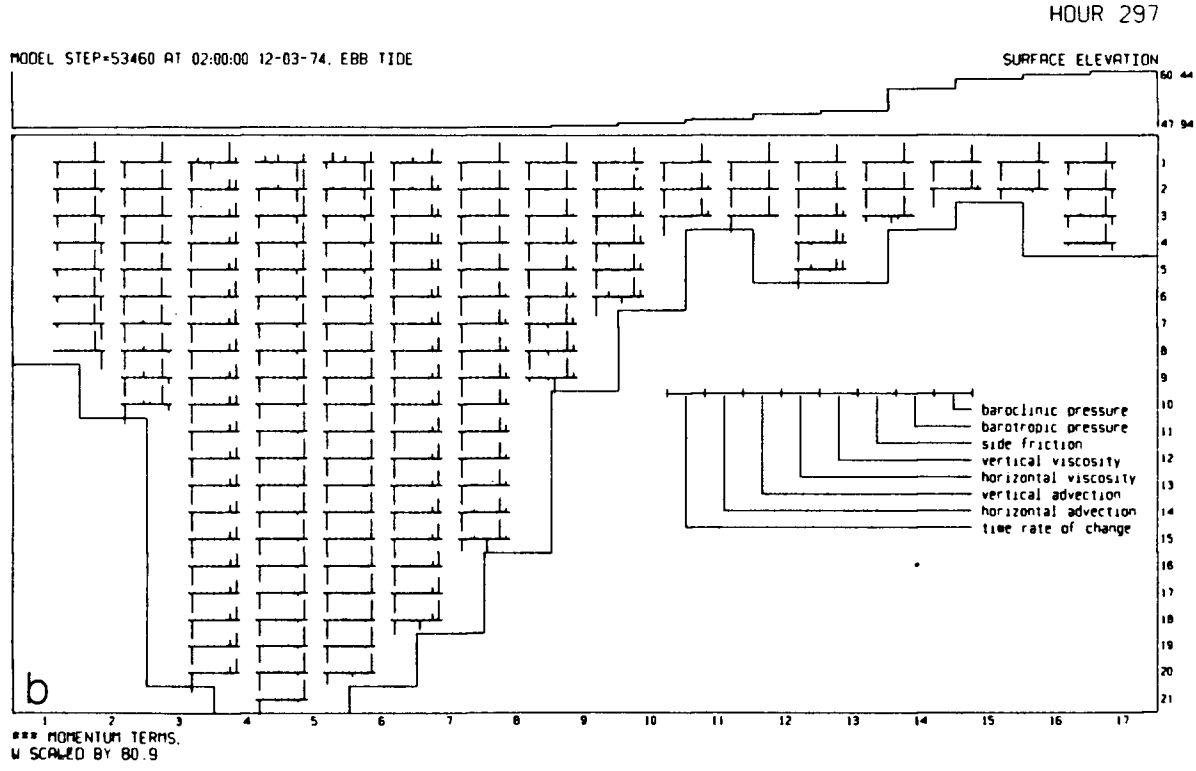

Figure 50(continued)

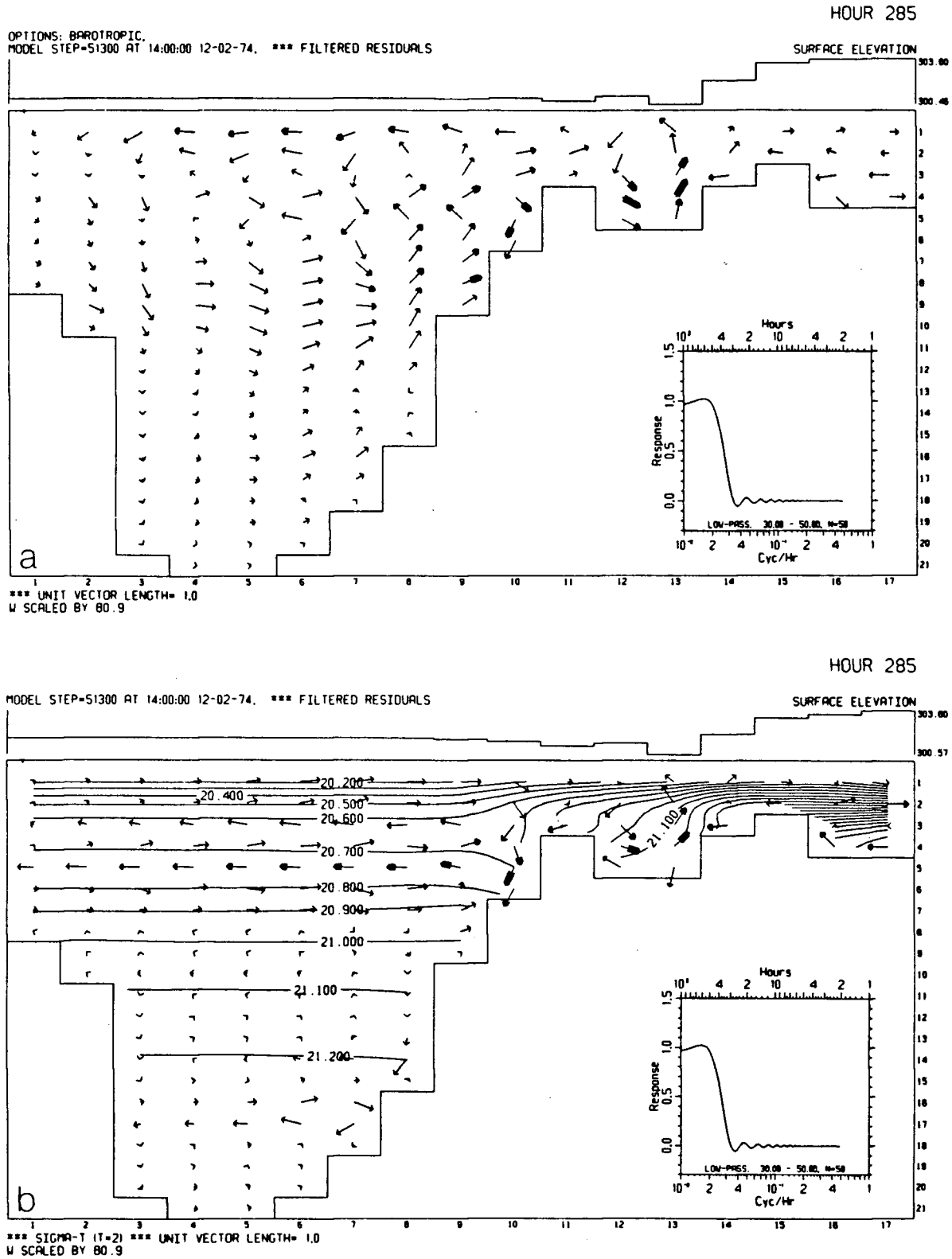

Figure 51. Residual surface elevation, current vectors and isopycnals for Class 4 model simulation of Indian Arm and Burrard Inlet. Vertical exaggeration is 80.9 and elevations are in *cm*. Unit vector length is 1 $cm\,s^{-1}$. Contours are in σ_t units. Inset shows response curve of digital filter used to calculate residuals. Plot (a): unstratified run. Plot (b): stratified run.

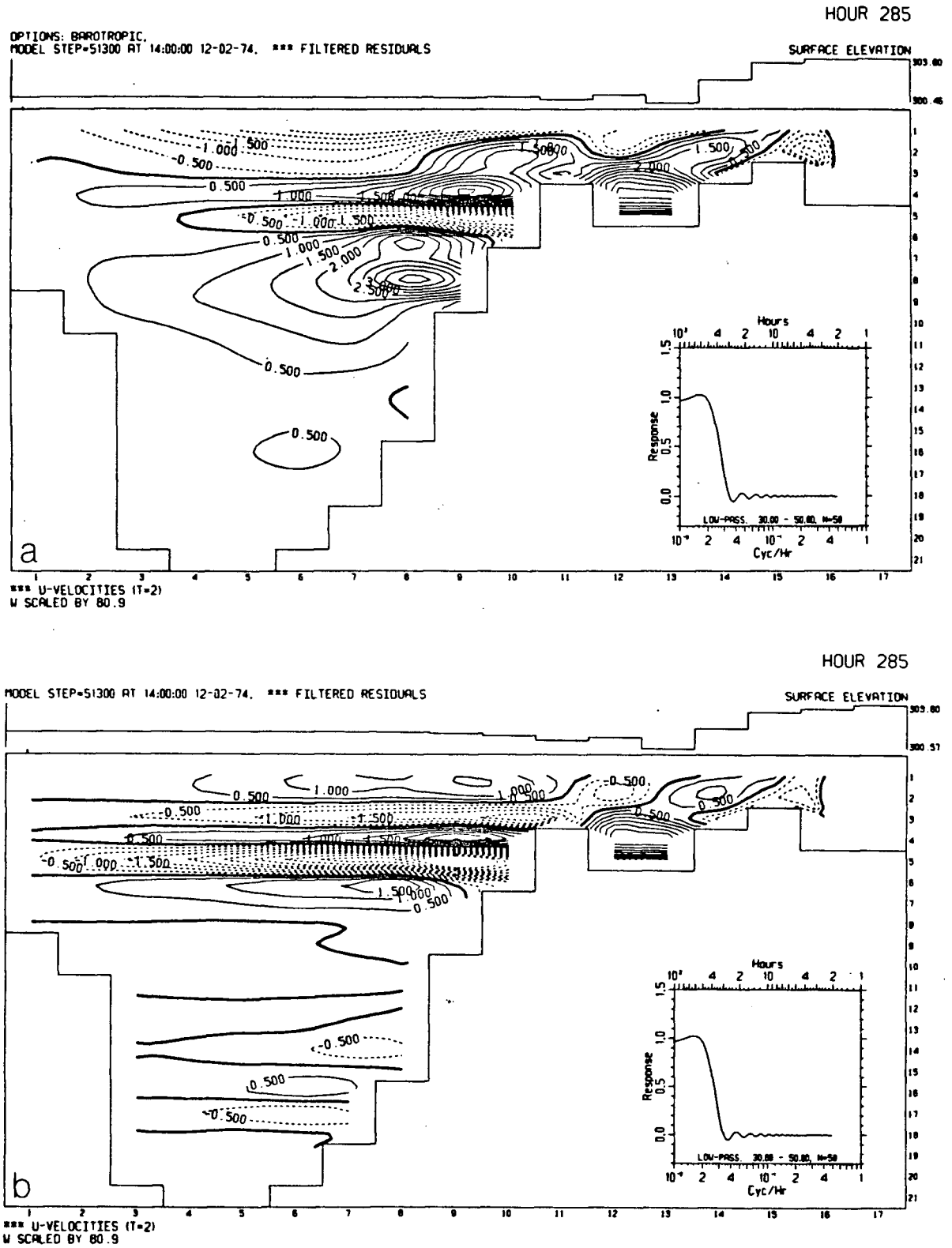

Figure 52. Residual surface elevation and contours of horizontal velocity for Class 4 model simulation of Indian Arm and Burrard Inlet. Vertical exaggeration is 80.9. Elevations are in *cm*. Contours are in $cm\,s^{-1}$. Inset shows response curve of digital filter used to calculate residuals. Plot (a): unstratified run. Plot (b): stratified run.

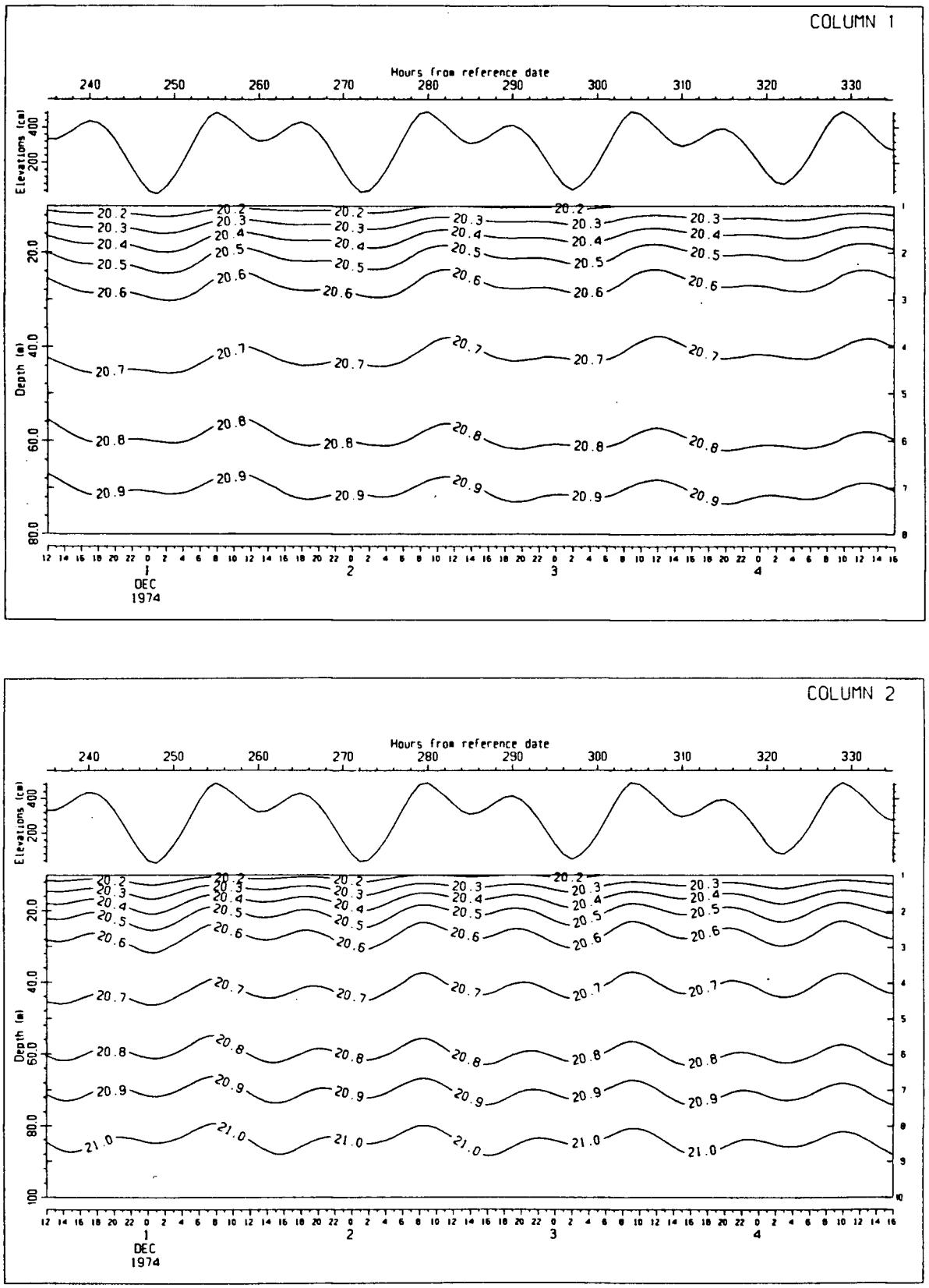

Figure 53. Time series of surface elevation and isopycnals for each column in the Class 4 model simulation of Indian Arm and Burrard Inlet. Isopycnals are in σ_t units. Elevations are in *cm*. (Note that vertical scale varies between plots).

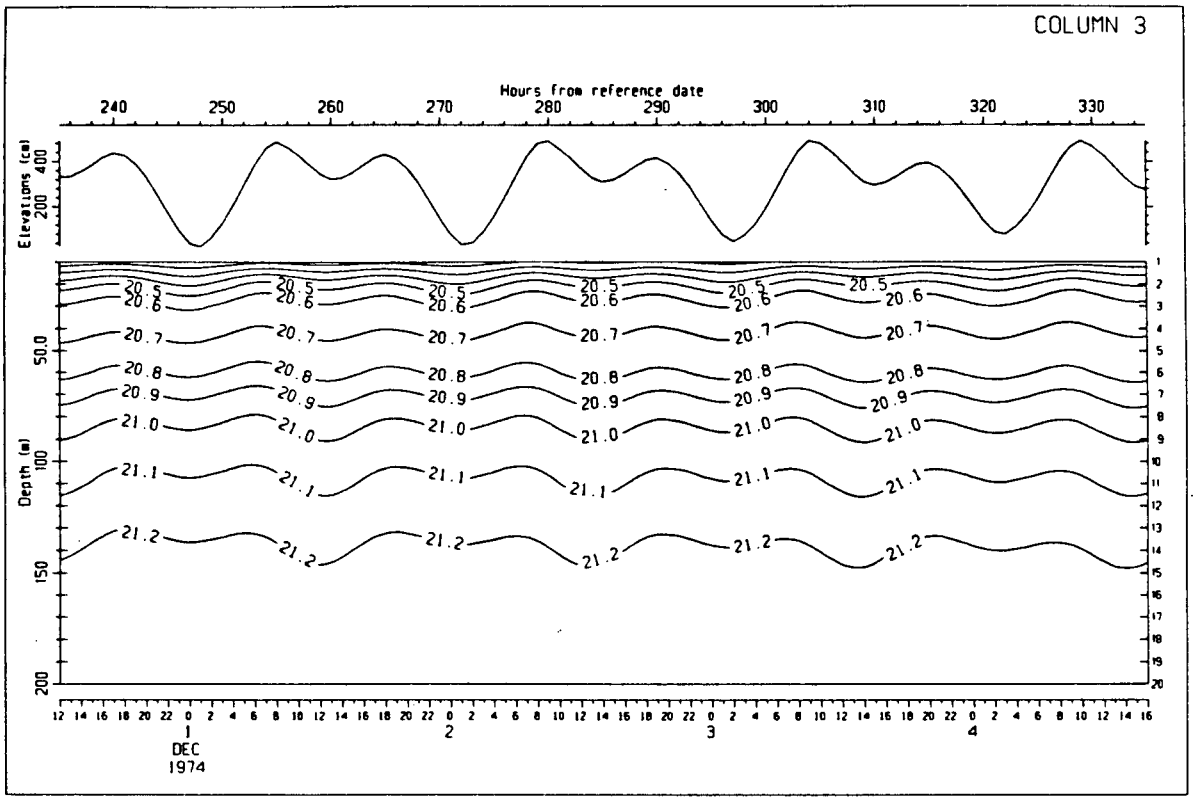

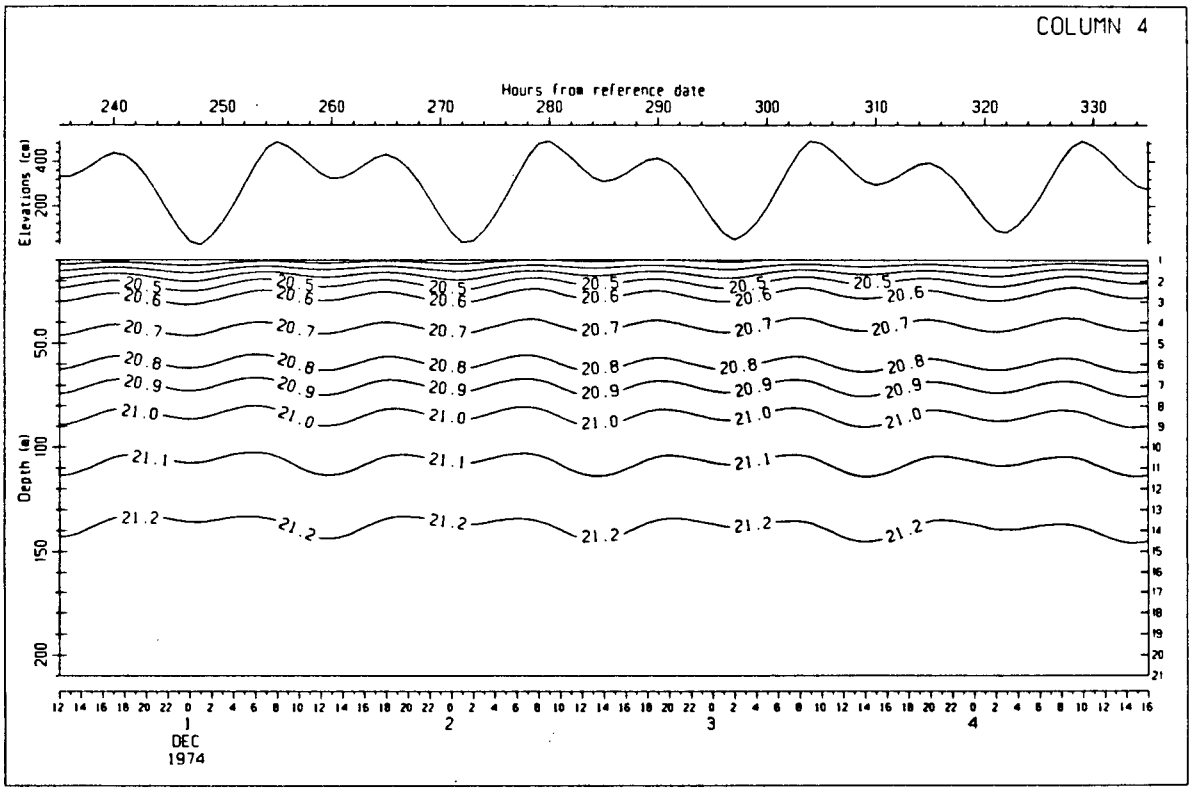

Figure 53(continued)

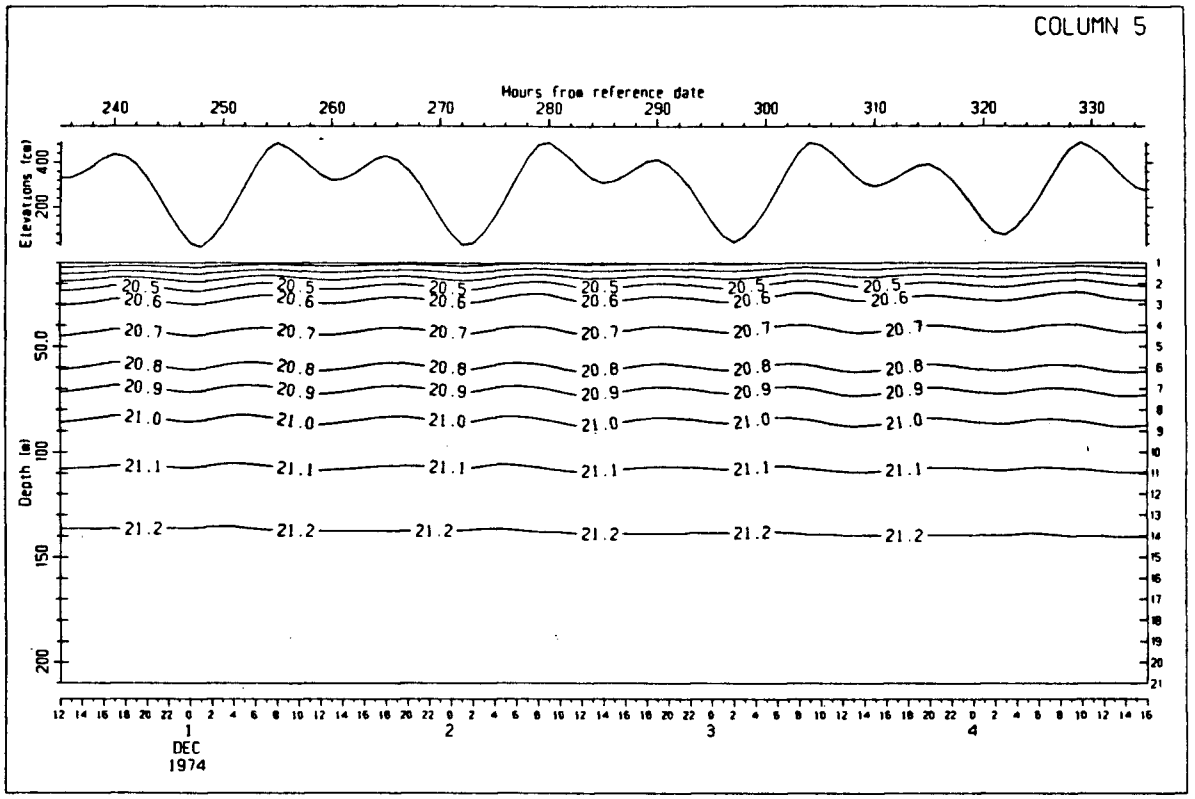

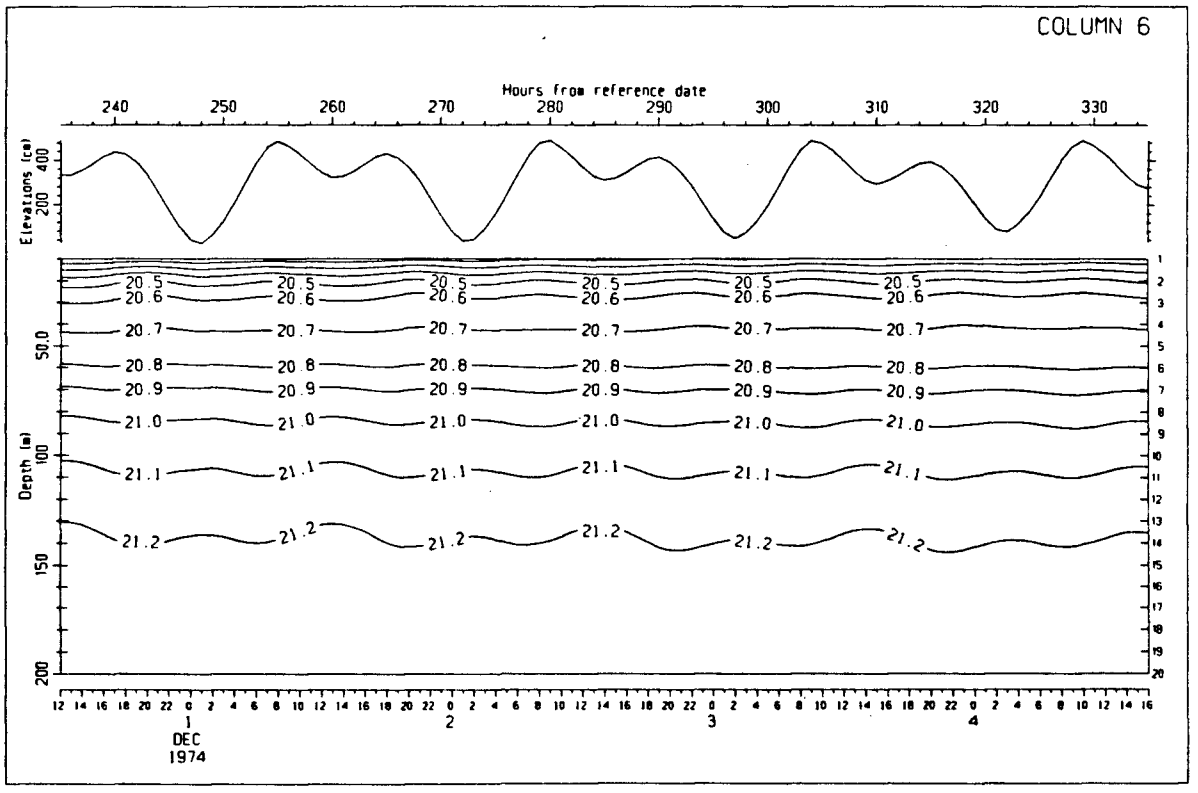

Figure 53(continued)

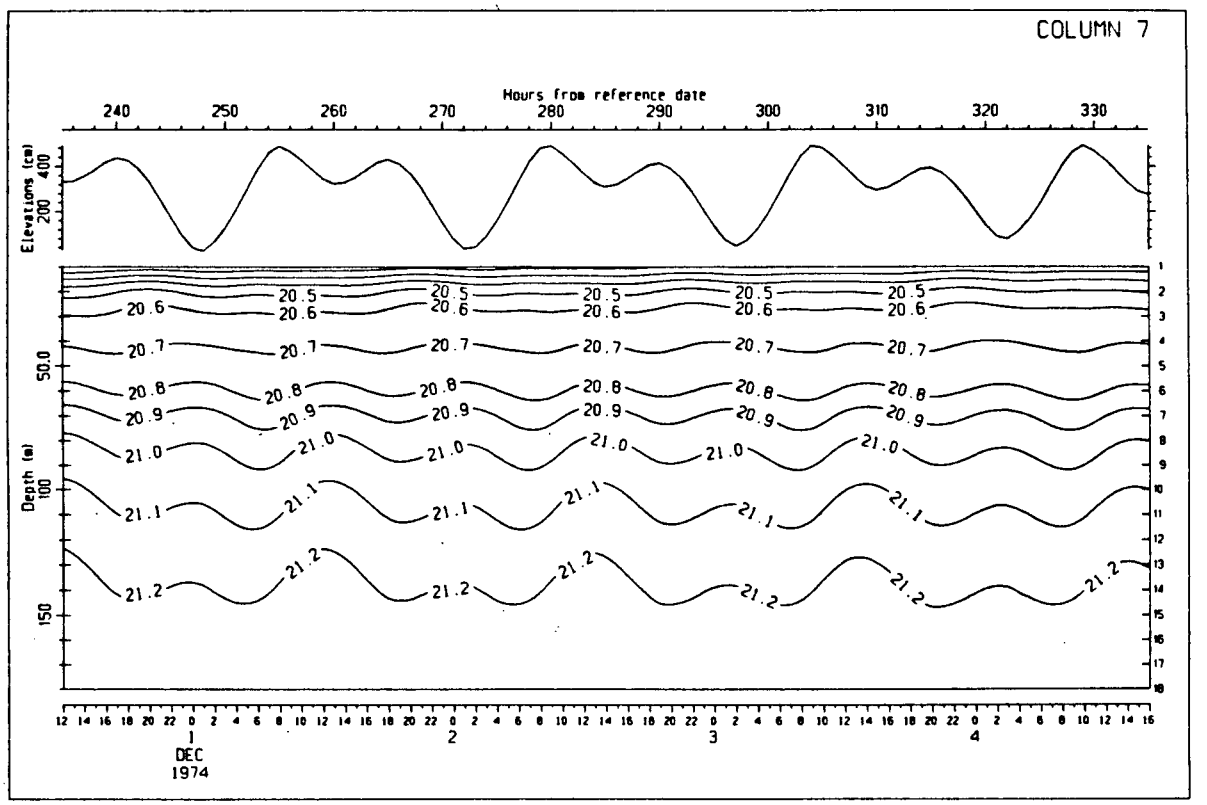

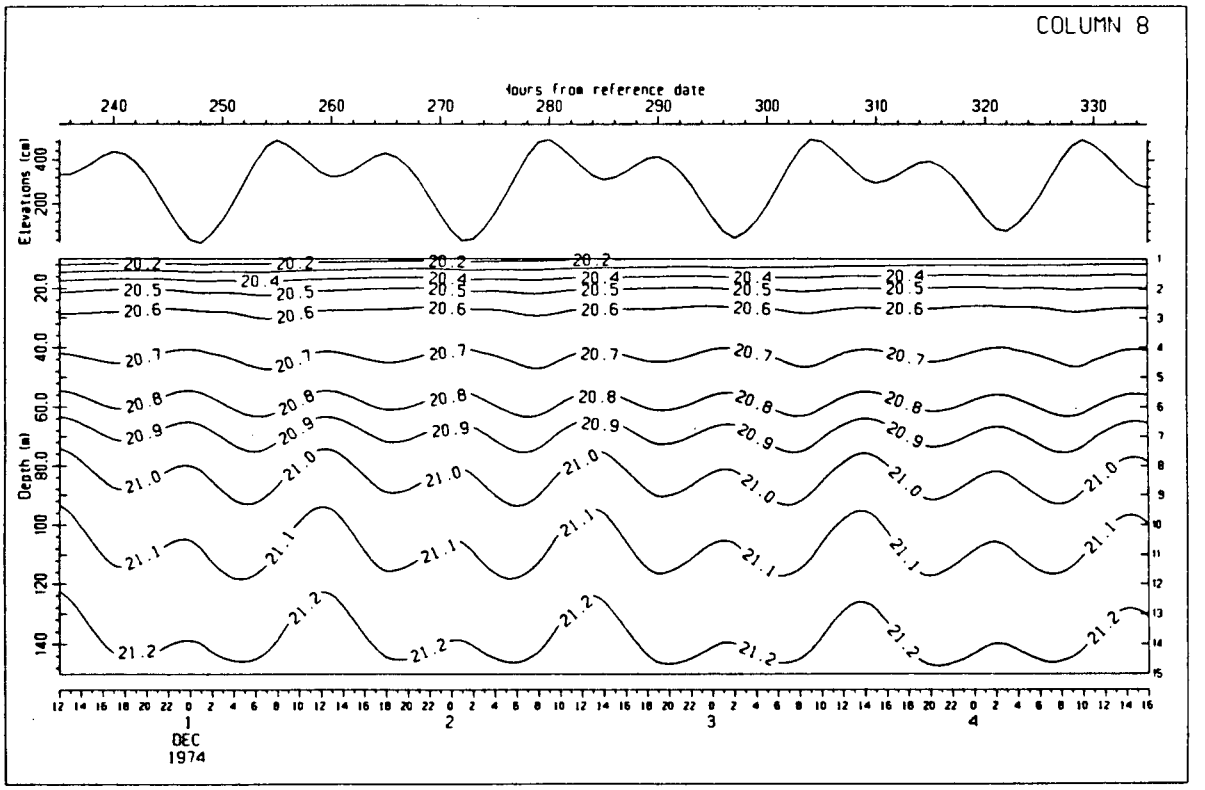

Figure 53(continued)

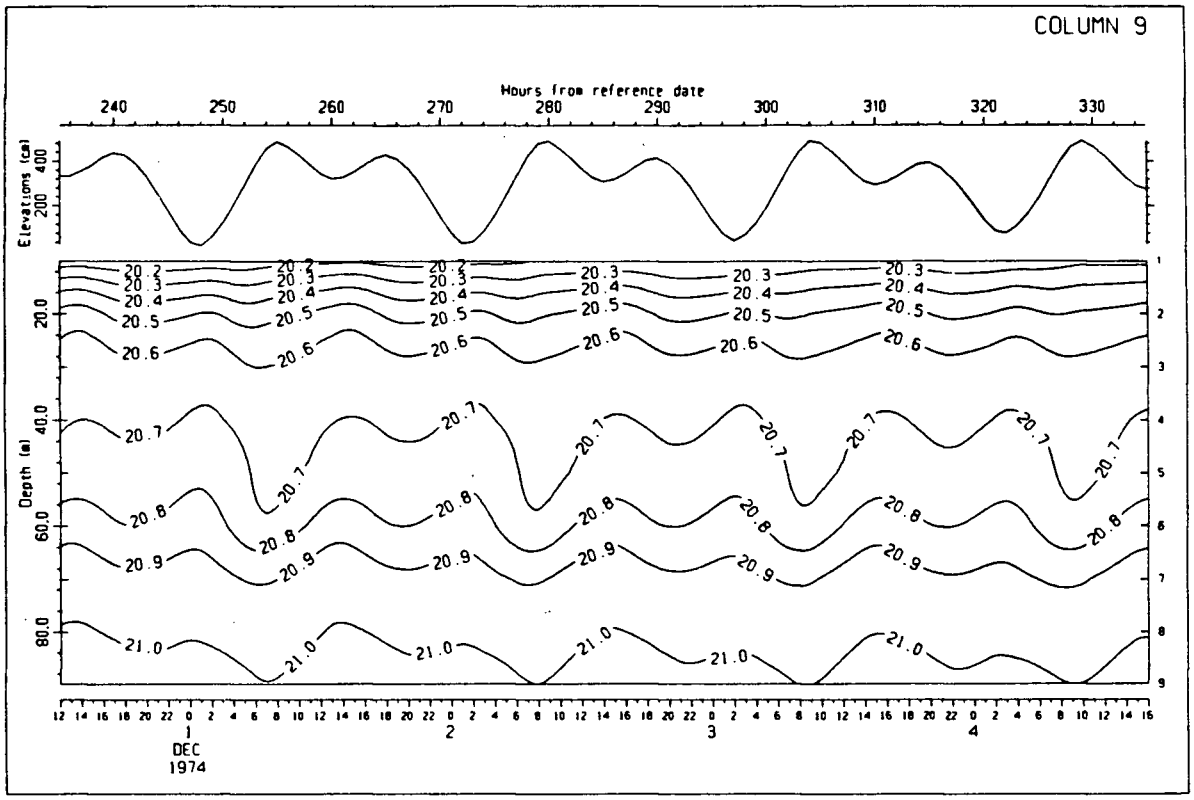

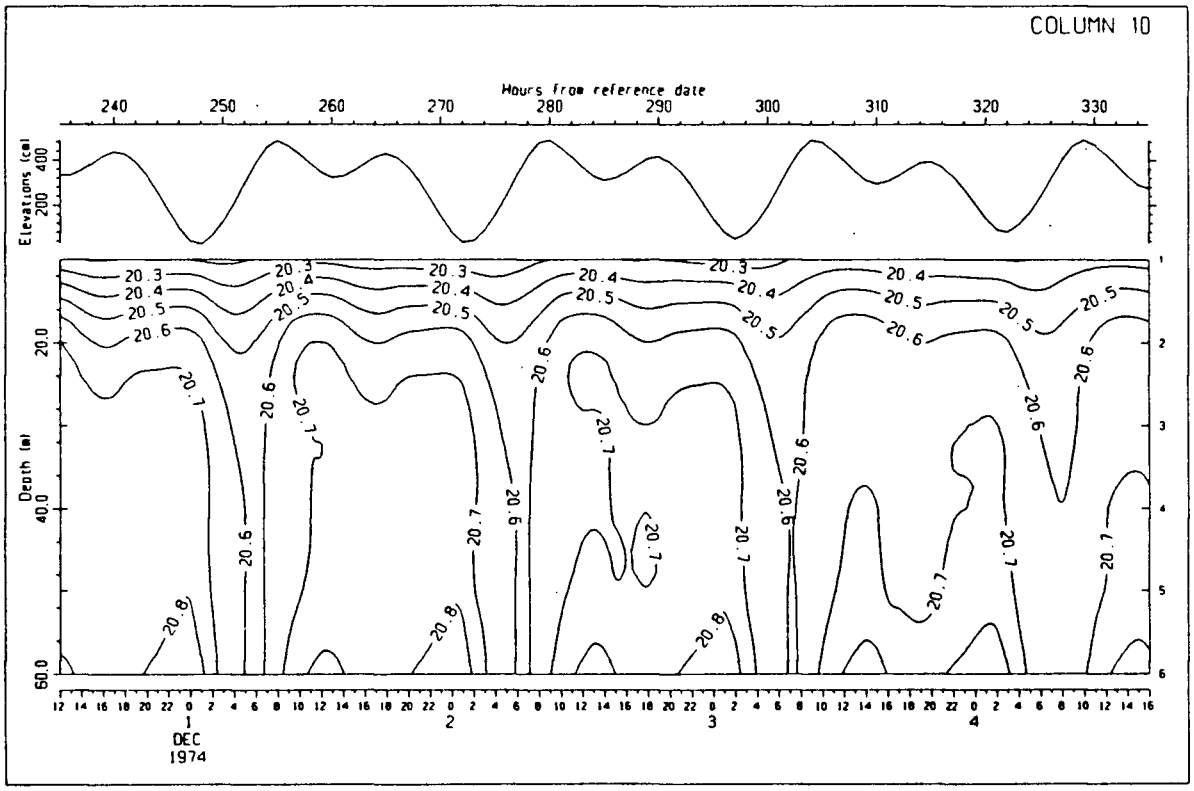

Figure 53(continued)

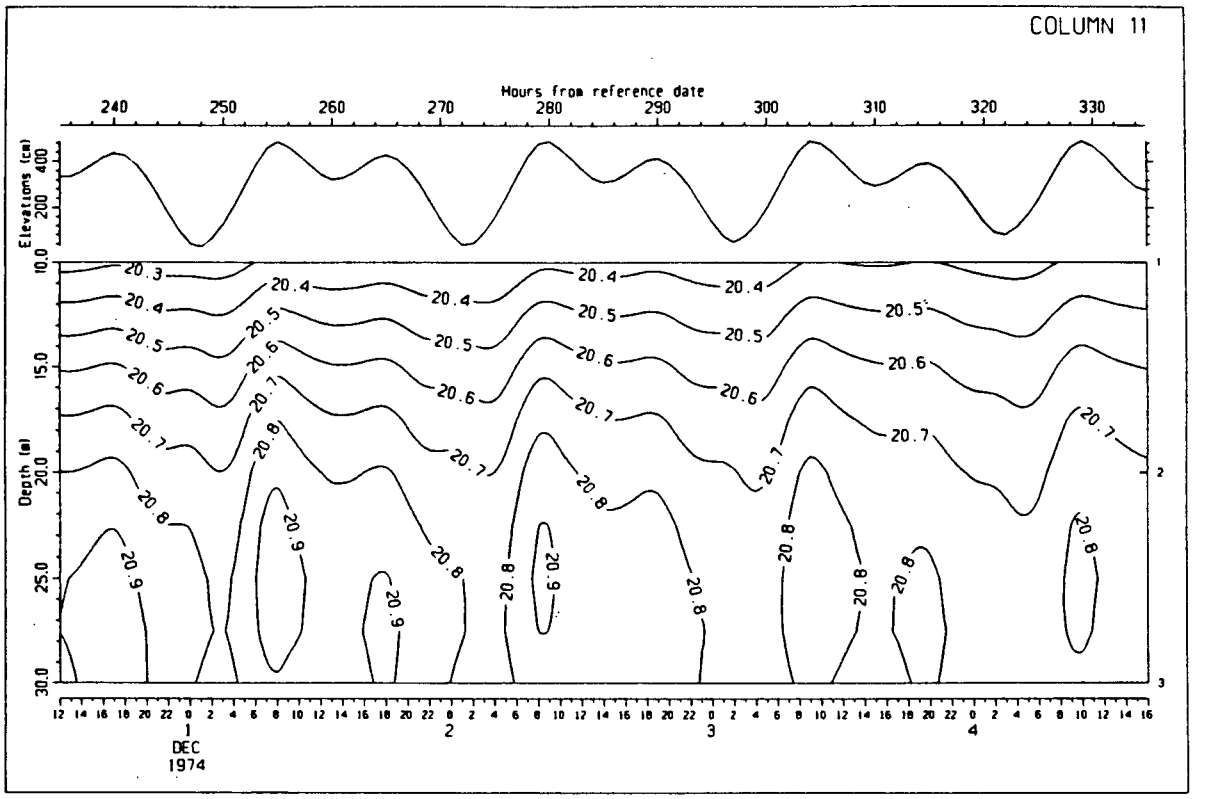

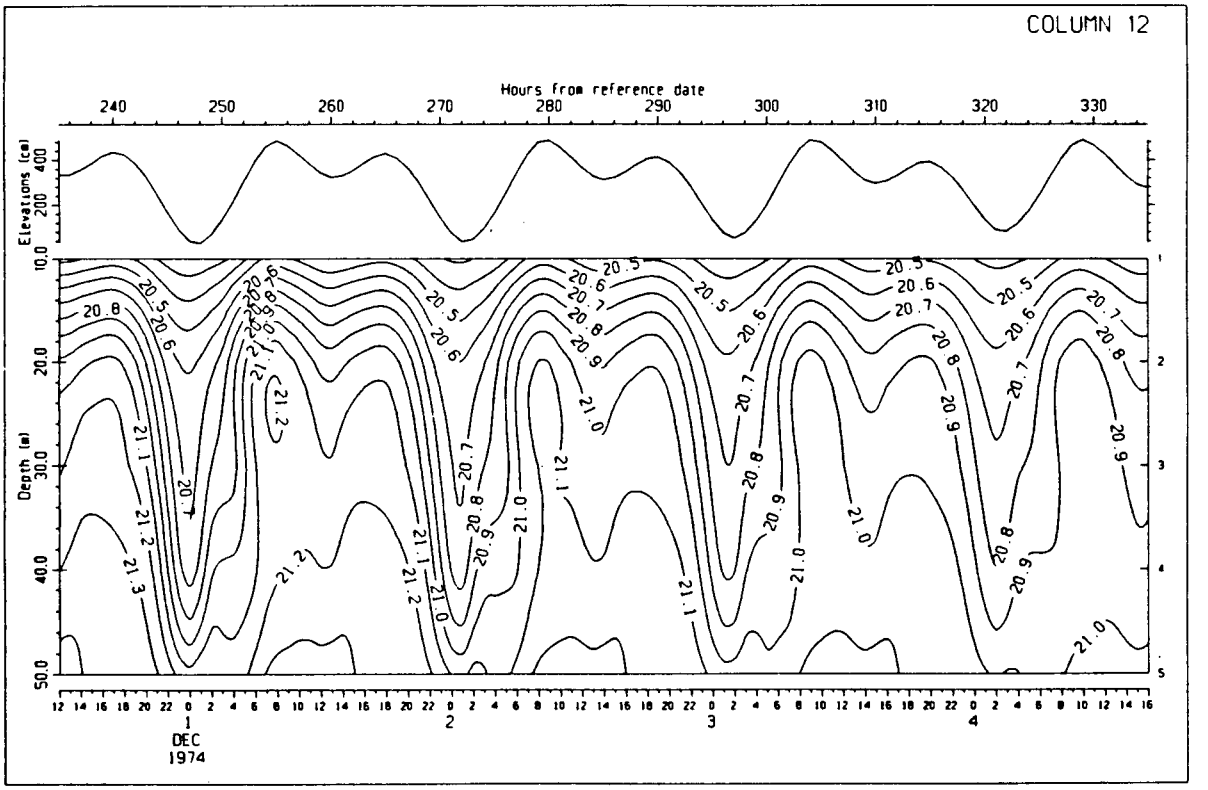

Figure 53(continued)

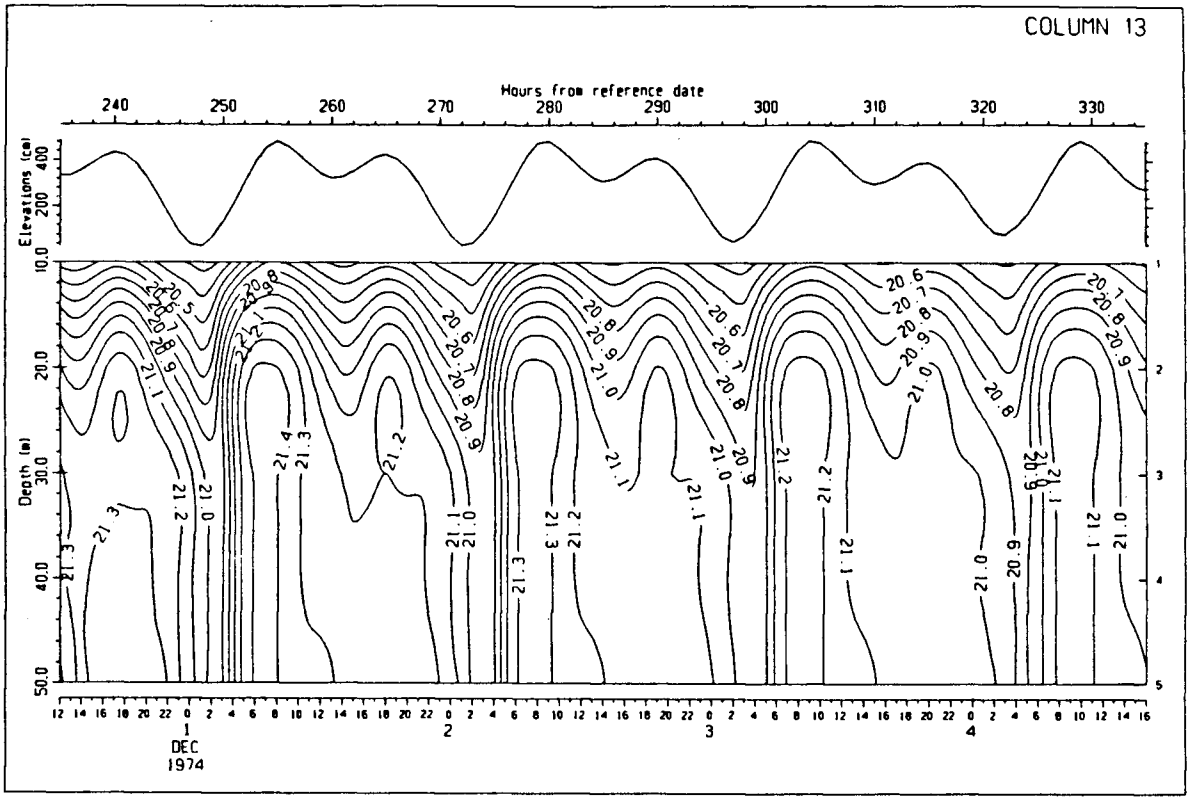

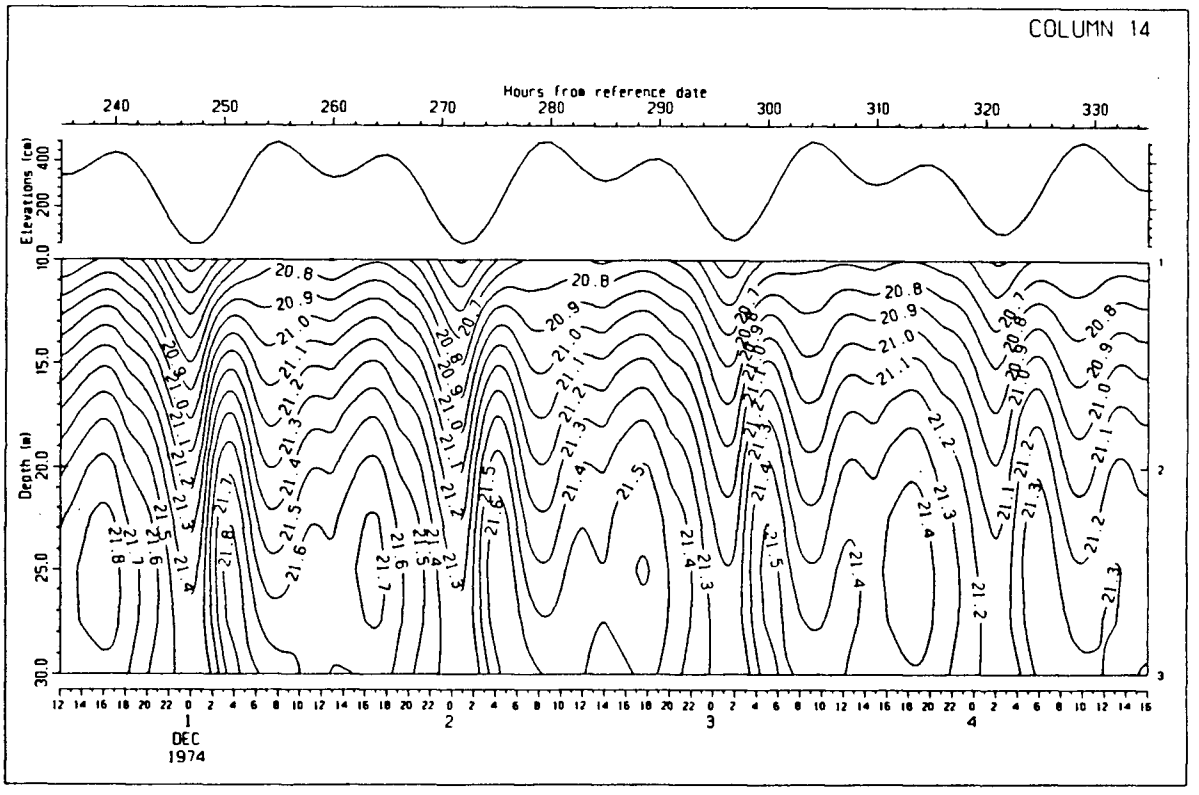

Figure 53(continued)

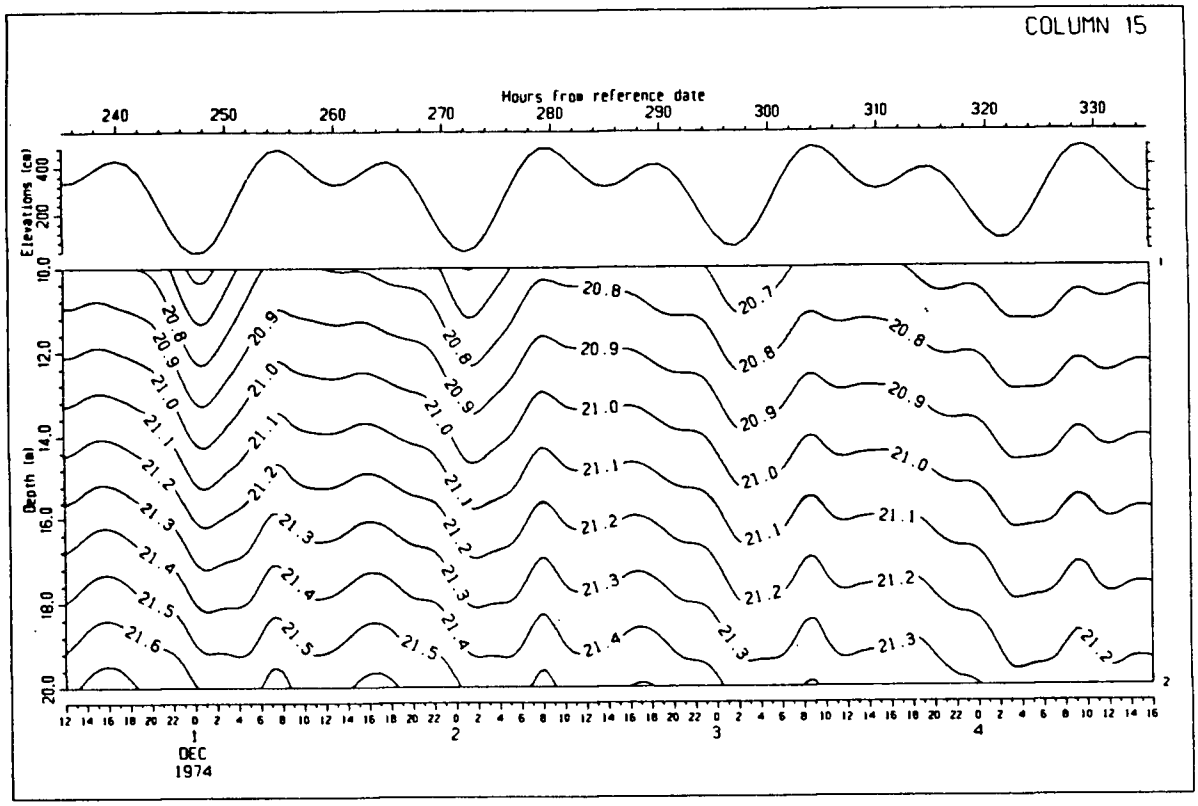

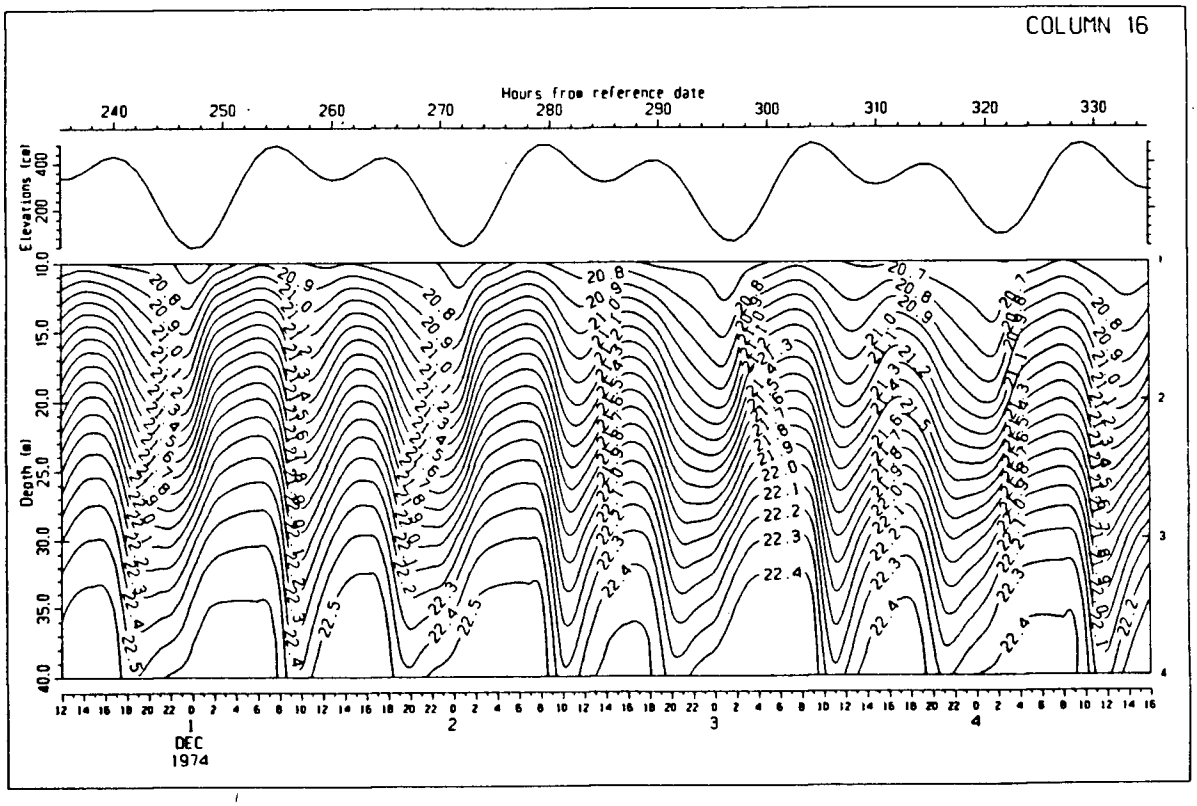

Figure 53(continued)

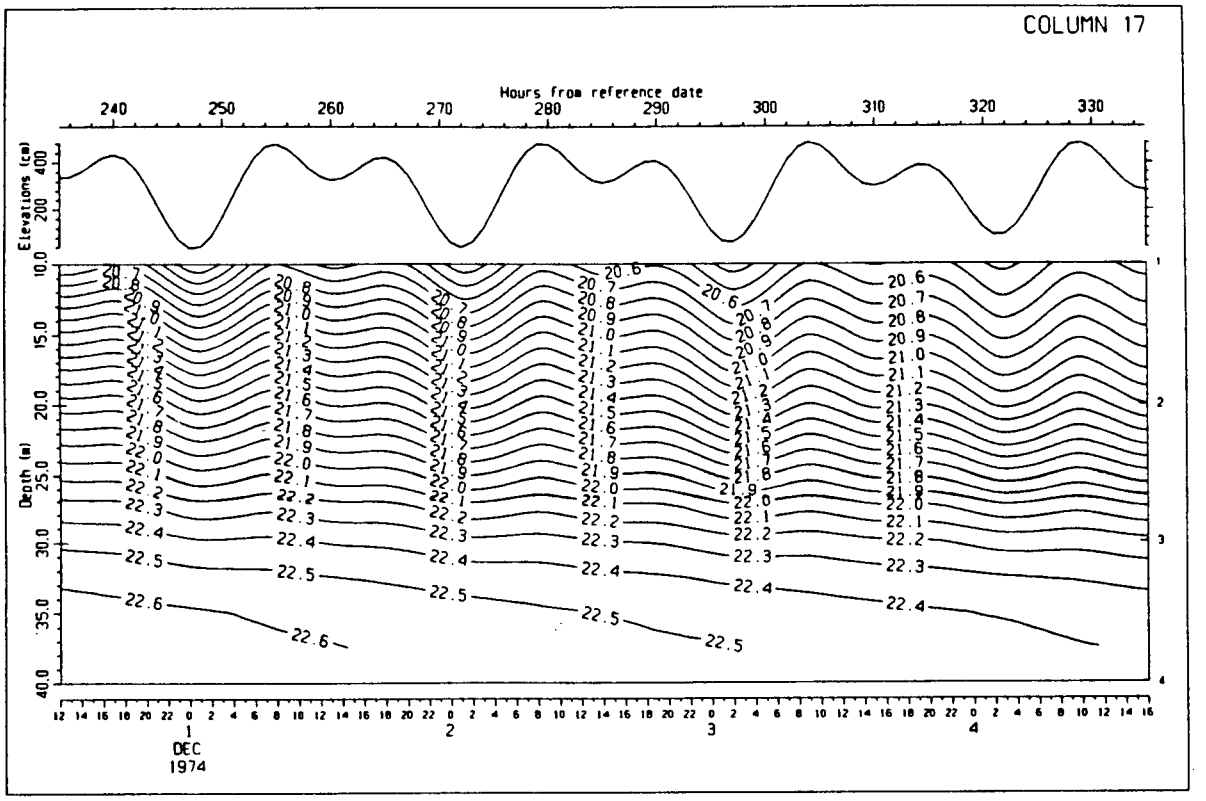

Figure 53(continued)

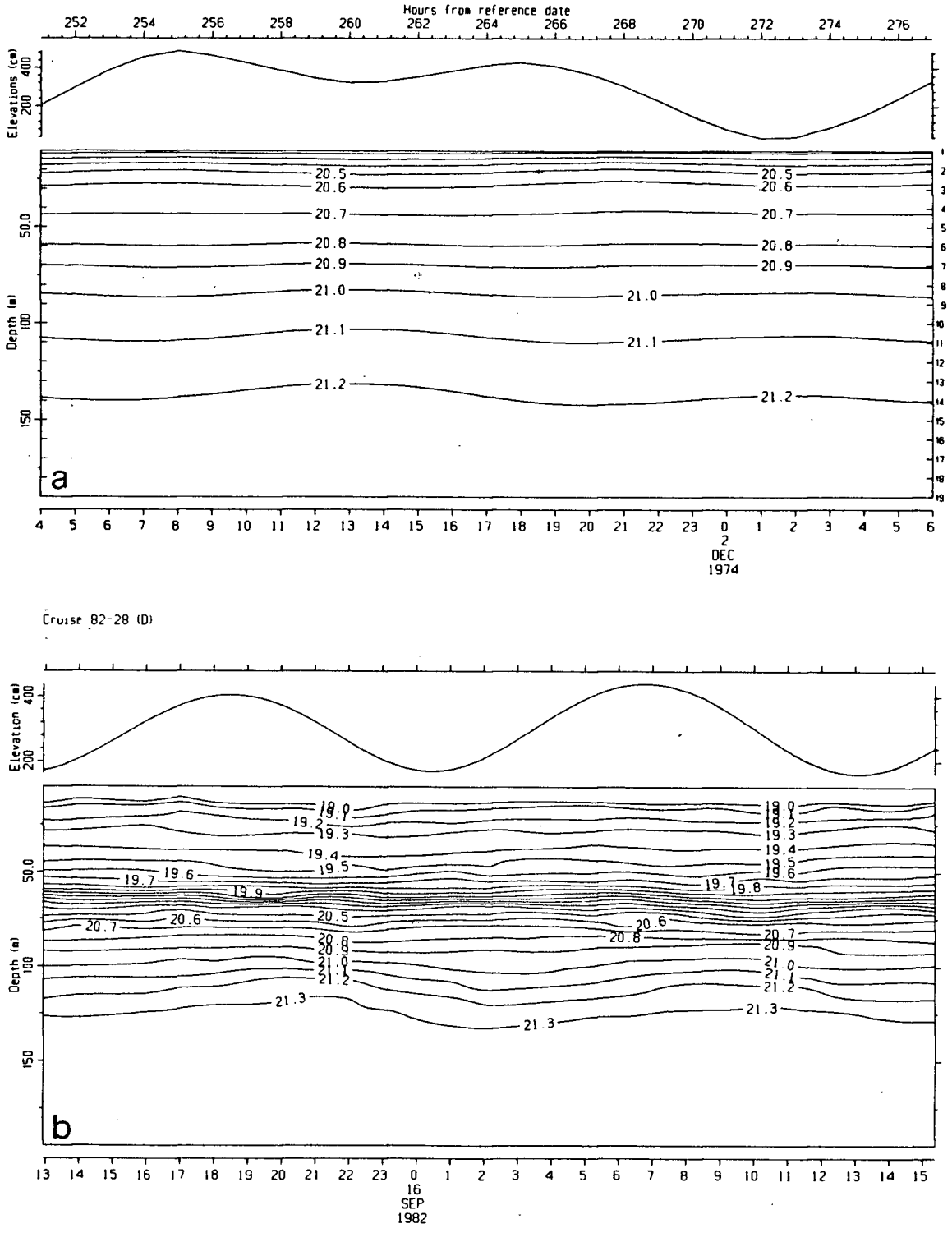

Figure 54. Isopycnal time series at model grids 6, 7 and 9. (Note different vertical scales between stations). Plot (a): Model. Plot (b): measured data

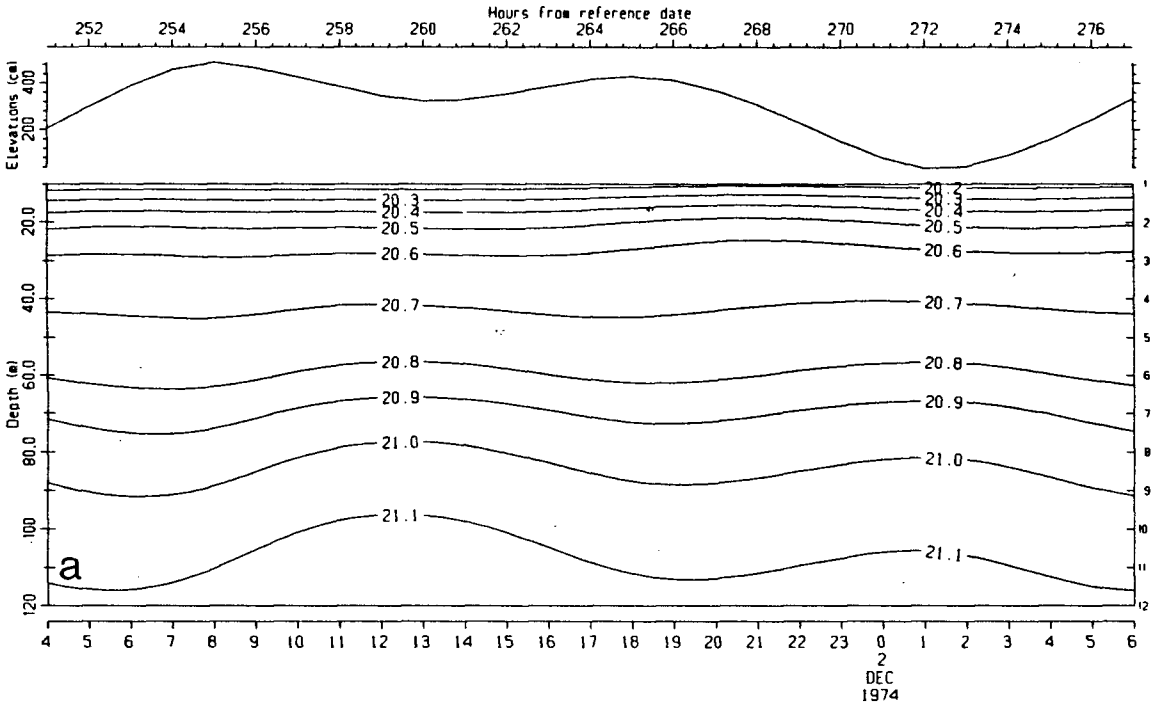

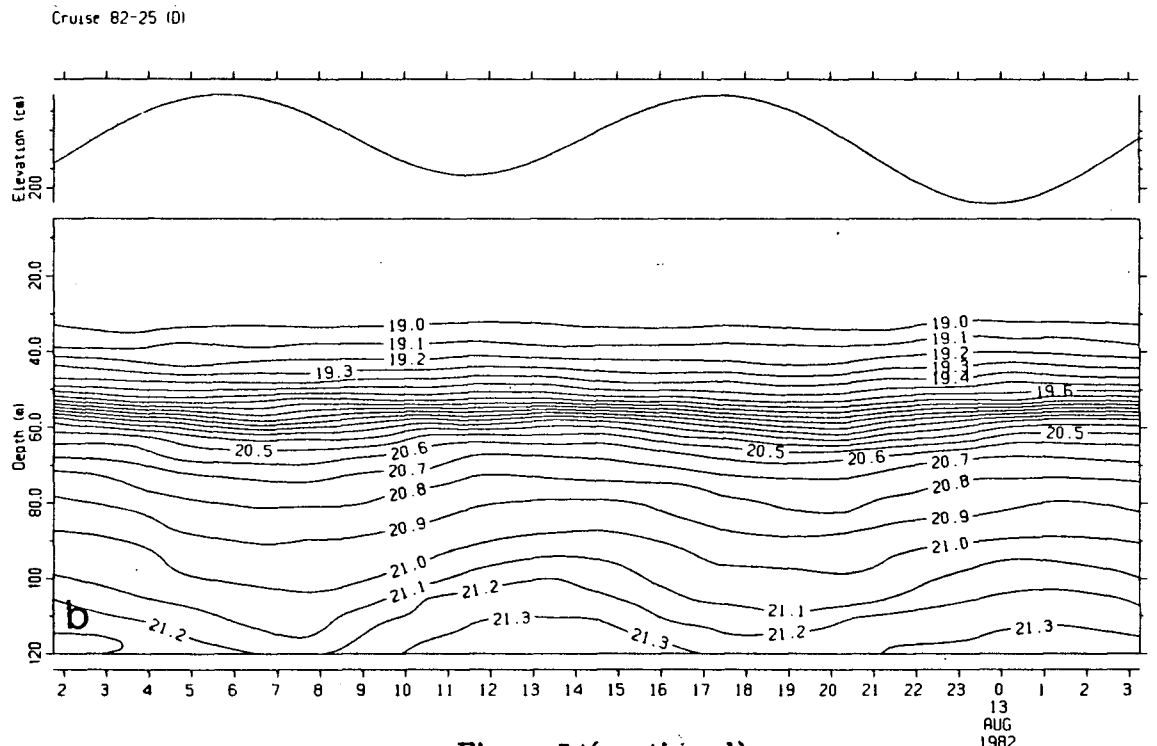

Figure 54(continued)

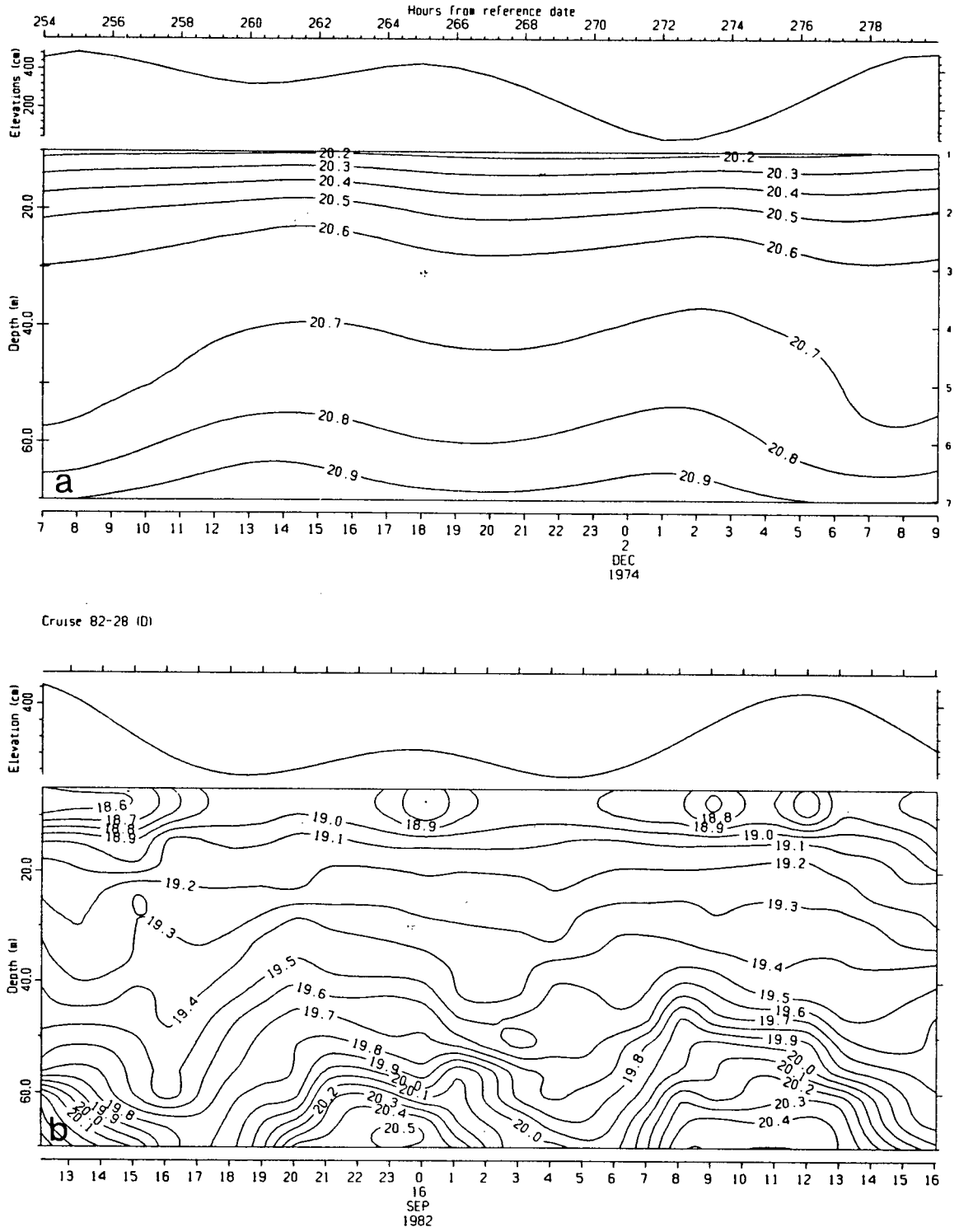

Figure 54(continued)

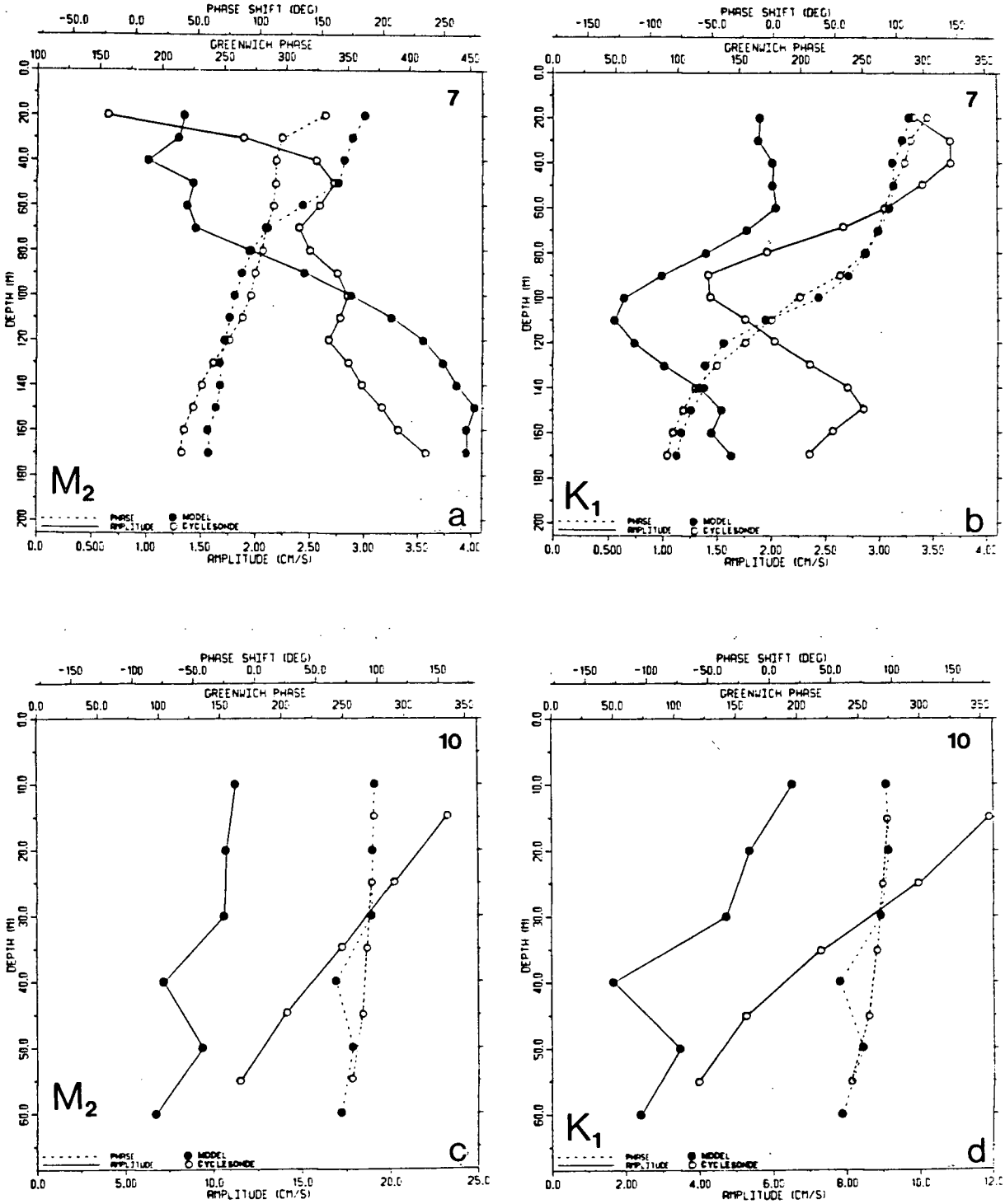

Figure 55. Vertical profiles of amplitude and phase from harmonic analysis of model and Cyclesonde time series centred on December 9, 1974 and January 5, 1983 respectively. The phase shift (top scale) is relative to the surface elevation. See Appendix A for a definition of Greenwich phase angles. Plot (a): M_2 at column 7. Plot (b): K_1 at column 7. Plot (c): M_2 at column 10. Plot (d): K_1 at column 10.

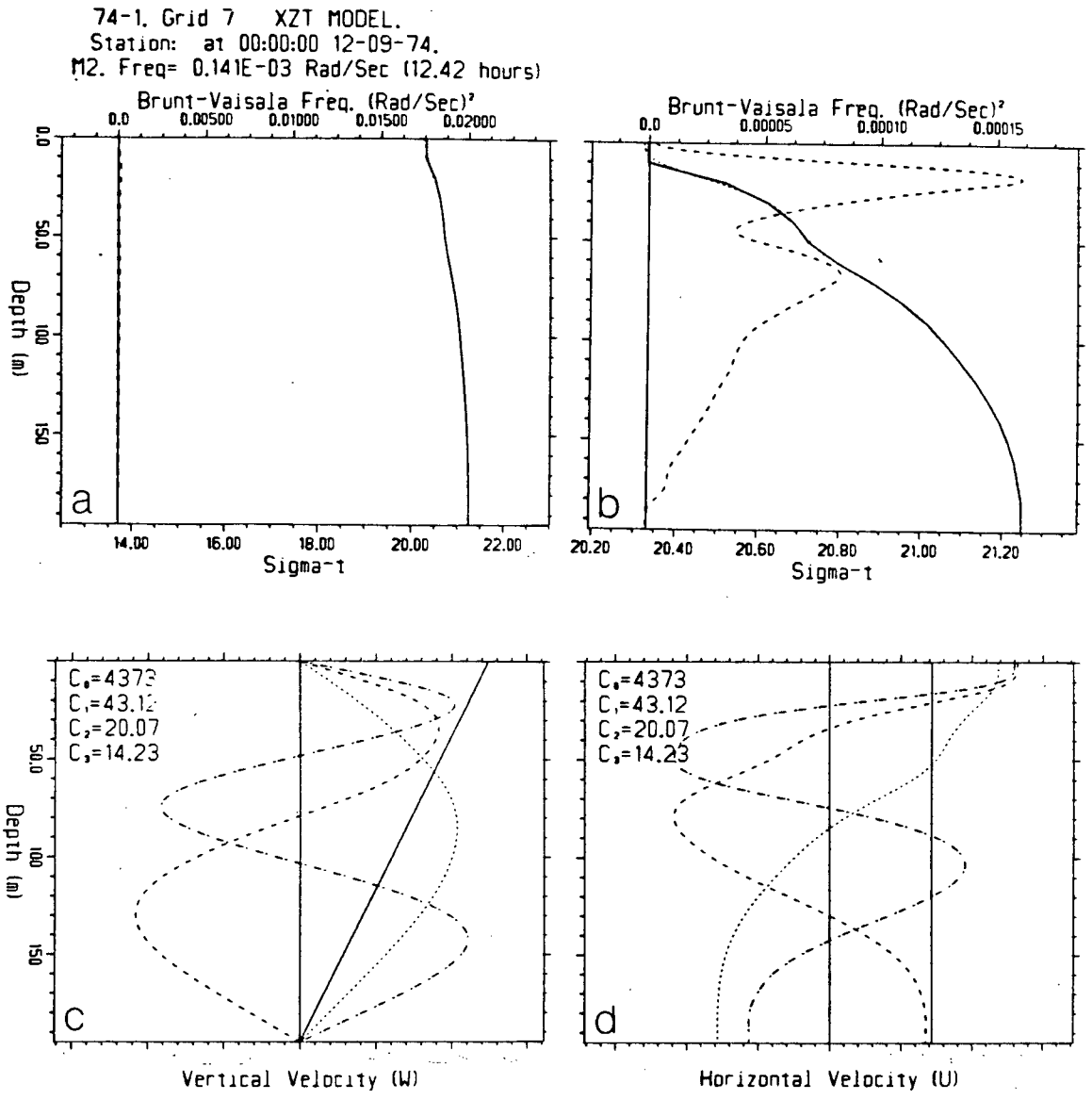

Figure 56. Vertical profiles for model section 7. Plots (a) and (b): N^2 (dashed line) and σ_t (solid line). Plot (c): Vertical modes for w. Plot (d): Vertical modes for u. Phase speeds c_0–c_3 for (c) and (d) are in $cm\,s^{-1}$.

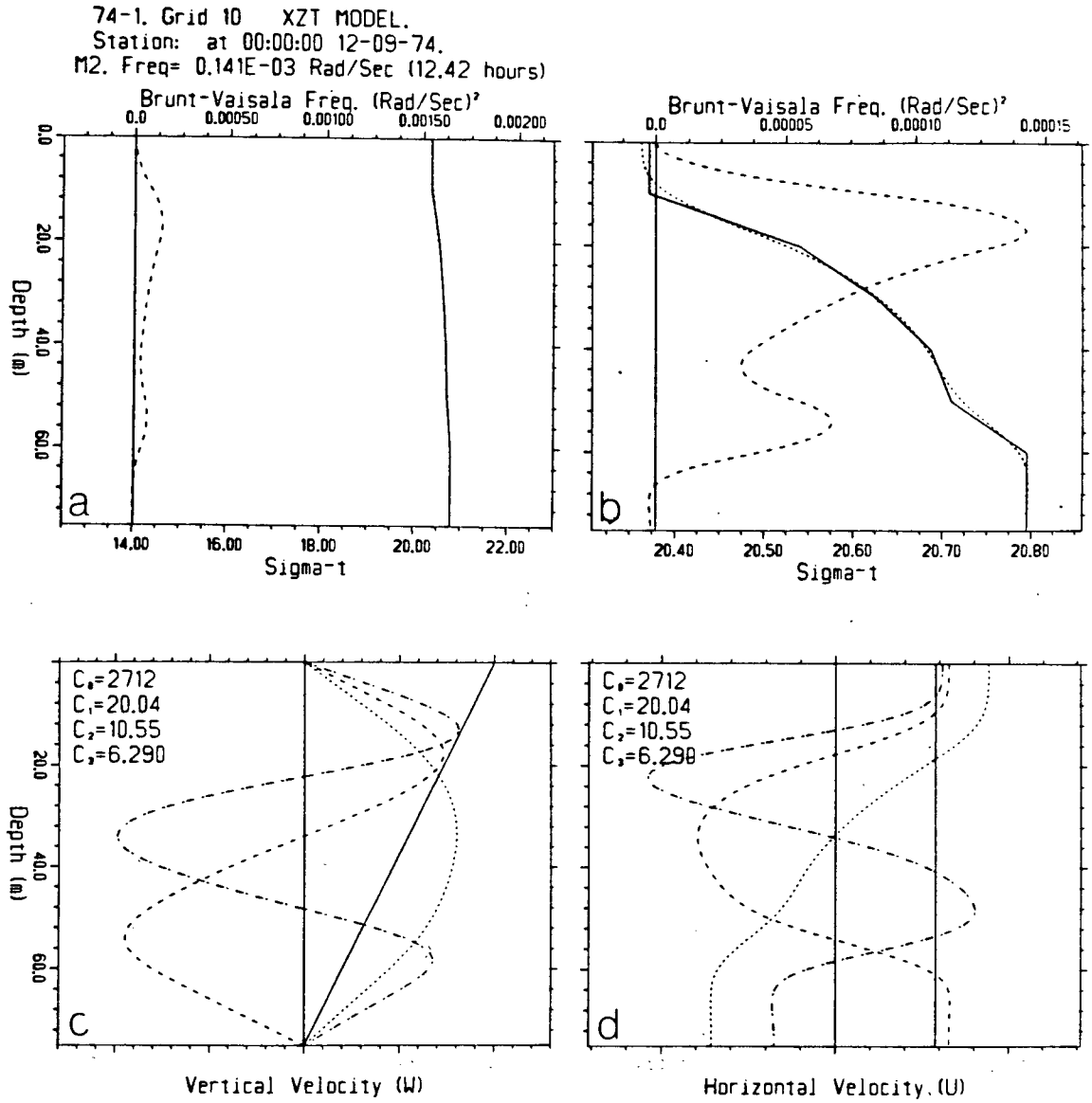

Figure 57. Vertical profiles for model section 10. Plots (a) and (b): N^2 (dashed line) and σ_t (solid line). Plot (c): Vertical modes for w. Plot (d): Vertical modes for u. Phase speeds c_0–c_3 for (c) and (d) are in $cm\,s^{-1}$.

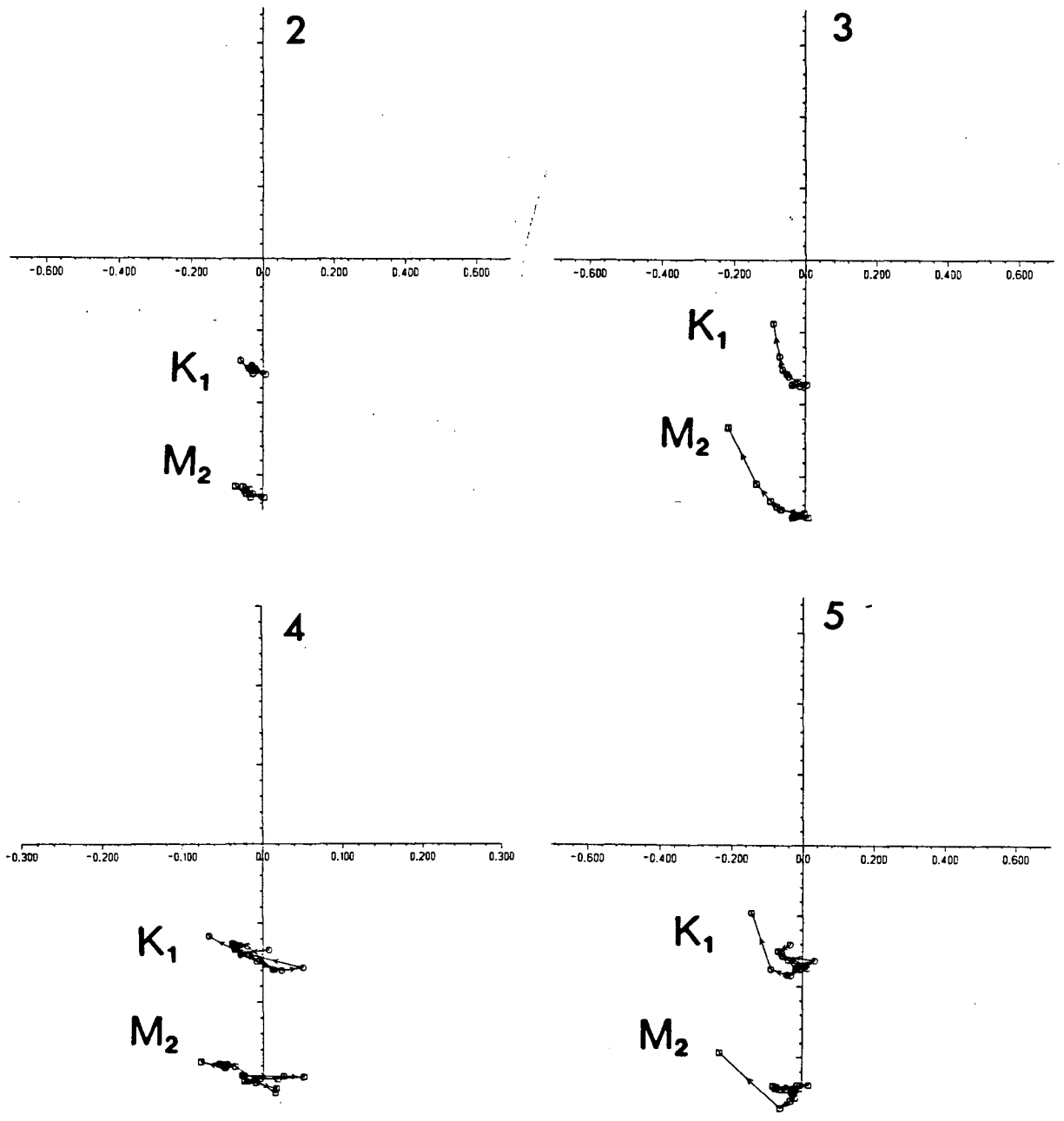

Figure 58. Argand diagrams of depth dependent amplitude (axes ticks indicate the scale in $cm\,s^{-1}$). and phase for M_2 and K_1 constituents at each column in the model from the Class 4 simulation of unstratified flow. Arrows on curves indicate the direction of increasing depth at $10\,m$ intervals from an initial value of $10\,m$.

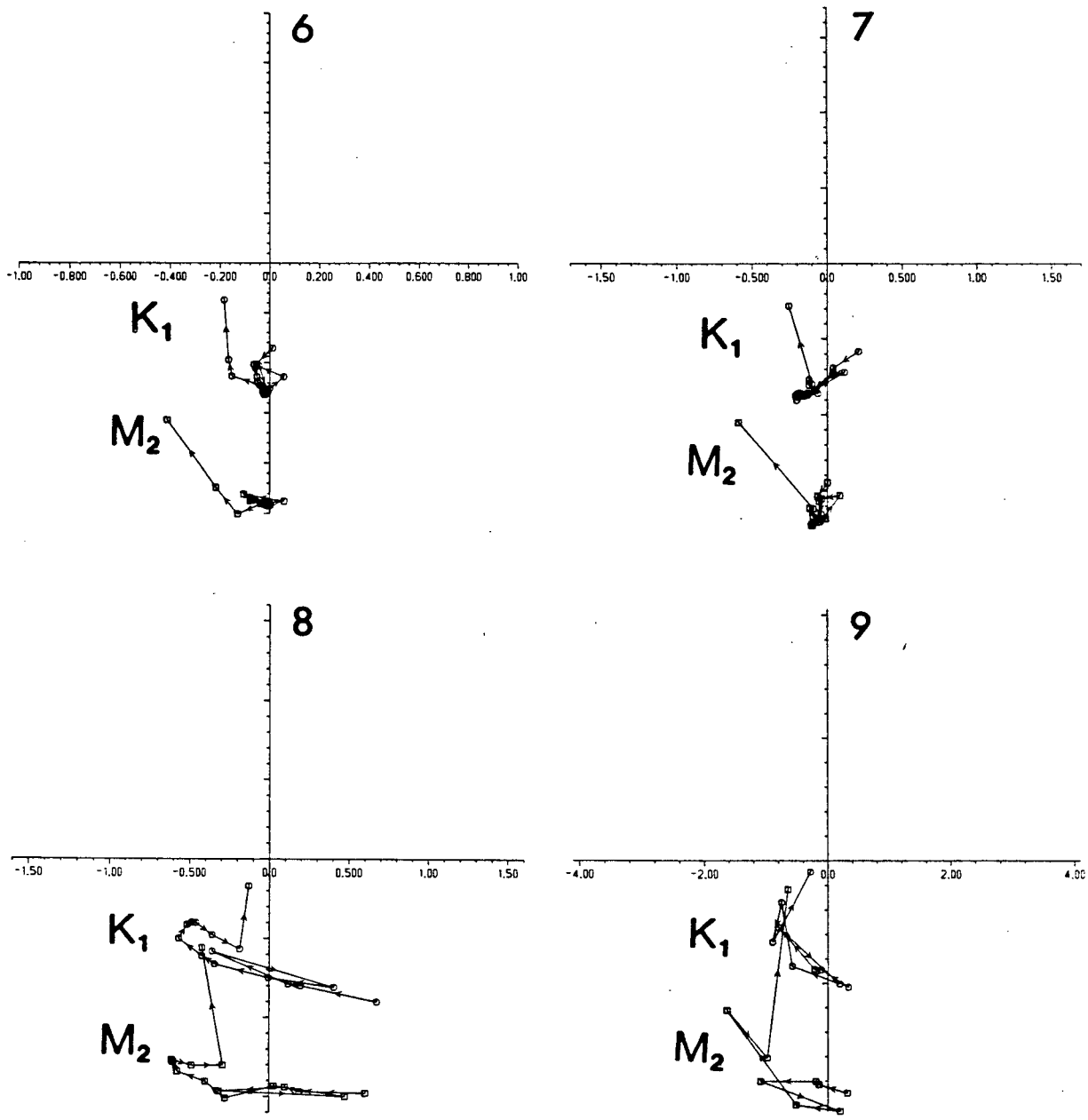

Figure 58(continued)

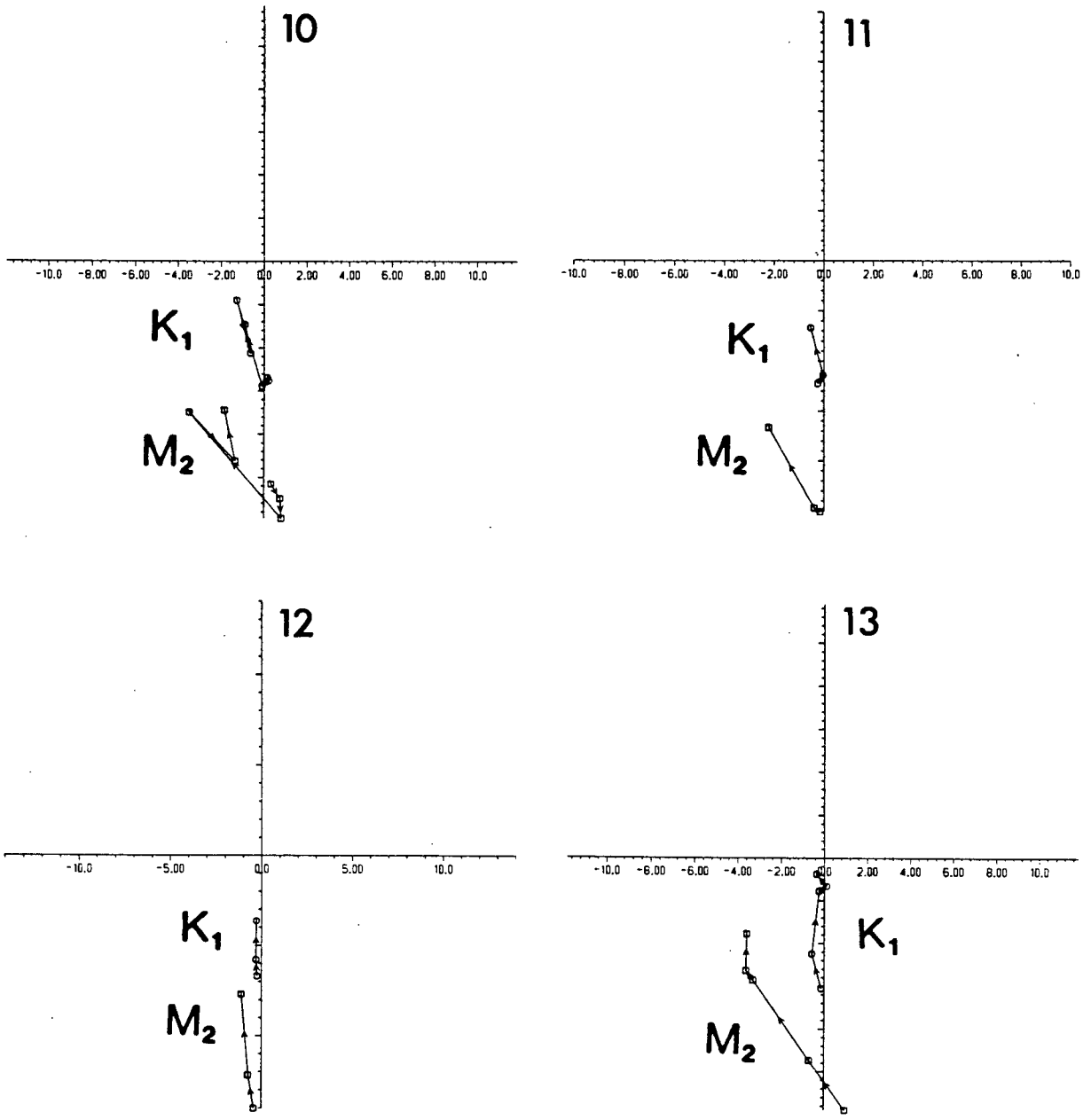

Figure 58(continued)

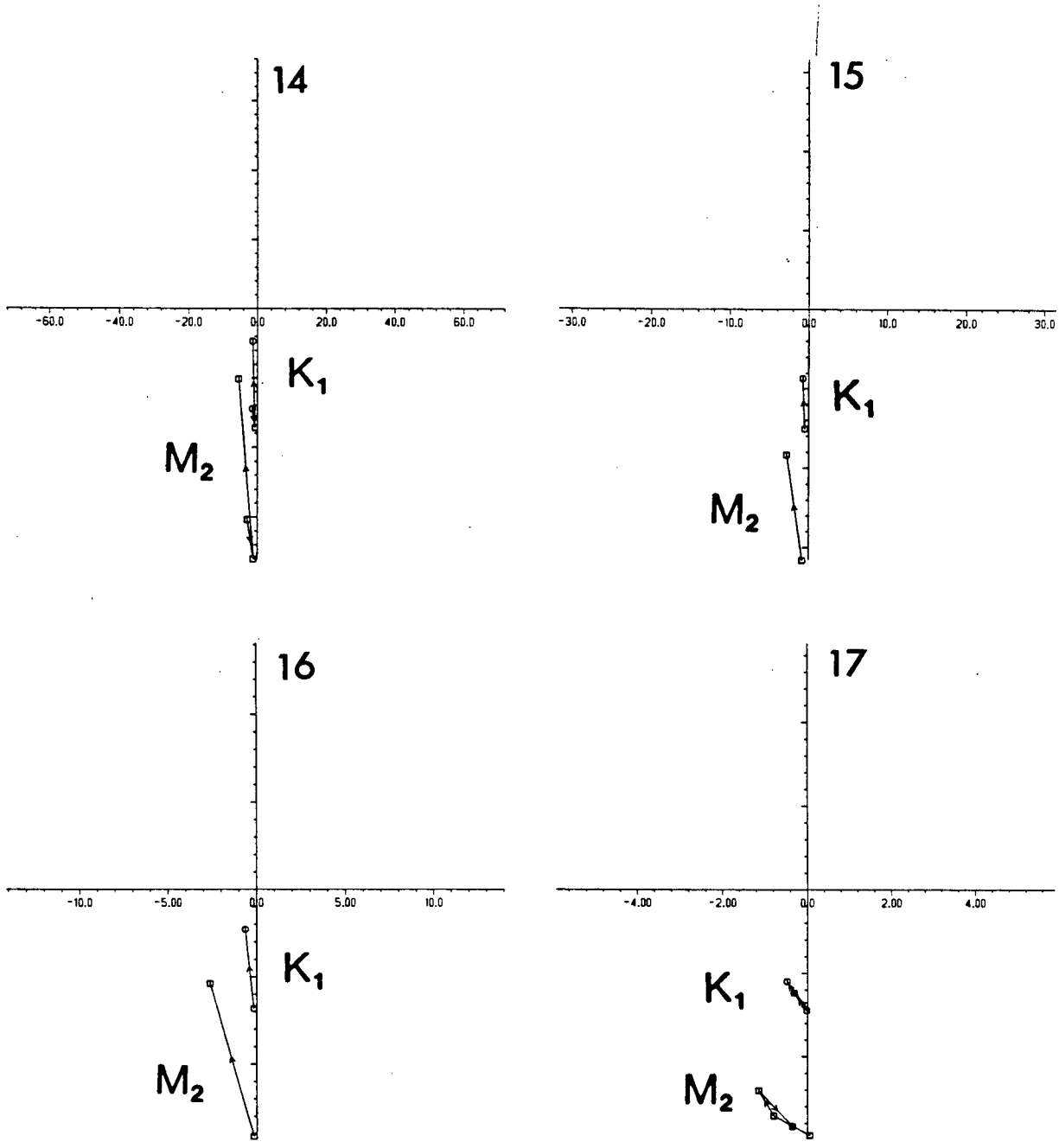

Figure 58(continued)

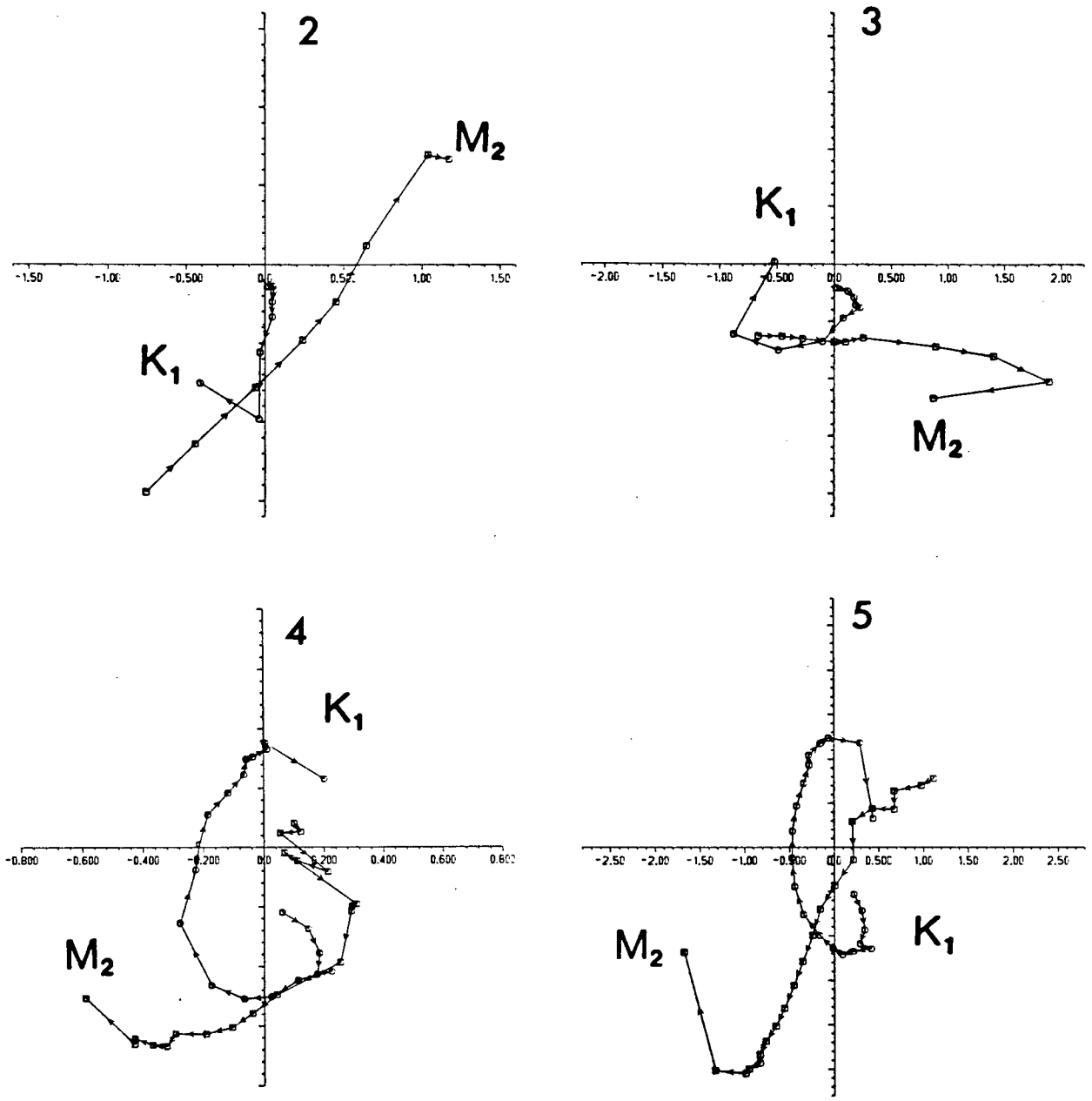

Figure 59. Argand diagrams of depth dependent amplitude (axes ticks indicate the scale in $cm\,s^{-1}$). and phase for M_2 and K_1 constituents at each column in the model from the Class 4 simulation of stratified flow. Arrows on curves indicate the direction of increasing depth at $10\,m$ intervals from an initial value of $10\,m$.

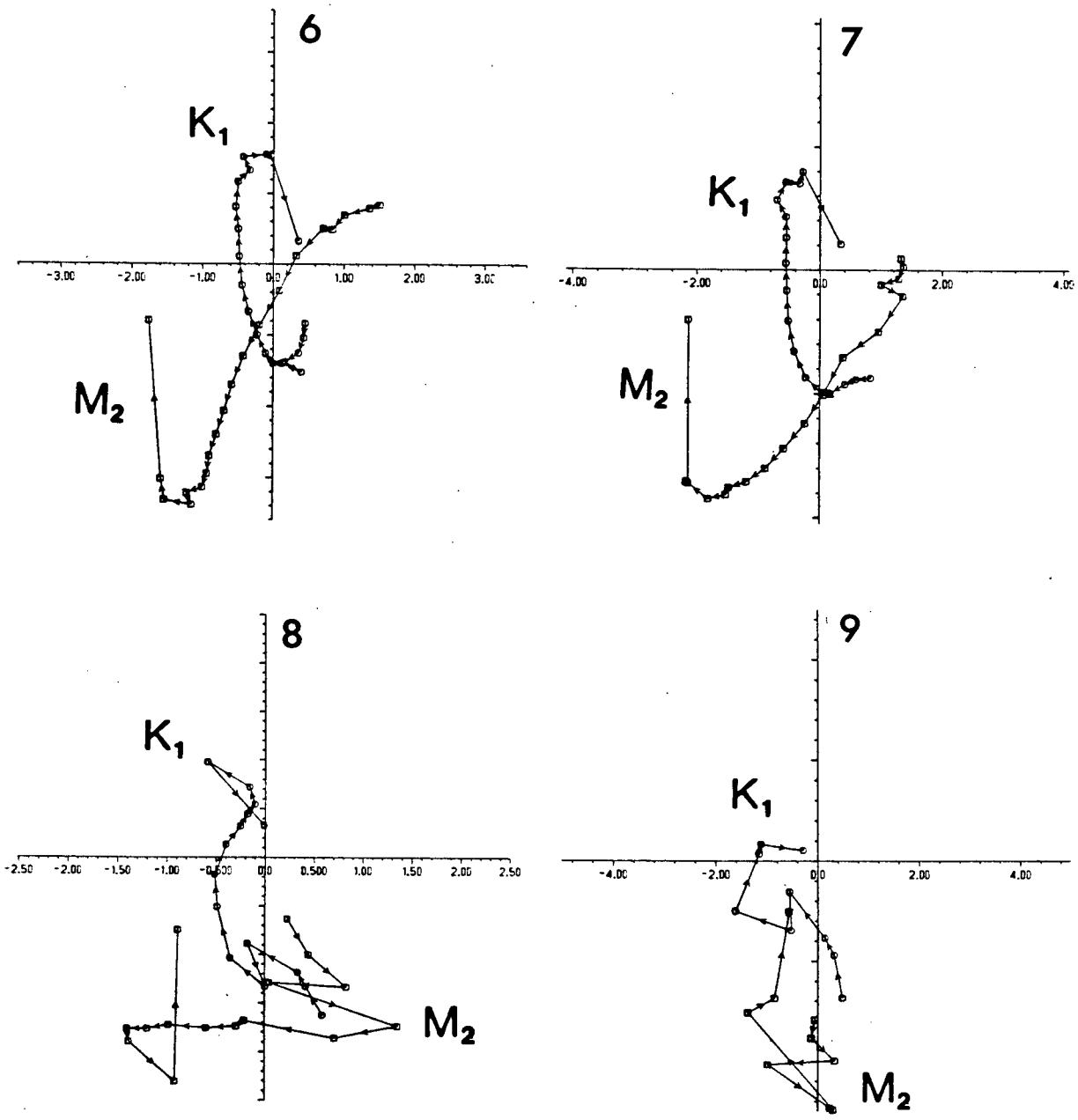

Figure 59(continued)

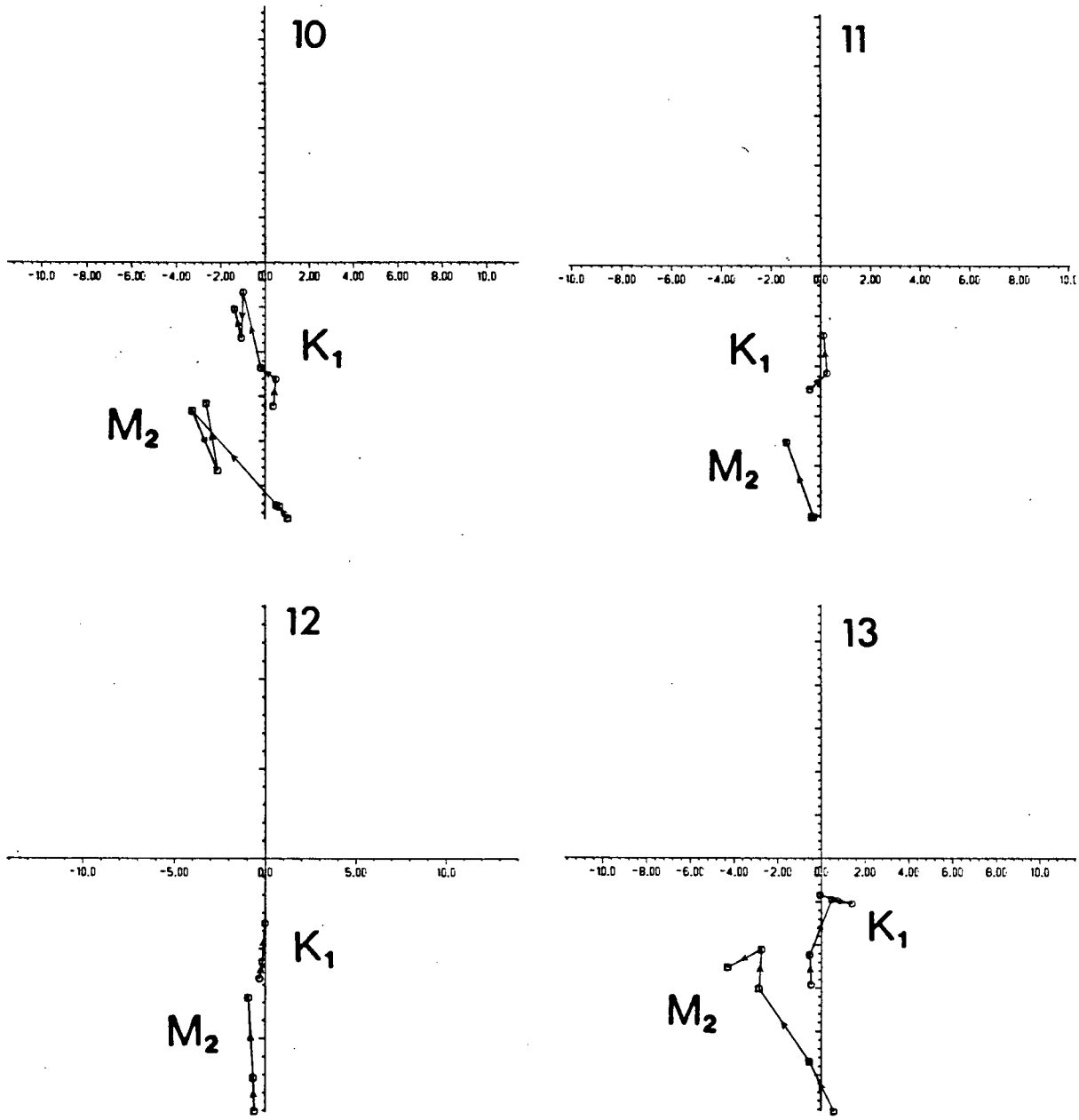

Figure 59(continued)

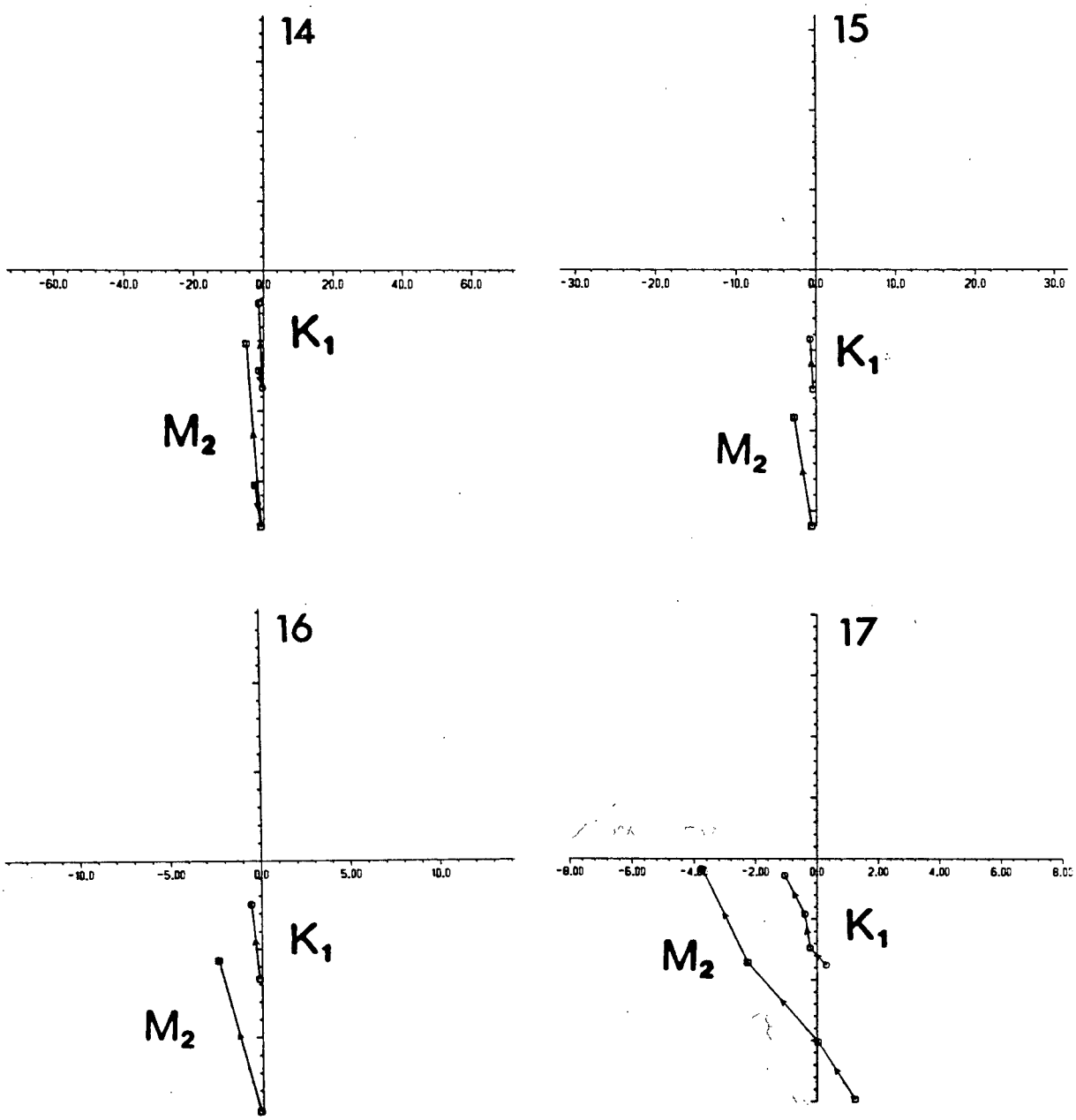

Figure 59(continued)

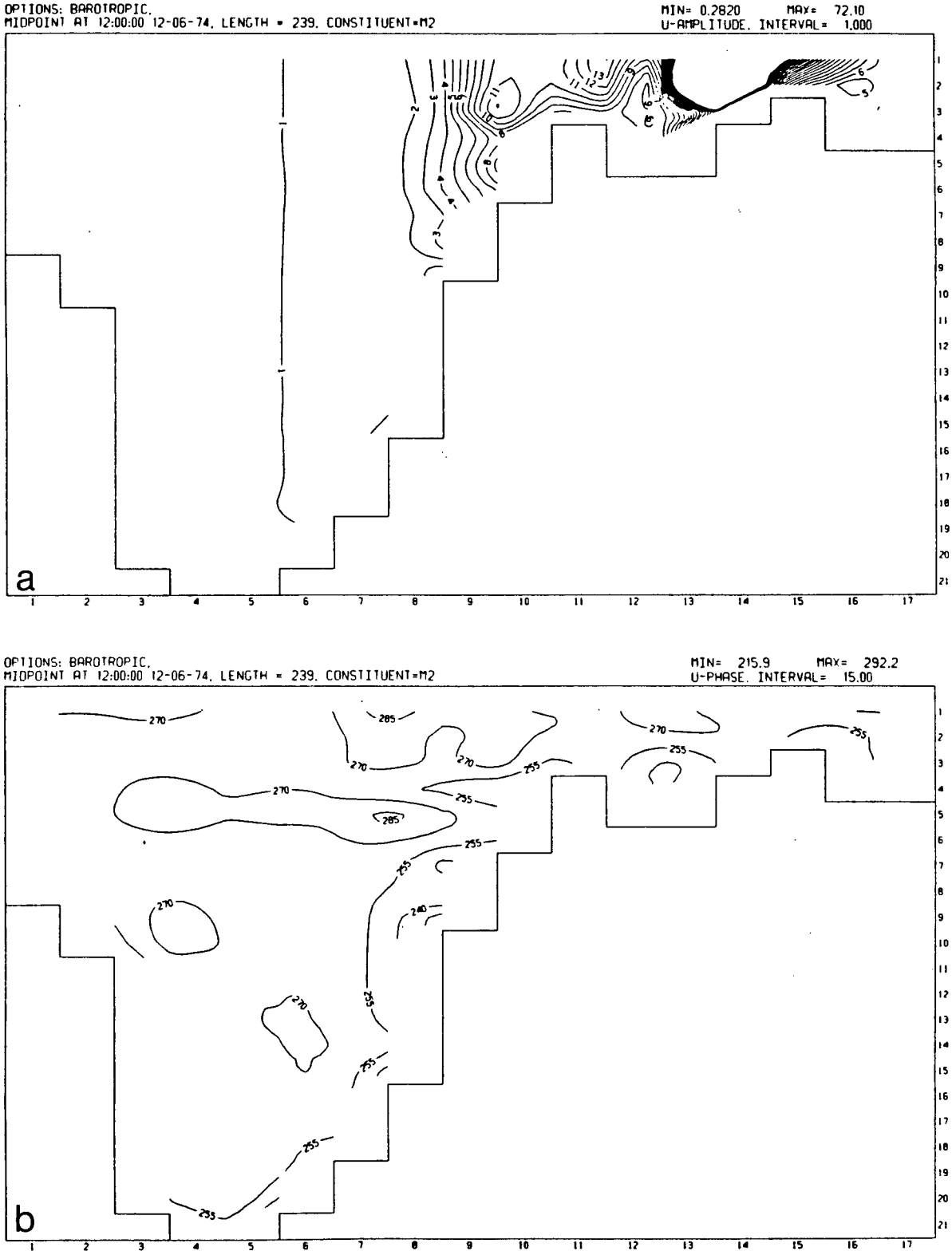

Figure 60. M_2 constituent of horizontal velocity from the Class 4 simulation of unstratified flow in Indian Arm and Burrard Inlet. Plot (a): Amplitude contours ($cm\,s^{-1}$) Plot (b): phase contours (degrees)

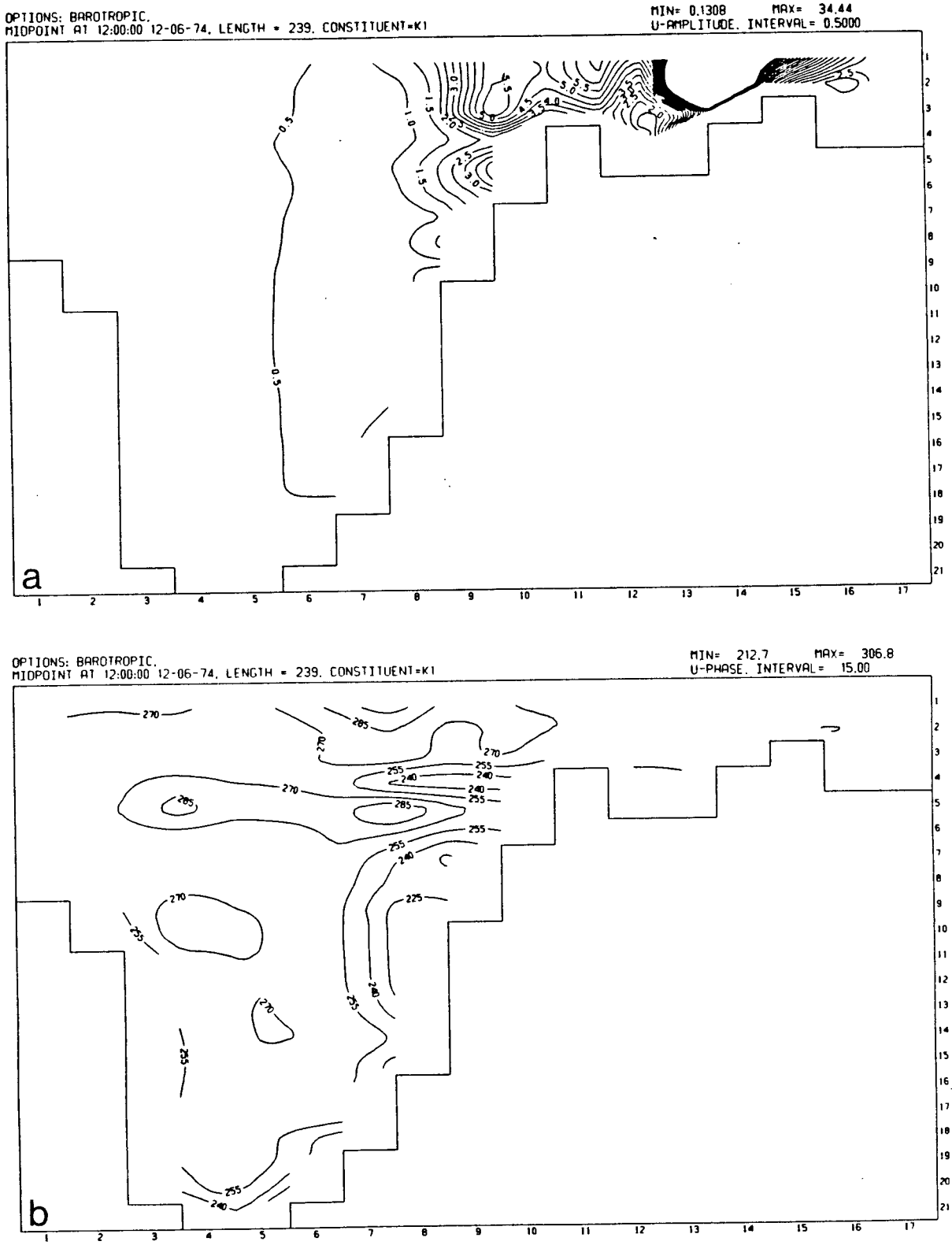

Figure 61. K_1 constituent of horizontal velocity from the Class 4 simulation of unstratified flow in Indian Arm and Burrard Inlet. Plot (a): Amplitude contours ($cm\,s^{-1}$) Plot (b): phase contours (degrees)

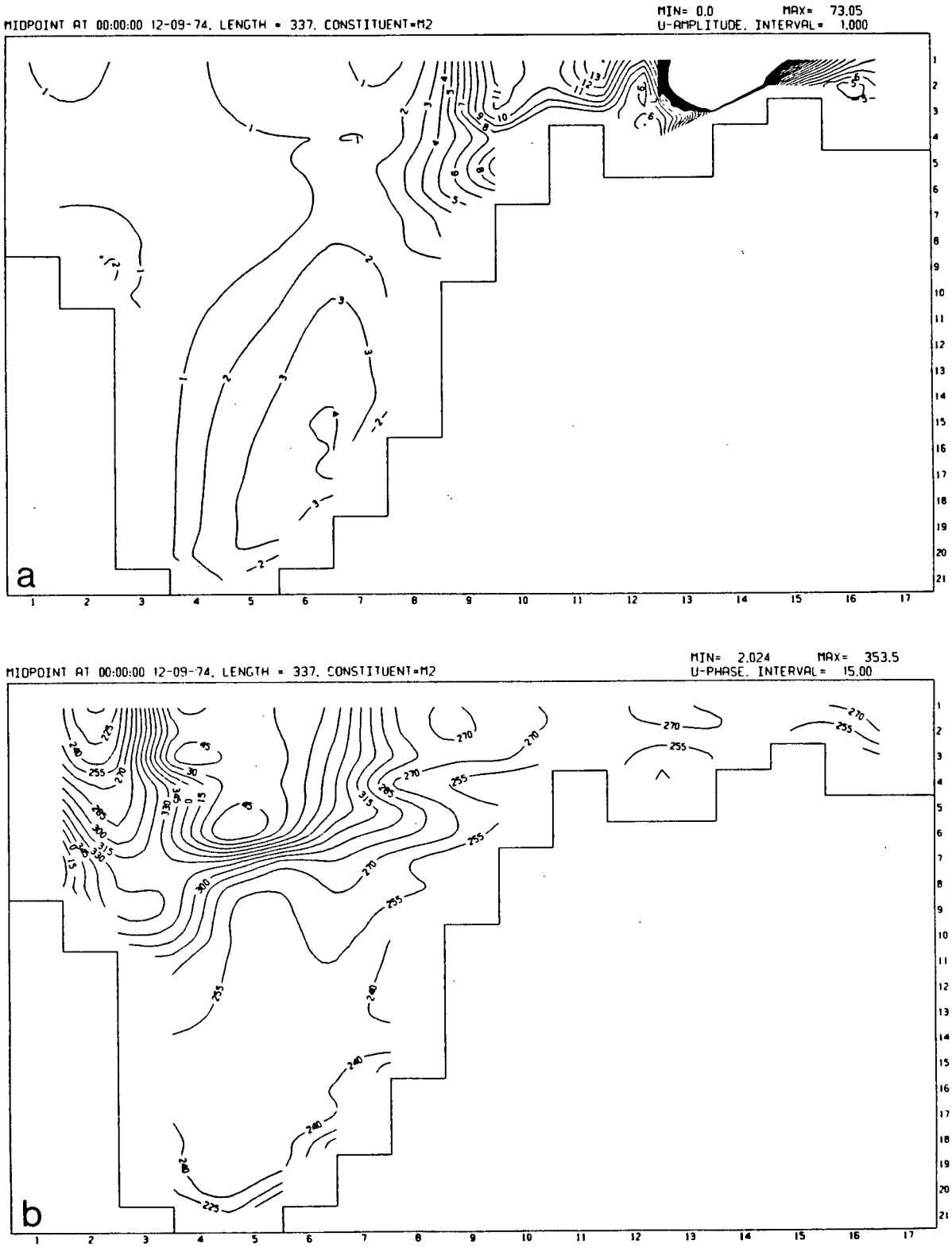

Figure 62. M_2 constituent of horizontal velocity from the Class 4 simulation of stratified flow in Indian Arm and Burrard Inlet. Plot (a): Amplitude contours ($cm\,s^{-1}$) Plot (b): phase contours (degrees)

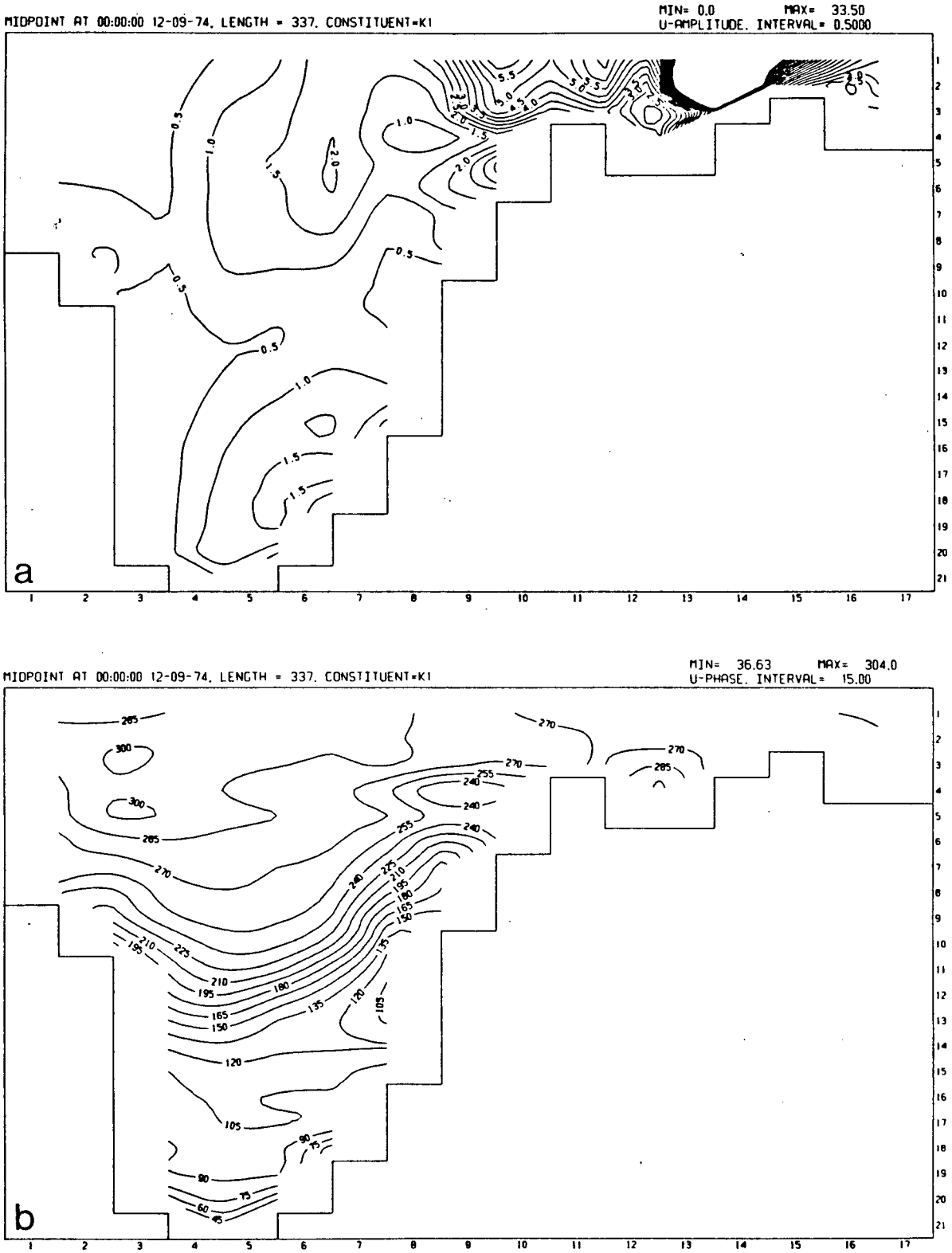

Figure 63. K_1 constituent of horizontal velocity from the Class 4 simulation of stratified flow in Indian Arm and Burrard Inlet. Plot (a): Amplitude contours ($cm\,s^{-1}$) Plot (b): phase contours (degrees)

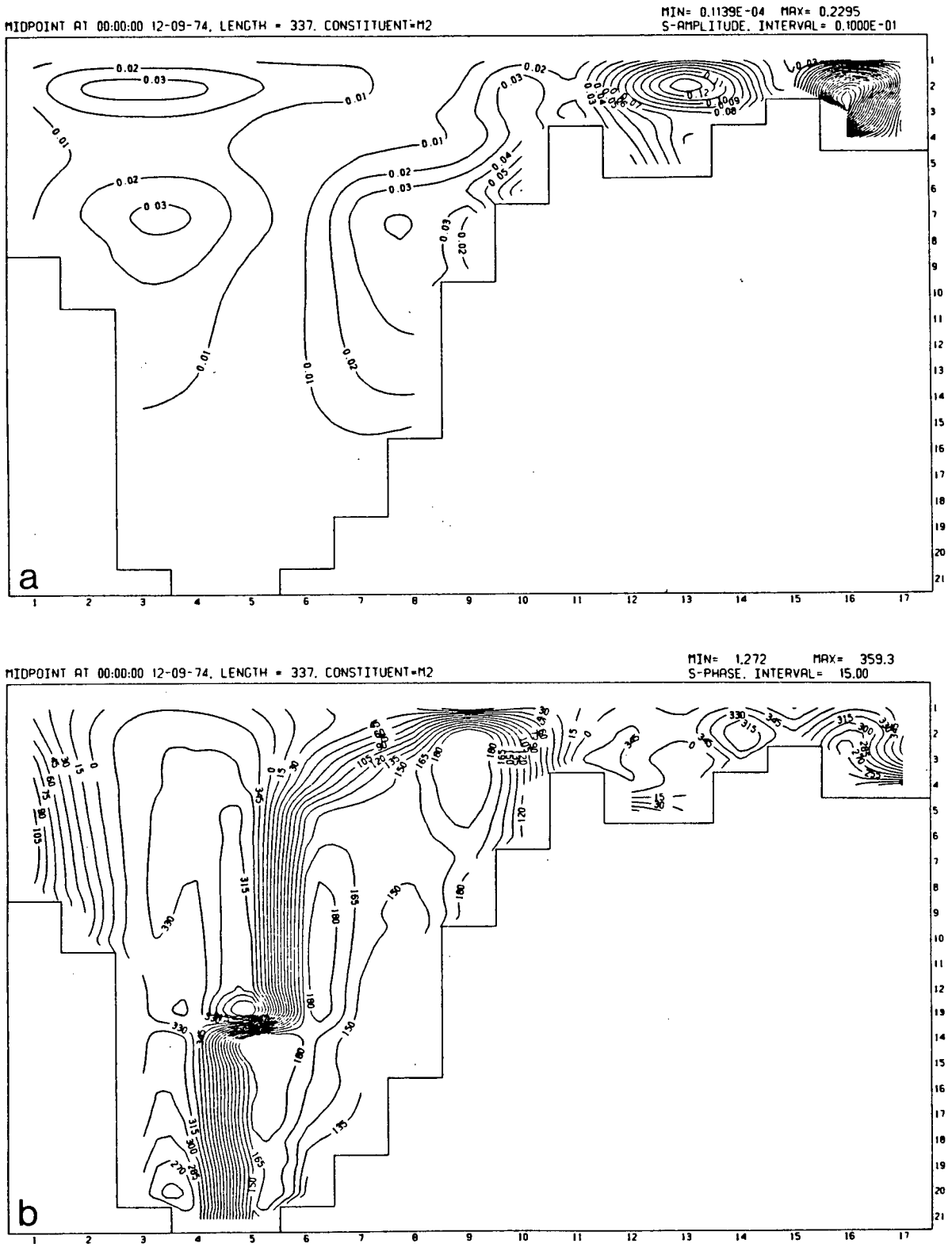

Figure 64. M_2 constituent of salinity from the Class 4 simulation of stratified flow in Indian Arm and Burrard Inlet. Plot (a): Amplitude contours ($cm\,s^{-1}$) Plot (b): phase contours (degrees)

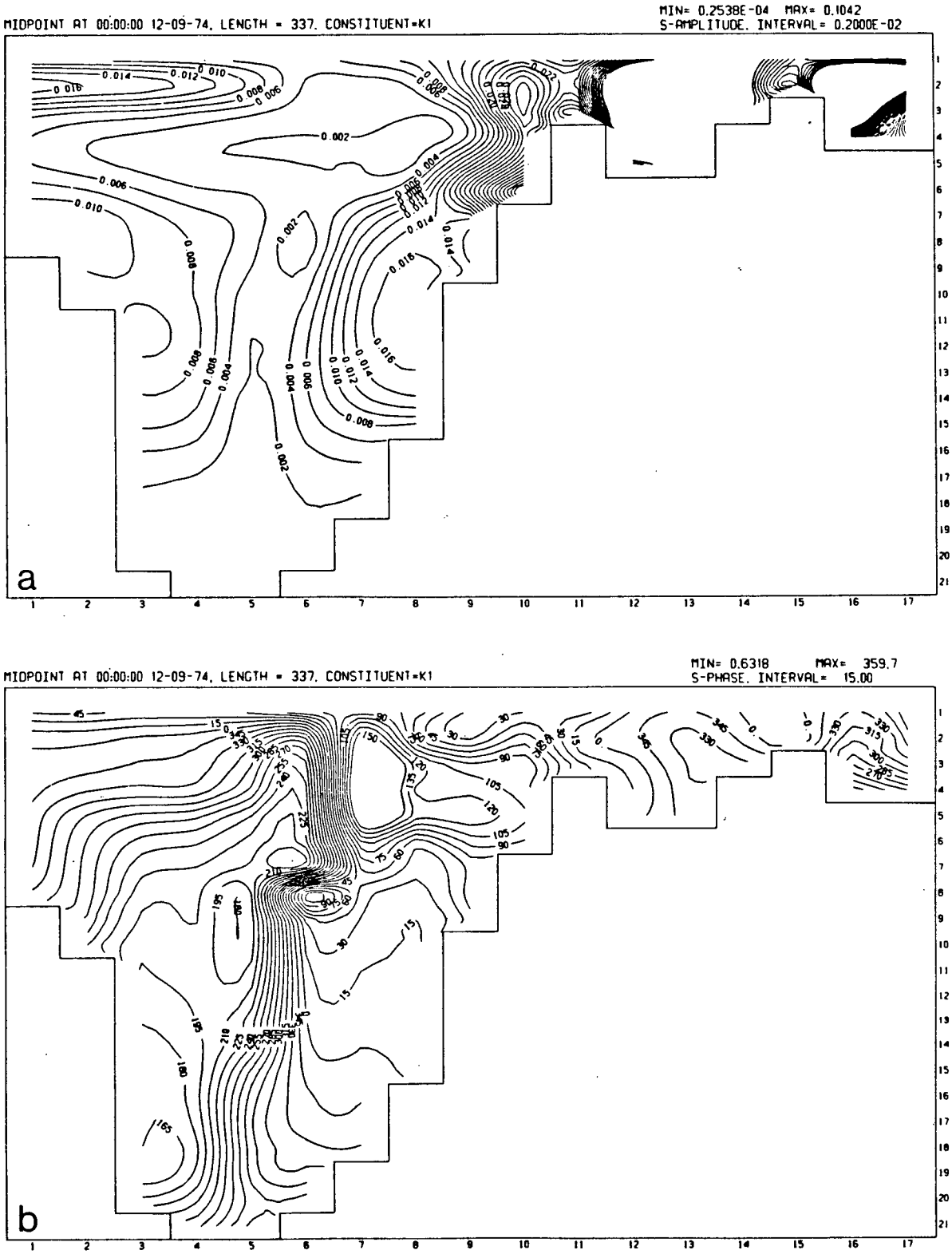

Figure 65. K_1 constituent of salinity from the Class 4 simulation of stratified flow in Indian Arm and Burrard Inlet. Plot (a): Amplitude contours ($cm\,s^{-1}$) Plot (b): phase contours (degrees)

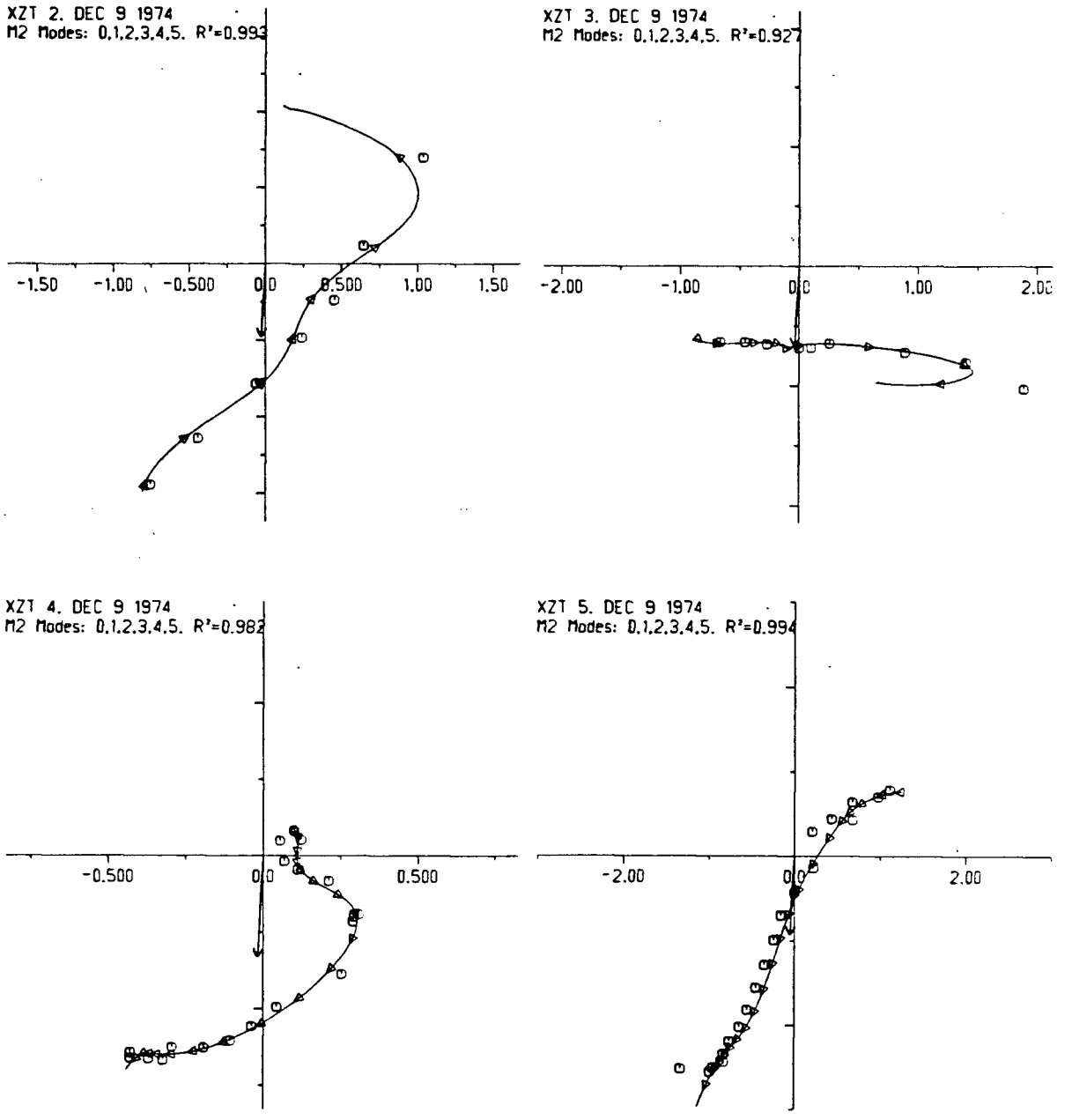

Figure 66. Argand diagrams of depth dependent amplitude (axes ticks indicate the scale in $cm\,s^{-1}$). and phase for the M_2 constituent of horizontal velocity from the Class 4 simulation of stratified circulation in Indian Arm and Burrard Inlet. Circles indicate harmonic constants from an initial depth of $10\,m$ at $10\,m$ intervals. Triangles — and solid lines connecting them — represent a least-squares fit of vertical modes. The vector indicates the barotropic mode. Note varying amplitude scale.

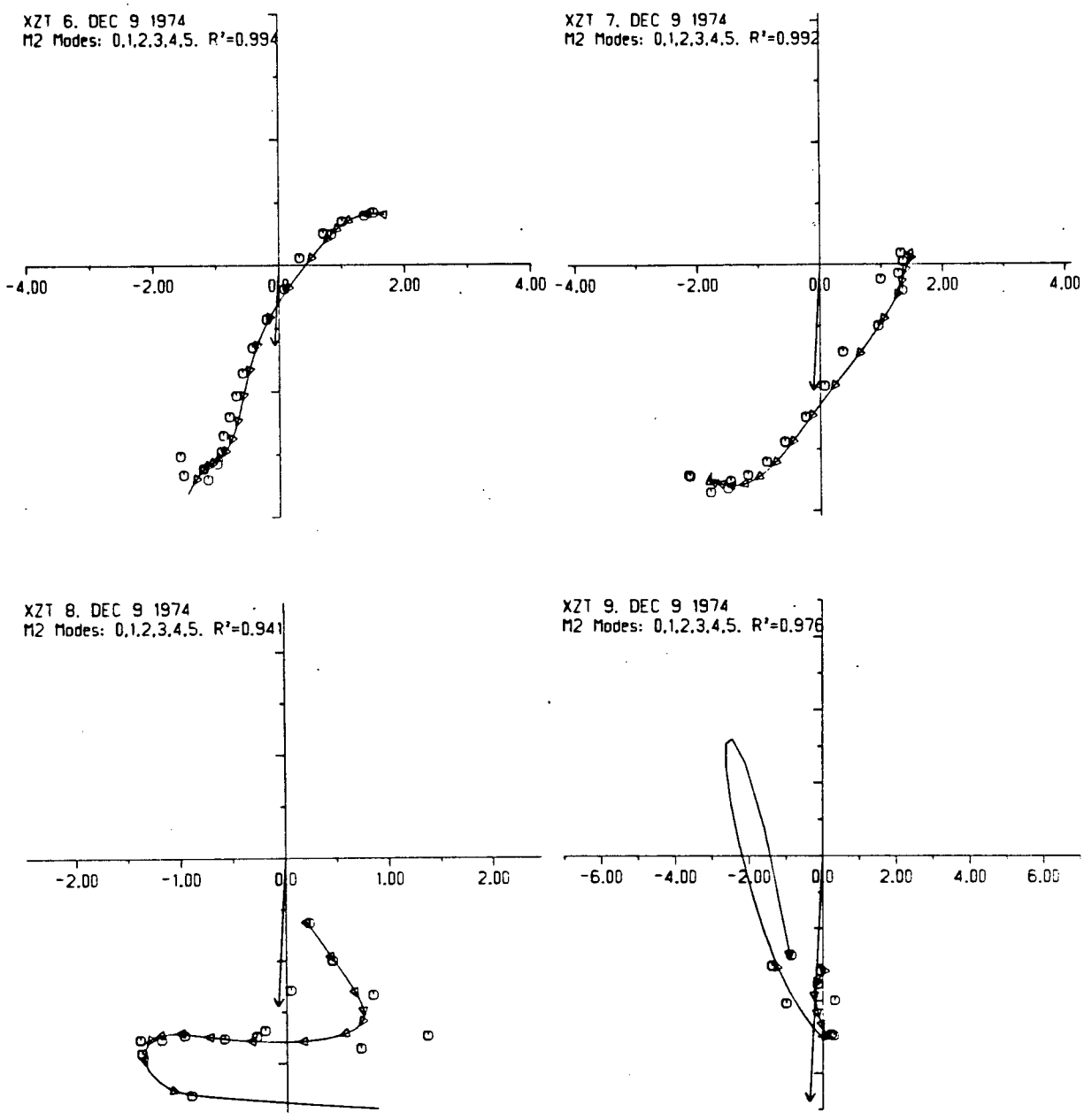

Figure 66(continued)

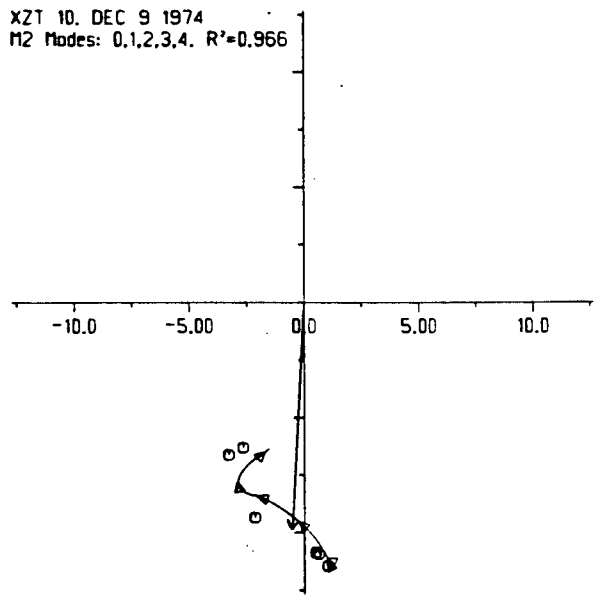

Figure 66(continued)

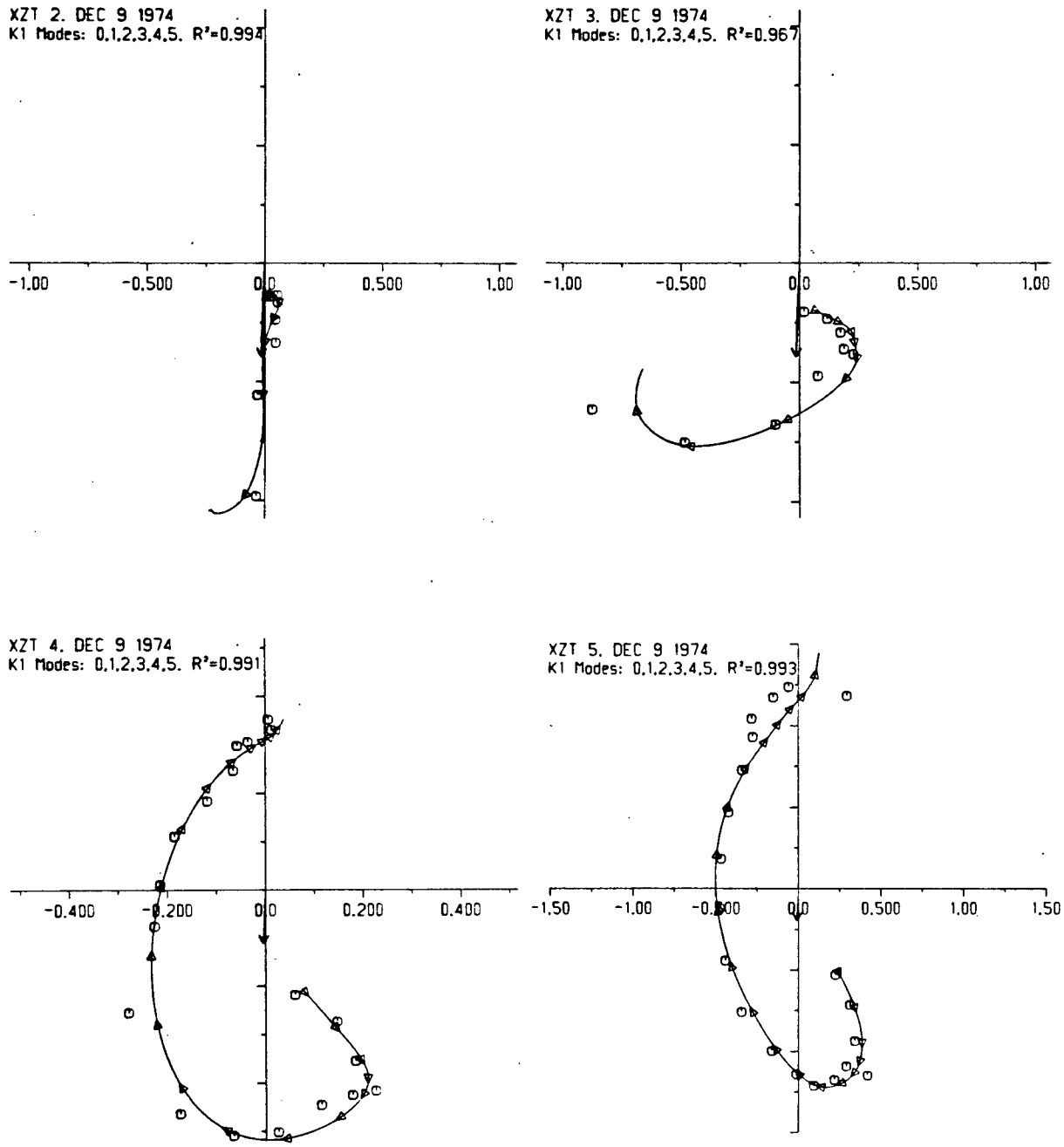

Figure 67. Argand diagrams of depth dependent amplitude (axes ticks indicate the scale in $cm\,s^{-1}$). and phase for the K_1 constituent of horizontal velocity from the Class 4 simulation of stratified circulation in Indian Arm and Burrard Inlet. Circles indicate harmonic constants from an initial depth of $10\,m$ at $10\,m$ intervals. Triangles — and solid lines connecting them — represent a least-squares fit of vertical modes. The vector indicates the barotropic mode. Note varying amplitude scale.

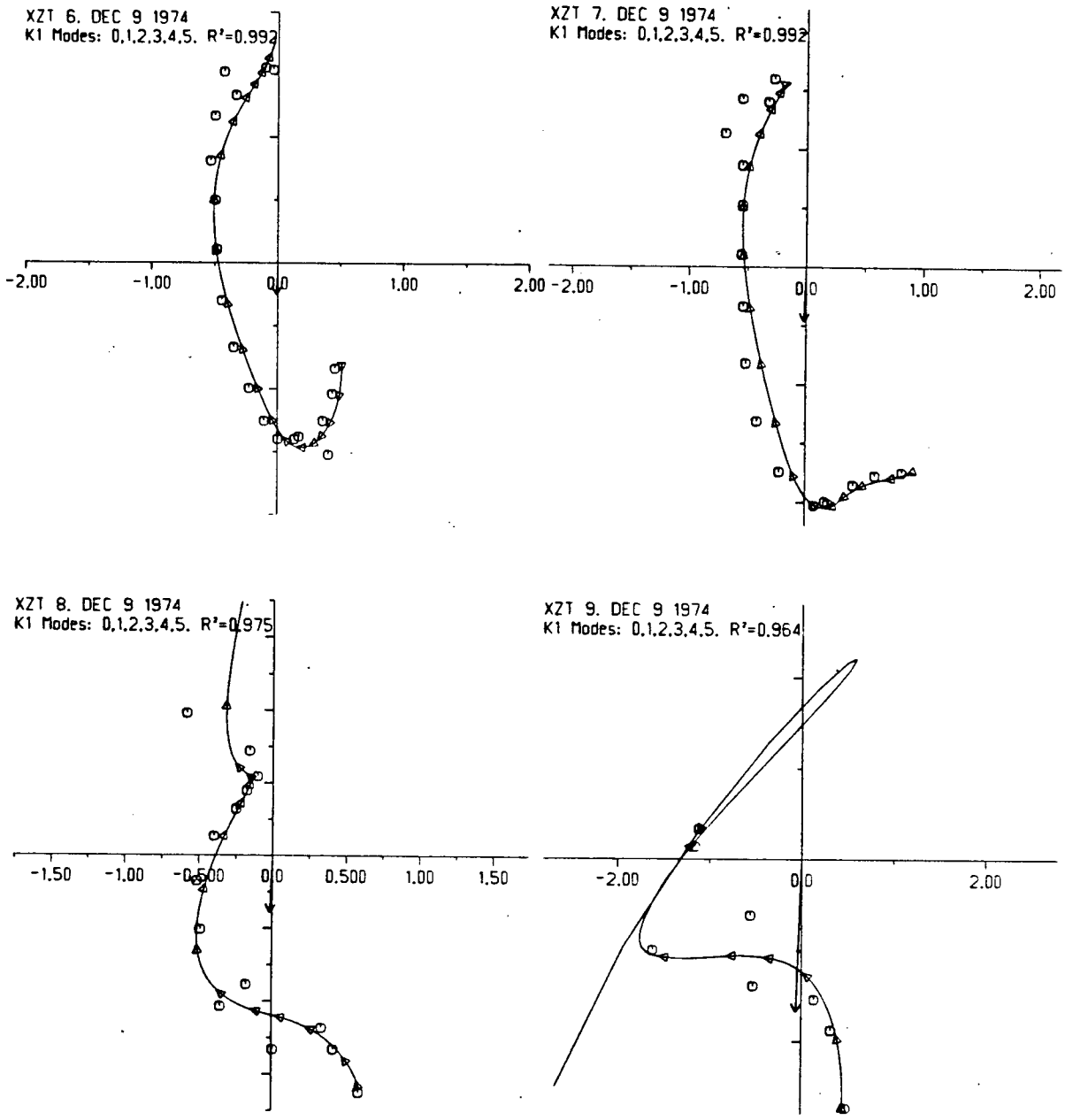

Figure 67(continued)

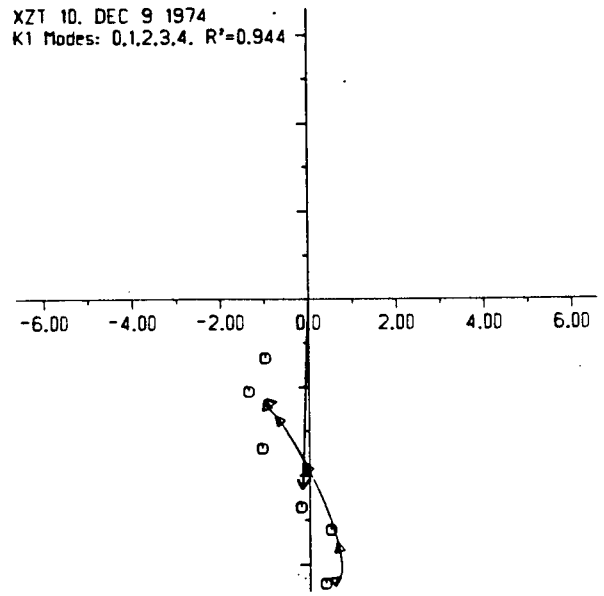

Figure 67(continued)

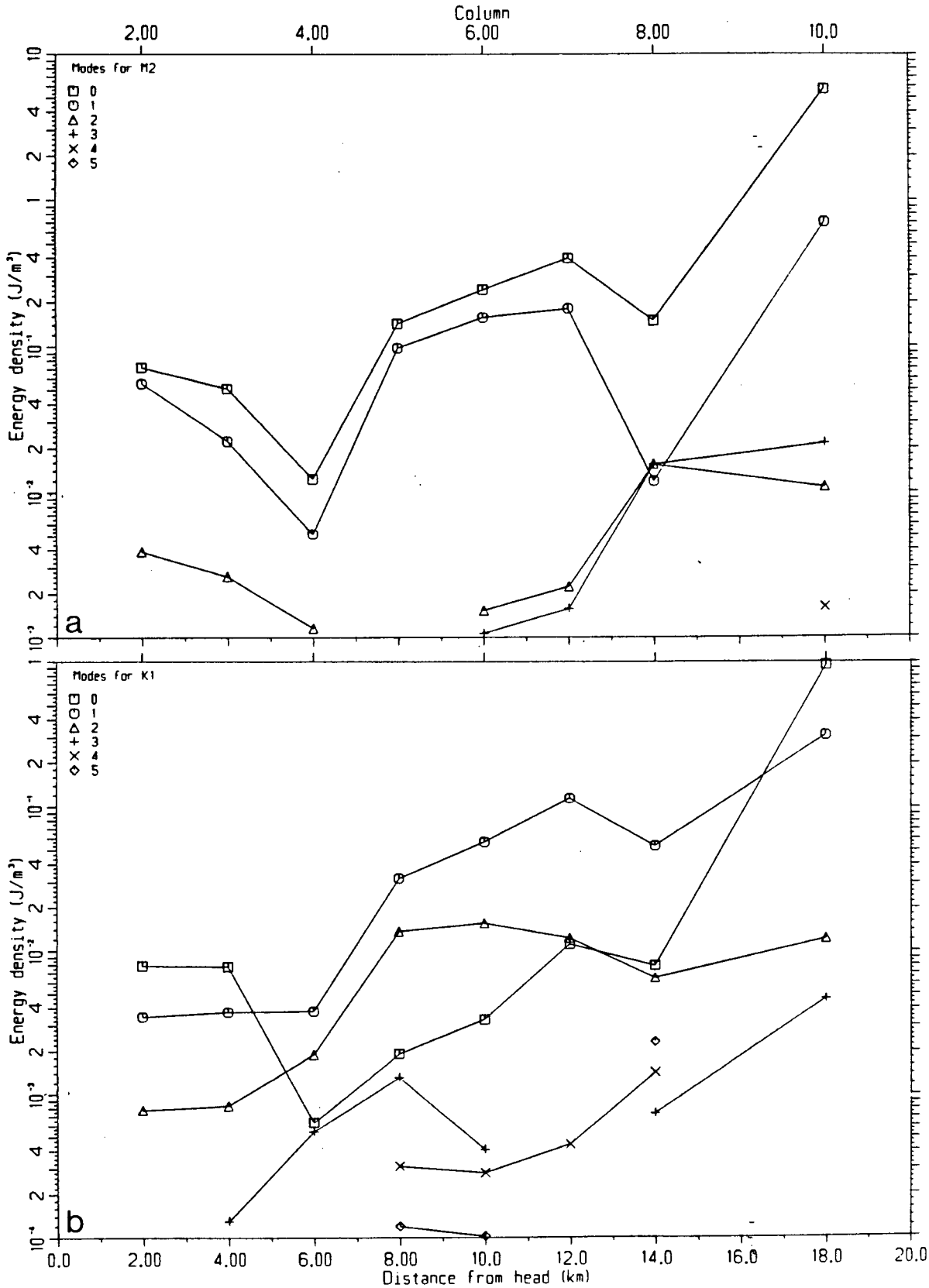

Figure 68. Kinetic energy in the barotropic, and first five baroclinic modes at columns 2–10 in the model based on the least-squares fit to harmonic analysis. Plot (a): M_2. Plot (b): K_1.

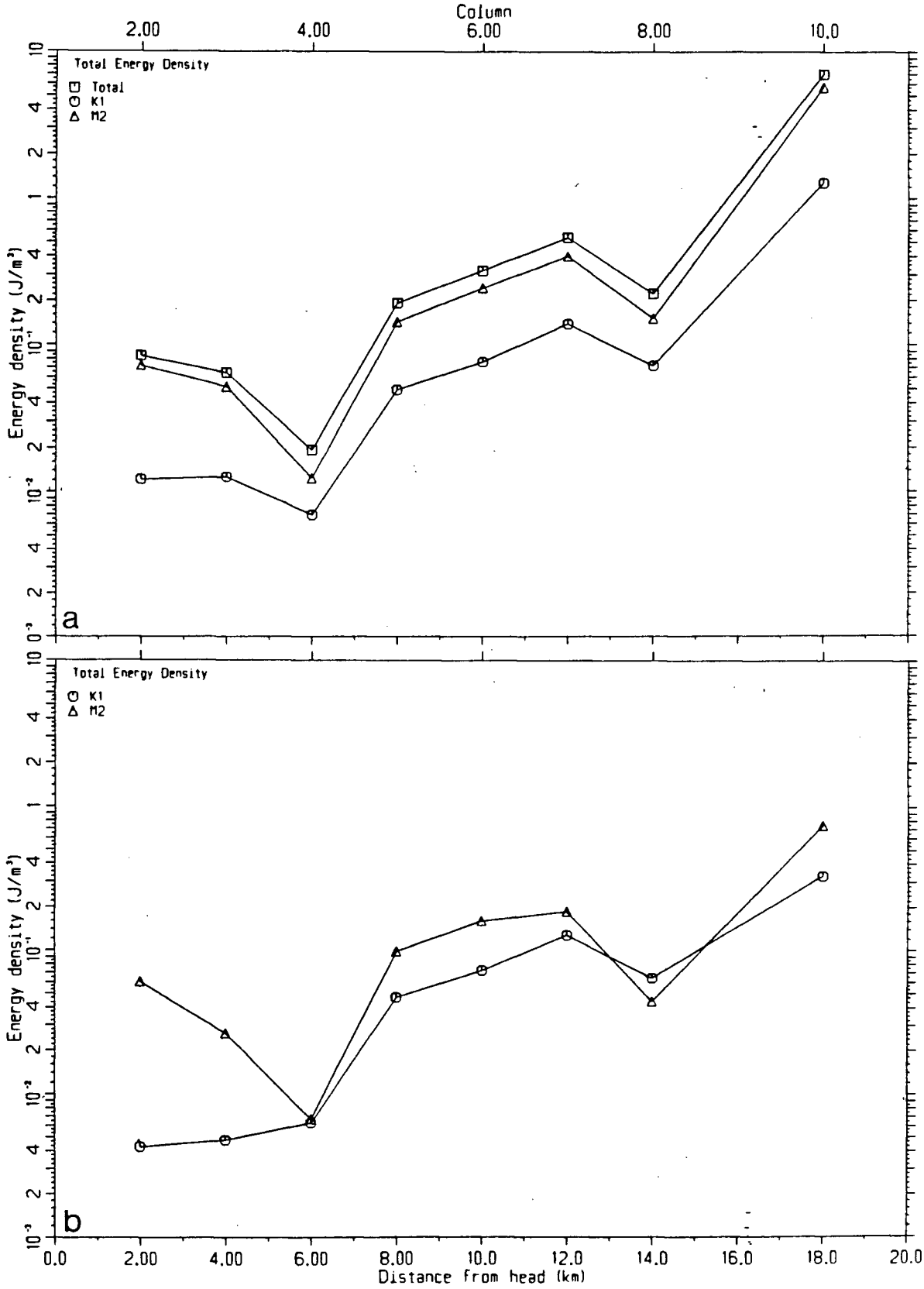

Figure 69. Total kinetic energy, and kinetic energy for each constituent at columns 2–10 in the model based on the least-squares fit to harmonic analysis. Plot (a): including barotropic mode. Plot (b): excluding barotropic mode.

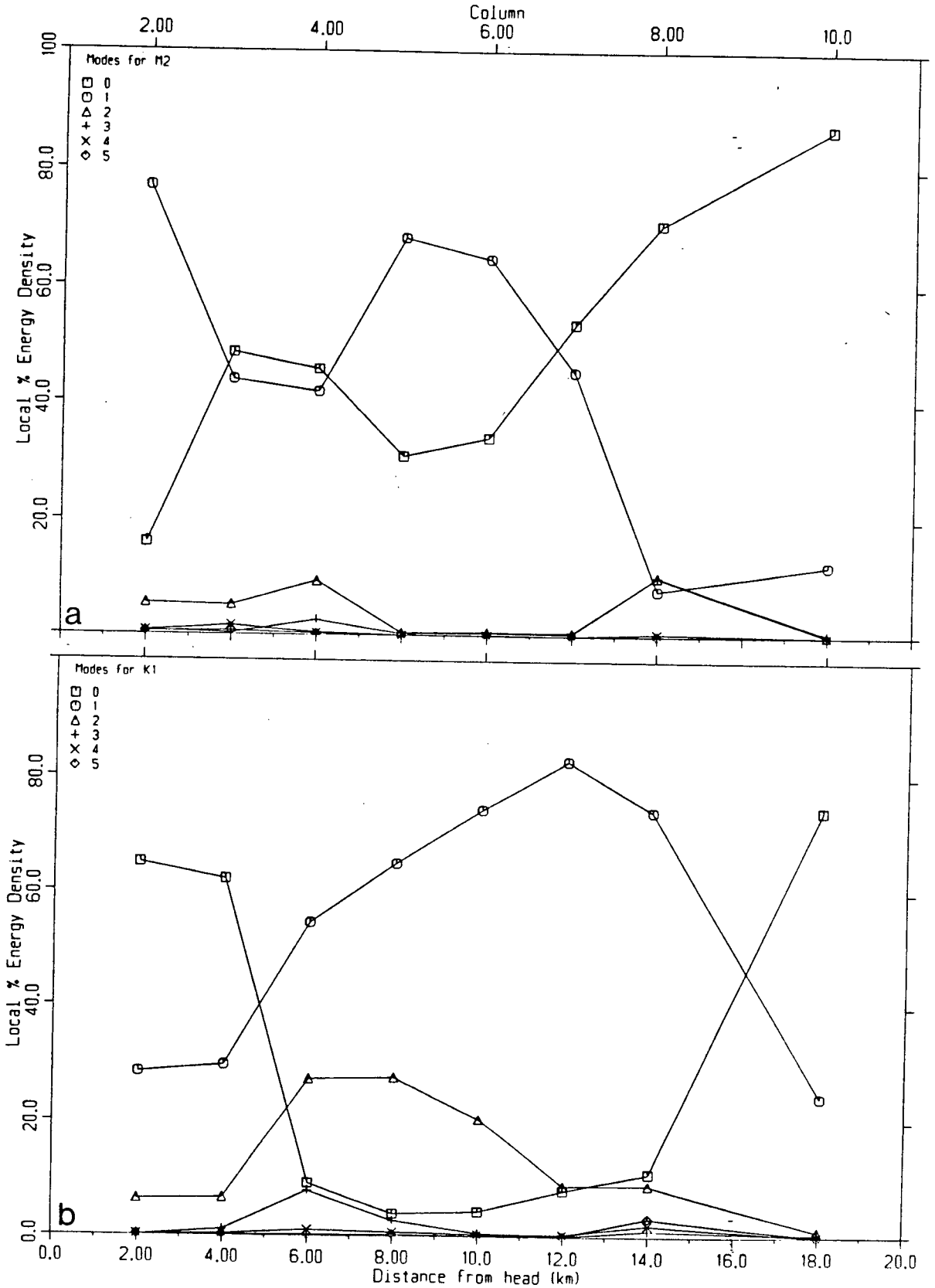

Figure 70. Percentage of kinetic energy in the barotropic, and first five baroclinic modes at columns 2–10 in the model based on the least-squares fit to harmonic analysis. Plot (a): M_2. Plot (b): K_1.

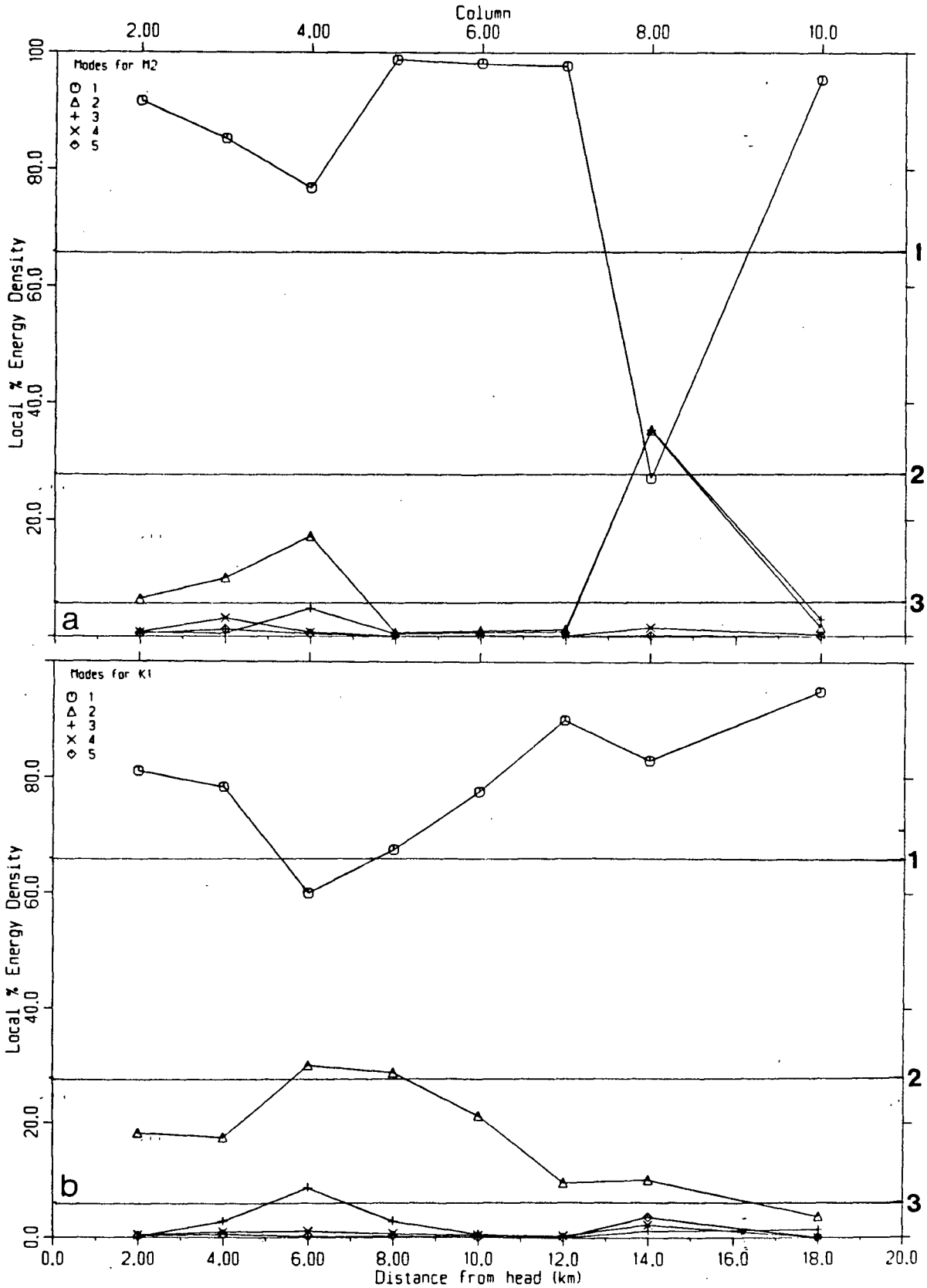

Figure 71. Percentage of kinetic energy in the first five baroclinic modes at columns 2–10 in the model based on the least-squares fit to harmonic analysis (less the barotropic contribution). Horizontal lines indicate theoretical levels for each mode — identified on the right of the diagram (*Stigebrandt*, 1981). Plot (a): M_2. Plot (b): K_1.

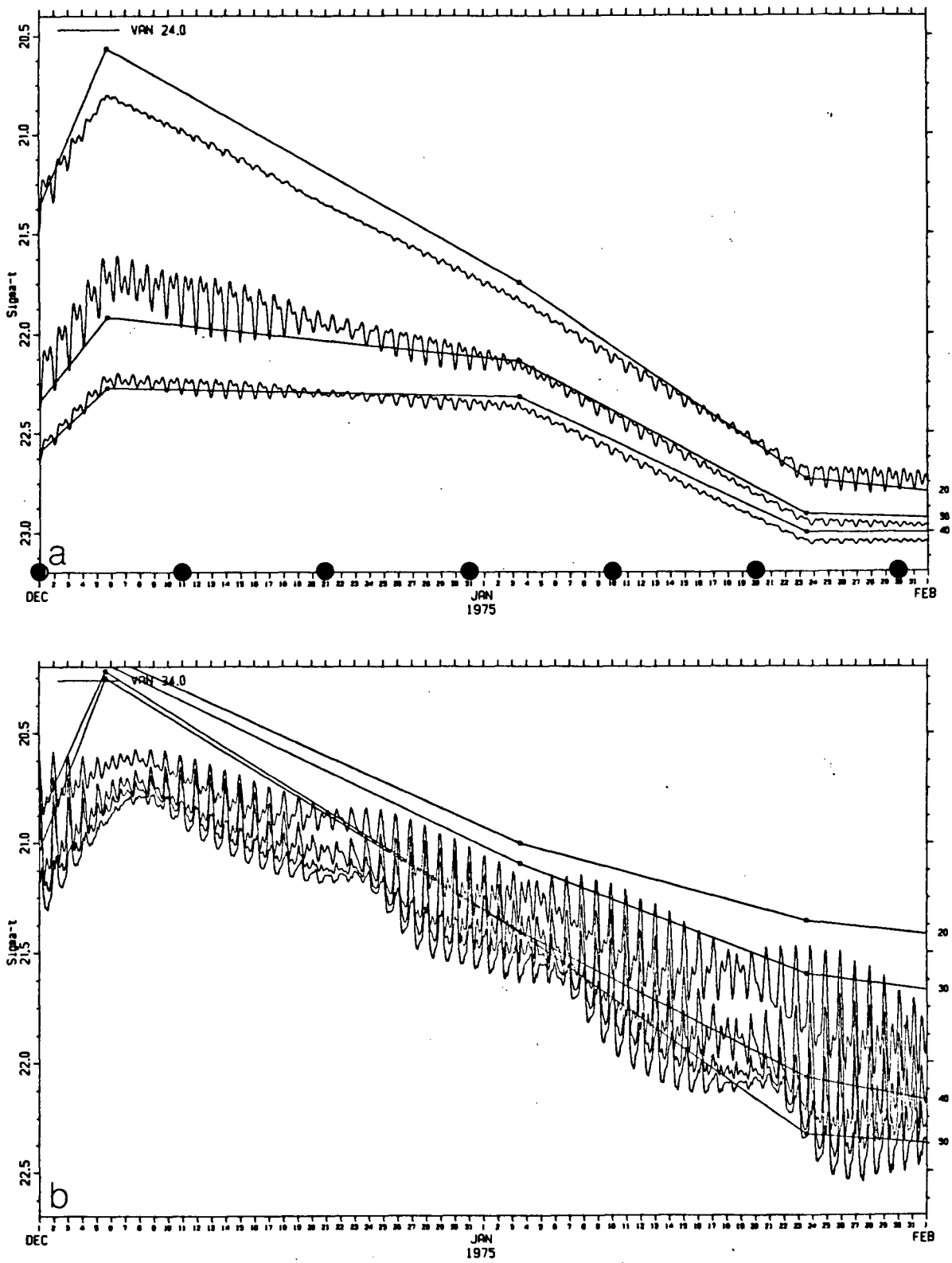

Figure 72. Time series (straight lines) of σ_t at four standard stations (located in *figures* 1 and 3) together with corresponding values from the model (fluctuating lines). Depths (m) are shown at right. Note change in vertical scale between plots. Circles on (a) and (c) indicate times of plots in *figure* 74. Plot (a): Van-24 (the open boundary). Plot (b): Van-34. Plot (c): Ind-0 (with TS — the observed time series). Plot (d): Ind-2.

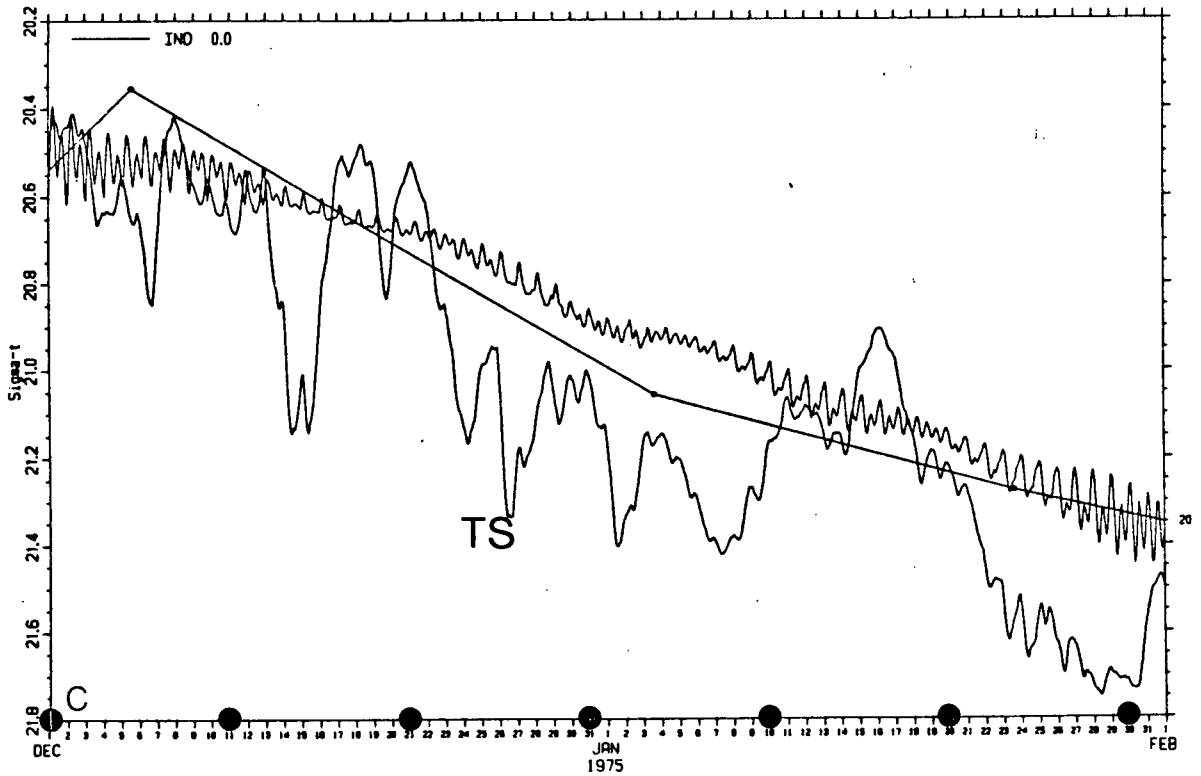

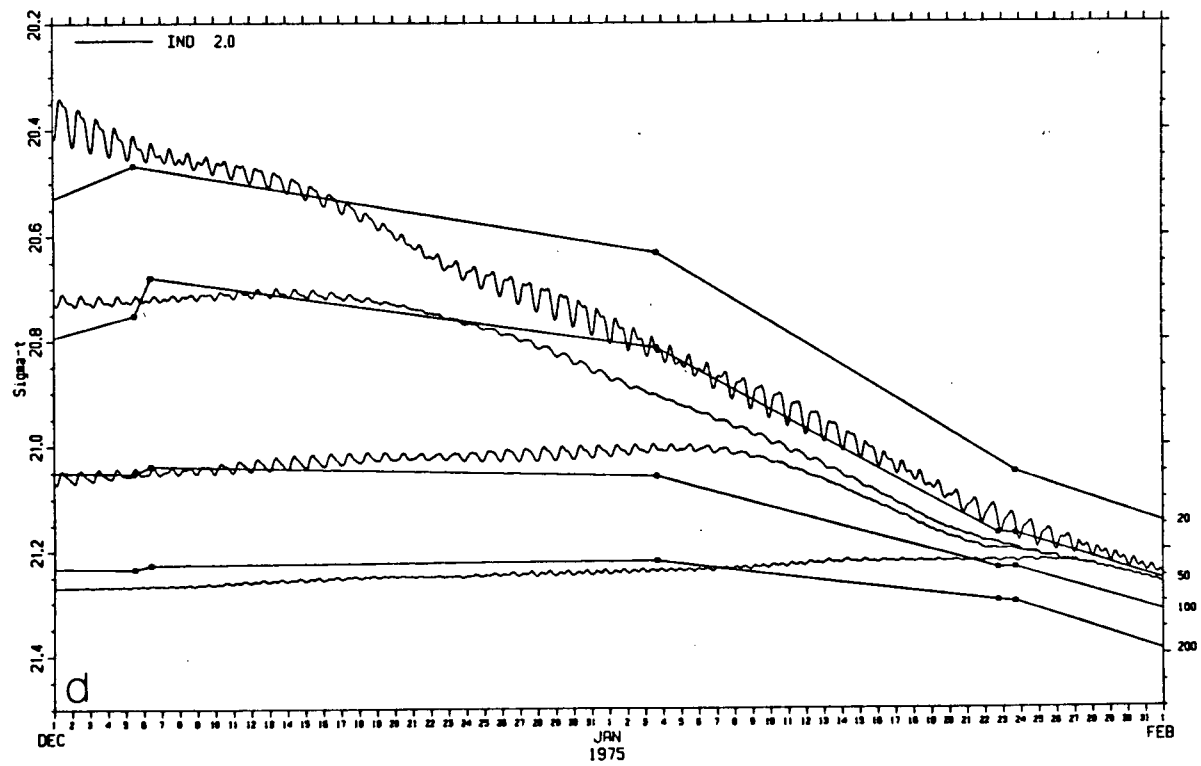

Figure 72(continued)

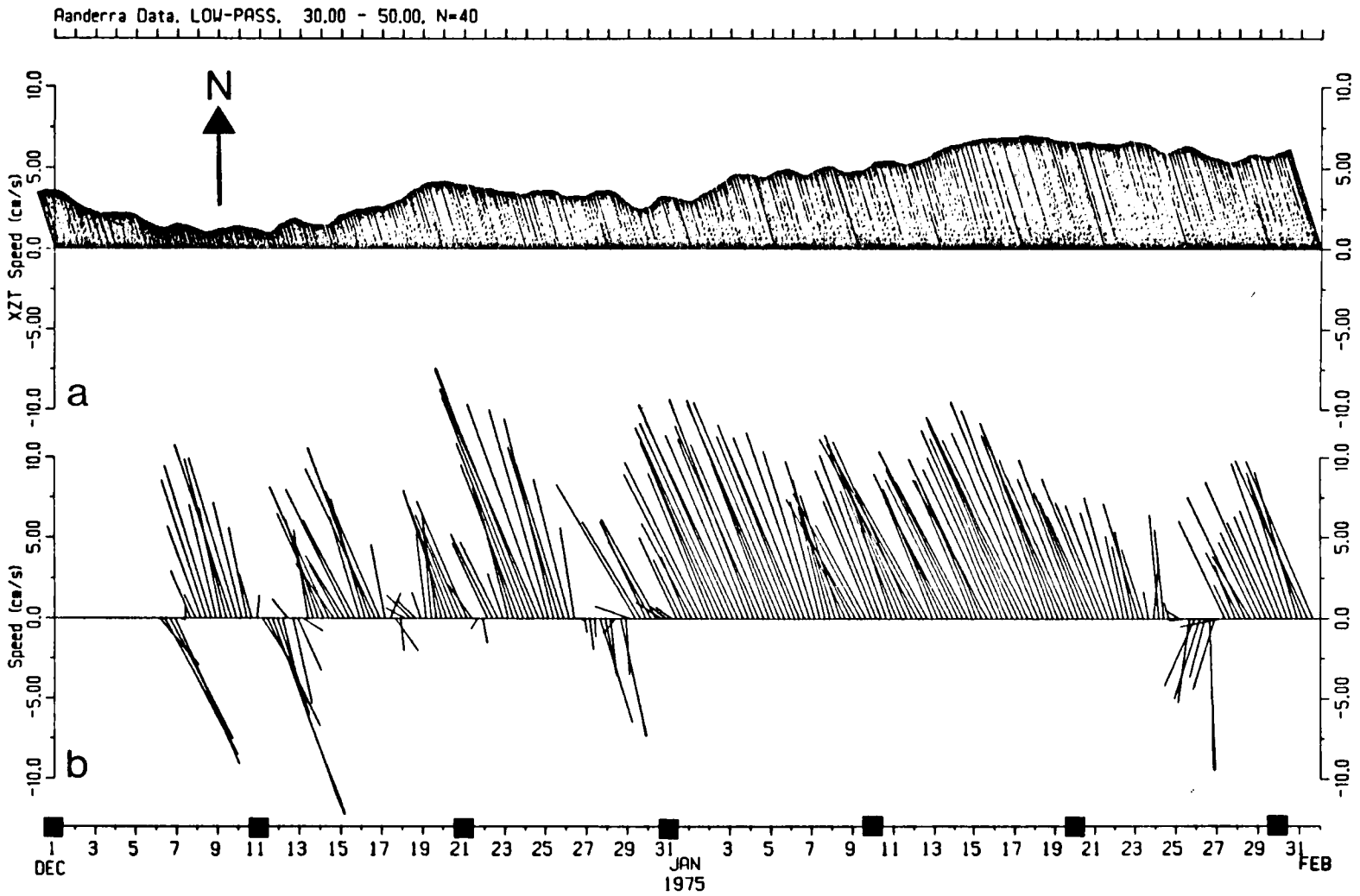

Figure 73. Current vectors from the model (a), and measured (b) near Ind-0. Positive values indicate flow into Indian Arm, and the velocity scale refers to the vector lengths. Squares along the bottom axis indicate times of plots for *figure* 74. A (30,50,40) digital filter was used to remove tidal oscillations from both series, and 6 hour vector means have been plotted in (b).

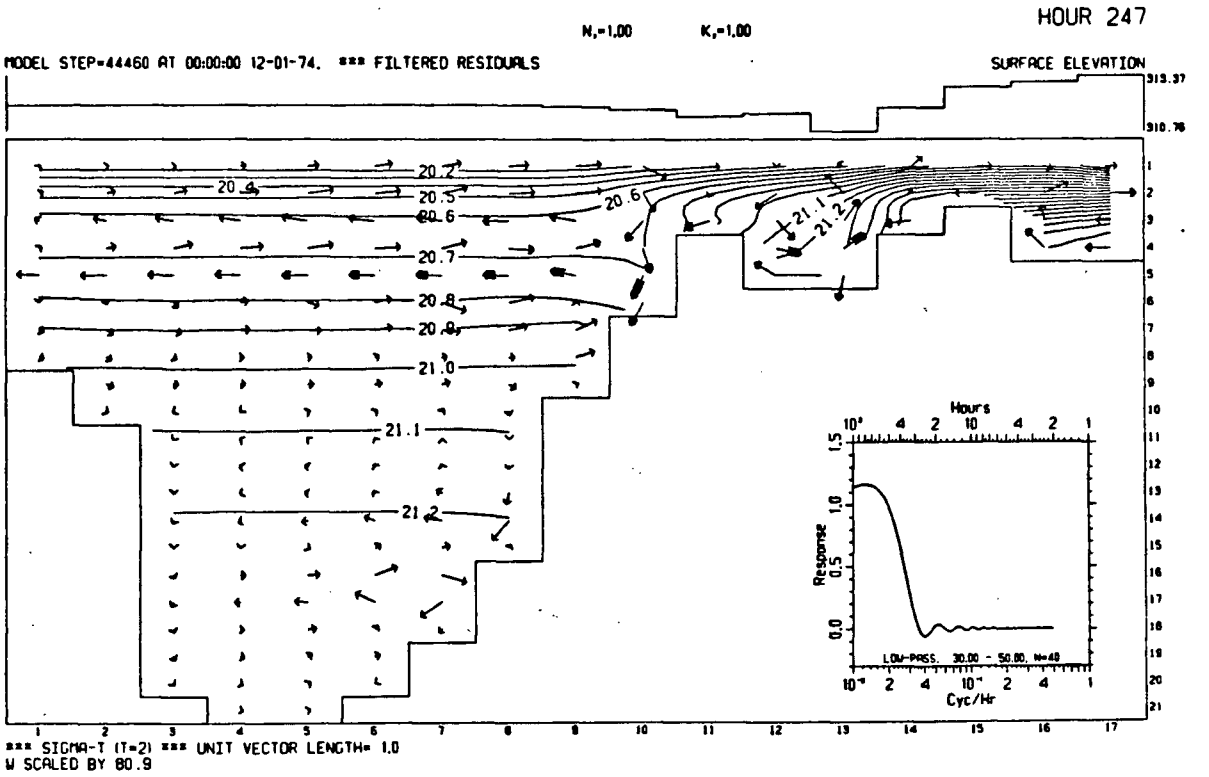

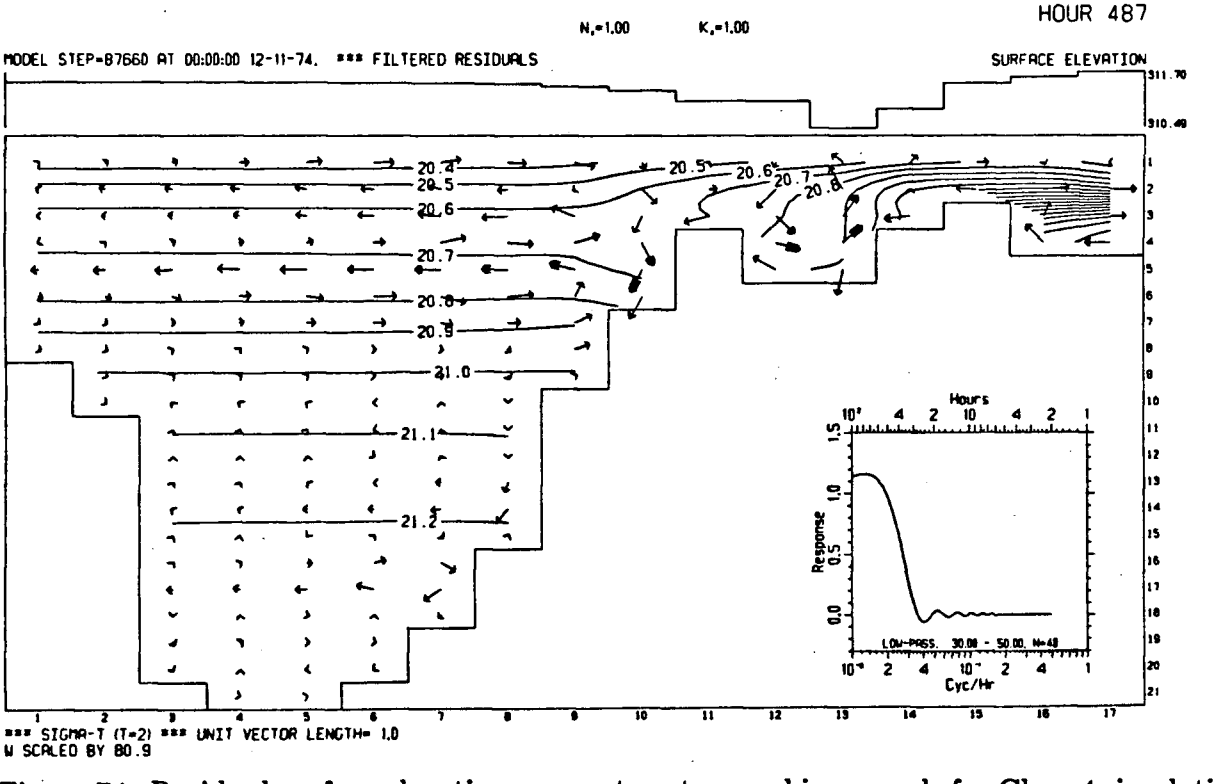

Figure 74. Residual surface elevation, current vectors and isopycnals for Class 4 simulation of tidal density flows into Indian Arm. Unit vector length is $1\,cm\,s^{-1}$ except at hour 1687 where it is $2\,cm\,s^{-1}$. Contours are in σ_t units (interval is 0.1). Inset shows response curve of digital filter used to calculate residuals.

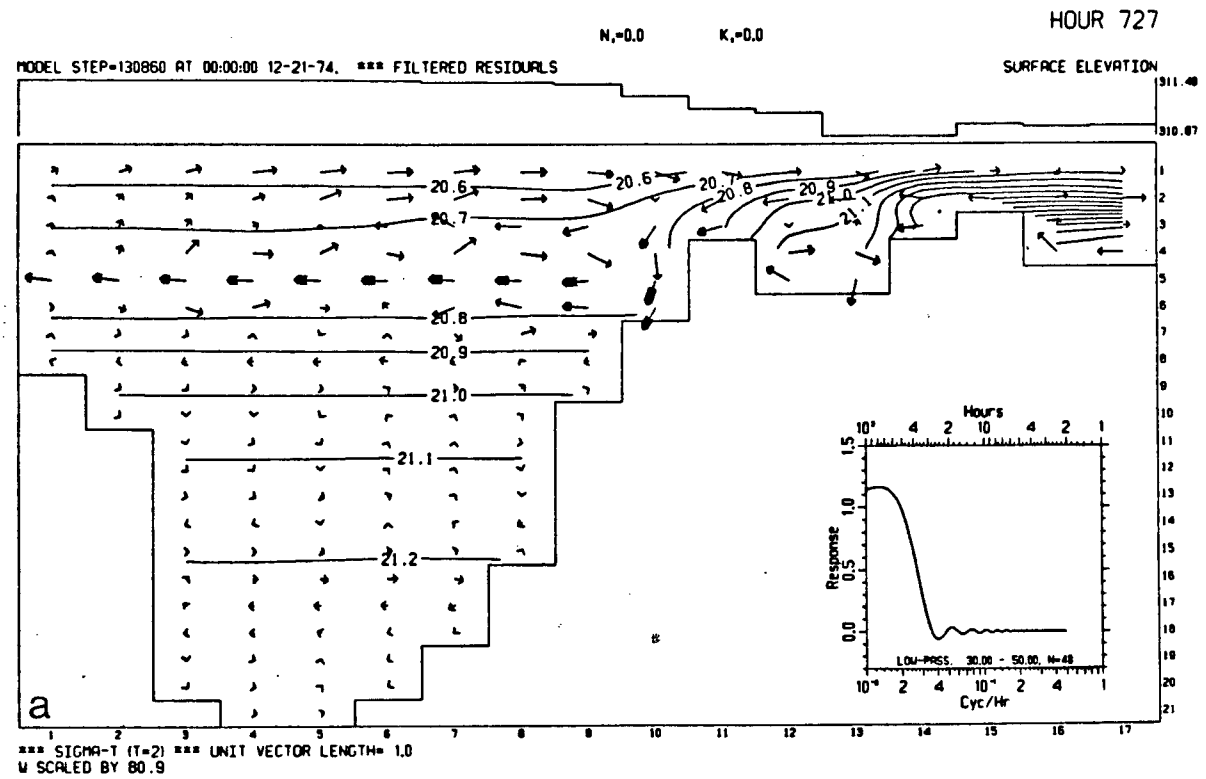

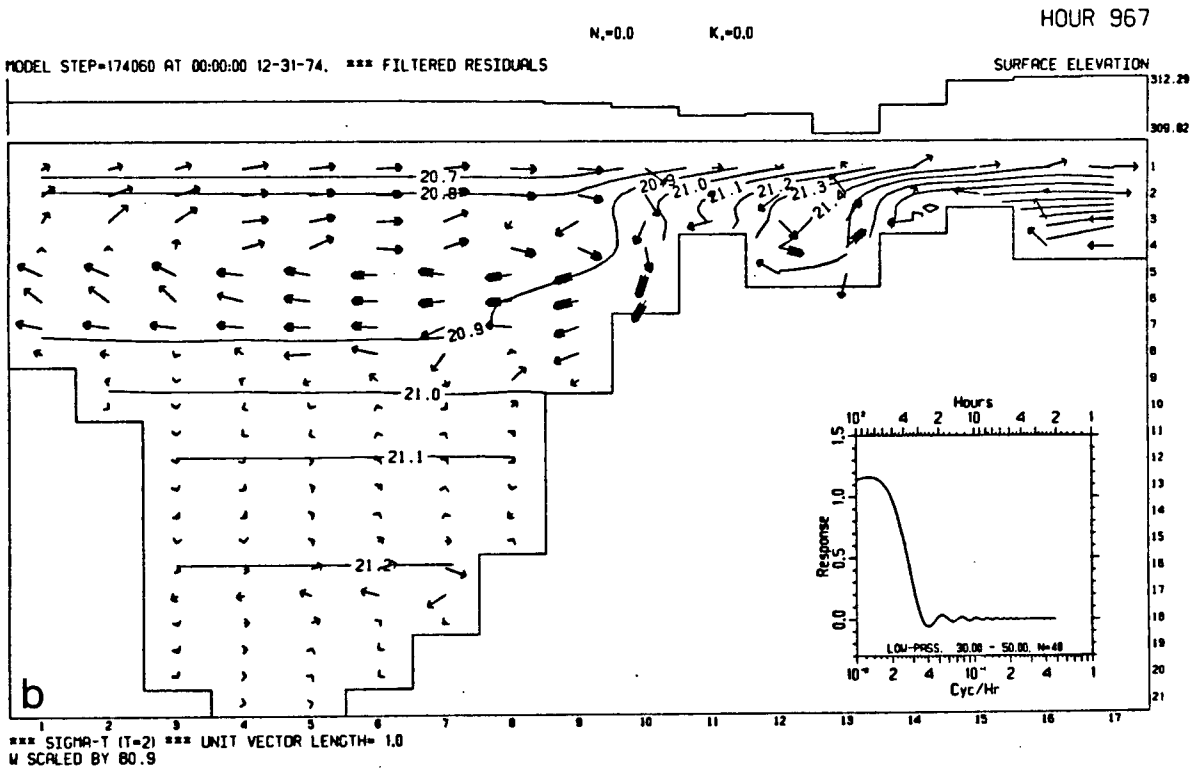

Figure 74(continued)

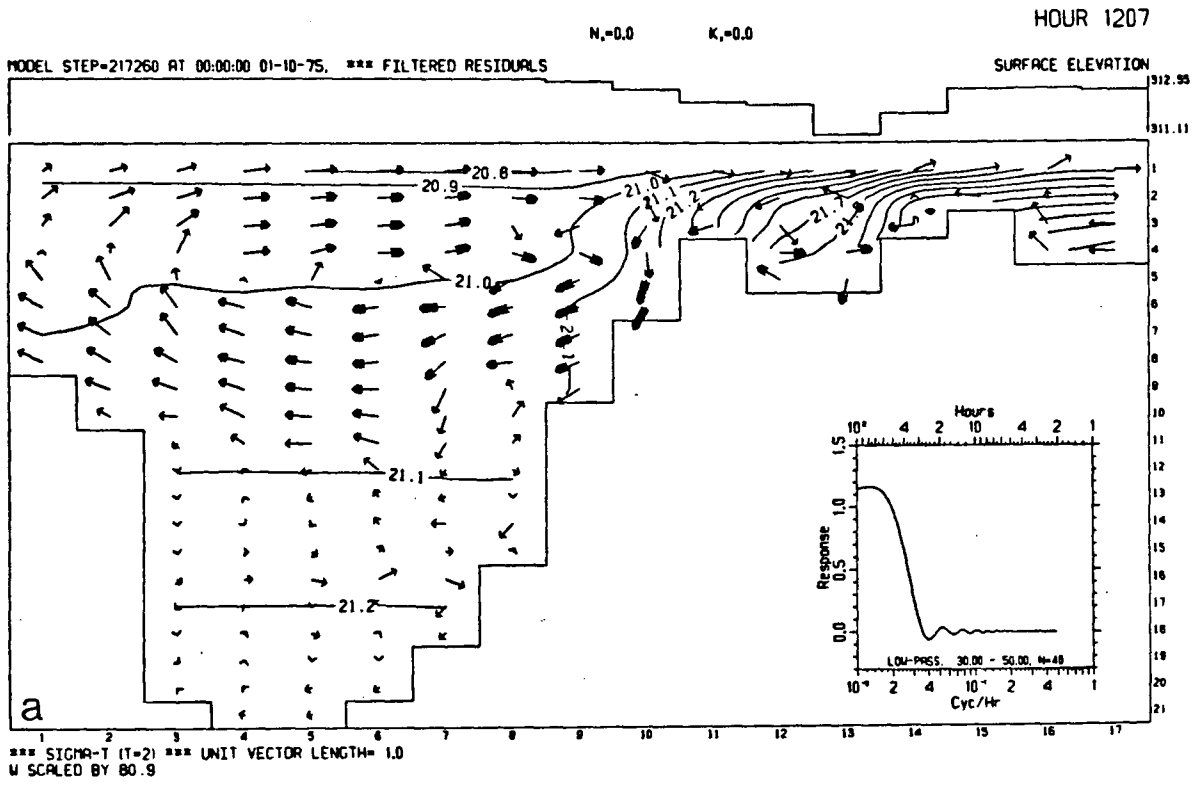

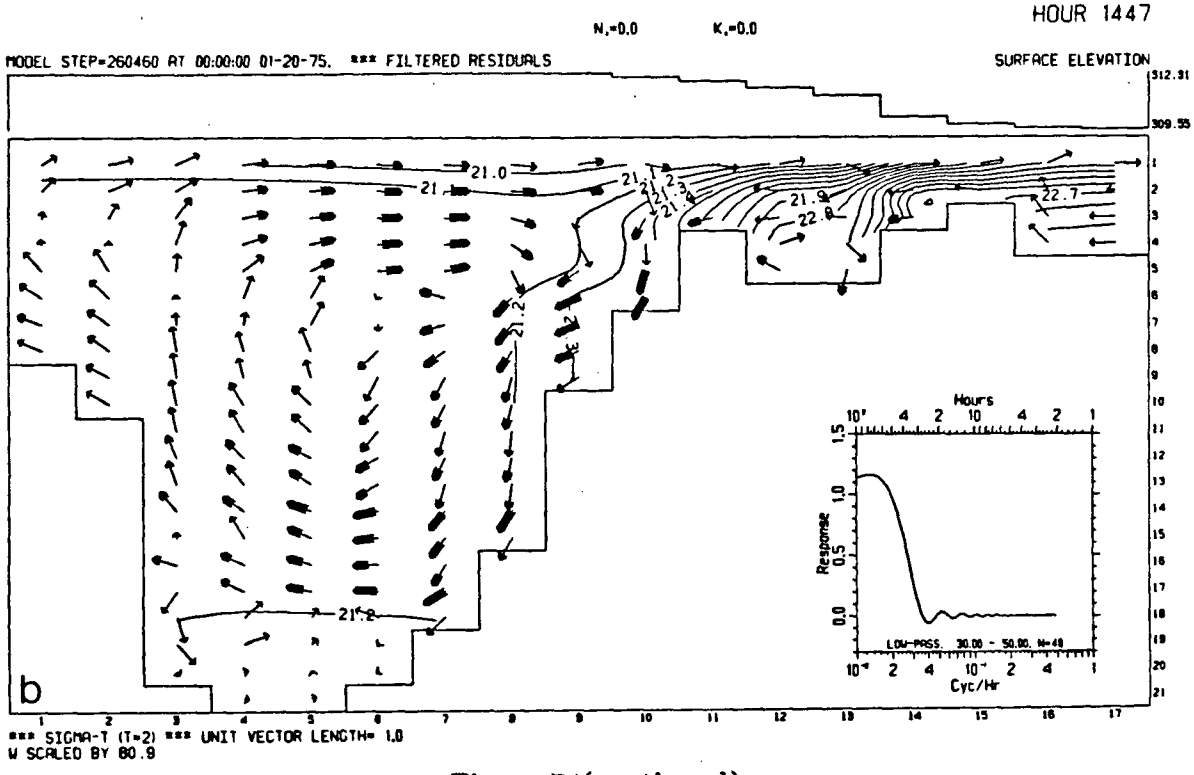

Figure 74(continued)

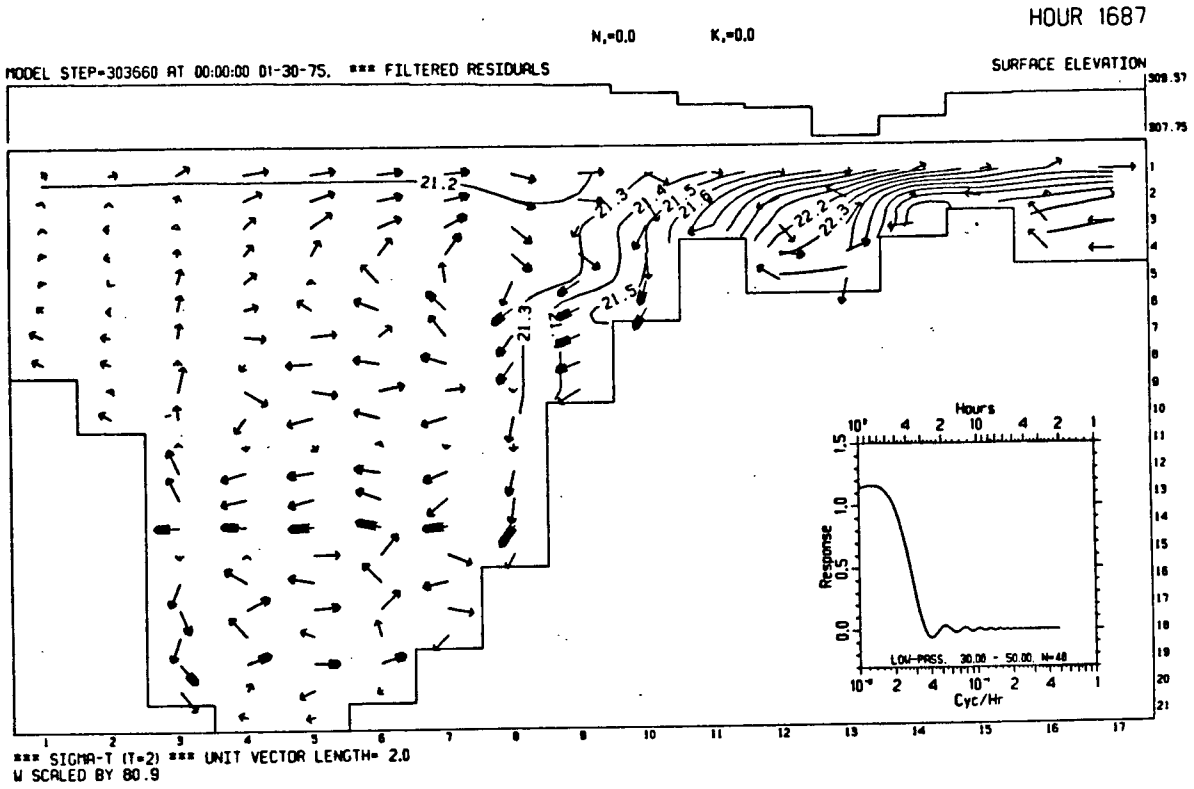

Figure 74(continued)

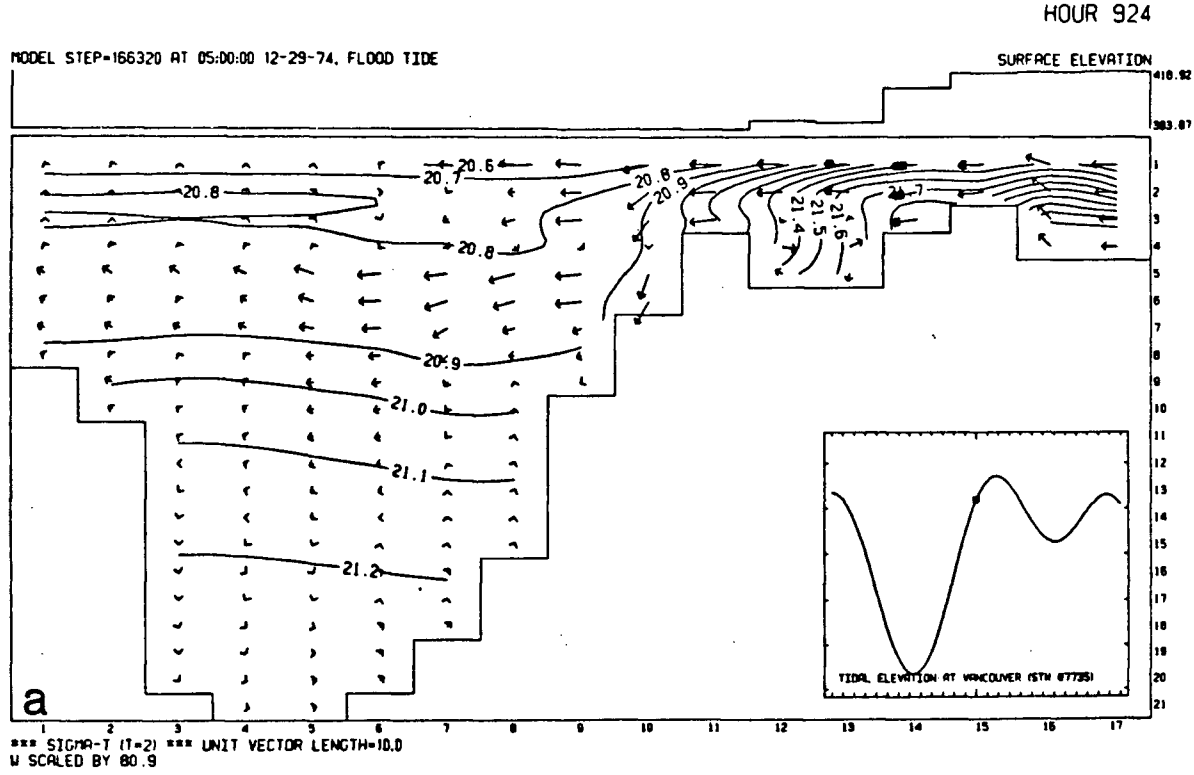

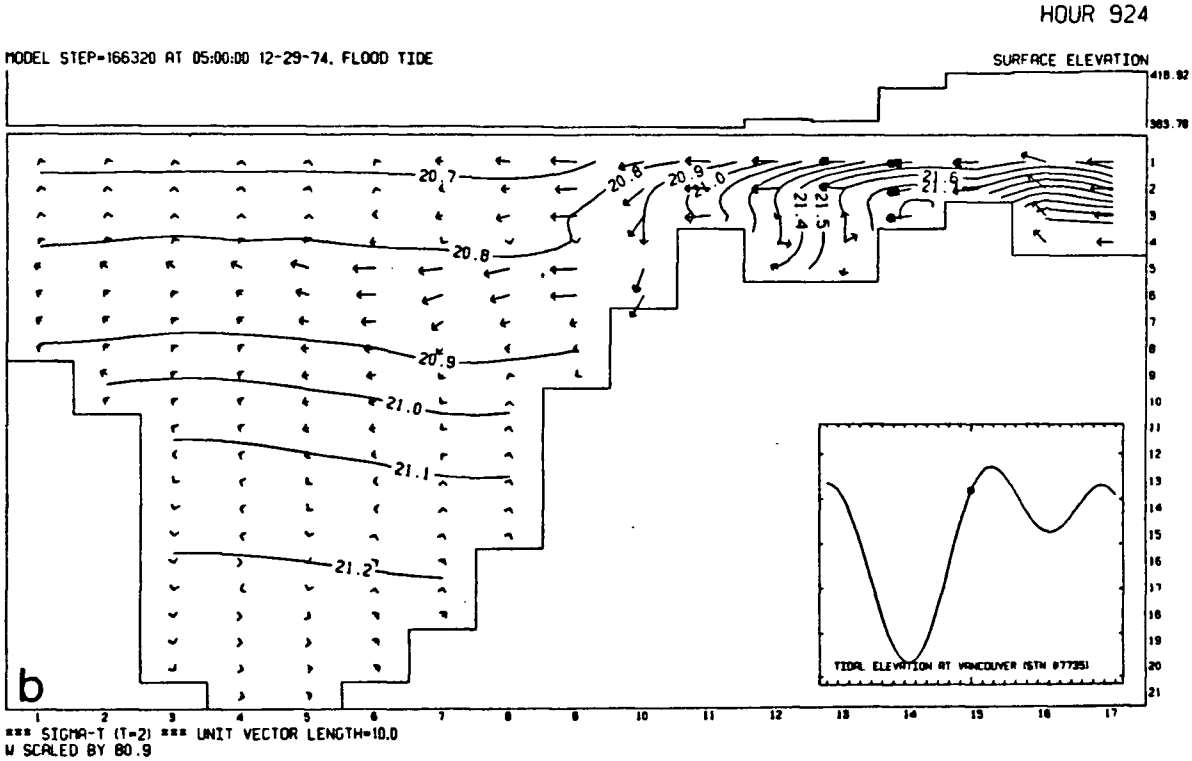

Figure 75. Fields of surface elevations, current vectors and isopycnals for two simulations using different values for $N^{(z)}$ and $K^{(z)}$, 250 hours after starting with the same initial conditions. Plot (a): $N^{(z)} = K^{(z)} = 0$. Plot (b): $N^{(z)} = K^{(z)} = 1\,cm^2\,s^{-1}$.

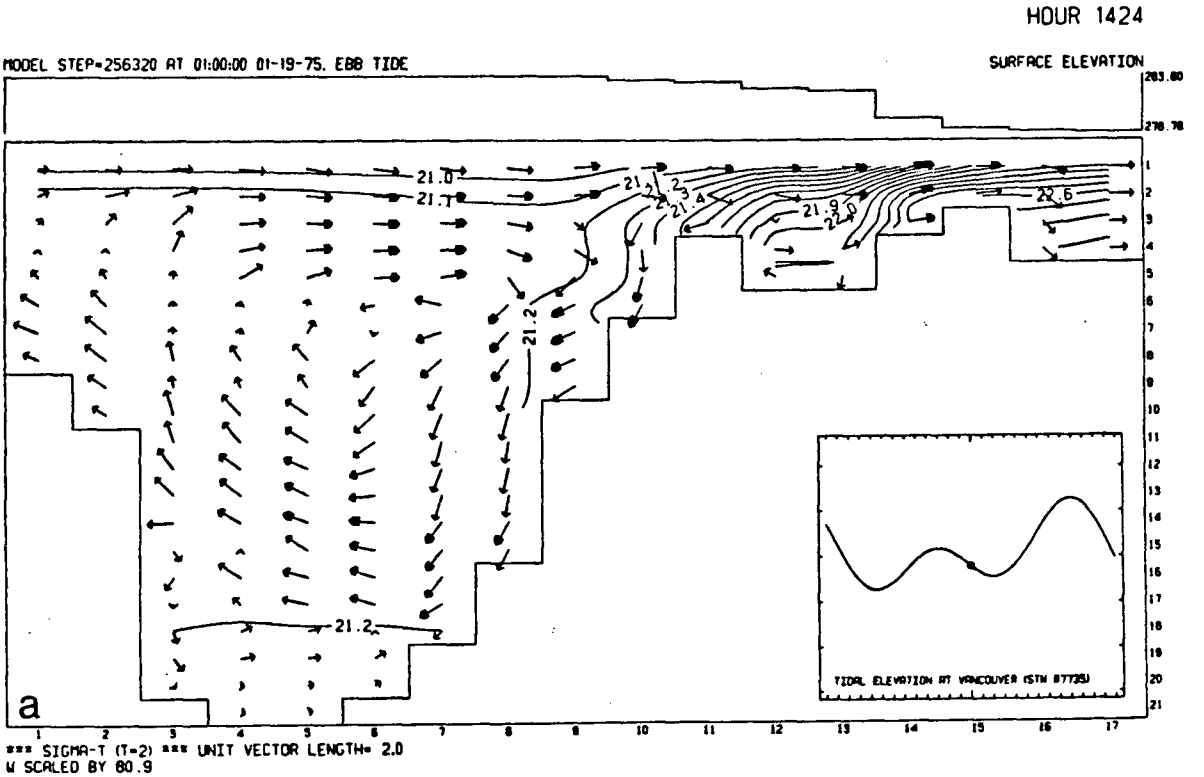

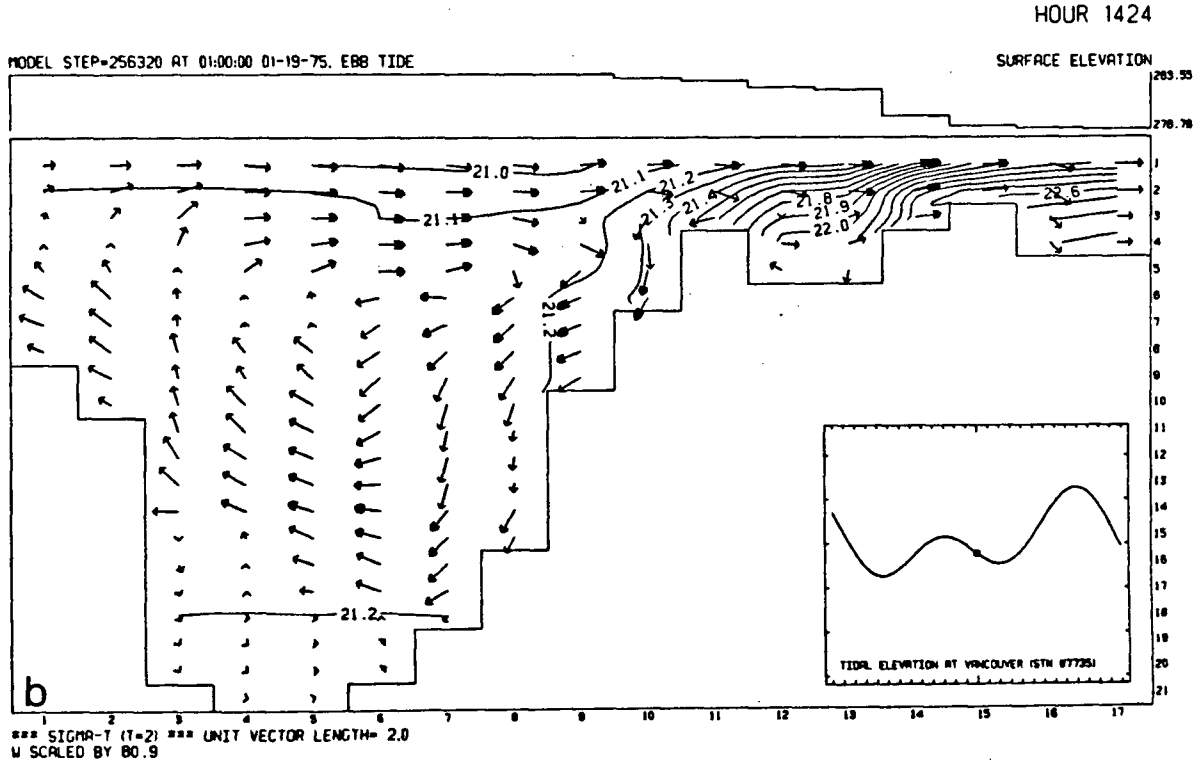

Figure 75(continued)

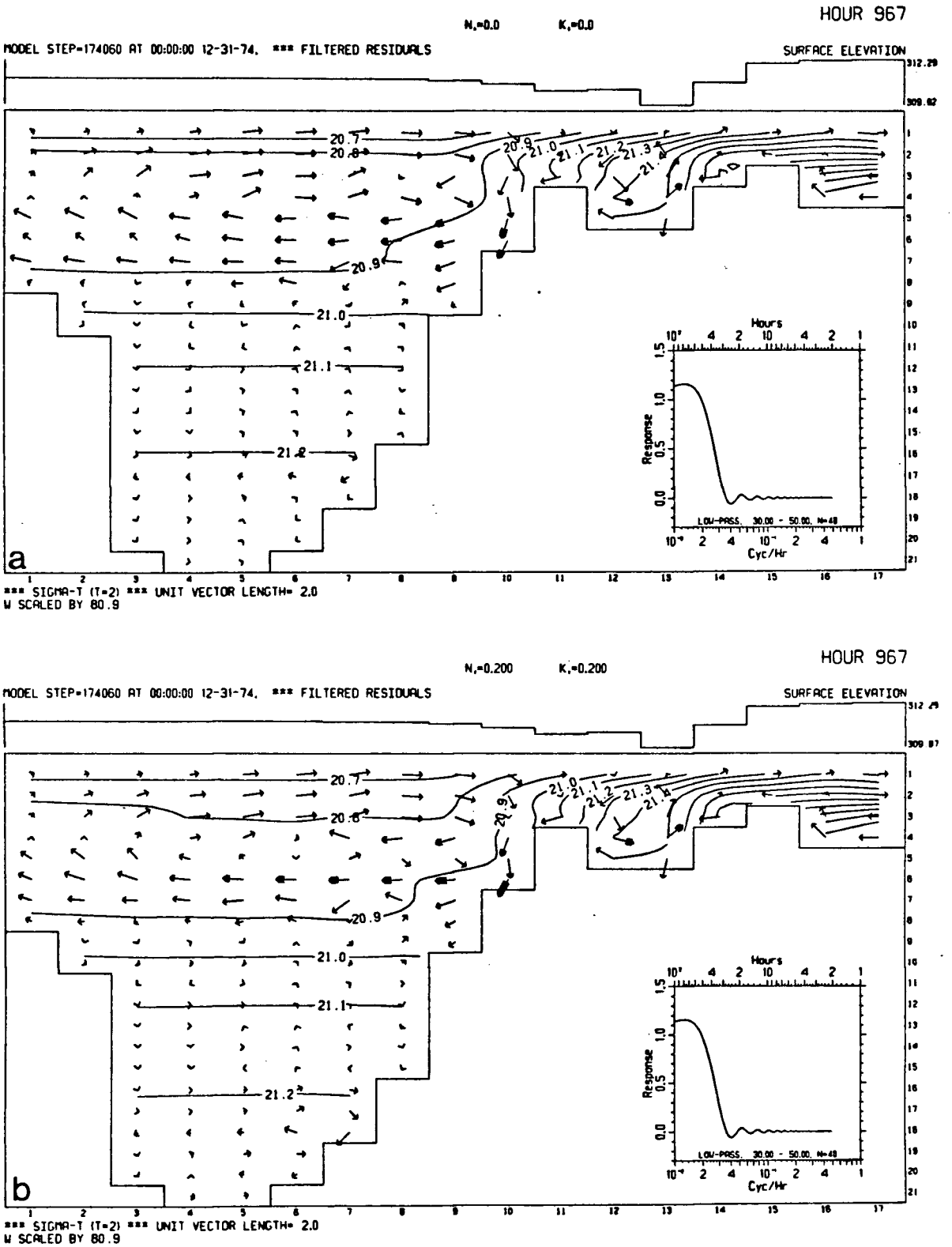

Figure 76. Residual surface elevations, current vectors and isopycnals for two simulations using different values for $N^{(z)}$ and $K^{(z)}$ after starting with the same initial conditions. Unit vector length is $2\,cm\,s^{-1}$. Contours are in σ_t units (interval is 0.1). Inset shows response curve of digital filter used to calculate residuals. Plot (a): $N^{(z)} = K^{(z)} = 0$. Plot (b): $N^{(z)} = K^{(z)} = 0.2\,cm^2\,s^{-1}$.

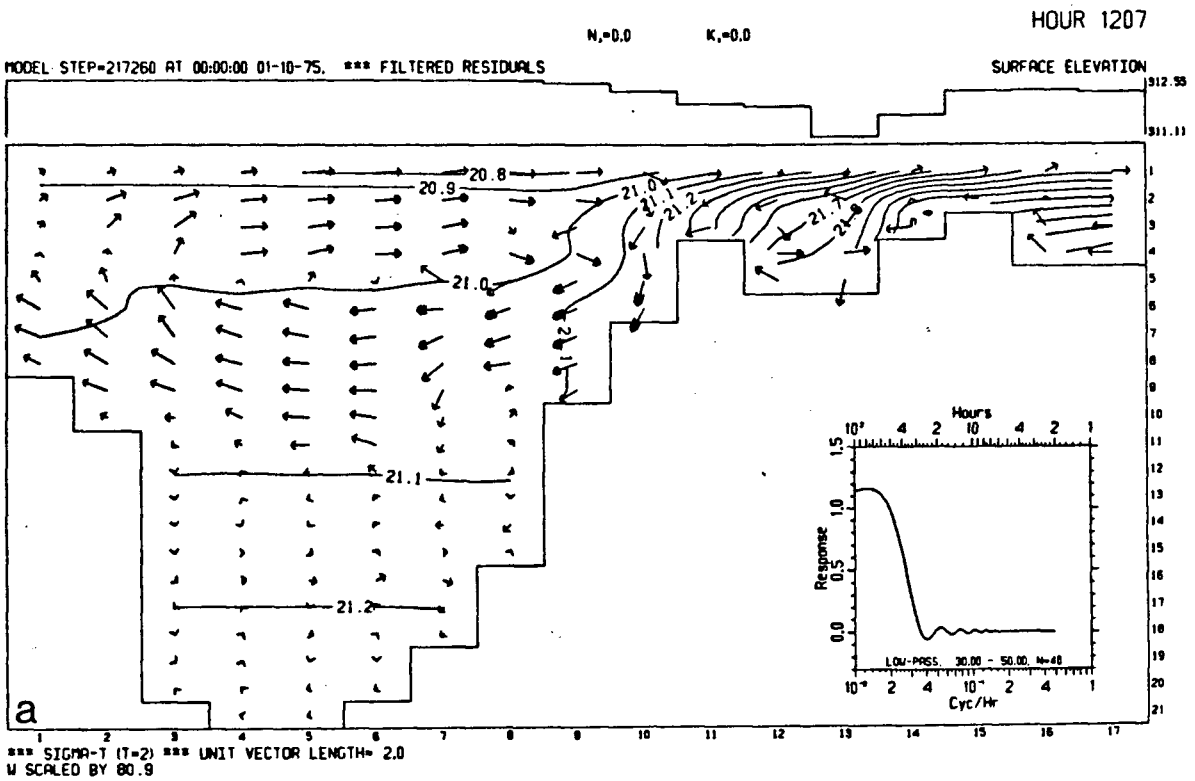

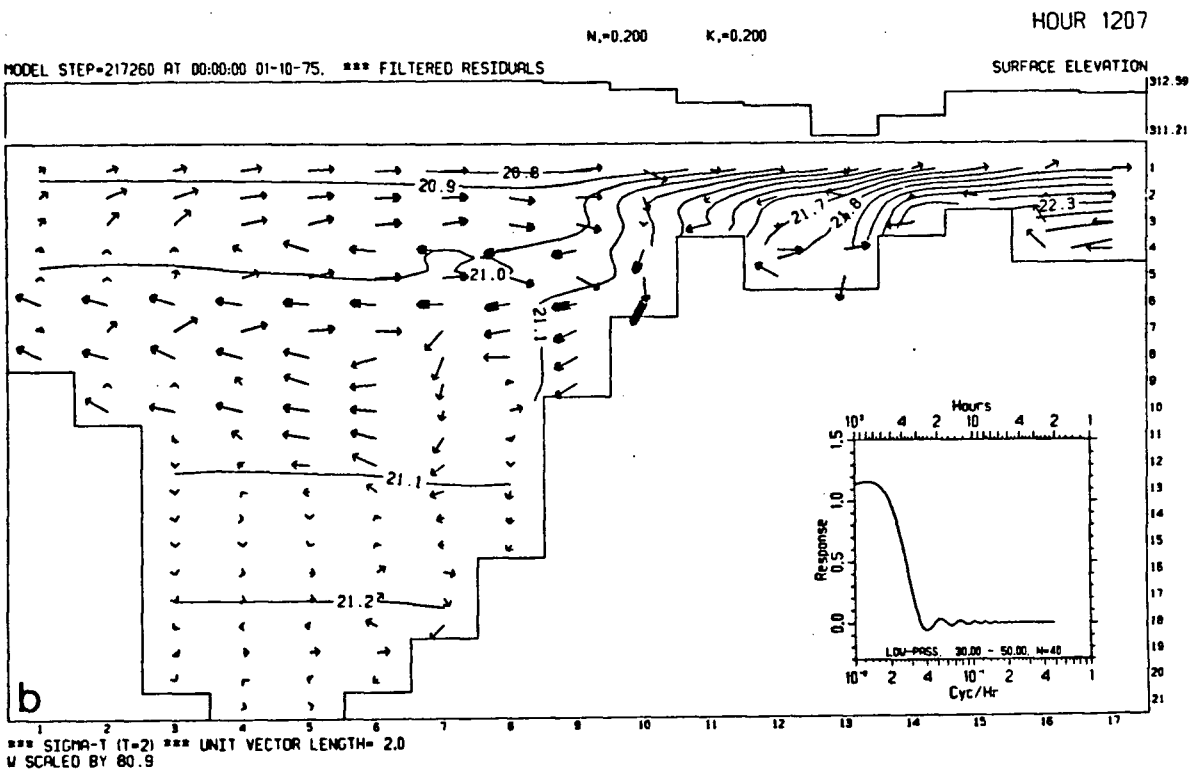

Figure 76(continued)

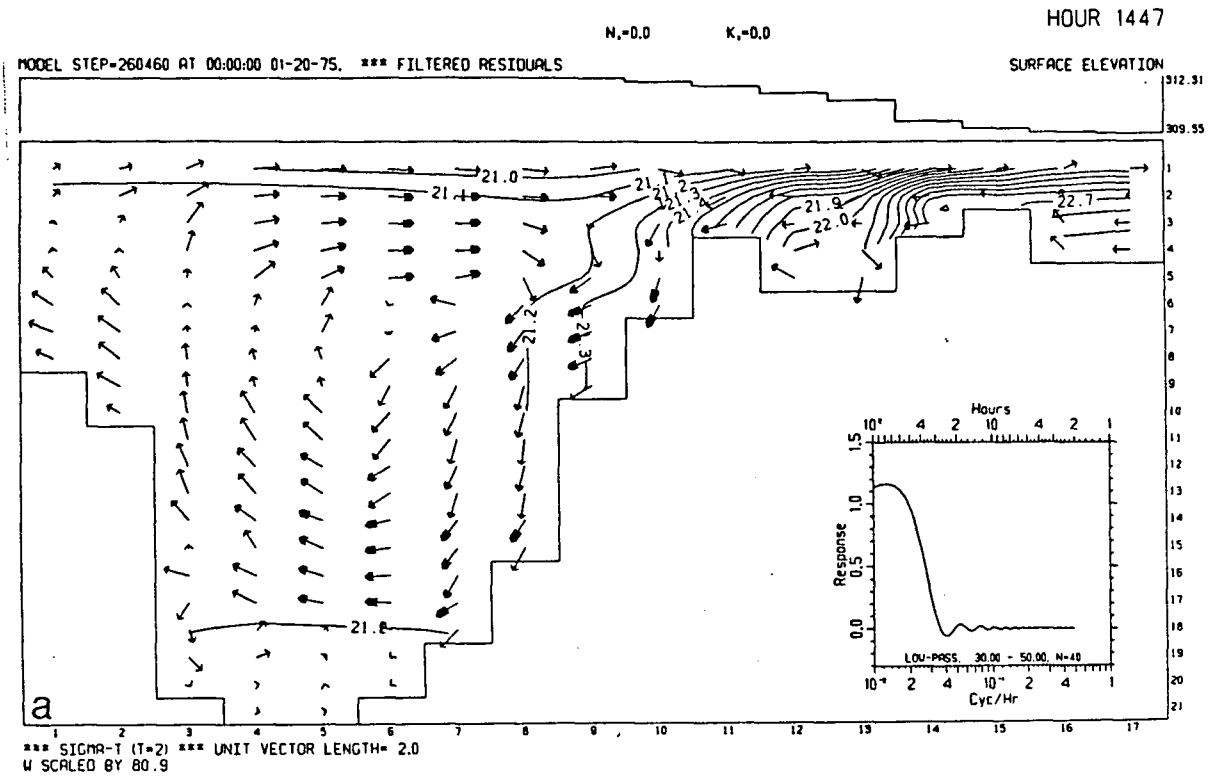

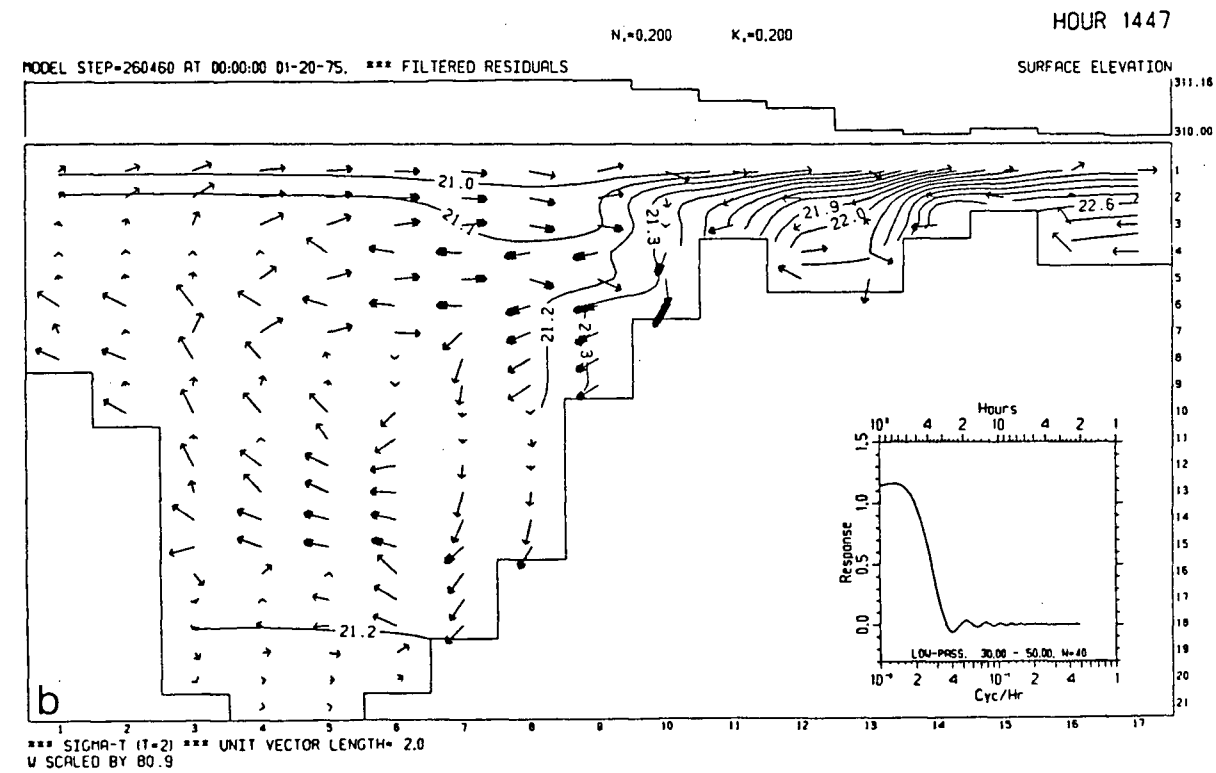

Figure 76(continued)